



UNIL | Université de Lausanne

Unicentre

CH-1015 Lausanne

<http://serval.unil.ch>

Year : 2017

Quantitative risk analysis for natural hazards at local and regional scales

Nicolet Pierrick

Nicolet Pierrick, 2017, Quantitative risk analysis for natural hazards at local and regional scales

Originally published at : Thesis, University of Lausanne

Posted at the University of Lausanne Open Archive <http://serval.unil.ch>

Document URN : urn:nbn:ch:serval-BIB_72FA1F0DF6660

Droits d'auteur

L'Université de Lausanne attire expressément l'attention des utilisateurs sur le fait que tous les documents publiés dans l'Archive SERVAL sont protégés par le droit d'auteur, conformément à la loi fédérale sur le droit d'auteur et les droits voisins (LDA). A ce titre, il est indispensable d'obtenir le consentement préalable de l'auteur et/ou de l'éditeur avant toute utilisation d'une oeuvre ou d'une partie d'une oeuvre ne relevant pas d'une utilisation à des fins personnelles au sens de la LDA (art. 19, al. 1 lettre a). A défaut, tout contrevenant s'expose aux sanctions prévues par cette loi. Nous déclinons toute responsabilité en la matière.

Copyright

The University of Lausanne expressly draws the attention of users to the fact that all documents published in the SERVAL Archive are protected by copyright in accordance with federal law on copyright and similar rights (LDA). Accordingly it is indispensable to obtain prior consent from the author and/or publisher before any use of a work or part of a work for purposes other than personal use within the meaning of LDA (art. 19, para. 1 letter a). Failure to do so will expose offenders to the sanctions laid down by this law. We accept no liability in this respect.



Faculté des Géosciences et de l'Environnement
Institut des Sciences de la Terre

Quantitative risk analysis for natural hazards at local and regional scales

Thèse de doctorat

présentée à la Faculté des Géosciences et de l'Environnement de l'Université de Lausanne par

Pierrick Nicolet

titulaire d'une Maîtrise universitaire ès Sciences d'ingénieur géologue délivrée par les Universités de Lausanne et de Genève

Devant le jury composé de :

Prof. Dr Michel Jaboyedoff, directeur

Prof. Dr Paolo Frattini, expert externe

Dr Alexander Garcia Aristizabal, expert externe

Dr Markus Imhof, expert externe

Dr Farrokh Nadim, expert externe

Sous la présidence de Prof. Dr Suren Erkman (colloque)

et de Prof. Dr Jean-Luc Epard (séance publique)

Lausanne, 2017

IMPRIMATUR

Vu le rapport présenté par le jury d'examen, composé de

Président de la séance publique :	M. le Professeur Jean-Luc Epard
Président du colloque :	M. le Professeur Suren Erkman
Directeur de thèse :	M. le Professeur Michel Jaboyedoff
Expert externe :	M. le Professeur Paolo Frattini
Expert externe :	M. le Docteur Alexander Garcia Aristizabal
Expert externe :	M. le Docteur Farrokh Nadim
Expert externe :	M. le Docteur Markus Imhof

Le Doyen de la Faculté des géosciences et de l'environnement autorise l'impression de la thèse de

Monsieur Pierrick NICOLET

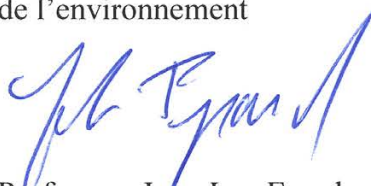
Titulaire d'une
*Maîtrise universitaire ès Sciences d'ingénieur géologue
des Universités de Lausanne et de Genève*

intitulée

**Quantitative risk analysis for natural hazards
at local and regional scales**

Lausanne, le 9 janvier 2017

Pour le Doyen de la Faculté des géosciences et
de l'environnement



Professeur Jean-Luc Epard

Abstract

Natural hazards can have damaging consequences for human activities, causing death or economic losses. This PhD thesis concentrates on the risk of natural hazard, where risk is defined as the combination of the likelihood of a damaging event and its negative consequences. The types of hazards considered in this work are mostly geological hazards such as landslides and sinkholes, but hail is also investigated.

The first part of this work focuses on the local scale, where local stands for a small group of objects, typically a few houses or a road. First, in order to improve the characterisation of the hazard, the potential of the photogrammetric method, which consists in retrieving the 3D position of objects from a set of 2D pictures, is tested. Together with this promising method, Unmanned Aerial System (UAS) are presented, since they permit to carry a camera and thus to take pictures for a photogrammetric analysis. Then, a tool to calculate the risk at local scale is presented. This tool is designed in Microsoft Excel and aims at calculating rapidly the risk using hazard maps produced according to the Swiss guidelines. A particular aspect of this model is presented in the next chapter ; it reviews the methods used to calculate the conditional probability for a falling object, such as a rock block, to impact a moving vehicle, taking into account the dimensions of the block and of the vehicles. Then, prospective aspects of such a risk model are presented and deal with the addition of multiple risk scenarios and the inclusion of uncertainty in the risk analysis using a Monte-Carlo approach. To conclude this part, a method which aims at taking the protection measures into account in the hazard maps without losing the initial hazard level is presented.

The second part of this work presents risk analyses at regional scale, where the region varies from the size of a canton to the size of a (small) country. The first study concerns the risk induced by evaporite sinkholes on a building portfolio. An inventory of damaged buildings is built from different sources and projections are made to estimate the losses that the public building insurance company could face if this type of hazard was insured. Then, a stochastic model which aims at modelling shallow landslides with regard to a precipitation event, and at calculating the probability of impact with buildings is presented. It shows that the location of the landslides

which occurred during the precipitation event considered in this study is positively correlated with the building location, suggesting a human influence in the landslides. To conclude this part, an analysis based on a hail event is presented and aims at relating the radar-derived maximum hailstone size reached during an event with the losses, at calculating the mean annual risk using this relation and at modelling random event to refine the risk analysis.

Although the basic principles of risk analysis are relatively simple, this work highlights the diversity of the risk analyses procedure and the need to adjust the procedure to the research question. In addition, it highlights the need for good inventories of events and consequences, since these inventories are crucial to perform a good risk analysis.

Résumé

Les dangers naturels peuvent avoir des conséquences dommageables pour les activités humaines en causant des pertes humaines ou financières. Cette thèse de doctorat se concentre sur le risque lié aux dangers naturels, le risque étant défini comme étant la combinaison entre la plausibilité d'un événement et ses conséquences négatives. Les types de dangers considérés dans ce travail sont principalement géologiques (glissements de terrain et effondrement de dolines, par exemple), même s'il est question de grêle dans un des chapitres.

La première partie de ce travail se concentre sur les analyses de risques à l'échelle locale. On considère par échelle locale un petit groupe d'objets tels que des maisons où une route. Premièrement, dans l'idée d'améliorer l'analyse des phénomènes dangereux, le potentiel de la méthode photogrammétrique, qui consiste à extraire la position d'un objet dans l'espace à partir d'un jeu de photos, est estimée. Conjointement à cette méthode prometteuse, une discussion sur les drones, qui permettent de transporter un appareil photo et de prendre des photos utilisables pour la photogrammétrie, est présentée. Ensuite, un outil permettant de calculer le risque à l'échelle locale est présenté. Cet outil, développé dans Microsoft Excel, vise à calculer rapidement le risque en utilisant des cartes de danger établies selon les standards suisses comme donnée de base. Un aspect particulier de ce modèle est présenté dans le chapitre suivant, qui passe en revue les méthodes utilisées pour calculer la probabilité conditionnelle qu'un projectile atteigne un véhicule, et propose une méthode tenant compte des dimensions des deux objets. Ensuite, des pistes de développement du modèle de risque sont présentées et concernent l'addition de multiples scénarios de risque et la prise en compte de l'incertitude dans l'analyse de risque en utilisant une simulation de Monte-Carlo. Pour conclure cette partie, une méthode visant à prendre en compte les mesures de protection dans les cartes de danger sans perdre le degré de danger initial est présentée.

La seconde partie de ce travail présente des analyses de risque à l'échelle régionale, avec une région variant de l'échelle du canton à celle d'un (petit) pays. La première étude se concentre sur le risque induit par la dissolution du gypse sur un portefeuille de bâtiments. Un inventaire de bâtiments endommagés est établi à partir de différentes sources et des projections sont

faites pour estimer le risque que prendrait l'assurance des bâtiments en assurant ce type de dommages. Ensuite, un modèle stochastique visant à modéliser des glissements superficiels liés à un événement de pluie intense ainsi que leur probabilité d'impact sur des bâtiments est exposé. Cette étude montre que la position des glissements est positivement corrélée avec la position des bâtiments, ce qui suggère une influence du bâti sur les glissements de terrain. Cette partie se conclut sur une analyse basée sur un événement de grêle, ou une relation entre la taille maximum des grêlons observée à l'aide d'un radar pendant un événement est corrélée à la proportion de bâtiments endommagés ainsi qu'à leur taux de dommage. Le risque annuel moyen est calculé sur la base de cette relation et de données extraites d'une carte de danger existante. Des événements aléatoires sont également créés sur la base de ces données, dans le but de voir comment les coûts se répartissent dans le temps.

Malgré que les principes du calcul de risque soient relativement simples et bien établis, ce travail met en évidence la diversité des procédures et le besoin de les ajuster aux questions de recherche. De plus, ce travail montre l'importance de bons inventaires des événements et de leur conséquences, puisque ces inventaires sont cruciaux pour effectuer une bonne analyse de risque.

Acknowledgements

Spending more than six years on a PhD with the opportunity to work on many projects and to meet many different persons is certainly tremendous, but it makes things difficult when the time of acknowledgements has come. Therefore, I am afraid that this short section does not enough reflect how much grateful I am to the people who helped me during that time and I hope not to forget too many!

I would like to mention first my supervisor, **Michel Jaboyedoff**, who accepted me as a PhD student without knowing me that much, but who trusted me from the beginning. Working with Michel is very interesting and challenging, since he comes with a lot of ideas and likes to debate them. He also created a very nice and motivating working environment and collaborating with him will always be a pleasure. It is hard to summarize all of Michel's input here, but I'm glad to be part of the IGAR family!

I would like to thank next the members of my jury, **Paolo Frattini**, **Alex Garcia**, **Markus Imhof** and **Farrokh Nadim**, who spent a lot of time reading and commenting the manuscript, and who provided very useful comments and discussion. The contributions of **Suren Erkman** as president of the private defence and **Jean-Luc Epard** as president of the public defence were also much appreciated.

The existence of this manuscript owes a lot to **Christian Gerber**, from the natural hazard unit (UDN) of the state of Vaud, who, having the project of sponsoring a PhD, convinced me to go back to the university to do it, and who gave me the opportunity to get familiarised with the work done by the administration and the private companies. I certainly owe you more than a Gløgg! I should not forget to mention **Nadia Christinet** and **David Giorgis** as well, who were also at the origin of this project and with whom I really appreciated working. I also had a lot of pleasure being integrated in the work and in the social life of the UDN. Thank you **Eric**, **Claire-Anne**, **Vincent**, **Guy**, **Mélanie** and **Dominique**, who were there for most of the duration of this work, but also to the others with whom I had been in contact through the UDN. In addition several discussions with private companies gave useful insights for this work.

Going more into the details of this work, I must thank **Sébastien Lévy** (DGE-Forêts, Etat de

Vaud), who came with the project that led to Chapt. 3–5, and **Catherine Cloutier** and **Giovanni Crosta**, who gave useful contributions for Chapt. 4. Chapt. 7 and 9 have benefited from the trust of public insurance companies, who provided data and inputs and authorised the publication of the results. Thanks to **Jean-Marc Lance** and **Marc Choffet**, from the "Etablissement d'assurance contre l'incendie et les éléments naturels du canton de Vaud", **Markus Imhof**, from the Inter-cantonal insurance union, and to the Aargauische Gebäudeversicherung. I am also grateful to **Bertrand Lauraux** who provided data for Chapt. 7. **Jonathan Demierre** developed the first hail event model (Chapt. 9), for which I was later given access to the cluster Argos, maintained by the university's IT service. When it comes to Chapt. 8, **Olivier Caspar** started the analysis, whereas **Stéphane Losey** and **Bernard Loup** (Federal Office of the Environment) provided data and comments and **Loris Foresti**, in addition to handling the precipitation part, provided guidance for the writing process.

Also, I couldn't have kept my motivation without my great office mates: **Clément**, who has been my mentor when I started, **Dario** and **Antonio**, and without great colleagues such as **Zar Chi**, **Meriam**, **Marie**, **Marc**, **Loris**, **Lucie**, **Martin**, **Antoine**, **Simon**, **Pascal**, **Florian**, **Agnès**, **Ryan**, **Céline**, **Papi**, **Raja**, **Battista**, **Giona**, **Richard**, **Emmanuel**, **Liliane**, **Roya**, **Andrea**, **Line**, **Benjamin**, **Karen**, **Mitch**, **Jérémie**, **Emmanuel**, and all the others who spent some time in the group or with whom I shared nice time at the university. I am also grateful to **Marc-Henri Derron**, who provided support all along this work.

Finally, I am very grateful to my parents, family and friends for their support and I would like to address a special thank **Ivanna** for her patience and support during the finalisation of this work.

Contents

Abstract	5
Résumé	7
Acknowledgements	9
Introduction	17
1 Introduction	19
1.1 Context of this PhD study	19
1.2 Natural hazards and risk	19
1.2.1 Section outline	19
1.2.2 Geological hazards	21
1.2.3 Hydro-meteorological hazards	24
1.2.4 Risk	26
1.2.5 Hazard mapping and risk management in Switzerland	40
1.3 Content of this manuscript	42
1.3.1 Outline	42
1.3.2 Contribution of the candidate	43
I Risk analysis and management at local scale	45
2 Landslide surveying with photogrammetry and UAS	47
2.1 Introduction	47
2.1.1 Chapter outline	48
2.2 State of the art	49
2.2.1 Photogrammetry	49

2.2.2	UAS	56
2.3	Photogrammetry versus LiDAR	59
2.3.1	Transportability	59
2.3.2	Errors	62
2.3.3	Sensitivity to the vegetation	62
2.3.4	Scaling and georeferencing	63
2.3.5	Simple georeferencing	66
2.3.6	Sensitivity to the reflector	69
2.3.7	Colour-based segmentation	69
2.4	Perspectives and conclusion	71
3	Cost-benefit analysis	77
3.1	Introduction	77
3.2	Formulas	78
3.2.1	Risk analysis	78
3.2.2	Cost of the measures	82
3.3	Architecture	83
3.4	Example	87
3.5	Conclusions	94
4	Direct impact of hazard on moving vehicles	97
	Foreword	97
	Abstract	97
4.1	Introduction	97
4.2	Temporal spatial probability of moving vehicles	98
4.2.1	Approaches neglecting the events dimension	98
4.2.2	Approaches neglecting the vehicle dimension	99
4.2.3	Approaches using both dimensions	102
4.3	Synthetic examples	104
4.4	Discussion and conclusions	105
	Appendices	107
	Demonstration of Roberds' (2005) approach	107
	Variable names	108
5	Addition of multiple risk scenarios accounting for the uncertainty	111
5.1	Introduction	111
5.2	Scenarios addition	112

<i>CONTENTS</i>	13
5.2.1 Introduction	112
5.2.2 Method	112
5.2.3 Results	115
5.2.4 Discussion	116
5.3 Accounting for the uncertainty	120
5.3.1 Introduction	120
5.3.2 Sampling from the triangular distribution	120
5.3.3 Correlation of random variables	120
5.3.4 Input parameters	124
5.4 Example	124
5.5 Discussion and conclusion	130
6 Accounting for protective measures in hazard mapping	131
6.1 Introduction	131
6.2 Forgetting the hazard, example of La Faute-sur-Mer	132
6.3 Proposed symbology	134
6.4 Examples	135
6.4.1 Rockfalls in Chardonne	135
6.4.2 Rockfalls in Veyrier-du-Lac	138
6.5 Conclusion	139
II Stochastic risk modelling at regional scale	141
Introduction to Part II	143
7 Evaporite sinkhole risk for a building portfolio	145
Foreword	145
Abstract	145
7.1 Introduction	146
7.2 Study area	147
7.2.1 Geology	147
7.2.2 Karst features	148
7.2.3 Insurance context	150
7.3 Method	151
7.3.1 Susceptibility map	151
7.3.2 Event inventory	152

7.3.3	Risk analysis	154
7.4	Results	156
7.4.1	Susceptibility map	156
7.4.2	Event inventory	158
7.4.3	Risk analysis	159
7.5	Discussion	162
7.6	Conclusion	165
Appendix	165
	List of variables	165
8	Shallow landslide's risk modelling	169
	Foreword	169
	Abstract	169
8.1	Introduction	170
8.2	The rainfall event of August 2005 in Switzerland	171
8.2.1	Study area	171
8.2.2	Description of the precipitation event	172
8.2.3	Landslide inventory	173
8.2.4	Damage	174
8.3	Risk modelling methodology	175
8.3.1	Introduction	175
8.3.2	Spatial analysis of rainfall	175
8.3.3	Landslide distribution	177
8.3.4	Impact assessment	181
8.4	Results	186
8.4.1	Impact assessment	187
8.5	Discussion	188
8.6	Conclusions	193
9	Hail risk modelling in the context of building insurance	195
9.1	Introduction	196
9.2	Data	197
9.2.1	Intensity maps	197
9.2.2	Hazard maps	197
9.2.3	Elements-at-risk and past losses	200
9.3	Methods	202

<i>CONTENTS</i>	15
9.3.1 Loss assessment	202
9.3.2 Average annual hail risk	204
9.3.3 Hail event modelling	208
9.4 Results	212
9.4.1 Loss assessment	212
9.4.2 Average annual hail risk	222
9.4.3 Hail events modelling	225
9.5 Discussion	249
9.6 Conclusions	250
General conclusions	253
10 Concluding remarks	255
10.1 Discussion and synthesis	255
10.1.1 Local risk analyses	255
10.1.2 Regional risk analyses	256
10.2 Research perspectives	258
10.3 Conclusion	259
Bibliography	261
Appendices	281
A Rockfall hazard and risk assessments along roads	283
B Multi-scale debris flow vulnerability assessment	301
C La gestion des risques naturels est une dynamique	333
D Using the consequence - frequency matrix to reduce the risk	371
E Analysis of the 12–13 July 2011 hail event in the Canton of Aargau	383

Introduction

Chapter 1

Introduction

1.1 Context of this PhD study

The first four years of this PhD work were the result of a collaboration between the University of Lausanne and the team in charge of coordinating the establishment of hazard maps at the State of Vaud. The idea was to strengthen the relation between these two entities and to provide a scientific support for the hazard maps dealing with geology. My role was then to assist the hazard mapping team, bringing in the competences of the University. As a result, part of the work of this PhD originated from the various problems encountered in the process of hazard mapping. In addition, the State of Vaud was interested in going further in the risk analysis and management, which was then chosen as a general topic for this PhD thesis.

In the meantime, natural hazard being more and more expensive for the building insurance companies, several mandates were granted to the University to try to assess the cost of natural phenomenon for their building portfolio. That gave the opportunity to access to sensitive data that are not often provided for purely academic work, and to go further in the risk analysis, as wished by the State of Vaud. This is the starting point of the chapters on sinkhole risk (Chapt. 7) and on hail risk (Chapt. 9).

1.2 Natural hazards and risk

1.2.1 Section outline

This thesis refers to the term "natural hazards". By natural, it is implied that there is no human action of any kind on the process. This is not always the case of the hazards presented in this thesis. As a matter of fact, as presented in Fig. 1.1, hazards are most of the time not completely

natural since almost every phenomena can be influenced by humans to some extent. The current work deals mostly with hazards belonging to the landslide group, but Chapt. 9 treats of hail, which could be placed together with tornado on Fig. 1.1. Both categories have then a large natural component, but can have a significant human influence as well. For hail, the human influence is for example the changes in the atmospheric system induced by the current climate change. When it comes to landslides, the human influence can be much more direct, for example by changing locally the stability conditions, especially the water intake and the slope profile (e.g. [Jaboyedoff et al., 2016](#); [Michoud et al., 2011](#)).

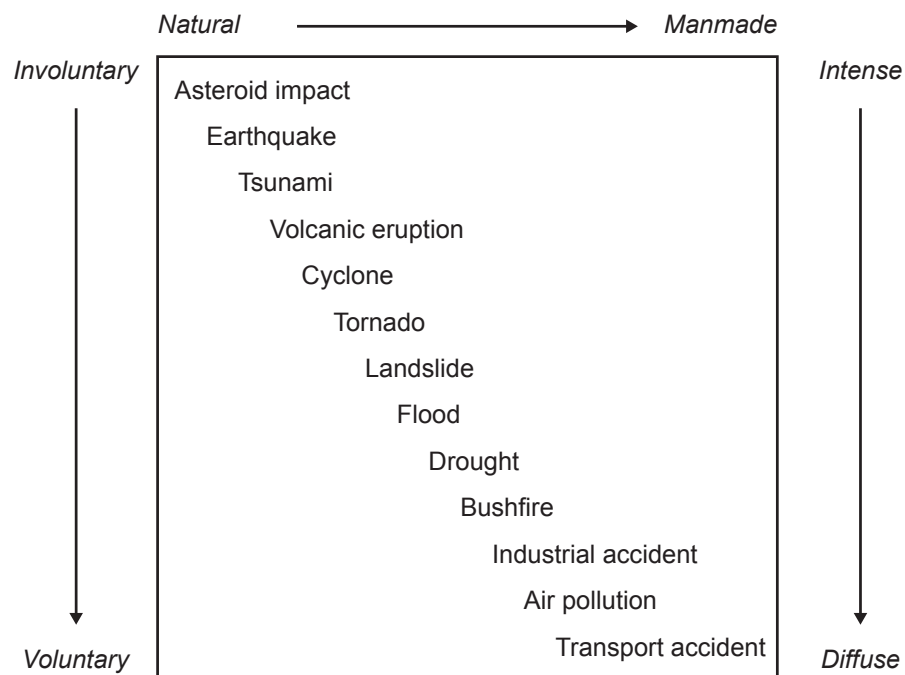


Figure 1.1: Classification of hazards according to the potential human influence, to the extent of the risk imposed (e.g. number of persons affected) and to the willingness of the exposure (from: [Smith and Petley, 2009](#)).

Section 1.2.2 presents briefly the geological hazards, to which landslides belong, whereas Sect. 1.2.3 reviews the hydro-meteorological hazards, especially hail. The notion of risk is then introduced in Sect. 1.2.4, and the specificities of hazard mapping and risk management in Switzerland are presented in Sect. 1.2.5.

1.2.2 Geological hazards

Introduction

Geological hazards, or geohazards (Komac and Zorn, 2013), is a group containing all hazards related to the earth, such as earthquakes, volcanic eruptions, landslides or subsidence. Tsunamis and floods are also sometimes included in this category since they are driven by the topography (e.g. Komac and Zorn, 2013; Guthrie, 2013). The terminology proposed by the United Nations International Strategy for Disaster Reduction (UNISDR, 2009) does not include floods in geological hazard and mentions that tsunamis are difficult to classify, since their origin is geologic, but their expression as a hazard is a water-related process. This more restrictive definition also corresponds to the category "Geophysical hazard" of the "Emergency Events Database" (EM-DAT) compiled by the CRED (Guha-Sapir and Vos, 2011), which is however a bit more restrictive since only "dry" landslides are included. In addition, landslides consequences are sometimes attributed to their triggering event (earthquake, storm, . . .) in the databases (Lacasse and Nadim, 2009). A description of the geological hazard studied in this manuscript, namely landslides and karstic subsidence, is given below.

Landslides

The term landslide does not only cover the slide of a land, but is rather defined as "the movement of a mass of rock, earth or debris down a slope" (Cruden, 1991). De Blasio (2011) considers that the density of the moving mass has to be at least 10 % greater than water for a gravity mass flow to be considered as a landslide. Landslides are commonly classified and named according to their movement type (Fig. 1.2) and to the material involved. Regarding the material, Cruden and Varnes (1996) distinguish rock from soil, and classify the soil materials in earth ($\geq 80\%$ of particles smaller than 2 mm) and debris (20–80 % of particles larger than 2 mm). Hungr et al. (2014) extends this list by proposing to use: rock, clay, mud, silt, sand, gravel, boulders, debris, peat, and ice, and to add descriptive adjectives such as strong or weak for rock material. The authors also add slope deformation to the movement type and summarize the classification as shown in table 1.1.

Landslides are also often characterised by their velocity, ranging from extremely slow (< 1.6 cm/year) to extremely rapid (> 5 m/s), as proposed by Cruden and Varnes (1996), and by their state of activity (active, suspended, reactivated, dormant, stabilized or relict).

Table 1.1: Classification of landslides according to [Hung et al. \(2014\)](#). When applicable, only one of the word in italics should be used. Landslide types in bold face usually reach velocities classified as extremely rapid (> 5 m/s).

Type of movement	Rock	Soil
Fall	1. <i>Rock/ice</i> fall	2. <i>Boulder/debris/silt</i> fall
Topple	3. <i>Rock block</i> topple 4. Rock flexural topple	5. <i>Gravel/sand/silt</i> topple
Slide	6. Rock rotational slide 7. <i>Rock planar</i> slide 8. <i>Rock wedge</i> slide 9. Rock compound slide 10. <i>Rock irregular</i> slide	11. <i>Clay/silt</i> rotational slide 12. <i>Clay/silt</i> planar slide 13. <i>Gravel/sand/debris</i> slide 14. <i>Clay/silt</i> compound slide
Spread	15. Rock slope spread	16. <i>Sand/silt</i> liquefaction spread 17. <i>Sensitive clay</i> spread
Flow	18. <i>Rock/ice</i> avalanche	19. <i>Sand/silt/debris</i> dry flow 20. <i>Sand/silt/debris</i> flowslide 21. <i>Sensitive clay</i> flowslide 22. <i>Debris</i> flow 23. <i>Mud</i> flow 24. Debris flood 25. <i>Debris</i> avalanche 26. Earthflow 27. Peat flow
Slope deformation	28. Mountain slope deformation 29. Rock slope deformation	30. Soil slope deformation 31. Soil creep 32. Solifluction

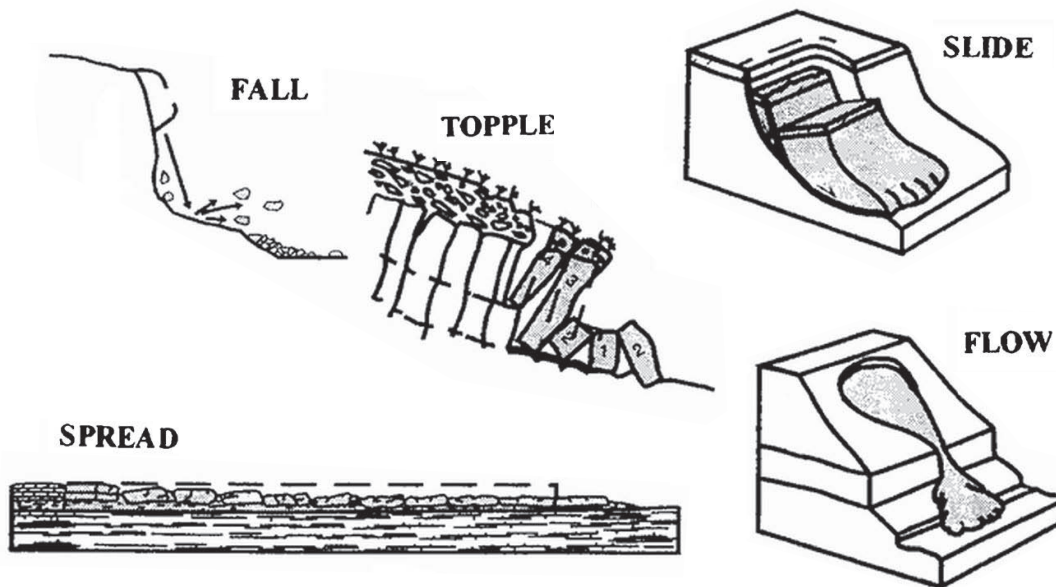


Figure 1.2: Type of landslide movements (modified from: [Cruden and Varnes, 1996](#); [Hungri et al., 2014](#))

Karstic subsidence

According to [Marker \(2013\)](#), subsidence is "the mainly vertical downward displacement of the Earth's surface generally due to insufficient support from beneath, a superimposed load, or a combination of both". According to the same source, it can result from the collapse or the settlement of natural or man-made underground cavities, from a movement along a fault during an earthquake, from ground compaction due to fluid withdrawal (e.g. water, oil, gas) or from compression of weak soils by a superimposed load or by shaking. Karstic subsidence belongs to the first of the above identified causes, since it is related to natural cavities.

Karst refers to the ensemble of specific landforms that occurs on soluble rocks such as limestones or evaporites. It includes the superficial landforms as well as the underground cavities and drainage systems. When it comes to subsidence, this latter group is the most important. [Ford and Williams \(2007\)](#) mention that the rock solubility needs to be combined with a favourable rock structure and lithology to produce karst. Sinkholes, or dolines, are the surface manifestation of subsidence and are circular to sub-circular enclosed depression with a diameter ranging from a few meters to around 1 km ([Ford and Williams, 2007](#)).

A classification of sinkholes, comparable to the one used for landslides, has been proposed by [Gutiérrez et al. \(2008b\)](#). It combines the movement type and the material involved (Fig. 1.4). The movement types considered are *sagging*, which corresponds to a progressive settlement,



Figure 1.3: Example of catastrophic sinkhole in the Italian municipality of Camaiore, in Tuscany (Picture by L. Micheli from: [Buchignani et al., 2008](#)).

suffosion, which is the result of unconsolidated material moving downwards (by washing or granular flow for example) and *collapse*, which is a sudden phenomenon. The material involved can be classified as bedrock, caprock and cover. Bedrock refers here to the rock formation in which the dissolution occurs, whereas caprock refers to a rock mass belonging to another formation, and located above the bedrock. Since most cases involve several processes or material, a combination of terms is possible as well (e.g. cover and bedrock collapse).

[Gutiérrez et al. \(2008a\)](#) lists the human activities that might trigger or accelerate the formation of sinkholes. The main processes concern the modification of water circulations (e.g. increased water input to the ground or lowering of the water table, which favours the percolation of unsaturated water) and the application of a load (static or dynamic).

1.2.3 Hydro-meteorological hazards

Introduction

Hydro-meteorological hazards are related to the atmosphere or to the hydrosphere. This category typically includes severe weathers such as cyclones, thunderstorms, hailstorms or tornadoes (classified by [Guha-Sapir and Vos, 2011](#), as meteorological hazards), more diffuse processes such as droughts and heatwaves (classified by [Guha-Sapir and Vos, 2011](#), as climatological hazards) as well as other hazards such as avalanches or floods ([UNISDR, 2009](#)). The CRED classifies

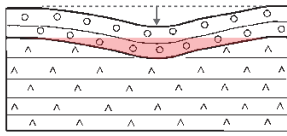
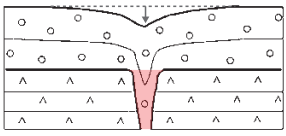
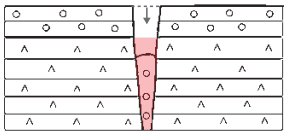
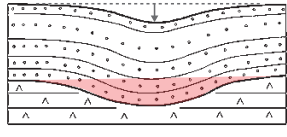
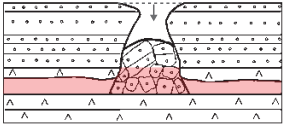
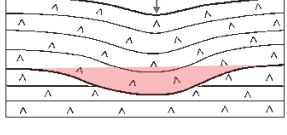
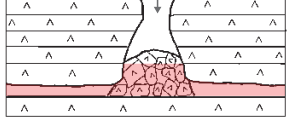
MAIN SINKHOLE TYPES			
MATERIAL	PROCESS		
	Sagging	Suffosion	Collapse
Cover	<p>Cover sagging sinkhole</p> 	<p>Cover suffosion sinkhole</p> 	<p>Cover collapse sinkhole</p> 
Caprock	<p>Caprock sagging sinkhole</p> 		<p>Caprock collapse sinkhole</p> 
Bedrock	<p>Bedrock sagging sinkhole</p> 		<p>Bedrock collapse sinkhole</p> 

Figure 1.4: Classification of sinkholes according to the movement type and the material involved. The layers are originally horizontal and with a constant thickness in these sketches, so that the deformations are only related to the sinkhole process. Dissolution is occurring in the rocks represented by upward-facing open triangles, and the initial position of the dissolute rocks is marked by a red overprint (modified from: [Gutiérrez et al., 2008b](#)).

floods as hydrological hazards and even add "wet" landslides ([Guha-Sapir and Vos, 2011](#)). A clear line can not be drawn between hydro-meteorological hazards and geological hazards since this latter group can be largely influenced by hydro-meteorological conditions (see for example the influence of rainfalls on landslides in [Chapt. 8](#)). Anyway, only hailstorms are directly investigated in this manuscript and will therefore be described below.

Hail

Hailstorms can form when a deep convective system is created, with strong updraft going up to the tropopause and forming an overshooting top ([Fig. 1.5](#), [Reynolds, 1980](#); [Bedka, 2011](#)). This requires an intense solar radiation, that heats the earth surface and favours the evapo-transpiration. This heat and humidity is then carried to upper levels of the atmosphere by convection. During its ascent, the air expands due to lower pressures and cools down as a consequence. This temperature

drop favours the condensation of the water, which releases latent heat and slows down the air cooling, maintaining thus the instability (Doswell, 2014). If a strong upward current exists, large hailstones can be maintained in suspension. In the absence of nucleus, water can reach temperatures far below zero and freeze rapidly when meeting a hailstone (Flossmann, 2006). This type of hailstone creation is known as wet growth and results in transparent hailstones. Dry growth characterizes the hailstones created by the transformation of vapour in ice (also called rimming) and results in translucent ice (Doswell, 2014). A single hailstone often displays an alternation of these two creation modes (Fig. 1.6)

In addition to hail, severe storms can produce lightning and thunder, as well as strong wind and tornadoes. Due to the convective systems, where the ascending air has to be replaced by descending air, hailstorms are generally organized in cells, which have a lifetime of around 20 to 40 minutes, although the storm itself might have a longer lifetime (Doswell, 2014).

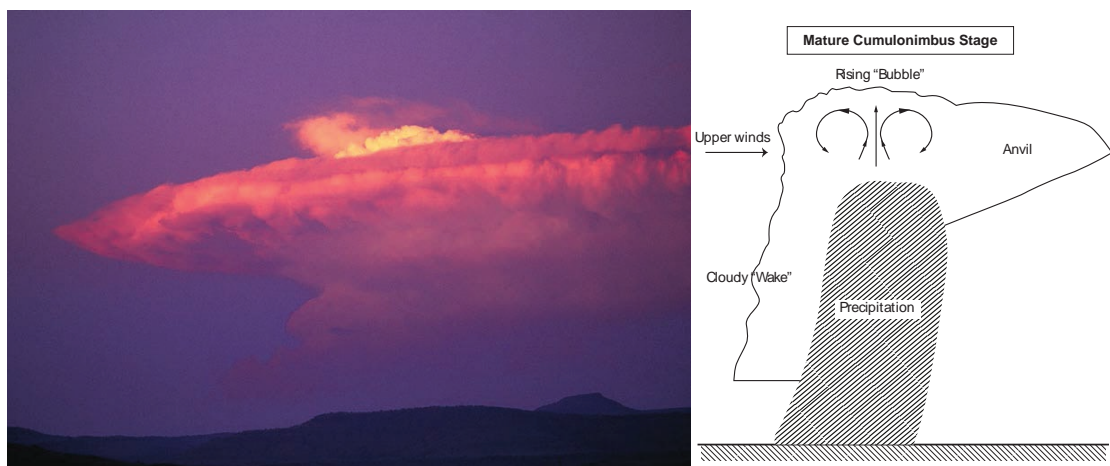


Figure 1.5: Example of deep convective storm cloud with the overshooting part on the top (compare to the sketch on the right) (modified from: Doswell, 2014).

1.2.4 Risk

The risk concept

All phenomena described above can have negative consequences for the humans. The combination of the likelihood of such an event and its negative consequences is known as risk. (Kaplan and Garrick, 1981) define risk as the answer to three questions:

1. "What can happen?"
2. "How likely is that?"

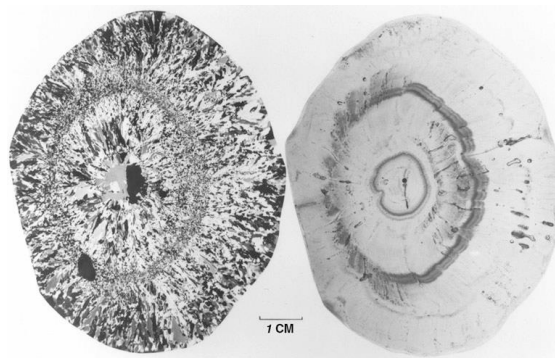


Figure 1.6: Hailstone section shown through polarized (left) and natural light and revealing its internal structure, which results from an alternation of wet and dry growth (from: [Doswell, 2014](#)).

3. "If it does happen, what are the consequences?"

The answer to the first question is the scenario, the answer to the second question is the likelihood and the answer to the third question is the consequences. These three elements form a risk triplet ([Kaplan and Garrick, 1981](#)). The same source of hazard can result in several triplets, reflecting the different potential outcome of a risk situation. If the analysis is performed quantitatively, a combination of several triplets can be used to form a risk curve, also known as FN curve (e.g. [Kaplan and Garrick, 1981](#); [Christian, 2004](#); [Fell et al., 2005](#)), which presents the frequency, generally in terms of number of events per year, at which a number of victims is reached or overpassed. An example is shown in Fig. 1.7, and compares risks from different sources. A different definition has been given recently by the International Organisation for Standardization in the standard ISO 31000:2009 and defines risk as the "effect of uncertainty on objectives" ([Purdy, 2010](#)). Although this interesting definition places the uncertainty in the heart of risk analysis, the definition of [Kaplan and Garrick \(1981\)](#) will be preferred in this manuscript since it is easier to translate in numbers. A critical discussion of this new definition is given in [Purdy \(2010\)](#) and [Aven \(2011\)](#).

Frequency or probability?

When defining the risk, some authors consider the hazard as a probability (e.g. [Einstein, 1988](#)), when some others consider the hazard as a frequency (e.g. [Cascini et al., 2005](#)). Some authors even use both terms almost indistinctly (e.g. [Fell et al., 2005](#)). Both concepts can be used to answer the second question in the previous list. However, these two concepts are not synonym. Starting with the (temporal) frequency, it can be defined as the number of time that a repetitive event occurs in a unit period of time. The frequency can take any value between 0 and ∞ . The

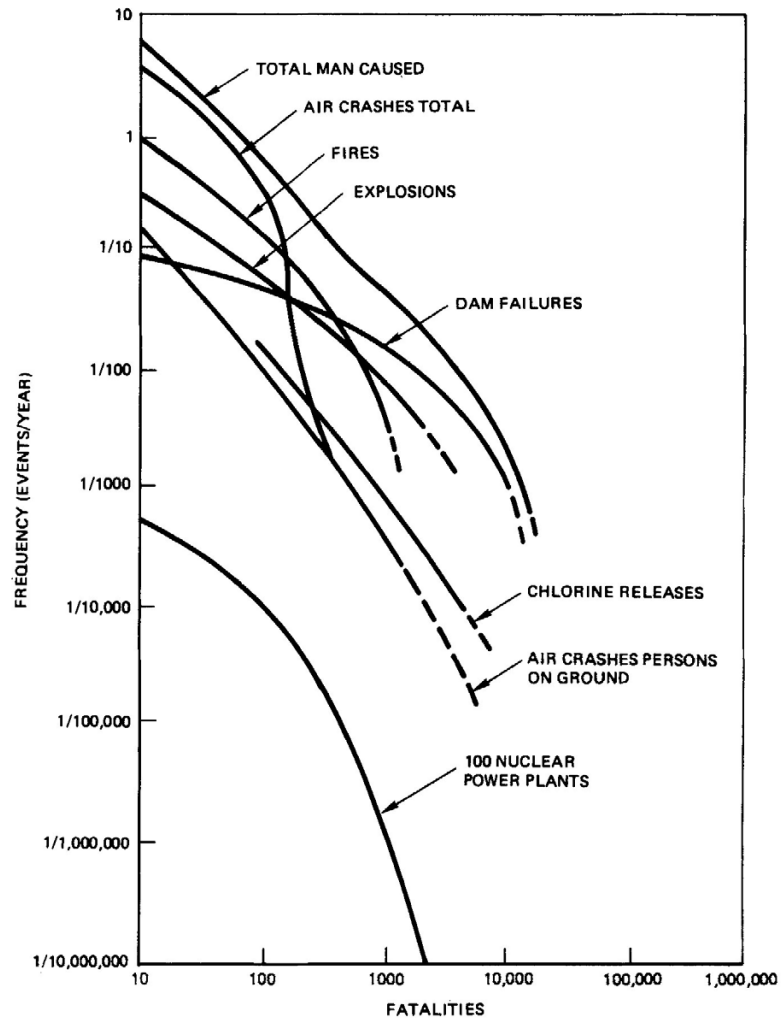


Figure 1.7: Risk curves for different hazard (Kaplan and Garrick, 1981, reproduced from: U.S. Nuclear Regulatory Commission, Reactor Safety Study: An Assessment of Accident Risks in US. Commercial Nuclear Power Plants, WASH-1400 (NUREG-75/014), 1975).

inverse of a temporal frequency is the return period and corresponds to the average time between two occurrences of the event. When talking about frequency, one generally thinks of something that repeats with constant intervals. However, in risk analysis, the term frequency is usually used for an average frequency, which means that the different occurrence of an event occurs with variable intervals. When it comes to landslides, it is unlikely that the exact same landslide occurs twice at the same location, since the slope conditions will change after the first one. However, when looking at a larger region, landslides can often be considered as repetitive events (van Westen et al., 2006).

When it comes to the term probability, it is harder to define. A first approach is to consider the probability as a relative frequency (e.g. Ross, 2010; Fell et al., 2008b), which is the number of time an event occurs divided by the total number of outcomes. This approach of the probability is also sometimes referred to as "objective" probability and can be related to the aleatory uncertainty (Kaplan, 1997), which is a random variability assuming that the model is correct (e.g. Beven, 2009). The other approach is to measure a personal degree of belief (e.g. Ross, 2010; Fell et al., 2008b). This type of probability is also called "subjective" and is closer to an "epistemic" uncertainty (Kaplan, 1997), which results from a lack of knowledge (e.g. Beven, 2009). This approach of probabilities is also suited to "one shot events" (Kaplan, 1997). Probabilities can only take values between 0 (impossible event) and 1 (certain event).

Frequency and probability can be linked by the Poisson law, which has the following form:

$$P(X = k) = \frac{\lambda^k}{k!} e^{-\lambda} \quad (1.1)$$

Where, $P(X = k)$ is the probability that event X occurs k times in the observation period, knowing that its mean frequency is λ (e.g. Ventsel, 1973). To fit this law, the occurrences need however to be independent, which is not always the case with natural hazards. For example, the occurrence of an earthquake along a specific fault has a large influence on the occurrence of other earthquakes along the same fault. Indeed, a strong earthquake comes generally with smaller earthquakes that are spatio-temporally related to the main one (e.g. Stein and Wyssession, 2003; Telesca et al., 2001). Therefore, the Poisson law is not adequate to reproduce the occurrence of earthquakes. On the other hand, the occurrence of hurricanes over the years often fits well with a Poisson law (e.g. Mooley, 1981; Elsner et al., 2004). Regarding landslides, Crovelli (2000) states that the Poisson law might be a suitable first approximation.

It can be seen from the Poisson law that when the frequency is small ($\lambda \rightarrow 0$), then the probability that the event occurs once in the time unit and the frequency are almost equal ($P(X = 1) \approx \lambda$). That is because, in this case, the probability of having more than one event in the time unit is negligible. For this reason, frequencies and probabilities are often used

indifferently in risk analysis (for example in [Fell et al., 2008b](#)). When the probability of having more than one event in a time unit is not negligible, then expected value should be used (as long as the damage can be repaired in the meantime). For the Poisson distribution, the expected value is equal to the frequency (e.g. [Ross, 2010](#)).

[Kaplan \(1997\)](#) states that the likelihood can also be defined by a "probability of frequency", which is, in other words, a probability distribution of the frequency. This is especially useful to include the uncertainties in risk modelling; uncertainties that can be defined using objective or subjective criteria ([Uzielli et al., 2009](#)).

Most of the time, especially when a frequency can't be measured, a risk estimation is subjective and is relative to the observer, as illustrated by this example:

"Some people put a rattlesnake in a man's mailbox. Now if you had asked that man: 'Is it a risk to put your hand in your mailbox?' He would have said, 'Of course not.' We however, knowing about the snake, would say it is very risky indeed." ([Kaplan and Garrick, 1981](#))

The consequence of this is that uncertainty is intrinsically enclosed in the concept of risk. [Aven and Renn \(2009\)](#) and [Rosa \(1998\)](#) insist also on the uncertainty since they consider that "risk refers to uncertainty about and severity of the consequences (or outcomes) of an activity with respect to something that humans value". Some risks contain a large uncertainty, when others are more predictable.

A category of unpredictable events are the Black Swans, defined by [Taleb \(2007\)](#) as events that are outliers (i.e. nothing indicates that it could happen), that have huge consequences and for which we tend to find *a posteriori* explanations and clues for their prediction. [Gilbert et al. \(2016\)](#) considers these risks as "unknown unknown", things we don't know we don't know, which is a concept presented by the former U. S. Secretary of Defence Donald Rumsfeld. The possibility to predict these risks or not is debated (e.g. [Werther, 2013](#); [Stein and Stein, 2014](#)). [Sornette and Ouillon \(2012\)](#) and [Paté-Cornell \(2012\)](#) think that considering such event as unpredictable is irresponsible, since it justifies inaction. From the studies of several authors (e.g. [Ancey, 2012](#); [Stein and Stein, 2014](#)) it seems that natural hazards are not susceptible to real black swans, but that, although if similar events are not available in an historic record, can be foreseen, for example by enlarging the scope of the analysis (or "pooling data from different sites" [Ancey, 2012](#)). In addition, potential error in the historic data must also be considered ([Ancey, 2012](#); [Kuczera et al., 2010](#)). [Paté-Cornell \(2012\)](#) and [Gilbert et al. \(2016\)](#) see in Bayesian probabilities a good approach to deal with such uncertainties.

Analysing the risk

Scenarios and event trees

A first step in a risk analysis is often to define scenarios both for the hazard and the consequences. According to the learner's dictionary of [Merriam-Webster](#), a scenario is "a description of what could possibly happen". According to [Garcia-Aristizabal et al. \(2015\)](#), a scenario should be synoptical, plausible and consistent. When defining a set of risk scenarios, [Kaplan et al. \(2001\)](#) point out that the set should be complete (i.e. cover the range of possibles), finite and disjoint (i.e. no overlap of the scenarios). The authors consider the process of defining scenario as a "partitioning" the risk space. A way to do this is to use an event tree (e.g. [Wong et al., 1997](#); [Lacasse and Nadim, 2009](#)). An event tree is a construction that divides a starting event into possible sequences of events. At each node of the tree, the incoming branch is divided into several branches that each represent a possible state. A probability is attributed to each branch so that the sum of the probabilities of the branches coming out from a node is equal to one ([Peila and Guardini, 2008](#)). As a consequence, the branches emerging from a node should be incompatible events (e.g. a tossed coin can't fall both on the head and on the tail at the same time) that covers the whole range of possibles (e.g. the same tossed coin can't fall on its edge, so head or tails cover the whole spectrum). All the probabilities in the tree are conditional to the occurrence of the starting event and to those of all the branches leading to the considered node. An example of event tree is presented in Fig. 1.8. For each end, the probability is calculated by multiplying the probabilities of all the branches leading to the end. In addition, consequences are estimated. Once the analysis has been done, each result is a combination of likelihood and consequences (in terms of run-up height in Fig. 1.8, but it might also be the number of victims or the economic losses). If the results are ranked by the magnitude of the consequences, it is possible to combine the results to build a risk curve giving the likelihood of an event reaching or overpassing a magnitude of consequences (FN curve, [Kaplan and Garrick, 1981](#)).

Risk as an expected value

Another way to express the risk is using an expected value, which is typically expressed in monetary loss per year or in death per year (e.g. [Fell et al., 2005](#)). As for FN curves, it is done by multiplying the frequency and the consequences. These latter are often calculated using a combination of three terms. One of these terms is the number of potential victims or the total value of the elements that can be affected. For humans in objects, since all the occupants will not die from the impact, the probability for an occupant to die in the scenario needs to be considered. At this point, it is important to mention that although risk analyses could also consider the injured

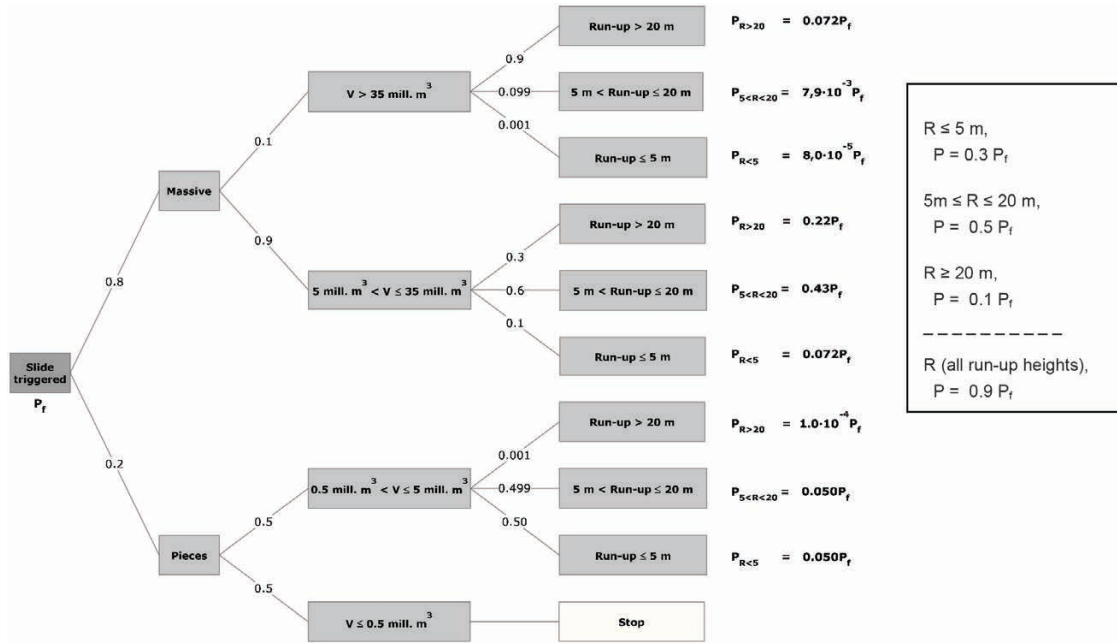


Figure 1.8: Example of an event tree for a tsunami created by the failure of Åknes in the municipality of Stranda, Norway. The starting point of the tree is the rock slope failure and its probability (P_f) is assessed with another tree, which is not presented here (from: Lacasse et al., 2008)

persons, most of them only consider the fatalities, which is easier since it is Boolean, and since the fatalities are generally more reported. Also, fatalities can be considered as a proxy for other consequences. The probability for a person to die, or the proportion of loss in case of an object, is called the vulnerability. Vulnerability is a function of the hazard intensity and the object type, among others (Fig. 1.9). The hazard intensity can be expressed in many ways, and a relevant and measurable indicator (total energy, landslide velocity, ...) needs to be selected (e.g. Fell et al., 2005). Finally, in some cases, a last parameter is needed. Indeed, if we consider the risk for persons in a house, it will depend on the time they spend there. This is done through the temporal spatial probability, also called exposition. A way to write the risk equation is then (modified from Agliardi et al., 2009; Corominas et al., 2013):

$$R_{i,j} = f(M_j) \times N \quad (1.2)$$

$$= f(M_j) \times P(X|M_j) \times P(T_i|X) \times V_{i,j} \times E_i \quad (1.3)$$

Where $f(M_j)$ is the frequency of the natural event (e.g. the landslide) with magnitude M_j in

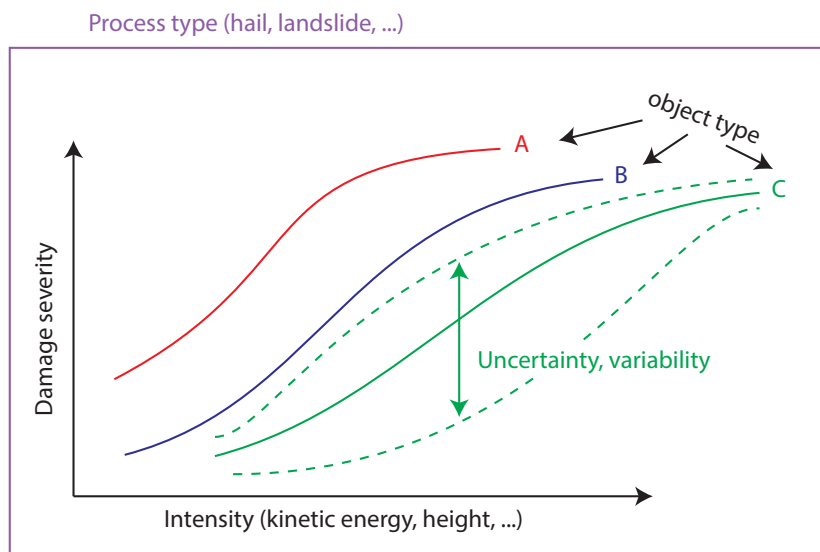


Figure 1.9: Synthetic example of vulnerability curves. The vulnerability (damage severity) is a function of the intensity and of the object type. Since it is generally a regression made from different situation, simplifying or disregarding many parameters, the realisation generally show a high variability around these curves.

scenario j and N are the consequences. These latter can be divided in $P(X|M_j)$, the conditional probability that the event reaches the location X , $P(T_i|X)$, which is also often denoted by P_{ST} for its spatial (S) and temporal components (T), the temporal spatial probability of the element-at-risk, i.e. the conditional probability, knowing that the landslide occurs and reaches location X , that the element-at-risk i is present at the impacted location, $V_{i,j}$, the vulnerability of the element-at-risk i in the scenario j and E_i is its monetary value, or a number of elements (e.g. persons). Finally, since $P(T_i|X)$ and $V_{i,j}$ are dimensionless, if $f(M_j)$ is a mean annual frequency, then $R_{i,j}$ is the average annual loss in CHF/year (or any currency) or in death/year.

In Eq. (1.3), the frequency is as a scalar. However, in most of the natural hazards, it exists a frequency-size relation, which can very often be fitted by a power law. This type of relation has been observed for example for landslides (e.g. Malamud et al., 2004), rockfalls (Fig. 1.10; e.g. Dussauge et al., 2003), and forest fires (e.g. Turcotte, 1999). Risk analysis is thus generally made considering scenarios of different magnitude and their associated frequency and consequences.

Qualitative approaches

Risk analysis has been presented here mostly with a quantitative approach, which is the focus of this thesis. However, risk is also very often analysed qualitatively. In the field of natural hazards, the Rockfall Hazard Rating System (Pierson, 1991, 2012) is one of the most used qualitative

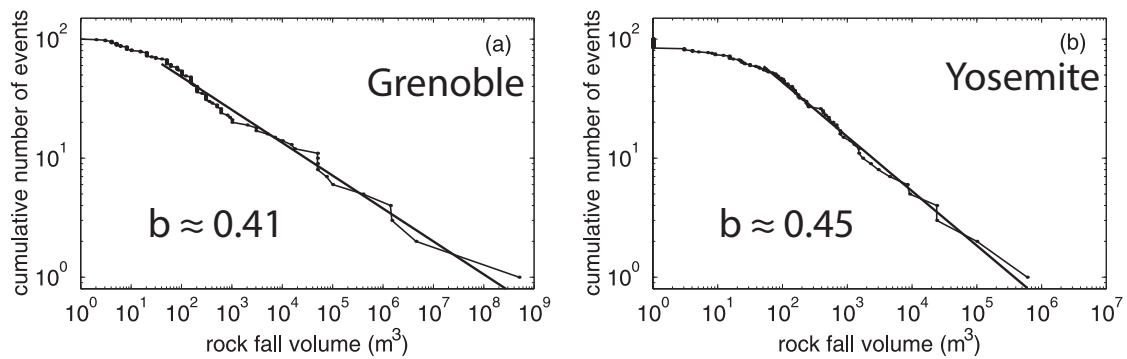


Figure 1.10: Example of inventory of rockfalls where the curves correspond to the number of blocks with a volume equal to or larger than the abscissa value. The distributions are fitted with power laws of the form $n(V) = aV^{-b}$, where $n(V)$ is the number of blocks with a volume equal to or larger than V , a is a scale parameter and b is a shape parameter (from: [Dussauge et al., 2003](#)).

methods. The qualitative methods often use a matrix approach that permits to define classes (e.g. [Haimes et al., 2002](#)). These approaches contain some limits, for example that quantitatively equivalent risks might be classified differently ([Cox, 2008](#)). An example of matrix analysis with the effect of proposed risk reduction methods is presented in Fig. 1.11.

Indirect consequences

Finally, only direct consequences have been presented here, but they are often eclipsed by indirect consequences. For risks along roads, the indirect consequences are for example the economical consequences of a road closure (e.g. [Shi et al., 2015](#)). These consequences are often complicated to estimate, even after an event.

Risk management

General considerations

The concepts above-mentioned permit to estimate the risk. They correspond, in Fig. 1.12, which presents the general framework of risk management, to the risk analysis section, especially to the danger characterisation (question 1 of the list presented on p. 26), the analysis of frequency (question 2) and the characterization of consequence scenarios and the analysis of probability and severity of consequences (question 3). Answering these questions permits then to estimate the risk, but this estimation is useless as long as it is not somehow taken into account in policies or to establish protection measures. The next question is thus to know if the estimated risk is acceptable or not. Different types of criterion can answer the question of acceptability, and

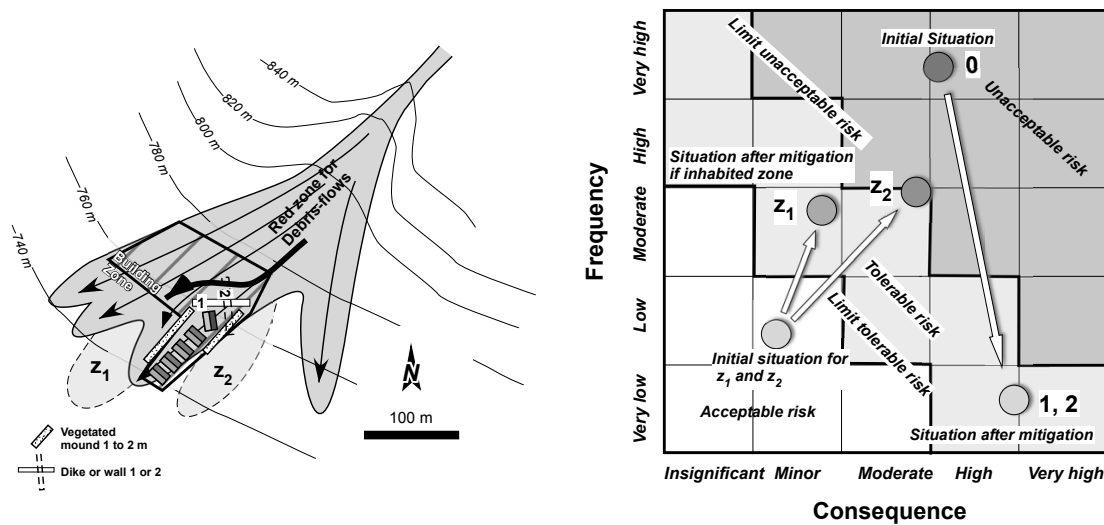


Figure 1.11: Example of qualitative risk analysis using a matrix. After the construction of dikes, the risk for the houses is reduced, since the frequency is reduced (0→1,2). However, the consequences in case of an event will be more important since only the largest events can reach the houses. On the other hand, the flux deviation by the dikes will increase the risk in areas Z1 and Z2, where the consequences are however lower (e.g. production loss if these areas are cultivated) (from: [Jaboyedoff et al., 2014](#))

depend a lot on the context. Several aspects can influence how a person or a society accepts a risk or not. The first aspect is the perceived benefit. Indeed, people will accept to be submitted to a risk only if they perceive a benefit in the situation. For example societies tends to settle in floodplains because of the good agricultural soils and the trade opportunities (e.g. [Di Baldassarre et al., 2013b](#)). A closely related aspect is the willingness. A person doing extreme sports accepts a much higher risk in this situation than the same person would accept on the workplace, for example. Figure 1.13 shows the example of a person climbing, who is willing to take a risk and sees a direct benefit in it (having fun). On the other hand, the same person will be less willing to accept the risk of a factory located close to his or her house, especially if this person does not have an interest in that factory (i.e. the person does not work there, does not consume their products, ...). [Litai et al. \(1983\)](#) cite other distinction in risks types that can affect the acceptability. For example, if the hazard is natural or not, if the event is ordinary or catastrophic, if the risk is future or immediate and if the risk is new or old.

Societal risk

A first way to decide if a risk is acceptable or not is to measure the societal risk, which corresponds to the expected number of fatalities or the economic losses. The societal risk is often represented

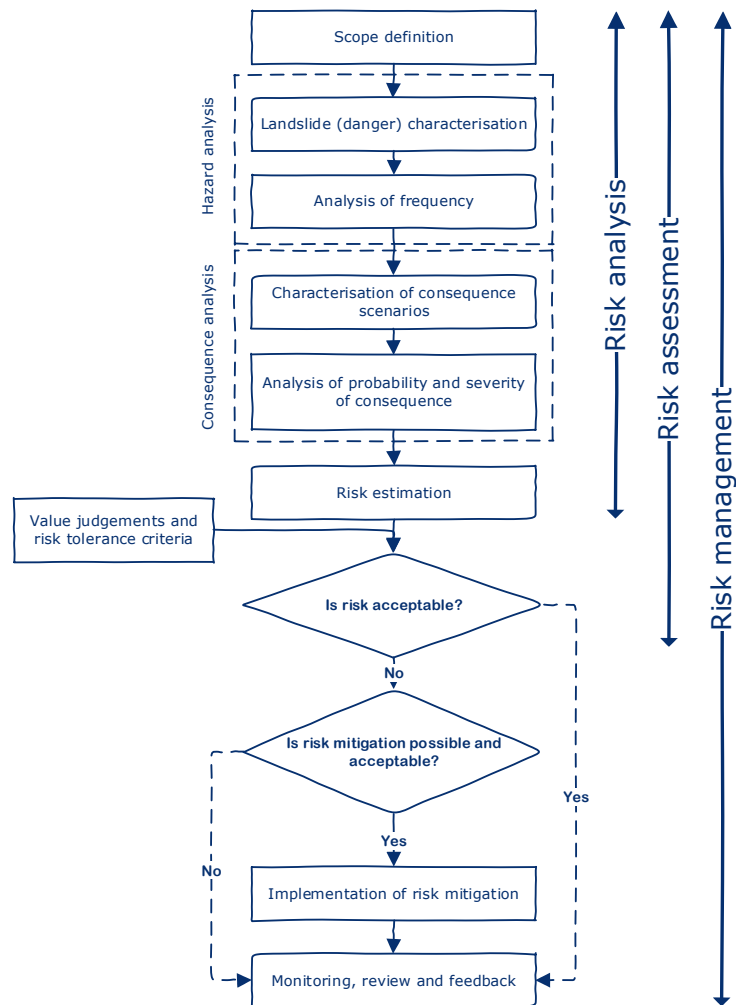


Figure 1.12: Risk management framework (modified from: [Fell et al., 2005](#))

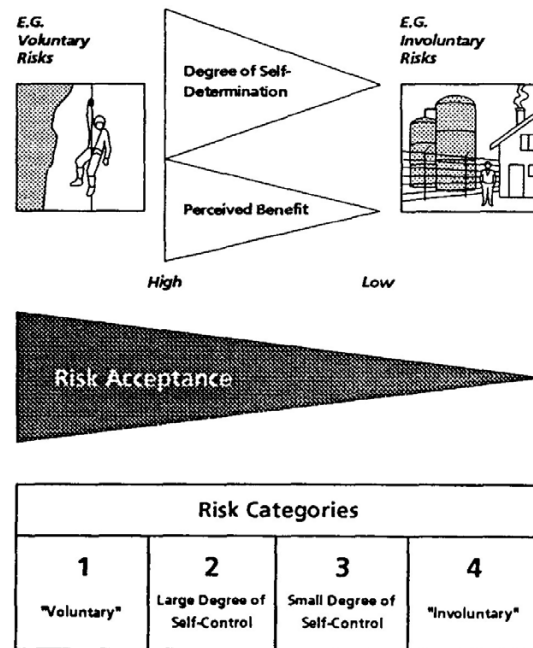


Figure 1.13: Risk acceptance as a function of self-determination and perceived benefits (from: [Bohnenblust and Slovic, 1998](#))

by a FN curve, where FN stands for frequency-number (Fig. 1.14). For example, such a curve has been developed for landslides in Hong-Kong (e.g. [Ho and Ko, 2009](#)) and permits to compare a risk value or a risk curve to an acceptability and a tolerability curve. Above a certain limit, all risks are unacceptable and measures should be taken, disregarding their cost. In the meantime, risks that are below this limit might fall in the ALARP zone, which stands for *as low as reasonably practicable*. This implies that such risks have to be reduced if possible. The possibility is generally evaluated by another criterion such as a cost-benefit analysis (see below). Generally, this zone spans two orders of magnitude, and risks that are below these two orders of magnitude (below a tolerability line) are considered to be too low to justify further analysis (Option A in Fig. 1.14). Independently from the frequency, a maximum number of victims is generally accepted, with a buffer zone (intense scrutiny region). That is because, as seen above, the catastrophic events are generally less accepted than more diffuse events. To account for the same effect, an aversion factor could be added, so that the limits are no longer iso-risk lines, but give a lower threshold in terms of mean risk (mean number of victims per year) to the events with a large number of fatalities (e.g. [Finlay and Fell, 1997](#); [Jonkman et al., 2003](#)). The curves presented for Hong-Kong have been developed for landslides along a slope with 500 m length and are adjusted in case of longer slopes ([Ho et al., 2000](#)). The same curve (or the same principle) is applied in many other

countries and, although an economic criterion could be used, they generally measure the number of victims. Evans and Verlander (1997) show that similar risks in terms of mean annual number of victims can be judged differently using a FN curve. Indeed, depending on the repartition of the type of events, the curve might cross the limit or not, although the mean risk is the same. Even if it doesn't discredit such analyses, it insists on their indicative nature.

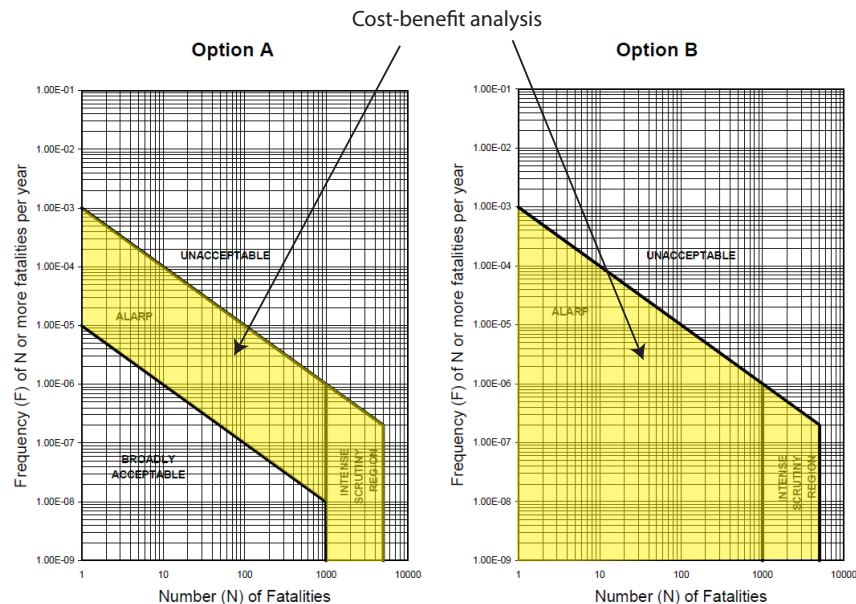


Figure 1.14: Two examples of FN diagrams with different criteria (modified from: Ho et al., 2000)

Individual risk

A second criterion that is often used is the measure of the individual risk, which is the risk encountered by one individual exposed to a hazard. This risk is expressed in terms of annual death probability (formally a frequency if the hazard is a frequency). This number is often compared to the normal death rate and aims at avoiding an unfair situation where an acceptable collective risk would be concentrated in one individual and have a large impact in the life of that individual (Bohnenblust and Slovic, 1998). For example, in Switzerland, the lower death rate is of about 10^{-4} between 5 and 10 years old (Fig. 1.15). Different threshold might be set according to the willingness of the exposure, for example. For natural hazard, Hong-Kong sets the limit at 10^{-4} for existing settlements and 10^{-5} for new developments (Ho et al., 2000). In New Zealand, Enright (2015) argues that the current threshold of 10^{-4} is far too high and that a limit of 10^{-5} for existing risks and 10^{-6} for new risks would be more suitable. It has to be mentioned that the individual

risk is an increment of risk that adds to the other risks of a person. Thus, the same person can for example be threatened by a risk at work and a different one at home, that might be individually below the limit, but above if they are summed.

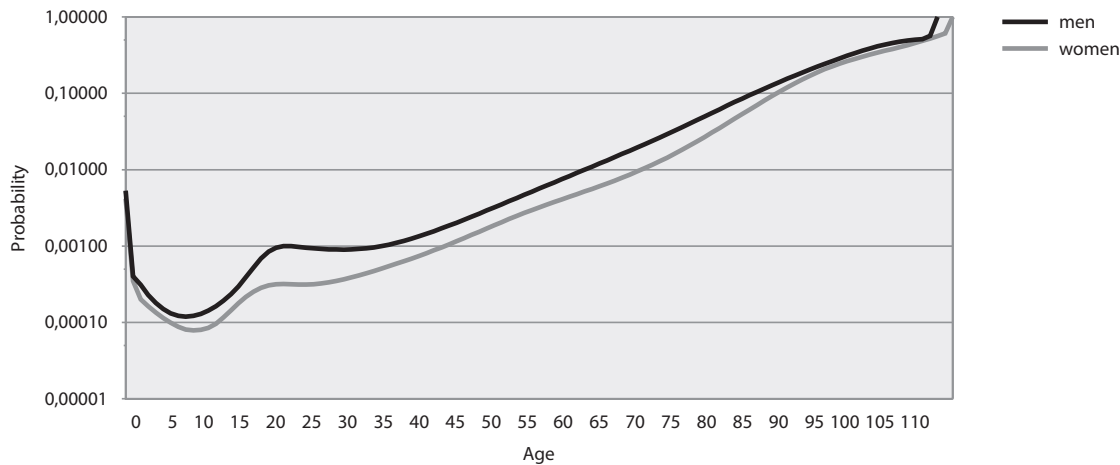


Figure 1.15: Death probabilities during the period 1998–2003 in Switzerland (modified from: Kohli, 2005)

Cost-benefit analysis

The third way to decide if a protection measure is needed is to perform a cost-benefit analysis. The idea of such an analysis is to compare the expected cost without measure (i.e. the mean annual risk) to the expected cost with measure, which is a combination of the annual cost of the measure and the residual risk, since the measure often only reduces the risk (Fig. 1.16). This requires to annualize the cost of the measure, and thus to divide the investment cost by the expected lifetime of the measure. Such an analysis requires a monetary risk. To include the potential fatalities in the analysis, the concept of willingness-to-pay or marginal costs has been created and corresponds to the price that a society is willing to pay to save a statistical life (Bohnenblust and Slovic, 1998). Different methods have been investigated to estimate this price and can for example be based on the potential economic production of a person or estimated from the money invested and the lives saved in past projects (Jonkman et al., 2003). In addition, this price might be weighted by different criterion, similarly to the individual risk thresholds. It is currently of 5 mio. CHF in Switzerland for natural hazards (Bründl et al., 2015), whereas Marzocchi and Woo (2009) estimate, from a mitigation action at Mount Vesuvius, that a minimum value of 800 000 Euros is reasonable for Italy.

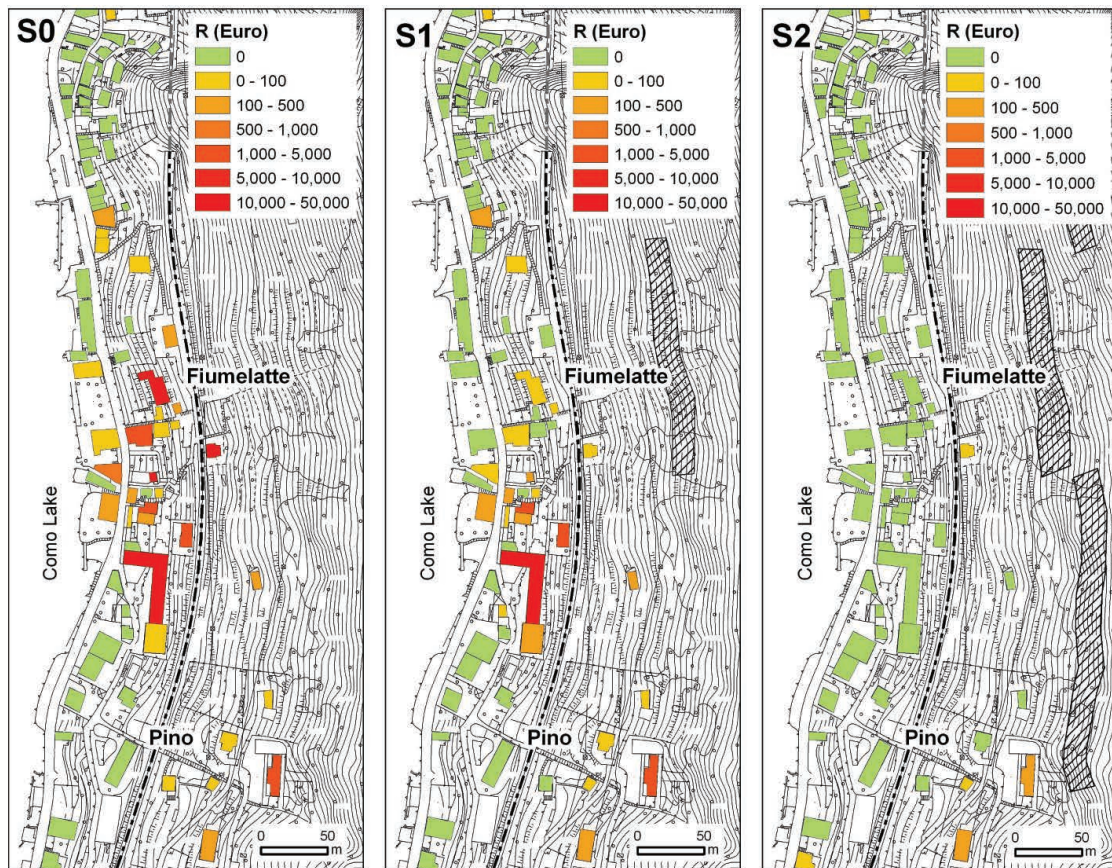


Figure 1.16: Example of risk analysis without protection measures (S0), with temporary embankments (S1) and with long-term protection measures (S2). The calculations consider several volume classes for the falling rock blocks and combine material and human consequences, with an economical value of one million EUR for the human lives (from: [Agliardi et al., 2009](#)).

1.2.5 Hazard mapping and risk management in Switzerland

Switzerland is exposed to several natural hazards, among which flood and hail cause the highest losses for the public building insurance companies ([Imhof, 2011](#)). ([Hilker et al., 2009](#)) have registered around 3 fatalities per year caused by floods or landslides between 1972 and 2007. These statistics does not include snow avalanches, neither accidents related to risky sport activities.

In 1987, a large flood and debris-flow event (e.g. [Rickenmann and Zimmermann, 1993](#)) highlighted the limits of constructive structures for the protection of buildings against natural hazards. As a result, The Federal Act of 21 June 1991 on Hydraulic Engineering (Art. 3), states that the priority has to be given to the maintenance of the rivers and to spatial planning for the protection against floods. Constructive measures such as dikes have to be considered only when

the protection can't be reached with spatial planning. When it comes to landslides, the Federal Act of 4 October 1991 on Forests states that the Cantons shall protect their population from landslides (ForA Art. 19), but it is less precise regarding the methods to use. However, the Ordinance of 30 November 1992 on Forests requires the Canton to prepare hazard maps and to document the natural events (ForO Art. 15). In addition, the forest law demands that the cantonal authorities identify and maintain the forests playing a role in the protection against natural hazards (ForA Art. 20 al. 5). The identification of protective forests has subsequently been harmonized at the federal level (Losey and Wehrli, 2013). Between the adoption of these laws and the publication of guidelines for hazard mapping, the landslide which occurred in 1994 in Falli-Höllli (Canton de Fribourg) and destroyed 41 houses showed an instructive example of bad planning. Indeed, the landslide, which reached velocities up to 6 m/day during the crisis, was the reactivation of a prehistoric landslide (Raetzo et al., 2002) that should have been identified by hazard maps.

Guidelines for hazard mapping and their consideration in spatial planning have been prepared for landslides (Lateltin, 1997; Raetzo et al., 2002; FOEN, 2016) and floods (Loat and Petrascheck, 1997; FOWG, 2001). Similar guidelines were already existing for snow avalanches (BFF, 1984). The maps are designed for land-use planning and are based on the same hazard matrix (Fig. 1.17), with small adaptations for some phenomena. The hazard maps are built by combining three scenarios for each class of return period and an intensity threshold is defined for each type of hazard. The idea of this matrix is that constructions are impossible in red areas, possible with some restrictions in blue areas and allowed without restriction in yellow areas. The limitation of these maps is that they do not solve the problem of already existing buildings and that they are not adapted for transportation network, since in that case, the frequency is often more important than the intensity. In addition, drawing these maps for the entire territory would use too much resources. Therefore, a first step is often to build preliminary hazard maps (Jaboyedoff et al., 2012), that are based on conservative computer models, and to combine the information of these maps with land use maps, in order to identify the area with a potential risk.

Although risk guidelines have been published in 1999 already (Borter, 1999), systematic risk analyses started in 2008 with the obligation for subsidized projects of protection measures to be analysed with the on-line tool EconoMe (Bründl et al., 2009). Comparable tools and guidelines have been developed for highways (Dorren et al., 2009) and for railways (Bründl et al., 2012).

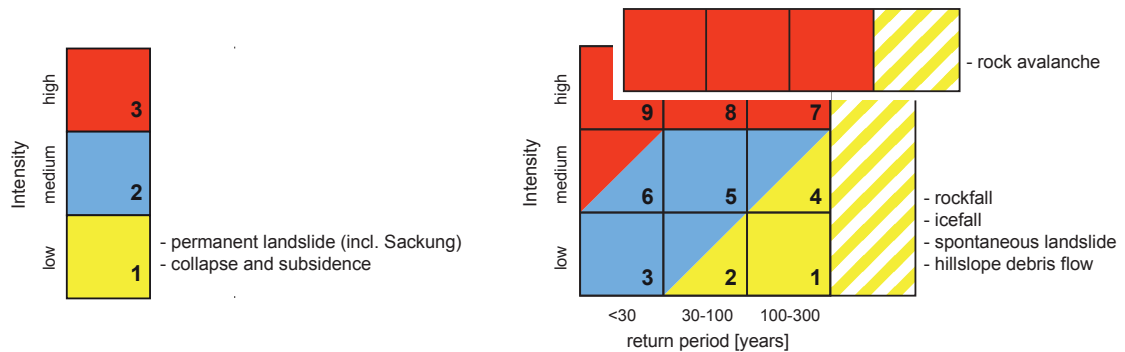


Figure 1.17: Matrix used for the hazard mapping in Switzerland (modified from: FOEN, 2016)

1.3 Content of this manuscript

1.3.1 Outline

Although from the perspective of the 3 questions presented on page 1.2.4, analysing the risk seems like an easy task, it is actually complicated for numerous reasons. One of the main reasons is that risk deals by definition with uncertainty and unknowns. In addition, risk analyses are generally based on scarce and uneven data from past events and need to compare different metrics (such as people and objects) and to simplify complex problems. Finally, risk depends on the end user. Indeed, a building insurance company is for example not concerned by the loss of human lives. As a consequence, this PhD tries to improve the quantitative risk analysis of natural hazards at local and regional scale addressing the previously enumerated issues. This manuscript is organised in two parts. The first one treats of risk analysis at local scale and covers the whole span of risk management, as described in Fig. 1.18, considering the role of public authorities. The second part takes the point of view of building insurance companies and treats of risk modelling at regional scale, where the focus is the portfolio and not the individual objects. This part also proposes solution to work with incomplete data and to deal with the related uncertainty. More precisely, the different chapters of this manuscript try to answer to the questions below.

At local scale (Part I), Chapt. 2 treats of the hazard characterisation by means of photogrammetry and unmanned aerial systems (UAS). Chapters 3 to 5 discuss questions related to the risk analyses that are performed for cost-benefit analyses, in order to estimate if protection measures are necessary. This part is especially relevant for the method used in Switzerland, where the risk analyses are made according to a homogenised procedure based on hazard maps. Chapter 3 presents a tool designed to perform such an analysis, with the goal of simplifying the process. Chapter 4 discusses on the specific problem of calculating the temporal spatial probability of a

vehicle being affected by an event and solves the problem of having a unique and simple method for all types of hazards and vehicles. Chapter 5 proposes a method to add the risk of different scenarios that account for the partial representation of the risk by the scenarios used for the hazard maps and discusses on the inclusion of uncertainties in the process. Finally, Chapt. 6 proposes a solution for the communication of the change in the hazard level when the protection measures are built.

At regional scale (Part II), Chapt. 7 to 9 present risk models based on incomplete data for different hazards including the uncertainties. These models are especially designed to work with insurance data, in order to calculate the risk of a portfolio, but are also helpful in order to understand the factors controlling the risk and to test mitigation strategies. Chapter 7 presents a study of gypsum dissolution-related risk for a building insurance company and focuses mainly on the inventory of past events, which permits to estimate the frequency of the events and the buildings vulnerability. Chapter 8 is based on a rainfall-induced large landslide event and is an attempt to create a probabilistic risk model based on the precipitation amounts and the buildings location. Finally, Chapt. 9 is based mainly on a hail event that occurred in 2011 in Northern Switzerland. It exploits a radar intensity map and insurance data in order to build a model, which aims at estimating quickly the damage after an event. In addition, the vulnerability model derived from these data is exploited in conjunction with hazard maps in order to estimate the mean annual risk and exceedance probability curves.

1.3.2 Contribution of the candidate

This manuscript has been written by the PhD candidate, with minor external contributions listed below. Chap. 4 and 8 have been published as articles and have been improved by the comments of the co-authors and reviewers. In addition, the sections of Chap. 8 treating of the description of the precipitation event and the spatial analysis of rainfall have been written by a co-author, whereas the first comparison of the rainfall amount and the landslides' position has been performed by co-authors. Chap. 7 has been submitted for publication in a journal and has been improved by the comments of the co-authors and reviewers. The other chapters have been written exclusively by the PhD candidate, but benefited from the comments of the PhD supervisor and of the PhD jury members.

When it comes to the appendices, the PhD candidate has participated in the different studies, but not as main contributor.

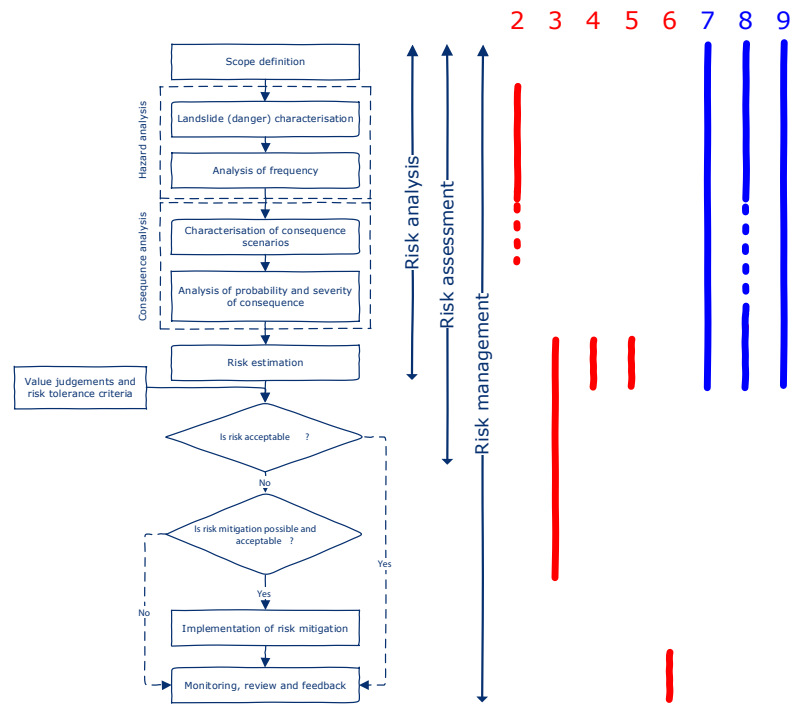


Figure 1.18: Range of the risk management framework (Fig. 1.12) covered by the chapters of this manuscript (modified from: Fell et al., 2005)

Part I

Risk analysis and management at local scale

Chapter 2

Landslide surveying with photogrammetry and UAS

2.1 Introduction

Landslide mapping and monitoring can be done using field techniques, but these ones have several limitations and remote-sensing techniques have been applied for a long time as a complement. In particular, photogrammetry has been used for several years in order to visualize the topography and to produce topographical maps, using the relative displacement of objects on pictures taken from different locations. However, for several years, landslide mapping and monitoring is benefiting from the development of new powerful remote-sensing techniques such as LiDAR ("Light Detection And Ranging"), which diminished the popularity of photogrammetry. Nevertheless, recent advances in the field of computer vision and increasing computing capabilities gave a new momentum to the photogrammetry field. In particular, the possibility to perform photogrammetry from the ground (and at close range) using market-grade non-calibrated cameras is making this method very popular. A particularly compelling example is the (successful) attempt to create 3D models using pictures of different monuments, such as the Colosseum in Roma (Fig. 2.1), retrieved from an internet image search (Snavely et al., 2008). In addition, the procedure has become very popular due to the availability of highly automated programs that does not require a detailed knowledge of computer vision such as VisualSFM (Wu, 2015) or Agisoft Photoscan (Agisoft LLC, 2014).

Since photogrammetry permits to obtain point clouds that are similar in many ways to LiDAR point clouds, this chapter compares both approaches in order to identify their strengths and weaknesses.

LiDAR technique consists in sending a laser pulse in a known direction and measuring the

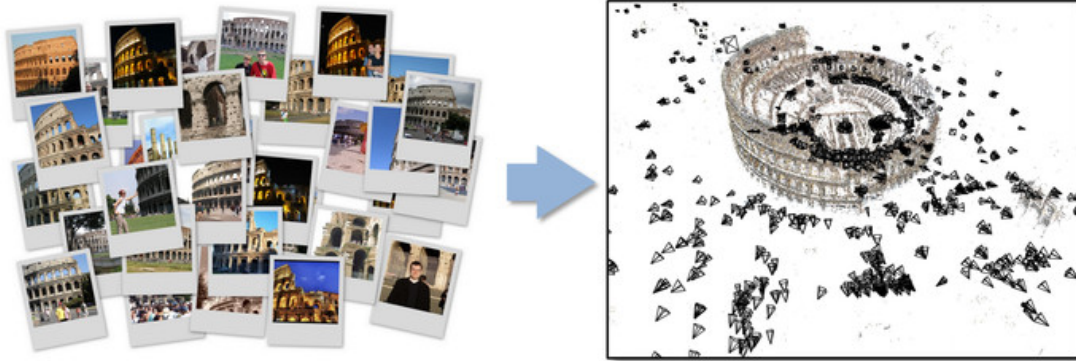


Figure 2.1: Reconstruction of the Colosseum, in Rome, using pictures found on the internet (from: [Snavely et al., 2008](#))

distance using the time of flight (TOF), the phase shift or by triangulation ([Jaboyedoff et al., in press](#)). TOF LiDAR is generally used for geoscientific applications thanks to its relatively long acquisition range. LiDAR devices can be located on different scanning platforms. Many areas have been scanned systematically using airborne laser scanning (ALS), where the LiDAR is carried by a plane or by a helicopter. The main application of this technique is to produce high-resolution DTM and DEM, with typical grid size ranging from 0.5 to 10 m. Another common method is the terrestrial laser scanning (TLS), where the LiDAR device remains at the same position on the earth surface. This technique is typically used to perform detailed scans of a specific area and, due to its simple set-up (as compared to ALS), can be used to perform change detection or monitoring. Finally, other moving platforms can carry a LiDAR, such as boats (e.g. [Michoud et al., 2015](#)), cars (e.g. [Lato et al., 2009](#); [Sampson et al., 2012](#)) or unmanned aircraft systems (UAS) (e.g. [Wallace et al., 2012](#)). They are generally referred to as mobile laser scanning (MLS) ([Michoud et al., 2015](#)).

2.1.1 Chapter outline

After a brief state of the art of the field of photogrammetry and UAS, this chapter outlines some advantages and disadvantages of the photogrammetry method as compared to LiDAR, using different case studied over the years.

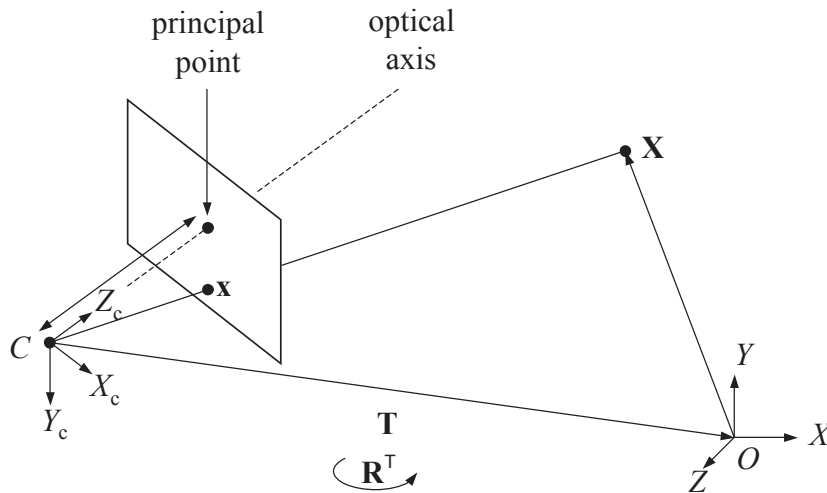


Figure 2.2: Relation between the different coordinates systems. C is the perspective center of the camera, whereas O is the origin of the real-world coordinate system. To simplify the schema, the picture plane is placed here in front of the centre of perspective, although it is actually behind (from: Robertson and Cipolla, 2009)

2.2 State of the art

2.2.1 Photogrammetry

Basic principles

Photogrammetry is a technique assessing the 3D position of a point $X = [X Y Z]$ from its coordinates on a set of 2D pictures. Assuming a pinhole camera (i.e. where all light rays converge through a dimensionless hole) that respects the collinearity (the real-world point, its projection on the sensor and the focal centre are located on a straight line), the coordinates in the camera coordinate system (see Fig. 2.2) are related to the real-world coordinates by the following equation:

$$\begin{bmatrix} X_c \\ Y_c \\ Z_c \end{bmatrix} = R \times \begin{bmatrix} X - X_0 \\ Y - Y_0 \\ Z - Z_0 \end{bmatrix} \quad (2.1)$$

This equation transposes the coordinate system to the perspective centre (C) of the camera by translating it using X_0 , Y_0 and Z_0 , which are the coordinates of the perspective centre in the real-world coordinate system. Then a (3×3) rotation matrix (R) representing the orientation of

the camera is applied. Once these 2 transformations have been made, the coordinates of the point $X = [X \ Y \ Z]$ can be expressed in the camera coordinate system (X_c, Y_c, Z_c) . However, when observing an image in 2D, the coordinate Z_c can obviously not be estimated. When it comes to X_c and Y_c , they can't be assessed either, since they actually depend on the distance between the focal centre and the image plan (i.e. the focal length). The 2D coordinates in the image plane are related with the 3D coordinates by the following equations (Robertson and Cipolla, 2009):

$$\begin{cases} x = f \frac{X_c}{Z_c} \\ y = f \frac{Y_c}{Z_c} \end{cases} \quad (2.2)$$

Where f is the focal length, i.e. the distance between the focal centre and the image. These coordinates can then be related to the pixel coordinate system. By applying a scaling factor to the right side of Eq. (2.1), it is possible to transform the equation as follows:

$$\begin{bmatrix} x - x_0 \\ y - y_0 \\ f \end{bmatrix} = c \times R \times \begin{bmatrix} X - X_0 \\ Y - Y_0 \\ Z - Z_0 \end{bmatrix} \quad (2.3)$$

Where x_0 and y_0 represent the potential (small) offset separating the optical axis from the geometric centre of the image¹. The scale factor can then be eliminated by solving the matrix multiplication and by dividing the scalar equations of $x - x_0$ and $y - y_0$ by the one of f (Mikhail et al., 2001). This gives the following equation system:

$$\begin{cases} x - x_0 = f \frac{r_{11}(X - X_0) + r_{12}(Y - Y_0) + r_{13}(Z - Z_0)}{r_{31}(X - X_0) + r_{32}(Y - Y_0) + r_{33}(Z - Z_0)} \\ y - y_0 = f \frac{r_{21}(X - X_0) + r_{22}(Y - Y_0) + r_{23}(Z - Z_0)}{r_{31}(X - X_0) + r_{32}(Y - Y_0) + r_{33}(Z - Z_0)} \end{cases} \quad (2.4)$$

Where r_{ij} are the elements of R . With this ideal system, one can calculate the number of similar points needed between 2 pictures or more to solve the equations system (Abellán et al., 2015). Indeed, the unknown common to every points are the coordinates of the two cameras (6 unknown) and the rotation angles (6 unknown). Assuming that the coordinates of the principal point and the focal length are common to the two images (3 unknown), then every point common to the two pictures adds three unknown (its coordinates) and 4 equations (the 2 Eq. 2.4, for both cameras). Therefore, with 15 common unknown, 15 common points are needed to solve the system. If we consider 3 pictures, then there is 21 common unknown, and each point visible in

¹Note that in the equation of Mikhail et al. (2001), f is replaced by $-f$. That is because the z-axis is pointing in direction of the image in Fig. 2.2. As a consequence, y-axis is pointing downwards.

the 3 pictures adds 3 unknowns to the system and 6 equations. Therefore, only 7 common points are needed to solve the system. Although in practice a larger number of points are considered, this example shows the potential of using a large set of pictures, with high redundancy. On the other hand, it might sometimes be better to use fewer pictures but with a better quality, since even for two pictures, the number of points required is relatively small.

Until now, we considered a pinhole camera, with no deformation. However, due to the use of a lens, which aims at getting more light into the camera, most cameras are affected by a radial deformation, and potentially by a less significant tangential deformation. These parameters also need to be estimated and represent the internal orientation. Different deformation models with diverse levels of complexity exist to account for these effects. For example, 3DM Analyst ([ADAM Technology, 2010](#)) uses a model with 11 parameters (including f , x_0 and y_0).

General workflow

The general workflow of modern photogrammetric techniques is presented in the next sections. Globally, it consists in:

1. defining key points on each image and searching for correspondence in the other images
2. retrieving the position and orientation of the cameras, together with their geometric parameters, building a sparse point cloud at the same time
3. building a dense point cloud

Finally, the point cloud can be georeferenced using different procedures.

Keypoint detection and matching

Area-based matching are very accurate methods, but only works with little perspective deformation and little light variations ([Scaioni et al., 2015](#)). Therefore, it is essentially used in traditional aerial photogrammetry. Another group of methods, namely feature-based matching is able to accommodate changes in scale, angle and light by describing the pictures gradients. They are also able to accommodate occlusions. An example of such a method is the "Scale Invariant Feature Transform" (SIFT; [Lowe, 2004](#)), which is integrated in VisualSFM with an algorithm using the graphical processing units (GPU) to accelerate the calculation ([Wu, 2007](#)).

Sparse reconstruction

Structure from motion (SfM) refers to the process of estimating simultaneously, from a collection of images, the camera locations and orientations (exterior orientation), the camera parameters

(interior orientation), such as the focal length and the radial distortion, and a sparse reconstruction of the scene (Snavely et al., 2006). It is also named "structure and motion" (SAM) in earlier articles (e.g. Pollefeys et al., 2004; Brown and Lowe, 2005), with reference to the structure of the scene and the motion of the camera.

The procedure is generally to select a pair of images with a large number of matches, but with a relatively large baseline (distance between the camera stations). The scale is often set by arbitrary attributing the value of 1 to the initial baseline (Pierrot-Deseilligny, 2013). Then, the camera with the largest number of features that already have an estimated position is added to the model and its interior and exterior orientation are estimated (the initial focal length value being often retrieved from the EXIF metadata). This procedure is repeated until all cameras have been added, or until the remaining cameras have no already positioned features (Snavely et al., 2006). It has to be mentioned that the camera interior orientation can be defined for each picture or adjusted globally, considering a unique camera with stable deformation.

A bundle adjustment is generally used as a last step, in order to refine the estimation of the parameters. This procedure is likely to converge to a local minimum, therefore, it needs a good initial estimate (Robertson and Cipolla, 2009). "Bundle" refers to the light rays emitted by the objects in the scene and converging in each camera focal point (Triggs et al., 2000).

Due to the process of self-calibration, SfM is subject to systematic errors like the "dome-effect" described by (James and Robson, 2014) and (Wu, 2014). Indeed, in some cases, if the block is poorly constrained, the simultaneous resolution of both interior and exterior orientation can be ambiguous. This is especially the case for a flat surface and sub-parallel cameras (Fig. 2.3), and can then occur using UAS or modelling a linear cliff (James and Robson, 2014). The solution is however simple, as Fig. 2.4 shows, since adding pictures taken with another angle can consolidate the block and remove the ambiguity.

Dense matching

Dense matching is also referred to as "Multi-View Stereo" (MVS) and consists in building a dense 3D model when the camera interior and exterior orientation have been established (Seitz et al., 2006). VisualSFM integrates the second version of Patch-based Multi-view Stereo (PMVS) software (Furukawa and Ponce, 2010). To use this algorithm with large sets of pictures, the sets need to be decomposed in several sub-sets that are processed in parallel with PMVS2 and merged at the end. This is usually done with the algorithm "Clustering Views for Multi-view Stereo" (CMVS) developed by Furukawa et al. (2010). An example of MVS procedure is presented in Fig. 2.5 and consists, for a specific pixel in an image, in projecting different hypothetical depth on other images and selecting the depth for which the window correspondence obtain the best score.

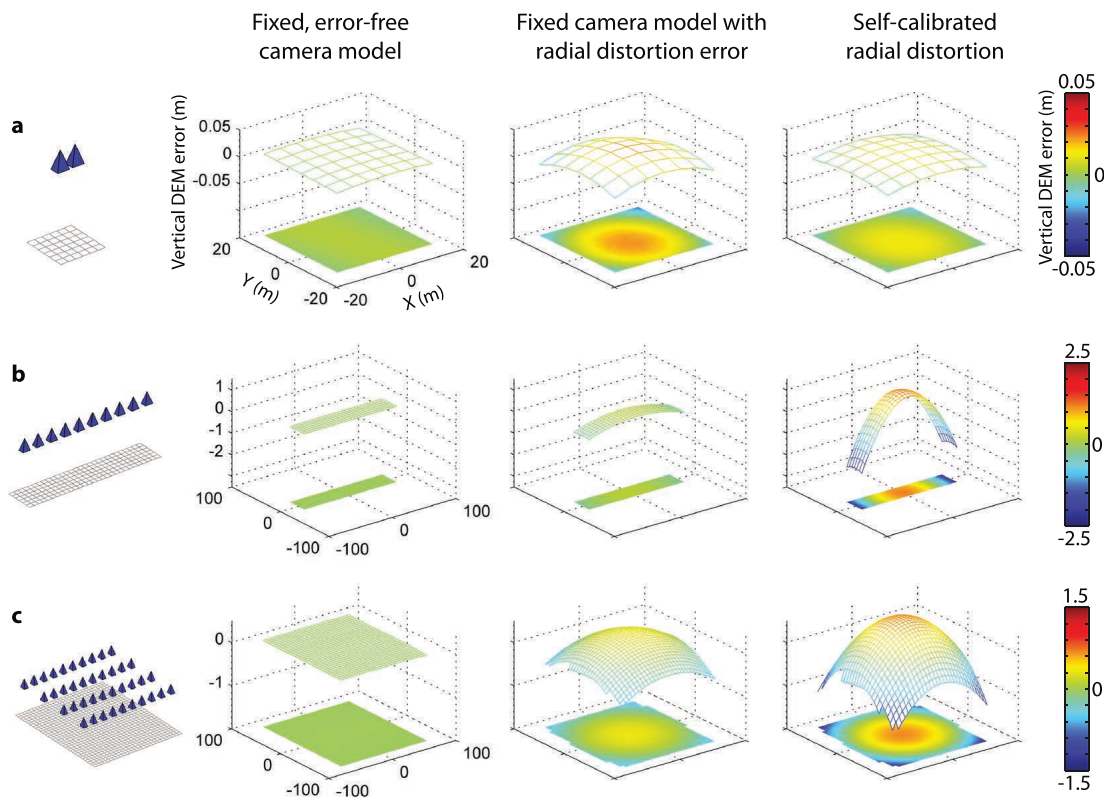


Figure 2.3: Examples of ambiguous configurations. The first column shows the acquisition procedure, the second column is the model obtained with an accurate camera calibration, the third column is the result obtained with a erroneous fixed calibration and is similar in shape to the model obtained using self-calibration (from: [James and Robson, 2014](#))

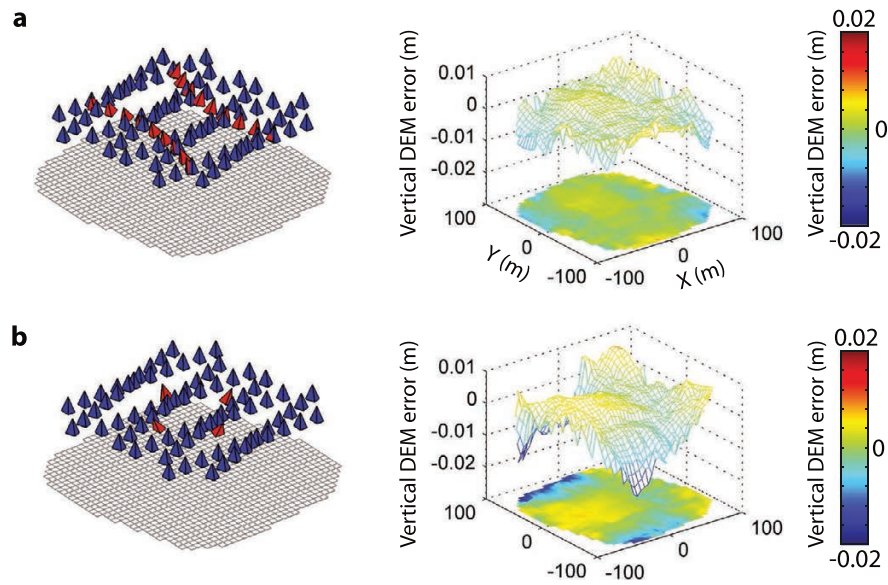


Figure 2.4: Examples of acquisition strategies eliminating the systematic errors. The camera added to consolidate the block are shown in red (from: [James and Robson, 2014](#))

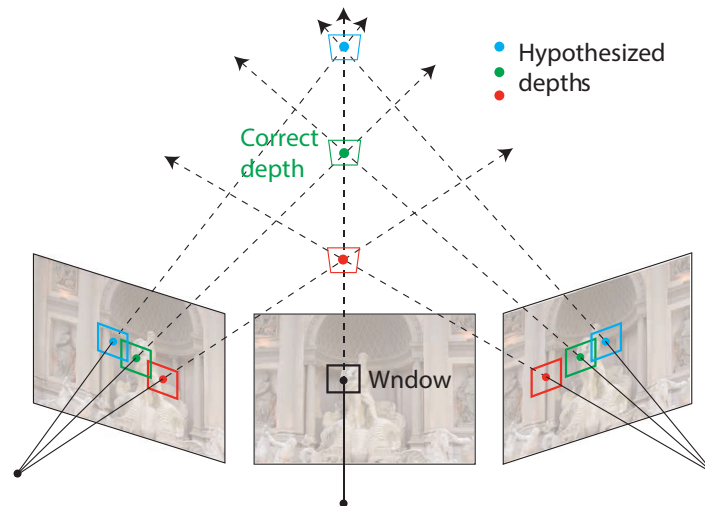


Figure 2.5: Different depth are hypothesized on the already orientated pictures and the one resulting with the best correspondence between the window's is kept (from: [Agarwal et al., 2011](#))

Several algorithms exist and their respective performance can be compared on the website of [Seitz et al. \(2015\)](#). Applying different algorithms to build a 3D point cloud of a landslide, [Stumpf et al. \(2015\)](#) obtained better results using the suite Apero/Micmac ([Pierrot-Deseilligny and Clery, 2011](#)) than using VisualSFM with PMVS2.

Apart from the performance regarding the accuracy, large difference in the number of points can be observed. Indeed, PMVS2 produces a unique 3D point for a feature present in several images, whereas Agisoft Photoscan can produce a point for each pixel of an overlapping photo pair, which means that a same feature can correspond to several points ([Remondino et al., 2014](#)). Therefore, filtering can be useful in the last case.

Georeferencing

As mentioned in the sparse reconstruction section, an arbitrary scale is attributed to the point cloud. Therefore, for many uses, the point cloud needs to be scaled. In addition, as for LiDAR point clouds, a georeferencing of the point cloud is often needed, in order to work with absolute coordinates. Table 2.1 summarizes the possible procedures that can be used to scale and georeference the point clouds.

Most of the geoscientific applications use ground control points (GCP) to register the point cloud in an absolute coordinate system (e.g. [Niethammer et al., 2012](#); [Fonstad et al., 2013](#); [Stumpf et al., 2015](#)). A smaller number of studies use another point cloud to co-register the SfM-MVS point cloud by manually picking the coordinates of recognizable features on the reference point cloud and by applying a transformation to the SfM-MVS point cloud including translation, rotation and scaling. An algorithm such as the iterative closest point (ICP; [Besl and McKay, 1992](#)) can then be applied to refine the co-registration by adjusting the translation and rotation (e.g. [James and Robson, 2012](#)). Finally, few studies only scale their point cloud by measuring a distance in the scene and by applying an homothetic transformation to the point cloud, and no study in the field of geosciences has been found applying no transformation at all, but it is frequently the case in papers concerning a methodological aspect (e.g. [Agarwal et al., 2011](#)).

As mentioned by [Fonstad et al. \(2013\)](#), georeferencing is often a seven-parameter linear transformation (one scale parameter, three translation parameters and three rotation parameters) applied after the point cloud processing. Therefore, if a non-linear error affects the model, as the dome effect mentioned in Sect. *Sparse reconstruction*, the quality of the point cloud might be seriously affected. However, some programs currently offer the possibility to use the GCP in the SfM process. Agisoft Photoscan offers an optimization tool, applied after a first bundle adjustment and a linear georeferencing, that tries to account for the GCP coordinates to optimize the bundle adjustment ([Agisoft LLC, 2014](#)). Apero, the bundle adjustment module of MicMac proposes

Table 2.1: Method used for scaling and georeferencing SfM-MVS point clouds

Method	Correction	Final use	Remark	Examples
—	—	Visualisation	—	Agarwal et al. (2011)
Distance measurement in the scene	Scale	Visualisation and relative comparison	Often imprecise	Volcanic bomb in James and Robson (2012) ; Morgenroth and Gomez (2014)
Ditto + compass orientation	Scale and orientation	Visualisation, relative comparison, structural analysis	Often imprecise	Approach A of Sturzenegger and Stead (2009)
Station location with GPS	Georeferencing	Visualisation, comparison, structural analysis	Precision depend on scale	—
Relative tie points	Co-registration (relative or absolute)	Visualisation, comparison (\pm structural analysis)	relative or absolute according to the reference	Coastal cliff section in James and Robson (2012) ; Micheletti et al. (2015)
Station location (and attitude) with DGPS	Georeferencing	Visualisation, comparison, structural analysis	Might improve the model	Forlani et al. (2014) ; approach B of Sturzenegger and Stead (2009)
Ground Control Points (GCP)	Georeferencing	Visualisation, comparison, structural analysis	Might improve the model, implies to access the scene	Niethammer et al. (2012)

to directly include GCP coordinates in the SfM process ([Pierrot-Deseilligny and Clery, 2011](#)). On the other hand, VisualSfM, which is widely used, does not offer this possibility. According to its developer, Changchang Wu, it is possible, although not straightforward, to incorporate 2D control points². Finally, to facilitate the georeferencing of point clouds after the SfM-MVS reconstruction, Sfm_georef³ ([James and Robson, 2012](#)) offers the possibility to locate the GCP on the original pictures rather than on the point cloud, and georeferences the point cloud on this basis.

2.2.2 UAS

Although drone and "Unmanned Aerial Vehicle" (UAV) are the most common terms used in the general public, "Unmanned Aircraft Systems" (UAS) is now the official term used by the International Civil Aviation Organization and correspond to the definition: "An aircraft and its

²<https://groups.google.com/forum/#!searchin/vsfm/GCP\protect\T1\textdollar20bundle\protect\T1\textdollar20adjustment/vsfm/aUApqoG4ARQ/jwQd9Pk511YJ>

³http://www.lancaster.ac.uk/staff/jamesm/software/sfm_georef.htm

associated elements which are operated with no pilot on board" (ICAO, 2011). This organisation also uses the acronym RPA, for "remotely piloted aircraft" to characterise the fact that a pilot is able to control the UAS when needed, even if the UAS is in flying autonomously the rest of the time. UAS is also the official term used by the US Department of Defence and by UK's Civil Aviation Authority (Colomina and Molina, 2014). These multiple terminologies reflect the recent an rapid development of the UAS field.

Eisenbeiß (2009), who gives a very detailed history and state of the art of UAS, classify the UAS according to the following categories:

Weight: heavier than air, lighter than air

Propelling: powered, unpowered

Wing type (when relevant): flexible (e.g kites, paragliders), fixed (e.g. planes) or rotating (e.g helicopters)

Eisenbeiss and Sauerbier (2011) review the use of UAS for archeological applications, which are quite similar to geoscientific application with regard, for example, to the dimensions or types of materials. Especially, they classify the UAS in different categories relevant to the archaeological applications, which adds the following distinctions:

Flight mode: manual, assisted or autonomous

Image acquisition mode: manual, stop-mode (the UAS hover at a waypoint, to insure stability in the image) or cruising mode.

The availability of UAS has been strongly increasing in the last decade. Indeed, although Eisenbeiss (2004) were already using an autonomous helicopter-like UAS, the use of such system was restricted to experimented users and the number of commercial models was low. Around 2008, MikroKopter started selling UAS component, that can be assembled following the instructions on their wiki, and that have been integrated in other projects (HiSystems GmbH, 2015). In 2009, Sensefly started selling turnkey autonomous fixed wing UAS, carrying a compact camera (Sensefly, 2015). The use of UAS has been greatly democratised when the DJI Phantom has been available, starting 2013. This UAS has been designed to carry a GoPro, to be very stable and easy to control, and is sold at a low price (around 500–1000 USD without the GoPro).

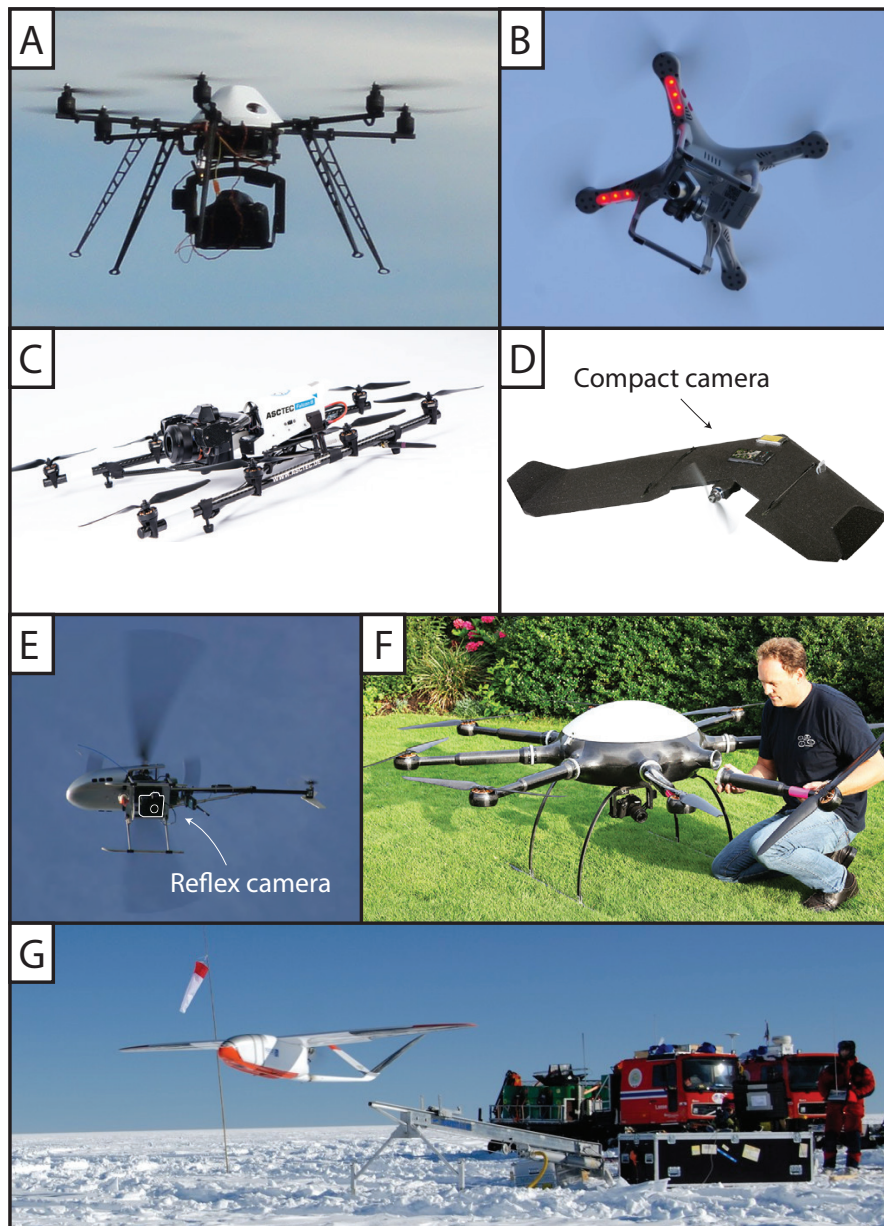


Figure 2.6: Different types of UAS used for aerial photography and SfM-MVS. A: Hexacopter in use at the University of Lausanne (photo: Marc Choffet); B: DJI Phantom Vision 2+ (photo: NGU); C: Octo-kopter (source: <http://www.asctec.de>); D: Fix-wing UAS (source: www.sensefly.com) E: Helikopter-like UAS (source: Eisenbeiß, 2009); F: BigOkto, a UAS in development designed for long operations (source: www.mikrokoetter.de); G: CryoWing, a UAS designed for polar regions by NORUT (source: <https://www.xsens.com/customer-cases/cryowing-fixed-wing-uav/>)



Figure 2.7: Pont Bourquin landslide viewed from the front and example of a target used for the georeferencing

2.3 Photogrammetry versus LiDAR

2.3.1 Transportability

One of the main advantages of SfM-MVS is the transportability. Since a consumer-grade camera is relatively light, it can easily be carried by a UAS. An example of Pont Bourquin landslide (Fig. 2.7) is described below. For a description of the landslide, see [Jaboyedoff et al. \(2009\)](#) or [Mainsant et al. \(2012\)](#).

The photos for the SfM-MVS model have been acquired on 25 August 2011 using a Canon 550D with a fix 20 mm lens carried by an Oktokopter produced by Mikrokopter ([HiSystems GmbH, 2015](#)) and assembled by FlyingEye⁴ (see Fig. 2.6 A). 39 pictures were acquired with the UAS and 9 from the ground (at the toe of the landslide). The UAS was operated manually with GPS and altimeter assisting modes and the pictures acquired manually in stop-mode in order to respect a 60 % overlap inside the bands.

The pictures have been processed in Agisoft Photoscan. Only 37 pictures have been used (including all the pictures from the toe) since the other pictures were causing problems to reconstruct the model. The model has been roughly georeferenced using 5 targets measured by total station on the 31 August 2011. Although the targets have not been significantly moving in six days, they are not ideal for georeferencing since their coordinates correspond to the reflector and not to the sphere located below (Fig. 2.7). Indeed, this latter has been used to georeference the point cloud since it is well visible on the pictures.

⁴<http://www.flyingeye.fr/>

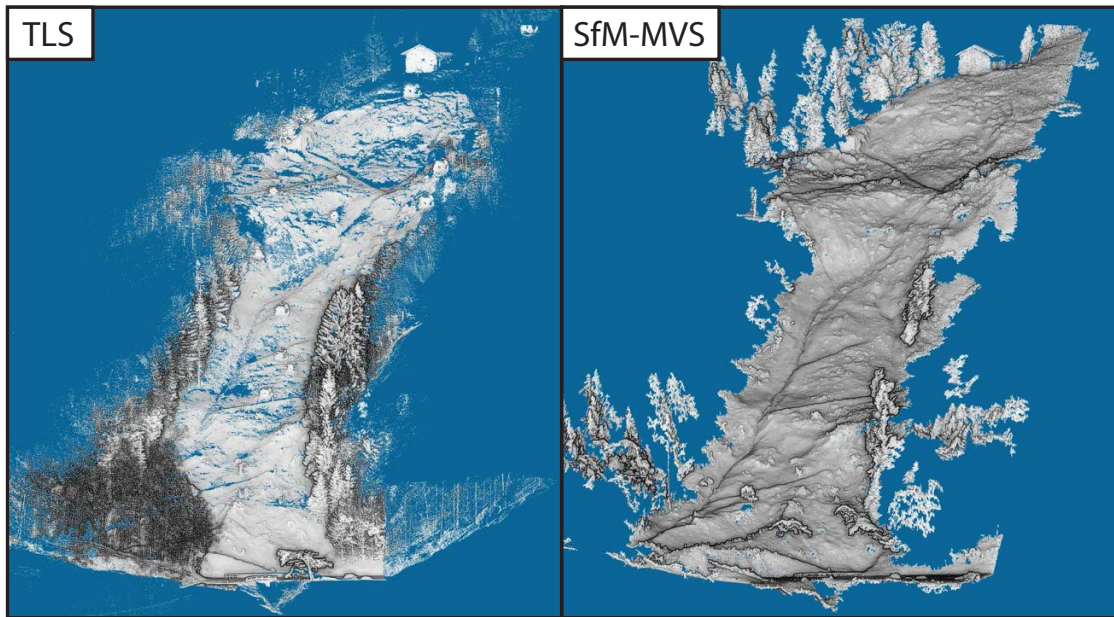


Figure 2.8: Comparison of the TLS and SfM-MVS point clouds of Pont Bourquin landslide viewed from the South. The shading is obtained using the Eye-dome Lighting function of CloudCompare

The SfM-MVS point cloud is compared with a LiDAR point cloud acquired on 11 May 2015. In order to cover all the landslide, 11 scans acquired at different position around the landslide were needed (Michoud et al., 2012b). The scans were then co-registered and georeferenced using the 1 meter aerial DEM as a reference.

In order to improve the alignment between the 2 clouds, a modified ICP (Besl and McKay, 1992) allowing scale variation was performed in CloudCompare, using the TLS point cloud as a reference.

A visual comparison of the resulting point clouds are given in Fig. 2.8 looking towards the North and in Fig. 2.9 viewed from above. It is possible to see from both comparison, but especially from the view from above, that the SfM point cloud allows a better coverage of the whole landslide. Indeed, ground-based LiDAR is not the best suited method for the flat areas or the counter-slopes formed by the trenches built to drain the landslide (lines visible on the LiDAR point cloud). Furthermore, the precision of the LiDAR is lower if the angle formed by the normal to the surface and the laser beam is too high.

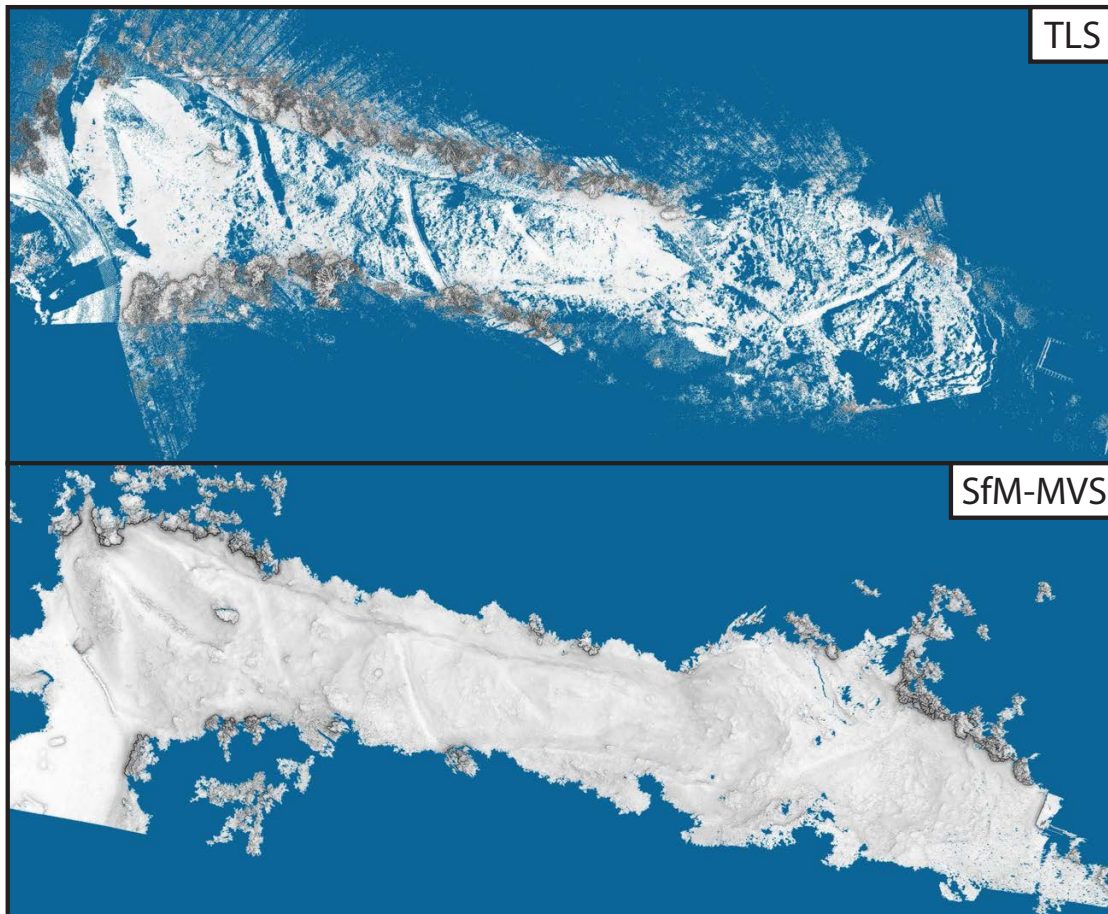


Figure 2.9: Comparison of the TLS and SfM-MVS point clouds of Pont Bourquin landslide viewed from above. The shading is obtained using the Eye-dome Lighting function of CloudCompare

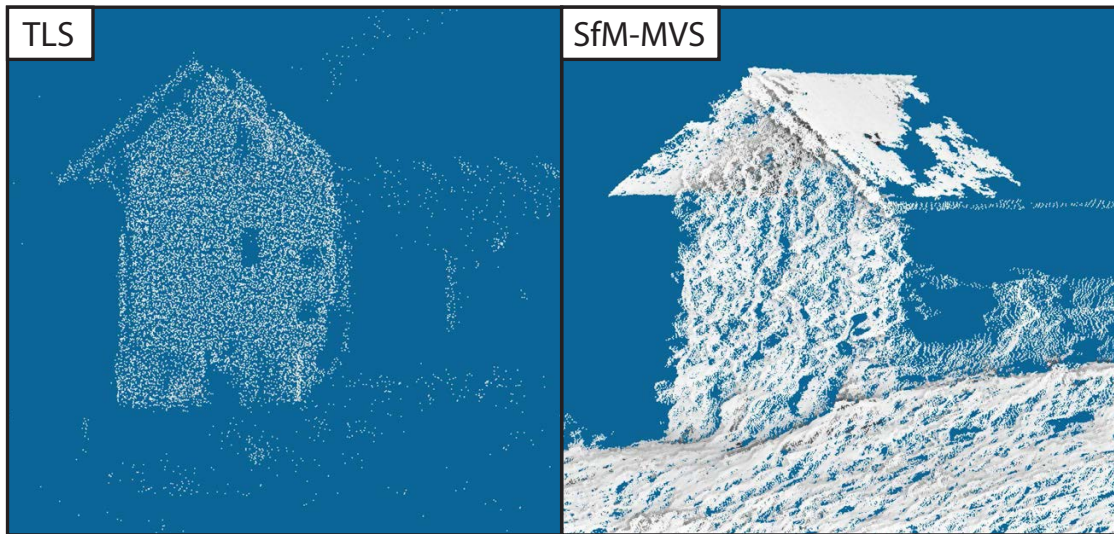


Figure 2.10: Comparison of the TLS and SfM-MVS point clouds of the house above Pont Bourquin landslide viewed towards the NW (325°). The shading is obtained using the Eye-dome Lighting function of CloudCompare

2.3.2 Errors

Although the results of Pont Bourquin landslide looks good when viewed globally, a more detailed look on the chalet above the landslide illustrate that SfM-MVS is not an error-free technique (Fig. 2.10), whereas LiDAR point clouds generally contain only small errors.

2.3.3 Sensitivity to the vegetation

When studying the temporal evolution of landslides, stable parts around the landslide are generally needed (e.g. [Oppikofer et al., 2009](#)). Often, vegetation covers these stable parts. This is for example the case of a landslide in Vully-Les-Lacs (Switzerland) presented in Fig. 2.11, where the landslide took place in a previously forested area. As a result of the landslide, the trees inside the landslide area have felt down, but logically not the ones located around.

A point cloud has been built using Agisoft Photoscan and is based on 27 pictures taken on 16 July 2013 with the same UAS and camera as in Sect. 2.3.1. The point cloud is roughly georeferenced by retrieving the position of the UAS at the time of each picture from the GPS track stored in the flight data recorder of the UAS using MKGPXExport⁵.

Figure 2.11 shows a comparison of a picture and the point cloud obtained with Agisoft Photoscan displayed with the colours and reproducing roughly the perspective of the picture.

⁵<http://www.mk-fr.info/forum/index.php?topic=651.0>

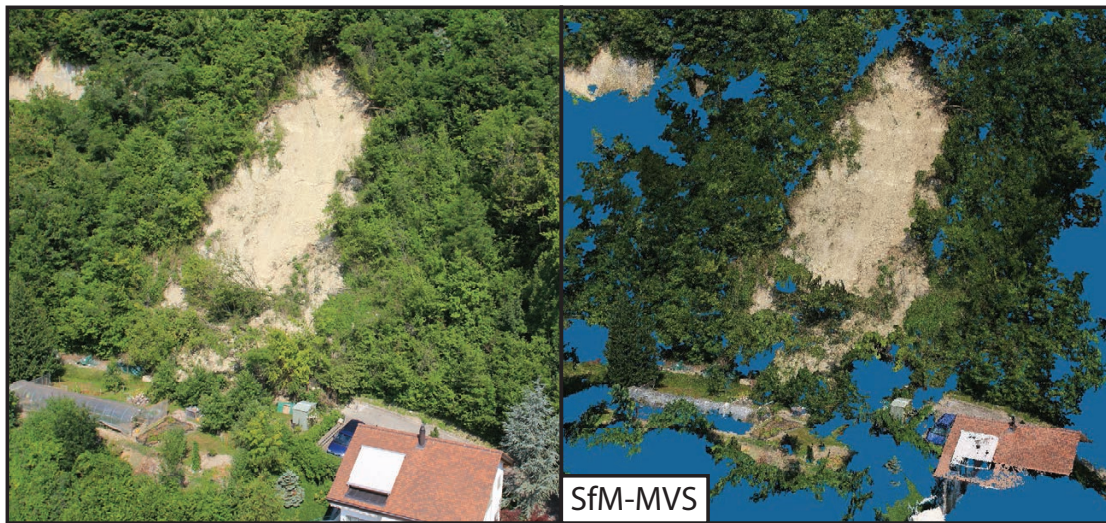


Figure 2.11: Pictures of a landslide in Vully-Les-Lacs (left) and SfM-MVS point cloud with RGB colours (right)

Although the point cloud is built also in stable parts such as the house, the road at the toe and the rock slope on the left, which would allow a co-registration with a point cloud acquired at another time, the points in the direct vicinity of the landslide are all vegetation. On the other hand, with a LiDAR point cloud, we could expect to have ground points as well in these areas. This is because part of the LiDAR laser beam might reach the ground, and, if the LiDAR is used in "last pulse" mode, the obtained range will often be the one of the ground, at least with sparse vegetation. When it comes to SfM-MVS, not only the ground needs to be visible in a picture, but the same ground point needs to be seen and recognised in another picture. Therefore, even sparse vegetation is often a problem with SfM-MVS. A synthetic explanation is given in Fig. 2.13.

2.3.4 Scaling and georeferencing

As mentioned in the state of the art, if no coordinates or reference scales are used in the reconstruction process, the point cloud is in a relative coordinate system and also possess a relative scale. Two case studies are presented below and aim at evaluating the performances of simple scaling and simple georeferencing, without using GCP. Sometimes, particularly for landslide applications the modelled scene does not allow the use of GCP, for example with unstable vertical rock faces, in which it would be complicated and dangerous to install targets.

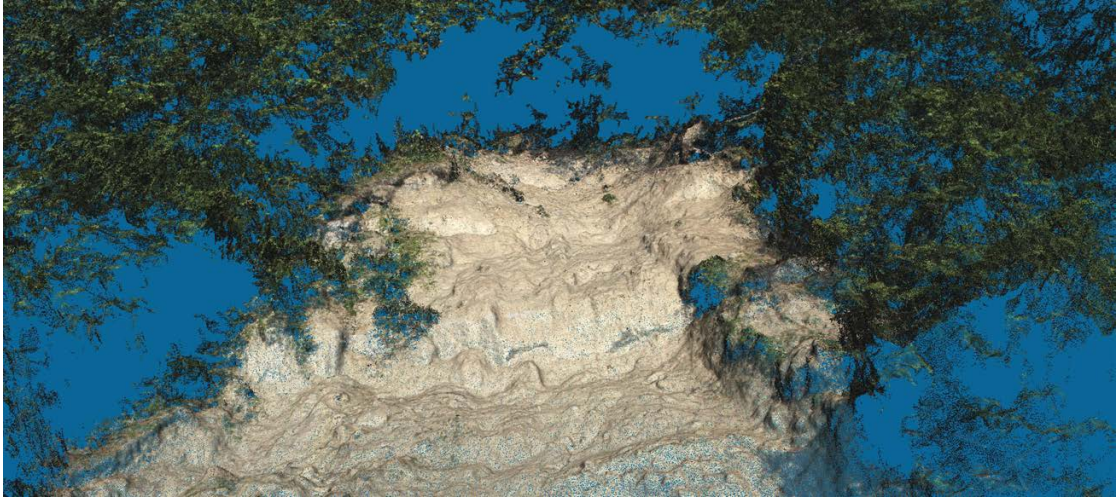


Figure 2.12: Upper part of the landslide point cloud seen from below. The ground around the landslide is not modelled although the vegetation is less dense in the direct vicinity of the landslide than farther.

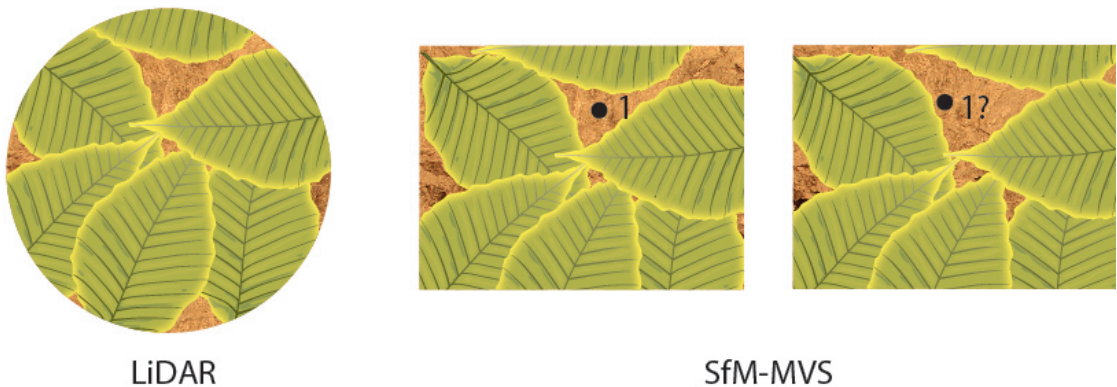


Figure 2.13: Synthetic example of the problem encountered with the vegetation using SfM-MVS. On the left, the LiDAR laser beam partly filtrates trough the leafs and the last pulse will correspond to the ground. On the other hand, point number 1, which is identified on the left picture, will be hard to identify on the right picture since the visible ground surface is small and the matching is affected by the surrounding leafs.

Simple scaling

An erratic block has been modelled several times in the framework of a master course. 5 sets of pictures have been taken in 2013 using a Canon 550D with a fixed-lens 20 mm objective, whereas in 2014, 3 sets have been acquired using the same material as well as 3 using the student's smartphones. The pictures have been taken every 0.5–1 meters along a circle at distance of around 4–5 meters from the block, representing a total of 30–40 pictures. To scale the model, the students measured an element of the scene, whereas the students of 2014 added a wooden board of known dimensions to the scene.

The pictures have then been processed using VisualSFM (Wu, 2015). The point cloud has then been segmented in CloudCompare (Girardeau-Montaut) in order to keep only the points belonging to the block. To close the volume, the part lying on the ground being not modelled, a Poisson reconstruction has been used (Kazhdan et al., 2006). This reconstruction allows forming a smooth surface, which is more realistic than using a plane. The octree depth being chosen by the students, the convexity is more or less pronounced on the different resulting models.

The point cloud has then been scaled by calculating the ratio of the reference length measured on the scene and the length of the same element in the point cloud.

Finally, the volume has been calculated in matlab using, in 2013, the script Alphavol (Lundgren, 2012) modified by Carrea et al. (2015). This script calculates the volume of a point cloud by defining tetrahedrons. If the volume is perfectly convex, then the script will give an exact result. Otherwise, the search radius has to be limited in order to avoid the closure of concavities. However, since the block contains no point inside, the search radius needs to be large enough to allow the block to be completely filled by tetrahedrons. To allow using a smaller radius, some points were manually added inside the volume.

In 2014, the mesh has been directly used to calculate the volume with a modified version of the script stlVolume (Suresh, 2010), which uses the divergence theorem.

The calculated volumes are presented in Fig. 2.16. The number of samples is too small to make definitive conclusions. However, some trends can still be explained. To start, the variability seems larger in 2013 and some volumes are largely inferior to the mean value. This is probably caused by a too small radius in the Alphavol calculation. Indeed, keeping an infinite radius (Fig. 2.15) gives a result only 7.8 % above the value obtained using stlVolume, which does not suffer from the problem of differentiating the inside from the outside. Indeed, with the model presented in Fig. 2.15, the (unscaled) volume obtained using stlVolume is 19.6 units³. The variability obtained using smartphones is larger than using a DSLR camera, which correspond to the expectation since the sensor is smaller. Finally, for all models, errors can be explained by the scaling process, in particular since the students measured a distance directly in the point

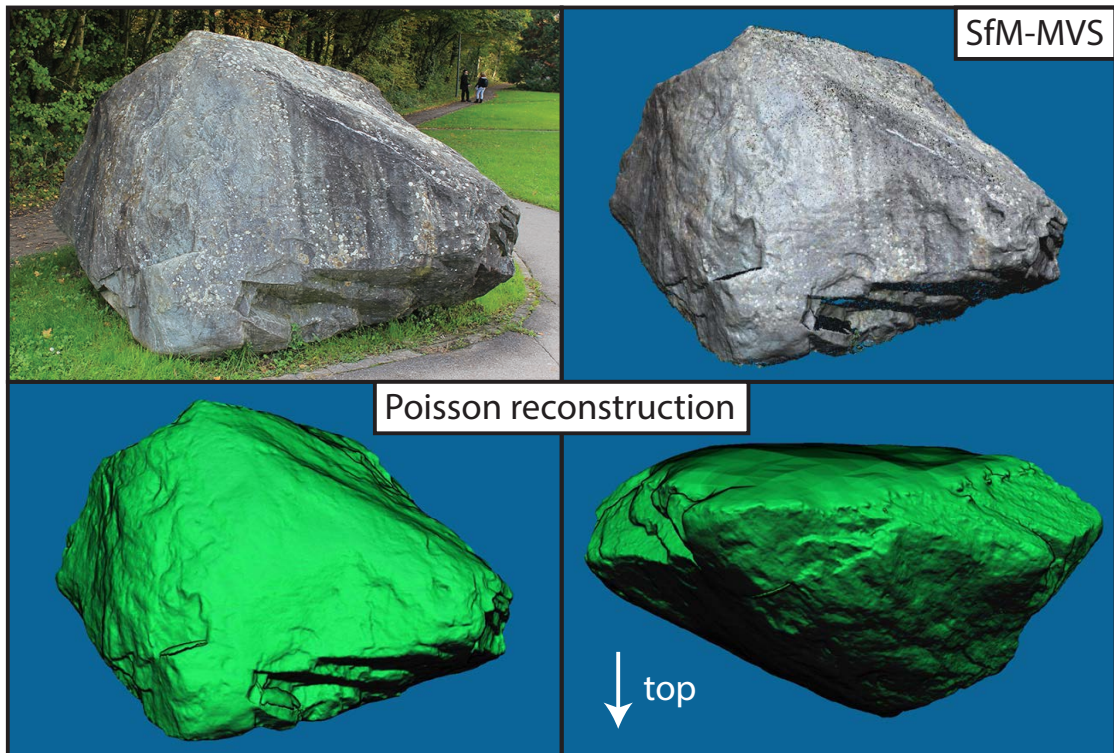


Figure 2.14: Picture of the modelled block and point cloud obtained with VisualSFM. The point cloud contain around one million points. The point cloud has then been transformed into a surface that is closed in the bottom part of the block.

cloud, which is not trivial (particularly with the less dense smartphone models). Better results could have been expected by measuring a distance in the pictures using, for example, `Sfm_georef` (James and Robson, 2012). If we consider that the points obtained using the reflex camera and `stlVolume` (2014) varies only because of the scaling, the dispersion is rather small, and thus the scaling quite accurate (keeping in mind that there is only 3 points and that the significance of the results is limited). In addition, part of the variability is explained by the octree depth used in the Poisson reconstruction.

2.3.5 Simple georeferencing

The Dent-du-Midi massif is located in Western Switzerland. In 2012, a rockfall event occurred and a team from the University of Lausanne went there to make measurements. The source area is about 60 meters high (Fig. 2.17) and is located on "La Forteresse", which is one of the peaks of the Dents-du-Midi massif.

LiDAR point clouds have been acquired for a large area including "La Forteresse" with an

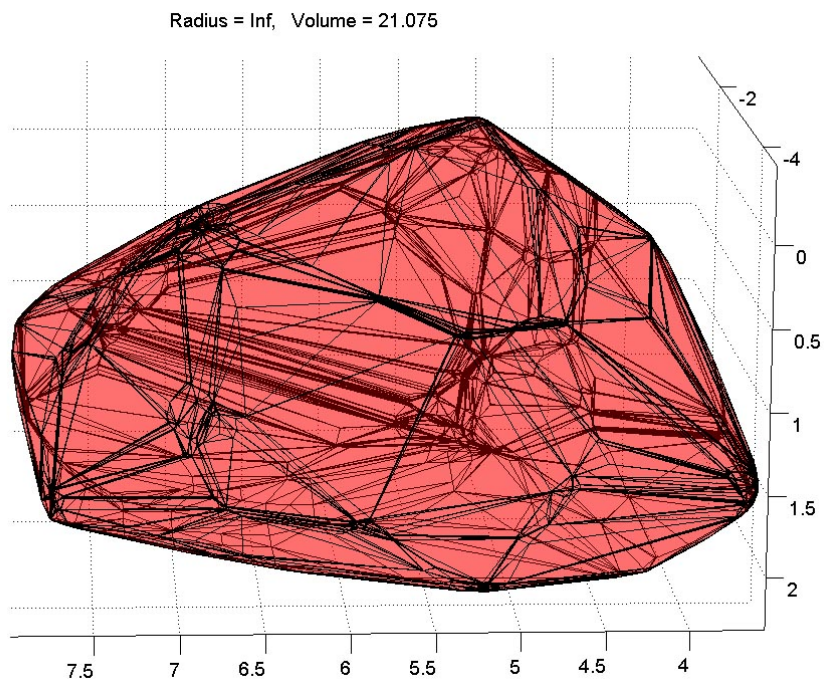


Figure 2.15: Using the script Alphavol with an infinite radius, the block has a volume of 21.075 units³. In this case the point cloud has not been scaled, so the volume is relative to the coordinate system. Calculating the volume of the same point cloud using stlVolume gives a volume of 19.6 units³

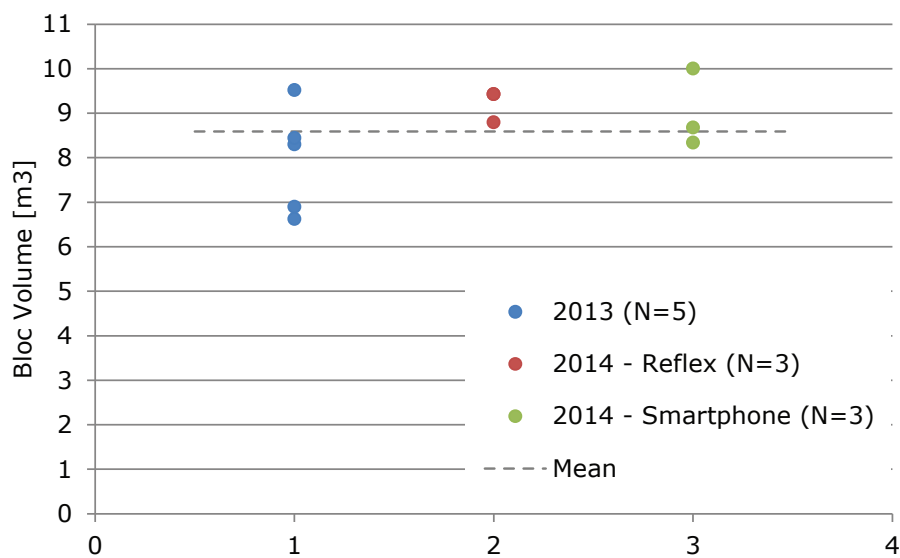


Figure 2.16: Volumes calculated by the students in 2013 and 2014. 2013 volumes are calculated using Alphavol, whereas 2014 volumes are computed with stlVolume.



Figure 2.17: Location of the rockfall scar on "La Forteresse" (modified from B. Rudaz, unpublished)

Optech Iris-LR (Matasci et al., 2015). In the meantime, 2 sets of pictures have been taken. The first set has been shot with a canon 550D using a 20 mm lens and covers roughly the same area as the LiDAR point cloud. The second set has been shot with the same camera, but with a 250 mm lens and focuses on "La Forteresse". The maximum range is of about 1200 m. The two models have been processed using VisualSFM (Wu, 2015). "La Forteresse" point cloud has been built using 528 images and has necessitated 58 hours of computation. 141 other images have been left out since no corresponding points have been found with the model. This might have been avoided by including pictures taken with a shorter focal to consolidate the block, as described in Pierrot-Deseilligny (2013). The resulting cloud contains 48 million points. The pictures have been taken from the locations shown in Fig. 2.18.

The cloud has been georeferenced using the GPS location of the stations, which are estimated with a precision of around 5 meters. To estimate the quality of the georeferencing, the SfM-MVS point cloud has been co-registered on the LiDAR mesh using a modified ICP (Besl and Mckay, 1992) allowing scale variation. The absolute coordinates of the LiDAR point cloud have been assessed by co-registering the point cloud on the 1 m DEM. The distribution of the distances from the SfM-MVS points to the LiDAR mesh are shown in Fig. 2.19 before and after the co-registration. The co-registration permits to centre the distribution on 0 and to reduce the standard deviation from 3.10 m to 0.66 m.

In addition, the point cloud has been scaled down by 0.42 % and rotated of 1.26° around the x-axis, -0.14° around the y-axis and -0.05° around the z-axis. Rotation angles have been estimated using the method described in Oppikofer et al. (2009). The smallest rotation angle around the z-axis (vertical) might be explained by the fact that GPS are more accurate on the XY plane. Indeed, although a barometer is often used to obtain a better precision on the vertical axis than the plane precision, the quality of the altitude estimation depends on the calibration

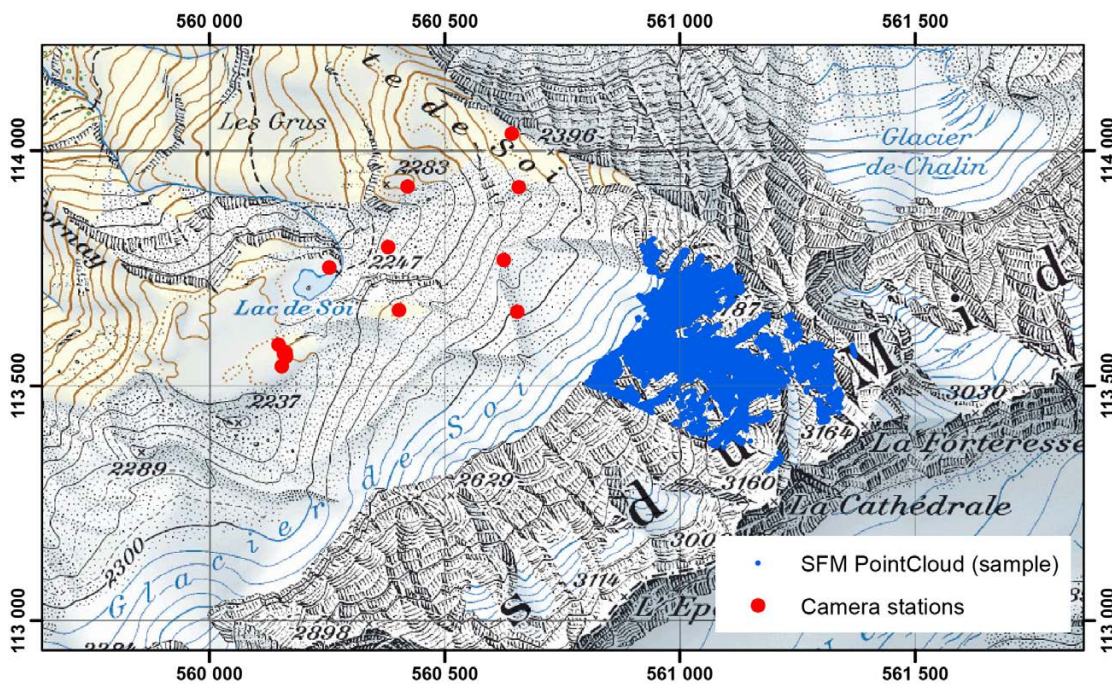


Figure 2.18: Location of the SfM-MVS stations and of the resulting point cloud

and on the time variations. Finally, the median distance between a point before and after the co-registration is 3.91 m.

2.3.6 Sensitivity to the reflector

In the case of the Dents-du-Midi rockfall event, the scar was partly covered by ice, as it can be seen on Fig. 2.17. In such situation, if the ice is pure, the LiDAR gets no return. On the other hand, VisualSfM has been able to model the ice covered part of the scar (Fig. 2.20).

2.3.7 Colour-based segmentation

By contrast with the LiDAR, which gives an intensity value, SfM-MVS returns a RGB colour based on the photography. To test the potential of semi-automatic segmentation based on the colour, the distribution of the colour intensity of the different formation are studied on the point cloud of the whole massif (Fig. 2.21). The same has been done with the LiDAR intensity of the Dents-du-Midi massif by [Matasci et al. \(2015\)](#), who obtained good results (Fig. 2.22). In addition, a similar comparison has been also been done by [Humair et al. \(2015\)](#), who obtained better results with the blue band of the SfM-MVS model than with the LiDAR.

For the LiDAR, as the intensity depend on the range and on the incidence angle, [Matasci et al.](#)

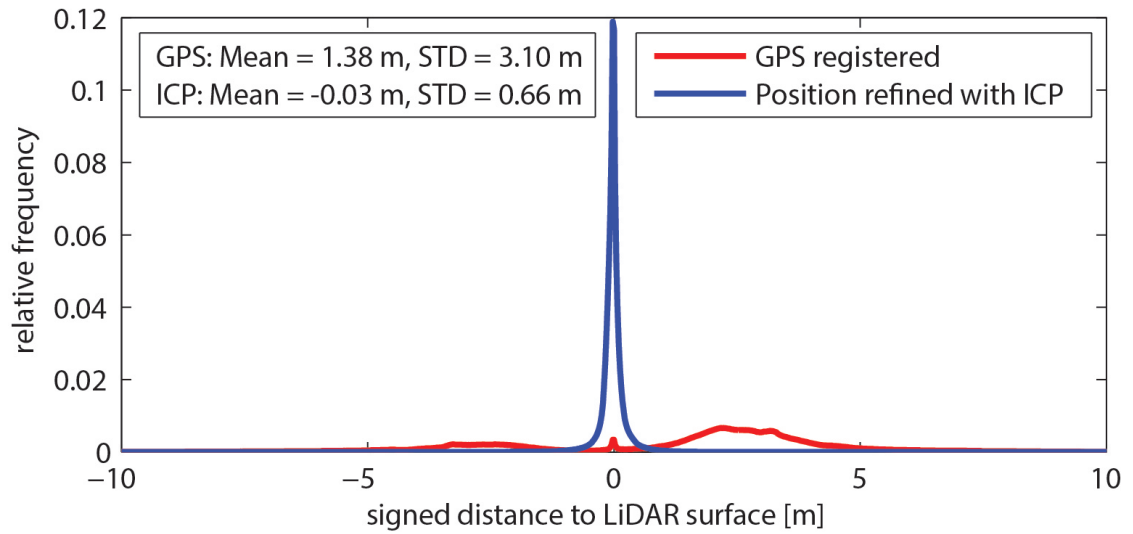


Figure 2.19: Distribution of the distances from the SfM-MVS points to the LiDAR mesh before (GPS registered) and after the co-registration (Position refined with ICP). The average distance and the standard deviation are also provided.

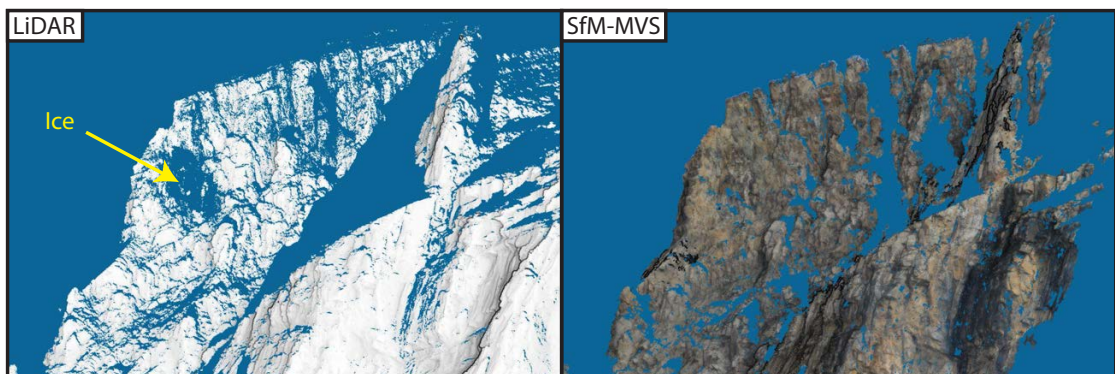


Figure 2.20: The part of the rockfall scar which is covered by ice did not return any signal from the LiDAR, whereas the SfM-MVS point cloud has not been affected by the presence of ice.

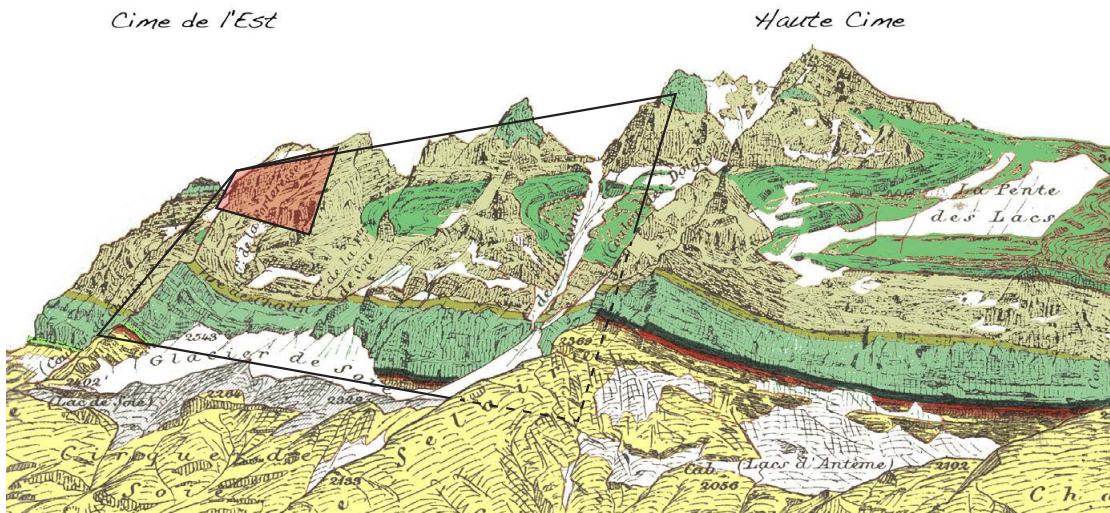


Figure 2.21: Geological cross-section from [De Loys and Gagnebin \(1926\)](#). The red window corresponds to Fig. 2.21 with another view angle (hence the perspective deformation of the window)

(2015) correct the intensity using the following equation:

$$I_{corr} = \frac{I_{raw} \times R^2}{\cos(0.75 \times \alpha)} \quad (2.5)$$

Where I_{raw} is the raw intensity, R is the range and α is the angle between the normal to the face and the incidence beam ([Carrea et al., 2016](#)).

When it comes to the SfM-MVS point cloud, it has been first segmented to keep only the interesting part and to remove the fringes, where the sky colour is attributed to the rock slope (Fig. 2.23). Then, it has been manually segmented in order to separate the different formations for the analysis. The distribution of the intensities for each band have been studied, and since they present similar characteristics, only the grayscale distribution is presented in Fig. 2.24. A colour-based segmentation seems not really possible since the overlapping of the distribution is quite large.

2.4 Perspectives and conclusion

To sum up, as compared to LiDAR, SfM-MVS possess the following advantages (modified from: [Pierrot-Deseilligny, 2013](#)):

- low-cost technique

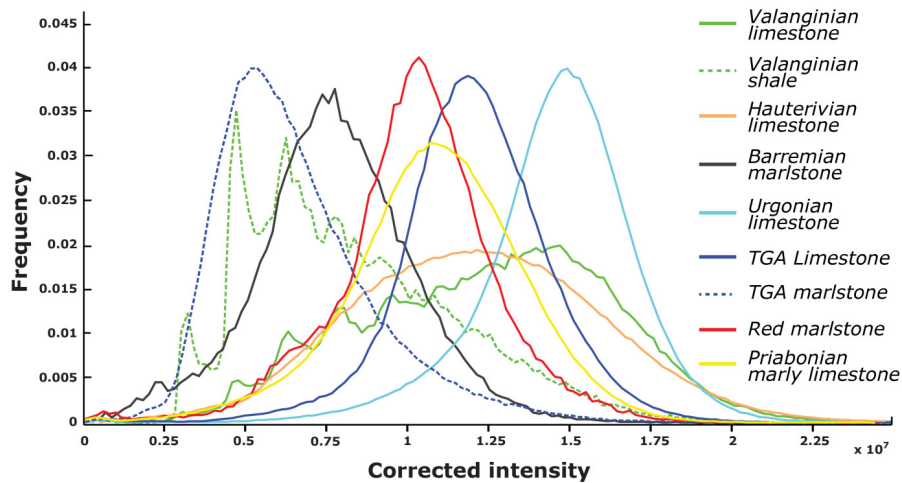


Figure 2.22: Corrected intensities obtained with the LiDAR for different lithologies (from: [Matasci et al., 2015](#))

- high portability (a camera can be carried by a small UAS)
- multiple working scales allowed, with varying precision
- can be performed with standard field equipment

On the other hand, SfM-MVS is affected by the following drawbacks:

- not error-free
- does not "penetrate" the vegetation
- the intensity is not univocal and depends on the lightening conditions
- scaling is needed and might affect the precision
- works on textured materials only, but sometimes on material for which a LiDAR gets no return
- the parameters such as the precision and the point density are harder to control

SfM-MVS techniques are expected to continue their development, in particular in the accessibility of such techniques and on the control of the precision. Some limitations will however remain such as the low ability to work with the vegetation. On the other hand, SfM is also assisting the development of UAS-borne LiDAR (Fig. 2.25). Indeed, apart from their weight, the main problem of using LiDAR on UAS is to precisely measure the position and the attitude of

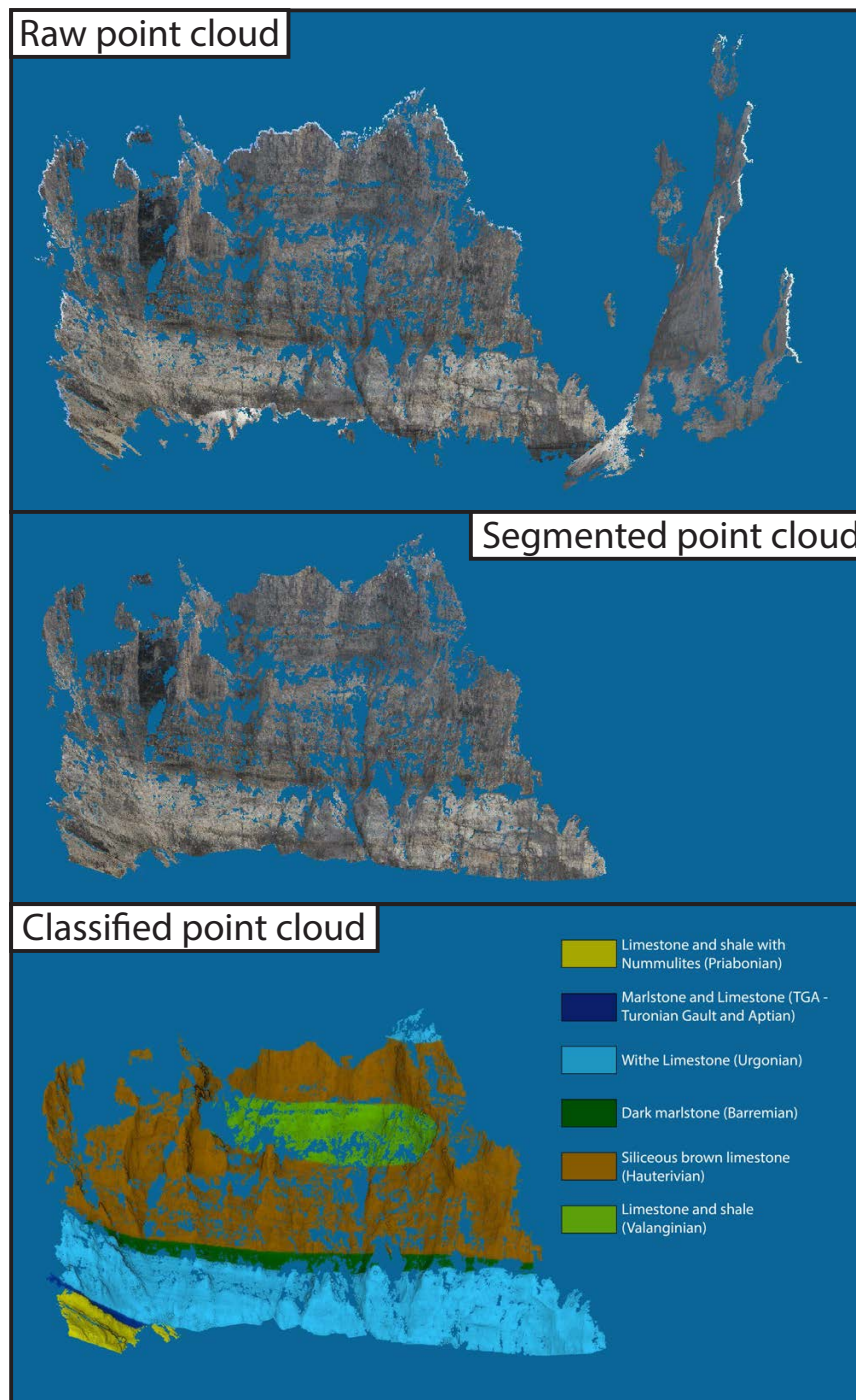


Figure 2.23: Procedure followed to classify the point cloud. A first operation is to segment the point cloud in order to remove the fringes where the sky colour is attributed to the cliff and to remove the small patches of points. Then, the point cloud is manually segmented in order to separate the different lithologies.

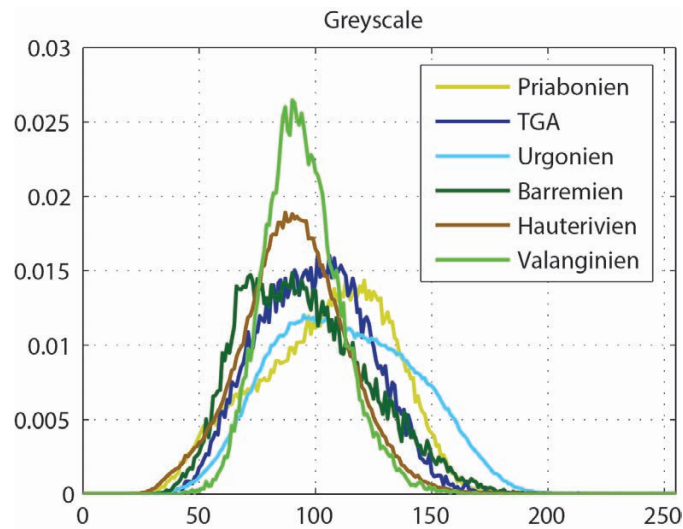


Figure 2.24: Distribution of the greyscale intensity for different lithologies. Although the Urgonian limestones have a slightly higher intensity as expected, the correlation is very small.

the UAS in order to know exactly where the LiDAR is shooting. Wallace et al. (2012) used SfM in order to refine the position and attitude of the UAS and to improve the LiDAR point cloud. They divided the horizontal RMSE by two by adding the SfM observation to the GPS and inertial measurement unit (IMU) measurements.

Finally, substantial improvements are expected in the UAS field, in particular regarding the system reliability and flight duration. In addition, a development of small LiDAR devices that can be carried by small UAS is awaited.

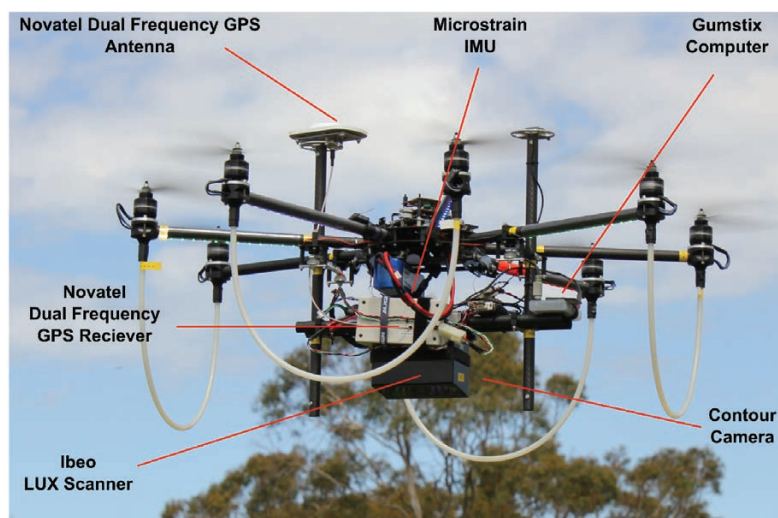


Figure 2.25: UAS carrying a LiDAR and other devices such as a HD video-camera (from: [Wallace et al., 2012](#))

Chapter 3

Cost-benefit analysis

3.1 Introduction

Cost-benefit analysis is one of the methods used to decide if protective measures should be implemented or not (e.g. [Fell, 1993](#); [Marzocchi and Woo, 2009](#); [Boonyanuphap, 2013](#)). It consists in comparing the cost of a protective measure to the risk reduction that this measure offers. In cost-benefit analyses, risk reduction is expressed in monetary terms, which distinguish this method from a cost effectiveness analysis, where the benefits are evaluated qualitatively (e.g. [Fuchs et al., 2007](#); [Ganderton, 2005](#)). It is therefore a tool that is appropriate for governmental institutions that need an objective method to allocate their resources. In the USA, the Federal Emergency Management Agency requires a protection measure to be cost-effective and offers a tool to assess that ([FEMA, 2015](#)). In Switzerland, such an analysis is also required for the funding of protective measures by the confederation ([Bründl et al., 2009](#)) and is also performed for national roads ([Dorren et al., 2009](#)) and railroads ([Bründl et al., 2012](#)). For the funding of measures protecting buildings, the Swiss Confederation offers an on-line tool named EconoMe to perform the analysis ([BAFU, 2016a](#)). Since the previous versions of this tool were relatively slow and complicated, a simplified version, based on an excel spreadsheet and named Valdorisk, has been developed and is presented here. These analyses are based on the products established during the standardised hazard mapping process.

For natural hazard considered as repetitive, Swiss hazard maps are made by combining scenarios of different return periods, which is an approach often used internationally, especially for floods (e.g. [Ward et al., 2011](#)). In Switzerland, three predefined classes of return periods are considered, namely 0–30, 30–100 and 100–300 years ([Loat and Petrascheck, 1997](#); [Raetzo et al., 2002](#), see also Sect. 1.2.5). In practice, the worst scenario of each class is chosen, which corresponds to the highest return periods, i.e. 30, 100 and 300 years. These return periods are

then used for the risk analysis. Such maps are established for snow avalanches, floods, debris-flow and rock falls. The procedure of hazard mapping is therefore to define a scenario for each of the return period classes (e.g. block size for rock falls, rate of overflow at a critical point for floods; this part is referred as the magnitude hereafter) and to model or estimate the spatial distribution of intensities, classified according to predefined thresholds. This approach is based on the fact that the frequency–magnitude of most natural hazard is characterised by a heavy-tailed distribution such as a power law (e.g. [Guzzetti et al., 2002](#)). The three scenarios are then combined keeping the highest class of hazard retrieved in a matrix (Fig. 1.17). The resulting hazard map is then used for land planning. However, when it comes to risk analysis, the intensity maps are used, since they assess the frequency and intensity of an event.

This chapter presents the formulas used in Valdorisk (Sect. 3.2) as well as the program architecture (Sect. 3.3).

3.2 Formulas

The formulas used to calculate the risk in Valdorsik are mostly similar to the ones used in EconoMe, which are described in detail in [Bründl et al. \(2016\)](#). A short summary is given here.

3.2.1 Risk analysis

Common parameters

Risk is calculated for different objects, both for the objects themselves (e.g. buildings) and for their occupants. Although the risk calculation is different for the different object types, some principles are used for all risk calculations. For example, for a single object, risk is calculated for each scenario (i.e. for each intensity map). Therefore, the final risk is the sum of the partial risk calculated for each scenario:

$$R_{\text{tot}} = \sum_j R_j \quad (3.1)$$

With R_j the risk for scenario j (e.g. for the scenario 30 years). For this sum to be correct, the scenarios should not contain other scenarios. Indeed, if the scenario 30 years is defined as the intensity that is reached or overpassed on average once in 30 years, then the 100 years scenario is included in the 30 years scenario. To illustrate this, an example that could correspond to rockfalls is presented in Fig. 3.1, where the volume of random events is calculated using a Pareto inverse cumulative distribution function:

$$F^{-1}(u) = \frac{x_{\min}}{u^{\frac{1}{b}}} \quad (3.2)$$

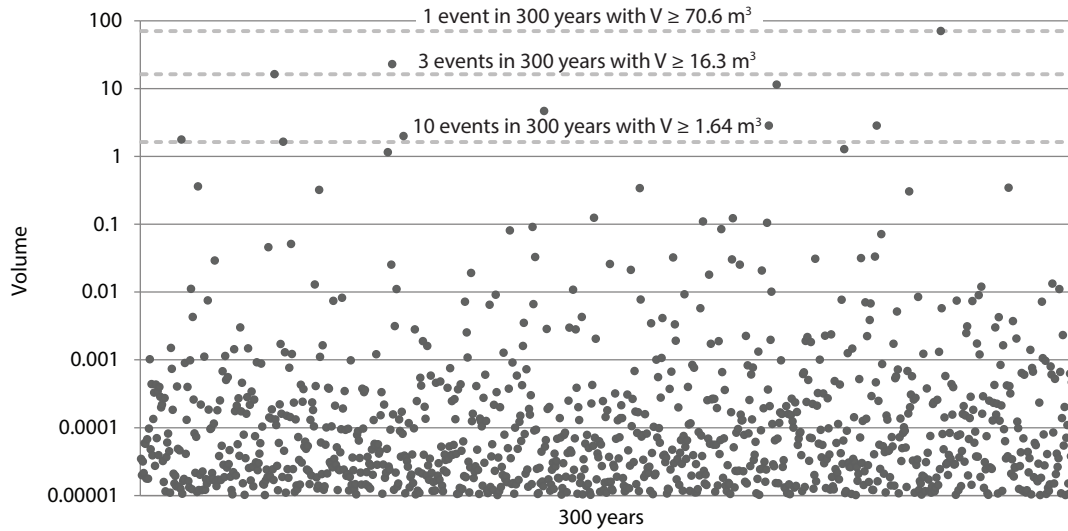


Figure 3.1: Simulation of rockfall volumes over 300 years using a value of 0.45 for parameter b of the power law. The simulations are computed using a Pareto inverse cumulative distribution function with threshold $x_{\min} = 10^{-5} \text{ m}^3$. The scenario 300 years is defined here as the volume that is reached once in a 300 years period (the scenario is defined on the raw data and, therefore, don't correspond precisely to the theoretical one). Similarly, the scenario 100 years is defined as the volume that is reached or overpassed on average once every 100 years, or 3 times every 300 years. As a result, the scenario 300 years is included in the scenario 100 years.

Where u is a random variable uniformly distributed between 0 and 1 and b the shape parameter of the distribution and corresponds to the parameter b of the power law (Fig. 1.10). x_{\min} is the minimum value of the distribution, since the power law needs to be truncated to allow a sampling process. The number of events N_{events} to create to represent N_{years} is given by:

$$N_{\text{events}} = N_{\text{years}} \times a \times x_{\min}^{-b} \quad (3.3)$$

Where a is a scale parameter and corresponds to the parameter a of the power law (Fig. 1.10). Figure 3.1 shows that the event used for the 300 years scenario is also included in the 100 years scenario and so on. Therefore, the frequency of the next scenario (if there is one) has to be removed:

$$f'_j = \begin{cases} f_j - f_{j+1} & \text{for } j \leq j_{max} \\ f_j & \text{for } j = j_{max} \end{cases} \quad (3.4)$$

This implies that the frequency of the 30 years scenario, which would individually be 1/30, becomes:

$$f'_{30} = f_{30} - f_{100} = \frac{1}{30} - \frac{1}{100} \cong \frac{1}{42.86} \cong 0.02333 \quad (3.5)$$

This implies that an event with a return period between 30 and 100 years occurs on average every 42.86 years.

Finally, since in the Swiss hazard mapping procedure, the frequency is defined at the source and does not vary spatially on the intensity maps, the spatial occurrence probability parameter P_S accounts for the fact that the area or the length actually affected in case of an event might be smaller than the area or the length defined in the intensity map (see Sect. 4.2.2 for further details). It is then defined as the proportion of the area (or length) that is actually affected.

$$P_S = \begin{cases} \frac{S_E}{S_H} & \text{for punctual/areal objects} \\ \frac{W_E}{L_H} & \text{for linear objects} \end{cases} \quad (3.6)$$

With S_E the expected affected surface in case of an event, S_H the surface affected in the intensity map, W_E the width of an event on a linear object (i.e. the expected affected length) and L_H the length affected in the intensity map.

When it comes to the risk before and after implementing the measure, they are calculated the same way, using the respective intensity maps. The economic efficiency of the measure is reached if the risk reduction, that is the difference between the risk before and the risk after measures, the "benefit", is greater than the annual cost of the measure, the "cost".

Punctual objects

The risk for static objects considered as punctual such as building is given by:

$$R_j = f'_j \times P_S \times V_{i,j} \times E_i \quad (3.7)$$

where $V_{i,j}$ is the vulnerability of the object i in scenario j and E_i is the value of the object i .

The collective monetised risk for people in punctual objects is obtained from:

$$R_j = f'_j \times P_S \times P_{ST} \times \lambda_{i,j} \times N_i \times 5 \times 10^6 [\text{CHF}] \quad (3.8)$$

where P_{ST} is the temporal spatial probability of the humans to be inside the object (i.e. the fraction of the time that they spend in this building, also known as exposure), $\lambda_{i,j}$ is the lethality of the process for the humans in object i considering the scenario j and N_i is the total number of persons that might be in the object. A value of 5 million CHF is used to monetise a human life.

In addition to the collective risk, which is used for the cost-benefit analysis, the individual risk is calculated in order to check that no individual is subject to an unacceptable risk. It is calculated as follows:

$$R_j = f'_j \times P_S \times P_{ST} \times \lambda_{i,j} \quad (3.9)$$

Linear objects

For linear objects such as roads, the damage to the road is considered, as well as the risk for the vehicle passengers. Risk for the road is very similar to the risk for punctual object, except that linear objects might be affected by different intensities of the process:

$$R_j = f'_j \times P_S \times V_{i,j} \times (l_l + l_m + l_h)_{i,j} \times E_i \quad (3.10)$$

Therefore, the value is calculated by multiplying the length affected by the different intensities (low: l_l , medium: l_m and high: l_h) by a unit value E_i expressed in CHF/m. The vulnerability of the road needs to be adjusted to the different intensities and is simply a mean intensity weighted by the respective lengths:

$$V_{i,j} = \frac{(V_l \times l_l) + (V_m \times l_m) + (V_h \times l_h)}{(l_l + l_m + l_h)} \quad (3.11)$$

The risk for the vehicle occupants is given by:

$$R_j = f'_j \times P_{ST} \times N_P^{\text{affected}} \times \lambda \times 10^6 [\text{CHF}] \quad (3.12)$$

Where P_{ST} is the temporal spatial probability of a vehicle being affected by the event. It is further discussed in Chapt. 4. It is obtained by:

$$P_{ST} = \frac{f_V \times (W_E + L_V)}{24000 \times v_V}, \quad (3.13)$$

where f_V is the average number of vehicles per day, v_V is the mean vehicle velocity, W_E

is the width of the event on the road and L_V is the average length of the vehicles. 24 000 is a correction factor that allows to express v_V in km/h and f_V in vehicles per day. λ is the weighted average lethality and is given by:

$$\lambda_{i,j} = \frac{(\lambda_l \times l_l) + (\lambda_m \times l_m) + (\lambda_h \times l_h)}{(l_l + l_m + l_h)} \quad (3.14)$$

The number of persons affected by the scenario is the lowest value from (i) the total number of persons in the vehicle and (ii) the number of persons in the length of the vehicle affected by the event plus a 4 m buffer. This correction avoids considering that all the passengers of a train are affected by an event and is further discussed in Chapt. 4:

$$N_P^{\text{affected}} = \min \left[\frac{N_P^{\text{total}} \times (W_E + 4)}{L_V}, N_P^{\text{total}} \right] \quad (3.15)$$

The individual risk is calculated in a comparable manner, considering a number of passages z for the temporal spatial probability:

$$R_j = f'_j \times P_{ST} \times \lambda \quad (3.16)$$

$$P_{ST} = \frac{z \times (W_E + 4)}{24\,000 \times v_V}, \quad (3.17)$$

The default z value is 4 (2 round-trips), but the parameter can be modified.

3.2.2 Cost of the measures

To be compared to the reduction of the risk, which is expressed in CHF/y, the cost of the measures has to be annualised. The cost generally depends mostly on the initial investment (I_0) and the life expectancy of the measure (n), but other costs might be important as well. These costs are related to the exploitation (K_b), the maintenance (K_u) or the reparation (K_r). In addition, an interest rate t is considered since the money invested for the measure is not invested for something else, that might have fructified. The annual cost is then:

$$K_{tot} = K_b + K_u + K_r + I_0 \times \frac{t}{1 - (1 + t)^{-n}} \quad (3.18)$$

Depending on the calculation, one can also consider that after n years, the measure still has a remaining value. This is not possible in the formula presented above, but *Valdorisk* uses the function "PMT" of excel, that allows for this possibility (Microsoft, 2016). This function is designed to calculate the amount of constant periodic payments that needs to be made in order to

reimburse a debt subject to a constant interest rate in a defined period of time.

3.3 Architecture

Valdorisk consists of an excel workbook with several worksheets. The different worksheets are listed in table 3.1. In addition to the worksheets, a VBA project contains scripts accessible from individual sheets or from the whole workbook¹. Some scripts are triggered by specific actions such as when a sheet is activated.

In addition to the sheets themselves, a number of forms are accessible and facilitate the data collection (an example is given in Fig. 3.2). The general work-flow followed by a user is presented in Fig. 3.3. The user first enters the basic parameters of the projects (name, date, ...) and selects the types(s) of processes for which he or she does the analysis. The workbook is designed to study the following phenomenon:

- Snow avalanches
- Rockfalls
- Deep-seated landslides with continuous movement
- Deep-seated landslides with episodic movement
- Debris-flows
- Static flood
- Dynamic flood
- Rock avalanches

The category "Deep-seated landslides with continuous movement" does not exist in EconoMe, where risk is calculated for this type of hazard using the usual 3 return periods. However, the intensity maps are not available for the 3 return periods for deep-seated landslides since the one column matrix presented in Fig. 1.17 (p. 42) is used. Therefore, this new category allows calculating a small damage occurring every year, or a damage occurring after some years of continuous movement. The limitation of this category is that the corresponding vulnerabilities are not known. Therefore, it should only be used with a greater care. Then, once the phenomena are selected, a sheet with the intensities and a sheet with the risk is created for each phenomena.

¹the workbook is accessible on the website of the Cantonal administration (<http://www.vd.ch/themes/environnement/forets/informations-techniques/subventions/prevention-dangers-naturels/valdorisk/>) and the scripts are accessible on a Bitbucket repository (<https://bitbucket.org/pnicolet/valdorisk>)

The screenshot shows a software window titled "Properties of object 1". It contains several input fields and sections:

- Category of object:** A dropdown menu set to "Bâtiments".
- Type of object:** A dropdown menu set to "01 - Unité de logement maison individuelle (2.24 personnes s)".
- Reference of the object (facultative):** A text input field containing "Blue house".
- Value of the object:** Two radio buttons: "Automatic" (unselected) and "Manual" (selected). The "Manual" option has a text input field with "650000" and a unit dropdown set to "CHF".
- Humans:** Two radio buttons: "Automatic" (unselected) and "Manual" (selected). The "Manual" option has two text input fields: "Average number" with "2" and "Exposure" with "1".
- Vulnerability and letality parameters:** A section with two radio buttons: "Automatic" (selected) and "Manual" (unselected). Below them is a "Phenomenon" dropdown set to "CPB" with left and right arrow buttons. Under "Intensity", there are three radio buttons: "Low", "Medium", and "High". Below these are two rows of three text input fields each: "Vulnerability" (0.03, 0.3, 0.6) and "Letality" (0.00003, 0.003, 0.18).
- Road and rail traffic:** A section with five text input fields: "ADT", "Length of the train", "Velocity", "Number of passengers", and "Number of daily crossings (individual risk)".

At the bottom of the window are four buttons: "Previous", "Cancel", "OK", and "Add an object".

Figure 3.2: Form designed to facilitate the collection of objects information. In this example, the form permits to enter the properties of an object such as its category and type, its value (calculated automatically from predefined values or entered manually), the number and exposure of humans, the vulnerability parameters (for each phenomenon if several are defined) and the road or railway specific parameters.

In the same sheet, the user can select the number and type of measures. The possible measures are similar to the ones available in EconoMe, with the exception of two new types. The first one is the object-based measure. The idea behind this measure type is that it is not the intensity for a given return period that is reduced, but the vulnerability of the object. If this measure is used, the operator does not input the intensity after measure in the intensity sheet, but the vulnerability of the object after the measures. The other new category is the maintenance of a protection forest. The idea behind this is to calculate the cost-benefit of an already existing measure, which has no investment cost, but only annual maintenance costs. The use of these new categories is however not trivial since no default value exists.

Table 3.1: Worksheets available in Valdorisk workbook. Intensities and risk sheets are copied from the templates for each process selected by the user. These copies are then visible and editable. 1+ and 2+ means that the sheets are visible as soon as one process or more or, respectively, two processes or more are selected. Finally, no data can be entered or modified by the user in the graphs and summary sheets, but some options can be selected.

Name	Visible	Editable	Content
Home	Yes	Yes	Basic information such as the name of the project and the date, but also the selection of the type of processes (snow avalanches, rockfalls, ...) and the number and type of protection measures.
Objects	Yes	Yes	Information on the studied objects (houses, roads, ...) such as the value, the human exposure and the vulnerability and lethality for each intensity (low, medium and high) of the studied processes.
Measures	Yes ^a	Yes	Basic information on the protection measures (price, life expectancy, ...)
XX_intensities	No	Yes	Template copied for each selected type of process containing the intensities for each object in each scenario
XX_risk	No	No	Template copied for each selected type of process containing the risk for each object in each scenario (as well as the aggregated risks)
Risk total	Yes ^b	No	Sum of the risk for all processes (if more than one is selected)
Graphs	Yes ^c	(No)	Different graphs to summarise the risk (some options on the graph types are available in drop-down lists)
Summary	Yes ^c	(No)	Printer-friendly summary of all the information. The summary is created automatically, but old versions can be kept as comparison. A logo can be added to the report
Vulnerability	Yes	No	Default values of vulnerability for each object type and each process type. These values are retrieved from EconoMe
Measures costs	Yes	No	Default values for the annual costs of the measures (that are proportional to the investment cost)
PrA	Yes	No	Default values of spatial occurrence probability

^aIf one or more protection measures are selected

^bIf 2 or more hazard types are selected

^cIf 1 or more hazard type is selected

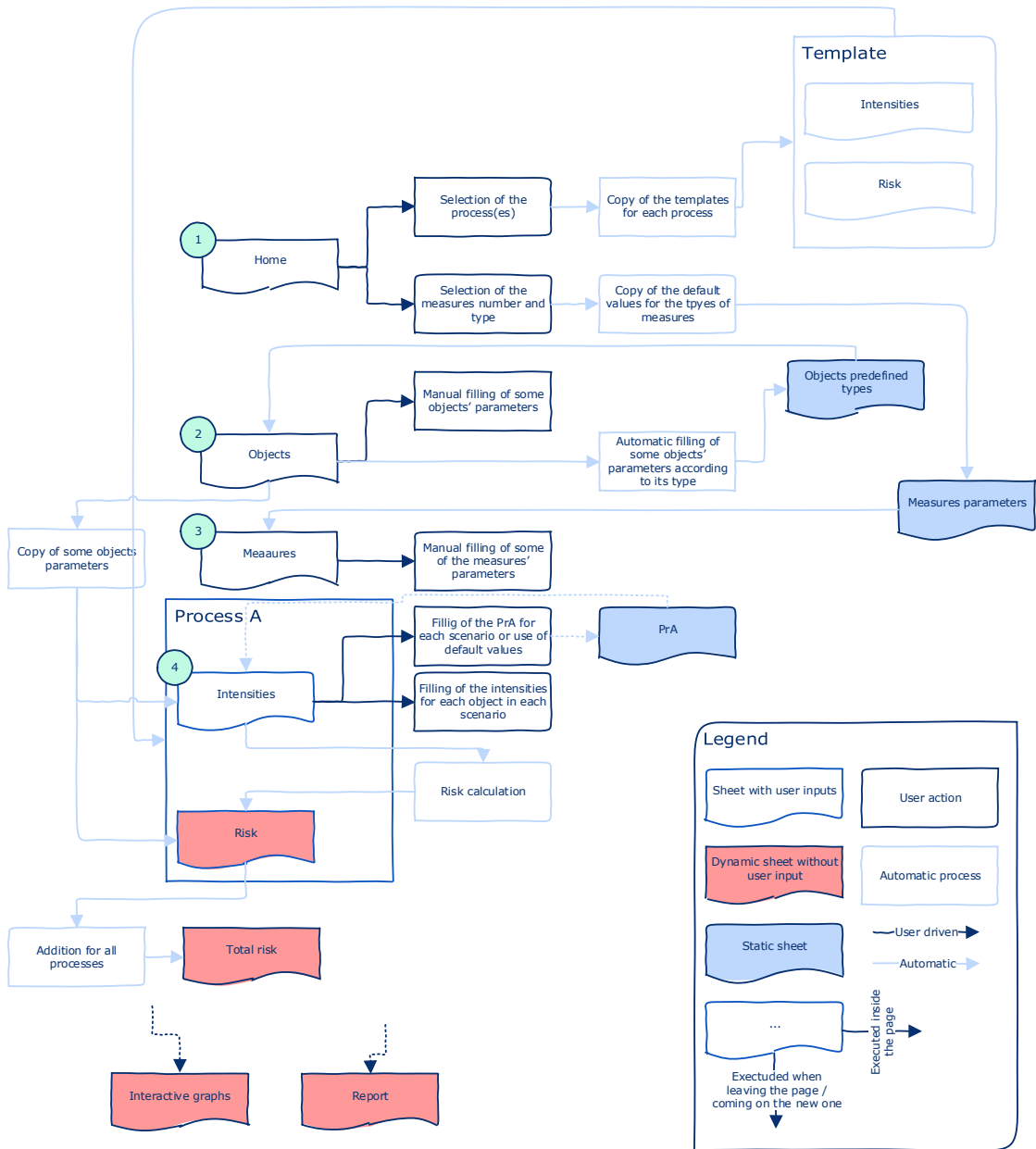


Figure 3.3: Flow chart of the general procedure used to assess the risk with Valdorisk including both the processes done by the user (dark blue) and the automatic procedures (light blue). The navigation between the different sheets generally follows the order indicated in the green rounds. Many procedures are triggered by an event such as entering or leaving a page. The graphs and the report aggregate data from many sheets. Therefore, the arrows have not been drawn to simplify the reading.

3.4 Example

To illustrate the use of this tool, an example is given hereafter. This example will be used through the following chapters, to illustrate the inclusion of uncertainty in the risk analysis (Chapt. 5) and to discuss the symbology of the hazard maps after measures are taken (Chapt. 6).

The village of Chardonne, in the Canton of Vaud, is located on the slope of the Mont Pélerin. Conglomerates and sandstones blocks from the Lower Freshwater Molasse sometimes detach from the rock slopes and fall on or close to infrastructures. This happened in 2007, when 3 blocks of 0.5 m³ fell in a garden in the area "en Courlaz" (Joliquin et al., 2010). After this event, a project of protection measures has been planned. To assess the efficiency of the measure, intensity and hazard maps have been established both without measures (Fig. 3.4–3.7) and with the expected effect of the planned protection measures (Fig. 3.8). Without protection measure, 4 scenarios have been established with return periods of 5, 30, 100 and 300 years. With the protection measure, Joliquin et al. (2010) expect that rockfall will occur only in the 300 years scenario. Then, a risk analysis has been made manually by using largely the principles of EconoMe (Winkler, 2010).

The risk analysis is reproduced with Valdorisk for the buildings only. Indeed, the risk analysis presented in (Winkler, 2010) considers also the risk to the roads and to the land parcels, but the number of objects (108) is too important for Valdorisk, which is limited to 50 objects for technical reasons. The buildings are positioned on Fig. 3.4 to 3.8 with the number of the land unit as label (several buildings can have the same number) and the intensity as symbol colour. Three types of buildings are present here: buildings with one housing unit ("individual houses"), buildings with several housing units ("multi-housing building") and garages. Each type of building has its individual predefined vulnerability for rockfalls for each intensity (table 3.2). (Winkler, 2010) also obtained the value of each building and the number of inhabitants from the municipality. The number of inhabitants (N_i) is used here, but since the values of the buildings are confidential, the default values presented in EconoMe are used here. The cost of multi-housing buildings is estimated considering two housing units. When it comes to the temporal spatial probability of the inhabitants, a value of one is considered, which corresponds to what Winkler (2010) used in the calculations. The parameters of each building, as well as the monetised risks are presented in tables 3.3 (before measures) and 3.4 (after measures).



Figure 3.4: Intensity map for the 5 years scenario without protection measure (modified from: Joliquin et al., 2010; Winkler, 2010)

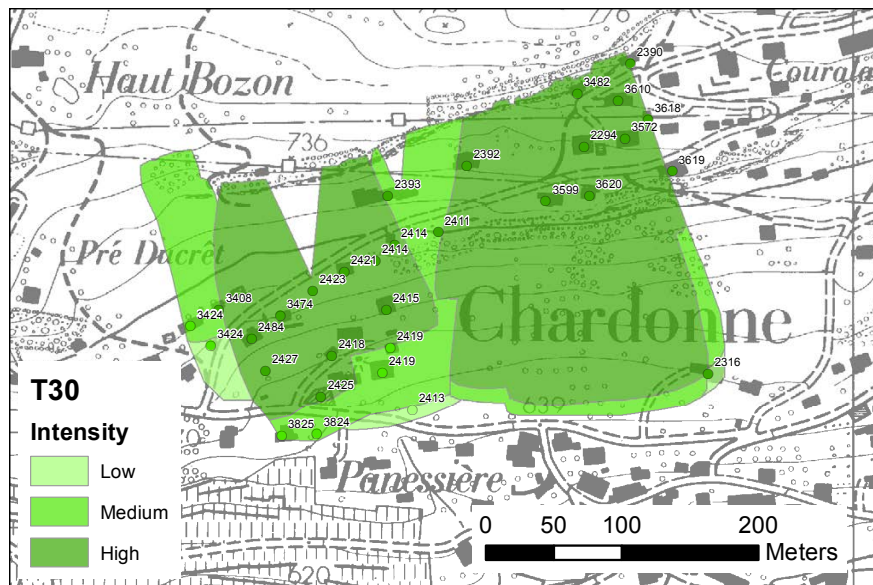


Figure 3.5: Intensity map for the 30 years scenario without protection measure (modified from: Joliquin et al., 2010; Winkler, 2010)

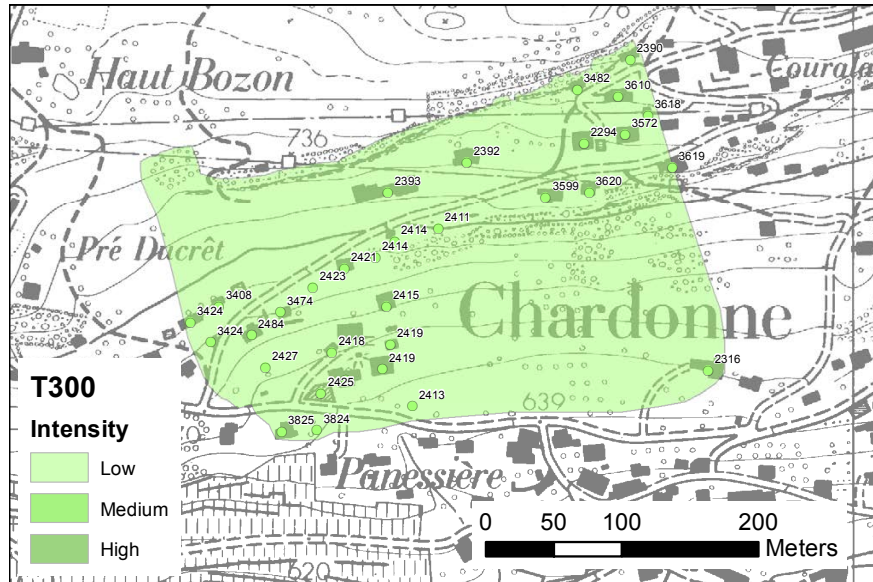


Figure 3.8: Intensity map for the 300 years scenario after the construction of protection measures (modified from: [Joliquin et al., 2010](#); [Winkler, 2010](#))

Table 3.2: parameters used for the vulnerability and the lethality. The values are extracted from EconoMe 3.0 ([BAFU, 2016b](#))

Intensity	Vulnerability ($V_{i,j}$)			Lethality ($\lambda_{i,j}$)		
	Low	Medium	High	Low	Medium	High
Individual house	0.03	0.3	0.6	0.00003	0.003	0.18
Multi-housing building	0.01	0.1	0.2	0.00001	0.0002	0.02
Garage	0.03	0.5	0.9	0.0003	0.05	0.54

Table 3.3: Parameters of the buildings and monetised risk before the construction of measures

Object type	Plot of land	E_i	N_i	P_{ST}	Material					Human					Total
					T5	T30	T100	T300	Total	T5	T30	T100	T300	Total	
Individual house	2294	650'000	2	1	3'250.00	455.00	104.00	65.00	3'874.00	15'000.00	2'100.00	480.00	300.00	17'880.00	21'754.00
Individual house	2316	650'000	2	1	3'250.00	455.00	104.00	65.00	3'874.00	15'000.00	2'100.00	480.00	300.00	17'880.00	21'754.00
Individual house	2390	650'000	2	1	-	455.00	104.00	65.00	624.00	-	2'100.00	480.00	300.00	2'880.00	3'504.00
Multi-housing building	2392	1'100'000	2	1	-	256.67	58.67	36.67	352.00	-	233.33	53.33	33.33	320.00	672.00
Multi-housing building	2393	1'100'000	12	1	916.67	256.67	58.67	36.67	1'268.67	100.00	1'400.00	320.00	200.00	2'020.00	3'288.67
Multi-housing building	2411	1'100'000	4	1	916.67	256.67	58.67	36.67	1'268.67	33.33	466.67	106.67	66.67	673.33	1'942.00
Garage	2413	60'000	0	0	15.00	2.10	8.00	5.00	30.10	-	-	-	-	-	30.10
Individual house	2414	650'000	1	1	-	455.00	104.00	65.00	624.00	-	1'050.00	240.00	150.00	1'440.00	2'064.00
Garage	2414	60'000	0	0	-	63.00	14.40	9.00	86.40	-	-	-	-	-	86.40
Individual house	2415	650'000	1	1	1'625.00	455.00	104.00	65.00	2'249.00	125.00	1'050.00	240.00	150.00	1'565.00	3'814.00
Individual house	2418	650'000	4	1	1'625.00	455.00	104.00	65.00	2'249.00	500.00	4'200.00	960.00	600.00	6'260.00	8'509.00
Garage	2418	60'000	0	0	250.00	63.00	14.40	9.00	336.40	-	-	-	-	-	336.40
Individual house	2419	650'000	1	1	1'625.00	227.50	52.00	32.50	1'937.00	125.00	17.50	4.00	2.50	149.00	2'086.00
Garage	2419	60'000	0	0	250.00	35.00	8.00	5.00	298.00	-	-	-	-	-	298.00
Individual house	2421	650'000	3	1	1'625.00	455.00	104.00	65.00	2'249.00	375.00	3'150.00	720.00	450.00	4'695.00	6'944.00
Individual house	2423	650'000	5	1	1'625.00	455.00	104.00	65.00	2'249.00	625.00	5'250.00	1'200.00	750.00	7'825.00	10'074.00
Individual house	2425-2426	650'000	0	1	1'625.00	455.00	104.00	65.00	2'249.00	-	-	-	-	-	2'249.00
Individual house	2427	650'000	3	1	162.50	455.00	104.00	65.00	786.50	3.75	3'150.00	720.00	450.00	4'323.75	5'110.25
Individual house	2484	650'000	5	1	162.50	455.00	104.00	65.00	786.50	6.25	5'250.00	1'200.00	750.00	7'206.25	7'992.75
Individual house	3408	650'000	2	1	1'625.00	455.00	104.00	65.00	2'249.00	250.00	2'100.00	480.00	300.00	3'130.00	5'379.00
Individual house	3424	650'000	0	1	-	227.50	52.00	65.00	344.50	-	-	-	-	-	344.50
Garage	3424	60'000	0	0	-	35.00	8.00	9.00	52.00	-	-	-	-	-	52.00
Individual house	3474	650'000	2	1	-	455.00	104.00	65.00	624.00	-	2'100.00	480.00	300.00	2'880.00	3'504.00
Individual house	3482	650'000	2	1	3'250.00	455.00	104.00	65.00	3'874.00	15'000.00	2'100.00	480.00	300.00	17'880.00	21'754.00
Individual house	3514	650'000	2	1	1'625.00	455.00	104.00	65.00	2'249.00	250.00	2'100.00	480.00	300.00	3'130.00	5'379.00
Individual house	3572	650'000	5	1	3'250.00	455.00	104.00	65.00	3'874.00	37'500.00	5'250.00	1'200.00	750.00	44'700.00	48'574.00
Individual house	3599	650'000	2	1	3'250.00	455.00	104.00	65.00	3'874.00	15'000.00	2'100.00	480.00	300.00	17'880.00	21'754.00
Individual house	3610	650'000	2	1	3'250.00	455.00	104.00	65.00	3'874.00	15'000.00	2'100.00	480.00	300.00	17'880.00	21'754.00
Garage	3618	60'000	0	0	-	63.00	14.40	9.00	86.40	-	-	-	-	-	86.40
Individual house	3619	650'000	4	1	-	455.00	104.00	65.00	624.00	-	4'200.00	960.00	600.00	5'760.00	6'384.00
Individual house	3620	650'000	2	1	3'250.00	455.00	104.00	65.00	3'874.00	15'000.00	2'100.00	480.00	300.00	17'880.00	21'754.00
Individual house	3824	650'000	4	1	-	227.50	52.00	32.50	312.00	-	70.00	16.00	10.00	96.00	408.00
Individual house	3825	650'000	3	1	-	227.50	52.00	32.50	312.00	-	52.50	12.00	7.50	72.00	384.00
Total					38'423.33	11'041.10	2'531.20	1'618.50	53'614.13	129'893.33	55'790.00	12'752.00	7'970.00	206'405.33	260'019.47

Table 3.4: Parameters of the buildings and monetised risk after the construction of measures

Object type	Plot of land	E_i	N_i	P_{ST}	Material					Human					Total
					T5	T30	T100	T300	Total	T5	T30	T100	T300	Total	
Individual house	2294	650'000	2	1	-	-	-	3.25	3.25	-	-	-	0.05	0.05	3.30
Individual house	2316	650'000	2	1	-	-	-	3.25	3.25	-	-	-	0.05	0.05	3.30
Individual house	2390	650'000	2	1	-	-	-	3.25	3.25	-	-	-	0.05	0.05	3.30
Multi-housing building	2392	1'100'000	2	1	-	-	-	1.83	1.83	-	-	-	0.02	0.02	1.85
Multi-housing building	2393	1'100'000	12	1	-	-	-	1.83	1.83	-	-	-	0.10	0.10	1.93
Multi-housing building	2411	1'100'000	4	1	-	-	-	1.83	1.83	-	-	-	0.03	0.03	1.87
Garage	2413	60'000	0	0	-	-	-	0.30	0.30	-	-	-	-	-	0.30
Individual house	2414	650'000	1	1	-	-	-	3.25	3.25	-	-	-	0.03	0.03	3.28
Garage	2414	60'000	0	0	-	-	-	0.30	0.30	-	-	-	-	-	0.30
Individual house	2415	650'000	1	1	-	-	-	3.25	3.25	-	-	-	0.03	0.03	3.28
Individual house	2418	650'000	4	1	-	-	-	3.25	3.25	-	-	-	0.10	0.10	3.35
Garage	2418	60'000	0	0	-	-	-	0.30	0.30	-	-	-	-	-	0.30
Individual house	2419	650'000	1	1	-	-	-	3.25	3.25	-	-	-	0.03	0.03	3.28
Garage	2419	60'000	0	0	-	-	-	0.30	0.30	-	-	-	-	-	0.30
Individual house	2421	650'000	3	1	-	-	-	3.25	3.25	-	-	-	0.08	0.08	3.33
Individual house	2423	650'000	5	1	-	-	-	3.25	3.25	-	-	-	0.13	0.13	3.38
Individual house	2425-2426	650'000	0	1	-	-	-	3.25	3.25	-	-	-	-	-	3.25
Individual house	2427	650'000	3	1	-	-	-	3.25	3.25	-	-	-	0.08	0.08	3.33
Individual house	2484	650'000	5	1	-	-	-	3.25	3.25	-	-	-	0.13	0.13	3.38
Individual house	3408	650'000	2	1	-	-	-	3.25	3.25	-	-	-	0.05	0.05	3.30
Individual house	3424	650'000	0	1	-	-	-	3.25	3.25	-	-	-	-	-	3.25
Garage	3424	60'000	0	0	-	-	-	0.30	0.30	-	-	-	-	-	0.30
Individual house	3474	650'000	2	1	-	-	-	3.25	3.25	-	-	-	0.05	0.05	3.30
Individual house	3482	650'000	2	1	-	-	-	3.25	3.25	-	-	-	0.05	0.05	3.30
Individual house	3514	650'000	2	1	-	-	-	3.25	3.25	-	-	-	0.05	0.05	3.30
Individual house	3572	650'000	5	1	-	-	-	3.25	3.25	-	-	-	0.13	0.13	3.38
Individual house	3599	650'000	2	1	-	-	-	3.25	3.25	-	-	-	0.05	0.05	3.30
Individual house	3610	650'000	2	1	-	-	-	3.25	3.25	-	-	-	0.05	0.05	3.30
Garage	3618	60'000	0	0	-	-	-	0.30	0.30	-	-	-	-	-	0.30
Individual house	3619	650'000	4	1	-	-	-	3.25	3.25	-	-	-	0.10	0.10	3.35
Individual house	3620	650'000	2	1	-	-	-	3.25	3.25	-	-	-	0.05	0.05	3.30
Individual house	3824	650'000	4	1	-	-	-	3.25	3.25	-	-	-	0.10	0.10	3.35
Individual house	3825	650'000	3	1	-	-	-	3.25	3.25	-	-	-	0.08	0.08	3.33
Total					-	-	-	85.30	85.30	-	-	-	1.63	1.63	86.93

The results are presented in Valdorisk in a risk worksheet (from where the data of tables 3.3 and 3.4 have been extracted) as well as in the Graphs and Summary worksheets. The graph worksheet contains a dynamic graph presenting the risk for each object (Fig. 3.9), a static graph comparing the total costs with and without protection measures (Fig. 3.10) and, if several types of processes are studied, a pie presenting the contribution of each type of process to the total risk. The summary worksheet presents all the values in a standardised manner. The values that do not correspond to the default values are highlighted. The global summary that is presented at the beginning of the report is presented in Fig. 3.11. In this example, since high intensities are reached already in the 5-years scenario before the measures, this scenario produces the main contribution to the total risk. The 30-years scenario also produces a significant contribution since higher intensities are reached in some places as compared to the 5-years scenario. Both the 100-years and 300-years scenarios contribute less to the total risk since they are relatively similar to the 30-years scenario in terms of intensity, but with a much lower frequency. When it comes to the risk after measures, since it results only from low intensities in the 300-years scenario, it is very low. Thus, since the protection measure has a cost of 111 938.13 CHF/year and reduces the risk from 260 019.47 CHF/year to 86.93 CHF/year, its benefit-cost ratio is 2.32 and the measure is therefore economical.

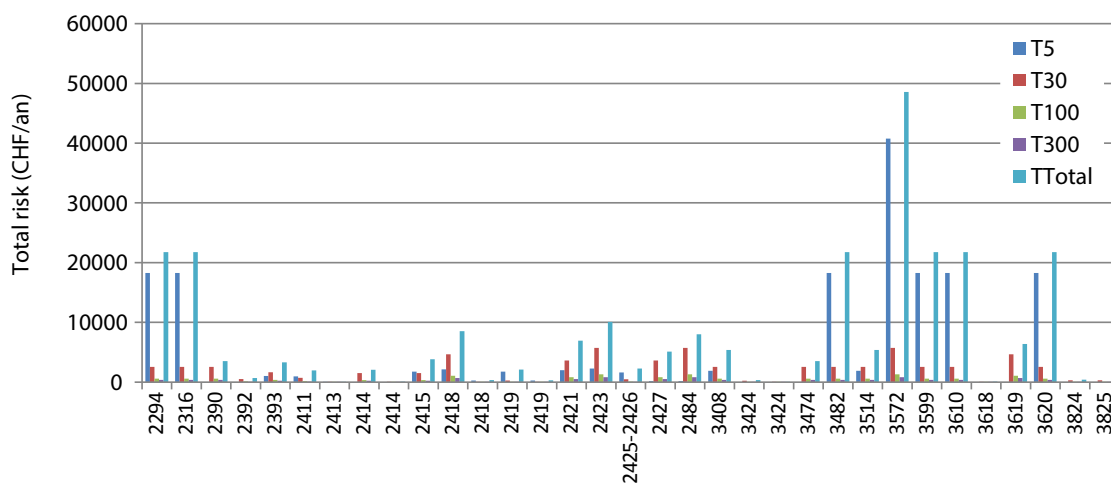


Figure 3.9: Monetise risk before measure (human and material). This graph is an output of Valdorisk (only the label of the buildings have been changed to display the number of the plot of land). In Valdorisk, it is possible to select the type of process (if several types of processes are studied), the type of risk (human monetised, material, ...) as well as the protection measure (without, with measure 1, ...).

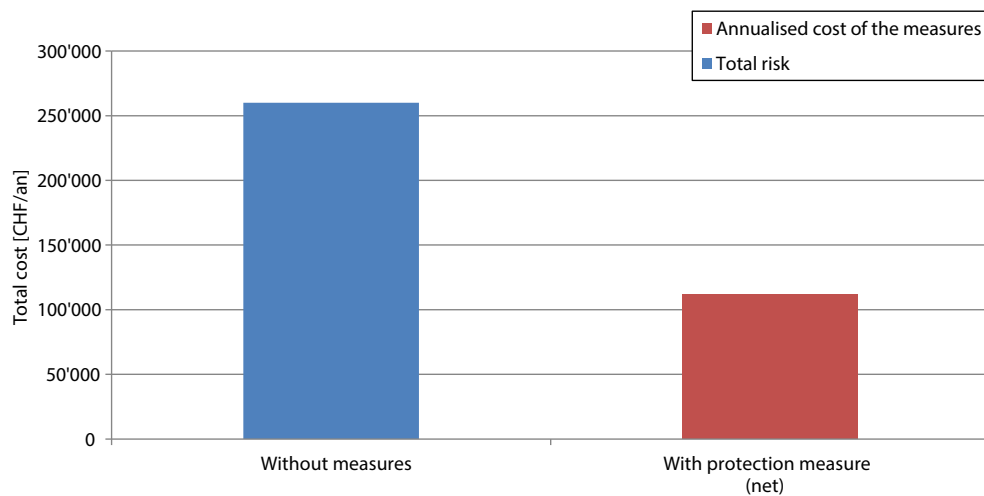


Figure 3.10: Comparison of the total cost without and with protection measures. With protection measures, the risk is the sum of the annualised cost of the measures and the residual risk (insignificant in this example). This graph is an output of Valdorisk

3.5 Conclusions

Valdorisk is mostly based on EconoMe, and can thus be seen as a simple copy. However, it is faster to use and permits to perform rapid tests for example, in order to see if a more detailed analysis is required (which can also be done with Valdorisk). This goal is now also reached with the new EconoMe Lite (OFEV, 2015).

In addition, in contrast with EconoMe, Valdorisk allows to modify most of the parameters, in order to see their potential effect on the risk analysis and test all different possibilities. Nevertheless, for some parameters such as the vulnerability, the parameters that do not correspond to the default values will be highlighted in the report and the modification should be justified by the operator. Indeed, since many parameters are hard to assess, using default values allows having more coherence between the different risk analyses.

Finally, one of the main advantages of Valdorisk is that it is used by a constrained group of users and administrators, whereas EconoMe is a central solution used in different regions, with different administrators. Therefore, it is more complicated to test new approaches in the latter. On the other hand, Valdorisk incorporates some new options such as the reduction of the vulnerability and the continuously moving landslides, which might be incorporated in EconoMe when they will be mature enough. The discussions presented in Chapt. 4 and Chapt. 5 also originated from the development of Valdorisk, and the calculation of the impact probability of a natural hazard on a moving vehicle has been modified in EconoMe thanks to these reflections.

Global summary		
Type	Without measures	With measures
Life expectancy of the measure		50
Initial cost (CHF)		2'160'000.00
Annual cost (CHF/year)		111'938.13
Total risk (CHF/year)	260'019.47	86.93
Benefit (CHF/year)	-	259'932.54
Benefit/cost ratio		2.32
Individual risk ¹	1.66E-02	1.25E-07

¹The total individual risk makes sense only if one person is exposed to the risk in all objects (for example, in a neighbourhood, a same person will not be exposed in all buildings, but for connected roads, one person can drive on all sections each day)

Figure 3.11: Extract of the automatic report generated in Valdorisk. After this global summary, Valdorisk presents the parameters for each object, as well as the risk without and with measures.

Chapter 4

Direct impact of hazard on moving vehicles

Foreword

This chapter has been published as:

Nicolet, P., Jaboyedoff, M., Cloutier, C., Crosta, G. B., and Lévy, S.: Brief communication: On direct impact probability of landslides on vehicles, *Nat Hazard Earth Sys*, 16, 995–1004, doi:[10.5194/nhess-16-995-2016](https://doi.org/10.5194/nhess-16-995-2016), 2016.

Abstract

When calculating the risk of railway or road users of being killed by a natural hazard, one has to calculate a temporal spatial probability, i.e. the probability of a vehicle being in the path of the falling mass when the mass falls, or the expected number of affected vehicles in case of such an event. To calculate this, different methods are used in the literature, and, most of the time, they consider only the dimensions of the falling mass or the dimensions of the vehicles. Some authors do however consider both dimensions at the same time, and the use of their approach is recommended. Finally, a method considering an impact on the front of the vehicle is discussed.

4.1 Introduction

Natural hazards impacting on transportation corridors can cause traffic disruption, with direct and indirect economic consequences, and affect the users by direct impact on vehicles (hereafter referred to as direct impact) or by impact of the user with deposited material.

When the indirect consequences (e.g. economical cost of the road closure) are taken into account, they generally largely outweigh the direct consequences. However, indirect consequences have no influence on the individual risk, which is often used as an acceptability criterion (e.g. [Ho and Ko, 2009](#)). Therefore, the impact of vehicles with falling or deposited material is worth attention. On the other hand, according to [Pantelidis \(2011\)](#), direct impact of a landslide on a moving vehicle is by far less likely than the impact of a vehicle with the landslide material deposited on the road. Nevertheless, using an inappropriate formulation to calculate the direct impact probability might still have a noticeable effect on the total risk assessment.

This paper reviews the approaches used to calculate the direct impact probability given that an event occurs. This is usually called temporal spatial probability (e.g. [Fell et al., 2005, 2008a; Ferlisi et al., 2012; Corominas and Mavrouli, 2013](#)), although, depending on the hypothesis and formulation, it is expressed as an expected number of vehicles rather than a formal probability. It has to be mentioned that some methods also consider traffic jam situations, or account for the possibility of a warning system or for the driver to see the event in advance and to respond by braking. These situations are however beyond the scope of this article, where we concentrate on the category named “impact of a falling rock on a moving vehicle” by [Bunce et al. \(1997\)](#), keeping in mind that the calculation applies also to other falling or flowing material such as for debris flow or snow avalanches. For this review, the approaches are divided into three categories, namely, neglecting the event dimension (Sect. 4.2.1), neglecting the vehicle dimension (Sect. 4.2.2) and, finally, taking both dimensions into account (Sect. 4.2.3).

4.2 Temporal spatial probability of moving vehicles

4.2.1 Approaches neglecting the events dimension

Most of the quantitative risk analyses for moving vehicles published in the literature concern rockfalls. To calculate the probability of a falling block hitting a car or a train, Eq. (4.1) is generally used (e.g. [Bunce et al., 1997; Fell et al., 2005; Ferlisi et al., 2012; Mignelli et al., 2012; Corominas and Mavrouli, 2013; Wang et al., 2014; Macciotta et al., 2015](#)):

$$P_{ST} = \frac{f_V \times L_V}{v_V}, \quad (4.1)$$

where (correspondence of the variables names used in this paper with those adopted in some of the cited works can be found in Appendix 4.4)

- P_{ST} is the temporal spatial probability of a vehicle being in the path of the rock when it falls, neglecting the rock dimensions and considering a single lane with no vehicle overlap;

- f_V is the traffic density expressed in number of vehicles per time unit (e.g. average annual daily traffic, with proper unit conversion);
- L_V is the length of the vehicle;
- v_V is the mean vehicle velocity.

The aim of this equation is to calculate, as the block falls, the probability of a car being present at the instantaneous position of the block's centre of mass. The simplification of using the geometric centre of the block is valid only for L_V significantly larger than the size of the falling block, which is usually the case for trains, but might become an oversimplification for cars. In this case, P_{ST} is formally a probability, since a value of 1 would mean that cars move bumper to bumper.

The approach proposed by [Peila and Guardini \(2008\)](#) and used by [Budetta et al. \(2015\)](#) falls in the same category, although it takes into account the length of the hazard zone and the vehicle length. However, if we multiply their spatial probability by their temporal probability and by the vehicle frequency, we obtain

$$\frac{L_V}{L_H} \times \frac{L_H}{v_V} \times f_V = \frac{L_V \times f_V}{v_V}, \quad (4.2)$$

where L_H is the length of road included in the hazard zone. The simplification is then similar to Eq. (4.1). It has to be noted that [Peila and Guardini \(2008\)](#) use a binomial distribution to calculate the probability of one or more impacts, using the rockfall frequency as the number of experiments, and the spatial probability as the probability of success. We neglected this transformation here in order to keep the rockfall frequency out of the calculation, but the general idea is the same. This method is modified from [Crosta et al. \(2001\)](#).

4.2.2 Approaches neglecting the vehicle dimension

In the following, we present two examples of methods neglecting the vehicle dimension: one is applied in Switzerland and the other is known as the average vehicle risk method.

Approach used in Switzerland

Risk analysis in Switzerland has been standardised by the requirement for the regional authorities to produce hazard maps ([Raetzo et al., 2002](#)), and by the attribution of subsidies for protective measures based on standardised cost–benefit analyses using intensity maps prepared during the procedure of hazard mapping ([Bründl et al., 2009](#)). Systematic risk assessment is also performed for highways ([Dorren et al., 2009](#)) and for railways ([Bründl et al., 2012](#)).

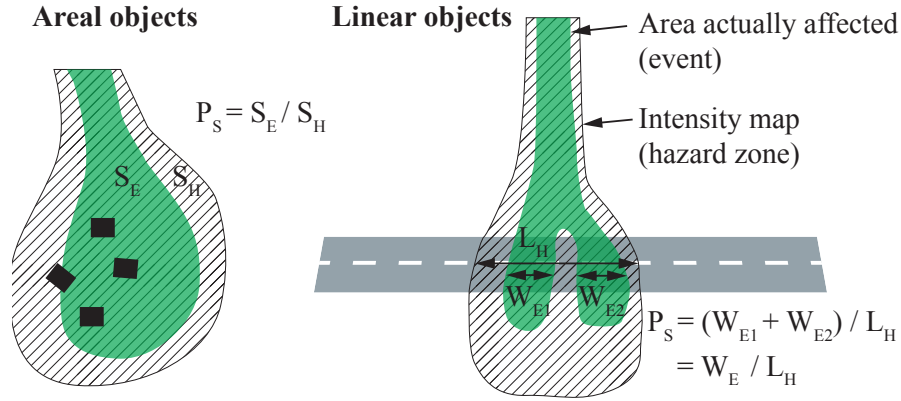


Figure 4.1: Calculation of the spatial occurrence probability (P_S) as used in the Swiss methodology. This probability corresponds to the proportion defined in the hazard map which is actually affected in the case of an event (left panel), or to the proportion of the length which is affected (modified from Bründl et al., 2015).

The procedure used to design hazard maps consists in establishing scenarios for three different return periods, namely 30, 100 and 300 years. The return period is defined for the source area, and intensity maps are built for each scenario, in order to identify the spatial distribution of the potential intensities. The conditional probability of the source material reaching any downslope location is considered only in a Boolean way, which means that the entire endangered area is considered as having the same probability of being affected. The three intensity maps are then combined to build the hazard, keeping the highest hazard level obtained by plotting the intensity–frequency combinations in a matrix. This last step is performed for land-use planning, but when it comes to risk analysis, intensity maps are used. Since intensity maps are characterised by the return period of the source and the total extension of the endangered area (generally considered as being equiprobable, which simplifies the calculation), the concept of spatial occurrence probability is introduced. This parameter aims to calculate the proportion of the area defined in the intensity map (or of the length if the object at risk is linear), which is actually affected in the case of an event (Fig. 4.1), or, roughly, the probability of a given location being affected in the scenario.

Risk is then calculated for each scenario – before being summed to obtain the total risk – using the following formula (modified from Bründl et al., 2009):

$$R = f \times P_S \times P_{ST}^* \times N_P \times \lambda, \quad (4.3)$$

where f is the frequency of the scenario; P_S is the spatial occurrence probability, which is defined in Eq. (4.4); P_{ST}^* is the temporal spatial term, i.e. the number of expected cars in the portion of the road included in the hazard map (of length L_H), and is defined in Eq. (4.5); N_P is the mean

number of persons per vehicle and λ is their vulnerability.

The spatial occurrence probability of the event is then

$$P_S = \frac{W_E}{L_H}, \quad (4.4)$$

with W_E being the actual width of the event on the road (i.e. the length of the road actually affected by the event) and L_H the length of the road included in the intensity map (i.e. the hazard zone, Fig. 4.1). The temporal spatial term is given by

$$P_{ST}^* = \frac{f_V \times L_H}{v_V}. \quad (4.5)$$

Multiplying Eq. (4.5) by (4.4), we can rewrite the temporal spatial term as follows:

$$P_{ST} = P_{ST}^* \times P_S = \frac{f_V \times W_E}{v_V}, \quad (4.6)$$

which represents the probability of the geometric centre of a moving vehicle being located in the section covered by the event (W_E). This approach is then valid only for W_E much larger than L_V . However, this is often not the case since rockfalls (with small W_E) are often a problem along roads or railways. Few technical papers in the literature use this approach (e.g. [Dorren et al., 2009](#); [Voumard et al., 2013](#), as a comparison with the risk that they calculate using a traffic simulator), but it is commonly used in practice. [Zischg et al. \(2005\)](#) use this formulation for snow avalanches impacting cars, which, in this case, is an acceptable simplification since W_E is generally large for snow avalanches.

With this approach, P_{ST}^* and P_{ST} are formally not probabilities, since several cars can be in the affected section simultaneously. It is indeed the expected number of affected cars.

The average vehicle risk method

A similar approach, neglecting the dimension of the vehicle, is the average vehicle risk (AVR) method used in the Rockfall Hazard Rating System (RHRS) ([Pierson and Van Vickle, 1993](#); [Budetta, 2002, 2004](#); [Pierson, 2012](#)). Although the RHRS is not intended to quantitatively assess the risk, the AVR criterion corresponds to a temporal spatial probability and is calculated as follows:

$$P_{ST} = \frac{f_V \times L_H}{v_V}, \quad (4.7)$$

where P_{ST} corresponds to the variable AVR of the original methodology, except that it is not expressed here in percent. This method uses L_H , which is the length of the hazard section (slope length in the original methodology), and neglects both the vehicle dimension (L_V) and the event dimension (W_E). In this formulation, P_{ST} often takes a value above 1, meaning that on average, more than one car is expected in the studied section.

Although this method is mostly used as an index rather than as a quantity, its use might lead to inexact results. Indeed, in [Pierson and Van Vickle \(1993\)](#) and [Budetta \(2004\)](#), the rating includes a frequency, which, for similar susceptibilities, is dependent on the considered slope length. At the same time, P_{ST} also reflects the slope length, which means that this parameter is considered twice in the classification. On the other hand, [Ferlisi et al. \(2012\)](#) modified the RHRS by using a frequency normalised to a unit slope length, which means that the section length is reflected only in P_{ST} , which is then coherent.

4.2.3 Approaches using both dimensions

Methods considering an impact on the side of the vehicle

Few authors in the literature use both event size and vehicle length for a more complete risk assessment. [Hantz \(2011\)](#) uses a risk calculation, where the block size varies according to a power law, and the target dimension is set to 0.5 m, corresponding to a hiker's "length". [Michoud et al. \(2012a\)](#) also use the dimensions of the cars (4 m) and of the falling rocks. [Borter \(1999\)](#), in the original Swiss risk methodology, takes into account both the dimension of the falling mass and the length of the vehicle when estimating the risk for a train. This approach has been integrated recently in the official risk calculator EconoMe for trains traffic ([Bründl et al., 2015](#)), but the approach presented in Sect. 4.2.2 is still used for road traffic. This approach has also been presented by [Hazzard \(1998, p. 185\)](#). In these studies, the temporal spatial probability is calculated as follows:

$$P_{ST} = \frac{f_V \times (W_E + L_V)}{v_V}. \quad (4.8)$$

The reason for the addition of W_E and L_V is illustrated in Fig. 4.2. P_{ST} is then independent of the length of the hazard area L_H . It has to be mentioned that this equation will give inexact results in the case of a multiple path event, as the one presented in Fig. 4.1. Indeed, to be exact, the vehicle length should be added to the width of every path, which is not the case if the total width of the event is used. [Cloutier \(2014\)](#) also uses the two dimensions, but the equation differs by considering, in addition, the braking time and the time since the last clearance (to account for the impact of deposited material), which is beyond the scope of this review.

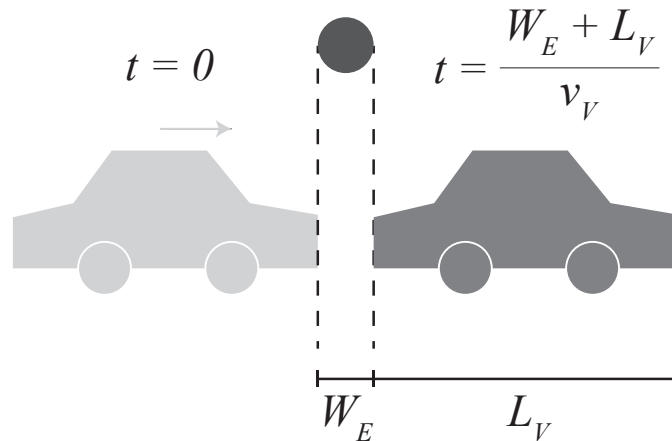


Figure 4.2: Temporal spatial probability considering both vehicle and event size. Every vehicle located between the left and the right position will be affected by the rockfall, which means that the temporal spatial probability will depend on the time needed to travel the distance $W_E + L_V$, as denoted in Eq. (4.8). Another way to see this is that a block will affect a car if its centre falls closer to $(1/2)W_E$ in front or behind the car.

In addition, [Borter \(1999\)](#) proposes calculating the number of affected people on a train using the length of the event and the total number of passengers on the train (N_P^{total}):

$$N_P^{\text{affected}} = \frac{N_P^{\text{total}} \times W_E}{L_V}. \quad (4.9)$$

N_P^{affected} then replaces N_P in the risk calculation (Eq. 4.3). Indeed, for long vehicles, many passengers might be located in a section of the vehicle that is not impacted and are therefore not expected to be affected. The passengers' "length" could also be added to the event's width in this equation, similarly to the addition of the event's width to the vehicle's length in P_{ST} (Eq. 4.8) or to the hiker's length in [Hantz \(2011\)](#), to account for the fact that a passenger with a geometric centre close to the path of the falling mass could actually be partly on its path. This is however a detail with respect to the fact that this last equation does not take the potential derailment of the train into account (see [Cloutier, 2014](#)), which could affect the passengers on a section of the train longer than the section directly affected by the falling material.

Methods considering an impact on the side and front of the vehicle

The most complete method is probably the one proposed by [Roberds \(2005\)](#), who uses a complex conditional probability model. The part of the model concerning the direct impact probability consists in calculating the probability of a falling mass passing between uniformly spaced vehicles,

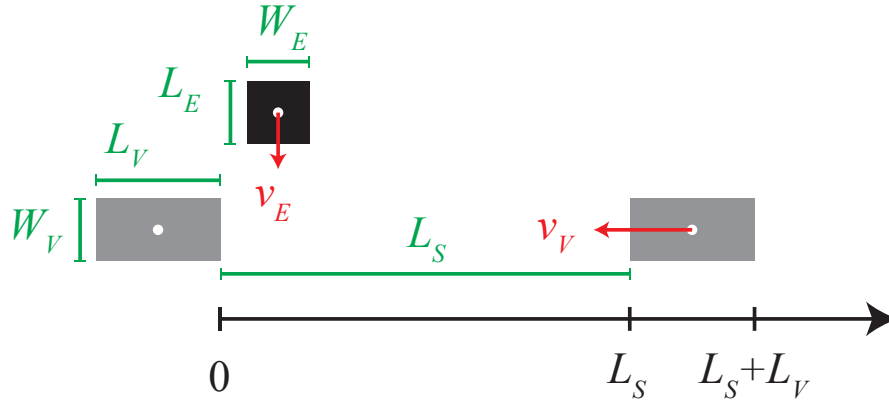


Figure 4.3: Parameters of the cars (in grey) and the falling mass (in black) used for the calculations in [Roberts' \(2005\)](#) method. The origin of the abscissa axis is located at the rear of the front car. The length of the hazard zone is not indicated in this figure because it does not influence the calculation.

and taking its complement to 1. The calculation is done as follows:

$$P_{ST} = 1 - \frac{\left[L_S - (L_E + W_V) \frac{v_V}{v_E} \right] - W_E}{L_S + L_V}, \quad (4.10)$$

where the vehicle V is characterised by a length L_V , a width W_V and a velocity v_V , while the falling mass is characterised by a length L_E (perpendicular to the vehicle length), a width W_E and a velocity v_E . L_S is the spacing between the vehicles and depends on the traffic density (Fig. 4.3). With this approach, the possibility for a car to collide frontally with an event occurring is taken into account (see Appendix 4.4). The limitation of this method consists in considering that vehicles are uniformly spaced, but the impact probability is actually higher if they are not. Indeed, since L_S is present in the numerator and in the denominator, and since the numerator is always smaller than the denominator, a negative change in L_S (denoted ΔL_S) will result in a positive change in P_{ST} (denoted ΔP_{ST}) larger, in absolute values, than the ΔP_{ST} resulting from an equivalent positive ΔL_S . Therefore, on average, P_{ST} with L_S varying around a mean \bar{L}_S will be larger than P_{ST} resulting from a constant $L_S = \bar{L}_S$.

4.3 Synthetic examples

Two examples of risk calculation using the different methods are given in Tables 4.1 and 4.2, respectively, for cars and for trains. The risk is calculated only for direct impacts. In the case of rockfalls affecting cars, the temporal spatial probability using Eq. (4.1), which is widely used in

the literature, is around 18 % lower than if both dimensions are used (Eq. 4.8) and 43 % lower than considering an impact on the side and front (Eq. 4.10). Neglecting the size of the vehicle (Eq. 4.6) gives a P_{ST} farther from the expected value (obtained with Eq. 4.10). For cars, the difference in P_{ST} is directly reflected on the risk estimation.

When it comes to trains, the temporal spatial probability is largely inferior with Eq. (4.6). However, if N_P^{affected} is used when needed, the risk estimations are quite similar to the different methods. We consider that N_P^{affected} is needed whenever L_V is taken into account. Indeed, if L_V is not used (Eq. 4.6), P_{ST} considers the vehicle as being dimensionless. Therefore, P_{ST} in Eq. (4.6) is somehow already the probability of a train user being affected.

4.4 Discussion and conclusions

Although risk resulting from direct impact of the event with a moving vehicle is generally lower than the risk of a moving vehicle hitting debris deposited on its way, it is not negligible. As a consequence, neglecting the dimension of the event or the dimension of the vehicle when calculating the direct impact risk might lead to an inexact result if the neglected dimension is not significantly lower than the other one. Therefore, we recommend using Eq. (4.8) rather than Eqs. (4.1) and (4.6), in order to avoid significant errors. Although, as shown in Table 4.2, the difference in risk evaluation for the passengers might be reduced to a reasonable level by using a suitable method to calculate the number of affected people, an incorrect P_{ST} could also affect other consequence scenarios, such as train derailment. Indeed, if P_{ST} is used to calculate the probability of a road or railway closure after a vehicle has been hit by a falling mass (disregarding whether a passenger has been affected or not), then the method used to calculate P_{ST} really matters (considering that the closure will be longer if a train has to be removed from the track than if the track only needs to be cleared of fallen material). In addition, the calculation of N_P^{affected} (Eq. 4.9) highlights the fact that the rest of the risk calculation has to be coherent with the calculation of P_{ST} . Indeed, if P_{ST} is the probability of a vehicle being hit by a falling mass, since some passengers might be in a part of the train that is not affected, then whether (1) the vulnerability is the conditional probability of a passenger dying if any part of the vehicle is affected (and might therefore be very low), or (2) the vulnerability is the conditional probability of a passenger dying if the part of the vehicle where he or she is located is affected, as a consequence, the number of people N_P should be computed with Eq. (4.9).

More in-depth analysis could be performed using the approach presented in Eq. (4.10), which takes into account the possibility of a frontal impact with a moving vehicle. However, this approach needs many parameters that are not always easy to assess, and the results are different if the spacing between the cars is not constant. Moreover, this latter method considers the impact

Table 4.1: Example of risk calculation for car passengers (direct impact only). Parameters are shown only when used in the calculation. In addition to the parameters presented in the text, the risk is calculated using the vulnerability of the car passengers (V) and the hazard frequency (H).

Parameter	Dimension	Eq. (4.1)	Eq. (4.6)	Eq. (4.8)	Eq. (4.10)
f_V	(vehicles day ⁻¹)	5000	5000	5000	5000
L_V	(m)	4.5	–	4.5	4.5
W_V	(m)	–	–	–	2
v_V	(km h ⁻¹)	80	80	80	80
W_E	(m)	–	1	1	1
L_E	(m)	–	–	–	1
v_E	(km h ⁻¹)	–	–	–	100
L_S	(m)	–	–	–	379.5
P_{ST}	(–)	1.17×10^{-2}	2.60×10^{-3}	1.43×10^{-2}	2.06×10^{-2}
H	(yr ⁻¹)	0.1	0.1	0.1	0.1
V	(–)	0.5	0.5	0.5	0.5
N_P	(persons)	1.76	1.76	1.76	1.76
R	(persons yr ⁻¹)	1.03×10^{-3}	2.29×10^{-4}	1.26×10^{-3}	1.81×10^{-3}

Table 4.2: Example of risk calculation for train passengers (direct impact only). Parameters are shown only when used in the calculation. In addition to the parameters presented in the text, the risk is calculated using the vulnerability of the car passengers (V) and the hazard frequency (H).

Parameter	Dimension	Eq. (4.1)	Eq. (4.6)	Eq. (4.8)	Eq. (4.10)
f_V	(vehicles day ⁻¹)	30	30	30	30
L_V	(m)	200	–	200	200
W_V	(m)	–	–	–	2
v_V	(km h ⁻¹)	150	150	150	150
W_E	(m)	–	1	1	1
L_E	(m)	–	–	–	1
v_E	(km h ⁻¹)	–	–	–	100
L_S	(m)	–	–	–	1.20×10^5
P_{ST}	(–)	1.67×10^{-3}	8.33×10^{-6}	1.68×10^{-3}	1.71×10^{-3}
H	(yr ⁻¹)	0.1	0.1	0.1	0.1
V	(–)	0.5	0.5	0.5	0.5
N_P^{total}	(persons)	175	175	175	175
N_P^{affected}	(persons)	0.9	–	0.9	0.9
R	(persons yr ⁻¹)	7.29×10^{-5}	7.29×10^{-5}	7.33×10^{-5}	7.49×10^{-5}

of a vehicle with a falling mass crossing the road, but, in many situations, the falling mass will stop on the road or on the railway, causing much higher risk. This is particularly critical for trains because they have limited chances of avoiding contact if rockfall debris is on the rail track and if the train operators are not informed of the situation ahead. Indeed, trains have large stopping distances (particularly freight trains) and cannot manoeuvre to avoid debris.

To conclude, it is important to understand that the present communication only aims at discussing the spatial interaction of two moving objects, namely the falling mass and the vehicle, and that other scenarios, such as the impact with deposited material or the economic consequences of a road or railway closure, should be analysed in addition if applicable.

Appendices

Demonstration of Roberds' (2005) approach

Consider a mass of debris of length L_E and width W_E falling on a road with a velocity v_E (Fig. 4.3). On the road, vehicles of length L_V and width W_V are moving with a velocity v_V , and are separated from each other by a constant distance L_S . The time needed by the falling mass to completely cross the vehicle's trajectory is

$$t = \frac{W_V + L_E}{v_E}. \quad (4.11)$$

During this time, the vehicles will move forward by the distance:

$$d = v_V \times t = v_V \times \frac{(W_V + L_E)}{v_E} = (W_V + L_E) \times \frac{v_V}{v_E}. \quad (4.12)$$

If we consider that the vehicles in Fig. 4.3 are static, the leftmost abscissa where the moving mass can cross the road equals

$$x_0 = \frac{1}{2}W_E. \quad (4.13)$$

This coordinate equals half of the debris width, since the reference system of the debris is located at its centre.

With static vehicles, the rightmost abscissa x_1 would be L_S minus half of the width of the falling mass, similarly to x_0 . However, since the vehicles are moving, the distance travelled by

the car during the time spent by the falling mass crossing the road (d) needs to be removed.

$$x_1 = L_S - d - \frac{1}{2}W_E \quad (4.14)$$

$$= L_S - \left((W_V + L_E) \times \frac{v_V}{v_E} \right) - \frac{1}{2}W_E \quad (4.15)$$

Therefore, the distance on the abscissa which is available for the block to cross without affecting a car is

$$\Delta x = x_1 - x_0 \quad (4.16)$$

$$= L_S - \left((W_V + L_E) \times \frac{v_V}{v_E} \right) - \frac{1}{2}W_E - \frac{1}{2}W_E \quad (4.17)$$

$$= L_S - \left((W_V + L_E) \times \frac{v_V}{v_E} \right) - W_E. \quad (4.18)$$

The probability of the block crossing the road without affecting a car $P_{\overline{ST}}$ is the proportion of favourable abscissa Δx compared to the total distance $L_S + L_V$. Therefore, the probability of the block affecting a car P_{ST} is the complement of $P_{\overline{ST}}$:

$$P_{ST} = 1 - P_{\overline{ST}} \quad (4.19)$$

$$= 1 - \frac{\left[L_S - (L_E + W_V) \frac{v_V}{v_E} \right] - W_E}{L_S + L_V}. \quad (4.20)$$

Variable names

A table of correspondence of the variable names in the literature is given in Table 4.3.

Table 4.3: Correspondence of selected variables names used in this paper with the original methodologies. P_{ST} is the temporal spatial probability, f_V the vehicle frequency, L_V the length of the vehicles, v_V their velocity, W_E the width of the event, P_S the spatial occurrence probability of the event in the Swiss methodology, P_{ST}^* is the temporal spatial term of the Swiss methodology and L_H the length of the hazard zone

	Name in this paper	f_V^a	L_V	v_V	W_E	P_S	P_{ST}^*	L_H
Bunce et al. (1997)	$P(S : H)$	N_V	L_V	V_V	–	–	–	–
Dorren et al. (2009)	Nc	AHT	–	Vmax	slide width	Pso	–	–
Bründl et al. (2009)	–	MDT	–	v	–	$p(s)$	$p(et)$	g
Pierson (1991)	AVR	ADT	–	posted speed limit	–	–	–	slope length
Borter (1999, p. 76)	p_{Pr}	F_Z	L_Z	v	g	p_{rA}	–	–
Roberds (2005)	P_{A_1}	λV	V_L	V_V	D_W	–	–	–
Peila and Guardini (2008)	$P(A)_{tot}^b$	$N_{V/a}$	L_V	V_V	–	–	–	L_P

^a The correction factors applied to f_V are not considered here.

^b The original variable considers the number of falling blocks in addition.

Chapter 5

Addition of multiple risk scenarios accounting for the uncertainty

Foreword

The part of this chapter dealing with uncertainties has been published as:

Nicolet, P., Jaboyedoff, M., and Lévy, S.: A Simple Method to Include Uncertainties in Cost-Benefit Analyses, in: *Engineering Geology for Society and Territory - Volume 2*, edited by Lollino, G., Giordan, D., Crosta, G. B., Corominas, J., Azzam, R., Wasowski, J., and Sciarra, N., pp. 1763–1766, Springer International Publishing, doi:[10.1007/978-3-319-09057-3_312](https://doi.org/10.1007/978-3-319-09057-3_312), 2015.

It has been partly modified for this chapter.

5.1 Introduction

When performing a cost-benefit analysis using the Swiss guidelines as described in Chapt. 3, several issues limit the quality of the results. Firstly, although the method seems to be conservative, underestimation arises from the method used to sum the scenarios. Indeed, in order to be conservative in the hazard mapping, the scenario with the highest return period (T) of the class is generally used, which means that 30, 100 and 300 years scenarios are established. Since these values are used to calculate the frequency, and not the middle of the class, it results in an underestimation, as it will be demonstrated in Sect. 5.2.

Secondly, despite an impression of precision and objectivity, this approach suffers from the large uncertainty affecting most of the risk parameters, as well as potential bias in the expert

judgement. When it comes to the uncertainties in risk analysis, they come especially from the lack of reference events (in a lot of places, no inventory exists), changes in the environment or by the multiple possible consequences of an event. Therefore, there is a need to include probability distributions in the risk analysis, in order to account for the natural variability of the process (for example, an event with a given intensity might produce different outcomes with a small change in the element at risk) and to permit the user to include his uncertainty. The challenge is to have a procedure as objective as possible, while being simple to use and to communicate. This problem is discussed in Sect. 5.3.

5.2 Scenarios addition

5.2.1 Introduction

Since, as seen in Chapt. 3, a scenario is defined by the magnitude which is reached or overpassed with a given frequency, a scenario j include the scenario $j + 1$ of lower frequency. This is illustrated in Fig. 3.1 (p. 79), where the 30 years scenario includes the 100 years scenario, and the 100 years scenario includes the 300 years scenario. Therefore, in order to take into account each event only once, the frequency of the next scenario needs to be subtracted. As a result, the frequency obtained by Eq. (3.4) (p. 80) is used for risk analysis. In this equation, f'_j is the frequency at which the magnitude of the scenario j is reached or exceeded, while the magnitude of scenario $j + 1$ is not reached. The result of this operation is to consider, for the scenario 30 years, only the events which are between the limit of the 30 years scenario and the next scenario, which is the 100 years scenario in this case. It implies that the return periods used for hazard mapping in Switzerland become 42.9, 150 and 300 years. The total return period is, as a consequence, equal to the lowest one, in that case 30 years. When the scenarios are defined, the procedure seems conservative since the scenario with the highest return period is chosen (e.g. 100 years for the class 100–300 years). However, since this return period is used for the risk calculation and not, for example, the average of the class, the calculation is not conservative any longer. On the contrary, the total risk is underestimated since it considers that the consequences for a return period applies up to the next studied return period. This issue is illustrated hereafter using a hail hazard analysis.

5.2.2 Method

Although hail is not included in Valdorisk and not subject to protection measures, except object measures, it is well suited for the example since a continuous function hailstone size vs. return period (Fig. 5.1), as well as a continuous model hailstone size vs. loss ratio (Fig. 5.2) have



Figure 5.1: Frequency at which a given hailstone size is reached or exceeded in the study area.

been established. The computation of the losses is here a two steps process, where the first step consists in determining for each building if it is damaged or not using a random sampling with a probability value dependent on the hailstone size (Fig. 5.2 left), whereas the second step consists in calculating the economic loss for the damaged buildings by sampling a damage ratio from a probability distribution function for which the parameters depend on the hailstone size (Fig. 5.2 right). The loss model used here is a simplified version of the one that will be presented in Chapt. 9 and is better suited for this analysis than the newer version since it includes less variability. As a result, there is no need to compute a large number of iterations to reach a stable value of loss for a given hailstone size. This simplified model uses a similar approach as the one used in Imhof et al. (2015), but the constraints are different. Since the purpose of this demonstration is mainly the hazard mapping, return periods between 30 and approximately 300 years are used. Calculations are made as follow: an initial return period of 30 years is used, and an increment in the hailstone diameter is chosen, in order that the hailstone size of the 30 years scenario plus the increment corresponds to a return period close to 300 years. A step of 1.6 cm is chosen, since it is a number with few digits that permits to have a highest return period equal to 342 years. Risk is then calculated and summed for these 2 scenarios, using Eq. (3.4) (p. 80) for the frequency and Fig. 5.2 for the damage. The same process is repeated using a half step and the same maximum value. 3 scenarios (30, 101 and 342 years) are then calculated. The same process is repeated and each time that the step is divided by 2, the number of scenarios increases to become $(n \times 2) - 1$, with n being the number of scenarios at the previous iteration. It is assumed that by reducing the step size, the risk gets closer to the "actual" value. The partial risks are calculated as in Valdorisk (Chapt. 3) using the following equations:

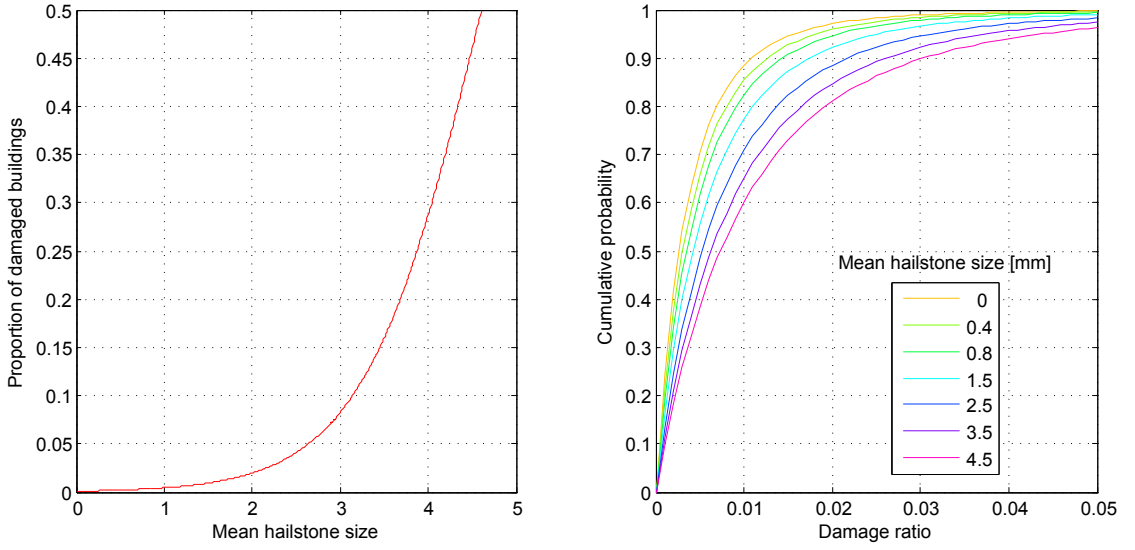


Figure 5.2: Vulnerability functions. The left graph shows the proportion of affected buildings, whereas the right graph shows a sample of the cumulative distribution function of the loss ratio for different hailstone size. The effectively used curve is defined by the exact hailstone size in the simulation.

$$R_i = \begin{cases} (f_i - f_{i+1}) \times D_i & \text{for } i \leq i_{max} \\ f_i \times D_i & \text{for } i = i_{max} \end{cases} \quad (5.1)$$

where D_i are the losses in scenario i .

In this example, it is relatively easy to calculate a large number of scenarios. However, many times, calculating or modelling many scenarios is time consuming, or even impossible. Therefore, 2 possible corrections are tested as well. The first uses a simple linear interpolation between the points and the risk can then be calculated using the following formula:

$$R_i = \begin{cases} (f_i - f_{i+1}) \times \left(\frac{D_i + D_{i+1}}{2} \right) & \text{for } i \leq i_{max} \\ f_i \times D_i & \text{for } i = i_{max} \end{cases} \quad (5.2)$$

As it can be seen in the formula, using a linear interpolation is similar to using the average of the losses in the studied scenario (i) and the next one ($i + 1$). This approach is similar to Meyer et al. (2009). The second tested solution consists in interpolating between the points using a power law with equation:

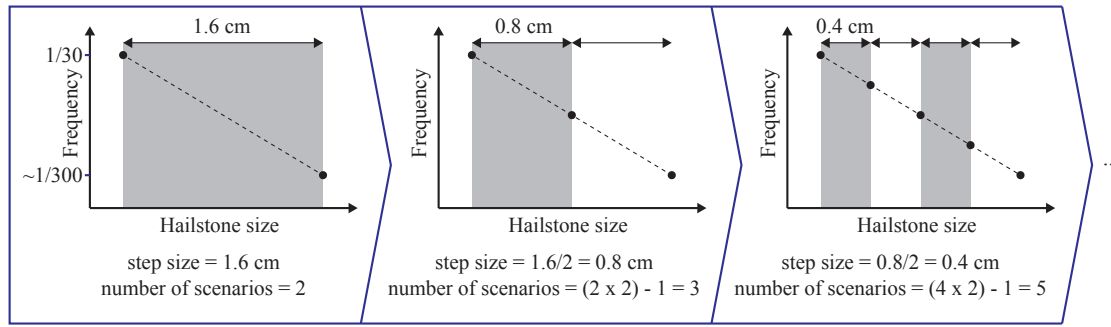


Figure 5.3: Schematic representation of the procedure used. First, a step is chosen so that when this step is added to the hailstone size of the 30 years scenario, the obtained size of the hailstones corresponds to a return period close to 300 years. The value of 1.6 cm satisfies this requirement and is then chosen. The risk is then calculated using these 2 scenarios. Then, the step is divided by two and three scenarios are required to calculate the risk between the same bounds, the 2 used before plus a new scenario in between. The scenarios used for the risk are represented by the dots on the graphs. The step is then divided by two again and the risk calculated using 5 scenarios. This process is repeated several times. For each value of the step, the risk is calculated using the same minimum and maximum return periods.

$$D = a f^{-b} \quad (5.3)$$

Risk can then be calculated using the following equations:

$$R_i = \begin{cases} \left[\frac{a}{1-b} (f_i^{1-b} - f_{i+1}^{1-b}) \right] b = -\frac{\log\left(\frac{D_i}{D_{i+1}}\right)}{\log\left(\frac{f_i}{f_{i+1}}\right)}; a = \frac{D_i}{f_i^{-b}} & \text{for } i \leq i_{max} \\ f_i \times D_i & \text{for } i = i_{max} \end{cases} \quad (5.4)$$

5.2.3 Results

The results using a step ranging from 1.6 cm to 0.0125 cm are presented in table 5.1 and Fig. 5.4, using respectively Eq. (5.1) (without corrections), Eq. (5.2) (linear correction) and Eq. (5.4) (power law correction). The risk without correction using the smallest step is considered as the reference value and is 18.7 million CHF/year. As expected, without correction, the risk for a small number of scenarios is underestimated. For the three scenarios with return periods corresponding to the ones used in the hazard maps in Switzerland, the obtain value is around 27.2 % below the expected value. The calculation is graphically illustrated in Fig. 5.5. Using a linear correction yields results closer to the expected value with 3 scenarios and more, but yields a result farther

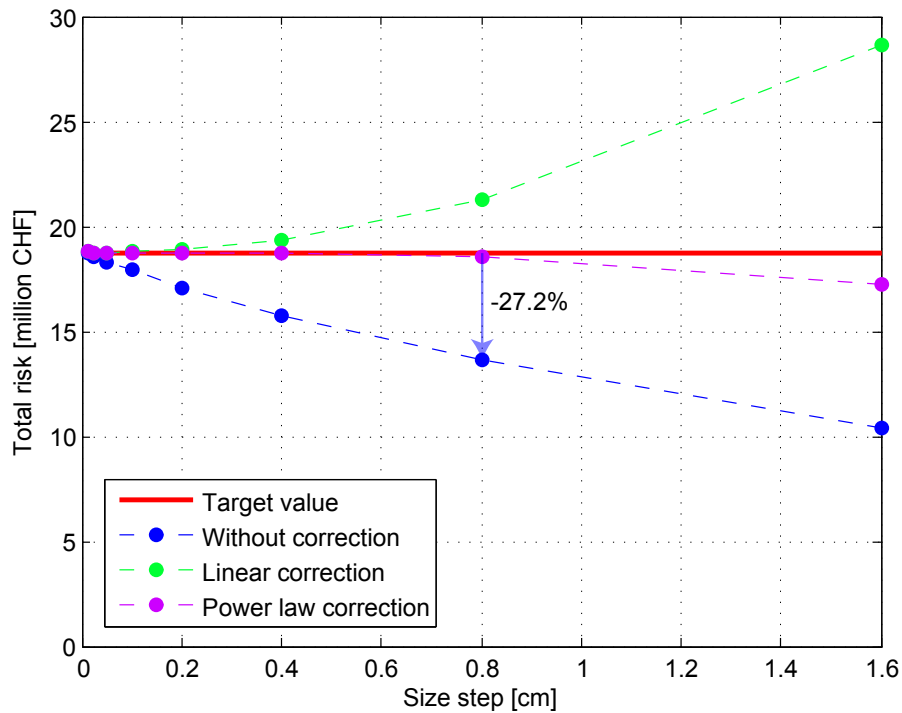


Figure 5.4: Total risk obtained with different hailstones step size (and thus different number of scenarios). The larger the number of scenarios, the higher the risk. Using three scenarios, similarly to the procedure used for the hazard maps yields a result 27.2% lower than using a large number of scenarios.

from the expected value using only two scenarios (+53.2 %). It can indeed be seen on Fig. 5.6 that the line does not perfectly correspond to expected shape. On the other hand, using the power law correction returns good results and with three scenarios, the result is very close to the expected value (Fig. 5.7).

5.2.4 Discussion

Using no correction at all is not recommended for a small number of scenarios since the obtained value will always be lower than the expected value. In this case, using three scenarios, the obtained value is indeed 27.2 % below the expected value. This proportion will obviously be different in other cases, but it is significant in this example. On the other hand, using a linear correction is slightly better here with three scenarios since it is only 13.7 % above the expected value. However, this correction is not good using only 2 scenarios. The main advantage of this method is that it is relatively simple to apply and that it doesn't need additional information. The linear correction has been integrated in Valdorisk (Chapt. 3) as an option.

Table 5.1: Results of the mean risk calculation using a different step size without correction, corrected with a linear regression or with a power law. The difference with the expected value (without correction using the smallest step) is given for each result (Δ risk max.).

Step size [cm]	1.6	0.8	0.4	0.2	0.1	0.05	0.025	0.0125
Number of scenarios	2	3	5	9	17	33	65	129
Risk [MCHF]	10.4	13.6	15.7	17.1	17.9	18.3	18.5	18.7
Δ risk max.	-44.3%	-27.2%	-15.8%	-8.51%	-4.18%	-1.97%	-0.865%	+0%
Linear regr. [MCHF]	28.6	21.2	19.4	18.9	18.8	18.8	18.8	18.8
Δ risk max.	+53.2%	+13.7%	+3.59%	+1.08%	+0.598%	+0.414%	+0.322%	+0.598%
Power law [MCHF]	17.2	18.6	18.7	18.7	18.8	18.8	18.7	18.8
Δ risk max.	-7.84%	-0.703%	+0.0442%	+0.191%	+0.377%	+0.358%	+0.308%	+0.593%

The second correction applied, which uses a power law, seems to fit better with the expected results. Indeed, even with 2 scenarios, the result is only 7.84 % above the expected value. That is because many frequency–magnitude relationships for natural hazard are well described by a power-law. It can indeed be seen on Fig. 5.7 that the results without correction using 129 scenarios are almost aligned on a log-log plot and in good agreement with the power law fits. This second method seems to be the best one, but is slightly more complicated to use than the linear correction.

This problem of using no correction has been discussed extensively in the working group of EconoMe, the risk calculator in use in Switzerland, but for now, the calculator uses no correction since risk analyses are generally over-evaluated by the operator according to the experience of the Federal Office for the Environmental (Bernard Loup, pers. comm.). However, for a project of the cantonal building insurance association, WSL et al. (2014) also uses a linear correction, that however differs by the fact that they establish a damage threshold, which is a first frequency at which damages occurs and permits to complete the analysis in the right-hand side of Fig. 5.5, towards a null damage amount. It is however not clear (neither in Meyer et al., 2009) if they consider that the damage amount of the scenario with the lower frequency applies to the all frequencies below (second line of Eq. 5.2). Although it needs more data, adding a damage threshold is probably often useful, as shown by Ward et al. (2011) in the context of a flood risk analysis, where the frequent floods have more influence on the total risk than extreme events. Another option could be to extrapolate the regression on both sides, but it has not been tested since a slight change in the slope would have a significant influence on the results. This would indeed put too much credit on the original points (blue points in Fig. 5.5–5.7).

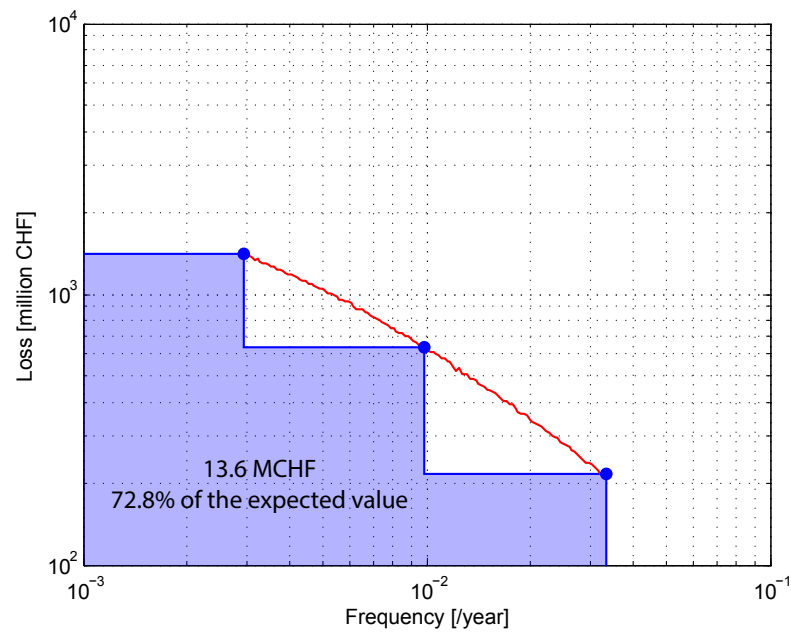


Figure 5.5: Risk calculation using three scenarios, without correction. The total risk corresponds to the integration of the blue area. The blue dots correspond to the scenarios used, whereas the red line corresponds to the risk obtained using the same procedure with the smallest steps, and is considered as being the "real" risk. The two triangles between the blue surface and the red curve are then missing from the calculation.

Besides the effect demonstrated in this section, [Ward et al. \(2011\)](#) also show the importance of properly selecting the return periods. Indeed, especially if the risk is not linear or contains steps (for example when a levee is over-topped), the number and values of the return periods used might have a great influence on the calculated risk.

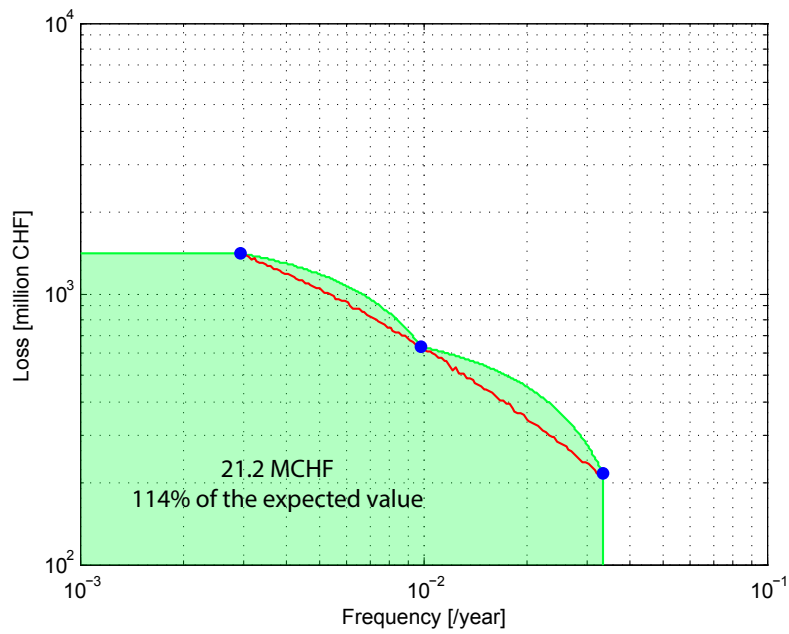


Figure 5.6: Risk calculation using three scenarios and linear interpolations between the points. The total risk corresponds to the integration of the green area and is close to the expected value.

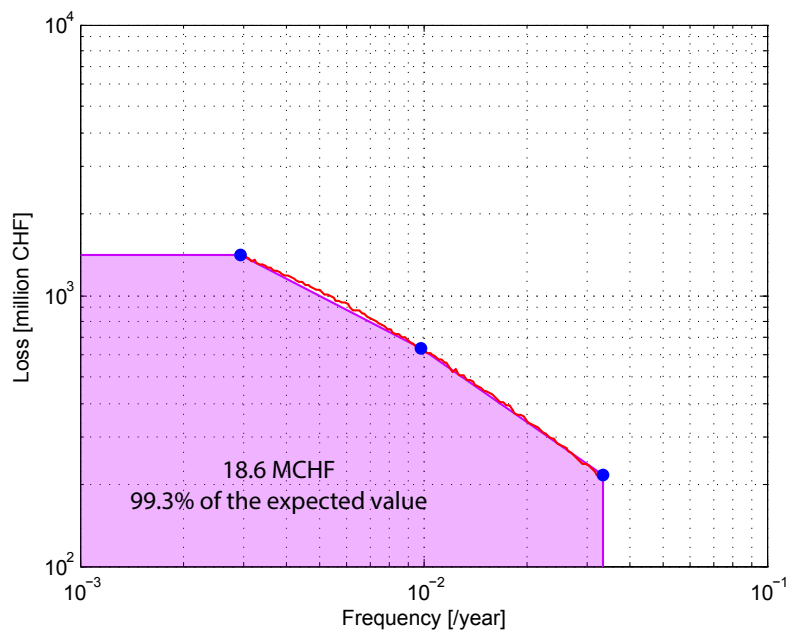


Figure 5.7: Risk calculation using three scenarios and power law interpolations between the points. The total risk corresponds to the integration of the pink area and is close to the expected value.

5.3 Accounting for the uncertainty

5.3.1 Introduction

This section focuses on the inclusion of the uncertainty on the risk calculation. This can be done, as presented in the introduction, by defining each parameter by a distribution of probability and by modelling the possible outcomes using a Monte-Carlo simulation (e.g. [Lari et al., 2012](#)). However, in order to be implemented in a risk calculator such as Valdorisk (Chapt. 3), this needs to be done simply, with as few additional parameters as possible. To achieve this goal, a method using a triangular distribution is presented here. First, the triangular distribution is presented (Sect. 5.3.2). Then, the possibility to correlate the random variables used for sampling the triangular distribution is discussed (Sect. 5.3.3). Finally, the implementation of this method is discussed, especially the input parameters (Sect. 5.3.4).

5.3.2 Sampling from the triangular distribution

The triangular distribution is defined by its mode (m) and by its minimum (a) and maximum (b) values. This makes it easy to use, since these parameters can be estimated more easily than, for example, the standard deviation of the normal distribution. Another advantage of this distribution is that impossible values can be excluded (for example a negative frequency). On the other hand, it doesn't have a fat tail, which could be suitable for some of the variables. The inverse cumulative distribution function (CDF) is ([Kotz and Van Dorp, 2004](#)):

$$F^{-1}(U) = x = \begin{cases} a + \sqrt{U(m-a)(b-a)} & \text{for } 0 \leq U \leq F(m) \\ b - \sqrt{(1-U)(b-m)(b-a)} & \text{for } F(m) \leq U \leq 1 \end{cases} \quad (5.5)$$

With $F(c) = (m-a)/(b-a)$ and U an number between 0 and 1. If U is a random variable uniformly distributed, the outputs are distributed according to the triangular distribution defined by parameters a , b and m .

5.3.3 Correlation of random variables

Let's assume that we want to add variability to the return period of the 3 usual scenarios. Sampling the inverse CDF with the same random value U for the 3 return periods would consider no uncertainty on the slope of the intensity–frequency relationship (Fig. 5.8 a). On the other hand, using independent variables would easily allow a scenario with a large intensity to be more frequent than one with a smaller intensity if the distributions are overlapping (Fig. 5.8 b). Similarly, if the vulnerabilities before and after measure are assessed using independent variables,

it would be possible to have a higher vulnerability after the measure, which does not make sense. As a consequence, different but correlated random variables are desirable (Fig. 5.8 c).

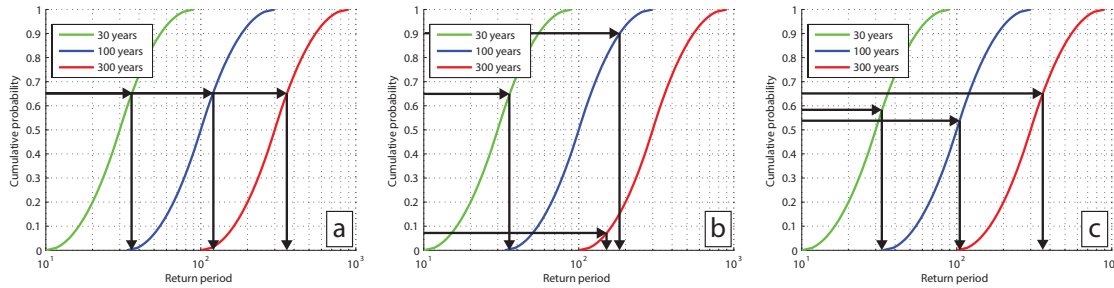


Figure 5.8: Sampling of return periods using the same random variable (a), independent random variables (b) or correlated random variables (c)

The following paragraphs describe a method to obtain correlated uniform random variables with domain [0-1], using independent variables with a random element in common described by Griffiths (1978) as a starting point.

Let (V_1, V_2) have the structure $V_1 = \alpha W_1 + (1 - \alpha)W_2$ and $V_2 = \alpha W_1 + (1 - \alpha)W_3$, W_1, W_2 and W_3 being mutually independent variables with uniform distribution [0-1] and α a coefficient [0-1] defined by the user. V_1 and V_2 follows a trapezoidal distribution (see Kotz and Van Dorp, 2004) with parameters a and d equal to 0 and 1 respectively, $b = \min(\alpha, 1 - \alpha)$ and $c = 1 - b$.

V_1 and V_2 can then be transformed into uniformly distributed variables by using the trapezoidal CDF, which is, in our case:

$$F(x) = \begin{cases} \frac{x^2}{2b(1-b)} & \text{for } x < b \\ \frac{x - (b/2)}{1-b} & \text{for } b \leq x < 1-b \\ 1 - \frac{(1-x)^2}{2b(1-b)} & \text{for } 1-b \leq x \end{cases} \quad (5.6)$$

Using this procedure, $F(V_1) = U_1$ and $F(V_2) = U_2$ are uniformly distributed, but are not independent if $\alpha > 0$. The process is illustrated in Fig. 5.9 and examples with $\alpha = 0$ and $\alpha = 0.75$ are given respectively in Fig. 5.10 and 5.11. We can roughly consider that highly correlated variables represent a situation where there is a low natural variability (i.e. a low aleatory uncertainty), and where the triangular distribution reflects mainly the epistemic uncertainty.

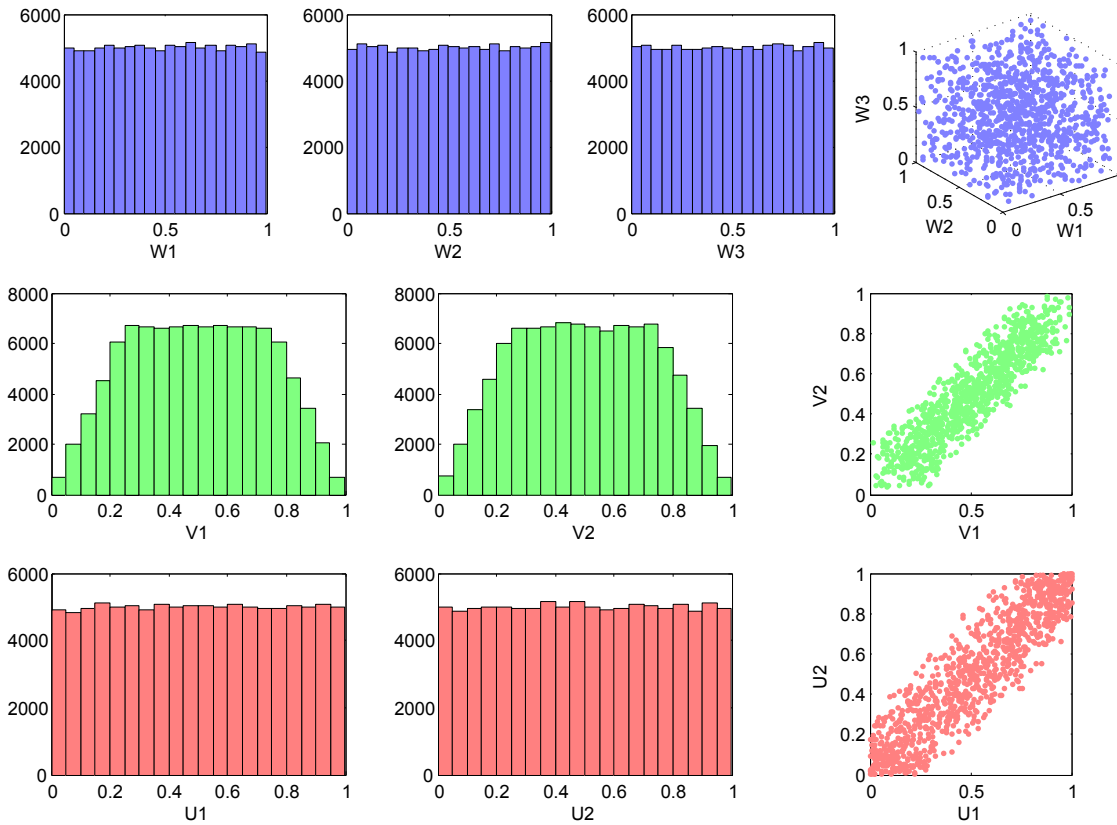


Figure 5.9: Process used to obtain two dependent random variables U_1 and U_2 with a correlation factor $\alpha = 0.75$. The process starts by generating three independent random variables W_1 , W_2 and W_3 that are uniformly distributed. V_1 and V_2 are then created by combining respectively W_1/W_2 and W_1/W_2 . V_1 and V_2 are correlated, but not uniformly distributed. Using the trapezoidal CDF, V_1 and V_2 are transformed into U_1 and U_2 respectively. These latter are uniformly distributed and dependant. The histograms show the distribution of 100 000 variables, whereas only 1000 points are displayed in the scatter plots.

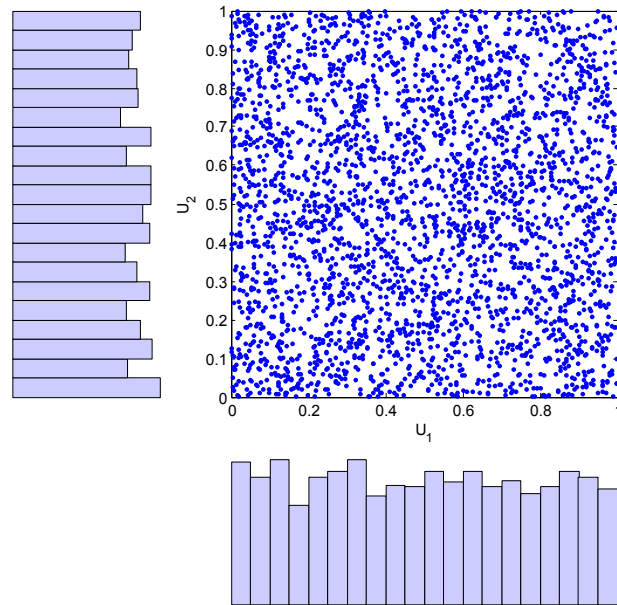


Figure 5.10: Scatter plot of 3000 pairs U_1, U_2 randomly generated with a correlation factor $\alpha = 0$. The marginal distributions are presented on the sides and show a uniform trend.

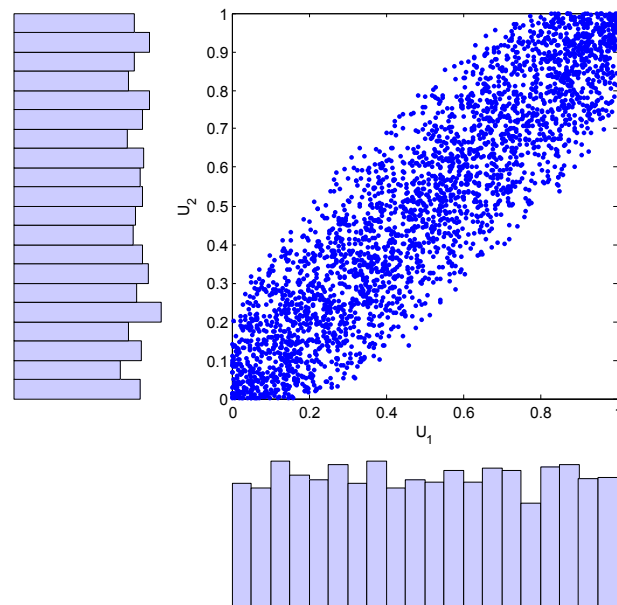


Figure 5.11: Scatter plot of 3000 pairs U_1, U_2 randomly generated with a correlation factor $\alpha = 0.7$. The marginal distributions are presented on the sides and show a uniform trend.

5.3.4 Input parameters

We propose to add a triangular distribution to every input parameter. However, since many parameters are considered in the analysis, and in order to stay simple for the user, we propose to limit the number of a and b parameters to assess. Since, the uncertainty on the return period of a scenario is generally related to those of the others, the user provides the lower range of the 30 years scenario (a_{30}), and the other a_j and b_j parameters are calculated by keeping a constant interval on a logarithmic scale.

When it comes to the spatial occurrence probability P_S (see Fig. 4.1), it is generally defined as constant for a given scenario in EconoMe. However, we propose to define it, as well as its a and b parameter, for each element at risk. This adds more input parameter to the analysis, but when a modelling is performed, P_S is usually better spatially defined than only by a general ratio.

When it comes to the vulnerability, since this parameter is not easy to define, we propose to keep the usual intensity classes as inputs (*low*, *medium* and *high*) and to add inter-classes: *very low* (vl), *low-medium* (lm), *medium-high* (mh) and *very high* (vh). These classes might help when the object is at the limit between two classes of intensities, or if the user considers it as being more or less resistant than the mean of the class. This parameter includes then both the hazard intensity and the objects vulnerability. The a , b and m parameters of the different classes are defined in Eq. (5.7) with v_l , v_m and v_h the vulnerabilities given in EconoMe. An example is given in Fig. 5.12.

$$\begin{pmatrix} a_{vl} & m_{vl} & b_{vl} \\ a_l & m_l & b_l \\ a_{lm} & m_{lm} & b_{lm} \\ a_m & m_m & b_m \\ a_{mh} & m_{mh} & b_{mh} \\ a_h & m_h & b_h \\ a_{vh} & m_{vh} & b_{vh} \end{pmatrix} = \begin{pmatrix} 0 & v_l/2 & (v_l + v_m)/2 \\ 0 & v_l & v_m \\ v_l/2 & (v_l + v_m)/2 & (v_m + v_h)/2 \\ v_l & v_m & v_h \\ (v_l + v_m)/2 & (v_m + v_h)/2 & (v_m + v_h)/2 \\ v_m & v_h & 1 \\ (v_m + v_h)/2 & (v_m + v_h)/2 & 1 \end{pmatrix} \quad (5.7)$$

5.4 Example

The example presented in Chapt. 3 is used here to demonstrate the use of the principles exposed above. The same parameters are used without variability for the value of the buildings, the number of inhabitants and their spatio-temporal probability and the intensities (see tables 3.3 and 3.4). However, when it comes to the return periods and the vulnerabilities, random distributions are used.

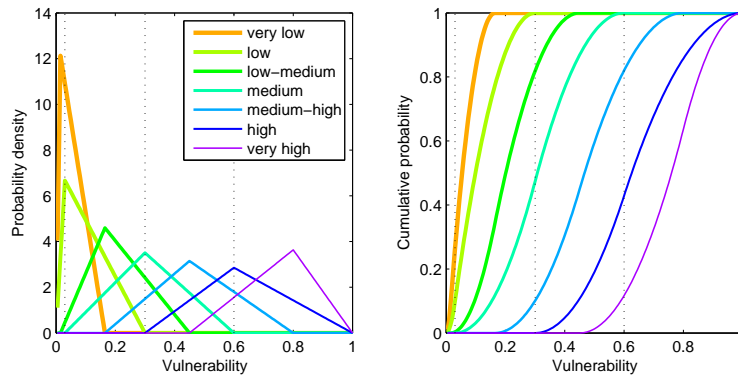


Figure 5.12: Vulnerability distributions built from 3 initial values, represented by the dotted lines (here 0.03, 0.3 and 0.6)

When it comes to the return periods, the lower limit of the most frequent scenario a_1 is chosen manually, whereas the others limits are automatically defined using the difference between the mode of the first scenario m_1 and a_1 on a logarithmic scale:

$$\begin{cases} a_i = 10^{\log(m_i) - \log\left(\frac{m_1}{a_1}\right)} \\ b_i = 10^{\log(m_i) + \log\left(\frac{m_1}{a_1}\right)} \end{cases} \quad (5.8)$$

The resulting values are presented in table 5.2 and Fig. 5.16. When a return period is sampled, the triangular inverse cumulative distribution function (Eq. 5.12) is always used with the logarithm of the values presented in table 5.2 in order for the function to be triangular on a logarithmic scale, as presented in Fig. 5.16.

Table 5.2: Parameters used for the triangular distributions of the return periods. The a and b values correspond to the minimum and maximum respectively, whereas m is the mode and corresponds to the initial value

a	m	b
2	5	12.5
12	30	75
40	100	250
120	300	750

Regarding the vulnerabilities, the values presented in table 3.2 are used together with the intensity values retrieved from the maps, but triangular distributions are used to add variability, as proposed in Eq. (5.7), although the additional intensity classes are not used. The resulting

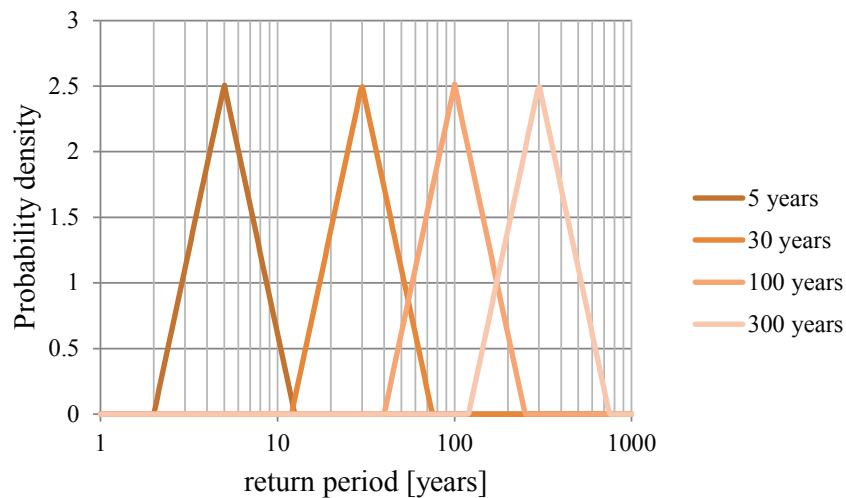


Figure 5.13: Probability density functions for the return period of the rockfall scenarios

distributions for the 3 types of buildings are presented in Fig. 5.14. To avoid too wide distributions, the lowest value of 1 and the double of the mode value of the distribution is used for the upper bound of the high intensities distributions. This is especially useful for multi-housing buildings since the vulnerabilities are generally low. The same principle is applied to the lethalties and this upper limit is also useful in that case since the lethality of persons in multi-housing buildings is very low (table 3.2). Without this limitation, the resulting risk could be several orders of magnitude higher.

Monte-Carlo analyses are then performed with the frequencies and the vulnerabilities and lethalties sampled randomly according to the distributions presented above. Several correlation factors are tested. First, the correlation factor α between the random variables used to assess the return periods is fixed to 0.9 and the correlation factor α of the random variables used for the intensities and lethalties is set respectively to 0, 0.5 and 1. The correlation is performed independently for each type of building, which means that in a same realisation, the vulnerabilities of one object type can be relatively high and the ones of another object type relatively low. The random variables used for one object for vulnerabilities and the lethalties are also independant. The results of this first test are presented in Fig. 5.15 in terms of total risk before the protection measures. The same test is then performed setting the correlation coefficient of the vulnerabilities and lethalties at 0.9 and setting the correlation coefficient of the return periods at respectively 0, 0.5 and 1. The results are presented in Fig. 5.16. It can be seen from these two figures that correlated random variables produces slightly more variability in the results. The variations of the correlation factor of the vulnerabilities and intensities produce more variability, although the random variables are independent for the different objects and for the vulnerabilities and

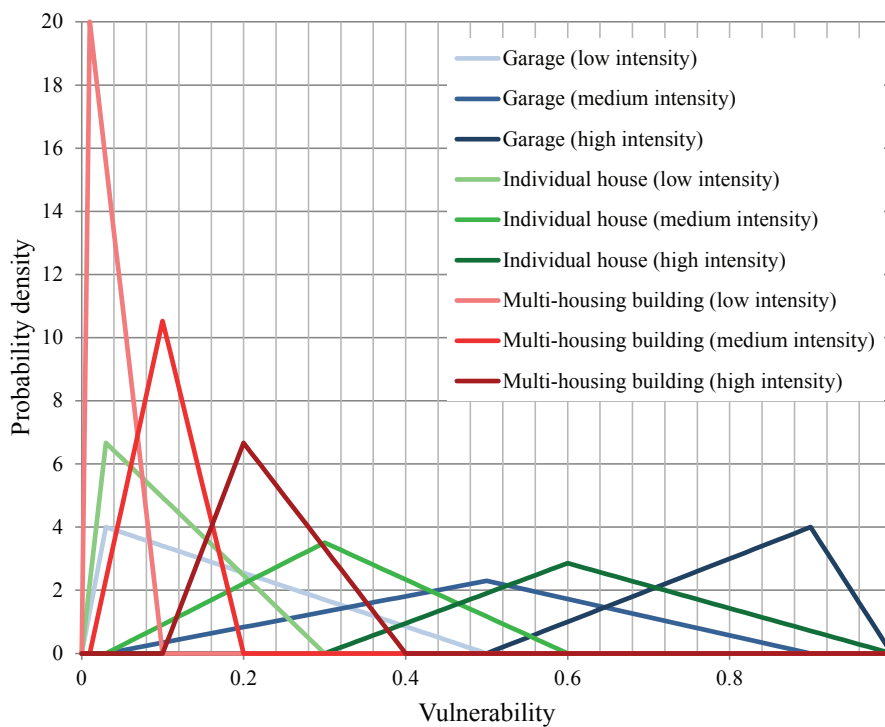


Figure 5.14: Probability density functions of the vulnerabilities for the encountered types of buildings for each intensity.

lethalities, which mean that there is 6 groups of random variables in this example. The variations of the correlation factor used for the return periods produce little variations in this example, which might be due to the link between the return periods (Eq. 3.4).

Finally, a test is made to see the result of using the same random variables with and without protection measures, i.e. the same return periods and vulnerability functions. Using the same values might indeed make sense in many situations, since, if protection nets are placed to stop rockfalls, the uncertainty on the frequency of the rockfalls would be the same with and without the protection measures. The results of this test are presented in Fig. 5.17 in terms of benefit/cost ratio and show no difference. The absence of difference is due in this case to the fact that the risk after the construction measure is several orders of magnitude below the risk without protection measures (see tables 3.3 and 3.4). Therefore, the risk reduction depends essentially on the risk before measures.

Compared to the risk calculation made in Chapt. 3, the values tend to be higher in the simulations. These tests also show that plausible uncertainty ranges can produce a high variability in the results.

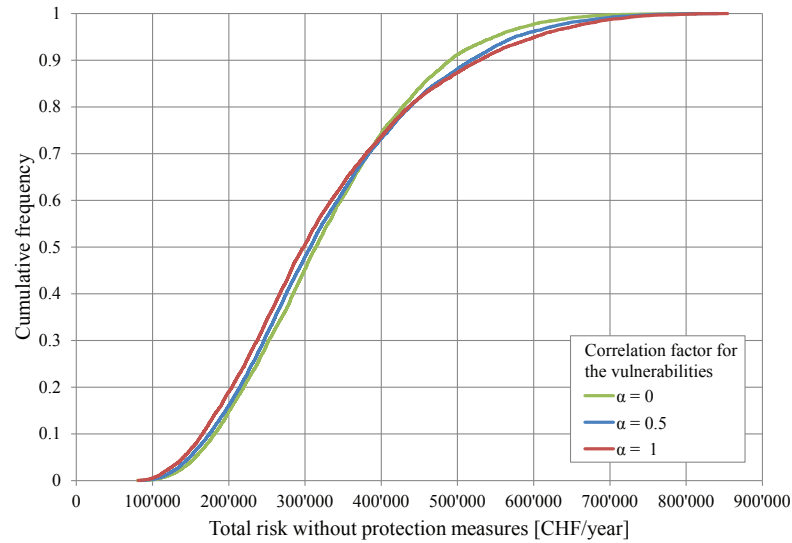


Figure 5.15: Monte-Carlo simulations made using three different correlation factors α to sample the vulnerabilities and lethality. The correlation factor α used to sample the return periods is set to 0.9 for the three analyses presented here. A higher correlation factor produces more variability in the results.

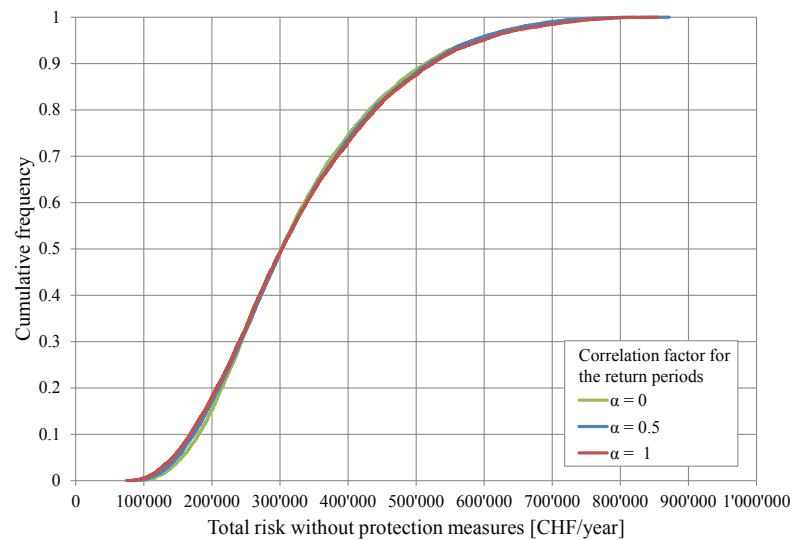


Figure 5.16: Monte-Carlo simulations made using three different correlation factors α to sample the return periods. The correlation factor α used to sample the vulnerabilities and lethality is set to 0.9 for the three analyses presented here. A higher correlation factor produces only slightly more variability in the results in that case.

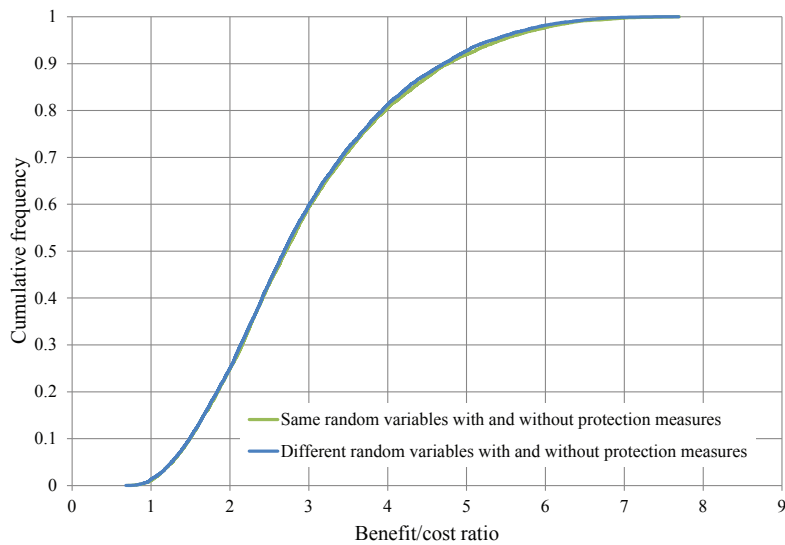


Figure 5.17: Monte-Carlo simulations made with correlation factors α of 0.9 to sample both the return periods and the vulnerabilities and lethalties. The green curve (hidden behind the blue one) is obtained by using the same random variables with and without protection measures, whereas the blue curve is obtained using different random variables. In this case, the two curves are similar since the risk after the construction of protection measure is several orders of magnitude below the risk without the protection measures. As a consequence the risk reduction (i.e. the benefit) depends almost only on the risk without protection measures.

5.5 Discussion and conclusion

This chapter presents simple methods to add the scenarios without underestimating the risk and, secondly, a method to allow the person in charge of a cost-benefit analysis to include his uncertainty, as well as the random variation in his analysis. This latter method is still under development and needs to be tested in practical cases.

Interpolating between the partial risks aims at being as correct as possible in the calculation. Indeed, although the error induced in the model is relatively small as compared to the large uncertainty affecting the risk estimation, introducing systematic errors that can easily be avoided is not desirable. Furthermore, when, for example, the scenario 30–100 years is studied, the estimator think that he is being conservative by keeping the scenario 100 years for this class. However, since we have seen that this scenario actually applies to the 100–300 years class, the conservative scenario becomes an optimistic scenario, without the estimator being aware of it.

When it comes to the method aiming at taking the uncertainty into account, the method to correlate the random variables for the sampling process might be useful for the parameters that change after the protection measures, but also for parameters that are related, such as the return periods.

The choice of the triangular distribution might seem peculiar since it is a statistical distribution that can only be encountered in very specific cases. Indeed, [Lari et al. \(2012\)](#) assume, in a similar analysis, that the Gaussian distribution is the most probable type of distribution for such parameters. However, the triangular distribution has been chosen here because we think that it is easier to define the minimum and maximum value than a standard-deviation and since negative values can easily be excluded. Furthermore, the cumulative of a symmetric triangular distribution is actually very similar to the one of a Gaussian with equivalent parameters. However, the choice of the distribution should actually rather be done by the user.

This way of including the uncertainty does however not correct the biasing (i.e. a systematic error, for example if the operator is too optimistic on its estimation). A way to correct it could be to use the method proposed by [Kahneman and Tversky \(1982\)](#), namely to use an estimated index of predictive accuracy and to correct the estimation by weighting the parameter estimation by a reference value, with a weighting degree depending on the index of predictive accuracy. However, this method needs a catalogue of reference values for different kind of situations (e.g. frequency of rockfalls in a unit area according to a type of rock).

To conclude, the cost-benefit analysis will always be limited by uncertainties and biases, as well as by simplification made in the methodology, but it is a useful decision support. Therefore, including some uncertainty in the parameters of the analysis allow to have a better understanding on the information contained in the results and permits to take more informed decisions.

Chapter 6

Accounting for protective measures in hazard mapping

6.1 Introduction

Natural hazard mapping is not a definite process, since many hazards depend on conditions that might change over time. This is for example the case for debris-flow on a cone, since the channel location might change, or for rock falls in a forest, since the tree population might change, for example after the apparition of a parasite. [Van Westen et al. \(2008\)](#) states that susceptibility and hazard maps are made for the present situation and should be updated in case of change in the causal factors. Among these changes, some are natural, but the hazard can also be modified by built protection measures. In Switzerland, built protection measures should only be applied to protect existing assets and not to increase the use of the land ([Lateltin et al., 2005](#)).

Since built protection measures change the hazard, the question of taking them into account or not for the hazard mapping arises. [Lateltin \(1997\)](#) and [FOEN \(2016\)](#) recommend to take the measure into account only if the two following conditions are fulfilled:

- the measure should be already built and not only be at the planning stage
- the protective function of the measure should be guaranteed on the long term

[Di Baldassarre et al. \(2013a\)](#), who theorise the floodplain occupation, note that the levee construction, since it is generally correlated with more intense urbanisation behind, produces a shift from frequent flooding of rural areas to rare but catastrophic flooding of urbanised areas. In the USA, the Federal Emergency Management Agency (FEMA) considers floodplain protected against a 100-year return period flood as being outside the official floodplain. Therefore, no

special requirement are issued for new constructions and the owners are often not even informed of the flood risk (Ludy and Kondolf, 2012). In 1993, a great flood affected the Mississippi and Missouri area and the limitation of assets in floodplains was recognised as the best solution to limit future flood losses. As a consequence, FEMA launched a program of buyouts to reduce the number of houses on floodplains. On the other hand, they allowed a large number of new construction in areas flooded in 1993, but protected by dikes afterwards (Pinter, 2005). Ludy and Kondolf (2012) did a survey on an area of the Sacramento-San Joaquin Delta of California, which is protected for the 100-year return period flood with levees. They found out that although the population was well educated, they were not aware of the risk. Some residents also consider that the authorities would not have allowed them to build at that place if it was not safe. It is observed in other regions of the world that the population considers the authorities as responsible for their protection (e.g. Terpstra and Gutteling, 2008). Ludy and Kondolf (2012) also point out that informed owners are more susceptible to take precautionary actions. Therefore, it seems important to inform people in protected area that there is still a residual risk.

This chapter discusses how and when protective measure should be taken into account in hazard maps. First, a bad example of development in "protected" area is discussed (Sect. 6.2), then, a symbology for hazard maps in protected areas is proposed (Sect. 6.3) and example are shown (Sect. 6.4).

6.2 Forgetting the hazard, example of La Faute-sur-Mer

An example of forgotten measure can be seen in La Faute-sur-Mer, in Western France, although the problems that lead to the crisis the village faced during the night of 27 to 28 February 2010 are more complex (e.g. Robert-Diard, 2015)

The storm Xynthia landed on the French Atlantic coast during the night of 27 to 28 February 2010. Although the winds associated with the storm were not exceptionally high in La Faute-sur-Mer, the level rise due to low pressures and the forcing of water towards the coast happened at the same time as a high tide with a relatively high coefficient. As a consequence, the sea level reached 4.8 m above its mean level in La Faute-sur-Mer (Chaveau et al., 2011) and flooded part of the village because of dike breaches inside the Lay estuary (Fig. 6.1). The natural dune on the open sea side was indeed high enough to sustain the sea rise (Fig. 6.2).

When it comes to the consequences, La Faute-sur-Mer is a village that developed a lot thanks to tourism and secondary residences. In 1959, the village was relatively small and dikes had been built to protect agricultural lands (Chadenas et al., 2011, Fig. 6.1). Subsequently, many new houses were built on these lands, in an area that seemed safe because of the dikes. However, the dikes had not been designed to protect houses, thus the design event might have been too small,

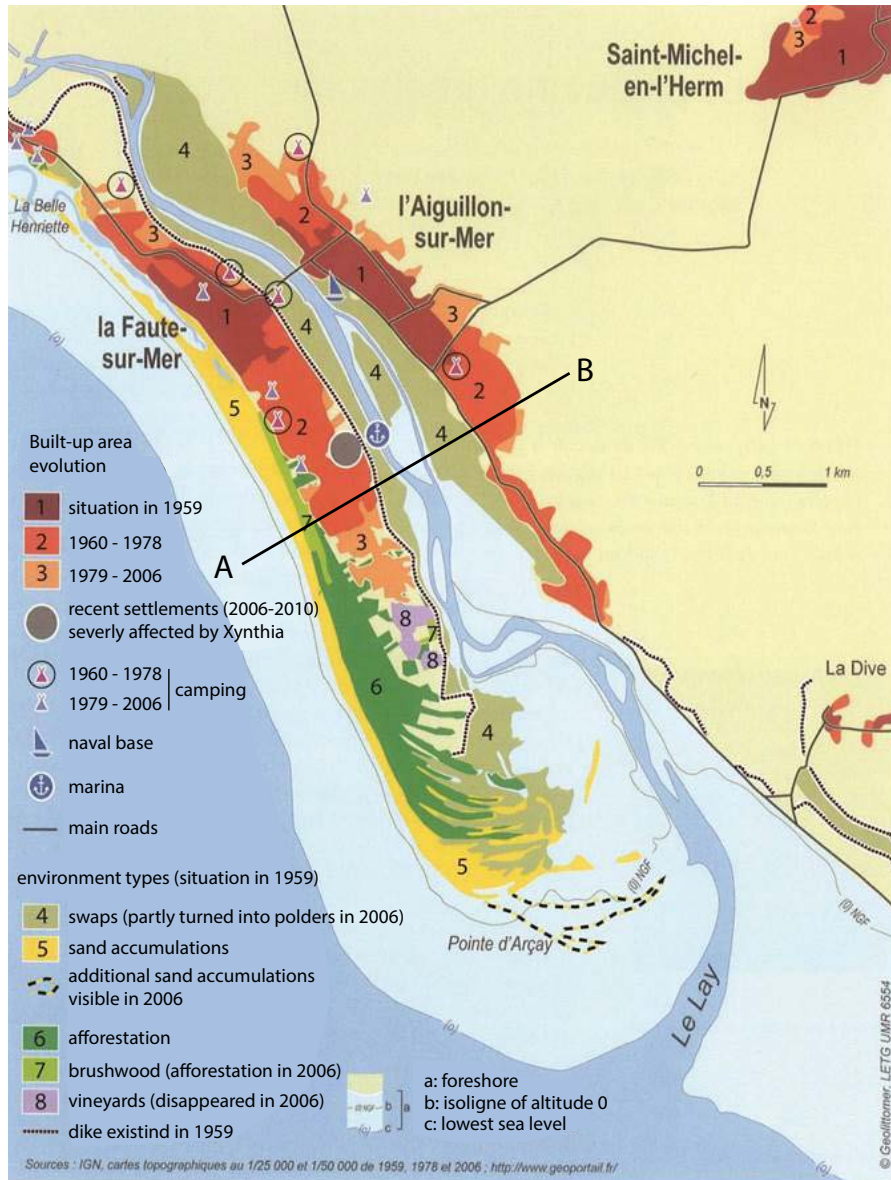


Figure 6.1: Land-use map of La Faute-sur-Mer. The black line indicates the position of the cross-section in Fig. 6.2. The gray circle marks the position of recent houses that where flooded. (modified from: Chadenas et al., 2011)

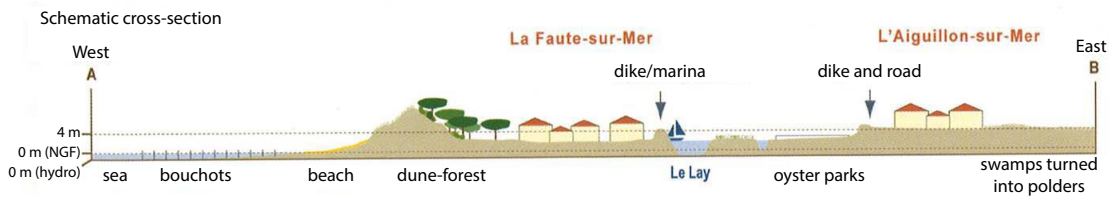


Figure 6.2: Cross-section of the Lay estuary (the position is given in Fig. 6.1). The altitude zero is given according to the general French levelling (NGF) and to the hydrological approach, that is the lowermost sea level (modified from: [Chadenas et al., 2011](#))

and the dikes lacked maintenance. In addition, the houses were not designed properly for an area susceptible for flooding. Indeed, many houses were single storey, with no escape to the roof and were equipped with electrical roller blinders (to reduce the premiums of anti-theft insurance) that are impossible to open in case of power cut ([Genovese et al., 2012](#)). In La Faute-sur-Mer and the region around, [Genovese et al. \(2012\)](#) highlights that 37 of the 41 casualties were persons in houses "protected" by dikes. Among the 41 victims, 27 were staying in La Faute-sur-Mer.

Although it seems like a perfect example of a forgotten risk, the problem is slightly more complex since the mayor and his ex-assistant were first found guilty of involuntary homicide ([Robert-Diard, 2015](#)). The sentence has then been reduced in appeal trial for the mayor and cancelled for his ex-assistant ([Robert-Diard, 2016](#)). The first trial pointed out that 9 of the victims were staying in houses built at a time when the risk was known and the mayor has always been opposed to the demands of the State and hid the risk to the population in order to benefit from the incomes ([Robert-Diard, 2015](#)). Whatever the responsibilities of the authorities are in this case, a good publicly available map could have forced the mayor to inform the population about the hazard and the protection measures.

Generally, in small municipalities, that are numerous in Switzerland, the knowledge of the authorities, that have to manage many different services with few employees, might be limited regarding natural hazards. Furthermore, the information is not always well transferred when the authorities change. As a consequence, it is important to ensure that the information on protection measure is well transferred to the next person in charge. In La Faute-sur-Mer, similar consequences could have happened if the mayor had recently changed and the new one had a limited knowledge on marine submersion.

6.3 Proposed symbology

A solution to this problem could be to use to color of the hazard level without protection measures on the background and to overprint the color of the hazard level with the protection measures using

hatching. This is the solution used in the Canton of Vaud, in Switzerland (UDN, 2014). A problem that appears with this solution is that the white pattern with yellow hatches can correspond both to the residual risk, which is the risk for return periods above 300 years (Fig. 1.17), and to a yellow area that has been protected.

The solution that we propose is to use the same system regarding the colors, but, instead of using hatches for the hazard level after protection measure, we propose to use a symbol representing the type of protection measure. This symbol would take the color of the hazard level after protection measure.

6.4 Examples

6.4.1 Rockfalls in Chardonne

The example presented in Chapt. 3 is used here to illustrate the method. The hazard map without protection measures is given in Fig. 6.3 and is obtained by combining the intensity maps presented in Fig. 3.4 to 3.7. It is expected, after anchoring the rock slope, that rockfall only occurs in the 300 years scenario with a small volume (Fig. 3.8). As a consequence, the hazard level after protection measures would be low (Fig. 6.4). However, the life expectancy of the protection measure is certainly lower than the one of a house. Therefore, it is especially important to keep track of the initial hazard level. A possible solution for the hazard map would be to use a nut as a symbol of the rock slope nailing, and to have the hazard map of Fig. 6.3 over-impressed by a yellow nut where the hazard is reduced to a low level (Fig. 6.5).

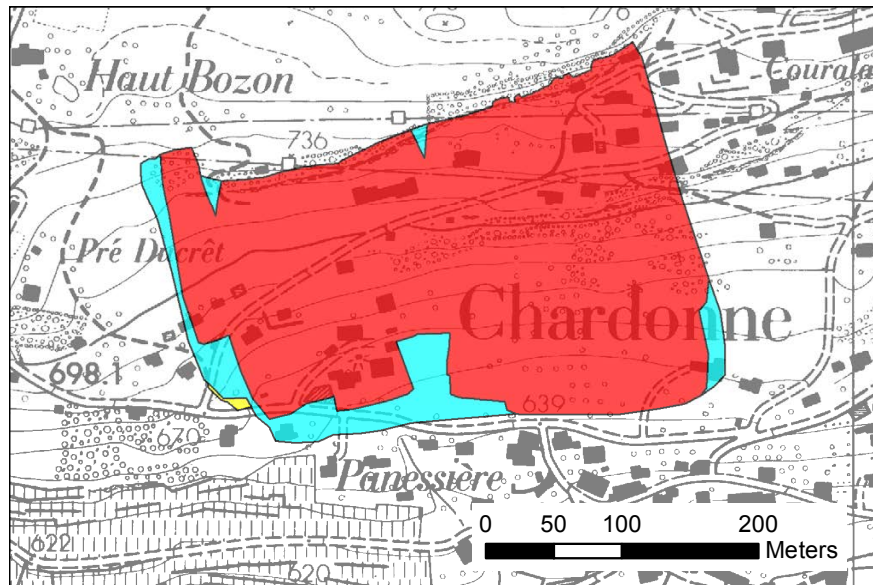


Figure 6.3: Hazard map before protection measure. The source area is located in the forest, on the northern side of the hazard area. (modified from: [Joliquin et al., 2010](#))

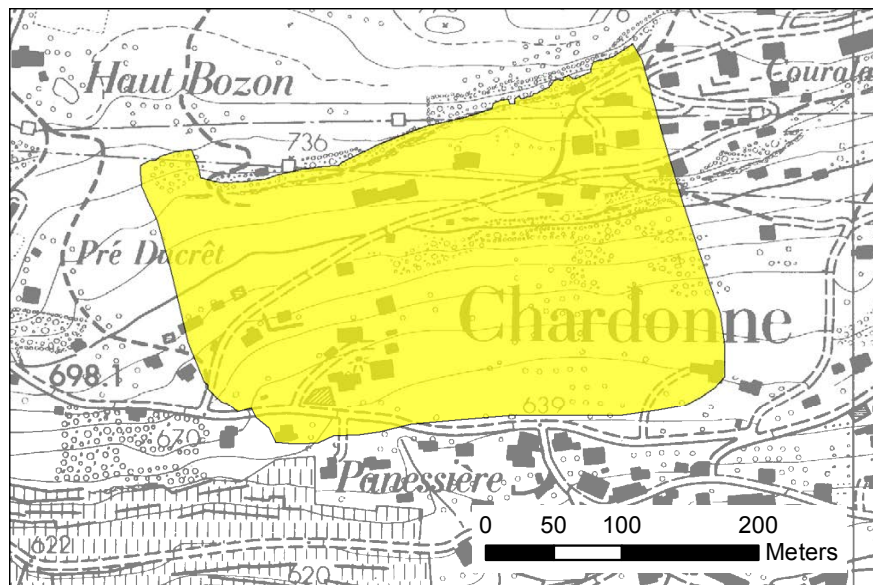


Figure 6.4: Hazard map after protection measures. Rockfall would occur only in the 300 years scenario and would have a low energy. (modified from: [Joliquin et al., 2010](#))

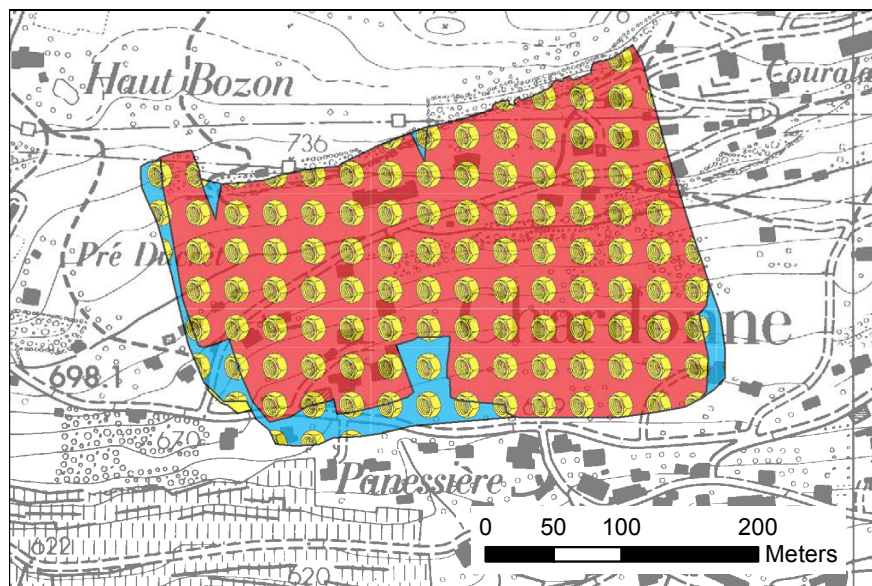


Figure 6.5: Proposed solution. The old hazard level would be over-impressed by yellow nuts to symbolize the protection measure and the hazard level with the protection measures (modified from: [Joliquin et al., 2010](#)).

6.4.2 Rockfalls in Veyrier-du-Lac

The second example is the village of Veyrier-du-Lac, in Haute-Savoie (Eastern France), which is subject to relatively frequent rockfalls (Monnet et al., 2010). However, the buildings are partly protected by a forest. In the french methodology of hazard mapping, forests are normally not taken into account (Berger and Rey, 2004). However, the rockfall propagation have been modelled both with an without the effect of the forest, using a matrix comparable to the one used in Switzerland (Monnet et al., 2010). Accounting for the effect of the forest, the propagation is much reduced. Figure 6.6 show what the map might look like using our symbology. The protection measure is symbolized here by a tree.

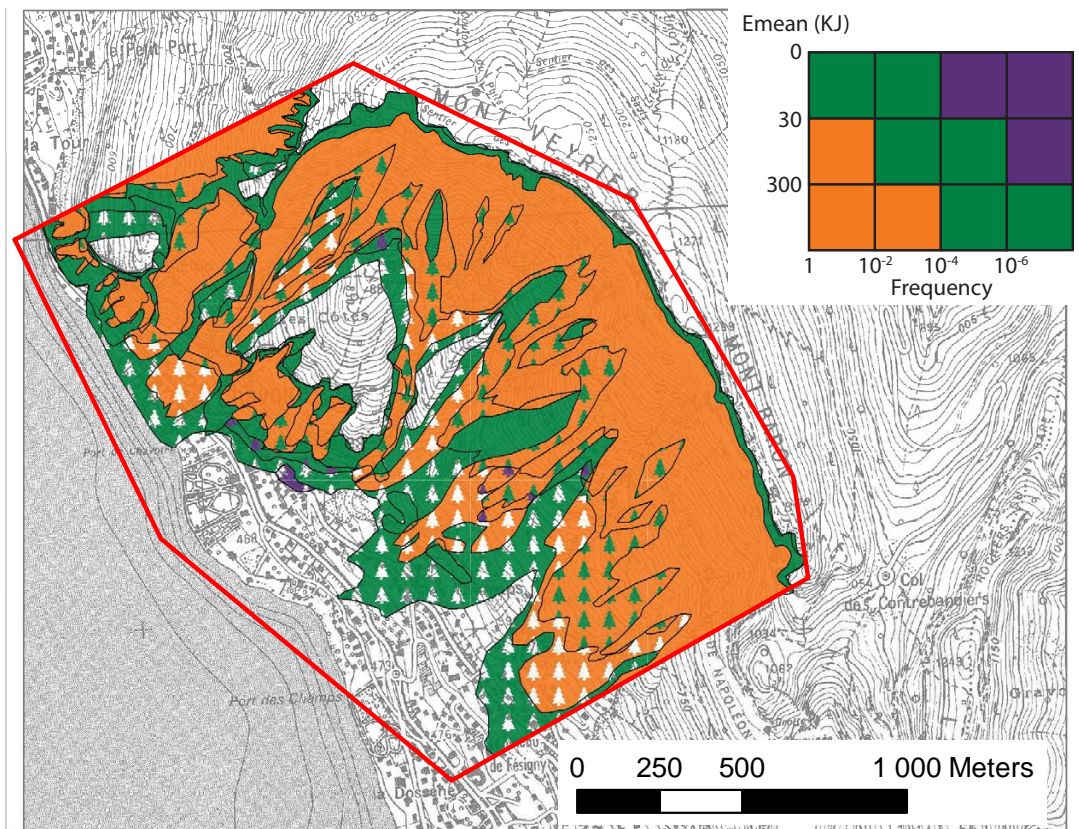


Figure 6.6: Proposed solution. Note that the axes of the matrix don't have the same direction as the Swiss matrix. Orange is then the highest hazard level (modified from: Monnet et al., 2010)

6.5 Conclusion

The building of protection measure is often correlated with an increase of constructions in the protected area (Di Baldassarre et al., 2013a), which should not be the goal in Switzerland (Lateltin et al., 2005). Furthermore, people in protected area are often not aware of the residual risk. Therefore, the method proposed here intends to make sure that the hazard level is known, both with and without the protection measures. This way, the population would be aware of the residual risk, and so would the authorities. Indeed, municipalities are often small in Switzerland and have therefore a small administration. This method is in agreement with Rouiller et al. (1998), who recommends, for rockfalls and rock slope failures, to always keep the original hazard degree with an overlay indicating that the area is protected.

Further research should however propose adequate symbols for all protection measures and make sure these symbols are easy to understand. Although this method is mostly designed for the Swiss methodology, it can easily be applied to other areas as long as hazard classes are used.

Part II

Stochastic risk modelling at regional scale

Introduction to Part II

This Part differs from Part I since it considers risk analyses at regional scale. If the principles or risk analysis are similar, analyses at regional scale generally face more uncertainties on all the risk parameters. Therefore, the use of a strategy to propagate the uncertainty is particularly important (e.g. Lari et al., 2009). All the models presented here have in common their non-deterministic nature and use stochastic (i.e. random) processes to provide a probability distribution of the models' outputs. Practically, the models consist in performing a large number of Monte-Carlo simulations with input values sampled randomly from a probability distribution.

These models (particularly Chapt. 7 and 9) are performed for insurance purposes. Indeed, the local-scale models presented in Part I permit to take decisions on protection measures, for example, whereas regional scale models aim at other goals that are more adequate for building insurance companies. These goals can be for example:

- Predict future losses to improve their management
- Test mitigation strategies
- Test our understanding of the factors controlling the risk
- Test the sensitivity of the output to each of the input factors
- Guide the collection of information on future events by identifying the key-parameters for the risk

The fitting of each of the models for these purposes is discussed in the general conclusions (Chapt.10).

In addition, these models need to cope with lack of data. Indeed, the collection of data at regional scale is more complicated and some parameters need to be estimated with different strategies. For example, the vulnerability is often not easy to assess, especially when an uncertainty exists on the actual intensity. Therefore, the vulnerability is not always related to the intensity in the following chapters. In addition, Chap. 8 and 9 use a random process to define if a building is affected or not before sampling, if needed, for a loss ratio.

Chapter 7

Evaporite sinkhole risk for a building portfolio

Foreword

This chapter has been submitted to Environmental Earth Sciences:

Nicolet, P., Choffet, M., Derron, M.-H., Jaboyedoff, M., and Lauraux, B.: Evaporite sinkhole risk for a building portfolio, Environmental Earth Sciences, Submitted.

Abstract

Karst-related hazard can be a problem for buildings, especially in the case of evaporite karst. This study aims at evaluating the risk posed by evaporite karst for a building portfolio in western Switzerland, using a susceptibility map and an event inventory. Since the inventory is not complete, different corrections aim at obtaining a frequency of sinkhole events damaging a building as close as possible to the actual frequency. These corrections account for the variation of the building stock during the inventory period, the varying inventory quality among the municipalities and the partial knowledge, even in the best case. This approach is preferred here to estimating spatially the hazard, since the amount of information on the frequency and magnitude is insufficient to draw a proper hazard map. The distribution of loss ratios is also retrieved from the inventory, thanks to the estimated or actual price of the remedial works. Annual losses are then estimated using a Monte-Carlo approach, which consists in sampling for a number of damaged buildings from a Poisson distribution, for a distribution of loss ratios and for a building value. Different exceedance curves relying on different hypotheses are presented, and the mean annual loss that the public insurance company might have to compensate is estimated at CHF 0.8–1.5 million.

7.1 Introduction

Karst-related hazard is periodically making the headlines due to spectacular collapses like in Winter Park, Florida (Tihansky, 1999), Ure Bank Terrace, UK (Cooper and Waltham, 1999) or in Camaioire, Italy (Buchignani et al., 2008). Beyond these spectacular cases, many regions in the world face engineering problems related to karst, in particular in evaporite rocks, since their solubility and dissolution rate are higher as compared to limestones and their mechanical strength is lower (Gutiérrez et al., 2008a). Furthermore, the higher solubility and higher dissolution rate of evaporite rocks makes them more sensitive to human activities, like water withdrawal or injection, since new cavities can develop at human time scale (e.g. Klimchouk, 2005)

Many studies have been made in order to map the susceptibility to sinkholes (e.g. Galve et al., 2009; Yilmaz et al., 2011; Pueyo Anchuela et al., 2015; Parise, 2015) or to propose good practices for land planning in karst areas (e.g. Sowers, 1996; Paukštys et al., 1999). On the other hand, relatively few studies quantify the hazard. A nice example of such an analysis is presented in Galve et al. (2011), who establish a magnitude-frequency analysis in the Ebro valley (Spain). This analysis is possible thanks to the very high occurrence rate of sinkholes in their study area.

When it comes to the induced risk, although sinkhole hazard is covered by insurances in some regions of the world like the United Kingdom (Cooper, 2008) or Florida (Cooper et al., 2011), relatively few studies try to assess quantitatively the risk induced by this phenomenon on human activities. Some examples can however be mentioned, like the long history of risk analysis in Russia (Ragozin and Yolkin, 2004; Tolmachev and Leonenko, 2011), which aims at classifying the relative risks. In addition, Cooper and Calow (1998) present an example of cost-benefit analysis and Galve et al. (2012) apply such an analysis to evaluate the best measure to mitigate sinkhole damage on roads.

Other studies present numbers on the reported loss event frequency, costs or victims, which permit to be aware of the orders of magnitude of the expected losses. De Bruyn and Bell (2001), for example, reports 38 victims and one billion ZAR (around USD 75 million) of losses during 30 years in the "dolomite lands", which is a large and densely populated area of the Gauteng Province, in South Africa. The particular severity of the consequences, especially regarding the number of fatalities, is a consequence of the very high susceptibility induced by the mining activity, more precisely by the drastic lowering of the water table. Tolmachev and Leonenko (2011) mention 73 cases of damage to construction (not only buildings) in around 50 years (1.3 events per year) in the city of Dzerzhinsk, in Russia, among which 14 events are characterised by the complete destruction of industrial sites. The population of the city is of around 250'000. Over all Russia, the cost has been estimated at 1-1.5 billion dollars per year (Ragozin, 1994, cited by: Ragozin and Yolkin, 2004). Cooper (1998) and Paukštys et al. (1999) report a major

subsidence every one to three years around the city of Ripon, in England, and estimate that the property loss is of around one million GBP in ten years (around USD 1.6 million, i.e. around 160,000 USD/year) for a city of around 16,000 inhabitants.

The present work aims at estimating the cost that would result of the inclusion of sinkhole-related hazard in a mandatory public building insurance, and at presenting a methodology to reach this goal with scarce data. It focuses on the Canton of Vaud, a state located in western Switzerland. Although part of the state is concerned by karstified limestones, this study focuses on the evaporite karst, which is present in the eastern part of the territory. This area is indeed more populated than the area where limestone karst is present. Therefore, as, in addition, evaporite karst is more sensitive to human activities, higher losses are expected in the evaporite karst area. This assumption is supported by the fact that no loss event was known for buildings located over limestones in the Canton when the study started. Recent ongoing investigations of the insurance company however reveal a surprisingly high number of damaged buildings. Although the damages are not formally attributed to karst processes yet, this needs to be further investigated.

7.2 Study area

7.2.1 Geology

The Canton of Vaud is located in South-Western Switzerland, and is composed, from North-West to South-East, of the Jura Mountains, the Molassic basin and the Alps (Fig. 7.1). A brief description of the geological framework of the canton is given below and is, for the most part, derived from [Trümpy \(1980\)](#), [Escher et al. \(1997\)](#), [Steck et al. \(2001\)](#) and [Pfiffner \(2014\)](#), where further information can be found.

The Jura Mountains is a fold and thrust belt composed, in the region, of around 1000 m of Dogger to Cretaceous Limestones and Marlstones. The Molassic basin is made of Tertiary sandstones and marlstones resulting from the erosion of the Alps, and except in the vicinity of the Alps, is almost not deformed. It is often covered by morainic deposits. When it comes to the Alps, the structure is more complex, but is of primary interest for the sinkhole process since evaporites are met in many places. From a paleogeographic perspective, the Alps can be divided in the Helvetic domain, which correspond to the European continental margin – the Ultrahelvetetic being the most distal part of the margin –, the Valais trough (corresponding to the lower Penninic tectonic unit), the Briançon rise (middle Penninic), the Piemont ocean (upper Penninic), and the Austroalpine domain, which corresponds to the Adriatic continental margin (e.g. [Escher et al., 1997](#)). During the Trias, shallow marine conditions were dominant, and evaporitic rocks were deposited in most of the domains listed above. In particular, the main units concerned by

evaporitic karst are the Submediane zone, which is often attributed to the external part of the Briançon domain, and the Ultrahelvetic Nappes (Fig. 7.1). As far as we know, no significant lithological characteristics differentiate the evaporites from these units, which are, in most places, composed of gypsum.

Regarding the Helvetic domain, pre-Triassic basement (Aiguilles-Rouges Massif) and cover (Morcles, Wildhorn) nappes form the South-Eastern edge of the Canton. Triassic rocks are present in the cover nappes, but are nevertheless thin and don't outcrop in the study area. On the other hand, although the Ultrahelvetic domain corresponds generally to higher deposition depth as compared to the Helvetic, the Ultrahelvetic Bex and Laubhorn Nappes contain a large sequence of Triassic evaporites. Together with other Ultrahelvetic nappes, they form the "Pass zone", which is a region of relatively low altitude in the North-West of the Helvetic nappes, resulting from the preferential erosion of the weak rocks which form these nappes.

When it comes to the lower and middle Penninic, The Niesen nappe originates from the most external part of the Valais domain, and is mainly composed of post-Jurassic rocks. On the other hand, Triassic series are well developed in the middle Penninic. Nappes of Briançon origin, namely the Préalpes Médiannes Rigides, the Préalpes Médiannes Plastiques and the Breccia nappe form the external part of the Alps in this region. However, evaporites acted as a décollement surface, and only few carnageules are outcropping. Nonetheless, as mentioned previously, evaporites outcrop in another unit attributed to the Briançon domain, the Submediane zone, which is a complex amalgamation of various types of rocks embedded in a wildflysch or gypsum matrix (Trümpy, 1980).

Finally, the Sarine nappe is a Late Cretaceous to Eocene flysch of Piemont origin, whereas The Simme is the only nappe of Austroalpine origin in the region, and is a wildflysch with Jurassic and Cretaceous elements. Therefore, both nappes contain no significant evaporite rocks.

7.2.2 Karst features

Karst features are widely present in the Jura, where limestones are generally outcropping or present at shallow depth, with typical collapse or suffosion sinkholes that remain well visible due to their marked shape and to the large portion of the territory used as pasture. Karstic features in the Prealpes are less spectacular, since they result mostly of the dissolution of evaporitic rocks, which is often marked by shallow depressions formed by the sagging of the overlaying cover (Fig. 7.2). Several evidences of karst have been observed in the area, as shown in Fig. 7.2, ranging from well-defined pipes visible on a quarry wall, to shallow, sometimes badly defined, depressions. Several rates of surface subsidence have also been measured, ranging from the sudden collapse of a small cavity to a continuous subsidence (e.g. Fig. 7.2 a). An intermediate

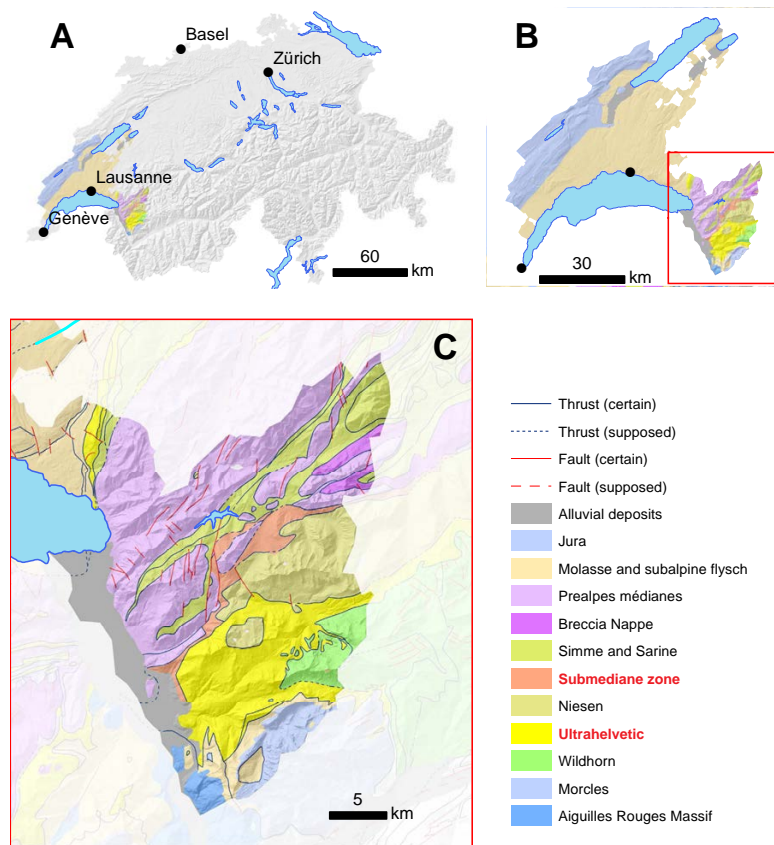


Figure 7.1: A: Location of the Canton of Vaud in Switzerland (coloured area). B: Canton of Vaud with the extent of map C, which contains the study area. C: Tectonic map of the Prealpine part of the Canton of Vaud (Modified from: [University of Bern and FOWG, 2005b](#); [Steck et al., 2001](#)). Evaporite rocks are present mainly in the Submediane zone and the Ultrahelvetic (in bold red). The attribution of certain formations to one or the other of these two unit is subject to debate, but is beyond the scope of this article (Hillshade and boundaries: © Swisstopo).

case can be illustrated by an event which occurred in 1984, where a 50–100 m wide zone subsided from up to 8 mm in two months, provoking fissures in at least three buildings. The observed diversity of processes is coherent with the observations of [Gutiérrez et al. \(2008b\)](#), who noted that the range of involved processes is wider in evaporite karst. In addition, in comparison to the Jura, denser and more urbanized municipalities are concerned in the Prealps, which means that the number and total value of exposed buildings is more important, but also that the traces of past event tend to be less visible. Furthermore, the mean building's value is also higher in the Prealps, where tourism is an important part of the economic sector. For this reason, this region is currently experiencing a faster development and this situation is expected to continue, although recent laws makes this prediction uncertain.

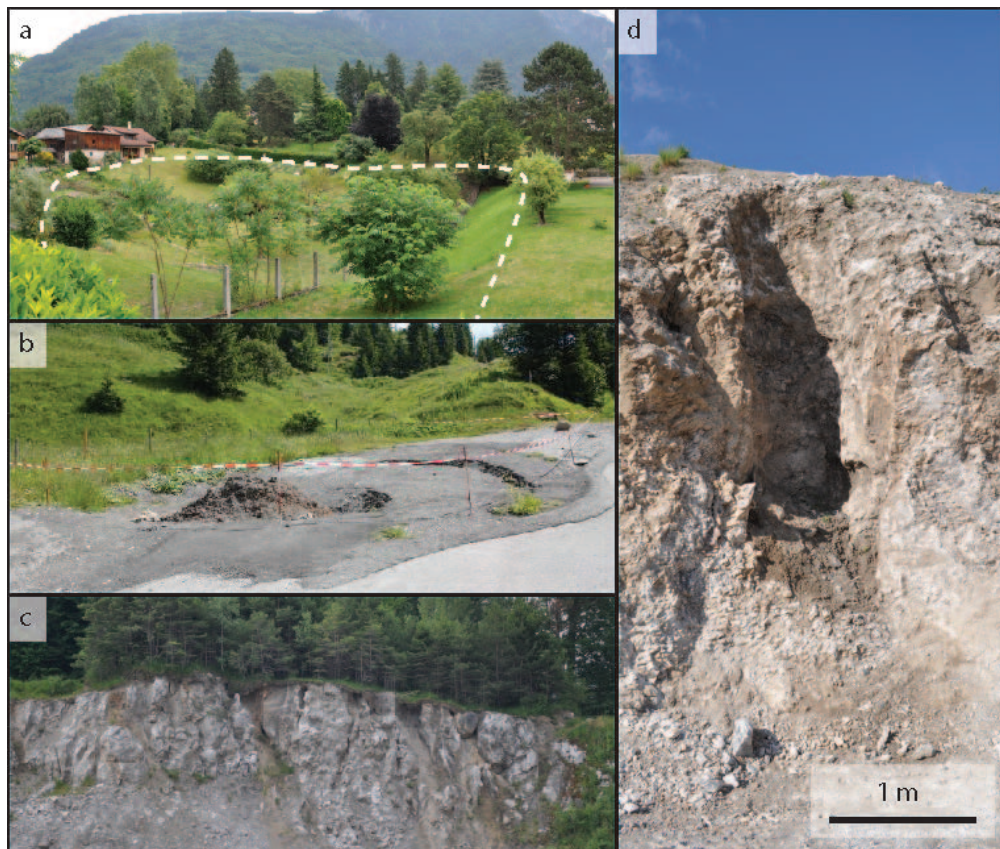


Figure 7.2: Examples of sinkhole encountered in the study area. **a:** Cover-sagging sinkholes in central Bex affecting the buildings on the left. **b:** collapse sinkhole on a road. **c and d:** Sinkholes cut by excavation in a quarry.

7.2.3 Insurance context

Every building of the canton is insured by a unique public insurance company, which represented a total of 203,261 buildings and a value of approximately CHF 230 billion end of 2014 (ECA, 2015). The insurance covers the losses resulting from fires and from natural hazards such as landslides, snow avalanches, snow creeping, floods, storms or meteorite impacts (Grand Conseil du Canton de Vaud, 1952, Art. 9). Losses resulting from insufficient foundations, water infiltration due to pipe breaking or earthquakes are not covered. Due to the potential difficulty of differentiating damage resulting from improper foundation design from damage induced by a shallow and slow-moving cover sagging sinkhole, sinkhole hazard was not covered. However, the insurance has been commissioned by the cantonal authorities to re-evaluate the exclusion of sinkholes from the insurance.

A reason for this re-evaluation is that the Canton is in charge of mapping the gravitational

hazards, namely floods, snow avalanches, rockfalls, debris-flow, deep-seated landslides, shallow landslides, and sinkholes; sinkhole being the only hazard of the list which was not covered by the insurance at the time of this study. Since the sinkhole hazard map will prohibit building in some areas, which, as mentioned by [Paukštys et al. \(1999\)](#), is the most cost-effective form of planning, imposing constructive measures in the less endangered areas and insuring the residual risk would be a coherent risk management strategy.

At the time of this study, a preliminary hazard map has been drawn by the authorities for the whole Canton, and detailed hazard maps are being established in the regions where buildings might be threatened by this hazard.

7.3 Method

Risk is defined as the hazard multiplied by the potential worth of losses. A risk analysis needs then to estimate the events frequency (i.e. the hazard), as well as the potential consequences, which depend both on the values of the element at risk and on their vulnerability, i.e. the degree to which the element is affected. Risk depends also on the spatial relation between the event and the element at risk. This study is based on a preliminary hazard map (subsection [7.3.1](#)), which aims at locating the potential events, and on an event inventory (subsection [7.3.2](#)), which can be used to estimate the frequency at which a sinkhole damages a building, as well as the building vulnerability.

7.3.1 Susceptibility map

The state of Vaud has established a susceptibility map for sinkholes ([Champod, 2011](#)), which aims at identifying the area for which more detailed hazard mapping is needed. This map takes several parameters into account, considers both carbonate and evaporite rocks and distinguishes several levels of susceptibility. However, for this study, we need to keep only the area potentially affected by evaporite dissolution. In addition, the method we use for risk analysis does not permit to differentiate susceptibility levels. This important limitation will be discussed in section [7.5](#), but to partly solve it, we will consider two different susceptibility maps.

- Susceptibility map A considers that all area located in a radius of 100 m around an evaporite-related sinkhole are susceptible. The sinkhole inventory has been produced by the cantonal administration and does not contain the rock type. Therefore, we interpreted it from the geological maps in order to suppress the limestone-related sinkholes. Since sinkholes are generally not visible in urbanised areas, known past events have been added to the sinkhole inventory.

- Susceptibility map B considers that all area where evaporite rocks occur at the surface or the "close" sub-surface, according to the geological maps and associated cross-sections, are susceptible. This map has been established for the preliminary hazard map of the administration (Champod, 2011).

Although a proper hazard map containing information on the frequency (such as in Galve et al., 2012) would be preferable, it is difficult to establish here since we have very few information on the temporal occurrence of sinkholes. In addition, other parameters such as the proximity to rivers or the tectonic lines are not considered here. However, as shown by Galve et al. (2009), the proximity to a sinkhole is the best proxy for the susceptibility.

7.3.2 Event inventory

In order to characterize the risk, an inventory of past events is desirable. However, since this type of hazard is not covered by the building insurance company yet, no centralized and standardized inventory of damaged buildings is maintained. Therefore, data have been collected when available from the municipalities' technical services and from Lauraux SA, a private civil engineering company active in one of the most concerned municipalities. Since no information is available on the sinkhole frequency, this inventory is used to estimate a frequency of events damaging a building and a distribution of loss ratio.

Frequency assessment

Since such an inventory is by nature incomplete and uneven, different corrections need to be applied in order to get as close as possible to the actual frequency of sinkhole events damaging a building. The adopted procedure, which is done separately for both susceptibility maps, is the following:

1. From the collected events, calculating for each municipality j , the mean number of events damaging a building per year, Λ_{raw}^j (to help the reader, a list of the variables used in this study is given in Appendix 7.6).
2. Correcting this number in order to account for the growth of the municipality building stock during the time span covered by the inventory, with the equation:

$$\Lambda_{obs}^j \left[\frac{\text{damaged building}}{\text{year}} \right] = \Lambda_{raw}^j \times \frac{n \times N_{y_n}^j}{\sum_{l=y_0}^{y_n} N_l^j} \quad (7.1)$$

Where Λ_{obs}^j is the observed frequency for municipality j , n is the number of years, ranging from y_0 to y_n (both included) and N_l^j is the number of at-risk buildings in municipality j in year i , whereas N_{y_n} is the number of buildings at the end of the inventory. We define the at-risk building as the buildings located in a susceptible area.

3. Calculating the observed frequency of event damaging a house per year and per at-risk building at the time of the end of the inventory :

$$\lambda_{obs}^j \left[\frac{\text{damaged building}}{\text{year} \times \text{at-risk building}} \right] = \frac{\Lambda_{raw}^j}{N_{y_n}^j} \quad (7.2)$$

4. Affecting the highest frequency per at-risk building (λ_{obs}^{max}) to all the municipalities and calculating the deduced frequencies:

$$\Lambda_{deduced}^j \left[\frac{\text{damaged building}}{\text{year}} \right] = \lambda_{obs}^{max} \times N^j \quad (7.3)$$

Where N^j is the current number of at-risk buildings in municipality j .

5. Summing the frequencies of all communities:

$$\Lambda_{deduced}^{total} \left[\frac{\text{damaged building}}{\text{year}} \right] = \sum_j \Lambda_{deduced}^j \quad (7.4)$$

6. Correcting the total frequency with an expert defined multiplication factor f , or by a range of factors $f_{min} \rightarrow f_{max}$ which accounts for the estimated proportion of known events in the municipality with the highest frequency per at-risk building (λ_{obs}^{max}) calculated in step 3.

This procedure permits to deduce a frequency for the municipalities where no or few events have been collected. The consistency of the frequency assessment relies then on several hypotheses, especially that the hazard is equivalent in any susceptible area, especially from one municipality to the other. It also assumes that the building conditions are similar, in particular the buildings foundation and the destabilizing factors such as leaking pipes. Finally, the multiplication factor presented at step 6 is hard to define, that is why it might be preferable to use a range rather than a unique value.

Vulnerability assessment

In order to identify the potential loss amount, the loss value (CHF) is compared to the building insurance value (CHF) with the aim of building a distribution of loss ratios. The loss ratio is

defined as the loss value (i.e. the amount of money the insurance has to compensate if there is no franchise) compared to the insured value. Since the year of the loss event is, in this case, always older than the year of the building value estimation, the consumers price index (CPI; [Federal Statistical Office, 2015](#)) is used to actualize the loss values to the building estimation year.

The term loss ratio is preferred here to the term vulnerability, as this latter term is generally related to the intensity of the event, which is not taken into account here. In addition, loss ratio better reflects the fact that we are concerned here only about a monetary loss and that we do not take into account other factors such as the building functionality. However, these terms are close and the variable V is used to denote the loss ratio.

The probability of total loss P_{TL} is defined as the proportion of damaged buildings which were too strongly damaged to be repaired (or which could only be repaired at a price higher than their insurance value, which means that their calculated loss ratio is above one). For the partially damaged buildings (i.e. with a loss ratio below 1), the observed distribution of loss ratios are fitted with a 2 parameters generalized Pareto distribution with cumulative distribution function (cdf):

$$F(V) = 1 - \left(1 + \alpha \frac{V}{\beta}\right)^{-\frac{1}{\alpha}} \quad (7.5)$$

where V is the loss ratio, α is a shape parameter and β a scale parameter. The parameters are fitted using the maximum likelihood estimation ([Embrechts et al., 1997](#)). Generalized Pareto distribution is used because it permits to fit well the data, especially the high proportion of small loss ratios, and because it is a relatively simple distribution. The main disadvantage of this distribution for this analysis is that it is not bounded to one. To take into account the representativeness of the sample, the distribution of the parameters between the upper and the lower 99 % confidence interval is retrieved. The distribution of α is normal, whereas β is defined by a log-normal distribution.

7.3.3 Risk analysis

The frequency of sinkhole events damaging a building, the distribution of loss ratios and the spatial distribution of buildings allow to establish a risk analysis based on a Monte-Carlo simulation, in order to estimate the distribution of aggregated losses (i.e. the sum of all the individual losses) over the years for the insurance company and to account for the uncertainty affecting some of the parameters. The general framework of the simulation is given in [Fig. 7.3](#), and is done once for each susceptibility map. The first step of the procedure is to define the correction factor f used to correct the deduced frequency. The analysis is performed both with a unique f (denoted "S" for "scalar") or with a uniform distribution ranging from f_{min} to f_{max} (denoted "U" for "uniform").

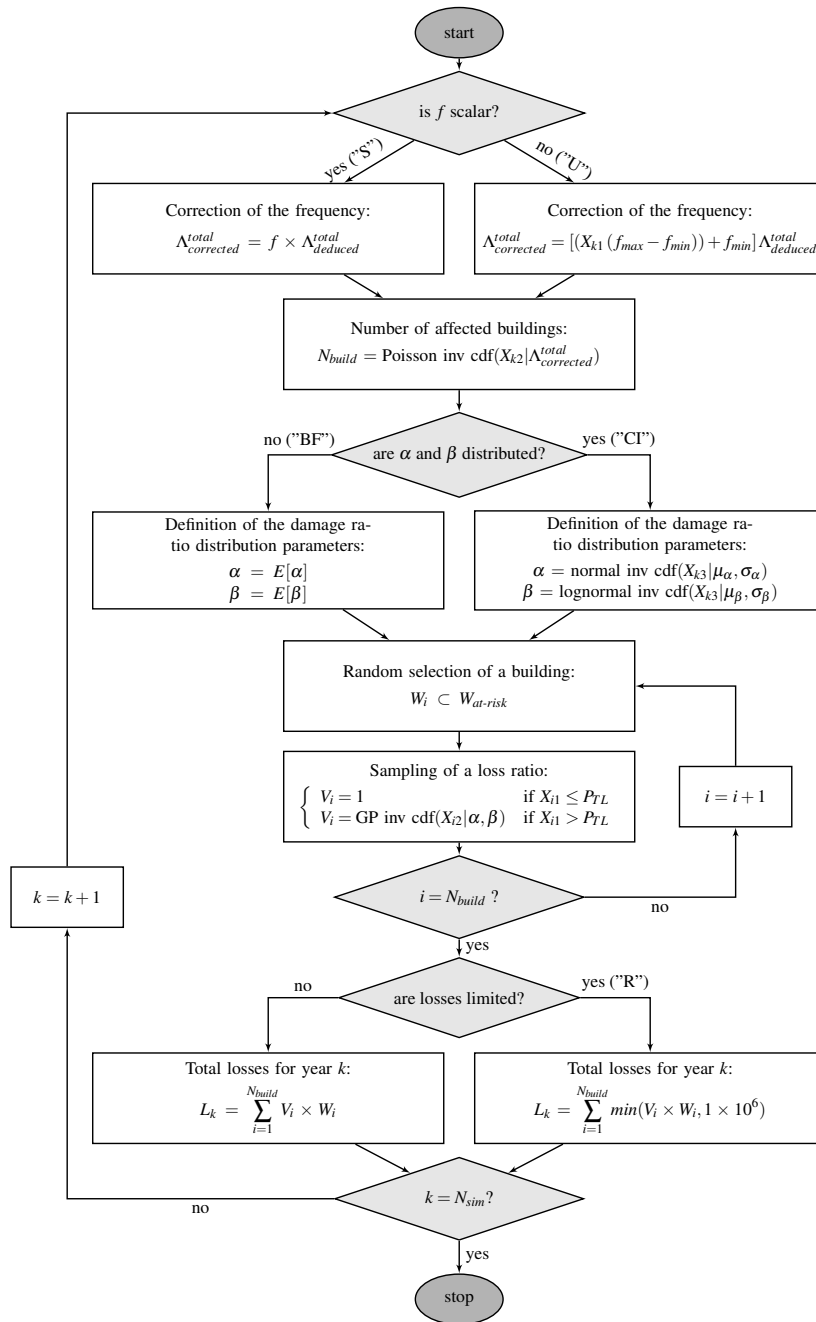


Figure 7.3: Flow-chart of the risk assessment procedure. Letters between quotation marks indicate the letters used to identify the type of analysis. Random variables are denoted by the letter "X" and their index indicates if the variable varies at each financial year ("k") or for each building ("i") and if the variable is used several times (same letter and number) or not. A list of variables is given in Appendix 7.6.

Then, the number of affected buildings in the considered year (N_{build}) is calculated. Considering that each event affects only one building and that the sinkhole occurrences are independent from each other, a Poisson distribution is used, which is in accordance with other areas (Tolmachev and Leonenko, 2011). Once the number of affected buildings (N_{build}) is defined, the value of each building (W_i) is chosen at random in the list of buildings inside the susceptible area ($W_{at-risk}$). For each of these N_{build} buildings, a loss ratio (V_i) is defined. If a random variable X_{i1} is lower than P_{TL} , the loss ratio is one. Otherwise, a generalized Pareto inverse cdf with parameters α and β is used to sample a value of V_i . α and β are defined using whether the best fit value (denoted "BF") or by sampling the distributions inside the confidence interval with an identical randomly defined quantile X_{k3} (denoted "CI"). In any case, α and β are kept unchanged for all affected buildings in year k . The total losses of year k are then given by:

$$L_k = \sum_{i=1}^{N_{build}} V_i \times W_i \quad (7.6)$$

This operation is repeated N_{sim} times in order to form an "exceedance probability curve", which gives the probability of exceeding a given amount of losses in a financial year (e.g. Michel-Kerjan et al., 2012). The same is tested using a maximum value for the individual losses (denoted "R" for "roof"). The reason for this roof is that we expect that expensive buildings have also a larger spatial extent, which reduces the probability for the entire building to be affected. It has to be noted that inside a financial year k , the parameters for which the distribution reflects the epistemic uncertainty (f , α , β) and not a "natural variability" do not vary, in order to properly reflect the uncertainty in the final outcome.

7.4 Results

7.4.1 Susceptibility map

The susceptibility maps obtained are given in fig. 7.4. As a comparison, a building density map with the location of the inventoried events is also shown. By comparing these maps, it is possible to observe that the municipalities of Bex, Gryon, Ollon, Ormont-Dessous and Ormont-Dessus are especially affected, since relatively high building densities intersect with sinkhole susceptibilities. On the other hand, the number of buildings located in the susceptible area is quite different for the two maps since 1 723 buildings are located inside a susceptible area in map A and 8 850 in map B. It has to be mentioned that susceptibility map B extends slightly outside of the studied municipalities (south of Bex and between Corbeyrier and Aigle), but the insurance data are not available in these areas.

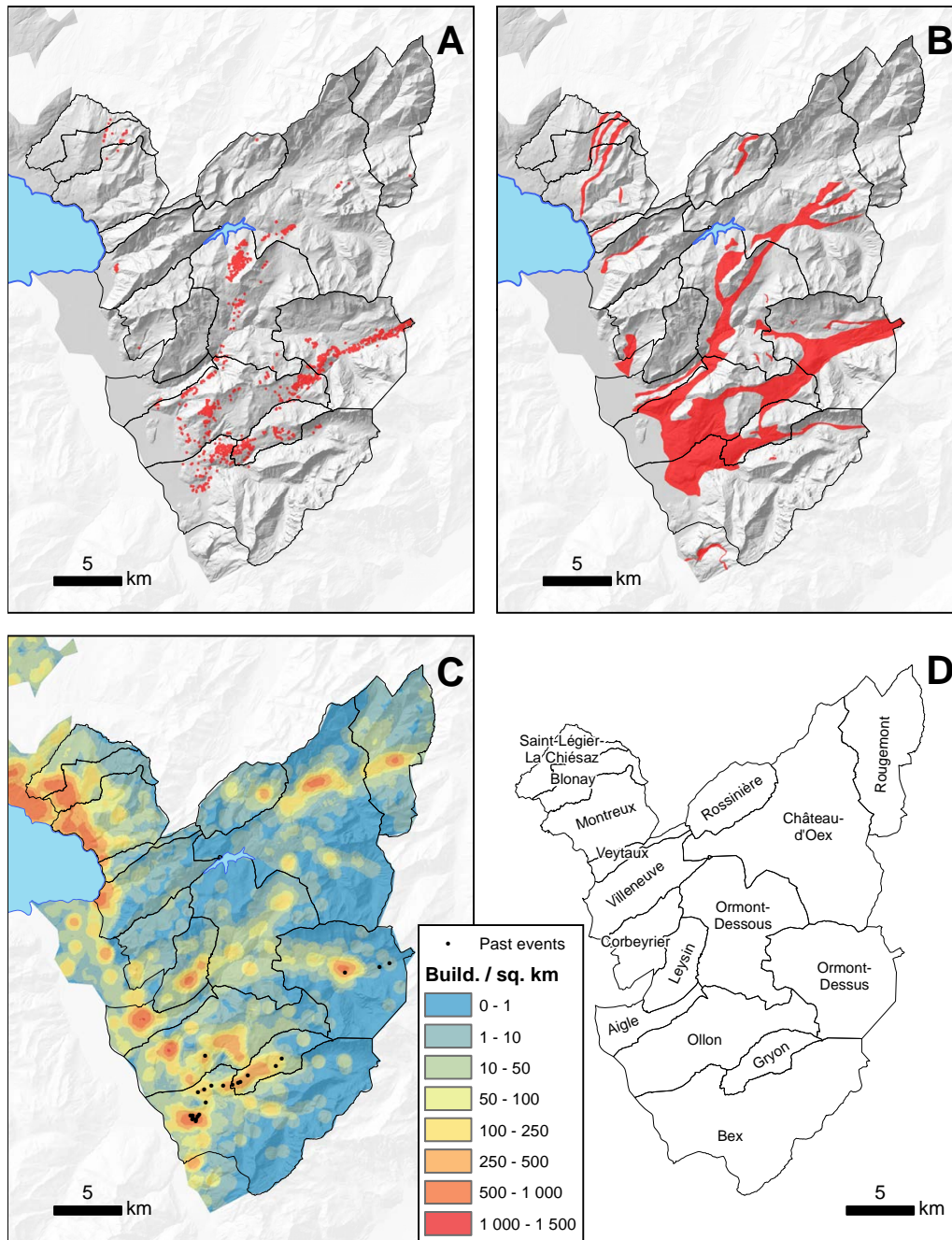


Figure 7.4: A: Susceptibility map A, established using the occurrences of sinkholes. B: Susceptibility map B, established by (Champod, 2011) using the occurrence of evaporitic rocks. C: Building density map showing the number of buildings per square kilometres in a 500 m radius. The location of the inventoried past events is shown as well. D: Municipality names (Basemaps © Swisstopo and Etat de Vaud)

7.4.2 Event inventory

During the inventory process, we identified 32 buildings affected by sinkholes in the past (see fig. 7.4 C for their location). The temporal extent of this inventory depends on the different sources. A value of loss is available for 14 of the events. This value is whether the actual repair cost or an estimation if the reparations have not been performed. The results of the inventory are very different from one municipality to another, according to the archives of the municipalities and the persons in charge.

Frequency

Since it turns out that the inventory in each municipality comes from a unique source, the number of events is compared to the temporal extent of this particular source. The frequencies are then corrected with Eq. (7.1), using the construction year of the buildings. We consider, with this correction, that no building has been dismantled during the period of time, which is an acceptable simplification since the population is growing. The total frequencies obtained at this step are presented in Fig. 7.5 ("Observed frequency"). These frequencies are then compared with the number of buildings located in a susceptible area in each municipality (the procedure is done separately for both maps). The maximum frequency per at-risk building (λ_{obs}^{max}) is observed in Bex. Therefore, this value is multiplied by the number of at-risk buildings of each municipality, which permits to obtain the "deduced frequencies" presented in Fig. 7.5. The sum of all these frequencies provides a value of 2.67 events per year using map A and 4.02 events per year using map B.

The transformation from observed frequency to deduced frequency is very significant for some municipalities, such as Ollon, Gryon or Ormont-Dessus. In Gryon, the observed frequency is multiplied by 11 and 8 respectively, although the inventory provided by the municipality technical service seems quite exhaustive. In Ollon, the multiplication factor is very important, but the person in charge of the technical service just arrived in the municipality and was for this reason not able to provide some information. The only known case of building affected by a sinkhole in Ollon has been provided by Lauraux SA.

Vulnerability assessment

One of the 14 events for which an amount of loss is available suffered a total destruction. Therefore, the probability of total loss is estimated at $P_{TL} = 0.0714$. The 13 other events are used to fit a generalized Pareto distribution (Fig. 7.6). The cdf of parameters α and β are presented in Fig. 7.7. The quantiles 0.5 % and 99.5 % of these parameters gives the 99 % confidence interval given in Fig. 7.6, whereas the median value correspond to the best fit. As mentioned in Sect. 7.3.2,

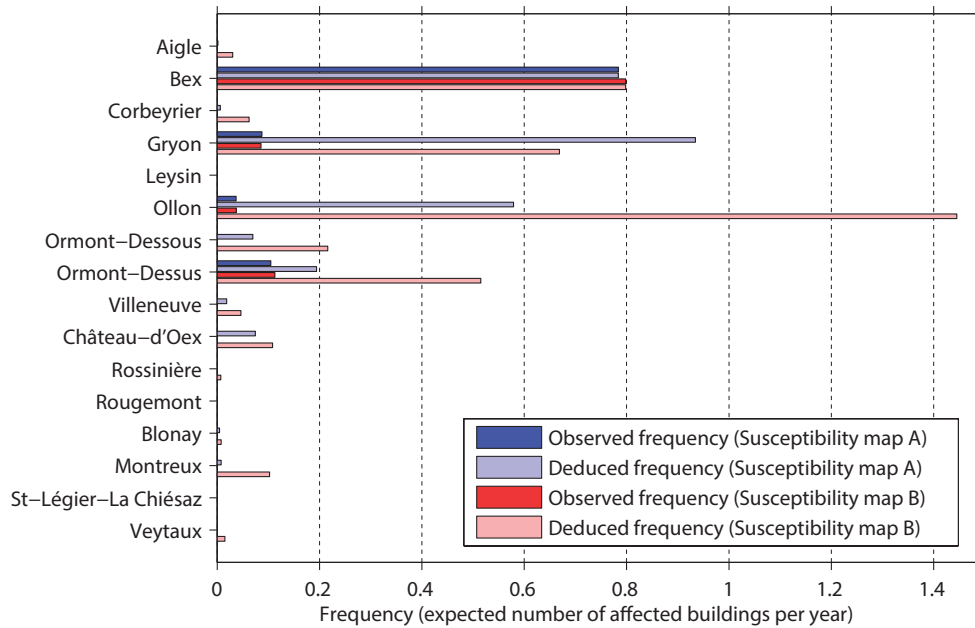


Figure 7.5: Frequency of building damaged by a sinkhole in each municipality of the study area. The observed frequency (Λ_{obs}^j) is the one after the correction accounting for the growth of the municipality building stock, as presented in step 2 of the list presented in Sect. 7.3.2, whereas the deduced frequency ($\Lambda_{deduced}^j$) attributes the maximum frequency per at-risk buildings (observed in Bex) to all the municipalities (step 4 of the list). The total deduced frequency ($\Lambda_{deduced}^{total}$) for the area is 2.67 events per year using map A and 4.02 events per year using map B. The observed frequencies are different for the two maps because the correction accounting for the growth of the municipalities only considers the susceptible areas.

the vulnerability distribution used can take values above one, which is not realistic for a loss ratio. Therefore, in such case, V_i is considered to equal one.

7.4.3 Risk analysis

Risk analysis is performed using the frequencies deduced at Sect. 7.4.2, which are multiplied by a factor representing the proportion of known events (item 6 of Sect. 7.3.2). This factor takes whether the value of the best guess, 1.5 ("S"), or is distributed uniformly between 0.5 and 5 ("U"). This factor should theoretically not be below 1, but we consider here the possibility that the rate defined in Bex might be too high for the other municipalities.

Regarding the loss ratio, the best-fit presented in Fig. 7.6 is whether used directly ("BF") or the distribution of parameters retrieved from the definition of the confidence interval presented in Fig. 7.7 is used ("CI"). In addition, all the combination have been tested with ("R") or without a roof of CHF 1 million per event. This limitation only affects the part of the curve above 1 million.

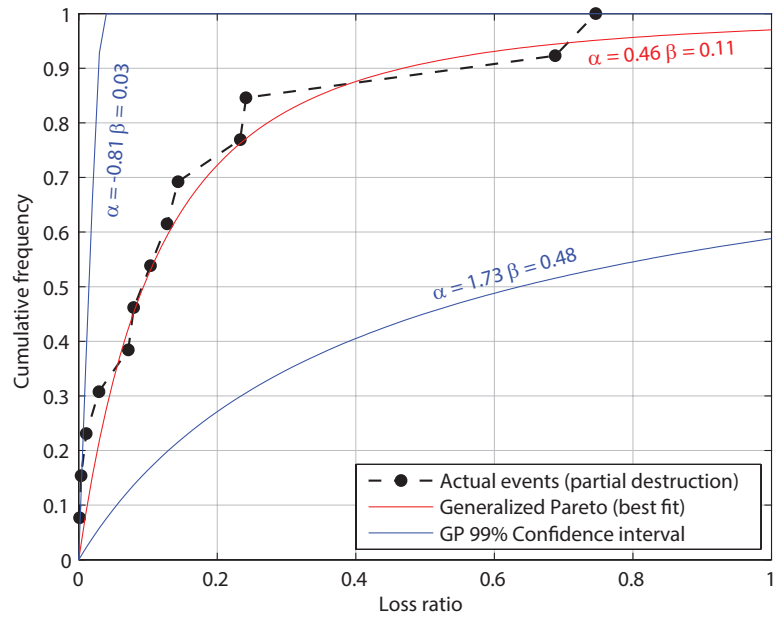


Figure 7.6: loss ratio of the partially affected buildings and generalized 2-parameters Pareto distribution adjusted to the data (red curve). The blue curves indicate the 99 % confidence interval.

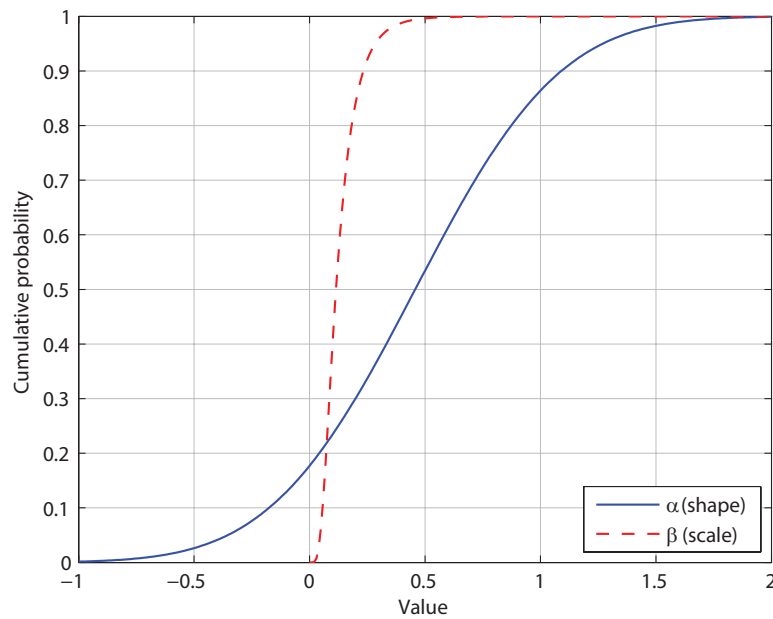


Figure 7.7: Distribution of the parameters α and β of the generalized Pareto distribution used to assess the loss ratio. The median value correspond to the best fit, displayed in red in Fig. 7.6. The values of the 0.5 % and 99.5 % quantiles are used to draw the 99 % confidence interval in Fig. 7.6.

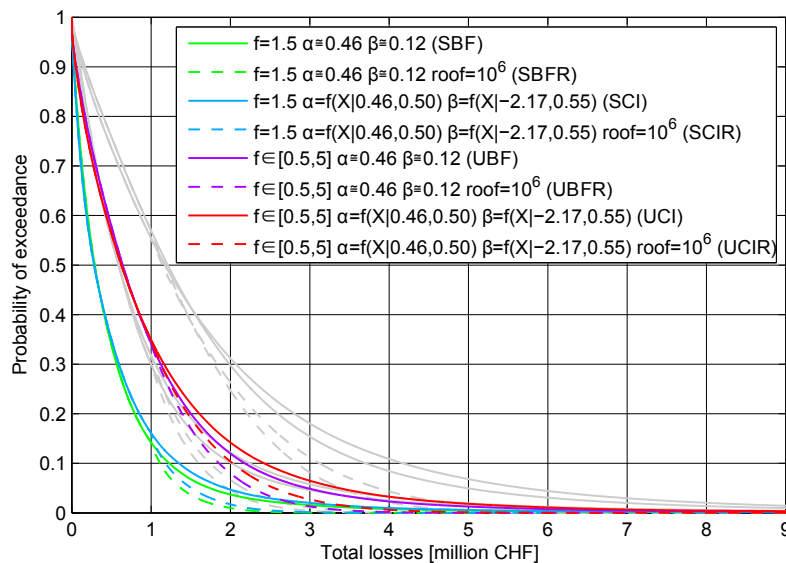


Figure 7.8: Probability of exceeding a total loss amount in a financial year, obtained with different approaches. Curves in grey have been obtained with susceptibility map B and show a similar pattern as the colour curves, which have been obtained with susceptibility map A. The first letter stands for a unique ("S") multiplication factor for the frequency or for a uniform distribution ("U"). Letters two and three indicate if the best fit ("BF") or the distribution of the parameters obtained from the confidence interval ("CI") are used for the parameters α and β of the generalized Pareto distribution. The values indicated inside the square brackets correspond respectively to the quantiles 0.5 % and 99.5 %. Finally, the "R" in 4th position indicates that a roof of 1 mio per loss event is used (dashed curves).

The results are presented in Fig. 7.8 as a exceedance probability curve and in table 7.1 in terms of mean, median and values for specific probabilities. The set of curves using Susceptibility map B is shown in grey, but apart from the fact that the expected losses are higher, they show a similar pattern as the other curves. A large separation is visible between the curves obtained with a unique multiplication factor and the curves obtained with a range of values. The generally lower values obtained with the unique value arise from the fact that this value (1.5) is significantly below the mean of the range (0.5–5). Compared to the values obtained with the best fit, the distribution obtained using the distribution of the generalized Pareto parameters tend to be more spread, which corresponds to the expectation. The difference is however relatively small (comparing for example the mean and median values). Finally, all the curves with a roof at 1 million CHF show a discrepancy above this value, which is significant in terms of average loss, since the extreme events are limited.

According to all the simulations, few years should see no loss at all, whereas a value of CHF 2 million should be exceeded every 3–100 years, depending on the curve used.

Table 7.1: Average and median annual losses using the different approaches (see Fig. 7.8 for the abbreviations). $P(L) = 0.1$, $P(L) = 0.05$ and $P(L) = 0.01$ correspond to the total losses that have a probability of respectively 10 %, 5 % and 1 % to be exceeded in a year. Values are in million CHF.

Susceptibility map A	SBF	SBFR	SCI	SCIR	UBF	UBFR	UCI	UCIR
Average [MCHF/year]	0.528	0.451	0.562	0.474	0.966	0.827	1.027	0.868
Median [MCHF/year]	0.289	0.289	0.280	0.280	0.641	0.641	0.624	0.624
$P(L) = 0.1$ [MCHF/year]	1.227	1.114	1.350	1.182	2.179	1.856	2.424	2.026
$P(L) = 0.05$ [MCHF/year]	1.739	1.374	1.938	1.507	2.966	2.275	3.367	2.551
$P(L) = 0.01$ [MCHF/year]	3.621	2.000	3.995	2.211	5.471	3.141	6.183	3.687
Susceptibility map B	SBF	SBFR	SCI	SCIR	UBF	UBFR	UCI	UCIR
Average [MCHF/year]	0.940	0.748	0.999	0.782	1.721	1.369	1.832	1.431
Median [MCHF/year]	0.591	0.591	0.589	0.589	1.209	1.175	1.176	1.143
$P(L) = 0.1$ [MCHF/year]	2.013	1.598	2.240	1.743	3.703	2.832	4.173	3.122
$P(L) = 0.05$ [MCHF/year]	2.876	1.954	3.226	2.160	4.977	3.385	5.702	3.855
$P(L) = 0.01$ [MCHF/year]	5.919	2.667	6.516	3.036	8.893	4.496	10.025	5.414

7.5 Discussion

Performing a risk analysis is often tricky, since standardized and complete inventory of past events – focused on affected buildings or on the natural process itself – are frequently not available. Furthermore, little information on vulnerability is generally available. This is especially the case for sinkholes, since no information on the vulnerability of buildings regarding this phenomenon has been found in the literature. In addition, would it exist, it might be inapplicable in a study area if defined somewhere else. However, since risk analysis is essential for the insurances, but also for the administrations, it needs to be performed anyway, taking care of the uncertainties and simplifications.

Using a Monte-Carlo analysis permits to account for part of the uncertainties and to estimate the variation of the losses over the year. Indeed, risk could also be calculated using the mean loss value of the event inventory (CHF 139,000) multiplied by a frequency of 4.01 or 6.03 events per year ($f = 1.5$). Doing this, the mean risk would be respectively 556 695 and 838 170 CHF/year, which is close to the average obtained with the methods using a single value for f . However, this would not permit to retrieve the loss distribution, which is useful for the insurance company since it allows estimating the needed reserves. Furthermore, it permits to estimate, after a few years of insurance coverage, if the compensations demanded to the insurance company are coherent with the analysis or if the parameters need to be adjusted.

In the present case study, the largest source of uncertainty is most probably the frequency of sinkhole events damaging a building. Indeed, the correction applied at the municipality level considers that all susceptible areas have the same hazard. Furthermore, the susceptibility maps are relatively simple and do neither take into account the local conditions (e.g. hydrogeology), human influence (see [Gutiérrez et al., 2008a](#)) or local sinkhole size-frequency distribution. This possible bias is supported by the fact that the application of the Bex rate to Gryon gives a frequency of sinkhole events damaging a building largely higher than the frequency deduced from the municipality data, which seems yet exhaustive. However, damages to buildings, when not spectacular, can be unnoticed by the technical service or by the elders, which have been consulted in this municipality. This is supported by the fact that according to the best fit (Fig. 7.6), 52 % of the losses represent less than 10 % of the building value. When it comes to Ollon, the past events are not known, but sinkholes close to buildings can be observed. Therefore, it is obvious that a risk exists, but since no data is available, it is impossible to know if the deduced frequency is realistic. As a result, a large uncertainty affects the frequency, and an over-estimation is possible according to the observations in Gryon. Finally, the correction factor f is based on an estimation and no observations allows to validate this factor. Therefore, the use of a relatively large range of possible values is advised.

The uncertainty on the susceptibility maps is addressed by using 2 maps. Although none of them gives directly information on the dissolution activity, map A gives a partial indication through the occurrence of sinkholes. This map is however limited in urbanised areas and map B is more representative in these areas, although it is generally more conservative. The results obtained with these two largely different susceptibility maps are comparable, which shows that the influence of the susceptibility map is relatively limited in the analysis. Furthermore, the comparison of susceptibility maps performed by [Galve et al. \(2009\)](#) shows that the proximity to a sinkhole is the best proxy for the susceptibility. Therefore, the exclusion of other parameters is expected to have a very low impact.

For the frequency modelling, the use of a Poisson distribution relies on the hypothesis that the loss events are independent in time. As a result, it considers that a single event can't impact two or more buildings at the same time. This assumption is likely true for most of the cases, but some of them concerned several buildings. However, this has no effect on the average annual loss, but only on the distribution over the year. Furthermore, the large sinkholes affecting several buildings often have a progressive movement, which means that the affected buildings might need to be repaired at different time. Therefore, the assumption behind the use of a Poisson law is not completely met, but has a limited impact on the results.

When it comes to the distribution of loss ratios, the lack of data makes the prediction difficult. The use of a confidence interval is then recommended, although it doesn't greatly affect the results

in this case. Furthermore, it is important to remember that a 99 % confidence interval doesn't mean that the "real" distribution lies within the interval for sure, neither does it mean that the type of distribution used is the best choice. In addition, no uncertainty has been used on the total loss probability, but it might be cautious to use one. However, since the ratio obtained from the generalized Pareto distribution are lowered to one if the retrieved value is higher, the proportion of loss ratio equal to one is actually often higher than P_{TL} and varies from one simulation to the other. Another limitation of the loss ratio distribution is that this evaluation takes into account the past and present building stock, but the building's vulnerability might vary in the future if the construction methods change. This will be the case since constructive measures will be demanded by the insurance company for every new building in a hazard zones.

The limitation of the individual loss event to 1 million CHF produces a sensitive change in the higher values of the distributions. This limitation seems however fair for the reasons described above. Furthermore, only 15 % of the at-risk buildings have a value above 1 million CHF, which supports the fact that the difference is the result of relatively few events. At the same time, the limitation of the vulnerability to one might be a bit too low, since it is cheaper to build a new building on a virgin terrain than if a damaged building has to be removed first. The insurance company can indeed give a compensation up to 115 % of the building value in case of important dismantling cost.

In view of the above discussion, we recommend to use the "UCIR" curves (Fig. 7.8), taking into account the range of multiplication factor for the frequency of sinkhole events damaging a building, the confidence interval for the loss ratio distribution, and the roof at 1 million CHF for each individual loss event. Using map B, which is more conservative, especially in urbanised areas, the average value of 1.431 million CHF/year would represent, for the insurance company, an increase of around 1.6 % of the aggregated losses, which has been of around 90 million CHF per year over the last 5 years, including fire as well (ECA, 2015). The inter-annual variation is relatively small due to the limited size of the events and to the absence of potential for very large events. Indeed, the value of 5.41 million CHF is expected to be exceeded on average once every hundred years, but is only 4.7 times the amount that is expected to be exceeded every two years (1.14 million CHF).

Another limitation of this study is that the limestones are not considered. This could seem unwise, but as mentioned in the introduction, no losses were known on limestones at the time of the study, and fewer and cheaper buildings are located on limestones than on evaporite. However, ongoing investigations of the building insurance company suggest to be careful with this hypothesis, since a relatively important number of buildings are damaged in limestone karst areas. As mentioned in the introduction, the damage cause is currently unknown, but this region will request a special attention in the first few years after the beginning of the insurance cover.

Finally, no validation of the results is possible yet. This is generally inherent to risk analysis, which can only rely on a careful estimation of the parameters, taking as much as possible all available sources of information into account. In addition, the assessment and communication of the uncertainty allows to reflect the state of knowledge of the system. As a consequence, future events need to be carefully collected, in order to enrich the database and to adjust the risk estimation.

7.6 Conclusion

This article presents a method that permits to perform a risk analysis in an area with relatively little information on the hazard. In this case, building an inventory of past sinkhole events damaging a building events seems to be the best data to estimate the risk, since it permits to estimate the event's frequency and the loss ratios. However, an inventory like this needs to be handled carefully, since it is biased in many ways. Therefore, we perform different corrections in order to reach a frequency of sinkhole events affecting a building as close as possible to the actual value. In addition, we add an uncertainty distribution on most of the risk analysis parameters, in order to get a distribution of annual losses and to estimate the probability for the losses to be above a given value.

A proper validation of the results is not possible yet, but, as a conclusion, this study highlights the importance of recording the past events, in order to constraint future analysis.

Appendix

List of variables

Table 7.2: Variable names

Name	Dimension	Description
Λ_{raw}^j		Number of damaged building inventoried in municipality j
Λ_{obs}^j		Number of damaged building inventoried in municipality j corrected for the building stock variation
$\Lambda_{deduced}^j$	$\frac{\text{damaged building}}{\text{year}}$	Number of damaged buildings deduced for municipality j using the maximum frequency per at-risk building observed in the area (λ_{obs}^{max})
$\Lambda_{deduced}^{total}$		Sum of the $\Lambda_{deduced}^j$ of all municipalities
$\Lambda_{corrected}^{total}$		$\Lambda_{deduced}^{total}$ corrected with a multiplication factor f accounting for the fact that only a fraction of the actual number of buildings damaged by sinkholes is known
λ_{obs}^j		Number of damaged building collected in the inventory for municipality j , corrected for the building stock variation and divided by the number of at-risk buildings
λ_{obs}^{max}	$\frac{\text{damaged building}}{\text{year} \times \text{at-risk building}}$	Maximum value of λ_{obs}^j obtained among all the municipalities
f		Multiplication factor accounting for the assumed proportion of known event in the municipality with the highest λ_{obs}^j
f_{min}	—	Lower bound of f if the latter is uniformly distributed
f_{max}		Upper bound of f if the latter is uniformly distributed
n		Number of years covered by the inventory
y_0	—	First year covered by the inventory
y_n		Last year covered by the inventory

Table 7.2: Variable names (continued)

Name	Dimension	Description
N_l^j	Number of buildings	Number of buildings in municipality j in year $l \in [y_0, y_n]$
$N_{y_n}^j$		Number of buildings in municipality j in year y_n
N^j		Current number of buildings in municipality j
N_{Build}		Number of buildings affected in an iteration of the model
P_{TL}	–	Conditional probability for a damaged building to be completely damaged (i.e. loss value equalling the building value)
V_i	–	Loss ratio of building i
L_k	CHF/year	Total losses in simulation k
i	–	index representing a building
j		index representing a municipality
k		index representing an iteration of the simulation
l		index representing a year
X_{k1}	–	random variable $[0,1]$ changing in every iteration k used to sample a value of f
X_{k2}		random variable $[0,1]$ changing in every iteration k used to sample a value of N_{build}
X_{k3}		random variable $[0,1]$ changing in every iteration k used to sample a value of α and β
X_{i1}		random variable $[0,1]$ changing for every affected building i used to determine if the loss for building i will equal the value of the building
X_{i2}		random variable $[0,1]$ changing for every affected building i used to sample the loss ratio distribution

Table 7.2: Variable names (continued)

Name	Dimension	Description
α	—	Shape parameter of the generalized Pareto distribution used for the loss ratios
β		Scale parameter of the generalized Pareto distribution used for the loss ratios
μ_α		Mean value of the normal distribution used for α
σ_α		Standard deviation of the normal distribution used for α
μ_β		Mean value of the log-normal distribution used for β
σ_β		Standard deviation of the log-normal distribution used for β
W_i	CHF	Insured value of building i
$W_{at-risk}$		Set containing all the at-risk building values

Chapter 8

Shallow landslide's stochastic risk modelling based on the precipitation event of August 2005 in Switzerland: results and implications

Foreword

This chapter has been published as:

Nicolet, P., Foresti, L., Caspar, O., and Jaboyedoff, M.: Shallow landslide's stochastic risk modelling based on the precipitation event of August 2005 in Switzerland: results and implications, *Nat Hazard Earth Sys*, 13, 3169–3184, doi:[10.5194/nhess-13-3169-2013](https://doi.org/10.5194/nhess-13-3169-2013), 2013.

Abstract

Due to their relatively unpredictable characteristics, shallow landslides represent a risk for human infrastructures. Multiple shallow landslides can be triggered by widespread intense precipitation events. The event of August 2005 in Switzerland is used in order to propose a risk model to predict the expected number of landslides based on the precipitation amounts and lithological units. The spatial distribution of rainfall is characterized by merging data coming from operational weather radars and a dense network of rain gauges with an artificial neural network. Lithologies are grouped into four main units, with similar characteristics. Then, from a landslide inventory

containing more than 5000 landslides, a probabilistic relation linking the precipitation amount and the lithology to the number of landslides in a 1 km² cell, is derived. In a next step, this relation is used to randomly redistribute the landslides using Monte Carlo simulations. The probability for a landslide to reach a building is assessed using stochastic geometry and the damage cost is assessed from the estimated mean damage cost using an exponential distribution to account for the variability. Although the model reproduces well the number of landslides, the number of affected buildings is underestimated. This seems to result from the human influence on landslide occurrence. Such a model might be useful to characterize the risk resulting from shallow landslides and its variability.

8.1 Introduction

Shallow landslides often represent a risk for housing, people and infrastructures. Compared with deep-seated landslides, shallow landslides usually trigger spontaneously, flow at higher speed and are not likely to affect repeatedly the same location due to the changes in soil stability conditions (e.g. [van Westen et al., 2006](#); [Corominas and Moya, 2008](#)). Consequently, most research efforts focus on the prediction of their exact location and, less frequently, their timing. Several methods for the mapping of landslide susceptibility exist and are based on physical models (e.g. [Pack et al., 1998](#); [Montgomery and Dietrich, 1994](#); [Godt et al., 2008](#)) or statistical approaches (e.g. [Carrara et al., 1991](#)). Since rainfall has been recognized as being a frequent triggering mechanism (e.g. [Wieczorek, 1996](#)), many authors, following [Campbell \(1975\)](#) and [Caine \(1980\)](#), proposed early-warning systems based upon criteria of precipitation intensity and duration (e.g. [Guzzetti et al., 2008](#)). Other studies also use the antecedent precipitation as a proxy for considering the groundwater level preceding the precipitation event ([Crozier, 1999](#); [Glade et al., 2000](#)). More direct approaches are based upon the real-time monitoring of soil moisture ([Matsushi and Matsukura, 2007](#); [Baum and Godt, 2010](#)) or the use of transfer functions to estimate the soil water content from precipitation measurements ([Cascini and Versace, 1988](#); [Capparelli and Versace, 2011](#); [Greco et al., 2013](#)).

Many rainfall-induced large landslide events have been recognized worldwide, for example in Italy ([Crosta, 1998](#); [Crosta and Frattini, 2003](#); [Crosta and Dal Negro, 2003](#); [Cardinali et al., 2006](#); [Gullà et al., 2008](#)), Spain ([Corominas and Moya, 1999](#)), the USA ([Campbell, 1975](#); [Whittaker and McShane, 2012](#)), New Zealand ([Crozier et al., 1980](#); [Glade, 1998](#); [Crozier, 2005](#)), Taiwan ([Yu et al., 2006](#)), the Portuguese island of Madeira ([Nguyen et al., 2013](#)) and in Switzerland ([Bollinger et al., 2000](#)).

Despite the numerous contributions to the physical understanding of the phenomenon itself (for a broad reference list, although not up to date, see [De Vita et al., 1998](#)), studies on the

assessment of landslide risk are less commonly found in the literature. Examples of quantitative risk analysis (QRA) at regional scale can be found in [Cardinali et al. \(2002\)](#), [Remondo et al. \(2005\)](#) and [Catani et al. \(2005\)](#). However, these studies provide a mean annual risk with no information on the expected distribution of annual costs. More recently, applications of regional-scale QRA providing exceedance probabilities were presented in [Jaiswal et al. \(2011\)](#) and [Ghosh et al. \(2012\)](#). Although most of the QRA methodologies are developed for local or regional scales, some of them, for example [Catani et al. \(2005\)](#), might be generalized to a larger area.

Switzerland was affected in August 2005 by a rainfall event with measured precipitation reaching 324 mm in 6 days. Although floods were the main cause of damage, more than 5000 landslides were reported ([Raetzo and Rickli, 2007](#)). Landslide-induced damage has been estimated by [Hilker et al. \(2007\)](#) at CHF 92 million (USD 99 million; debris-flows not included) and represents 4.5 % of the total damage cost.

As already mentioned by [Jaboyedoff and Bonnard \(2007\)](#) and by [Rickli et al. \(2008\)](#), landslide density was highly correlated with the total precipitation amount. Following their ideas, this article proposes a risk model for shallow landslides based on the event of August 2005. The input parameters of the model include a rainfall and a lithological map. The map of 6 day rainfall accumulations is constructed by interpolating a high resolution rain gauge network using weather radar data as external drift. A geotechnical map is interpreted in order to group different units into 4 main lithological settings. The expected number of landslides is predicted as a function of rainfall level conditional to the lithological type. A geometrical probability concept is then employed to predict the potential number of landslides affecting buildings and the corresponding damage cost.

The paper is structured as follows. Section 8.2 details the rainfall event of August 2005 in Switzerland both from a meteorological and lithological viewpoint. Section 8.3 explains the methodology to assess the landslide probability as a function of rainfall accumulation and lithological context. Section 8.4 presents the risk analysis results in terms of expected number of landslides, number of affected buildings and associated cost. Finally, Sects. 8.5 and 8.6 discuss and conclude the paper.

8.2 The rainfall event of August 2005 in Switzerland

8.2.1 Study area

The study area covers the entire Swiss territory (around 42 000 km², which extends from the Jura Mountains in the northwest, to the Alps, in the southeast, through the Molassic Plateau, where most of the population is concentrated. Special attention is given to the location where most of

the landslides occurred, which is the central part of Switzerland, between the cities of Bern and Lucerne (Fig. 8.1). Landslides occurred in the tectonic units described below (Trümpy, 1980; University of Bern and FOWG, 2005a,b), which are listed along a northwest–southeast direction (perpendicularly to the geological structures).

- Upper freshwater molasse from middle and early upper Miocene (consisting of floodplain sediments including puddings, sandstones and silty shales).
- Other types of molasse (narrower areas of upper marine molasse, lower freshwater molasse and lower marine molasse, the lower part of this series being in sub-Alpine position).
- Sub-Alpine flysch.
- Upper Penninic flysch (Schlieren flysch).
- Ultrahelvetic and Helvetic nappes (including Tertiary shallow marine formations and Cretaceous limestones from the Wildhorn nappe and Jurassic limestones from the Axen nappe).

The bedrock is mostly covered by soil (regolith) and loose materials. Most of these shallow and superficial formations have not been mapped, except for the cases where the formation reaches a sufficient extension or thickness to be considered relevant at the map scale. This is for example the case of morainic material deposited by the glaciations during the Quaternary, which is visible at several places, especially on the plateau (Trümpy, 1980). The properties (e.g. mechanical, hydrological) of the local soils strongly depend on the underlying bedrock.

8.2.2 Description of the precipitation event

The rainfall event of August 2005 in central and eastern Switzerland resulted in severe damage due to flooding and induced slope instabilities (Rotach et al., 2006). The presence of the Alps played a key role in controlling the spatial distribution of rainfall due to orographic precipitation enhancement processes. Persistent precipitation patterns were mostly found on the exposed upwind slopes under northerly and northeasterly flow conditions as studied by Foresti and Pozdnoukhov (2012) and Foresti et al. (2012). In particular, the stratiform precipitation was locally enhanced by smaller-scale orographic features leading to persistent initiation and enhancement of the embedded convection.

The most intense period of the event was observed between 21 and 22 August. Driven by cyclonic conditions during the first day, the moist air from the Mediterranean Sea circumvented the Austrian Alps and started approaching slightly crosswise the northern slopes of the Swiss

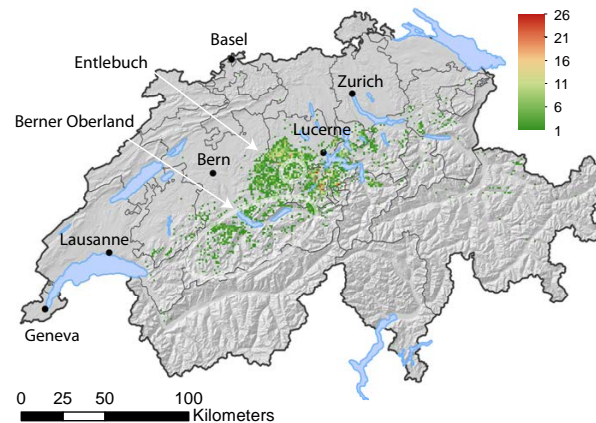


Figure 8.1: Number of landslides in 1 km² cells (after [Raetzo and Rickli, 2007](#)). White circles represent the Berner Oberland and Entlebuch regions (hillshade: © Swisstopo).

Alps from the east. The atmospheric flow gradually turned from easterly to northerly conditions during the second day. The reduced supply of air moisture was compensated by a stronger upslope rainfall enhancement which extended the duration of precipitation. The return period for 48 h rainfall accumulations largely exceeded 100 yr at several weather stations mostly located in the Berner Oberland ([Rotach et al., 2006](#)). It is worth mentioning that the uncertainty of this estimation is quite important as an event of such intensity was never observed in the past at the considered weather stations.

8.2.3 Landslide inventory

As a consequence of this extreme rainfall event, many shallow landslides were triggered, mainly in the Entlebuch part of Lucerne canton and in the Bern canton. Some deep-seated landslides were observed as well and are mainly located farther southeast. A landslide inventory has been collected by [Raetzo and Rickli \(2007\)](#) from cantonal authorities' information and contains 5756 landslides. Although some additional attributes such as the exact timing have been registered for some of the landslides, we only dispose of the version provided in the above publication and, as a result, we only know the approximate location. However, the Federal Office of the Environment (FOEN) also provides to the cantonal authorities a tool to register the events ([FOEN, 2012](#)). An extract of this database has been provided by the FOEN, but contains less landslides than the one built by [Raetzo and Rickli \(2007\)](#), since some of the cantons report every landslide, whereas others only report one point for each set of close landslides. The uncertainty about the location of landslides complicates the analysis of their geological context.

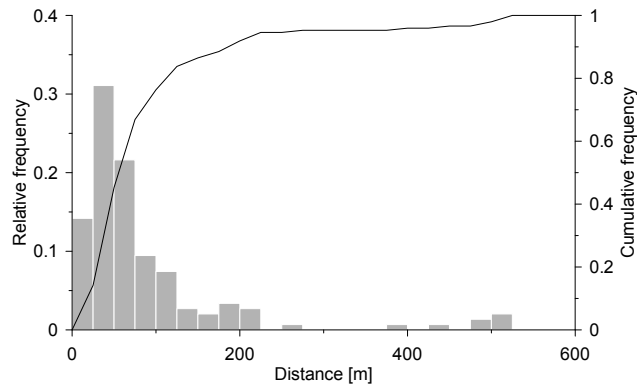


Figure 8.2: Relative and cumulative frequency of the distance travelled by 148 landslides (Raetzo and Rickli, 2007).

Statistics on the landslides can be found in Raetzo and Rickli (2007) and in Rickli et al. (2008) and investigations on specific sites in Mueller and Loew (2009) and von Ruetten et al. (2011). The travel distance of shallow landslides has been analysed for 148 cases and ranges from a few metres up to 500 m (Raetzo and Rickli, 2007). Around 75 % of the landslides travelled less than 100 m and 90 % less than 200 m (Fig. 8.2).

8.2.4 Damage

According to the Swiss Federal Institute for Forest, Snow and Landscape Research WSL, the 2005 event has been the most costly since the beginning of the collection of damage data in 1972, with a total damage cost estimated at CHF 1.83 billion (around USD 2 billion). On the other hand, in spite of being the most important event recorded, other years have been equally or more damaging regarding landslides in the past 40 yr (Hilker et al., 2009; WSL, 2012).

Hilker et al. (2009) divided the damage values into three categories according to the cause, namely floods, debris flows and landslides (including mudflows). Landslides represent around 4.5 % of the total cost and affected private properties (22 %, CHF 16.3 million) and public infrastructures (88 %, CHF 75.6 million) (Hilker et al., 2007). Private damage includes damage to buildings as well as furniture, vehicles, other property damage and loss of profits. Comparatively, public damage includes damage to waterways, roads (except small ones), railways, farming and forests. In addition to economic consequences, six casualties are to be deplored.

8.3 Risk modelling methodology

8.3.1 Introduction

Risk is defined by [Einstein \(1988\)](#) as

$$\text{Risk} = \text{hazard} \times \text{potential worth of loss}, \quad (8.1)$$

where the *hazard* is the “probability that a particular danger occurs in a given period of time” and the potential worth of loss characterizes the estimated potential loss caused by an event of given intensity, which depends on the economic value and vulnerability of the object. We prefer to define hazard in terms of frequency, rather than in terms of probability since we are dealing with events that can be considered as repetitive over a large area ([van Westen et al., 2006](#)). Indeed, if the events are repetitive, [Kaplan \(1997\)](#) suggests to use the frequency rather than the probability (or the frequency expressed as a probability distribution), which is also more rigorous since risk is expressed in terms of cost per year.

The methodology described hereafter is a partial risk calculation. Indeed, a single precipitation event is used as an input, which does not allow accounting for the temporal component of the hazard. However, the hazard is considered by its spatial aspect. In a first phase, the spatial distribution of the total rainfall accumulation is estimated using data from a dense network of rain gauges and 3 additional operational C-band weather radars (Sect. [8.3.2](#)). The second phase studies the statistical distribution of landslides as a function of precipitation accumulation and lithological type (Sect. [8.3.3](#)) and is used to estimate the probability of landsliding in $1 \text{ km} \times 1 \text{ km}$ cells given the occurrence of the precipitation event. These first steps do not however completely consider the spatial aspects of the hazard. Indeed, the exact location as well as the propagation probability are virtually assessed using principles of stochastic geometry, and represent the probability of buildings to be affected by circular landslides within a given cell. The potential worth of loss is then assessed by using the estimation of the mean cost of the event and by artificially adding a variability accounting for the diversity of the element at risk values and vulnerabilities, as well as the landslide intensities (see Sect. [8.3.4](#)).

8.3.2 Spatial analysis of rainfall

MeteoSwiss operates an automatic network of 76 weather stations and a dense network of additional 363 rain gauges. The automatic network measures rainfall with a temporal resolution of 10 min while the second only reports daily accumulations from 05:40 to 05:40 UTC of the next calendar day. An additional network of 3 C-band radars is used to measure precipitation

with higher spatial resolution. The operational radar data processing chain for quantitative precipitation estimation (QPE) at MeteoSwiss includes the removal of ground clutter, correction for the vertical profile of reflectivity in connection with the bright band effect, climatological rain gauge adjustment, the interpolation from polar coordinates to a Cartesian grid, and the use of a fixed climatological $Z-R$ relationship (refer to [Germann et al., 2006](#), for more details). A geostatistical method for real-time adjustment with rain gauges was only recently implemented by [Sideris et al. \(2013\)](#). For long-term evaluation of the radar QPE accuracy against rain gauges refer to [Gabella et al. \(2005\)](#). The radar QPE product used in this paper is a $1\text{ km} \times 1\text{ km}$ grid of the rainfall accumulation during the period 18–23 August 2005.

Despite these corrections, the product still contains residual ground clutter and biases due to the blockage of low level radar beams, particularly in the inner Alpine valleys. To partially account for these issues, an artificial neural network was applied to blend the radar-based QPE map with the rain gauge rainfall accumulations. A 3-H-1 multiLayer perceptron (MLP) was trained to predict the rainfall amount observed at the rain gauges as a function of 3 variables: the geographical location represented by the Swiss easting and northing coordinates and the radar QPE product which acts as an external drift. The geographical coordinates account for the observed biases between rain gauges and radar-based QPE, which show a significant spatial dependence. A conjugate gradient algorithm was employed to train the network. A low number of hidden neurons $H = 6$ was chosen to obtain a smooth representation of the spatial rainfall biases. The optimal model was selected by minimizing the leave-one-out cross-validation root-mean-square error (RMSE). A randomly sampled test set of 137 stations was kept to evaluate the expected prediction RMSE, which is of 25.3 mm. No quantitative assessment of the performance of the MLP model against geostatistical approaches (e.g. ([Sideris et al., 2013](#))) was carried out. Some preliminary comparisons with kriging with external drift and additional details on the MLP model are reported in [Foresti et al. \(2010\)](#). The regularized MLP solution is a smooth compromise between the radar and rain gauge measurements. This allows being robust to local radar overestimations due to ground clutter and the different sampling volume of radar and rain gauge measurements. The Machine Learning Office software was used for the computations ([Kanevski et al., 2009](#)).

Figure 8.3 illustrates the spatial analysis of the rainfall accumulation from 18 to 23 August 2005. The highest accumulations are observed on the northern slope of the Alps, in particular along a line from the Berner Oberland to the mountain range of Saentis. The spatial distribution of landslides is strongly correlated to the spatial distribution of rainfall amounts. The remaining unexplained spatial variability is due especially to the local geological and morphological settings, which control the sensitivity of the soil to the input rainfall.

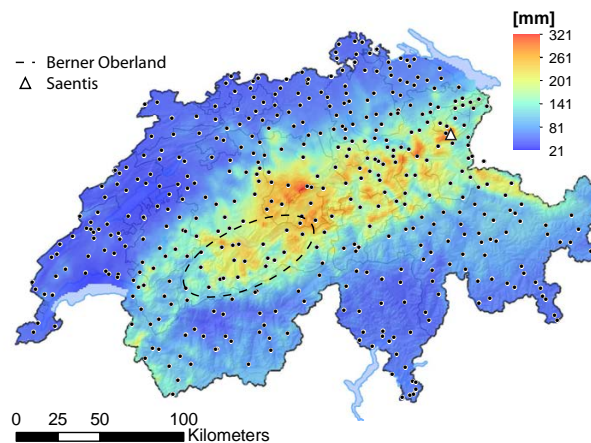


Figure 8.3: Total rainfall accumulation from 18 to 23 August 2005 [mm] estimated by MLP. Dots represent the stations used for the interpolation. The dashed area (Berner Oberland) and the triangle (Saentis) correspond to the end points of a line segment representing the regions with the highest rainfall accumulation.

8.3.3 Landslide distribution

In order to improve the georeferencing of the landslide localization extracted from [Raetzo and Rickli \(2007\)](#), the StorMe database ([FOEN, 2012](#)) has been used as a reference. The points known to correspond to multiple landslide events in the latter database have been removed. The remaining points are then supposed to correspond to a subset of the first landslide map. As a result, each point of the StorMe database should have its equivalent in the landslide map. The distance from each point of the StorMe database to its nearest neighbour in the landslide inventory has then been reduced by optimizing 2 scale and 2 position factors affecting the coordinates of the points in the landslide inventory. For the optimization, the median distance was preferred to another parameter, such as the RMSE, in order to ignore potentially remaining points corresponding to multiple landslides. The median distance obtained after optimization is 104 m. To be consistent with the precipitation map, the landslide points have been transformed into a raster grid with a resolution of $1 \text{ km} \times 1 \text{ km}$, by counting the number of landslides in each cell ([Fig. 8.1](#)).

To establish a predictive relation linking the precipitation amounts and the lithological type to the landslide probability, a categorical lithological information should be coded into a set of variables describing the presence of a given lithological type into a cell. For this purpose, the geotechnical map of Switzerland has been used ([SGTK, 2012](#)). This map combines the shape of the 1 : 500 000 geological map ([University of Bern and FOWG, 2005b](#)) with the attributes of the four 1 : 200 000 geotechnical maps ([de Quervain and Frey, 1963, 1965, 1967](#); [de Quervain](#)

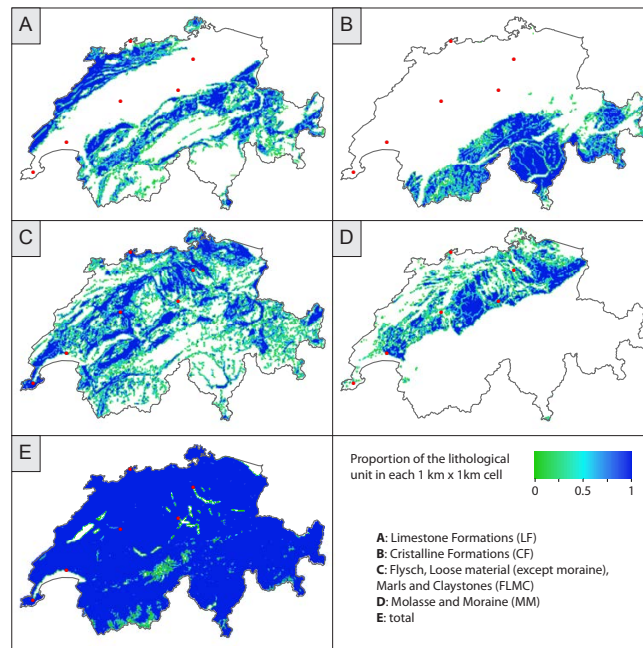


Figure 8.4: Probabilistic lithological maps showing the proportion of each lithological unit. Values range from green (lithological group slightly present) to blue, whereas white means that the lithological group is non-existent in the cell; **(A)** limestone formations (LF); **(B)** crystalline formations (CF), **(C)** flysch, loose material (except moraine), marls and claystones (FLMC), **(D)** molasse and moraine (MM) and **(E)** total. In map **(E)**, white tones mark the absence of lithological formations (i.e. lakes, glaciers) and other countries, while green tones depict their partial presence within the model cell, which occurs when the cumulative proportion of the 4 units is below 1.

and Hofmänner, 1964). The purpose of the latter maps is to transmit the geological information relevant for non-geologists involved in different activities dealing with the ground, especially for civil engineering. The map has been simplified into 4 units, loosely based on the 6 units used by Rickli et al. (2008) to assess the landslide density distribution of the event:

- limestone formations (LF),
- crystalline formations (CF),
- flysch, loose material (except moraine), marls and claystones (FLMC),
- molasse and moraine (MM).

The vector map is transformed into 4 raster maps displaying the proportion covered by the lithological groups in each cell (Fig. 8.4a–d). These products do not allow to relate directly each

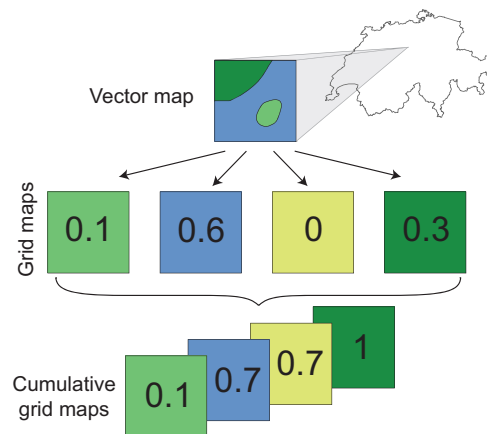


Figure 8.5: Schematic transformation of the vector geotechnical map into 4 grids containing the proportion of each lithology individually and, then, into 4 grids which give, for each cell, the lithological units' cumulative distribution. A lithology is assigned at each model iteration by choosing a random number $0 \leq u \leq 1$. In this example, if $u = 0.5$, the second geology would be assigned, since $0.1 < u < 0.7$.

landslide to only one lithological unit. Therefore, in order to take into account the uncertainty on the lithology involved in each landslide, a stochastic strategy is employed. A lithology is randomly assigned to each cell according to the initial lithological proportions. This is achieved by sampling a random variable $0 \leq u \leq 1$ and comparing it to the cumulative probability distribution of lithology classes (Fig. 8.5). This operation is performed several times to average the results.

Cells that contain water (lakes or glaciers) or that are located on the Swiss border have a cumulative value below 1, since the lithology polygons only cover a fraction of the surface (Fig. 8.4e). As a result, if the random value u is above their total cumulated value, they are not taken into account in the iteration. To build the probabilistic relation, the total number of landslides considered might then be lower than the actual number of landslides. To account for this effect, the landslide map is divided by the cumulated value of the lithological grids. This operation actually expresses the landslide map in terms of the number of landslides per km^2 , since the cumulated value of the lithological grids is the surface of land (in km^2).

The precipitation field has been divided into 6 classes to have a sufficient number of landslides in each class while being enough discriminative in terms of precipitation levels. As visible in Fig. 8.6, the histogram is highly skewed and only 10 % of Switzerland exceeds 200 mm of rain.

Figure 8.7 summarizes the data processing workflow. The output of the model is a cumulative distribution of the expected number of landslide given the geology and the precipitation

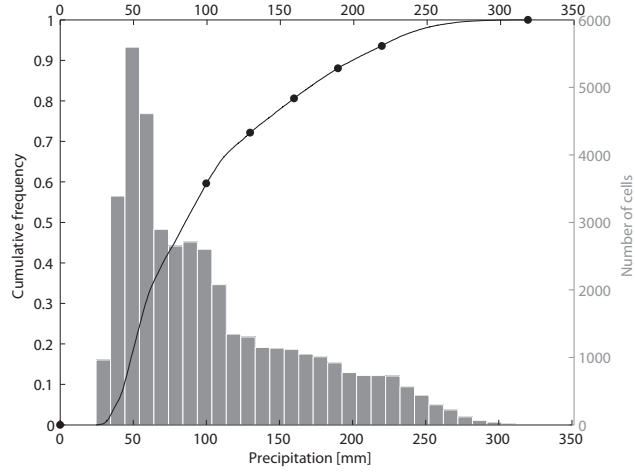


Figure 8.6: Cumulative distribution of the spatial precipitation amounts. Dots show the limits of the 6 classes and are rounded to the upper value.

amount. To allow a generalization of these results, gamma distributions were fitted to the data by minimizing the RMSE between the observed and modelled distributions in order to model the number of landslides as a function of precipitation amount. The 2 parameter form of the gamma cumulative distribution function is given by (Johnson and Kotz, 1970)

$$F(x) = \frac{1}{\beta^\alpha \Gamma(\alpha)} \int_0^x t^{(\alpha-1)} e^{-\frac{t}{\beta}} dt, \quad (8.2)$$

where α is the shape parameter, β is the scale parameter and $\Gamma(x)$ is the generalized form of the factorial function, such as $\Gamma(x) = (x-1)!$ if x is a positive integer. The gamma function is defined as

$$\Gamma(x) = \int_0^\infty e^{-t} t^{x-1} dt. \quad (8.3)$$

Since the gamma distribution is a continuous distribution whose domain is $0 \rightarrow \infty$, it is not exactly suitable to fit discrete data, especially as the most frequent number of landslides is expected to be $x = 0$ and as $F(x = 0)$ is null, whatever the values of α and β . As a workaround for these issues, the distribution has been virtually modified to extend the definition domain from $-1 \rightarrow \infty$ as:

$$F(x) = \frac{1}{\beta^\alpha \Gamma(\alpha)} \int_0^{x+1} t^{(\alpha-1)} e^{-\frac{t}{\beta}} dt. \quad (8.4)$$

This modification is virtual since the distributions' fitting is made by shifting the x values,

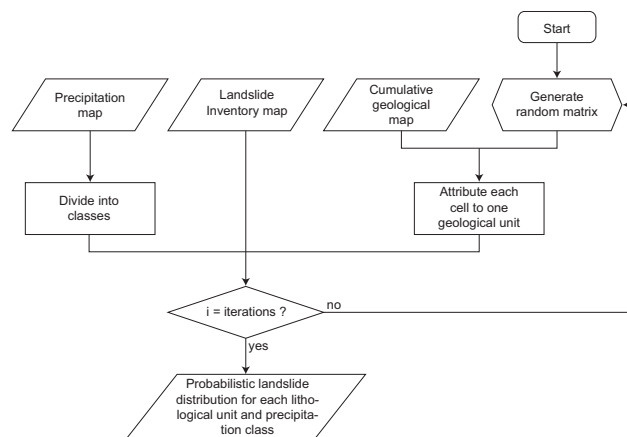


Figure 8.7: Flow diagram showing the assessment methodology used to obtain the cumulative frequency of the number of landslides per lithological unit and precipitation class.

i.e. by using the value $F(x = 0)$ for $x = 1$, which is easier than modifying the function. The consequences of this modification are discussed below.

To estimate the predictive ability of the model, a second part consists in using the distribution of the number of landslides according to the precipitation class and lithology previously assessed to simulate different potential consequences of the precipitation event using a Monte Carlo approach. This step illustrates the uncertainty of the model on the consequences of a given precipitation event. Indeed, since we consider that the landslides are controlled only by the precipitation and the lithology, this step gives the variability resulting from this simplification. The workflow of this step is given in Fig. 8.8. Both the raw distributions and the gamma distributions are used.

Since gamma parameters have been fitted with shifted values, the unmodified inverse distribution will overestimate the number of landslides. However, as the gamma distribution is continuous and as we need to obtain the number of landslides in integers, the results of the inverse function for a given quantile can be rounded down to be consistent with the original data. Matlab[®] was used to iteratively derive the gamma cumulative distribution as there is no analytical solution (Johnson and Kotz, 1970).

8.3.4 Impact assessment

The impact assessment consists of two main steps, which are evaluating how many buildings will be reached and estimating an associated cost.

In order to assess the number of affected buildings, geometrical probabilities are used. The

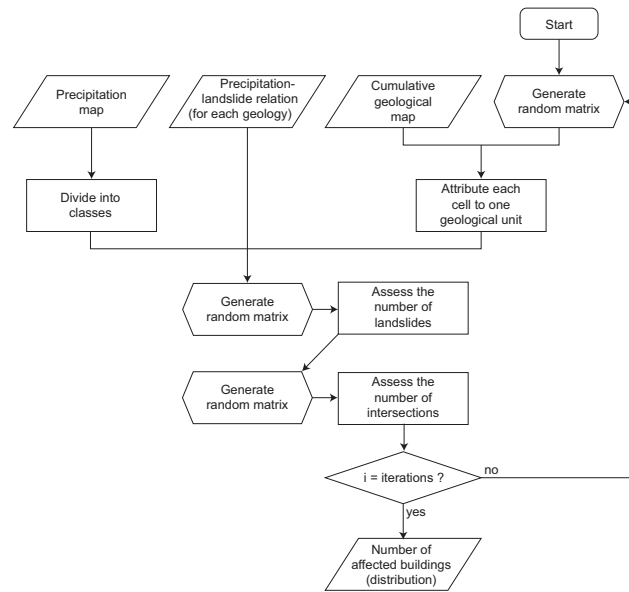


Figure 8.8: Flow diagram showing the assessment methodology used to obtain the number of affected buildings.

concept used in this model is inspired from Buffon's clean tile problem, which consists of calculating the probability for a coin to fall on the crack separating two tiles of a paved ground (Mathai, 1999; Weisstein, 2013). For square tiles, the probability that a circular coin of diameter d falls completely inside a square of side l (with $l > d$), is given by the ratio of a square of side $l - d$ with the tile of side l . The smaller square corresponds to the tile eroded by a buffer of size $d/2$ (Fig. 8.9, left). Therefore, the probability for the coin to fall on the crack is the ratio of the area between the plain and the dashed lines $(l^2 - (l - d)^2)$ and the area of the bigger square. Buffon also investigated the "needle problem", which consists of calculating the probability that a needle falling on a ground made of infinite parallel strips of equal width falls on one of the lines (Mathai, 1999). In contrast, the falling object is, in the needle problem, not only characterized by the position of its centre, but also by its orientation. As a result, dilating the lines by a buffer is not suitable to solve the problem and Buffon's solution cannot be straightforwardly extended to other objects than the straight lines.

To assess the conditional probability for a landslide to reach a building, the coin of Buffon's problem is replaced with circular landslides of diameter d , and the cracks between the tiles are replaced with the actual buildings (Fig. 8.9, right). Therefore, adding a buffer of a distance $d/2$ to the buildings allows one to compare the area covered by the expanded buildings with the total area, which corresponds to the conditional probability for a landslide to reach a building. At this

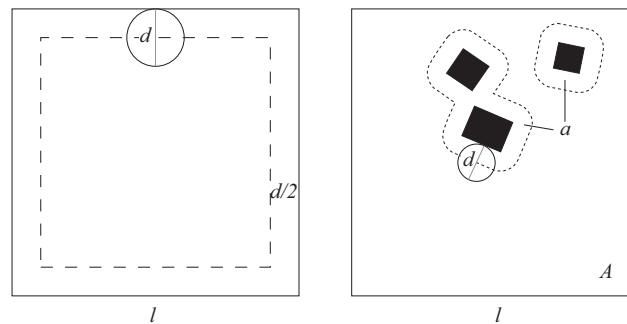


Figure 8.9: Left: Buffon's clean tile problem (modified from Mathai, 1999). The probability for the coin to touch the limit of the tile is given by the ratio between the dashed square (area = $(l - d)^2$) and the plain square (area = l^2). Right: The probability for a circular landslide of diameter d to reach a house is given by the ratio of the buildings expanded with a $d/2$ buffer (a) with the total area (A).

step, it is considered that the landslide has the same probability to occur anywhere inside the considered area.

Assuming circular landslides is a simplification which might have consequences on the model, since, as illustrated by the needle problem, an elongated shape is more likely to affect the buildings. Moreover, the shape of the landslides is expected to be elongated. As a consequence, the circle diameter is set to 200 m in order to completely include 90 % of the landslides, since the distance measure corresponds to the largest dimension (Fig. 8.2), i.e. the length of the landslide. This diameter results in an overestimation of the landslide surface, but it takes indirectly into account the landslide geometry and provides a slightly pessimistic risk estimation in terms of the number of affected buildings. Thus, a 100 m buffer has been added to the 1 814 667 buildings extracted from the vectorized landscape model of Switzerland (Vector25, ©swisstopo). Then, the total surface has been compared with each cell surface to obtain the impact probability. It has to be mentioned that impact is only considered with a Boolean approach, which means that a landslide can affect a building or not, but the potential for one landslide to affect several buildings is not considered. It should also be noted that the buffers are made before cutting shapes into cells in order to take into account the possibility for a landslide occurring in a given cell to reach a house located close to the border of an adjacent cell.

However, a shallow landslide preliminary hazard map exists at Switzerland scale (Geotest et al., 2006) and provides a global area where shallow landslides can occur, including both the initiation and propagation zones. This map is based on a global analysis in two steps: first the stability is assessed using an infinite slope analysis (model SLIDISP, Liener et al., 1996), then propagation prone areas are assessed with a model adapted from debris flow (model SLIDESIM,

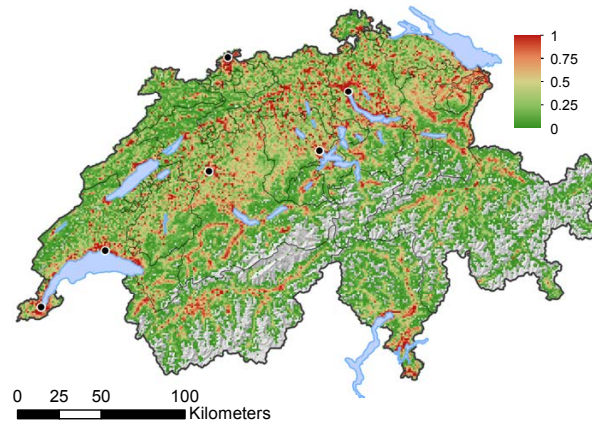


Figure 8.10: Impact probability map displaying the conditional probability for a 100 m radius circular landslide to affect a house for each cell of the model. Dots correspond to the cities visible in Fig. 8.1 (hillshade: ©Swisstopo).

based on [Gamma, 2000](#)). The final version of this map combines both areas without further attributes. Thanks to this map a small modification is made to the impact probability. If a landslide occurs in a cell where the hazard map exists, it is considered that the landslide will occur inside the area covered by the hazard map. Therefore, the ratio a/A described in Fig. 8.9 becomes $(a \in S)/S$, where S is the surface covered by the hazard map. The impact probability map including this modification is given in Fig. 8.10. The hazard map has however not been used yet to assess the location of the landslides, but a usage of this map for the landslide distribution has to be considered. Indeed, only 8 landslides (0.14 %) were located in cells with no hazard according to the map and 133 (2.31 %) were located within cells where less than 10 % of the surface is covered by the hazard map. This tends to indicate that this preliminary hazard map is realistic, but since there is an uncertainty on the landslide locations, an in depth analysis of the landslide locations with regard to the hazard map cannot be made.

The estimation of the associated cost is more complicated as the value of the buildings is not known. This information could be obtained from the buildings' insurances for 19 of 26 cantons, for which a public insurance exists and is mandatory. However, a suitable vulnerability curve linking the landslide intensity, characterized by parameters such as depth or area, to the damage rate, is difficult to assess. The lack of knowledge on the precise landslide characteristics and location as well as the inherent variability of the elements at risk complicates even more the assessment of the vulnerability ([Galli and Guzzetti, 2007](#)). Therefore, in order to keep the precision of the model consistent with the previous step, we chose not to use a value and a vulnerability curve to assess the damage cost, but to assess it directly from the 2005 event mean

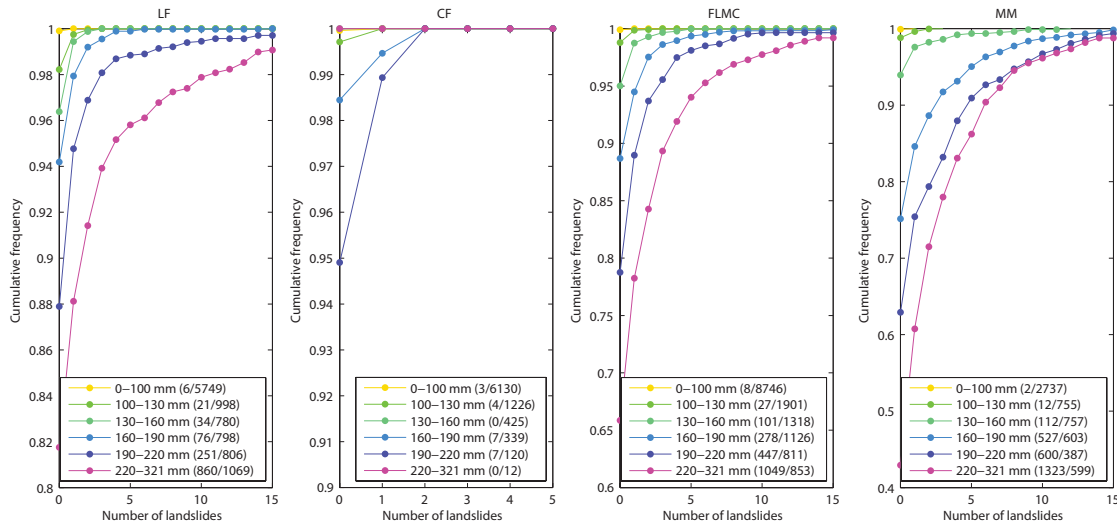


Figure 8.11: Landslide relation with precipitation and lithological group. The curves for small precipitation amounts are not always visible because of the low number of landslides. Note that scales are different. Numbers between brackets are respectively the number of landslides in the cells and the number of cells in the class, averaged over the iterations.

damage cost. This cost is estimated by dividing the total damage cost induced by landslides to private infrastructures (CHF 16.3 million) by the expected number of affected buildings. The latter is obtained by summing over all grid cells the product between the number of landslides (Fig. 8.1) and the impact probability (Fig. 8.10). This approach results in 2260 affected buildings, implying a mean cost \bar{x} of CHF 7211 per building. No uncertainty is considered for this parameter.

It is apparent that damage costs are varying. Therefore, to reproduce a possible distribution of costs, a statistical distribution is chosen. Thus, the expected damage cost x for a given building is assumed to follow an exponential distribution with probability density function (e.g. Ross, 2010) as

$$f(x) = \begin{cases} \lambda \exp(-\lambda x), & x \geq 0 \\ 0, & x < 0 \end{cases}. \quad (8.5)$$

The distribution is only defined in terms of its first moment $1/\lambda$, which is equal to \bar{x} , namely the expected mean damage cost per building assumed for the 2005 event.

The generation of exponential variates is obtained by sampling from the quantile distribution,

which is given by the inverse function of the exponential cumulative distribution as

$$F^{-1}(u) = x = -\frac{\ln(1-u)}{\lambda}, \quad (8.6)$$

where u is a uniformly distributed random number between 0 and 1. The exponentially distributed damage cost is sampled for each case of impact identified by the model.

The fat-tailed nature of the exponential distribution allows obtaining a more realistic estimate of the damage costs than a normal or triangular distribution and does not need the estimation of the second moment characterizing the variance of the distribution. The latter is a useful feature as the statistical distribution of the damage costs per building is not known in our particular case. The log-normal distribution also has heavy tails and was successfully used to model the cost associated to floods (Merz et al., 2004). However, due to the larger number of degrees of freedom, it is also not suitable for our application.

8.4 Results

The statistical distribution of landslides as a function of precipitation amount and lithological group is given in Fig. 8.11 and results from 10 000 iterations of the model. The probability to observe a given number of landslides in a given lithological group is a monotonically increasing function of the precipitation amount. CF show a very little susceptibility to landslides compared to the other groups as evidenced by the low number of observed landslides. With similar precipitation amount, MM formations tend to have a higher probability to contain at least one landslide than FLMC or LF. However this relation is less evident for a larger number of landslides.

Table 8.1 shows the fitted values of the gamma distribution (missing data denotes that the fitting did not converge in the allowed number of iterations), whereas Fig. 8.12 displays these values graphically. CF have to be considered with caution because of the low number of samples. The α parameter (shape), characterizes the central location of the distribution, while the β parameter (scale) characterizes its dispersion. A general increase in both α and β parameters with precipitation amount can be observed, although some values are not following the general linear trend. This is especially the case for α for LF and for β for the highest precipitation class.

The general increase of both parameters is a desirable property and is in accordance with our prior expectations. In fact, increasing precipitation amounts increase the expected number of landslides (represented by α) and the dispersion of the distribution (represented by β). Higher β values are representative of heavy tails, which means that the probability of observing a high number of landslides rises with increasing precipitation amount.

The spatial distribution of the number of landslides was computed following the procedure

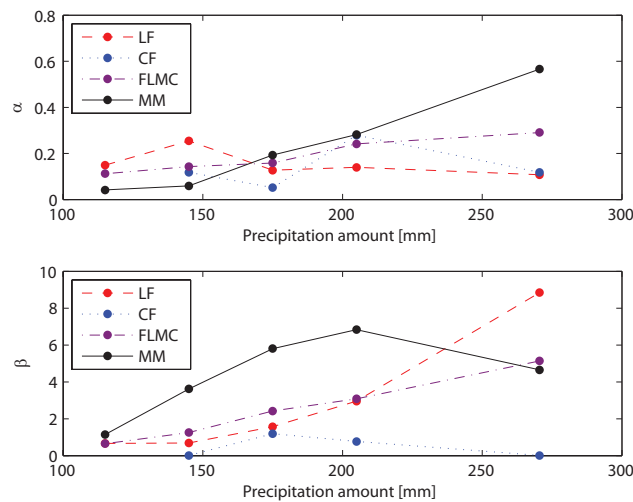


Figure 8.12: Fitted parameters for α and β of the gamma distribution.

described in Fig. 8.8 using both the raw data and the gamma fits and performing 10 000 iterations for each. However, since gamma distributions have not been fitted for some of the precipitation classes, raw data have been used instead of gamma distributions when not available. The mean modelled number of landslides with gamma fits is given in Fig. 8.13 and is very similar to the mean number of landslides modelled with raw data (not shown). The spatial pattern is relatively similar to the spatial distribution of rainfall amounts, with two remarkable differences. First, the relation between precipitation amount and number of landslides is not linear, which implies that areas with low precipitation amounts show a null to very low number of landslides. The second difference is due to the sharp geographical transitions between the lithological units, which lead to sharp transitions in the modelled number of landslides. An illustrative example occurs when moving from the MM formations to the CF, which strongly reduces the number of landslides (see Fig. 8.4). These results seem to be in good agreement with the observed distribution of landslides (Fig. 8.1).

8.4.1 Impact assessment

Although the number of landslides is reproduced, the expected number of hit buildings is almost never reached in the simulations (Fig. 8.14). Indeed, the expected number of affected buildings for the event is 2260, whereas the simulations return a mean of 1689.5 for raw data and 1665.8 for gamma fits. As a consequence, the damage amount is not reached either since it is derived from the latter. It is not yet clear why the observed total number of hit buildings is underestimated by the model. One possible reason could be that the landslide localization is highly correlated

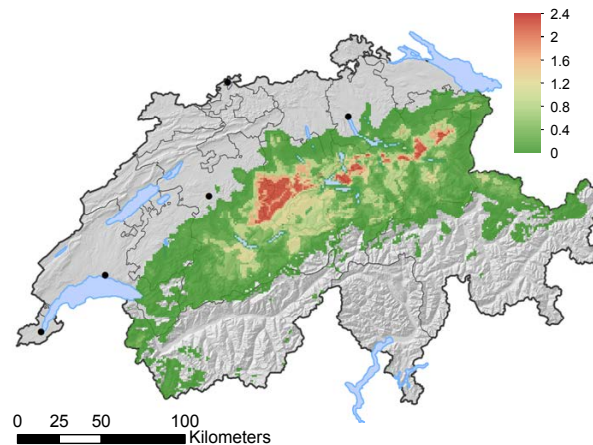


Figure 8.13: Mean modelled number of landslides with the gamma functions. No colour is displayed on the cells that never contain landslides.

with the location of the buildings. To test this hypothesis, we compared the impact probability of cells within which landslides actually occurred to the impact probability of cells in which landslides were modelled (the impact probability is taken into account n times if the number of landslides n in the cell is greater than 1, for both curves). This comparison indicates that the modelled landslides tend to occur in cells with lower impact probability than the actual landslides (Fig. 8.15).

8.5 Discussion

The landslide model presented in this paper only considers precipitation amounts and geology as input parameters. However, other variables such as terrain slope, soil thickness and permeability contrast, for example, play a key role in shallow landslide generation. These variables are either hard to measure over a large domain, e.g. the soil thickness, or show spatial variability at extents which are smaller than $1 \text{ km} \times 1 \text{ km}$ resolution, e.g. the terrain slope. Additionally, the uncertainty of the landslide inventory does not allow matching the location of the landslide with such high resolution variables. As a consequence, the $1 \text{ km} \times 1 \text{ km}$ resolution model only gives information about the large-scale pre-conditioning factors for landslide generation. Smaller-scale features may affect the process of landslide triggering in a significant way and should be taken into account to extend this kind of model to a higher resolution. Furthermore, this model is based only on one single event and should be compared with other similar rainfall events. In particular, it should be compared with similar events producing landslides in different geological settings,

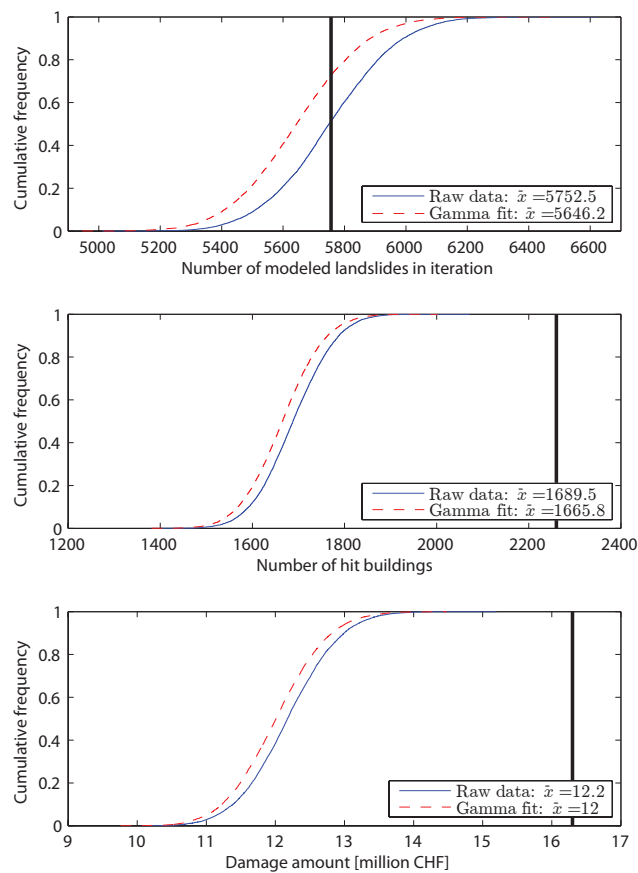


Figure 8.14: Number of landslides, number of hit buildings and damage amount calculated from raw data and gamma fits. Mean value \bar{x} for each line is displayed on the graph, whereas black lines correspond to the data of the event or the expected number of affected buildings. 10 000 iterations have been computed.

to validate the aggregation of the different lithologies into four main units. Indeed, landslide susceptibility might be different in Jura limestones than in pre-Alpine limestones, for example. Lithological information is also very coarse at the working scale and local variations could affect the susceptibility. Furthermore, shallow landslides are sensitive to the properties of the soil layer, for which generally no map exists.

The annual probability to exceed a given total damage cost could be assessed by analysing different precipitation events, which are weighted based on their frequency of occurrence (return period). This step is essential in order to obtain a mean annual cost as well as an exceedance probability curve. One possibility to generate a large number of rainfall fields to appropriately represent the full risk estimation could be based on design storms (Seed et al., 1999). Stochastic

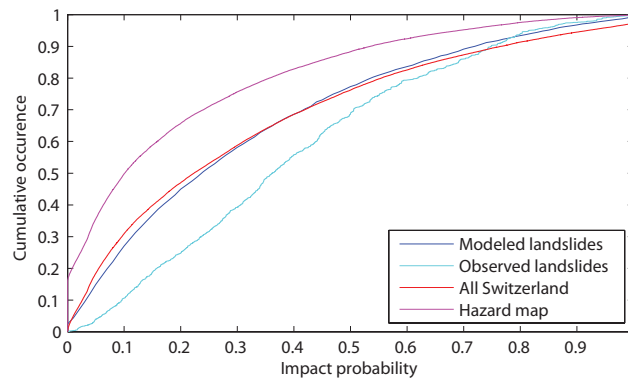


Figure 8.15: Comparison of the impact probability of the cells where landslides occurred and where landslides have been modelled (if $n > 1$ landslides occur in a cell, the impact probability of the cell is considered n times). As a comparison, the distribution over all of Switzerland is shown, as well as the results for the existing hazard map (weighted by the surface of the cell included in the hazard map).

rainfall fields could be generated according to a given return period and be used to simulate the spatial distribution of landslides under extreme rainfall conditions. Attempts have been made to use a return period in order to predict landslide triggering, but they were mainly performed at local scale (e.g. Iida, 1999; D'Odorico et al., 2005; Iida, 2004; Tarolli et al., 2011) and would therefore not be suitable for a larger area, since the spatial variability is not taken into account. However, the spatial distribution of rainfall by means of data with a smaller time step (in this case satellite data) has been used for early warning (e.g. Apip et al., 2010), but as far as we know, it has not been used as a starting point to simulate potential future events. Furthermore, for precipitation events with long return periods, the uncertainty on the frequency is rather high, as mentioned in Sect. 8.2.3 for this event. This would add uncertainty to the risk analysis.

Another issue concerns the landslide timing. We used the precipitation amount of the whole event (6 days) as a predictor for landslide occurrence. But, shallow landslides are known to be sensitive to the intensity and duration of the rainfall, as well as to the hyetograph shape (D'Odorico et al., 2005). There are two main reasons for this simplification. The first is the lack of data on the exact timing of landslides, which does not allow the analysis of the temporal precipitation pattern preceding their triggering. The second reason is due to the uncertainty of the radar QPE product, which is higher when used to analyse rainfall time series at high temporal resolutions, for instance hourly or 10 min accumulations. The spatial distribution of QPE accuracy can still be affected by some residual ground clutter, which overestimates the true rainfall amount, and by the blockage of low level beams, which leads to the underestimation of ground rainfall due to using only the beams aloft. Wüest et al. (2010) present a method to obtain hourly precipitation

fields by disaggregating the daily rain gauge measurements with higher resolution radar fields. If the timing of landslide occurrence was known, this dataset would be a valuable source of information. However, the product is not accompanied by uncertainty estimates. A possible solution could involve the generation of stochastic ensembles to represent the uncertainty of the radar QPE product with respect to the automatic network of 76 meteorological stations. This approach was recently implemented at MeteoSwiss (Germann et al., 2009) and could be a smart alternative to integrate ensembles of precipitation fields together with ensembles of lithological types into the landslide model.

When it comes to the damage cost assessment, due to the lack of information on the number of affected buildings and corresponding distribution of costs, a few important assumptions were made. The total number of affected buildings was estimated by means of an impact probability and this number was used to obtain a mean cost per hit building. The number of hit buildings is an uncertain estimation since it depends on the exact location of the landslides inside the cell. Indeed, we consider the probability of landsliding to be uniform within a grid cell, or within the hazard zone if it exists in the cell (which is the case in most of the cells in which landslides actually occurred). For the latter case, it takes partly into account the position of each element inside the cell, in particular the position of the slopes that might fail relatively to the buildings. However, since the hazard map is only indicative, no distinction is made between low hazard area and high hazard area. As a result, if buildings are located relatively more on low hazard area, our estimation of the number of affected buildings would be too high and, as a consequence, the mean price would be too low.

The distribution of costs was assumed to be exponential, which has a desirable long-tail property and is completely defined by its mean value. Despite being only defined in terms of the average costs, the obtained variability is supposed to adequately represent the reality. Nevertheless, with a mean cost of CHF 7211 per building, the probability to overcome CHF 500 000 is almost null (8×10^{-31} , i.e. one case over 1×10^{30}). Since the mean price of a building is around CHF 1 million, this value is quite low as we know that at least one – but probably more – building has been destroyed. This could be the result of a too high number of affected buildings (since they have been estimated), which reduces the mean damage cost, or an indication of the need for using a distribution of damages with a fatter tail. However, this confirms the fact that a distribution with a fat tail is suitable. Nevertheless, since the damage cost varies independently for each affected house and since the number of affected houses is relatively high in the simulations, the effect of varying the individual damage costs is attenuated when summing over all of Switzerland. Another problem concerns the absence of data about the type of damage. Therefore, we assumed that all of the private costs are related to buildings. This simplification is not an issue as long as the cost is related to objects located close to or inside the buildings (e.g. furniture, parked cars), but is

more problematic, for example, for costs related to loss of profits. However, we suppose that the vast majority is related to buildings. As a result, this model could be improved considerably if the type of damage was known. Thus, the damage assessment part has to be considered more as an example than as a reference for further vulnerability assessment.

Regarding the total number of landslides, hit buildings and the amount of damage in each simulation, the variability of the results follows more or less a normal or a log-normal distribution (Fig. 8.14). This distribution reflects the uncertainty induced by the lack of knowledge in the assessment of the consequences of a given precipitation event. Since the model is based on the observed landslides, to redistribute the landslides and assess the consequences, the number of modelled landslides using raw data is logically centred around the observed value. Gamma fit results tend, however, to be slightly lower than using raw data. When it comes to the number of hit buildings, the expected value is hardly ever reproduced. Since the same concept of impact probability, with the same buffer value, is used to assess the expected number of hit buildings of the 2005 event and of the simulation results, this should not be observed. By comparing the impact probability of the cells in which landslides occurred with those of the cells in which the landslides were modelled, we can observe that the cells in which landslides occurred have higher impact probability. Different hypotheses can be made in order to explain this effect. First, we might have neglected an important parameter for the localization of landslides which would be correlated to the built areas such as the repartition of the forested and non-forested areas, redistributing then the landslides in less populated areas. This seems however to be in contradiction with the fact the grid cells covered by the preliminary hazard map have a lower impact probability than the ones where landslides occurred or than the cells of the entire Swiss territory (Fig. 8.15). A second interpretation could be related to the quality of the inventory, which would be more complete in urbanized areas. Correcting for this effect would imply a greater total number of landslides, with more landslides on areas with low impact probability. The third one, which seems to us the most probable, would be that the urbanization tends to increase the susceptibility. Indeed, human activities can contribute to landslides, acting directly as a trigger or indirectly by destabilizing the slope, according to the classification of [Michoud et al. \(2011\)](#). Since, the trigger of the 2005 event is undeniably the rain, human activities could have played a role only as destabilizing factors. Examples of landslides triggered by rain events on slopes destabilized by the modification of pore pressure induced by pipe leaks have been observed in Switzerland, in Les Diablerets ([Jaboyedoff and Bonnard, 2007](#)) and in Lutzenberg ([Valley et al., 2004](#)). This second example is especially interesting since the landslide occurred within an event involving hundreds of landslides and debris flows, and since this particular landslide would not have occurred, thanks to the authors, without the pipe leak. Besides modifying pore pressure, pipe leaks can also destabilize slopes by weakening clay minerals ([Preuth et al., 2010](#)). In addition, the degradation of an old canalization

network led to a landslide in 1930 in La Fouvrière hill in Lyon (France), killing 39 persons ([Allix, 1930](#); [Albenque, 1931](#)). It would therefore be wise to include a parameter linked to the buildings to take account of this effect.

All things considered, the model makes simplifications in order to assess the risk for a large area rather than to be precise at local scale. Indeed, the lack of knowledge and data at the sub-grid scale is balanced by the use of stochastic simulations, which allows one to obtain a probabilistic model for landslide occurrence and associated cost.

Such kind of model might be useful to provide a rapid damage estimation following a precipitation event. Indeed, after a widespread event, the time needed by the insurance to process all claims is rather long and the exact consequences might need several months, even years to be known. Applying this model quickly after the event could provide a rough estimation of the damage costs. In a second step, modelling precipitation events assigned to a frequency could make possible the calculation of exceedance probability curves. Developments are also ongoing to assess the consequences of a landslide event for a road network with comparable models ([Taylor et al., 2013](#)).

8.6 Conclusions

This article proposes a model to assess the risk due to shallow landslides for a large region using the data from the rainfall event of 2005 in Switzerland. The first step assesses the distribution of landslides with regard to precipitation and lithology. Then the landslides are redistributed in a second step according to the relation obtained. Damage cost is obtained by means of an impact probability, which gives the probability, if a landslide occurs, that it reaches a building.

Some improvements have to be made to the model, to corroborate the relation obtained, and to improve the assessment of the impact probability, as well as the distribution of costs. Moreover, the human influence on landslide susceptibility has to be evaluated carefully in a further step, since it appears that the landslide locations are highly correlated with the buildings. This observation tends to indicate that the human influence on slope stability is substantial. Further developments are also conceivable to complete the risk analysis by simulating stochastic rainfall events characterized by a given frequency and to analyse the consequences. This would result in a complete risk analysis able to provide the temporal distribution of damage costs.

Table 8.1: Fitted parameters of the gamma distribution.

Precipitation [mm]	LF			CF		
	α	β	RMSE	α	β	RMSE
0–100	–	–	–	–	–	–
100–130	0.149	0.666	1.77×10^{-5}	–	–	–
130–160	0.255	0.685	6.28×10^{-5}	0.118	0.012	0
160–190	0.127	1.57	2.44×10^{-4}	0.052	1.195	3.54×10^{-4}
190–220	0.139	2.962	3.28×10^{-3}	0.279	0.775	4.60×10^{-4}
220–321	0.108	8.846	3.57×10^{-3}	0.118	0.012	0

Precipitation [mm]	FLMC			MM		
	α	β	RMSE	α	β	RMSE
0–100	–	–	–	–	–	–
100–130	0.112	0.643	9.56×10^{-5}	0.042	1.148	1.94×10^{-4}
130–160	0.144	1.245	7.19×10^{-4}	0.059	3.632	1.72×10^{-3}
160–190	0.159	2.421	1.26×10^{-3}	0.193	5.798	2.14×10^{-3}
190–220	0.242	3.077	2.45×10^{-3}	0.282	6.835	6.65×10^{-3}
220–321	0.29	5.133	3.18×10^{-3}	0.566	4.653	3.71×10^{-3}

Chapter 9

Hail risk modelling in the context of building insurance

Abstract

Hail is becoming very expensive for building insurance companies. Therefore, there is a need to improve the risk assessment procedures. This chapter is mainly based on an event that occurred in 2011 and caused important losses for the building insurance of the canton of Aargau, in Northern Switzerland. Detailed insurance data are available for this canton, and, in addition, aggregated data are available for other cantons, for the same event as well as for an event that occurred in 2009. First, a loss model is created and relates the maximum hailstone diameter reached during the event in a grid of 1 km x 1 km cells (hereafter intensity map) to a probabilistic model of the proportion of damaged buildings and to a probabilistic model of loss ratios for the damaged buildings. This model is then tested using the available intensity maps and the building's locations retrieved from a topographical landscape model (SwissTLM3D). The goal of this operation is to test the potential of the intensity maps to estimate the losses directly after an event. The second part of this study uses available hazard maps, from which a hailstone size–frequency relation is deduced, to calculate the average annual risk, using the loss model previously defined. This average annual risk is estimated for the canton of Aargau, as well as for the 19 cantons with a public building insurance company. Since the loss model is probabilistic, the results are presented with an exceedance probability curve. Regarding the 19 cantons with a public insurance company, the mean losses of the 20 last years has a probability of 79 % to be exceeded. A third part proposes a model that allows generating random events, which are created in agreement with the hazard maps. The goal of this part is to estimate the cost of individual events, in order to understand how the costs are distributed. The model contains two modules. The first module adjusts a set

of 2D Gaussian functions on the available intensity maps and retrieves key characteristics of these Gaussian functions. Then, the second module uses these characteristics to generate random events. The agreement of these events with the hazard maps is achieved using a rejection method. According to the simulations for the canton of Aargau, an event with losses equal or higher to the one which occurred in 2011 is to be expected with a return period of 45 years.

9.1 Introduction

Recent hail events such as the 2013 event in Germany, which was responsible for around 4 billion EUR of losses (Munich RE, 2014), are a reminder that hailstorms can be very costly for insurance companies. According to Swiss Re (2015), around 24 % of natural hazard related insured losses worldwide in 2014 were caused by hail. As a consequence, hailstorms as natural processes or as insurer concerns are currently actively studied (e.g. Martius et al., 2015).

Establishing relations between hailfall intensity and loss ratio for crop, building or vehicles is being performed for many years (e.g. Changnon, 1971; Katz and Garcia, 1981). In regions where meteorological radars are available, the latter have been used to derive a hail intensity, which are used to build similar relationships (e.g. Schiesser, 1990; Hohl et al., 2002a,b; Schuster et al., 2006). These kinds of relationships permit to estimate the losses quickly after an event and, if information regarding the hail hazard is available, to estimate the mean annual risk. It necessitates however, in addition to the radar data, to have similar information on the elements at risk (crop type and maturity, building type, location and value, ...)

In some cases, models have been developed in order to predict event-related damage, and thus to obtain the distribution of losses over the year. The most known is probably RMS-HailCalc (e.g. Grieser et al., 2014), which is based on the work of Roman Hohl (Hohl et al., 2002a,b). Other models include G-CAT, developed by Guy Carpenter & Co. (Strasser et al., 2015). However, most of the available models have been developed by private companies and at least some parts of the models are not publicly available. Some academic models can however be mentioned (e.g. Schmidberger et al., 2014; Deepen, 2006). To assess the losses, Katz and Garcia (1981) and Hohl et al. (2002a) use a logistic function connecting the total hail kinetic energy derived from the radar to a loss ratio.

In Switzerland, three recent events were particularly costly for the insurance companies. The first one affected mainly the Canton of Thurgau (North-East Switzerland), in May 2009 (47 million CHF of losses), whereas the second, which also happened in 2009, but in July, caused 267 million CHF of losses in the cantons of Vaud, Fribourg, Bern and Lucerne (Imhof and Choffet, 2012). The third event caused 151 million CHF losses in the canton of Aargau (Northern Switzerland) in July 2011 (Imhof et al., 2015).

Thanks to the mandatory insurance coverage for buildings in 19 of the 26 Swiss cantons, this study takes advantage of the insurance data from the "Aargauische Gebäudeversicherung", the public insurance company in the Canton of Aargau, and partly from data from the other insurance companies, in order to assess the vulnerability of the buildings to hailstones (Sect. 9.3.1). In addition, Sect. 9.3.2, uses the established relation with hazard maps in order to estimate the related risk, whereas Sect. 9.3.3 proposes a model to estimate the frequency at which a given loss amount is reached for a defined region.

9.2 Data

9.2.1 Intensity maps

Switzerland is covered by 3 C-band weather radars operated by the Federal Office of Meteorology and Climatology (MeteoSwiss). Using the information provided by these radars, *meteoradar ltd* ([meteoradar gmbh](#)) estimates the maximum hailstone size reached during an event. Their estimation is based on the height difference between the 55 dBZ reflectivity contour (which is a high reflectivity that might correspond to hail) and the 0 °C isotherm (indicating strong up-drafts), which is a method adapted from [Waldvogel et al. \(1979\)](#). They also extend the observation made in altitude with a buffer of 1-5 km to account for the potential oblique trajectory of the hailstones between the cloud and the ground [Schmid and Schiesser \(2014\)](#), making useless the optimisation used in [Schiesser \(1990\)](#) and ([Schmid et al., 1992](#)), for example. The approach of these authors is to find the translation vector producing the best correlation between the radar observation and the insurance losses.

For this study, the intensity maps established for the 26 May 2009 event (Fig. 9.1), hereafter refer to as the 2009 event (although there was another one in July, as seen above), and the 12–13 July 2011 (Fig. 9.2) event are used. The intensity is provided in classes of maximum hailstone size and have a step of 1 cm. For this study, the mean value of the class is considered. Since the first class of these maps is graupel (aka soft hail) and the second class is hail from 0 to 1 cm, we interpolated linearly the intensity such as class 3 is attributed the value of 2.5 cm. Therefore, graupel obtain the value of 0.4 cm and the class 0–1 cm hailstones the value of 0.8 cm (Fig. 9.3).

9.2.2 Hazard maps

According to [Stucki and Egli \(2007\)](#), the entire Swiss territory is concerned with hail, but the Alps are less often affected. This observation is corroborated by two more recent hazard maps based on radar data and insurance claims that have been published by Schweizer Hagel¹, a

¹http://hagel.ch/fileadmin/customer/Diverses/3052_Hagelkarte.jpg

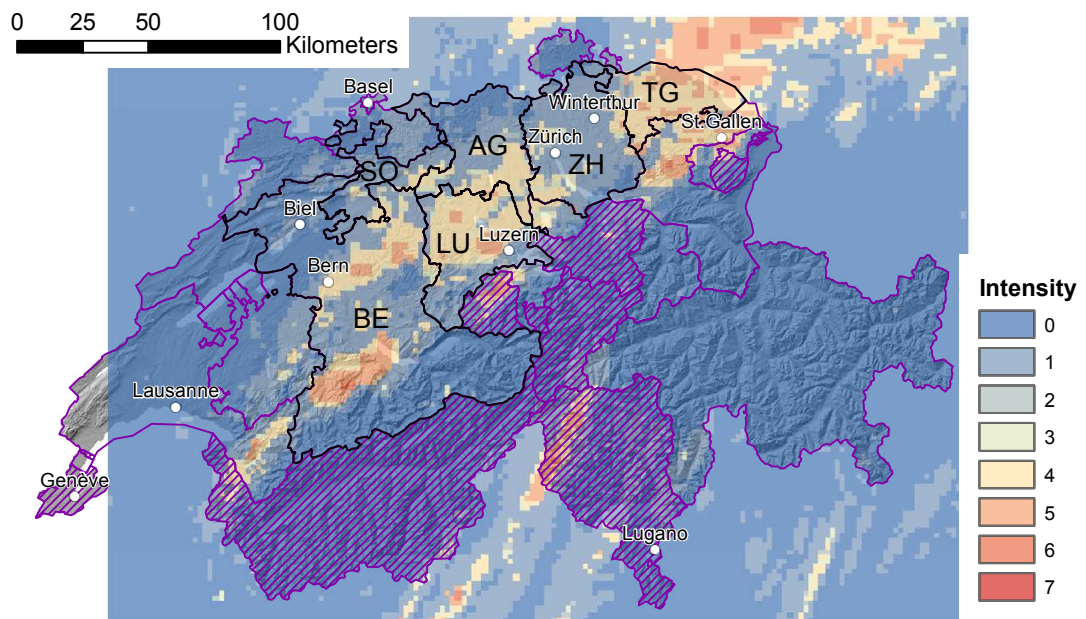


Figure 9.1: Maximum intensity reached during the 26 May 2009 event ([meteoradar gmbh](#)). Cantons in black are the ones mentioned in the text (AG = Aargau, BE = Bern, LU = Lucerne, SO = Solothurn, TG = Thurgau, ZH = Zurich), whereas dashed cantons do not have a public and mandatory insurance company. To convert the intensity values in hailstone sizes, the relation provided in Fig. 9.3 is considered in this study. (hillshade and borders © swisstopo)

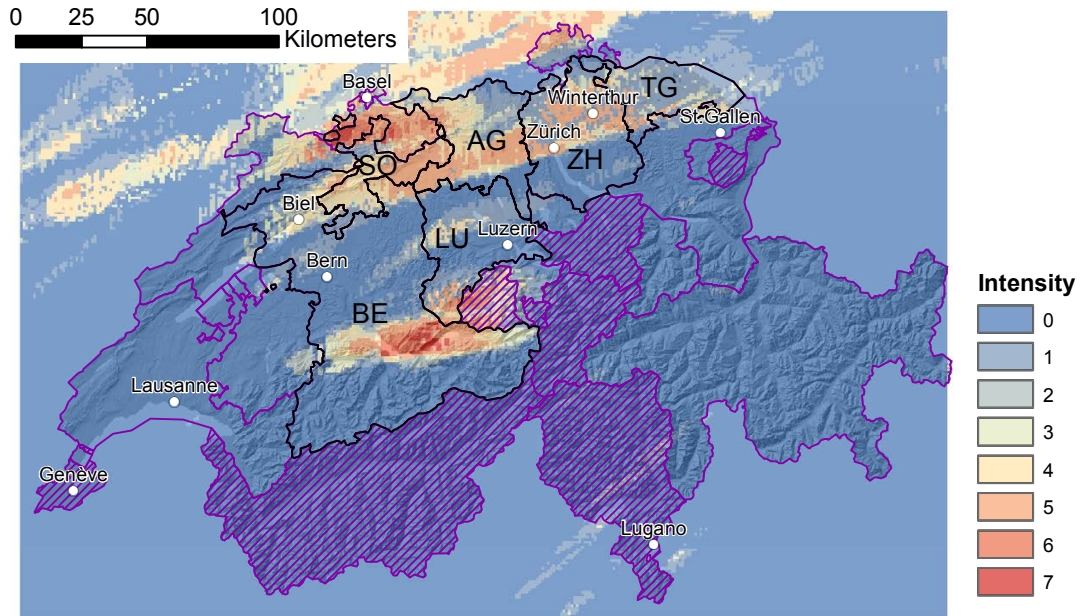


Figure 9.2: Maximum intensity reached during the 12–13 July 2011 event ([meteoradar gmbh](#)). Cantons in black are the ones mentioned in the text (AG = Aargau, BE = Bern, LU = Lucerne, SO = Solothurn, TG = Thurgau, ZH = Zurich), whereas dashed cantons do not have a public and mandatory insurance company. To convert the intensity values in hailstone sizes, the relation provided in Fig. 9.3 is considered in this study. (hillshade and borders © swisstopo)

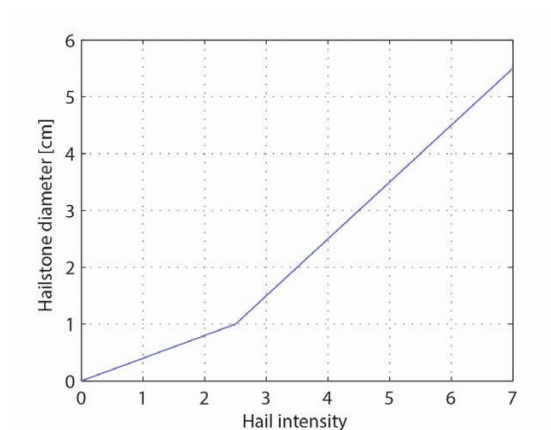


Figure 9.3: Assumed relation between the hail intensity and the maximum hailstone size

crop insurance company, and by the University of Bern, together with the Mobiliar insurance company². From these latter maps, it is possible to observe that the most affected areas are the Prealps (particularly central Switzerland and the South of Bern), the South Ticino and North East Switzerland. Although these latter two maps are more detailed and take into account insurance data, the map provided by [Stucki and Egli \(2007\)](#) is used for this study since it gives not only a relative frequency, but the minimum hailstone size to expect for different return periods. To establish the return periods, [Schuesser \(2006\)](#) divided Switzerland in 11 different regions (Fig 9.4a).

From the minimum hailstone size to expect for different return periods, a distribution can be adjusted to try to predict return period of any hailstone size. If the same size is expected to be exceeded at different return periods, it is only considered for the shorter return period. The Marshall-Palmer exponential law is used since it is in good agreement with the return periods presented in [Stucki and Egli \(2007\)](#). This law is often used to describe the distribution of particle size in a hail event, as mentioned by [Pruppacher and Klett \(2010\)](#). This is expressed as follows:

$$n(d) = n_0 e^{-\lambda d} \quad (9.1)$$

Where $n(d)$ is the number of hailstones with a diameter equal or superior to d , whereas n_0 and λ are parameters controlling respectively the scale and the shape. The resulting frequency–size relations are given in Fig. 9.4b. As an example, the points used to build the curve of the Aargau region are also displayed.

9.2.3 Elements-at-risk and past losses

Switzerland is divided in 26 cantons, among which 19 possess a mandatory public building insurance company. Altogether, 2.23 Million buildings are insured by these companies, for a total value of 2,209 Billion CHF. The insured values of the buildings are estimated by each insurance company, who also register the loss related to the events. When it comes to the location of the buildings, the insurance companies often have a postal address only, and the geographic coordinates can only be retrieved from other sources such as the cantonal administrations or the Swiss postal company ([Swiss Post, 2016](#)), at the condition that the data can be linked by some of the attributes. Buildings footprint are available in the SwissTLM3D, a topographical landscape model from the Federal Office of Topography ([swisstopo, 2015](#)), but these footprints cannot directly be linked with insurance data. In addition, the number of buildings in the swissTLM3D is different from the number of insured buildings, since a same shape can correspond to several insurance policies (for example in the case of attached houses). For this study, we have access to

²<https://www.mobi.ch/de/die-mobiliar/medien/neuer-schub-schweizer-hagelforschung.html>

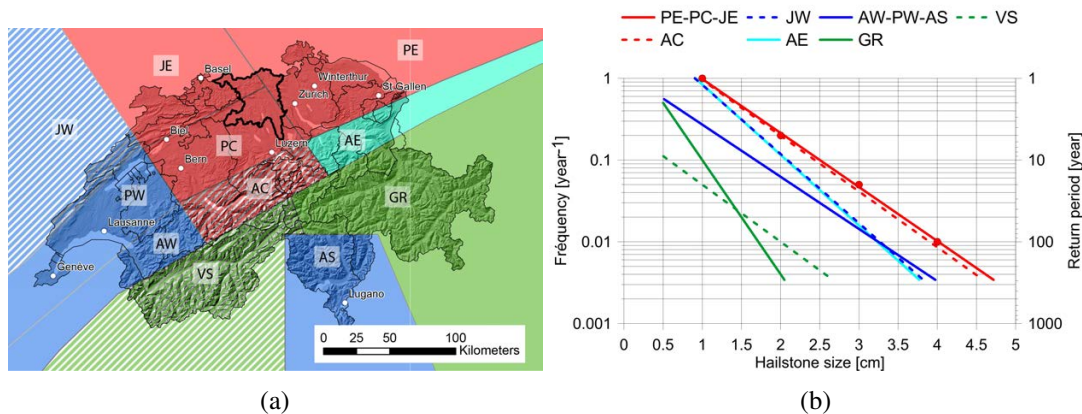


Figure 9.4: (a) Hazard area defined by [Schuesser \(2006\)](#) using radar data and published in [Stucki and Egli \(2007\)](#). (b) frequency–size relations adjusted to the return period of different hailstone sizes for each of these zones. The original data are shown as points for the Aargau area (PE-PC-JC)

data for several cantons, but with different level of detail.

For Aargau, which is the canton on which this study focuses since it suffered from high losses in 2011, the insurance data are directly available. The insurance portfolio contains 219,042 buildings, among which 194,221 (88.7 %) have been georeferenced using the Post Office database and the address fields as link. The total losses related to the georeferenced buildings in the 2011 event are 123 Million CHF.

The losses which occurred during the 2009 event in Thurgau have already been well studied ([Imhof and Choffet, 2012](#)). Losses reaching 47 million CHF have been reported to the insurance company, which was insuring 93'240 buildings for a value of 74 billion CHF at the end of 2009 ([GVTG, 2010](#)). Diverse statistics have been published after aggregation at the municipality scale and are now available with this level of detail ([Imhof and Choffet, 2012](#)).

For all cantons except Aargau, the centres of the building footprints retrieved in the swisTLM3D database, developed by Swisstopo, are used ([swisstopo, 2015](#)). Since the number of buildings in the SwissTLM3D is not equal to the number of insured buildings, it is not possible to use the average building value published by the insurance. Therefore, we divide the total insured value by the number of shapes in the SwissTLM3D for the purposes of this analysis. This operation is done for the whole canton, or municipality by municipality if the insured value is available with this level of detail. In addition, the number of insured buildings is also divided by the number of buildings in the SwissTLM3D. If this is done municipality by municipality, this permits to refine the proportion of affected buildings in the models.

For the cantons of Zurich, Lucerne and Solothurn, the number of affected buildings and the

Table 9.1: Portfolio data and loss statistics used in this study. When the building location is retrieved from the SwissTLM3D, a correction factor is applied to make the number correspond to the number of insured buildings. This correction is done at different scale depending on the available data. In addition, the loss data are available with different level of aggregation.

Canton	Event	Building location	Correction factor	Loss data granularity
Aargau (AG)	12-13 July 2011	Geopost	-	Building
Thurgau (TG)	26 May 2009	SwissTLM3D	Canton	Municipality
Zurich (ZH)	12-13 July 2011	SwissTLM3D	District	Municipality ¹
Lucerne (LU)	12-13 July 2011	SwissTLM3D	Municipality	Municipality
Solothurn (SO)	12-13 July 2011	SwissTLM3D	Canton	Canton

¹Data presented in classes

monetary losses are provided by the association of building insurance companies (AEAI). They are aggregated at the cantonal level for Zurich and Solothurn and at the municipality level for Lucerne. These data are however estimations since the reparation had not been all made at the time of the statistics.

The data used for this study are summarised in Table 9.1, regarding both the building portfolio and the loss statistics.

9.3 Methods

9.3.1 Loss assessment

Loss model

The loss model aims at answering the following questions: given hail intensity, what is the probability for a building to be damaged, and, if the building is damaged, how much will it cost? Both parts are indeed important since for an insurance company, a high number of damaged buildings will induce a high load of administrative work, disregarding the final reparation cost. This approach differs from the traditional vulnerability function, which defines the expected degree of loss as a function of the hazard intensity (e.g. Ciurean et al., 2017), or from the fragility curves, which indicate the conditional probability to reach or exceed a limit state as a function of the hazard intensity (e.g. Silva et al., 2014). On the other hand, it is comparable to the approach

of [Pei and van de Lindt \(2009\)](#) who use a zero loss probability, a collapse probability and a log-normal distribution for the partial damage. Here, an equivalent to the collapse probability is not used, since hail is not expected to destroy completely a building. Due to the many parameters influencing the losses, which are related both with the hazard (e.g. hailstone size distribution and event duration) and the element at risk (e.g. specific equipment such as solar panels, blinders type and state), defining a proxy for the intensity and a loss model is not trivial. Obviously, the choice is strongly limited by the available data. For example, the buildings' materials are most of the time not known, or at least not in a standardised manner. In the meantime, spatio-temporal distribution of the hailstone sizes and kinetic energies can only partially be estimated.

When it comes to the losses, it can be seen from the 2011 event that although the proportion of damaged buildings is correlated with the hail intensity, there is a high variability in the proportion of damaged buildings for a given hailstone size (it will be presented in the results, in [Fig. 9.9](#)). Indeed, the intensities in the Canton of Zurich are in many places similar with the intensities observed in the Canton of Aargau, although the proportion of damaged buildings is significantly lower in Zurich, particularly in the Eastern part of the Canton. Therefore, the proportion of damaged building is calculated for each pixel of the radar intensity map and the distribution of these proportions is analysed. This analysis is performed for the 4 cantons for which some information is available on the proportion of damaged buildings at the municipality or the building scale.

The obtained empirical distributions of damaged buildings are adjusted with a 2-parameters gamma cumulative distribution function:

$$F(p) = \frac{1}{\beta^\alpha \Gamma(\alpha)} \int_0^p t^{(\alpha-1)} e^{-\frac{t}{\beta}} dt, \quad (9.2)$$

where p is the proportion of damaged buildings, α is a shape parameter and β a scale parameter ([Johnson and Kotz, 1970](#)). $\Gamma(x)$ is the gamma function, which is the generalized form of the factorial function, such as $\Gamma(x) = (x-1)!$ for a positive integer. The parameters α and β retrieved are then adjusted with a linear function, that permits to predict their value for any hailstone size (see also [Chapt. 8](#)).

This first function returns the probability for a building to be affected, but provides no information on the damage extent. For this, the loss ratios of the affected buildings are analysed in each intensity class and adjusted using a two-parameter Pareto cumulative distribution function:

$$F(r) = 1 - \left(1 + \lambda \frac{r}{\gamma}\right)^{-\frac{1}{\lambda}} \quad (9.3)$$

Where r is the loss ratio, λ is the shape parameter and γ is the scale parameter (Embrechts et al., 1997).

Model validation

To test the model validity, the loss model is applied to all the affected cantons for which a loss figure is available for the 2009 or the 2011 event. That is the 4 cantons used to build the loss model (see table 9.2) as well as Solothurn, for which the figure is only available at the cantonal scale. To model the predicted losses, a Monte-Carlo simulation is performed using the intensity map of the respective events and the building location retrieved from the SwissTLM3D (except for Aargau, where the insurance database is used), as well as the loss model previously defined.

The total insured value of each canton, district (an administrative level between the canton and the municipalities) or municipality is divided by the corresponding number of buildings in the SwissTLM3D to obtain the individual building value. The total loss and proportion of damaged buildings are compared to the actual values for the whole cantons. The proportions of damaged buildings per district or municipality are also compared to the actual values, when available. For Thurgau, although the loss per municipality is available, it is not compared to the actual value, since only the net loss is available and since the excess (amount paid by the insured party) is not linear, but depend on the loss for each building. However, the losses are closely related to the proportion of damaged buildings, therefore, this parameter is a good proxy to assess spatially the quality of the results.

9.3.2 Average annual hail risk

The frequency–size relation presented in Fig. 9.4b can be used to calculate the mean annual risk. The mean annual risk is calculated between two bounds, and is the sum of the partial risks:

$$R = \sum R_i = \sum (f_i - f_{i+1}) \times L_i \quad (9.4)$$

Where R_i is the partial risk for scenario i , f_i is the frequency of scenario i , f_{i+1} is the frequency of the next calculated scenario (which is 0 for the last scenario), i.e. with the return period immediately higher and L_i are the losses (in CHF or number of damaged buildings), calculated with the loss model defined in Sect. 9.3.1. Since the damage L_i is applied for the interval $i \rightarrow i+1$, the interval should be small to avoid the need for a correction (see Chapt. 5). To simplify the process, we define a minimum return period, calculate the corresponding hailstone size, then we increase the hailstone size of a defined value (e.g. 0.1 cm) and calculate the corresponding return period. The size is then iteratively increased until the user-defined maximum return period is reached or exceeded (Fig. 9.5).

The mean annual risk can be compared with the statistics of the insurance companies. Indeed, between 1994 and 2013, the mean loss amount for all 19 cantons with a mandatory public insurance company was around CHF 86 million per year, and the average number of affected buildings of around 17,000 (loss statistics of the AEAI). To generalize the data, a Pareto function is fitted on both empirical functions (fig. 9.6). This gives better idea of the expected value.

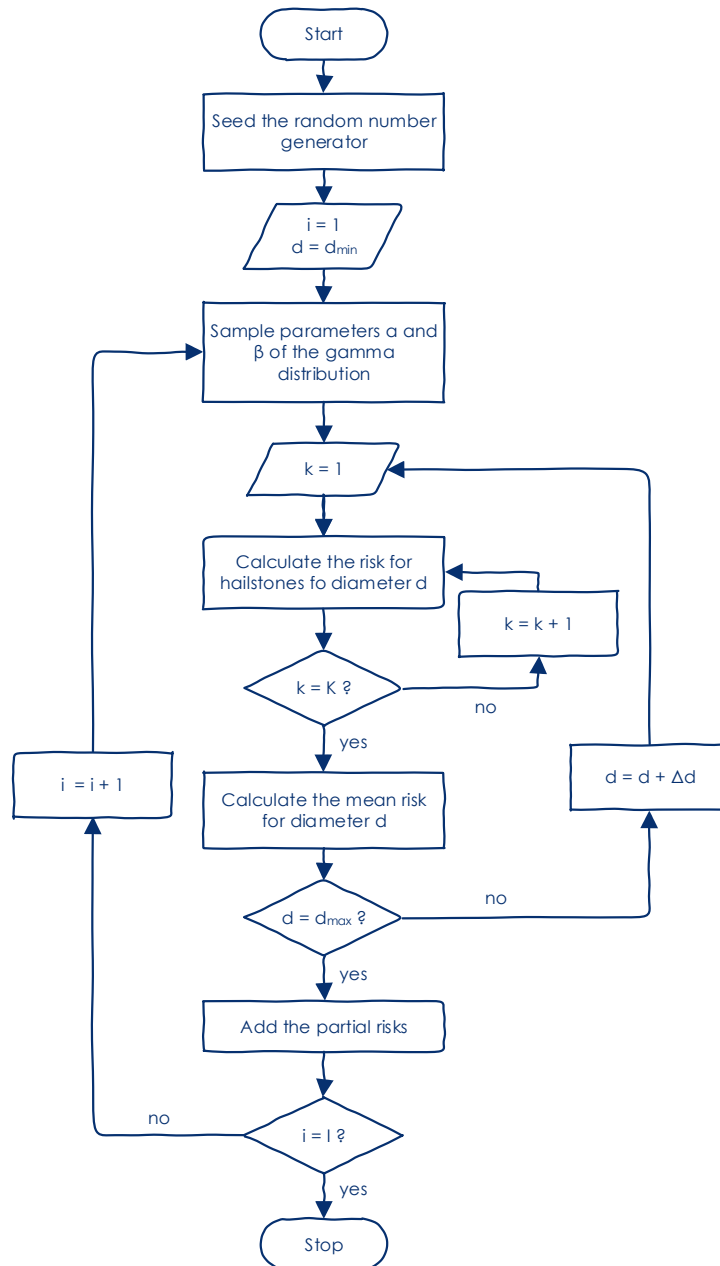


Figure 9.5: Flow-chart of the mean risk assessment procedure. The analysis is executed I times with different α and β parameters for the gamma distribution. In each of these analyses, the consequences are evaluated for hailstone sizes between d_{min} and d_{max} , increasing progressively the size of an increment Δd . For each size of hailstone, the analysis is performed K times to account of the variability in the loss model.

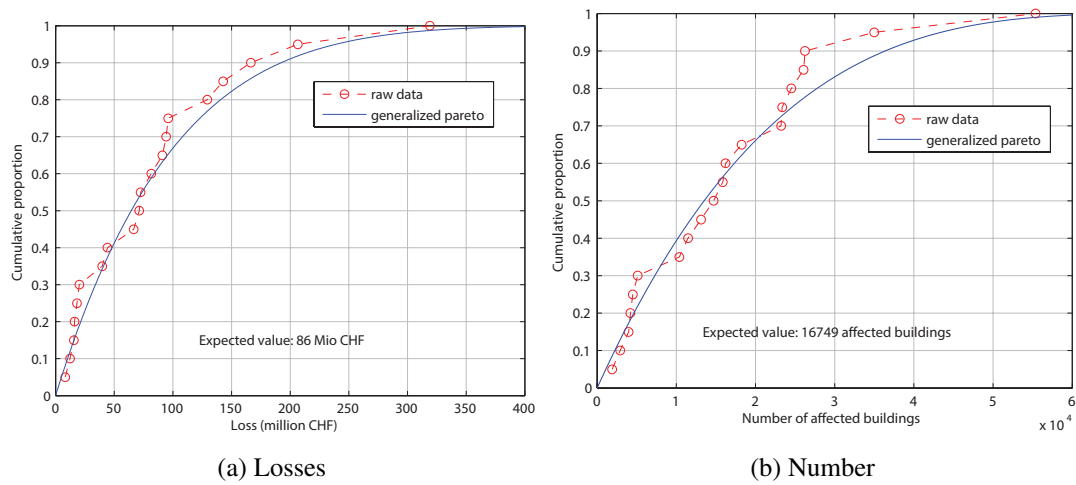


Figure 9.6: Statistics of the monetary losses and damaged buildings from 1994 to 2013 in the 19 cantons with a public building insurance (loss statistics if the AEAI). The values are ranked and fitted with a cumulative Pareto distribution function.

9.3.3 Hail event modelling

Goal of a model

Evaluating the mean risk thanks to hazard maps leaves a question unanswered: what cost can we expect for a single event? Having a constant cost with small variations over the years is indeed not the same as handling large and rare events. An event-based model can try to answer this question and can be used to test changes in the buildings (construction materials, number, location, ...) or in the hazard (frequency, size of the events, ...), as long as these parameters are included in the model. This section presents a first basic attempt of such a model.

The idea of the model is that an intensity map such as the ones presented in Fig. 9.2 and 9.1 can be approximated by a set of 2D Gaussian functions. After reproducing these 2 events, new events can be modelled using key characteristics of these Gaussian functions, as well as frequency-size ratios derived from the hazard map (Fig. 9.4). Sect. *Model calibration* presents the reproduction of past event, whereas Sect. *New events modelling* presents the modelling of new events.

Model calibration

The idea of the model is that the intensity map of the event can be reproduced with a set of 2D Gaussian functions. This part of the model is slightly modified from Demierre (2012) and Choffet et al. (2012) and their subsequent work. Although they presented only the version with 1D Gaussian functions, that necessitate to divide the study area in slices, they already developed a version with 2D Gaussian functions. A 2D Gaussian (which is not a statistical distribution) is defined by 6 parameters, which are presented in Fig. 9.7, and are the x_0 and y_0 coordinates of the mode, the angle θ of the great axis, the scale factor ϕ (corresponding to the maximum value), the standard deviation along the great axis σ_x and along the small axis σ_y . This latter parameter can be replaced by the eccentricity κ , which is defined by:

$$\kappa = \frac{\sigma_x}{\sigma_y} \quad (9.5)$$

The equation of a 2D Gaussian function is given by:

$$f(x, y) = \phi e^{-\left(\frac{(x-x_0)^2}{2\sigma_x^2} + \frac{(y-y_0)^2}{2\sigma_y^2}\right)} \quad (9.6)$$

This assumes a great axis along the x-axis. In practice, θ is used in a rotation matrix and x_0 and y_0 in a translation matrix that are used to calculate the x and y coordinates of each grid cell of the study area, relatively to the ellipse coordinate system. Equation (9.6) is then used to calculate

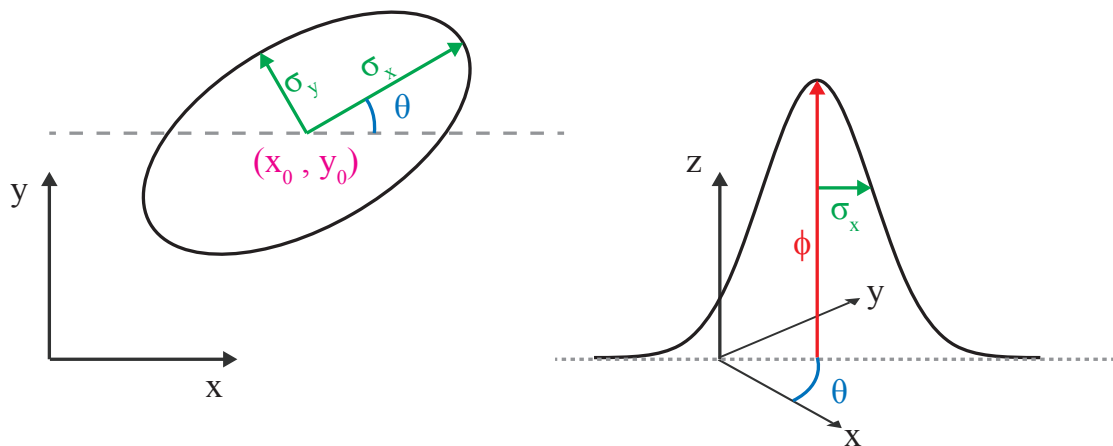


Figure 9.7: Parameters of the Gaussian functions on the XY-plane (left) and in cross-section along σ_x . For practical reasons, the standard-deviation of the Gaussian is not respected between the two figures

the intensity of the ellipse in each cell of the grid. The same process is performed for all ellipses and the intensities of all ellipses are summed.

Due to the potentially large number of Gaussian functions, the number of parameters to optimize can be very large. Therefore, a relatively good initial solution is needed. This initial solution is obtained by smoothing the intensity map. The smoothing is performed by convolving the intensity map with a Gaussian window (also called a kernel or a mask in image processing [Gonzalez and Woods, 2002](#)). The size of the Gaussian window determines the degree of smoothing. Then, the maxima are localized on the smoothed map, by checking for each pixel if its value is the highest of a neighbourhood of user-defined dimensions. A minimal intensity can also be set in order to avoid fitting Gaussian function on very small peaks produced during the smoothing procedure.

The initial solution is then optimized using a genetic algorithm Matlab toolbox ([Chipperfield et al., 1994](#); [Chipperfield and Fleming, 1995](#)). The principle of genetic algorithm is to produce generations of individuals by recombining elements of the previous generation, and by attributing a higher probability of the fittest individuals to be kept for the next generation. Each individual represents a potential solution, i.e. a vector with a value for each of the parameters that need to be optimised. The fitness is determined by the results obtained using an objective function. In that case, the objective function is the rooted mean squared error of the map obtained with the values of an individual (transformed in a grid) compared to the initial (non-smoothed) map. The genetic algorithm approach necessitates, for each variable, to set a minimum and a maximum value.

The properties of the Gaussian functions are then analysed under different aspects, in order to

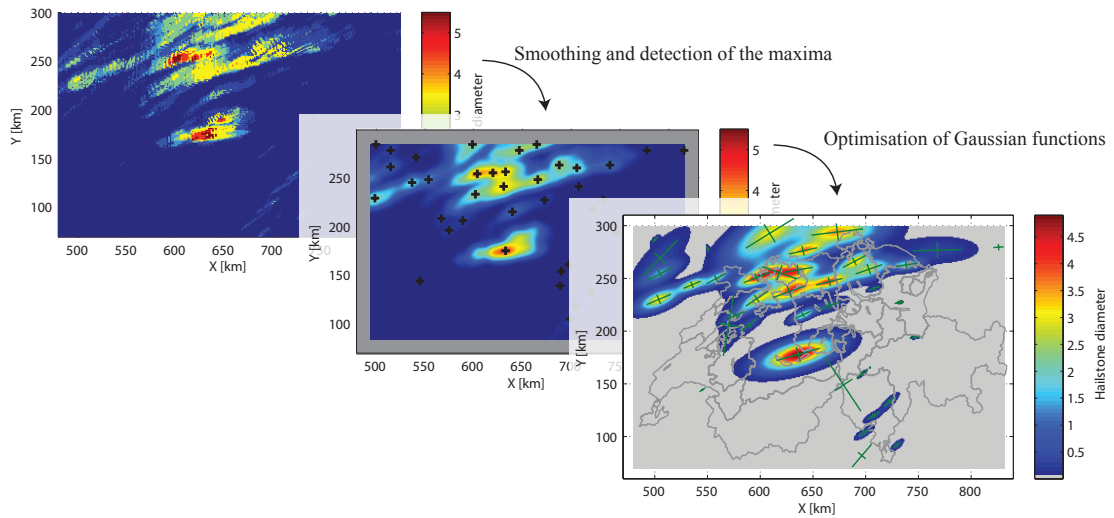


Figure 9.8: Schematic representation of the optimisation procedure: the original map is smoothed through a convolution with a Gaussian function. The dimensions of the window with the Gaussian function control the degree of smoothing. Then, the local maxima are detected on the smoothed map. The position of these maxima and the hailstone intensity at their respective position serves as initial solution for the optimisation procedure.

guide the creation of new events.

New events modelling

The modelling of new events is constituted of two parts:

1. Creation of the general location and shape of the event, according to the hazard map
2. Creation of Gaussian functions inside the event

The general shape of the event (first part) is depicted by an ellipse, which is defined by the angle of its great axis (A), the length of its great axis (L) and the ratio between its great axis and its small axis (K). For each realisation, random values are attributed to each of these parameters according to predefined distributions. The area of the obtained ellipse is compared to the area of 1 million ellipses created from the same distributions, in order to check if the surface covered by the ellipse is large or not. Thus, the quantile at which the random ellipse is located in the distribution of ellipses is retrieved. It is considered for this model that a large quantile corresponds to an event with a high magnitude. From the quantile of the ellipse size, a magnitude is then attributed (on an arbitrary scale) and is used to define:

- a dummy hailstone size, which is used to calculate a frequency map for the entire study area
- the distribution of the Gaussian functions scale factors.

The frequency at which the dummy hailstone size is reached is estimated based on the frequency–size relationships (Fig. 9.4) and the mean frequency in the ellipse is calculated. This mean frequency is then compared to the product of the frequency of 0.5 cm hailstones in Aargau and a random value between 0 and 1. If the mean frequency in the ellipse is higher or equal to the latter product, the ellipse is kept. Otherwise, the ellipse is rejected and a new one is created. The idea of this procedure is to respect a size distribution of events locally, but also to account for the spatial distribution of the events. Indeed, thanks to this procedure, an event in an area with low frequencies is less likely to be kept than the same one in an area with higher frequencies.

When it comes to the Gaussian functions scale factor (ϕ), it is defined by an exponential cumulative distribution function:

$$F(\phi) = 1 - e^{-\frac{\phi}{\mu}} \quad (9.7)$$

where μ is defined by a uniform distribution, which is sampled according to the event magnitude defined above. Thus, an event with a larger magnitude will be more susceptible to produce hail cells with large hailstones.

The position of each Gaussian function inside an event is defined by an iterative procedure. A probability of one is attributed inside the ellipse to each cell of a raster with the same extent and cell size as the hazard map. Then the first Gaussian function is positioned randomly using the weights of this probability raster. The other parameters of the Gaussian function are defined using their respective probability distributions. Then, the value of the probability raster is reduced to 0 in an ellipse corresponding to the area where the Gaussian function value is equal or higher to 20 % of its maximum value, which means that the center of another Gaussian function can't be located in that area any more. The next Gaussian function is then placed in the updated probability map. Although Gaussian function can still interact, this prevents Gaussian functions to be too close to each other and to build unrealistic hailstone size. New Gaussian functions are added as long as the sum of all the cells of the probability raster is above ten.

Once this process is over, a raster map adding all the Gaussian functions is computed and the damage expected for this event are calculated using the loss model previously defined.

Finally, several rasters store the number of events reaching or overpassing a given threshold. The threshold considered have values from 0.5 to 15 cm with a step of 0.1 cm. Then, a Marshall-Palmer distribution (Eq. 9.1) is adjusted for every pixel in a rectangle containing all the Swiss

territory (the grid is reduced compared to the simulations to accelerate the computing and to avoid border effects). The results are then scaled according to the mean n_0 parameter obtained with the simulations in the area of interest (a rectangle defined to contain all the buildings), and the value derived from the hazard map for the same area (Fig. 9.4b). The obtained λ parameter is compared to the expected one and some parameters are adjusted in order to reproduce as well as possible this parameter.

9.4 Results

9.4.1 Loss assessment

Loss model

Using the intensity maps transformed in hailstone size and the proportion of damaged buildings retrieved whether directly from the building portfolios or from the statistics of the association of building insurances (AEAI), the statistical distribution of the proportion of damaged buildings in each class of hailstone size can be assessed (Fig. 9.9). The proportions are weighted by the number of buildings in each cell. The most representative graphs are the one of Aargau, where the actual proportions are available, and the ones of Thurgau and Lucerne, since the data available at the municipality level is relatively representative of the local variations. To some extent, the data of Zurich are also representative, but the classification of the proportion of damaged buildings offers less detail as compared to the other cantons. The Zurich data are however useful to represent a situation where relatively high radar-derived hailstone sizes are not translated in high proportion of damaged buildings. The scale parameters β and the shape parameters α are plotted in Fig. 9.10 and 9.11 respectively. These parameters are fitted with a linear function constrained to go through the origin. For β , this is to avoid having a probability for a building to be damaged if there is no hailstone, whereas for α , this is mainly to simplify the calculation, but it does not really affect the regression. The linear regression is weighted by the number of buildings in the class, which is denoted by the size of the circle. In view of the parameters of the different cantons, for the simulations, a range of 0.1–0.4 is chosen for the slope of α and a range of 0.01–0.08 for the slope of β .

The second part of the model, which is the loss ratio of the damaged buildings in Aargau, is presented in Fig. 9.12. The plain curves are the empirical curves. These latter are fitted with 2-parameters generalized Pareto distributions, presented with a dashed line. The estimated parameters of the distributions are plotted in Fig. 9.13, with circles proportional to the number of buildings in the category. The shape parameter λ shows no obvious trend. On the other hand, the scale parameter γ shows a tendency to increase with increasing the hailstone size, which

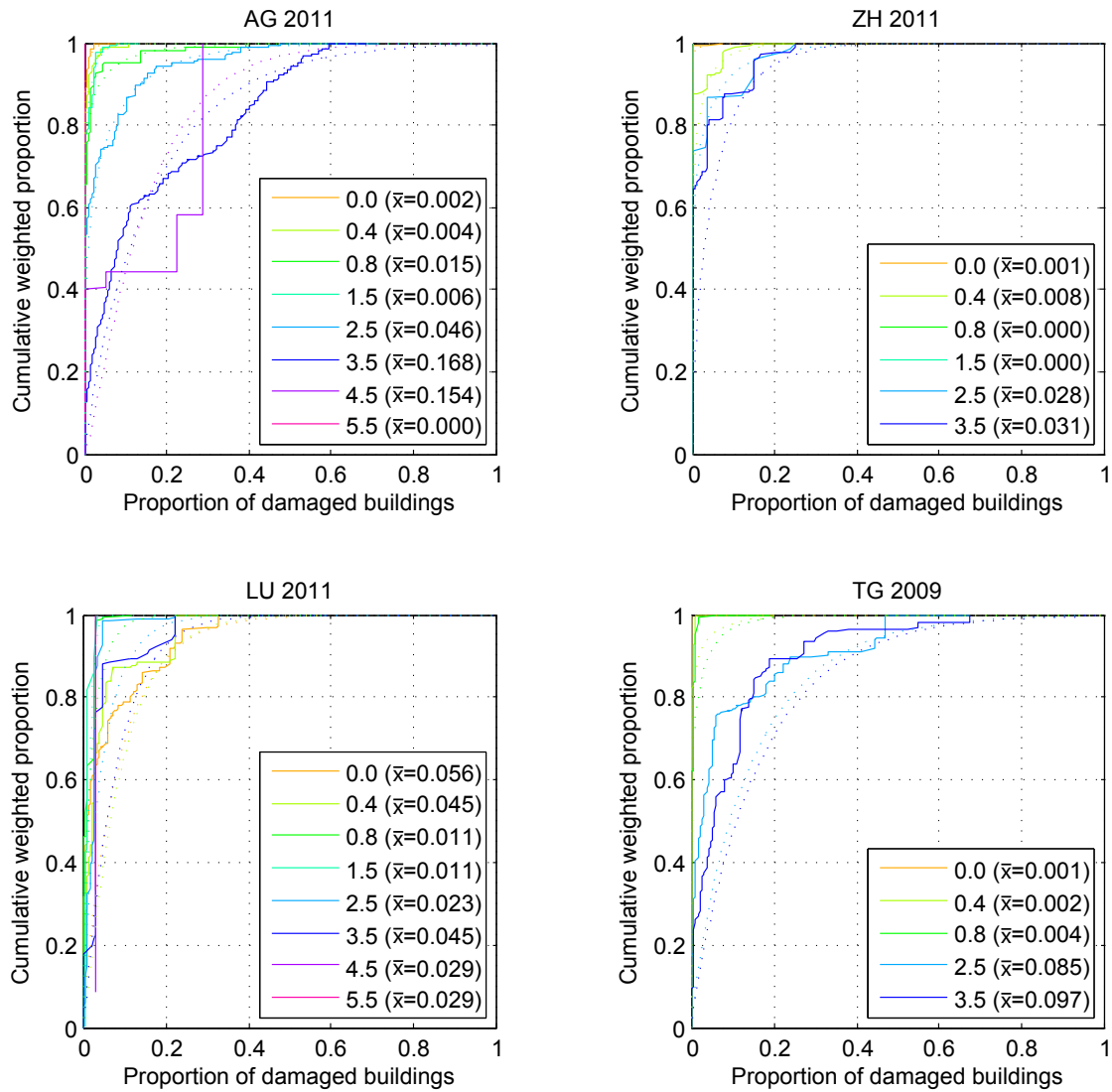


Figure 9.9: Observed cumulative weighted proportion of damaged buildings in each pixel of the defined intensities. The weighted mean of the class (\bar{x}) is indicated in the legend. For Zurich, the middle of the class indicated in (GVZ, 2012) is used, whereas for Lucerne, the proportion indicated for the district is used, which is obviously not detailed enough (note that the x-scale is different).

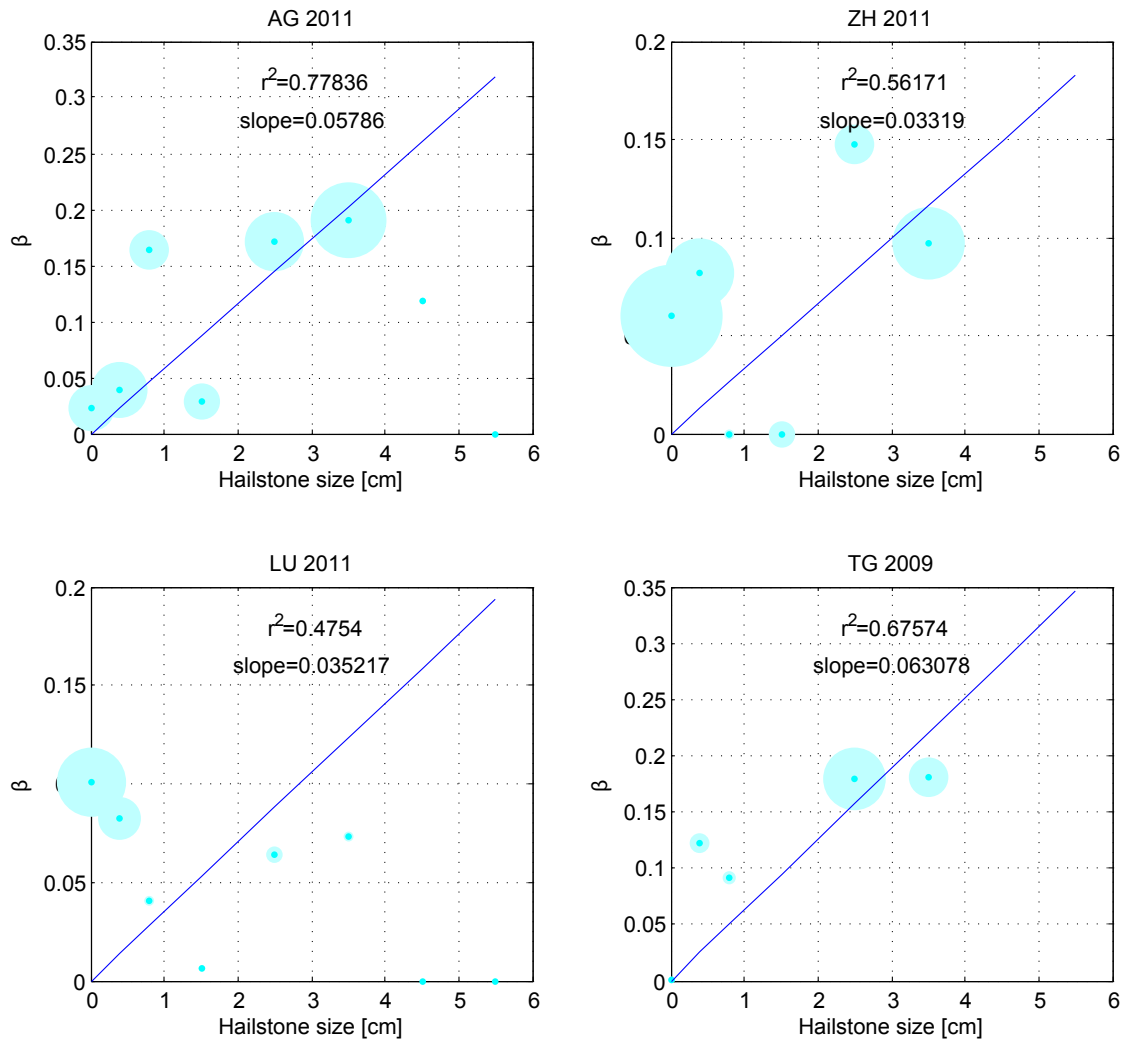


Figure 9.10: Scale parameters of the gamma fits retrieved from the proportion of damaged buildings. Note that the vertical scales vary.

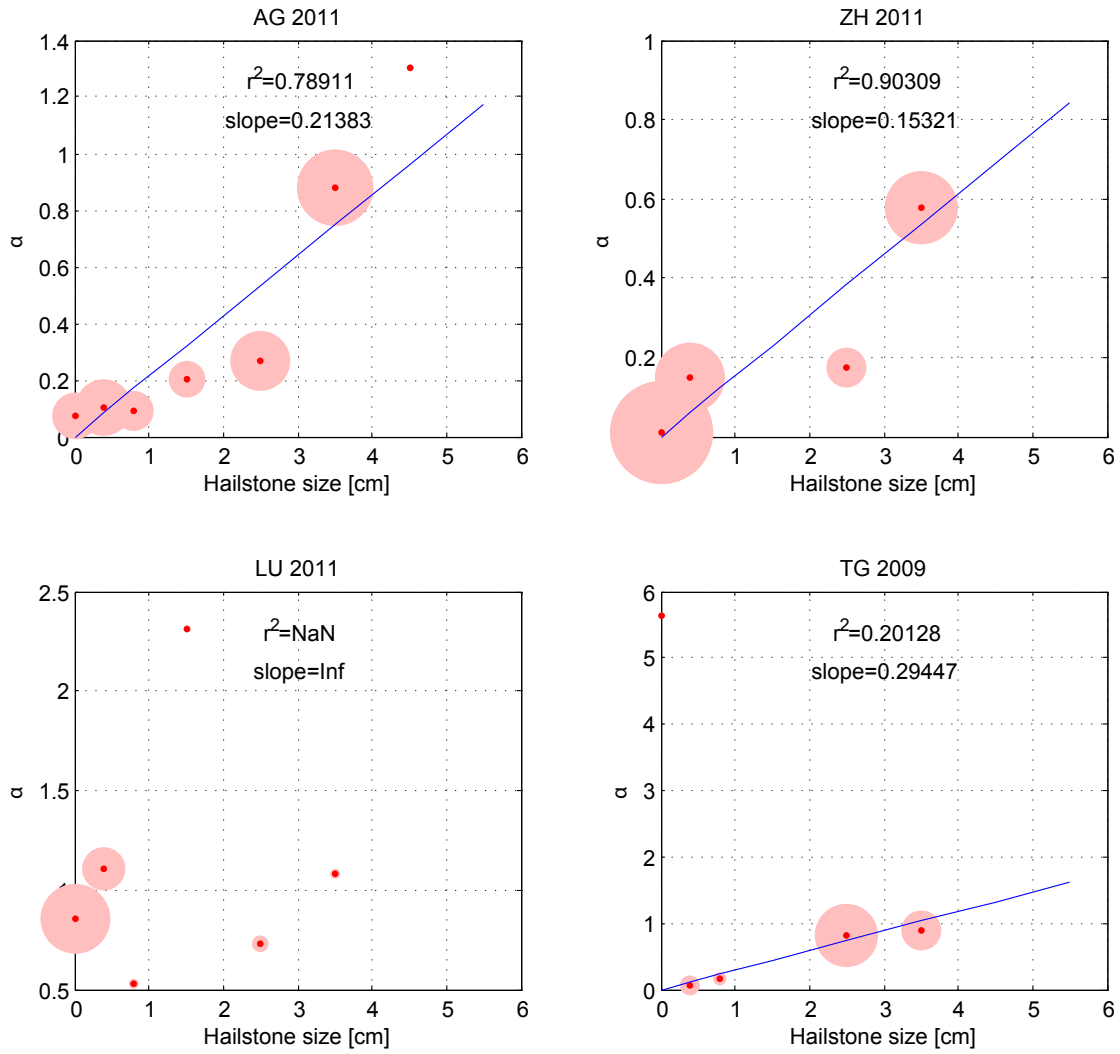


Figure 9.11: Shape parameters of the gamma fits retrieved from the proportion of damaged buildings. Note that the vertical scales vary.

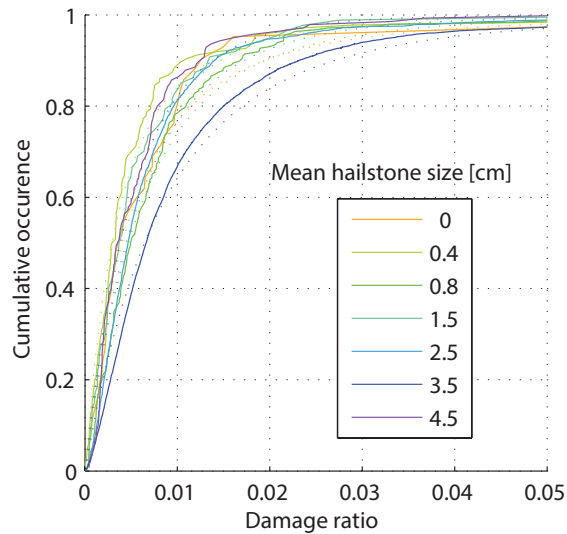


Figure 9.12: Cumulative distribution of damage ratio in each class of hailstone size (plain curves) and fitted 2-parameters generalized Pareto distributions (dashed curves).

corresponds to the expectation. This parameter is then fitted with a linear function, which is used, together with the weighted mean of λ , to draw the functions of Fig. 9.14. When assessing the damage of any location, the linear regression is used to assess the γ value corresponding to the hailstone size of this location which is then used to establish the probability distribution.

Model validation

The loss model is applied to the 4 cantons used to build the model, as well as to Solothurn, using the radar intensity maps (Fig. 9.1 and 9.2). The results are presented graphically in Fig. 9.15 and in Table 9.2. The high variability of the loss model results in a large spread of the results, which always include the actual value. Table 9.2 shows at which quantile of the model the actual value corresponds. For example, the real damage cost in Lucerne corresponds to the quantile 0.16 of the modelled values, which is not a perfect result, since it means that 84 % of the simulations give a result above the real value. A quantile close to 0.5 would indeed be desirable. On the other hand, if all the results were close to a quantile of 0.5, that would mean that the variability of the model is too large. An important characteristic to notice is that except for Aargau, the quantile of the proportion of affected buildings is always higher than the quantile of the damage cost, which means that the damage cost per building in Aargau is particularly high compared to other events. Detailed damage data from other event would then be beneficial to the second part of the model.

The coefficient of correlation in Table 9.2 shows the correlation between the median modelled proportion of damaged buildings and the actual proportion of damaged buildings. This comparison

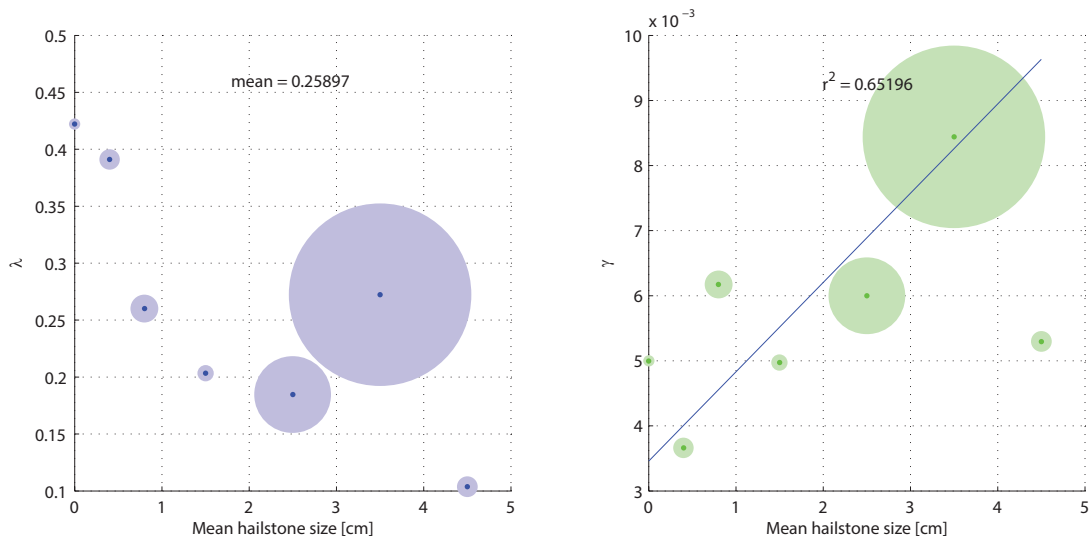


Figure 9.13: **Left:** Shape parameter (λ) of the generalized Pareto distribution. Since no tendency is visible, the weighted mean is used. **Right:** Scale parameter (γ). The weighted linear regression is used to build the curves presented in Fig. 9.12 right.

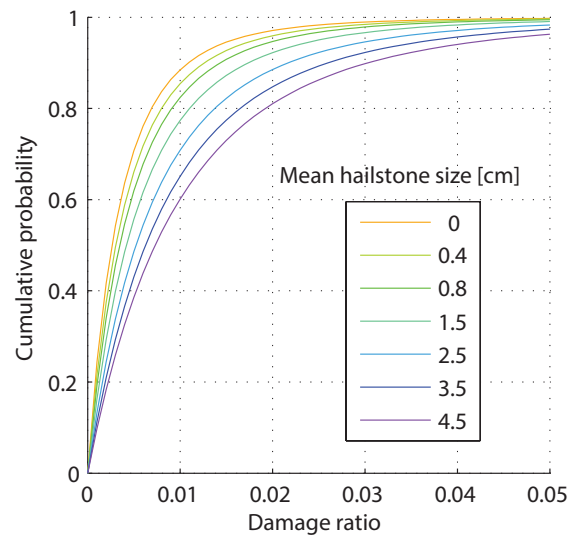


Figure 9.14: 2-parameters generalized Pareto distribution obtained using the parameters deduced from Fig. 9.13.

is done at the municipality level. For Zurich, the actual proportions are only given as class, so the actual proportion is considered to be the average of the class. Except for Aargau, the correlation is not very good. It is particularly bad for Lucerne, which shows no correlation at all. This highlights the limit of using the radar intensity as a proxy for the proportion of damaged buildings. Indeed, for a given intensity, the observed proportion of damaged buildings might be very different. This is true locally, which could be the result of the radar resolution, but also regionally. Indeed, the 2011 event in Zurich and Lucerne resulted in very low proportion of damaged buildings even though the intensities are relatively high. For Lucerne, although no correlation is observed, it is possible to see that the radar intensities and the actual damage are more spatially related than the absence of correlation suggests (Fig. 9.16). As long as the derivation of hail intensity from the radar is not improved, little improvement can be expected of such a damage model. However, this model already gives a first estimation and together with other information (hailstone size reported from the ground, newspapers, first insurance claims, . . .), it might help to estimate the damage cost to expect at the scale of a canton.

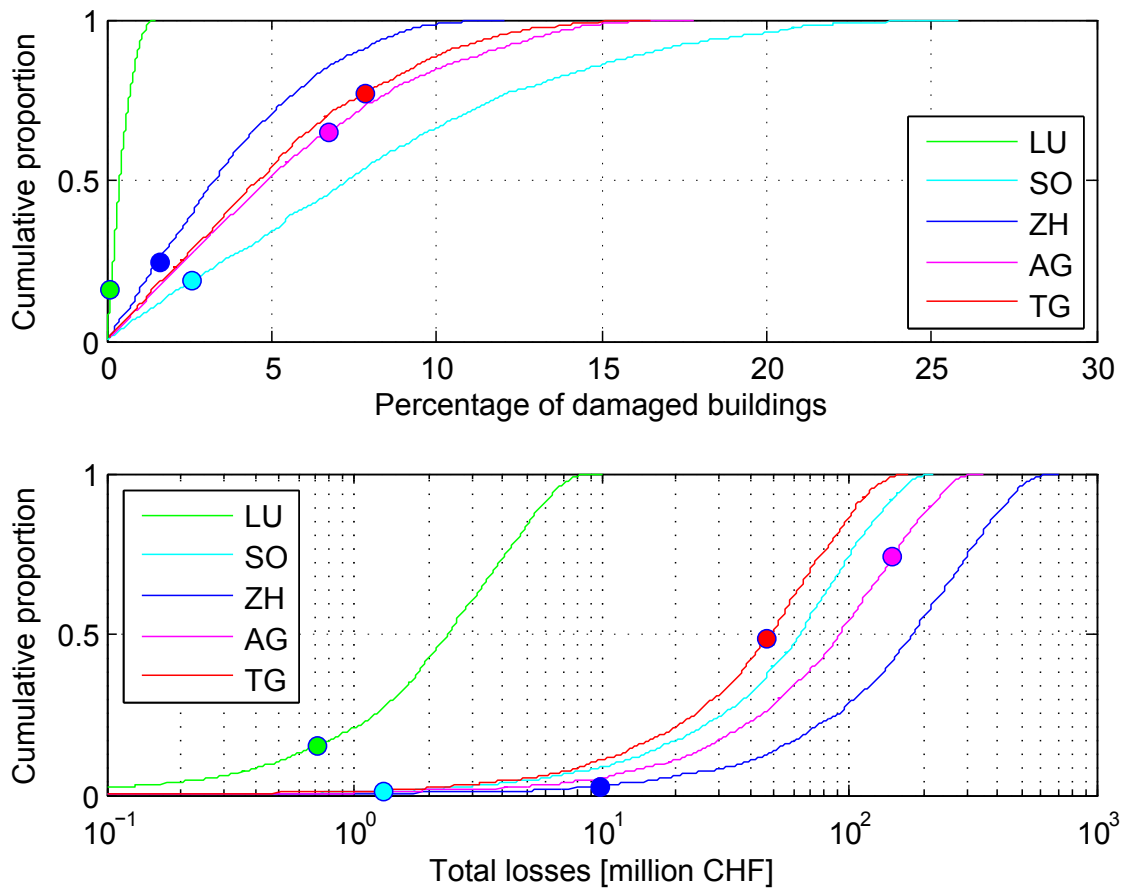


Figure 9.15: Results of the damage assessment from the radar images. The points represent the actual values and are located at the quantile where the respective curves reach these values.

Table 9.2: Results of the damage assessment compared to the expected values (compare to Fig. 9.15). For both the proportion of damaged buildings and the damage amount, several quantiles are given (0.1, 0.5, 0.9). The quantile at which the modelled value is similar to the observed value is also given. The coefficient of correlation is the correlation of the modelled proportion of damaged buildings to the actual proportion of damaged building at the municipality scale.

Parameter	LU	SO	ZH	AG	TG
Actual proportion of affected buildings	0.1%	2.6%	1.6%	6.7%	7.9%
Median modelled proportion	0.4%	7.4%	3.3%	4.9%	4.7%
Quantile 0.1	0.1%	1.4%	0.7%	1.0%	0.9%
Quantile 0.9	1.0%	16.6%	7.6%	11.6%	10.3%
Quantile of the actual value	0.16	0.19	0.25	0.65	0.77
Coefficient of correlation	-0.02	-	0.37	0.55	0.29
Actual damage cost [MCHF]	0.7	1.3	9.9	151.0	47.0
Median modelled cost [MCHF]	2.4	63.3	181.4	91.9	48.5
Quantile 0.1 [MCHF]	0.5	11.6	37.7	18.9	9.1
Quantile 0.9 [MCHF]	5.8	143.1	426.3	216.1	107.4
Quantile of the actual value	0.15	0.01	0.03	0.74	0.49

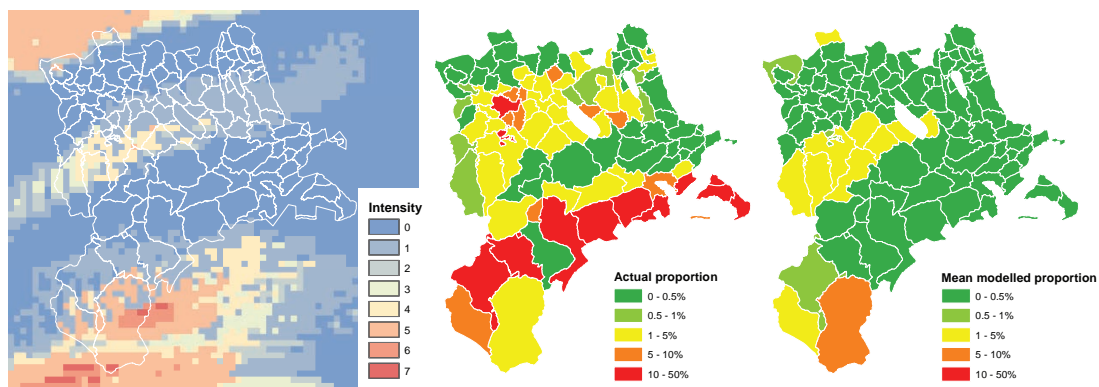


Figure 9.16: Comparison, at the municipality level, of the hail intensities derived from the radars, the actual proportion of damaged buildings and the modelled proportion of damaged buildings. The actual proportion of damaged buildings shows trends similar as the intensities (SW-NE bands), but with a partial overlap only. For example, the group of strongly affected communities in the South-Eastern border of the Canton does not overlap the high intensities.

9.4.2 Average annual hail risk

The region presented in [Stucki and Egli \(2007\)](#) are shown in [Fig. 9.4a](#), whereas the exponential fitted relations are presented in [Fig. 9.4b](#). From these relation and the loss model, the mean annual risk is calculated for Aargau alone, and for the 19 cantons with a public buildings insurance company, using the parameters given in [Table 9.3](#). The number of runs is quite low, because the time needed for one run using one processor of a cluster node is around 7.5 hours.

The distributions of the mean annual risks and the mean annual numbers of affected buildings are given in [Fig. 9.17](#) for Aargau, and in [Fig. 9.18](#) for the 19 cantons with a public building insurance company. In this latter figure, the expected values retrieved from [Fig. 9.6](#) are displayed as vertical lines. 88 % of the time, the modelled cost is above the expected value, and in 79 % of the realizations, the number of affected buildings is above the expected number.

The expected cost is then more often overpassed in the realizations than the expected number of affected buildings. This tends to confirm the observation made on [Fig. 9.15](#) and [Table. 9.2](#), that the real damage costs per building in Aargau are especially high.

Table 9.3: Parameters used for the mean risk calculation. The variable names refer to the flow-chart in [Fig. 9.5](#).

Parameter	Variable	Value
Lower return period [years]	–	1
Upper return period [years]	–	1000
Size step [cm]	Δd	0.1
Number of simulation per return period	K	10
Number of mean risk simulations	I	100

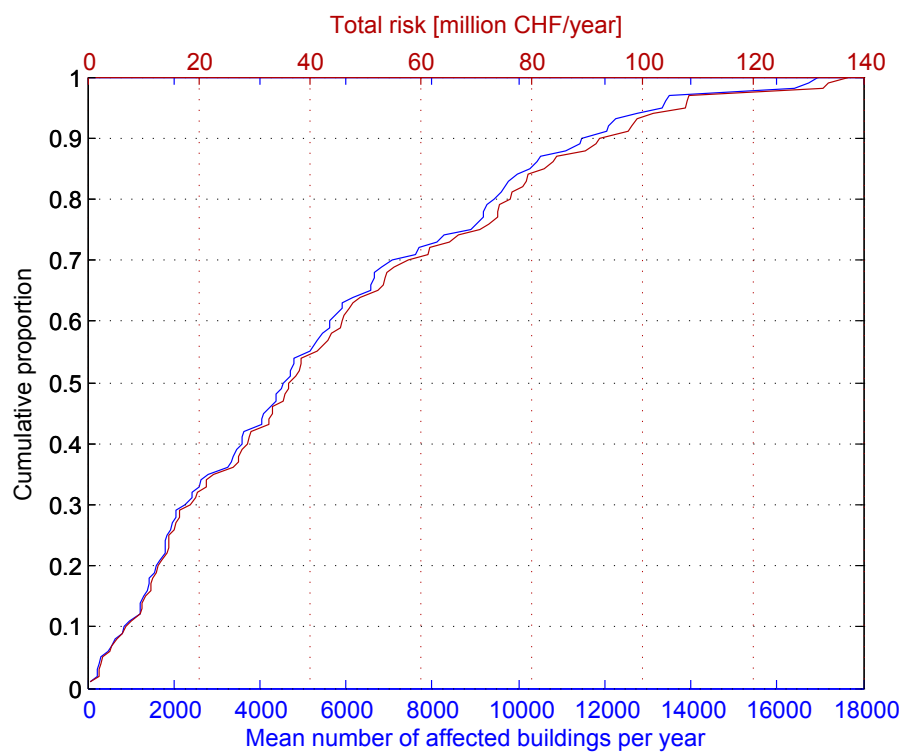


Figure 9.17: Mean annual risk for the canton of Aargau in terms of losses per year and (blue curve) and number of affected buildings (red curve)

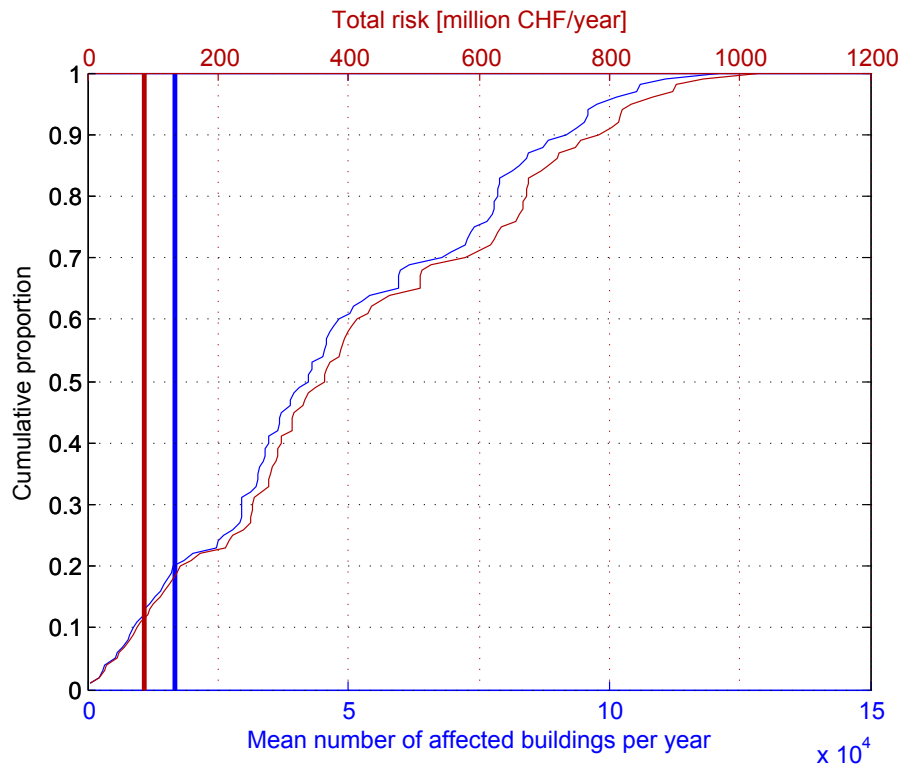


Figure 9.18: Mean annual number of affected buildings for the 19 cantons with a public building insurance company in terms of losses per year and (blue curve) and number of affected buildings (red curve)

9.4.3 Hail events modelling

Model calibration

The calibration is made using the images radar of both analysed events (Fig. 9.2 and 9.1). Several parameters can be changed both for the fitting and for the genetic algorithm optimisation. The size of the smoothing window is expected to be a very sensitive parameter, since it controls the level of detail. Therefore, tests are made with Gaussian windows between 10 and 50 pixels (Table 9.4). This parameters influences mainly the number of Gaussian functions. A tolerance of 2 pixels is used for the detection of the maxima, which needs to have an intensity (hailstone size) of at least 0.2 cm to be kept.

When it comes to the optimisations, reasonably large bounds are used for all parameters (Table 9.5). Very large bounds can however not be used, because it would make the optimisation more difficult, but also because the optimisation needs to help defining parameters for the simulations. It is particularly important to limit the stacking of the different Gaussian functions, because this is more difficult to reproduce in the simulations. Therefore, a maximum size and eccentricity has to be selected. The same can be said of the number of Gaussian functions. Indeed, a large number of functions are expected to better reproduce the initial map, but to be more complicated to reproduce. Therefore, a balance between the number of functions and the generalisation has to be found.

The genetic algorithm toolbox settings are presented in Table 9.5 as well. The optimisation is stopped after 30 000 iterations (one iteration being one generation), or when an improvement of the RMSE of less than 10^{-5} is obtained on the last 500 generations. At each generation, 30 individuals are created, with a generation gap of 0.9, which means that 90 % of the individuals are newly created by recombination, and the best 10 % are directly propagated from the previous generation.

The properties of the Gaussian functions in the 10 optimisations are then retrieved in order to keep the important characteristics for the simulations. Figure 9.19 shows the orientation of the great axis of each individual Gaussian function in the optimisations. In most cases, the orientation corresponds to the orientation of the main event with small variations. The optimisation in Thurgau using a large number of Gaussian is an exception. Indeed, using a lot of functions, they represent more the local characteristics than they generalize the characteristics of the event. Figure 9.20 shows the cumulative distributions of the length-width ratios (κ) in the optimisations. The results are not obviously related to the size of the smoothing window and are comparable for all optimisations. Figures 9.21 and 9.22 shows similar analysis for the standard deviation along the small axis and the maximum intensity respectively. The standard deviation is clearly related to the number of Gaussian functions. Logically, the higher the number of Gaussian functions,

Table 9.4: Parameters used for the smoothing.

Parameter	Value
Size of the Gaussian window [pixels]	10,20,30,40,50
Tolerance for the searching of maxima [pixels]	2
Cut-off intensity	0.2

the smallest are their standard-deviation, since a single function does not need to apply to a large area. Indeed, an extreme case would be to have one Gaussian function per pixel with a standard-deviation small enough so that they do not influence the neighbouring cells. This would be a solution reproducing perfectly the initial map. When it comes to the scaling factor (ϕ), a relation with the size of the smoothing window can't be observed, but the scaling factors tend to be smaller in the 2009 event than in the 2011 event.

The optimisations are presented spatially from Fig. 9.23 to Fig. 9.44. Figures 9.23 and 9.34 present the original raster maps with the same color scale as the optimisation results. Figures 9.24—9.33 present the results of the optimisations for the 2011 event, whereas Fig. 9.35—9.44 present the same results for the 2009 event. The green cross represent the great and small axis of each Gaussian functions (their length representing the standard-deviations σ_x and σ_y). The results are always presented in terms of hailstone sizes and residuals.

Table 9.5: Parameters used for the genetic algorithm optimization.

Bounds for the Gaussian functions	Min	Max
Displacement of the initial x_0 and y_0 [km]	0	10
Ratio of the initial hailstone diameter ϕ_{initial}	0.1	2
Smaller standard deviation σ_y [km]	0.5	10
Length-width ratio κ	1	20
Angle θ [deg]	0	180
Optimisation parameters	Value	
Maximum number of generations	30000	
Number of individuals per generation	30	
Generation gap	0.9	
Stopping criterion	10^{-5}	
Number of generations considered before stopping	500	

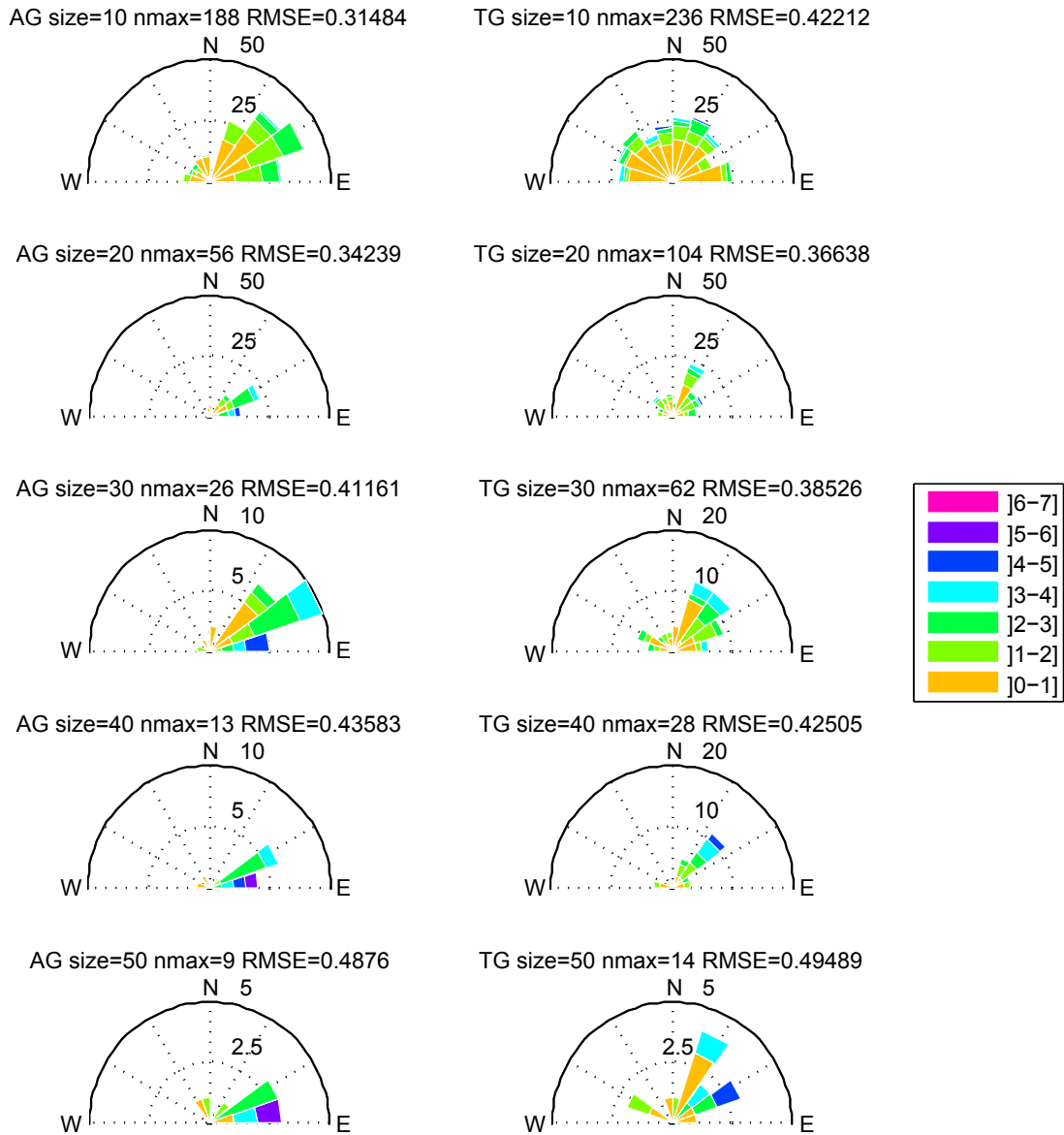


Figure 9.19: Orientation of the great axis of the Gaussian functions in the optimisations. The colors represent the maximum hailstone size of the Gaussian function (ϕ). $nmax$ is the number of Gaussian functions (number of detected maxima in the smoothed map) and RMSE is the rooted mean squared error, where the error is the difference of the resulting map and the original one.

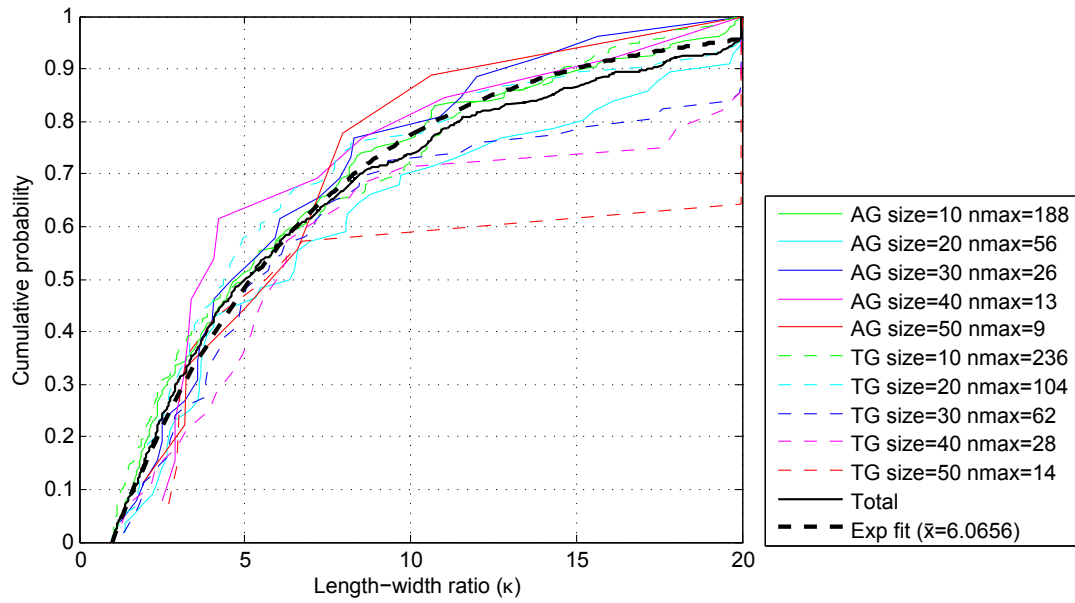


Figure 9.20: Cumulative distributions of the length-width ratio (κ) in the optimisations. The combined distribution for all the optimisations is fitted with a exponential distribution.

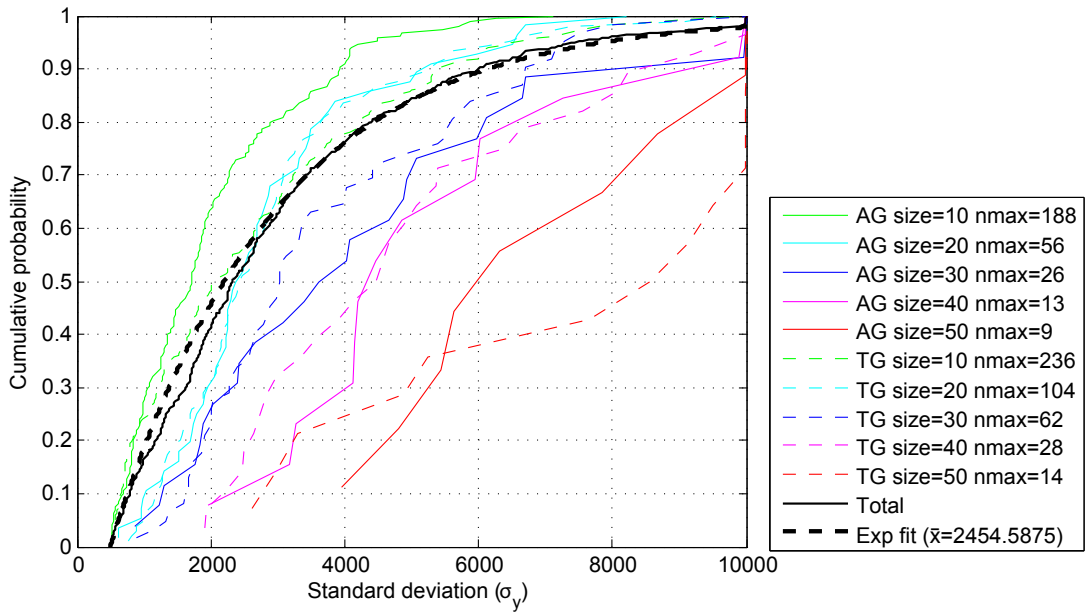


Figure 9.21: Cumulative distributions of the standard deviation along the small axis (σ_y) in the optimisations. The combined distribution of all the Gaussian functions in all the optimisations is fitted with an exponential distribution.

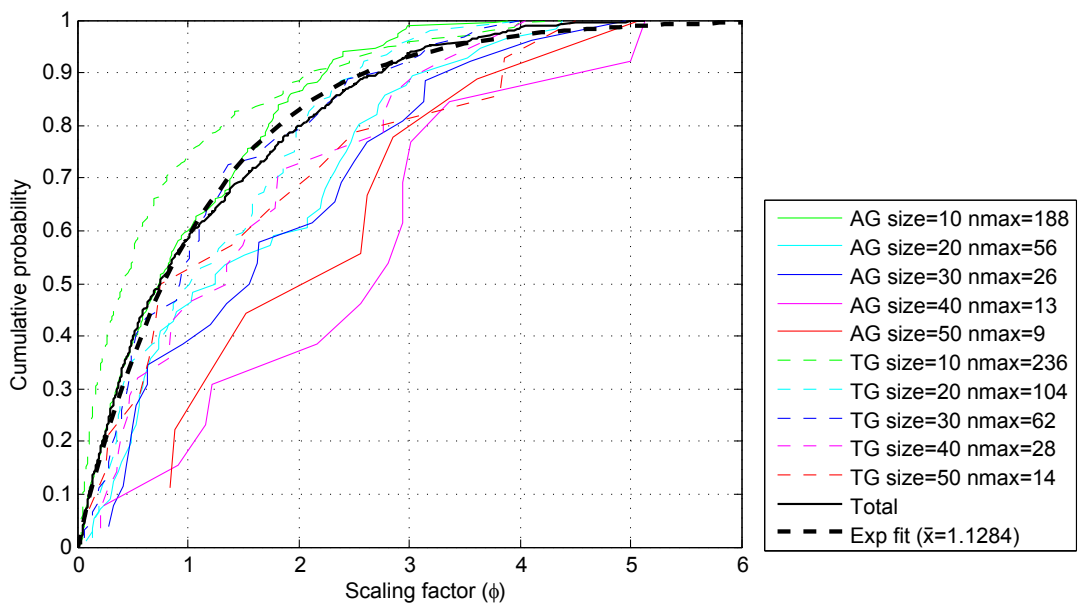


Figure 9.22: Cumulative distributions of the scaling factors of the Gaussian functions (ϕ) in the optimisations. The combined distribution of all the Gaussian functions in all the optimisations is fitted with a exponential distribution.

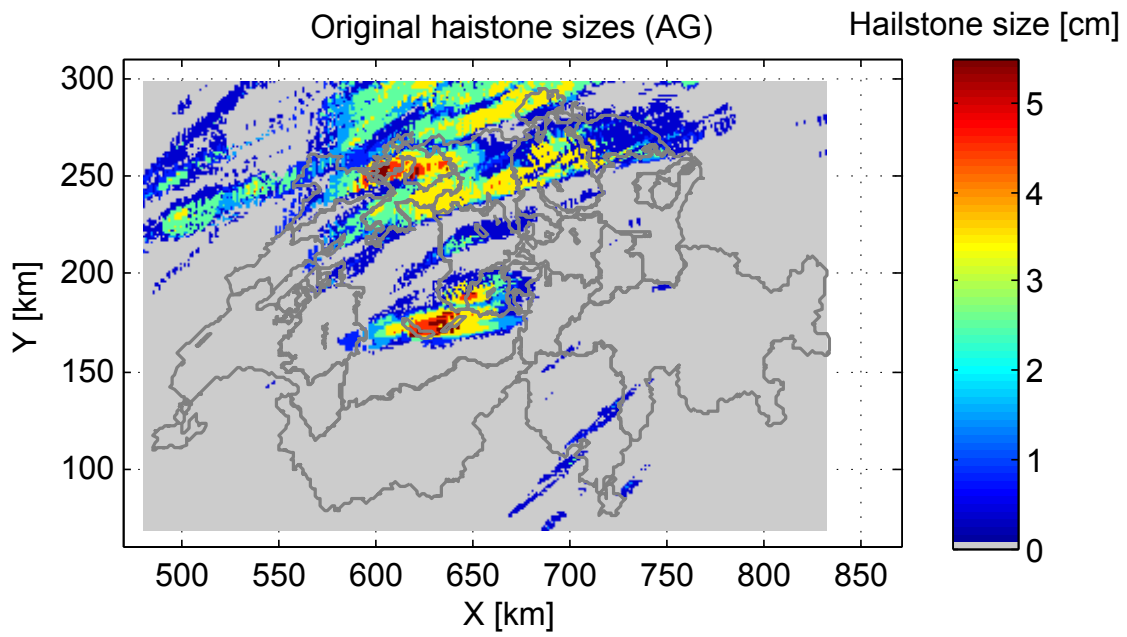


Figure 9.23: Maximum intensity reached during the 2011 event. The data are similar to Fig.9.2, but displayed with the same layout and scale as the optimisation results.

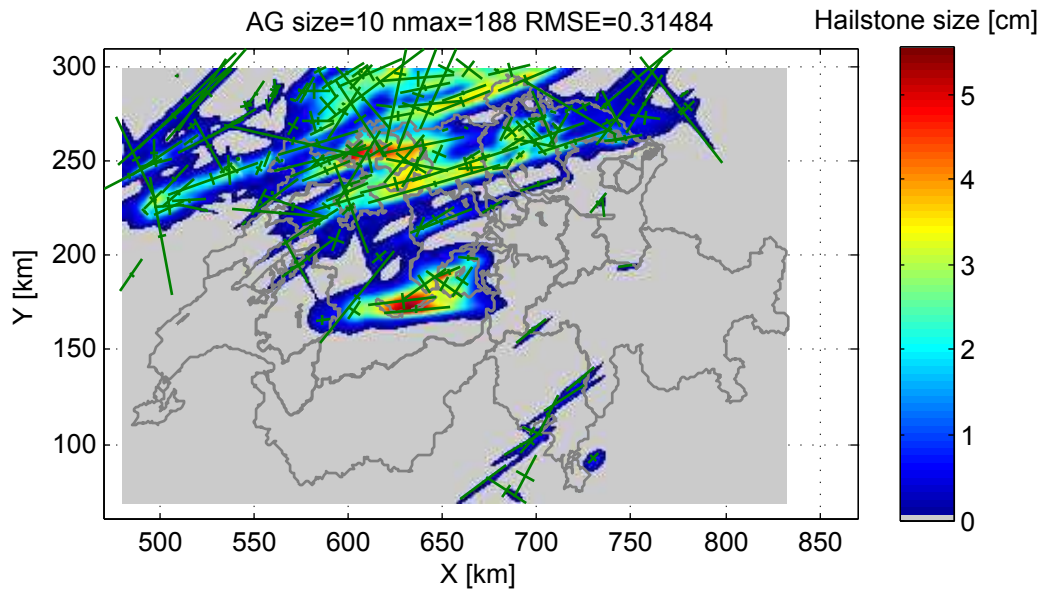


Figure 9.24: Result of the optimisation for the 2011 event using a smoothing window of 10 pixels

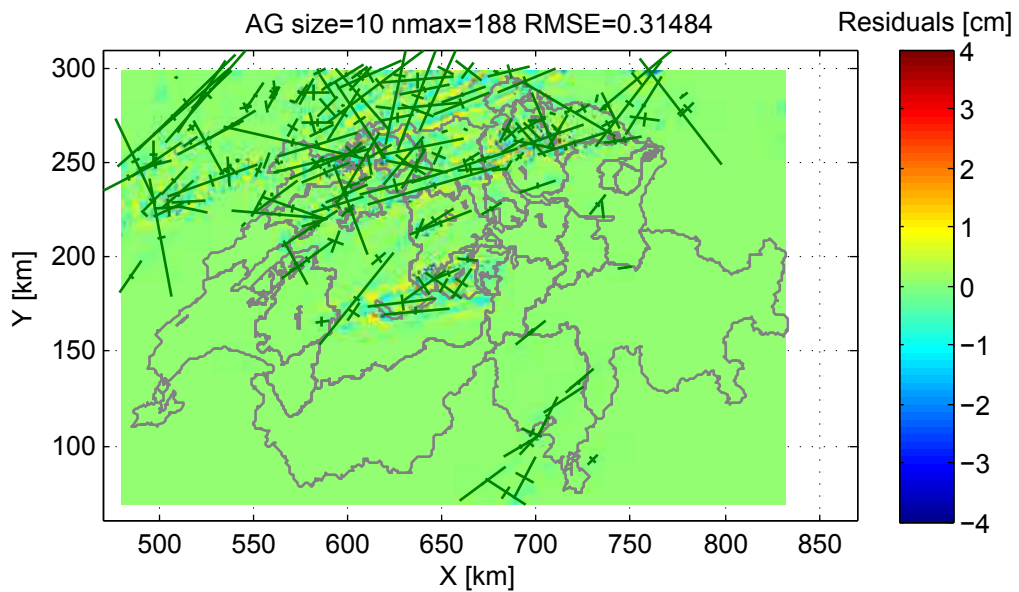


Figure 9.25: Residuals of the optimisation for the 2011 event using a smoothing window of 10 pixels

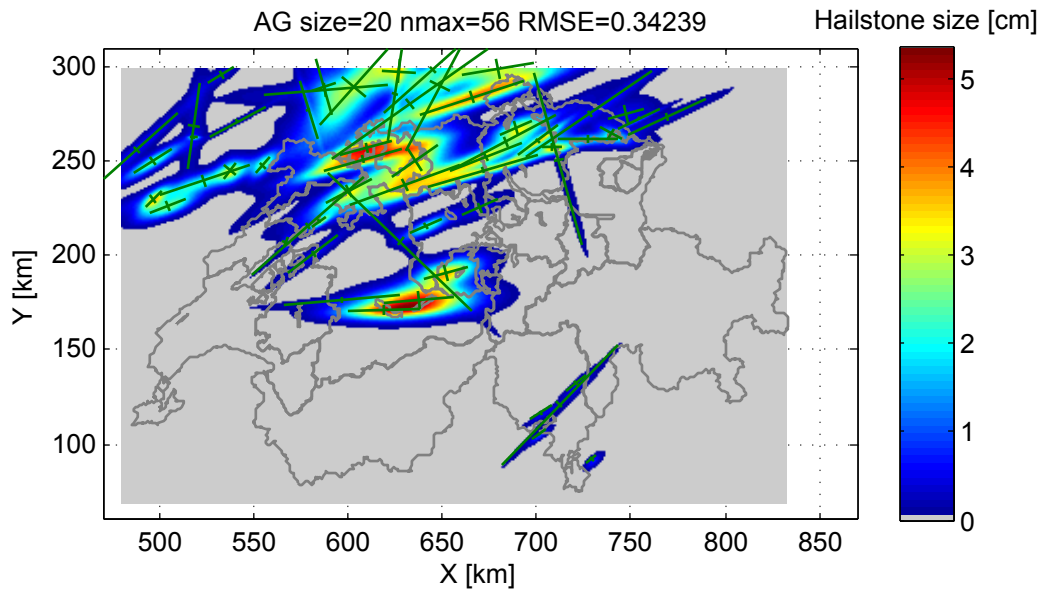


Figure 9.26: Result of the optimisation for the 2011 event using a smoothing window of 20 pixels

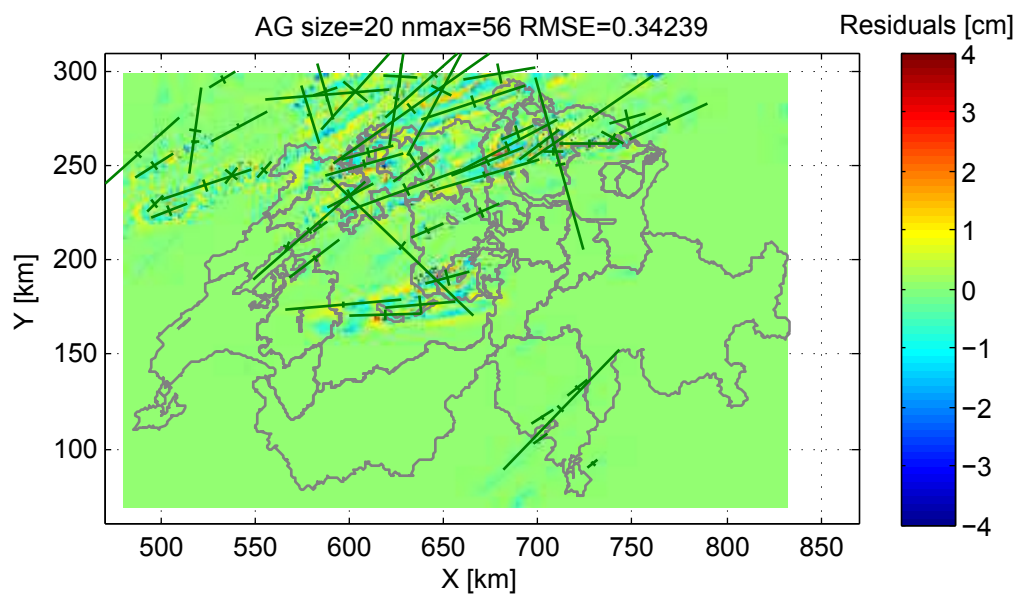


Figure 9.27: Residuals of the optimisation for the 2011 event using a smoothing window of 20 pixels

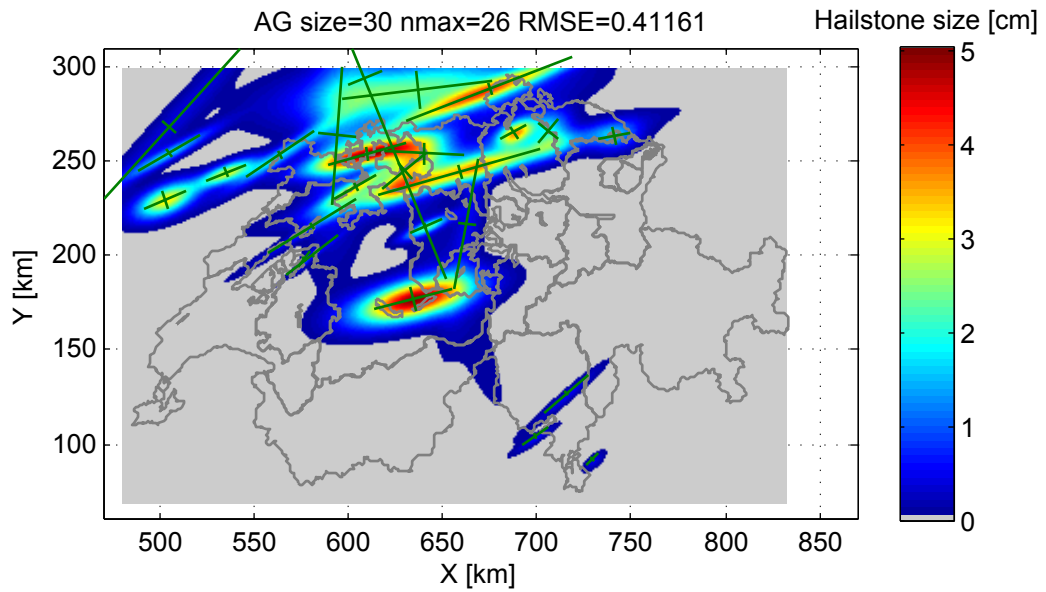


Figure 9.28: Result of the optimisation for the 2011 event using a smoothing window of 30 pixels

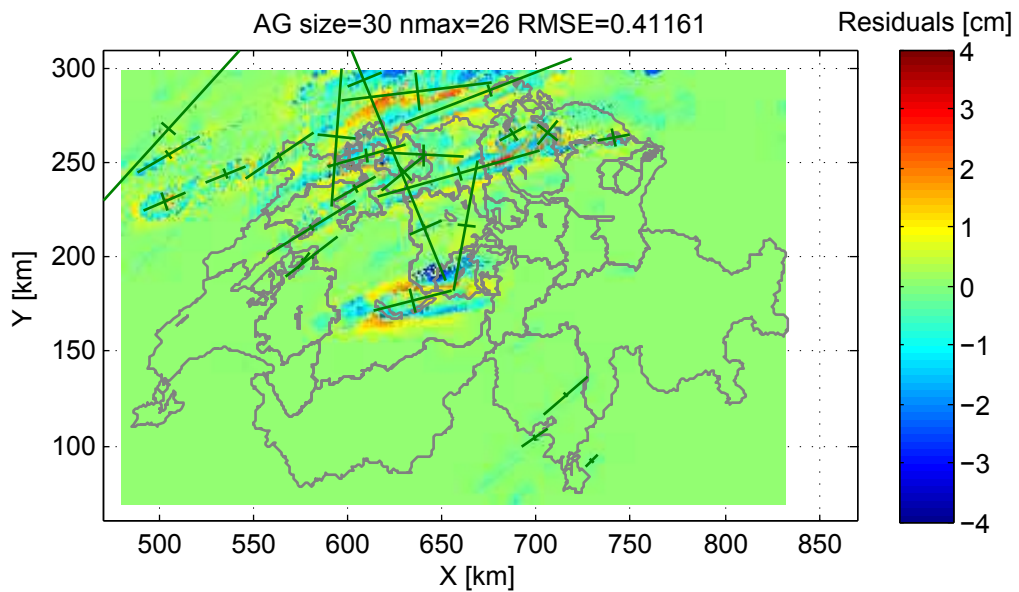


Figure 9.29: Residuals of the optimisation for the 2011 event using a smoothing window of 30 pixels

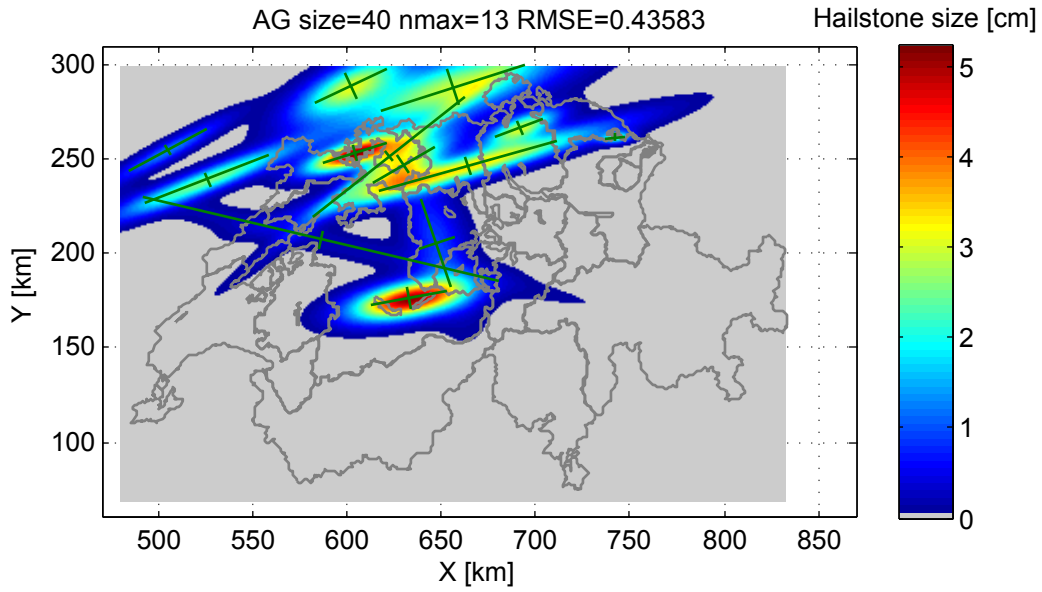


Figure 9.30: Result of the optimisation for the 2011 event using a smoothing window of 40 pixels

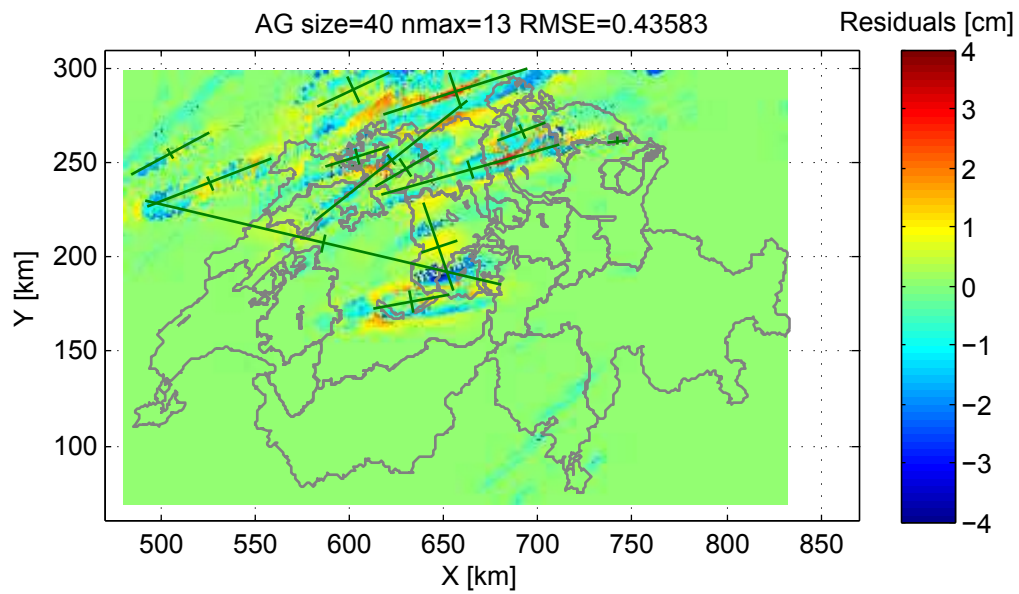


Figure 9.31: Residuals of the optimisation for the 2011 event using a smoothing window of 40 pixels

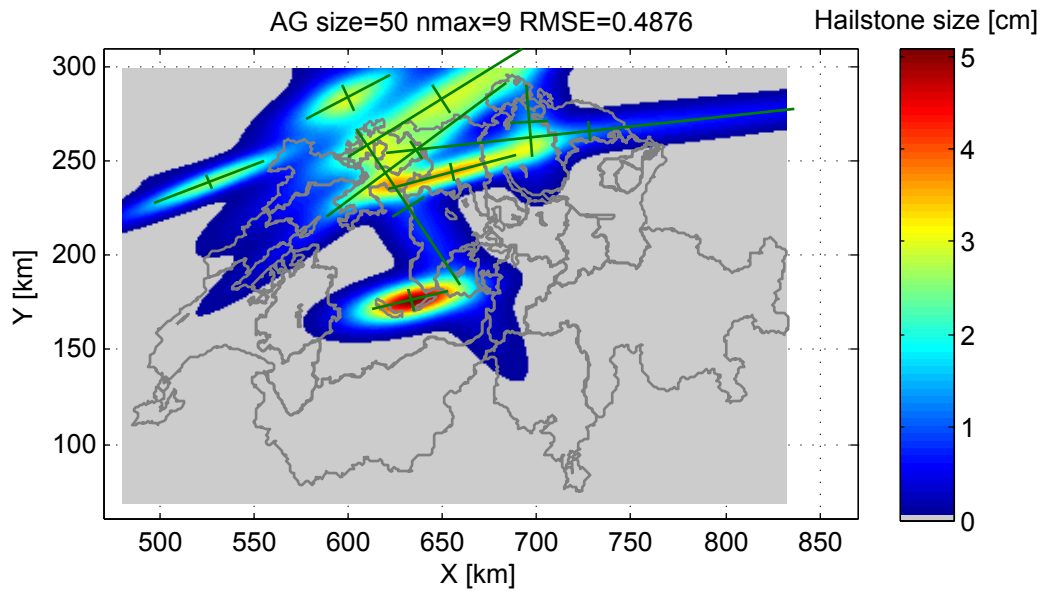


Figure 9.32: Result of the optimisation for the 2011 event using a smoothing window of 50 pixels

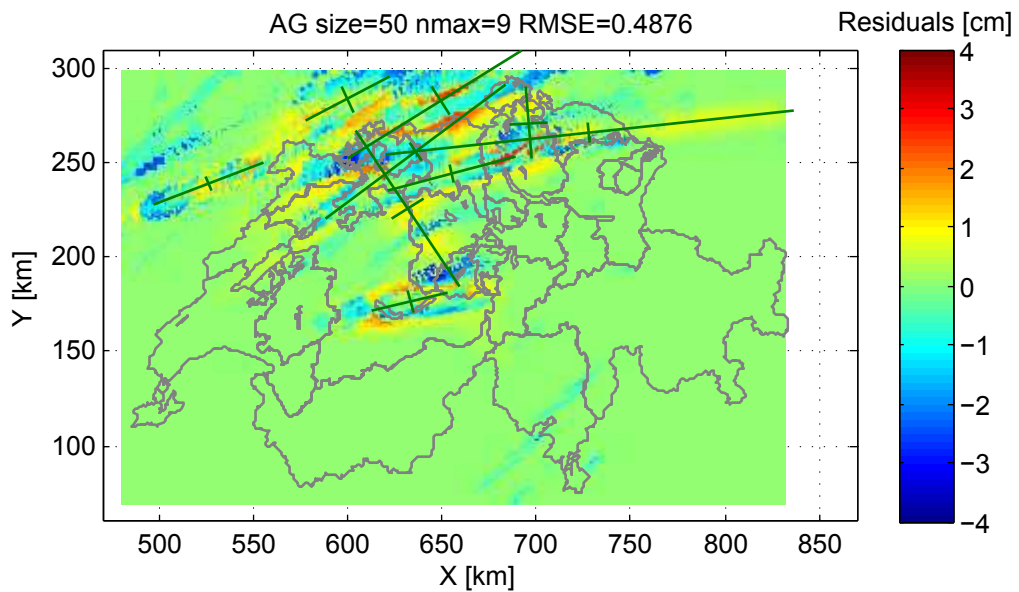


Figure 9.33: Residuals of the optimisation for the 2011 event using a smoothing window of 50 pixels

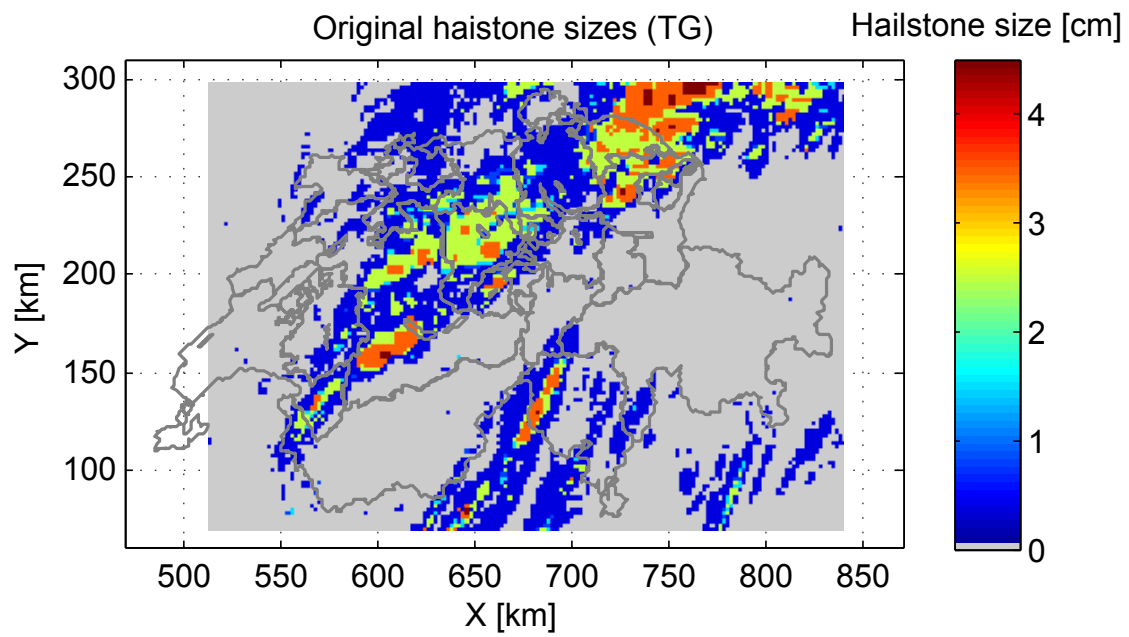


Figure 9.34: Maximum intensity reached during the 2009 event. The data are similar to Fig.9.1, but displayed with the same layout and scale as the optimisation results.

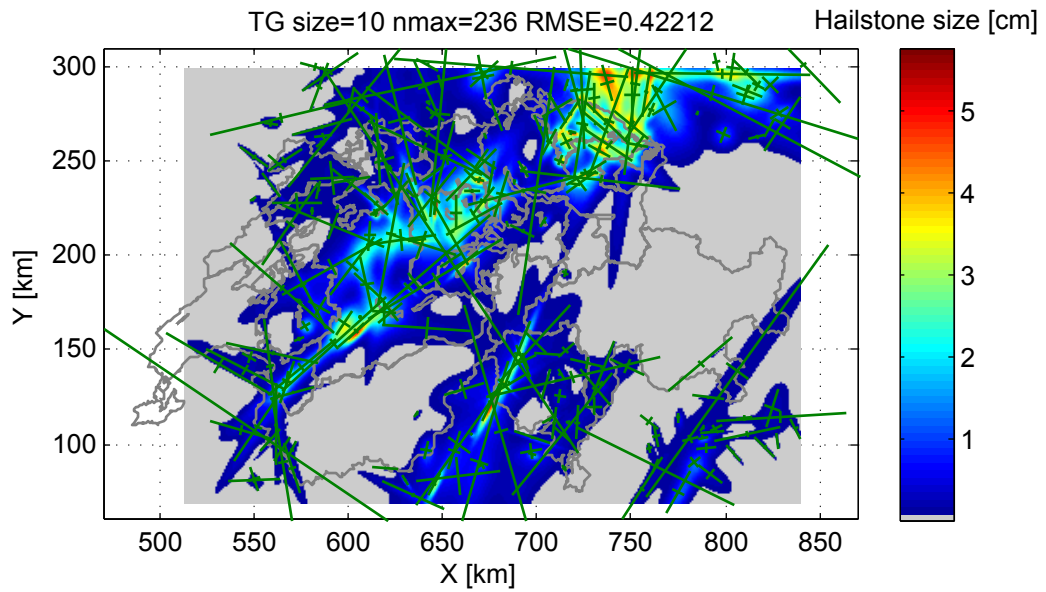


Figure 9.35: Result of the optimisation for the 2009 event using a smoothing window of 10 pixels

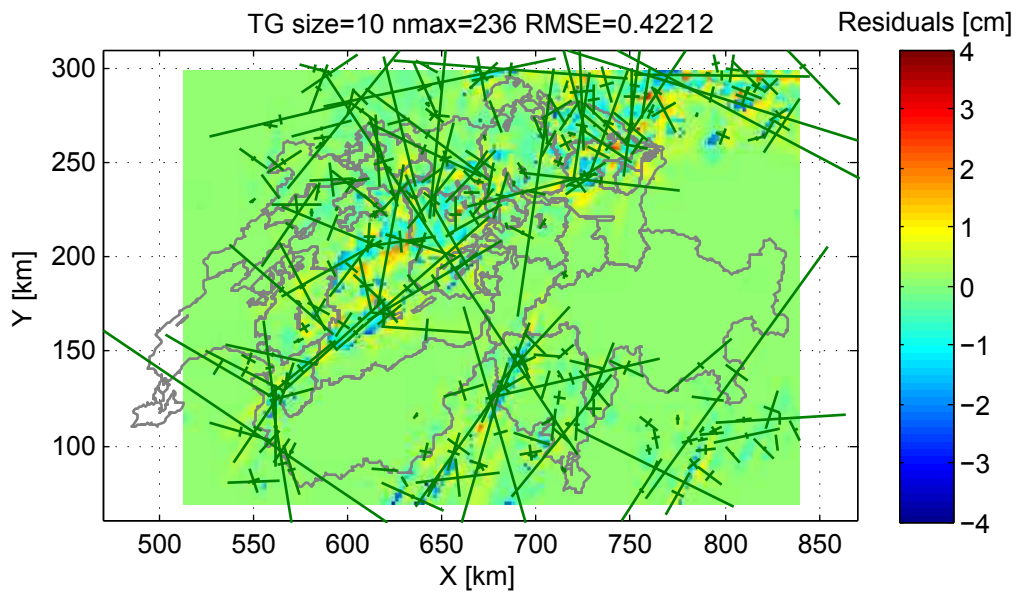


Figure 9.36: Residuals of the optimisation for the 2009 event using a smoothing window of 10 pixels

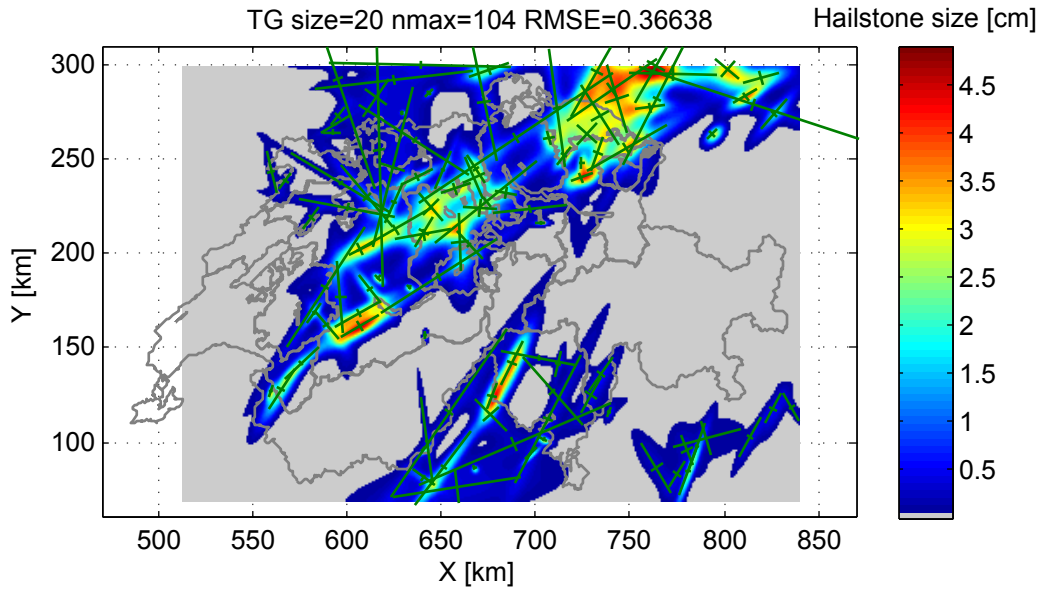


Figure 9.37: Result of the optimisation for the 2009 event using a smoothing window of 20 pixels

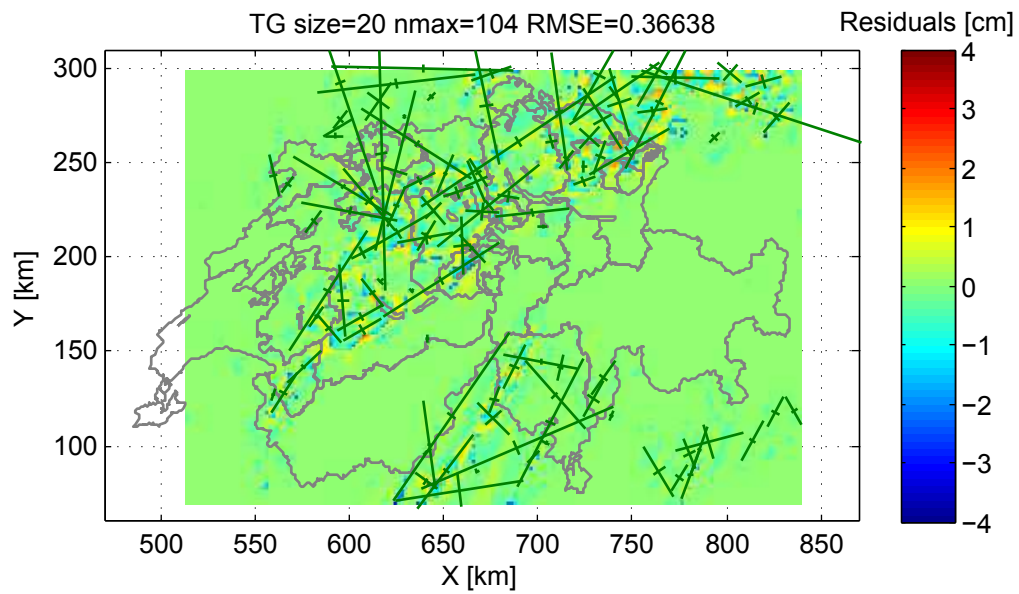


Figure 9.38: Residuals of the optimisation for the 2009 event using a smoothing window of 20 pixels

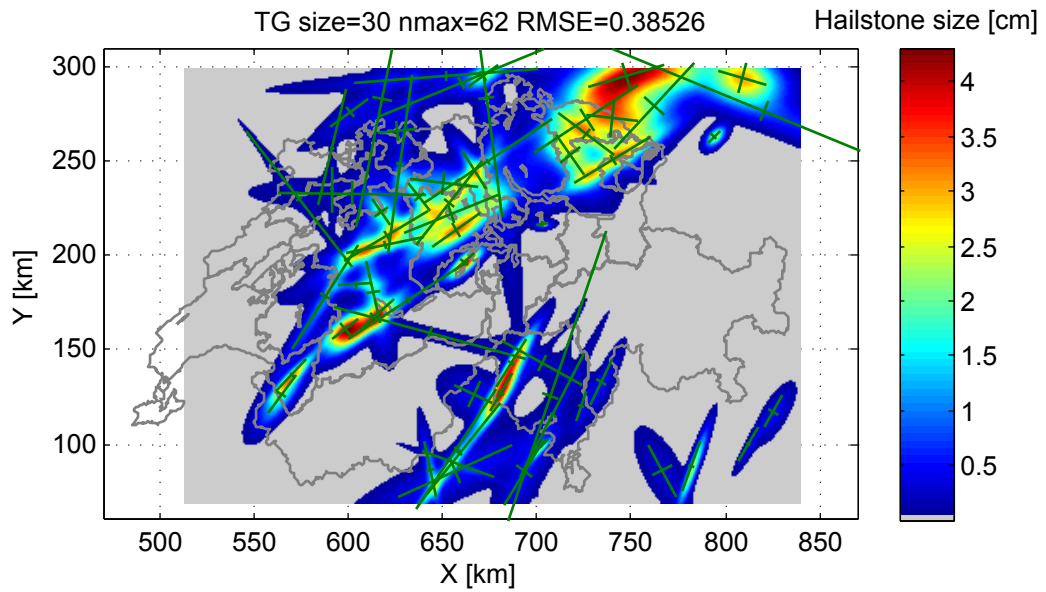


Figure 9.39: Result of the optimisation for the 2009 event using a smoothing window of 30 pixels

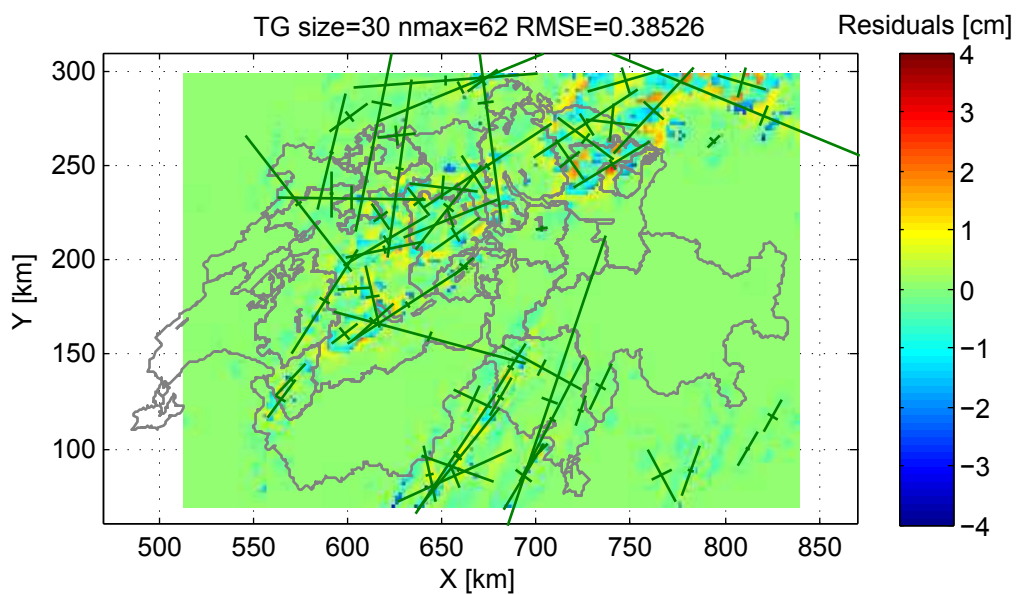


Figure 9.40: Residuals of the optimisation for the 2009 event using a smoothing window of 30 pixels

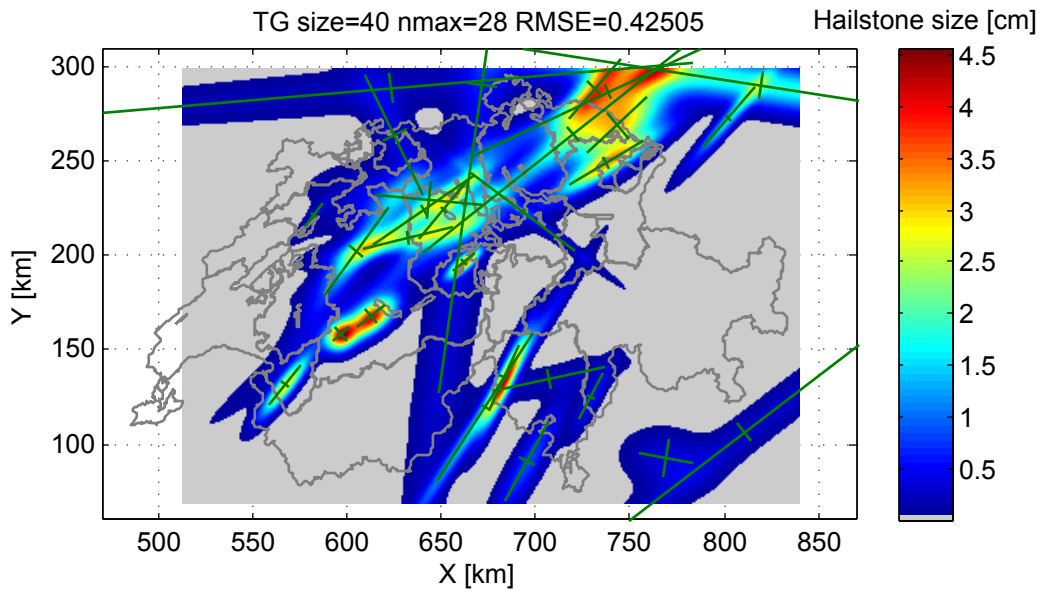


Figure 9.41: Result of the optimisation for the 2009 event using a smoothing window of 40 pixels

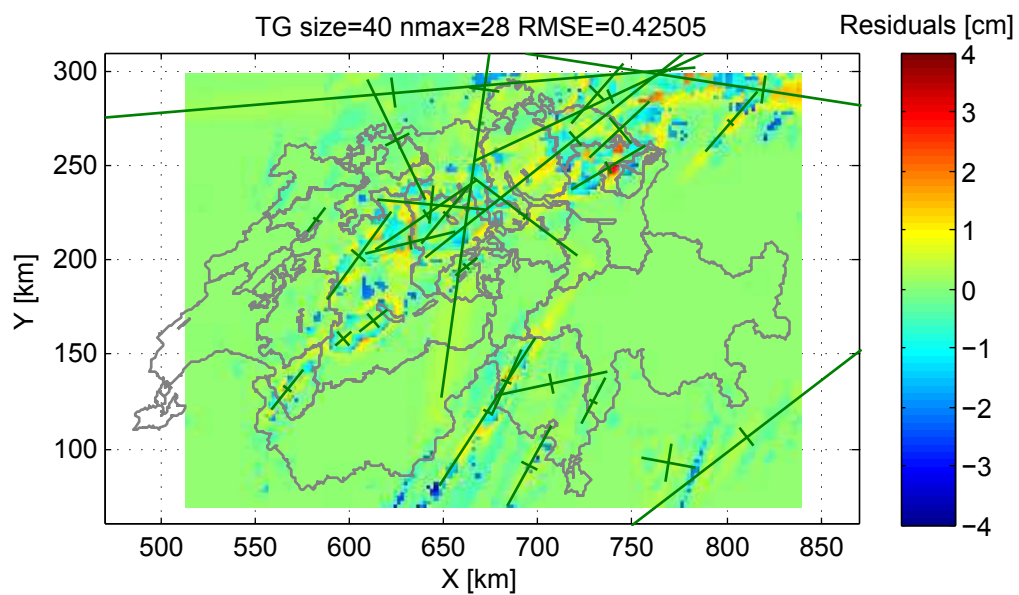


Figure 9.42: Residuals of the optimisation for the 2009 event using a smoothing window of 40 pixels

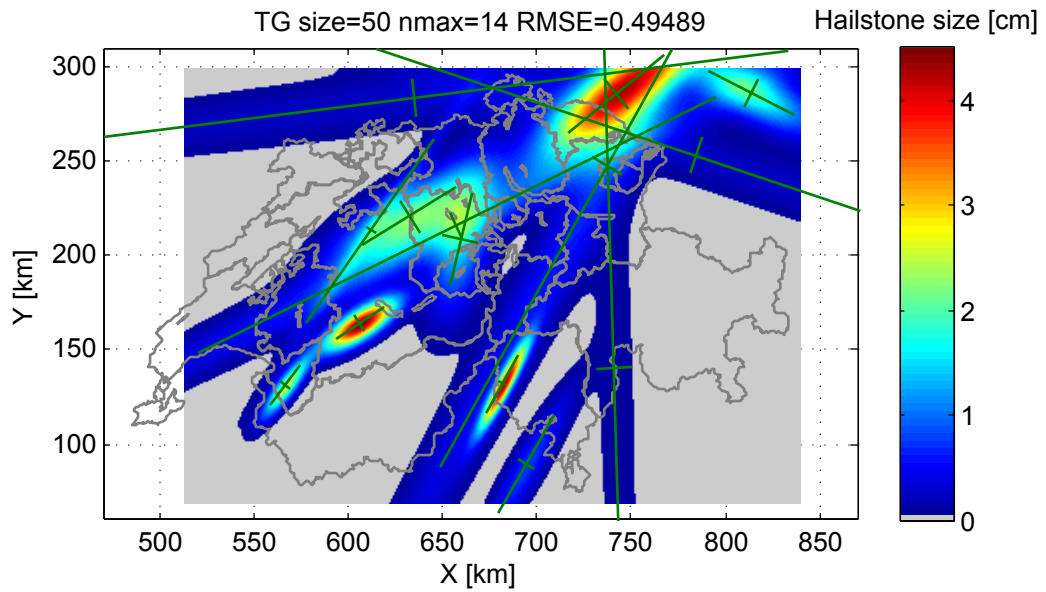


Figure 9.43: Result of the optimisation for the 2009 event using a smoothing window of 50 pixels

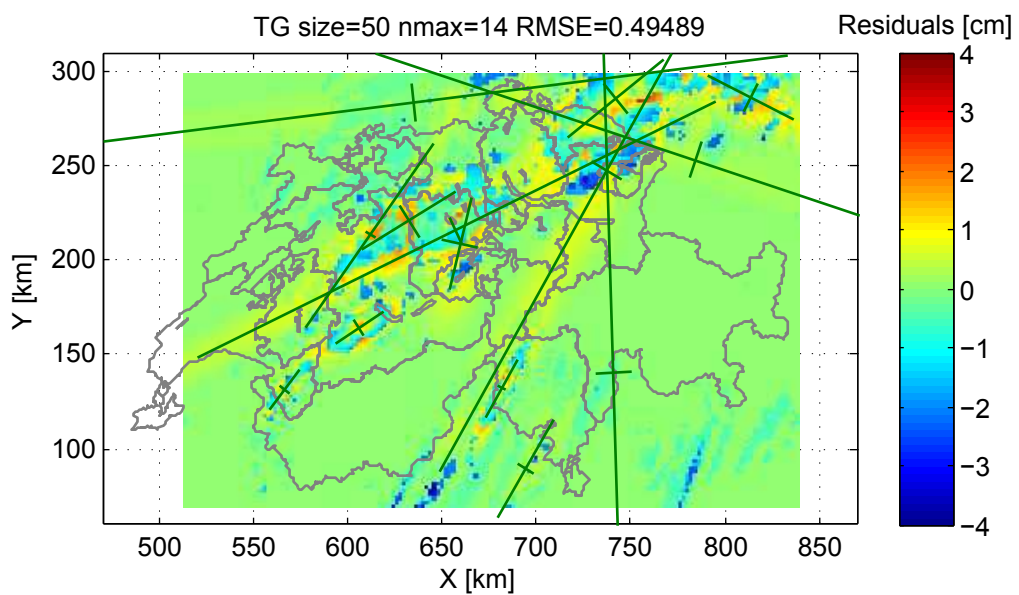


Figure 9.44: Residuals of the optimisation for the 2009 event using a smoothing window of 50 pixels

New events modelling

New events are created according to the parameters in Tables 9.6 and 9.7. A total of 500'000 events have been created and necessitated around 1'000 processor hours.

The parameters have been partially adapted from the results of the *Model calibration*, and most of them come from previous analyses and have slightly changed in the final results. However, due to the long computation time, the modelling of new events has not been completely adapted yet. For instance, the bounds used for μ are 1.2533 and 80 % of this value, whereas a value of 1.1284 is obtained in the new model calibration. The value of 1.2533 has previously been obtained from a similar analysis and the bounds of 80 % has been adjusted by trial and error so that the slope of the Marshall-palmer law adjusted on the results (Fig. 9.46 and 9.47) follows a slope similar as what is expected from the function adjusted on the hazard maps (Fig. 9.4b). The distribution used here assumes that events covering a larger surface have a larger probability of having large hailstones. This trick might however be solved by the μ value obtained in the new model calibration, since it is roughly in the middle of the bounds used here.

Table 9.6: General parameters of the event (ellipse). For random uniform sampling, the parameters correspond to the upper and lower bounds, for normal uniform sampling, the parameters correspond to the mean and the standard deviation, whereas for the uniform sampling, the parameters correspond to the quantile and to the lower and upper bounds. Thus, to define μ , the surface of the ellipse is used, and its corresponding quantile in the distribution of event's size is used to sample the uniform distribution between the given bounds.

Param	Distribution
Great axis length [km]	$L = \text{rand_uniform}(1, 100)$
Eccentricity [-]	$K = \text{rand_uniform}(2, 10)$
Angle [deg]	$A = \text{rand_normal}(45, 20)$
Size distribution	$\mu = \text{uniform}(M, 0.8 \times 1.2533, 1.2533)$

The length-width ratio is lower here than in most of the analyses (Fig. 9.20). This is because large ratios produce very big and elongated Gaussian functions that are more susceptible to be added to each other and to produce uncontrollable results. The same bounds should however be tested on the calibration since they might affect the other parameters. With the same goal of limiting the extent of the Gaussian functions, the standard deviation σ_y is bounded to 1000 m. When it comes to the distribution used, in this case as well the value of 3025 used in the

Table 9.7: Gaussian function parameters. The name of the distribution used for the sampling and their parameters is indicated.

Param	Distribution
Position	according to the probability raster
Max. height	$\phi = \text{rand_exponential}(\mu)$
Eccentricity	$\kappa = \text{rand_uniform}(1, 3)$
Standard deviation in y	$\sigma_y = \min(500 + \text{rand_exponential}(3025), 1000)$
Direction of the great axis	$\theta = \text{rand_normal}(A, 10)$

exponential distribution comes from previous results and is higher to the one presented in Fig. 9.21.

The mean $n0$ parameter obtained in the simulations is 4.10×10^{-3} . Therefore, to transform the number of simulations reaching or overpassing a threshold in annual frequencies, the values are multiplied by:

$$\frac{\frac{\text{expected } n0}{\text{modelled } n0}}{\text{number of simulations}} = \frac{4.49}{\frac{4.10 \times 10^{-3}}{500000}} = 2.19 \times 10^{-3} \quad (9.8)$$

Where 4.49 is the expected $n0$ value for Aargau (Fig. 9.4b). Figure 9.48 shows the variation in percent between the simulated values and the expected ones for the entire Swiss territory. If the value is logically correct for Aargau, it is also correct for the South-Eastern Switzerland (Tessin). On the other hand, it is especially wrong for the eastern Switzerland (GR on Fig. 9.4) and for the borders of zones PW-AW and VS.

The mean lambda parameter obtained through the simulations is 1.51 for the canton of Aargau, when a value of 1.52 is expected. The agreement of this parameter with the expected values is generally good, except again for zone GR. From these two maps, it is possible to see that the model is not able to reproduce the function of zone GR, which has a slope quite different from the other regions (Fig. 9.4b).

When it comes to the losses, the mean risk obtained through the simulations is 17.1 million CHF/year, which is low compared to the results of the mean risk analysis (Fig. 9.17), since it corresponds roughly to the quantile 30 %. Furthermore, since the λ parameter adjusted on the simulation results is slightly higher than the one used to calculate the mean annual risk, we would rather expect a higher risk with this model.

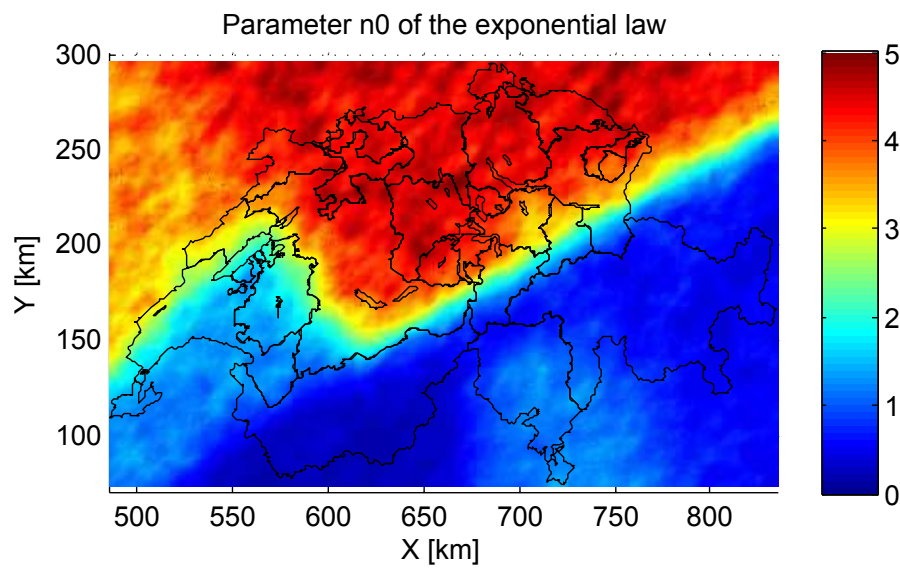


Figure 9.45: Parameter n_0 of the adjusted Marshall-Palmer law fitted on the results and scaled so that the mean for the rectangle containing all the buildings is 4.49. This figure is to be compared with the expected n_0 for each area of Switzerland (Fig. 9.4)

Finally, the frequency at which a given amount of losses is expected to be reached is given in Fig. 9.50. According to this set of simulations, the 2011 event has a return period of 45.7 years for the Aargau insurance company in terms of losses.

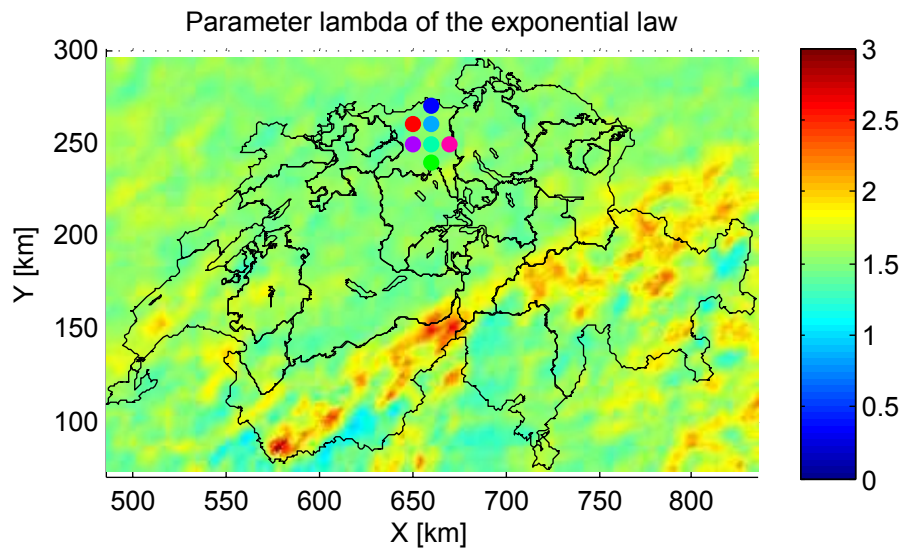


Figure 9.46: Parameter λ of the adjusted Marshall-Palmer law fitted on the results. The modelled frequency-size relation for the color points is given in Fig. 9.47

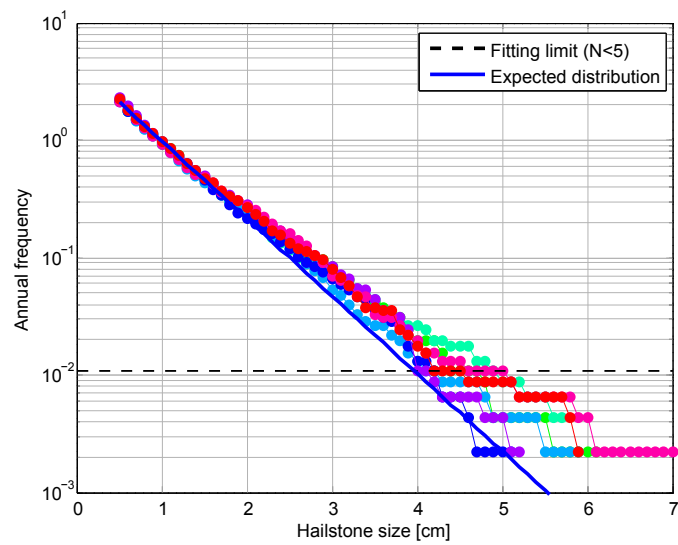


Figure 9.47: Modelled frequency-size relation for different points in the Canton of Aargau (see Fig. 9.46). The expected distribution is retrieved from the hazard maps (Fig. 9.4b).

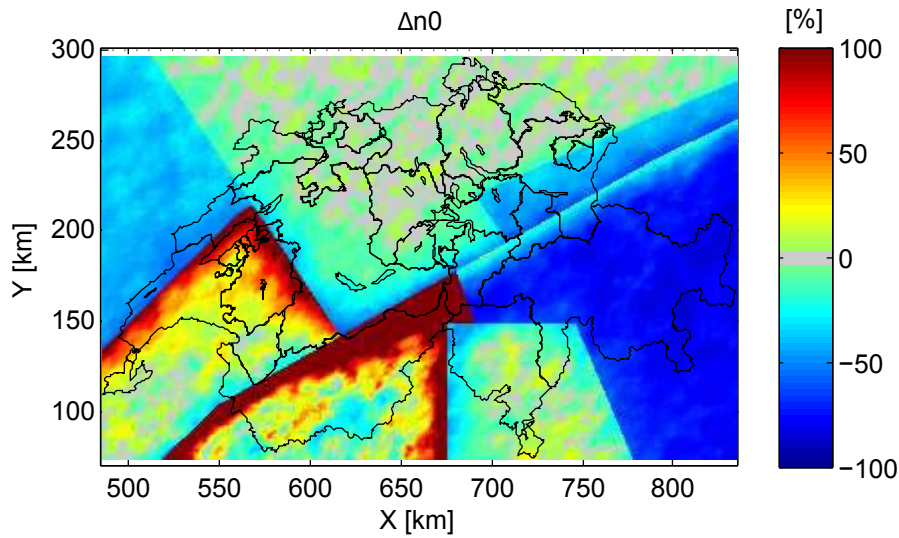


Figure 9.48: Difference in percentage between the simulated value and the expected value of the parameter n_0 of the size–frequency law. A value above 0 means that the parameter is higher in the simulations than its expected value. The scale has been bounded to 100 % on both side in order to better see the values on the Aargau region, where the variations are relatively small

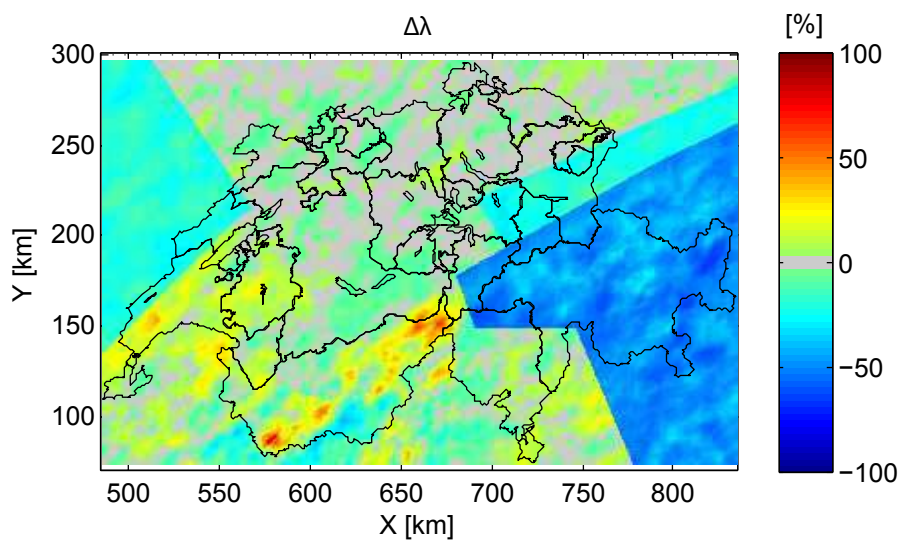


Figure 9.49: Difference in percentage between the simulated value and the expected value of the parameter λ of the size–frequency law. A value above 0 means that the parameter is higher in the simulations than its expected value. The scale has been bounded to 100 % on both side in order to better see the values on the Aargau region, where the variations are relatively small

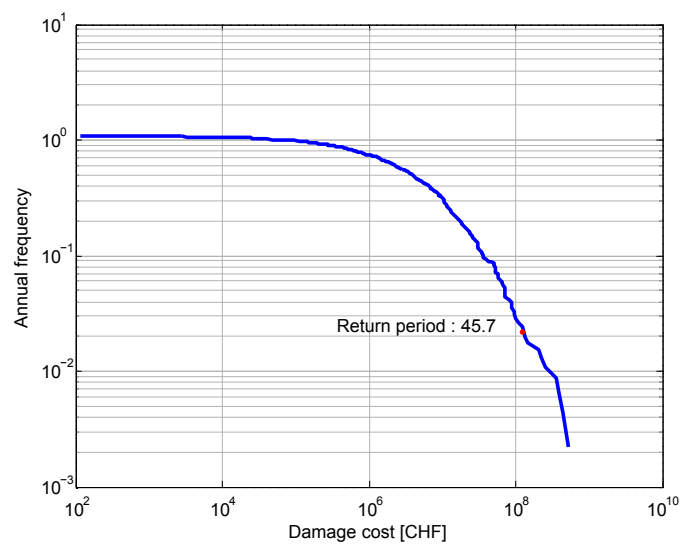


Figure 9.50: Annual frequency of events with a given damage cost. According to this model, the 2011 event corresponds, for the Aargau building insurance, to a return period of 45.7 years in terms of cost.

9.5 Discussion

The loss model retrieved from the different events shows that there is a large part of variability and that the available data do not allow the creation of a very precise model. Several reasons can be raised to explain this:

- The maximum hailstone size might not be a good proxy for the losses and might be replaced for example by the total kinetic energy (as in [Hohl et al., 2002a,a](#)). This would however make the analysis more complicated since there is no intensity map based on this parameter that is easy to obtain.
- The radar might be not precise enough or even wrong in some areas. This is supported for example by the difference in terms of losses between the cantons of Aargau and Zurich, although the radar intensity map is comparable for both cantons. This is also supported by the low coefficient of correlation of the modelled proportion of damaged buildings with the observed ones at the municipality level (ZH, AG, TG and LU in [Table 9.2](#)).
- The building portfolio might be too much different between one canton and another. This would also explain especially the higher loss per building in Aargau as compared to the other cantons.
- There might be some important difference in the event itself, for example when it comes to the wind intensity or the time of the day. Indeed, an event occurring at night might damage more blinders than one occurring during the day. However, this effect should be limited since most of the analysis is done on one event.

Although it is difficult to confirm or infirm these hypotheses, it is still manifest that there is a link between the radar intensity and the losses. Furthermore, the losses where the radar indicates an hailstone size below 2 cm are quite limited, which is in agreement with [Imhof and Choffet \(2012\)](#). Therefore, we can consider that the model has a predictive capability, although the variability is quite large, in order to be in accordance with the different cantons. The loss model somehow includes thus the uncertainty of the actual hailstone size with regard to the one indicated by the radar.

When it comes to the mean risk, the median value obtained for the 19 cantons with public building insurance is large compared to the statistics. Indeed, a value of 86 million CHF/year is expected, whereas the mean modelled value is 363 million CHF/year. However, due to the large variability of the loss model, the expected value is not exceeded in 12 % of the models. The reasons for a risk higher than expected from the statistics can be of two natures. The first

hypothesis is that the model is not accurate, whereas the second hypothesis is that the statistics of the past events does not reflect the current risk. To support this second hypothesis, Imhof (2011) reveals that the hail damage has increased both in terms of proportion of damaged buildings and in monetary losses. This could result from change in the hazard, or, more probably, from changes in the construction materials. However, the model is probably still affected by some limitations:

- The hazard maps might be too pessimistic. Indeed, they are based on radar data, which, as suggested by the difficulties encountered when building the loss model, seems to be affected by false positive.
- The loss model might not reflect all the parameters controlling the reality. As suggested above, this model has indeed a limited predictive ability due to its large variability. This could indicate that the parameters α and β of the gamma distribution should tend towards the lowest values rather than the upper ones.

Finally, the event modelling still contains a lot of uncertainty on many parameters, but allows obtaining a first estimation of the return period at which a given amount of losses is to be expected. Thus, the 2011 event can be estimated as having a return period of around 50 years, which seems to make sense. The modelling approach is however very sensitive to the parameters and the good agreement of the modelled slope of the frequency–size relation (λ) with the expected one resulted of a lot of trial and error. In addition, the model is based on only two intensity maps, that both concerns relatively important events. Therefore, the characteristics that can be retrieved from these two maps are quite limited. This study would greatly benefit from more intensity maps of diverse events.

9.6 Conclusions

Although the models developed in this chapter are still affected by large uncertainties, different lessons can be learnt from them. First, the loss model offers the possibility of estimating rapidly after an event the damage extent. Although the model will give a large range of possible values, first reports from the ground can help to know in which part of the range the actual damage will be. They also give an indication on the reliability of the hail intensity maps when it comes to the losses estimation. In addition, the analysis shows that the losses per damaged buildings in the 2011 event in Aargau tends to be higher than for other regions, which could result from a different type of buildings. In addition, further information on the buildings could easily be included in the model, for example regarding their age or their function.

When it comes to the risk, the model gives an idea of the risk to expect, although the results are quite uncertain. If the loss model is modified, the mean risk estimation could also help

in testing the effect of different measure that the insurance companies could take, especially regarding the building materials.

Finally, when it comes to the event modelling, much improvement can be made. However, such a model is useful to test different actions that the insurance companies could take and offers more details than the mean risk estimation.

General conclusions

Chapter 10

Concluding remarks

10.1 Discussion and synthesis

10.1.1 Local risk analyses

Chapter 2 compares Structure-from-Motion photogrammetry with LiDAR, in order to estimate the potential of this first method for hazard analysis. The main advantages are that this method is low cost and that a camera can easily be carried by a drone, thus offering the possibility to acquire data in inaccessible or hidden area. The main drawbacks are the registration issues and the poor performance in vegetated areas.

For risk analysis analyses at local scale, the tool Valdorisk is discussed first (Chapt. 3). It is based on EconoMe (Bründl et al., 2009) and offers the advantage of being easy to use and allows for fast estimations of risk, but it is also suited for an in-depth analysis. It aims at performing a risk analysis at local scale, for a relatively small group of objects. It is suited for multi-hazard risk assessment, but not for multi-risk assessment (according to the terminology of Garcia-Aristizabal et al., 2015), since the interactions of the hazards are not considered.

Then, the question of the impact of a landslide on a moving vehicle is discussed. When it comes to risk analysis in Switzerland, the method that was used up to EconoMe 2.0 and that is still used for cars in EconoMe 3.0 neglects the dimension of the vehicle. Thus, for rockfalls on trains, the impact probability used to calculate the risk only depends on the size of the block. On the other hand, many articles dealing with rockfalls neglects the dimension of the block and take only the one of the vehicle into account. Chapter 4 proposes a simple solution that accounts for the dimensions of the landslide and for the dimension of the moving vehicle. Another method, that is more complex since it considers the impact on the front of the vehicle as well, is discussed.

Chapter 5 discusses the problem of summing the risk of 3 scenarios by showing how a

supposedly conservative approaches actually underestimates the risk. It proposes two solutions that allow being as close as possible to the expected risk curve using no additional input. The simplest of the two approaches is also included in Valdorisk. The same chapter proposes an approach that allows including the uncertainties in the risk analysis by using triangular distribution functions with a limited number of user-defined parameters. This approach is not included in Valdorisk yet, but also aims as being as simple as possible to use.

To conclude this part, which is mostly devoted to cost-benefit analyses at local scale, Chapt. 6 discusses the matter of communicating the risk when protection measures have been built. It shows through the example of La Faute-sur-Mer that building behind protection measures is not always safe and that the authorities and the population should be aware that the hazard is reduced, and that this reduction is only guaranteed as long as the protection measure is efficient. Indeed, the protection measures have a limited life time in most cases. The proposed method consists in overlaying the hazard level without protection measures with symbols of the protection measure. These symbols take the colour of the new hazard level.

This part covers the whole span of local-scale risk analysis, and takes the point of view of public authorities, who have the need to protect both the society and its individuals. For this purpose, risk analysis helps in allocating the financial resources where protection measures are most effective. In this process, consistent local risk analyses have to be made to insure an homogeneity among all the territory, which can be reached using a standardised risk calculator such as EconoMe or Valdorisk (Chapt. 3). However, this part highlights that the simplifications that are made need to be re-evaluated when the method is applied for a slightly different purpose (Chap. 4 and 5). Also, since these analyses suffer from high uncertainties, a simple method for uncertainty analysis is proposed (Chapt. 5) and would allow for more representative results. Finally, once measures are taken, a good risk management procedure should permit to identify the protected area in order to avoid increasing the risk again by building new assets (Chapt. 6).

10.1.2 Regional risk analyses

For regional risk analyses, several models have been presented. In Chapt. 7, the developed model presents an estimation of the costs and the number of affected buildings to expect for a building insurance company. The analysis is based on data collected from a private civil engineering company and from the municipalities that are the most affected. The risk analysis is based on scarce data, and the results are given in the form of exceedance probability curves, which give an idea for the insurance company of how the losses should vary over the year. The different curves present different hypotheses and give a measure of the sensitivity of the analysis to some of the least known parameters. Since this first analysis, hazard map have been made and a comparison

of the hazard levels with the indicative hazard level is done for each building. This gives the insurance an overview of the risk for their portfolio.

Chapter 8 presents a risk model for shallow landslides based on a rainfall-induced large landslide event. It discusses the relation of precipitation amounts with the landsliding probability and the probability for a landslide to impact a building. Then, using these probabilities and the rainfall event used for the calibration, it is possible to analyse the potential consequences of the rainfall event. From this analysis, it is possible to see that the landslides are positively correlated with the building density. As a result, we suspect that the landslides are partly human induced (see also [Jaboyedoff et al., 2016](#)).

When it comes to hail risk (Chapt. 9), the amount and quality of available data permits to establish a vulnerability model, using the maximum hailstone size derived from meteorological radar data as a proxy. This model needs however to include a lot of variability since it can be seen that the link between the hail intensity assessed with meteorological data and the vulnerability is fuzzy. This model can still be used to obtain a first idea of the losses directly after an event, using a radar-based intensity map and the location of the buildings. The vulnerability model is then used together with hazard maps to establish the mean annual risk. The obtained results are above the expected values, but it might be related to an augmentation of the risk due to changes in the construction materials. However, an event-based approach is preferable for an insurance company since it also helps to plan for the compensation and for the extra workload related to a large event. A first attempt of such a model is presented in this document and uses Gaussian functions to reproduce the variability in hailstone sizes inside an event.

These three chapters present different approaches of risk analysis at regional scale. The differences between the methods used in these chapters are mainly driven by the available data, which are and will always be incomplete since many parameters can have an influence on the risk, and can't be assessed at a regional scale. As a consequence, the approach of stochastic risk modelling has been chosen for these studies since it is relatively versatile and permits to include additional data when they become available. In the context of building insurance, stochastic risk modelling permits to predict future losses (for example in Chapt. 7) and to test mitigation strategies, for example requiring a minimum hail resistance for the building materials (see Appendix E). In addition, stochastic risk modelling permits to test our understanding of the factors controlling the risk. This is well illustrated by Chapt. 8 since a relatively simple risk modelling indicates that the human influence on landslides should be investigated further to improve the model. Stochastic risk modelling permits in addition to test the sensitivity to each of the factors. This is for example done in Chapt. 7 and shows that the correction factor which accounts for the incomplete dataset even in the best case is an important parameters that would need to be better constrained to improve the reliability of the analysis.

This part also uses non traditional approaches to assess the degree of loss of the buildings. In in Chapt. 7 and 8, the degree of loss is not a function of the intensity, but is a statistical distribution that does not depend on any parameter. The hazard intensity is thus implicitly included in this statistical distribution, since if the intensities are generally low, the statistical distribution will tend to give low degrees of loss. On the other hand, in Chapt. 9, the model is more complex and is composed of two parts, to better differentiate the buildings that are not damaged from the buildings that are damaged. This approach is not standard, but a similar one has for example been applied for earthquakes (Pei and van de Lindt, 2009). This highlights that other approach than the vulnerability curves traditionally used for landslides might be more suitable for stochastic risk models, especially when the number of affected buildings needs to be known.

When it comes to the hazard, one could argue that the models used are too basic, when more sophisticated models have been described in the literature (especially for Chapt. 7 and 8). This is only partly true, since many models described in the literature are susceptibility models and do not give a real frequency, neither do they give a relative frequency. Therefore, although these susceptibility models give precious information to identify the most affected area or to help in the land-use planning, the information they provide can't be directly transferred into a risk model. Therefore, the models proposed here permit to deal with the lack of spatial frequency assessment.

10.2 Research perspectives

At local scale, many limitations have been observed in the risk analysis. Of particular importance is the coherence of the methodology used and its clarity, in order to be sure that the operator is using it properly. The tool presented in Chapt. 3 tries to be as open and clear as possible, offering targeted explanations when needed. Subsequently to this work, this tool has now been adapted with a cartographic interface based on Aye et al. (2016), which offers the user a better visual check of the results. Further developments have to be made in order to obtain a simple yet correct approach that would adapt to every particular situation. Furthermore, cost-benefit analyses are limited by the need of having an estimation of the price and effect of the planned measure and it is therefore not trivial to use this approach on a more regional scale, for example in order to establish priorities in the protection works. Therefore, standard values could help identifying the sites where the benefit-cost ratio would be the more optimal.

At both local and regional scale, one of the main problems in risk analysis is the vulnerability. Indeed, vulnerability is not a straightforward parameter since it can express the damage in different ways. In the present work (particularly in Chapt. 7 and 9), it is mostly reflecting the reparation cost and is therefore quite well constrained. In other research that are not taking the point of view of an insurance, the vulnerability is often expressed in terms damage class (e.g.

Jakob et al., 2012) and/or assessed visually based on the affected elements of the building (e.g. Gutiérrez and Cooper, 2002). The access to insurance data in Chapt. 9 shows the potential of using such data and the need to work with the company in order to improve the exploitability of the data (see Appendix E). This question is also discussed in Appendix B (Ciurean et al., 2017) or in Papathoma-Köhle et al. (2011). In Valdorisk (Chapt. 3), the vulnerabilities are taken from EconoMe, but it is also not clear how these vulnerabilities have been established. This is a problem when reusing the vulnerabilities since, as seen with the problem of the temporal spatial probability (Chapt. 4), the vulnerability needs to be adapted to the risk calculation. Indeed, for example, one could wonder if the vulnerability is the conditional probability for a train passenger to die if any part of the train is affected, if the wagon is affected or if the area where the passenger is located is affected. If this is not known when the risk analysis is performed, it will most probably give erroneous results. For this issue, a transparent catalogue of event with characterisation of the event properties and the consequences is required (e.g. Voumard et al., 2016).

When it comes to the hazard, as shown by the simple models presented in Part II, there is a need for further research on regional models that can be used for risk analysis. Indeed, as discussed above, the existing models (e.g., for shallow landslides, Pack et al., 1998) often lack a frequency or do not assess the frequency in a way that can directly be used in a risk analysis. Other models are focussed on the process itself and produce data that are not necessary for the risk model. Therefore, a right balance between a simple model such as the one used here for hail (Chapt. 9) and a model integrating all the knowledge on the process has to be found. When it comes to the model used in Chapt. 8, it should be tested with other events, and probably adapted to something closer to the rainfall thresholds that uses both duration and intensity (e.g. Crosta, 1998). Indeed, as is, it is difficult to adapt to other events, since these parameters, as well as the antecedent rainfall, are important. These curves do however not predict the probability of landslide.

10.3 Conclusion

Although the basic principles of risk analysis have been established for a long time, it is still not a straightforward process since many parameters influence the risk. This manuscript highlights that the procedure used to analyse the risk needs to be adjusted to each case and that one need to be careful with the assumptions made, especially when a model is transferred to another case study. In addition, the importance of accounting for the uncertainties is highlighted. This manuscript also shows the relevance of stochastic risk modelling at regional scale, which, in addition to providing an estimation of the risk, permits to test the sensitivity of the factors controlling the

risk, to better understand these parameters or to test mitigation strategies. It also permits to work with incomplete data, which are often the only available data, especially at regional scale.

Bibliography

- Abellán, A., Carrea, D., Guerin, A., Humair, F., Derron, M.-H., and Jaboyedoff, M.: Short course SC41: Use of 3D point clouds in Geosciences: Acquisition, Processing and Applications, in: European Geosciences Union General Assembly 2015, Vienna, Austria, 12–17 April 2015, 2015.
- ADAM Technology: 3DM Analyst Mine Mapping Suite 2.3.4 User's Manual, 1 edn., revision 1.0.137, 2010.
- Agarwal, S., Furukawa, Y., Snavely, N., Simon, I., Curless, B., Seitz, S. M., and Szeliski, R.: Building Rome in a Day, *Commun Acm*, 54, 105–112, doi:10.1145/2001269.2001293, 2011.
- Agisoft LLC: Agisoft PhotoScan User Manual: Professional Edition, Version 1.1, http://www.agisoft.com/pdf/photoscan-pro_1_1_en.pdf, 2014.
- Agliardi, F., Crosta, G. B., and Frattini, P.: Integrating rockfall risk assessment and countermeasure design by 3D modelling techniques, *Nat Hazard Earth Sys*, 9, 1059–1073, doi:10.5194/nhess-9-1059-2009, 2009.
- Albenque, A.: L'éboulement de Lyon, *Annales de Géographie*, 40, 105–106, 1931.
- Allix, A.: L'éboulement de Fourvière (note préliminaire), *Les Études rhodaniennes*, 6, 454–455, 1930.
- Ancey, C.: Are there "dragon-kings" events (i.e. genuine outliers) among extreme avalanches?, *The European Physical Journal Special Topics*, 205, 117–129, doi:10.1140/epjst/e2012-01565-7, 2012.
- Apip, Takara, K., Yamashiki, Y., Sassa, K., Ibrahim, A., and Fukuoka, H.: A distributed hydrological–geotechnical model using satellite-derived rainfall estimates for shallow landslide prediction system at a catchment scale, *Landslides*, 7, 237–258, doi:10.1007/s10346-010-0214-z, 2010.
- Aven, T.: On the new {ISO} guide on risk management terminology, *Reliability Engineering & System Safety*, 96, 719–726, doi:<http://dx.doi.org/10.1016/j.res.2010.12.020>, 2011.
- Aven, T. and Renn, O.: On risk defined as an event where the outcome is uncertain, *J Risk Res*, 12, 1–11, doi:10.1080/13669870802488883, 2009.
- Aye, Z. C., Jaboyedoff, M., Derron, M. H., van Westen, C. J., Hussin, H. Y., Ciurean, R. L., Frigerio, S., and Pasuto, A.: An interactive web-GIS tool for risk analysis: a case study in the Fella River basin, Italy, *Nat Hazard Earth Sys*, 16, 85–101, doi:10.5194/nhess-16-85-2016, 2016.
- BAFU: EconoMe 4.0: Wirtschaftlichkeit von Schutzmassnahmen gegen Naturgefahren, Bundesamt für Umwelt, <http://www.econome.admin.ch/>, last access: 3.7.2016, 2016a.
- BAFU: EconoMe 3.0 Objektparameter, http://www.econome.admin.ch/doc/Objektparameter_generate.php, last access: 17.09.2016, 2016b.
- Baum, R. and Godt, J.: Early warning of rainfall-induced shallow landslides and debris flows in the USA, *Landslides*, 7, 259–272, doi:10.1007/s10346-009-0177-0, 10.1007/s10346-009-0177-0, 2010.
- Bedka, K. M.: Overshooting cloud top detections using {MSG} {SEVIRI} Infrared brightness temperatures and their relationship to severe weather over Europe, *Atmos Res*, 99, 175 – 189, doi:10.1016/j.atmosres.2010.10.001, 2011.
- Berger, F. and Rey, F.: Mountain Protection Forests against Natural Hazards and Risks: New French Developments by Integrating Forests in Risk Zoning, *Nat Hazards*, 33, 395–404, doi:10.1023/B:NHAZ.0000048468.67886.e5, 2004.

- Besl, P. J. and McKay, N. D.: A method for registration of 3-D shapes, *Ieee T Pattern Anal*, 14, 239–256, doi:[10.1109/34.121791](https://doi.org/10.1109/34.121791), 1992.
- Beven, K.: *Environmental Modelling: An Uncertain Future?*, CRC Press, 2009.
- BFF: Richtlinien zur Berücksichtigung der Lawinengefahr bei raumwirksamen Tätigkeiten, Vollzug Umwelt VU-7500-D, Bundesamt für Forstwesen, Eidgenössisches Institut für Schnee- und Lawinenforschung, <http://www.bafu.admin.ch/publikationen/publikation/00778/index.html?lang=de>, 1984.
- Bohnenblust, H. and Slovic, P.: Integrating technical analysis and public values in risk-based decision making, *Reliability Engineering & System Safety*, 59, 151–159, doi:[10.1016/S0951-8320\(97\)00136-1](https://doi.org/10.1016/S0951-8320(97)00136-1), 1998.
- Bollinger, D., Hegg, C., Keusen, H., and Lateltin, O.: Ursachenanalyse der Hanginstabilitäten 1999, *Bulletin für angewandte Geologie*, 5, 5–38, 2000.
- Boonyanuphap, J.: Cost-benefit analysis of vetiver system-based rehabilitation measures for landslide-damaged mountainous agricultural lands in the lower Northern Thailand, *Nat Hazards*, 69, 599–629, doi:[10.1007/s11069-013-0730-y](https://doi.org/10.1007/s11069-013-0730-y), 2013.
- Botter, P.: Risikoanalyse bei gravitativen Naturgefahren: Methode, Umwelt-Materialien 107/I, Bundesamt für Umwelt, Wald und Landschaft (BUWAL), (In German), 1999.
- Brown, M. and Lowe, D. G.: Unsupervised 3D object recognition and reconstruction in unordered datasets, in: *International Conference on 3-D Digital Imaging and Modeling (3DIM 2005)*, Ottawa, Canada (June 2005), 2005.
- Bründl, M., Romang, H. E., Bischof, N., and Rheinberger, C. M.: The risk concept and its application in natural hazard risk management in Switzerland, *Nat Hazard Earth Sys*, 9, 801–813, doi:[10.5194/nhess-9-801-2009](https://doi.org/10.5194/nhess-9-801-2009), 2009.
- Bründl, M., Winkler, C., and Baumann, R.: "EconoMe-Railway" a new calculation method and tool for comparing the effectiveness and the cost-efficiency of protective measures along railways, in: *12th Congress INTERPRAEVENT 2012 – Grenoble / France*, 2012.
- Bründl, M., Ettl, L., Burkard, A., Oggier, N., Dolf, F., and Gutwein, P.: *EconoMe: Wirksamkeit und Wirtschaftlichkeit von Schutzmassnahmen gegen Naturgefahren*, Formelsammlung, Federal Office for the Environment (FOEN), Schweizerische Bundesbahnen (SBB), (In German), 2015.
- Bründl, M., Ettl, L., Burkard, A., Oggier, N., Dolf, F., and Gutwein, P.: *EconoMe: Wirksamkeit und Wirtschaftlichkeit von Schutzmassnahmen gegen Naturgefahren*, Formelsammlung, Federal Office for the Environment (FOEN), Schweizerische Bundesbahnen (SBB), (In German), 2016.
- Buchignani, V., Avanzi, G., Gianecchini, R., and Puccinelli, A.: Evaporite karst and sinkholes: a synthesis on the case of Camaiore (Italy), *Environ Geol*, 53, 1037–1044, doi:[10.1007/s00254-007-0730-x](https://doi.org/10.1007/s00254-007-0730-x), [10.1007/s00254-007-0730-x](https://doi.org/10.1007/s00254-007-0730-x), 2008.
- Budetta, P.: Risk assessment from debris flows in pyroclastic deposits along a motorway, Italy, *B Eng Geol Environ*, 61, 293–301, doi:[10.1007/s10064-002-0161-6](https://doi.org/10.1007/s10064-002-0161-6), 2002.
- Budetta, P.: Assessment of rockfall risk along roads, *Nat Hazard Earth Sys*, 4, 71–81, doi:[10.5194/nhess-4-71-2004](https://doi.org/10.5194/nhess-4-71-2004), 2004.
- Budetta, P., De Luca, C., and Nappi, M.: Quantitative rockfall risk assessment for an important road by means of the rockfall risk management (RO.MA.) method, *B Eng Geol Environ*, pp. 1–21, doi:[10.1007/s10064-015-0798-6](https://doi.org/10.1007/s10064-015-0798-6), 2015.
- Bunce, C., Cruden, D., and Morgenstern, N.: Assessment of the hazard from rock fall on a highway, *Can Geotech J*, 34, 344–356, 1997.
- Caine, N.: The Rainfall Intensity–Duration Control of Shallow Landslides and Debris Flows, *Geografiska Annaler. Series A, Physical Geography*, 62, 23–27, 1980.
- Campbell, R. H.: *Soil Slips, Debris Flows, and Rainstorms in the Santa Monica Mountains and Vicinity, Southern California*, Professional paper 851, U. S. Geological Survey, 1975.
- Capparelli, G. and Versace, P.: FLAIR and SUSHI: two mathematical models for early warning of lands-

- lides induced by rainfall, *Landslides*, 8, 67–79, doi:[10.1007/s10346-010-0228-6](https://doi.org/10.1007/s10346-010-0228-6), 2011.
- Cardinali, M., Reichenbach, P., Guzzetti, F., Ardizzone, F., Antonini, G., Galli, M., Cacciano, M., Castellani, M., and Salvati, P.: A geomorphological approach to the estimation of landslide hazards and risks in Umbria, Central Italy, *Nat Hazard Earth Sys*, 2, 57–72, doi:[10.5194/nhess-2-57-2002](https://doi.org/10.5194/nhess-2-57-2002), 2002.
- Cardinali, M., Galli, M., Guzzetti, F., Ardizzone, F., Reichenbach, P., and Bartoccini, P.: Rainfall induced landslides in December 2004 in south-western Umbria, central Italy: types, extent, damage and risk assessment, *Nat Hazard Earth Sys*, 6, 237–260, doi:[10.5194/nhess-6-237-2006](https://doi.org/10.5194/nhess-6-237-2006), 2006.
- Carrara, A., Cardinali, M., Detti, R., Guzzetti, F., Pasqui, V., and Reichenbach, P.: GIS techniques and statistical models in evaluating landslide hazard, *Earth Surf Processes*, 16, 427–445, doi:[10.1002/esp.3290160505](https://doi.org/10.1002/esp.3290160505), 1991.
- Carrea, D., Abellan, A., Derron, M.-H., and Jaboyedoff, M.: Automatic Rockfalls Volume Estimation Based on Terrestrial Laser Scanning Data, in: *Engineering Geology for Society and Territory - Volume 2*, edited by Lollino, G., Giordan, D., Crosta, G. B., Corominas, J., Azzam, R., Wasowski, J., and Sciarra, N., pp. 425–428, Springer International Publishing, doi:[10.1007/978-3-319-09057-3_68](https://doi.org/10.1007/978-3-319-09057-3_68), 2015.
- Carrea, D., Abellan, A., Humair, F., Matasci, B., Derron, M.-H., and Jaboyedoff, M.: Correction of terrestrial LiDAR intensity channel using Oren–Nayar reflectance model: An application to lithological differentiation, *Isprs J Photogramm*, 113, 17–29, doi:[10.1016/j.isprsjprs.2015.12.004](https://doi.org/10.1016/j.isprsjprs.2015.12.004), 2016.
- Cascini, L. and Versace, P.: Relationship between rainfall and landslide in a gneissic cover, in: *Proceedings of the 5th International Symposium on Landslides*, Lausanne, Switzerland, edited by Bonnard, C., vol. 1, pp. 565–570, 1988.
- Cascini, L., Bonnard, C., Corominas, J., Jibson, R., and Montero-Olarte, J.: Landslide hazard and risk zoning for urban planning and development, in: *Landslide Risk Management*, edited by Hungr, O., Fell, R., Cou-
 ture, R., and Eberhardt, E., chap. 7, pp. 199–235, Taylor and Francis, London, 2005.
- Catani, F., Casagli, N., Ermini, L., Righini, G., and Menduni, G.: Landslide hazard and risk mapping at catchment scale in the Arno River basin, *Landslides*, 2, 329–342, doi:[10.1007/s10346-005-0021-0](https://doi.org/10.1007/s10346-005-0021-0), 2005.
- Chadenas, C., Pottier, P., Mercier, D., Chaveau, E., and Pourinet, L.: Le prix d’une urbanisation abusive, in: *Xynthia, une tragédie prévisible*, edited by Mercier, D. and Acerra, M., pp. 25–29, Place Publique (hors série), 2011.
- Champod, E.: Carte Indicative du Danger d’effondrement (CID-EFF): Méthodologie développée pour le Jura et le Chablais Vaudois, Tech. rep., Etat de Vaud, Département de la Sécurité et de l’Environnement, Unité Dangers Naturels, (In French), 2011.
- Changnon, S. A.: Hailfall Characteristics Related to Crop Damage, *J Appl Meteorol*, 10, 270–274, 1971.
- Chaveau, E., Chadenas, C., Comentale, B., and Pourinet, L.: Une tempête banale ?, in: *Xynthia, une tragédie prévisible*, edited by Mercier, D. and Acerra, M., pp. 19–23, Place Publique (hors série), 2011.
- Chipperfield, A., Fleming, P., Pohlheim, H., and Fonseca, C.: Genetic Algorithm Toolbox For Use with MATLAB®, Department of Automatic Control and Systems Engineering, University of Sheffield, 1.2 edn., <http://codem.group.shef.ac.uk/index.php/ga-toolbox>, 1994.
- Chipperfield, A. J. and Fleming, P. J.: The MATLAB genetic algorithm toolbox, in: *IEE Colloquium on Applied Control Techniques Using MATLAB*, pp. 10/1–10/4, doi:[10.1049/ic:19950061](https://doi.org/10.1049/ic:19950061), 1995.
- Choffet, M., Demierre, J., Imhof, M., and Jaboyedoff, M.: Impact of a hailstorm on a building portfolio. Analysis of Cost structure and modeling of hail event consequences, in: *Geophysical Research Abstracts*, vol. 14, 2012.
- Christian, J. T.: Geotechnical Engineering Reliability: How Well Do We Know What We Are Doing?, *J Geotech Geoenviron*, 130, 985–1003, doi:[10.1061/\(ASCE\)1090-0241\(2004\)130:10\(985\)](https://doi.org/10.1061/(ASCE)1090-0241(2004)130:10(985)), 2004.

- Ciurean, R. L., Hussin, H., van Westen, C. J., Jaboyedoff, M., Nicolet, P., Chen, L., Frigerio, S., and Glade, T.: Multi-scale debris flow vulnerability assessment and direct loss estimation of buildings in the Eastern Italian Alps, *Nat Hazards*, 85, 929–957, doi:10.1007/s11069-016-2612-6, 2017.
- Cloutier, C.: Évaluation du comportement cinétique et du risque associé aux glissements de terrain rocheux actifs à l'aide de mesures de surveillance: Le cas du glissement de Gascons, Gaspésie, Canada, Ph.D. thesis, Université Laval, <http://www.theses.ulaval.ca/2014/30635/>, 2014.
- Colomina, I. and Molina, P.: Unmanned aerial systems for photogrammetry and remote sensing: A review, {ISPRS} *Journal of Photogrammetry and Remote Sensing*, 92, 79–97, doi:10.1016/j.isprsjprs.2014.02.013, 2014.
- Cooper, A.: The classification, recording, databasing and use of information about building damage caused by subsidence and landslides, *Q J Eng Geol Hydroge*, 41, 409–424, doi:10.1144/1470-9236/07-223, 2008.
- Cooper, A. H.: Subsidence hazards caused by the dissolution of Permian gypsum in England: geology, investigation and remediation, Geological Society, London, *Engineering Geology Special Publications*, 15, 265–275, doi:10.1144/GSL.ENG.1998.015.01.27, 1998.
- Cooper, A. H. and Calow, R. C.: Avoiding gypsum geohazards: guidance for planning and construction, Tech. Rep. WC/98/5, British Geological Survey, 1998.
- Cooper, A. H. and Waltham, A. C.: Subsidence caused by gypsum dissolution at Ripon, North Yorkshire, *Q J Eng Geol Hydroge*, 32, 305–310, doi:10.1144/GSL.QJEG.1999.032.P4.01, 1999.
- Cooper, A. H., Farrant, A. R., and Price, S. J.: The use of karst geomorphology for planning, hazard avoidance and development in Great Britain, *Geomorphology*, 134, 118 – 131, doi:10.1016/j.geomorph.2011.06.004, special issue "Geomorphology and Natural Hazards in Karst Areas", 2011.
- Corominas, J. and Mavrouli, O.: Rockfall Quantitative Risk Assessment, in: *Rockfall Engineering*, edited by Lambert, S. and Nicot, F., pp. 255–301, John Wiley & Sons, Inc., London and Hoboken, doi:10.1002/9781118601532.ch8, 2013.
- Corominas, J. and Moya, J.: Reconstructing recent landslide activity in relation to rainfall in the Llobregat River basin, Eastern Pyrenees, Spain, *Geomorphology*, 30, 79–93, doi:10.1016/S0169-555X(99)00046-X, landslides triggering factors, 1999.
- Corominas, J. and Moya, J.: A review of assessing landslide frequency for hazard zoning purposes, *Eng Geol*, 102, 193–213, doi:10.1016/j.enggeo.2008.03.018, special issue: Landslide Susceptibility, Hazard and Risk Zoning for Land Use Planning, 2008.
- Corominas, J., Westen, C., Frattini, P., Cascini, L., Malet, J.-P., Fotopoulou, S., Catani, F., Eeckhaut, M., Mavrouli, O., Agliardi, F., Pitilakis, K., Winter, M., Pastor, M., Ferlisi, S., Tofani, V., Hervás, J., and Smith, J.: Recommendations for the quantitative analysis of landslide risk, *B Eng Geol Environ*, pp. 1–55, doi:10.1007/s10064-013-0538-8, 2013.
- Cox, L. A. T. J.: What's Wrong with Risk Matrices?, *Risk Anal*, 28, 497–512, doi:10.1111/j.1539-6924.2008.01030.x, 2008.
- Crosta, G.: Regionalization of rainfall thresholds: an aid to landslide hazard evaluation, *Environ Geol*, 35, 131–145, doi:10.1007/s002540050300, 1998.
- Crosta, G. and Dal Negro, P.: Observations and modelling of soil slip-debris flow initiation processes in pyroclastic deposits: the Sarno 1998 event, *Nat Hazard Earth Sys*, 3, 53–69, 2003.
- Crosta, G., Frattini, P., and Sterlacchini, S.: Valutazione e gestione del rischio da frana, vol. 1 of *Valutazione della pericolosità e del rischio da frana in Lombardia*, Regione Lombardia, Milano, (in Italian), 2001.
- Crosta, G. B. and Frattini, P.: Distributed modelling of shallow landslides triggered by intense rainfall, *Nat Hazard Earth Sys*, 3, 81–93, 2003.
- Crovelli, R. A.: Probability Models for Estimation of Number and Costs of Landslides, Open-File Report 00-249, U. S. Geological Survey, <http://pubs.usgs.gov/of/2000/ofr-00-0249/ProbModels.html>, last access: 20.07.2016, 2000.
- Crozier, M.: Multiple-occurrence regional landslide events in New Zealand: Hazard management issues, *Landslides*, 2, 247–256, doi:10.1007/s10346-005-0019-7, 2005.

- Crozier, M. J.: Prediction of rainfall-triggered landslides: a test of the Antecedent Water Status Model, *Earth Surf Processes*, 24, 825–833, doi:[10.1002/\(SICI\)1096-9837\(199908\)24:9<825::AID-ESP14>3.0.CO;2-M](https://doi.org/10.1002/(SICI)1096-9837(199908)24:9<825::AID-ESP14>3.0.CO;2-M), 1999.
- Crozier, M. J., Eyles, R. J., Marx, S. L., McConchie, J. A., and Owen, R. C.: Distribution of landslides in the Wairarapa hill country, *New Zeal J Geol Geop*, 23, 575–586, doi:[10.1080/00288306.1980.10424129](https://doi.org/10.1080/00288306.1980.10424129), 1980.
- Cruden, D. M.: A simple definition of a landslide, *Bulletin of the International Association of Engineering Geology - Bulletin de l'Association Internationale de Géologie de l'Ingénieur*, 43, 27–29, doi:[10.1007/BF02590167](https://doi.org/10.1007/BF02590167), 1991.
- Cruden, D. M. and Varnes, D. J.: Landslide types and process, in: *Landslides Investigation and Mitigation*, edited by Turner, A. K. and Schuster, R. L., Special Report 247, pp. 36–75, Transportation Research Board, National Research Council, National Academy Press, Washington, DC, 1996.
- De Blasio, F. V.: *Introduction to the Physics of Landslides*, Springer Netherlands, doi:[10.1007/978-94-007-1122-8_1](https://doi.org/10.1007/978-94-007-1122-8_1), 2011.
- De Bruyn, I. A. and Bell, F. G.: The occurrence of sinkholes and subsidence depressions in the far west Rand and Gauteng Province, South Africa, and their engineering implications, *Environmental & Engineering Geoscience*, 7, 281–295, doi:[10.2113/gseegeosci.7.3.281](https://doi.org/10.2113/gseegeosci.7.3.281), 2001.
- De Loys, F. and Gagnebin, E.: *Monographie géologique de la Dent du Midi. Matériaux pour la carte géologique de la Suisse*, Commission Géologique de la Société Helvétique des Sciences Naturelles, 1926.
- de Quervain, F. and Frey, D.: *Geotechnische Karte der Schweiz 1:200000: Blatt Nr. 2 Luzern–Zürich–St. Gallen–Chur: Erläuterungen*, Schweizerischen Geotechnischen Kommission, 2 edn., [in German], 1963.
- de Quervain, F. and Frey, D.: *Carte Géotechnique de la Suisse 1:200000: Feuille n° 3 Genève–Lausanne–Sion: Texte explicatif*, Commission Géotechnique Suisse, 2 edn., [in French and German], 1965.
- de Quervain, F. and Frey, D.: *Carta Geotecnica della Svizzera 1:200000: Foglio n° 4 Bellinzona–St. Mortiz: Note esplicative*, Commissione Geotecnica Svizzera, 2 edn., [in Italian and German], 1967.
- de Quervain, F. and Hofmänner, F.: *Carte Géotechnique de la Suisse 1:200000: Feuille n° 1 Neuchâtel–Bern–Basel: Texte explicatif*, Commission Géotechnique Suisse, 2 edn., [in French and German], 1964.
- De Vita, P., Reichenbach, P., Bathurst, J. C., Borga, M., Crosta, G., Crozier, M., Glade, T., Guzzetti, F., Hansen, A., and Wasowski, J.: Rainfall-triggered landslides: a reference list, *Environ Geol*, 35, 219–233, doi:[10.1007/s002540050308](https://doi.org/10.1007/s002540050308), 1998.
- Deepen, J.: *Schadenmodellierung extremer Hageleereignisse in Deutschland*, Master's thesis, Institut für Landschaftsökologie der Westfälischen Wilhelms-Universität Münster, 2006.
- Demierre, J.: *Stochastic Model for Hail Damage Risk Assessment*, Tech. rep., Institute of Geomatics and Risk Analysis, University of Lausanne, 2012.
- Di Baldassarre, G., Kooy, M., Kemerink, J. S., and Brandimarte, L.: Towards understanding the dynamic behaviour of floodplains as human-water systems, *Hydrol Earth Syst Sc*, 17, 3235–3244, doi:[10.5194/hess-17-3235-2013](https://doi.org/10.5194/hess-17-3235-2013), 2013a.
- Di Baldassarre, G., Viglione, A., Carr, G., Kuil, L., Salinas, J. L., and Blöschl, G.: Socio-hydrology: conceptualising human-flood interactions, *Hydrol Earth Syst Sc*, 17, 3295–3303, doi:[10.5194/hess-17-3295-2013](https://doi.org/10.5194/hess-17-3295-2013), 2013b.
- D'Odorico, P., Fagherazzi, S., and Rigon, R.: Potential for landsliding: Dependence on hyetograph characteristics, *J Geophys Res-earth*, 110, n/a–n/a, doi:[10.1029/2004JF000127](https://doi.org/10.1029/2004JF000127), 2005.
- Dorren, L., Sandri, A., Raetzo, H., and Arnold, P.: Landslide risk mapping for the entire Swiss national road network, in: *Landslide processes: from geomorphologic mapping to dynamic modelling*, edited by Malet, J.-P., Remaître, A., and Bogaard, T., CERG, Utrecht University and University of Strasbourg, 6-7 February 2009, Strasbourg, http://eost.u-strasbg.fr/omiv/Landslide_Processes_Conference/Dorren_et_al.pdf, 2009.

- Doswell, C. A. I.: Severe Storms, in: *Encyclopedia of Remote Sensing*, edited by Njoku, E., *Encyclopedia of Earth Sciences Series*, pp. 767–780, Springer New York, doi:10.1007/978-0-387-36699-9_170, 2014.
- Dussauge, C., Grasso, J.-R., and Helmstetter, A.: Statistical analysis of rockfall volume distributions: Implications for rockfall dynamics, *Journal of Geophysical Research (Solid Earth)*, 108, ETG2.1–ETG2.11, doi:10.1029/2001JB000650, 2003.
- ECA: Rapport annuel 2014, Tech. rep., Etablissement d'assurance contre l'incendie et les éléments naturels du canton de Vaud, 2015.
- Einstein, H. H.: Special lecture: Landslide risk assessment procedure, in: *Proceedings of the 5th International Symposium on Landslides*, Lausanne, Switzerland, edited by Bonnard, C., vol. 2, pp. 1075–1090, *landslides and rockslides risk*, 1988.
- Eisenbeiss, H.: A mini unmanned aerial vehicle (UAV): system overview and image acquisition, *International Archives of Photogrammetry. Remote Sensing and Spatial Information Sciences*, 36, 2004.
- Eisenbeiß, H.: UAV photogrammetry, Ph.D. thesis, Zürich, Eidgenössischen Technischen Hochschule, http://www.igp-data.ethz.ch/berichte/Blaue_Berichte_PDF/105.pdf, 2009.
- Eisenbeiss, H. and Sauerbier, M.: Investigation of uav systems and flight modes for photogrammetric applications, *The Photogrammetric Record*, 26, 400–421, doi:10.1111/j.1477-9730.2011.00657.x, 2011.
- Elsner, J. B., Niu, X., and Jagger, T. H.: Detecting Shifts in Hurricane Rates Using a Markov Chain Monte Carlo Approach, *J Climate*, 17, 2652–2666, doi:10.1175/1520-0442(2004)017<2652:DSIHUR>2.0.CO;2, 2004.
- Embrechts, P., Klüppelberg, C., and Mikosch, T.: Modeling extremal events for insurance and finance, vol. 33 of *Applications of Mathematics*, Springer Berlin Heidelberg, doi:10.1007/978-3-642-33483-2, 1997.
- Enright, P.: Is there a tolerable level of risk from natural hazards in New Zealand?, *Georisk: Assessment and Management of Risk for Engineered Systems and Geohazards*, 0, 1–8, doi:10.1080/17499518.2014.1000341, 2015.
- Escher, A., Hunziker, J. C., Marthaler, M., Masson, H., Sartori, M., and Steck, A.: Geologic framework and structural evolution of the western Swiss Italian Alps, in: *Deep Structure of the Swiss Alps – Results from NRP 20*, edited by Piffner, O. A., Lehner, P., Heitzmann, P., Müller, S., and A., S., pp. 205–222, Birkhäuser AG, Basel, 1997.
- Evans, A. W. and Verlander, N. Q.: What Is Wrong with Criterion FN-Lines for Judging the Tolerability of Risk?, *Risk Anal*, 17, 157–168, doi:10.1111/j.1539-6924.1997.tb00855.x, 1997.
- Federal Statistical Office: Consumer Price Index, http://www.bfs.admin.ch/bfs/portal/en/index/themen/05/02/blank/key/basis_aktuell.html, last access: 07.08.2015, 2015.
- Fell, R.: Landslide risk assessment and acceptable risk, *Can Geotech J*, 31, 261–272, 1993.
- Fell, R., Ho, K. K. S., Lacasse, S., and Leroi, E.: A framework for landslide risk assessment and management, in: *Landslide Risk Management*, edited by Hungr, O., Fell, R., Couture, R., and Eberhardt, E., pp. 3–26, Taylor & Francis Group, London, 2005.
- Fell, R., Corominas, J., Bonnard, C., Cascini, L., Leroi, E., and Savage, W. Z.: Guidelines for landslide susceptibility, hazard and risk zoning for land-use planning, *Eng Geol*, 102, 99–111, doi:10.1016/j.enggeo.2008.03.014, special issue : "Landslide Susceptibility, Hazard and Risk Zoning for Land Use Planning", 2008a.
- Fell, R., Corominas, J., Bonnard, C., Cascini, L., Leroi, E., and Savage, W. Z.: Guidelines for landslide susceptibility, hazard and risk zoning for land-use planning, *Eng Geol*, 102, 85–98, doi:10.1016/j.enggeo.2008.03.022, special issue : "Landslide Susceptibility, Hazard and Risk Zoning for Land Use Planning", 2008b.
- FEMA: Benefit-Cost Analysis, <https://www.fema.gov/benefit-cost-analysis>, last update: 28.09.2015, last access: 10.09.2016, 2015.
- Ferlisi, S., Cascini, L., Corominas, J., and Matano, F.: Rockfall risk assessment to persons travelling in vehicles along a road: the case study of the Amalfi coastal road (southern Italy), *Nat Hazards*, 62, 691–721, doi:10.1007/s11069-012-0102-z, 2012.

- Finlay, P. J. and Fell, R.: Landslides: risk perception and acceptance, *Can Geotech J*, 34, 169–188, doi:[10.1139/t96-108](https://doi.org/10.1139/t96-108), 1997.
- Flossmann, A. I.: Models of Clouds, Precipitation and Storms, in: *Encyclopedia of Hydrological Sciences*, John Wiley & Sons, Ltd, doi:[10.1002/0470848944.hsa034](https://doi.org/10.1002/0470848944.hsa034), 2006.
- FOEN: Naturereigniskataster – StorMe, <http://www.bafu.admin.ch/naturgefahren/11421/11426/index.html>, 2012.
- FOEN: Protection against Mass Movement Hazards. Guideline for the integrated hazard management of landslides, rockfall and hillslope debris flows, no. 1608 in *The environment in practice*, Federal Office for the Environment, Bern, http://www.bafu.admin.ch/publikationen/publikation/01850/index.html?lang=en&show_kat=/publikationen, last access: 7.7.2016, 2016.
- Fonstad, M. A., Dietrich, J. T., Courville, B. C., Jensen, J. L., and Carbonneau, P. E.: Topographic structure from motion: a new development in photogrammetric measurement, *Earth Surf Processes*, 38, 421–430, doi:[10.1002/esp.3366](https://doi.org/10.1002/esp.3366), 2013.
- Ford, D. and Williams, P. D.: *Karst Hydrogeology and Geomorphology*, John Wiley & Sons, 2007.
- Foresti, L. and Pozdnoukhov, A.: Exploration of alpine orographic precipitation patterns with radar image processing and clustering techniques, *Meteorol Appl*, 19, 407–419, doi:[10.1002/met.272](https://doi.org/10.1002/met.272), 2012.
- Foresti, L., Pozdnoukhov, A., Tuia, D., and Kanevski, M.: Extreme Precipitation Modelling Using Geostatistics and Machine Learning Algorithms, in: *geoENV VII – Geostatistics for Environmental Applications*, edited by Atkinson, P. M. and Lloyd, C. D., vol. 16 of *Quantitative Geology and Geostatistics*, pp. 41–52, Springer Netherlands, doi:[10.1007/978-90-481-2322-3_4](https://doi.org/10.1007/978-90-481-2322-3_4), 2010.
- Foresti, L., Kanevski, M., and Pozdnoukhov, A.: Kernel-Based Mapping of Orographic Rainfall Enhancement in the Swiss Alps as Detected by Weather Radar, *Ieee T Geosci Remote*, 50, 2954–2967, 2012.
- Forlani, G., Pinto, L., Roncella, R., and Pagliari, D.: Terrestrial photogrammetry without ground control points, *Earth Science Informatics*, 7, 71–81, doi:[10.1007/s12145-013-0127-1](https://doi.org/10.1007/s12145-013-0127-1), 2014.
- FOGW: Flood Control at Rivers and Streams, Guidelines of the FOWG, Federal Office for Water and Geology, 2001.
- Fuchs, S., Thöni, M., McAlpin, M. C., Gruber, U., and Bründl, M.: Avalanche Hazard Mitigation Strategies Assessed by Cost Effectiveness Analyses and Cost Benefit Analyses—evidence from Davos, Switzerland, *Nat Hazards*, 41, 113–129, doi:[10.1007/s11069-006-9031-z](https://doi.org/10.1007/s11069-006-9031-z), 2007.
- Furukawa, Y. and Ponce, J.: Accurate, Dense, and Robust Multiview Stereopsis, *Ieee T Pattern Anal*, 32, 1362–1376, doi:[10.1109/TPAMI.2009.161](https://doi.org/10.1109/TPAMI.2009.161), 2010.
- Furukawa, Y., Curless, B., Seitz, S., and Szeliski, R.: Towards Internet-scale multi-view stereo, in: *2010 IEEE Conference on Computer Vision and Pattern Recognition (CVPR)*, pp. 1434–1441, doi:[10.1109/CVPR.2010.5539802](https://doi.org/10.1109/CVPR.2010.5539802), 2010.
- Gabella, M., Bolliger, M., Germann, U., and Perona, G.: Large sample evaluation of cumulative rainfall amounts in the Alps using a network of three radars, *Atmos Res*, 77, 256–268, 2005.
- Galli, M. and Guzzetti, F.: Landslide Vulnerability Criteria: A Case Study from Umbria, Central Italy, *Environ Manage*, 40, 649–665, doi:[10.1007/s00267-006-0325-4](https://doi.org/10.1007/s00267-006-0325-4), 2007.
- Galve, J., Gutiérrez, F., Remondo, J., Bonachea, J., Lucha, P., and Cendrero, A.: Evaluating and comparing methods of sinkhole susceptibility mapping in the Ebro Valley evaporite karst (NE Spain), *Geomorphology*, 111, 160–172, doi:[10.1016/j.geomorph.2009.04.017](https://doi.org/10.1016/j.geomorph.2009.04.017), 2009.
- Galve, J. P., Remondo, J., and Gutiérrez, F.: Improving sinkhole hazard models incorporating magnitude–frequency relationships and nearest neighbor analysis, *Geomorphology*, 134, 157–170, doi:[10.1016/j.geomorph.2011.05.020](https://doi.org/10.1016/j.geomorph.2011.05.020), special issue "Geomorphology and Natural Hazards in Karst Areas", 2011.
- Galve, J. P., Gutiérrez, F., Guerrero, J., Alonso, J., and Diego, I.: Application of risk, cost-benefit

- and acceptability analyses to identify the most appropriate geosynthetic solution to mitigate sink-hole damage on roads, *Eng Geol*, 145/146, 65–77, doi:[10.1016/j.enggeo.2012.07.002](https://doi.org/10.1016/j.enggeo.2012.07.002), 2012.
- Gamma, P.: dfwalk — Ein Murgang-Simulationsprogramm zur Gefahrenzonierung, Ph.D. thesis, University of Bern, Switzerland, 2000.
- Ganderton, P. T.: 'Benefit-Cost Analysis' of Disaster Mitigation: Application as a Policy and Decision-Making Tool, in: *Mitigation of Natural Hazards and Disasters: International Perspectives*, edited by Haque, C. E., pp. 113–133, Springer Netherlands, Dordrecht, doi:[10.1007/1-4020-4514-X_6](https://doi.org/10.1007/1-4020-4514-X_6), 2005.
- Garcia-Aristizabal, A., Gasparini, P., and UHINGA, G.: Multi-risk Assessment as a Tool for Decision-Making, in: *Urban Vulnerability and Climate Change in Africa: A Multidisciplinary Approach*, edited by Pauleit, S., Coly, A., Fohlmeister, S., Gasparini, P., Jørgensen, G., Kabisch, S., Kombe, J. W., Lindley, S., Simonis, I., and Yeshitela, K., pp. 229–258, Springer International Publishing, Cham, doi:[10.1007/978-3-319-03982-4_7](https://doi.org/10.1007/978-3-319-03982-4_7), 2015.
- Genovese, E., Przyluski, V., Vinit, F., and Déqué, M.: Xynthia : le déroulement de la tempête et ses conséquences en France, in: *Gestion des risques naturels : Leçons de la tempête Xynthia*, edited by Przyluski, V. and Hallegatte, S., chap. 1, Quae, 2012.
- Geotest, Geo7, and Oeko-B: SilvaProtect-CH: Schutzwaldhinweiskarte der Schweiz: Modul EVENT (Los 1: Prozess Steinschlag / Blockschlag und Los 2: Prozesse Hangmure / Rutschung, Murgang), Tech. rep., Zollikofen, Switzerland, 2006.
- Germann, U., Galli, G., Boscacci, M., and Bolliger, M.: Radar precipitation measurement in mountainous region, *Q J Roy Meteor Soc*, 132, 1669–1692, 2006.
- Germann, U., Berenguer, M., Sempere-Torres, D., and Zappa, M.: REAL - Ensemble radar precipitation estimation for hydrology in mountainous region, *Q J Roy Meteor Soc*, 135, 445–456, 2009.
- Ghosh, S., van Westen, C. J., Carranza, E. J. M., and Jetten, V. G.: Integrating spatial, temporal, and magnitude probabilities for medium-scale landslide risk analysis in Darjeeling Himalayas, India, *Landslides*, 9, 371–384, doi:[10.1007/s10346-011-0304-6](https://doi.org/10.1007/s10346-011-0304-6), 2012.
- Gilbert, R. B., Habibi, M., and Nadim, F.: Accounting for Unknown Unknowns in Managing Multi-hazard Risks, in: *Multi-hazard Approaches to Civil Infrastructure Engineering*, edited by Gardoni, P. and LaFave, M. J., chap. Accounting for Unknown Unknowns in Managing Multi-hazard Risks, pp. 383–412, Springer International Publishing, Cham, doi:[10.1007/978-3-319-29713-2_18](https://doi.org/10.1007/978-3-319-29713-2_18), 2016.
- Girardeau-Montaut, D.: CloudCompare v2.6, <http://www.danielgm.net/cc/>.
- Glade, T.: Establishing the frequency and magnitude of landslide-triggering rainstorm events in New Zealand, *Environ Geol*, 35, 160–174, doi:[10.1007/s002540050302](https://doi.org/10.1007/s002540050302), 1998.
- Glade, T., Crozier, M., and Smith, P.: Applying Probability Determination to Refine Landslide-triggering Rainfall Thresholds Using an Empirical "Antecedent Daily Rainfall Model", *Pure Appl Geophys*, 157, 1059–1079, doi:[10.1007/s000240050017](https://doi.org/10.1007/s000240050017), 2000.
- Godt, J., Baum, R., Savage, W., Salciarini, D., Schulz, W., and Harp, E.: Transient deterministic shallow landslide modeling: Requirements for susceptibility and hazard assessments in a GIS framework, *Eng Geol*, 102, 214–226, doi:[10.1016/j.enggeo.2008.03.019](https://doi.org/10.1016/j.enggeo.2008.03.019), special issue: "Landslide Susceptibility, Hazard and Risk Zoning for Land Use Planning", 2008.
- Gonzalez, R. C. and Woods, R. E.: *Digital Image Processing*, Pearson Education, Inc., ISBN 0-201-18075-8, 2002.
- Grand Conseil du Canton de Vaud: Loi concernant l'assurance des bâtiments et du mobilier contre l'incendie et les éléments naturels, http://www.rsv.vd.ch/dire-cocoon/rsv_site/doc.pdf?docId=5522, 1952.
- Greco, R., Giorgio, M., Capparelli, G., and Versace, P.: Early warning of rainfall-induced landslides based on empirical mobility function predictor, *Eng Geol*, 153, [10.1016/j.enggeo.2012.11.009](https://doi.org/10.1016/j.enggeo.2012.11.009), 2013.
- Grieser, J., Marescot, L., Smith, M., and Lai, M.: Estimating hail insured loss from radar images – application to the 2013 events in Germany, in: *1st European Hail Workshop*, 25–27 June 2014, University

- of Bern, Switzerland, edited by Romppainen-Martius, O., Kunz, M., Hering, A., Nisi, L., and Germann, U., http://www.oeschger.unibe.ch/events/conferences/hail/presentations/13_Grieser.pdf, 2014.
- Griffiths, R. C.: On a bivariate triangular distribution, *Aust J Stat*, 20, 183–185, doi:10.1111/j.1467-842X.1978.tb01304.x, 1978.
- Guha-Sapir, D. and Vos, F.: Quantifying Global Environmental Change Impacts: Methods, Criteria and Definitions for Compiling Data on Hydro-meteorological Disasters, in: *Coping with Global Environmental Change, Disasters and Security: Threats, Challenges, Vulnerabilities and Risks*, edited by Brauch, G. H., Oswald Spring, Ú., Mesjasz, C., Grin, J., Kameri-Mbote, P., Chourou, B., Dunay, P., and Birkmann, J., pp. 693–717, Springer Berlin Heidelberg, Berlin, Heidelberg, doi:10.1007/978-3-642-17776-7_40, 2011.
- Gullà, G., Antronico, L., Iaquina, P., and Terranova, O.: Susceptibility and triggering scenarios at a regional scale for shallow landslides, *Geomorphology*, 99, 39–58, doi:10.1016/j.geomorph.2007.10.005, 2008.
- Guthrie, R.: Geological/geophysical disasters, in: *Encyclopedia of Natural Hazards*, edited by Bobrowsky, P. T., pp. 387–400, Springer, doi:978-90-481-8699-0, 2013.
- Gutiérrez, F. and Cooper, A. H.: Evaporite Dissolution Subsidence in the Historical City of Calatayud, Spain: Damage Appraisal and Prevention, *Nat Hazards*, 25, 259–288, doi:10.1023/A:1014807901461, 2002.
- Gutiérrez, F., Cooper, A. H., and Johnson, K. S.: Identification, prediction, and mitigation of sinkhole hazards in evaporite karst areas, *Environ Geol*, 53, 1007–1022, 2008a.
- Gutiérrez, F., Guerrero, J., and Lucha, P.: A genetic classification of sinkholes illustrated from evaporite paleo-karst exposures in Spain, *Environ Geol*, 53, 993–1006, doi:10.1007/s00254-007-0727-5, 2008b.
- Guzzetti, F., Malamud, B. D., Turcotte, D. L., and Reichenbach, P.: Power-law correlations of landslide areas in central Italy, *Earth Planet Sc Lett*, 195, 169–183, doi:10.1016/S0012-821X(01)00589-1, 2002.
- Guzzetti, F., Peruccacci, S., Rossi, M., and Stark, C.: The rainfall intensity–duration control of shallow landslides and debris flows: an update, *Landslides*, 5, 3–17, doi:10.1007/s10346-007-0112-1, 2008.
- GVVG: Geschäftsbericht 2009, Gebäudeversicherung Thurgau, <http://gvvg.ch/cms/geschaeftsberichte/gvtg-gb-2009/index.html>, (In German), 2010.
- GVZ: Geschäftsbericht 2011, Gebäudeversicherung Kanton Zürich, <http://www.gvz.ch/LinkClick.aspx?fileticket=FUKaoEQ4DJo%3d&tabid=816&language=de-CHindex.html>, (In German), 2012.
- Haimes, Y. Y., Kaplan, S., and Lambert, J. H.: Risk Filtering, Ranking, and Management Framework Using Hierarchical Holographic Modeling, *Risk Anal*, 22, 383–397, doi:10.1111/0272-4332.00020, 2002.
- Hantz, D.: Quantitative assessment of diffuse rock fall hazard along a cliff foot, *Nat Hazard Earth Sys*, 11, 1303–1309, doi:10.5194/nhess-11-1303-2011, 2011.
- Hazzard, J.: Risk analysis of landslides affecting major transportation corridors in southwestern British Columbia, Master's thesis, University of British Columbia, <http://circle.ubc.ca/handle/2429/8933>, 1998.
- Hilker, N., Aller, D., and Hegg, C.: Ereignisanalyse Hochwasser 2005 : Teil 1 – Prozesse, Schäden und erste Einordnung, chap. Schäden, pp. 127–148, Bundesamt für Umwelt BAFU, Eidg. Forschungsanstalt WSL, 2007.
- Hilker, N., Badoux, A., and Hegg, C.: The Swiss flood and landslide damage database 1972–2007, *Nat Hazard Earth Sys*, 9, 913–925, doi:10.5194/nhess-9-913-2009, 2009.
- HiSystems GmbH: Company, <http://www.mikrokopter.de/en/contact/company>, last access: 02.11.2015, 2015.
- Ho, K. and Ko, F.: Application of quantified risk analysis in landslide risk management practice: Hong Kong experience, *Georisk: Assessment and Management of Risk for Engineered Systems and Geohazards*, 3, 134–146, doi:10.1080/17499510902873074, 2009.
- Ho, K., Leroi, E., and Roberds, B.: Quantitative risk assessment: application, myths and future direction, in: *Proceedings of the International Conference on Geotechnical Engineering (GeoEng 2000)*, Melbourne, pp. 269–312, 2000.
- Hohl, R., Schiesser, H.-H., and Aller, D.: Hailfall: the

- relationship between radar-derived hail kinetic energy and hail damage to buildings, *Atmospheric Research*, 63, 177–207, doi:[10.1016/S0169-8095\(02\)00059-5](https://doi.org/10.1016/S0169-8095(02)00059-5), 2002a.
- Hohl, R., Schiesser, H.-H., and Knepper, I.: The use of weather radars to estimate hail damage to automobiles: an exploratory study in Switzerland, *Atmospheric Research*, 61, 215–238, doi:[10.1016/S0169-8095\(01\)00134-X](https://doi.org/10.1016/S0169-8095(01)00134-X), 2002b.
- Humair, F., Abellan, A., Carrea, D., Matasci, B., Epard, J.-L., and Jaboyedoff, M.: Geological layers detection and characterisation using high resolution 3D point clouds: example of a box-fold in the Swiss Jura Mountains, *Eur. J. Remote Sens.*, 48, 569–591, 2015.
- Hungr, O., Leroueil, S., and Picarelli, L.: The Varnes classification of landslide types, an update, *Landslides*, 11, 167–194, doi:[10.1007/s10346-013-0436-y](https://doi.org/10.1007/s10346-013-0436-y), 2014.
- ICAO: Unmanned Aircraft Systems (UAS), Cir 328, International Civil Aviation Organization, 999 University Street, Montréal, Quebec, Canada H3C 5H7, 2011.
- Iida, T.: A stochastic hydro-geomorphological model for shallow landsliding due to rainstorm, *Catena*, 34, 293–313, <http://www.sciencedirect.com/science/article/B6VCG-3VTYVWW-5/1/272affa188fa14bbfd4d7290700da4c3>, 1999.
- Iida, T.: Theoretical research on the relationship between return period of rainfall and shallow landslides, *Hydrol Process*, 18, 739–756, doi:[10.1002/hyp.1264](https://doi.org/10.1002/hyp.1264), 2004.
- Imhof, M.: Analyse de données à long terme relatives à des dommages causés à des bâtiments: Analyse des données de la statistique des dommages AEAI sur plusieurs années, Analyse statistique, Union intercantonale de réassurance (UIR), 2011.
- Imhof, M. and Choffet, M.: Grêle 2009: Etude des orages de grêle du 26 mai et du 23 juillet 2009, Analyse des événements, Union intercantonale de réassurance UIR, <http://irv.ch/IRV/Downloads.aspx>, (In French and German), 2012.
- Imhof, M., Nicolet, P., Voumard, J., and Jaboyedoff, M.: Hail 2011: Analysis of the 12–13 July hail event in the Canton of Aargau, Event analysis, Intercantonal Reinsurance (IRV), http://irv.ch/getmedia/8007ce65-e40a-48d2-961f-0cd5c0d2f0c6/VKF_Brosch_Hagel_2011_DT_GzDb.pdf.aspx, (In German and French), 2015.
- Jaboyedoff, M. and Bonnard, C.: Report on landslide impacts and practices in Switzerland: Need for new risk assessment strategies, in: *The 2007 International Forum on Landslide Disaster Management*, edited by Ho and Li, pp. 79–97, 2007.
- Jaboyedoff, M., Loye, A., Oppikofer, T., Pedrazzini, A., Güell i Pons, M., and Locat, J.: Earth-flow in a complex geological environment: the example of Pont Bourquin, Les Diablerets (Western Switzerland), in: *Landslide Processes: from Geomorphologic Mapping to Dynamic Modelling: Proceedings of the Landslide Processes Conference*, edited by Malet, J.-P., Rémaitre, A., and Bogaard, T., 2009.
- Jaboyedoff, M., Choffet, M., Derron, M.-H., Horton, P., Loye, A., Longchamp, C., Mazotti, B., Michoud, C., and Pedrazzini, A.: Terrigenous Mass Movements: Detection, Modelling, Early Warning and Mitigation Using Geoinformation Technology, chap. Preliminary Slope Mass Movement Susceptibility Mapping Using DEM and LiDAR DEM, pp. 109–170, Springer Berlin Heidelberg, Berlin, Heidelberg, doi:[10.1007/978-3-642-25495-6_5](https://doi.org/10.1007/978-3-642-25495-6_5), 2012.
- Jaboyedoff, M., Derron, M.-H., Aye, Z. C., Nicolet, P., and Olyazadeh, R.: Using the consequence - frequency matrix to reduce the risk: examples and teaching, in: *International Conference on the Analysis and Management of Changing Risk for Natural Hazards*, 18–19 November 2014, Padua, Italy, CO1, http://www.changes-itn.eu/Portals/0/Content/2014/Final%20conference/abstracts/CO1_Abstract_Jaboyedoff_et_al.pdf, 2014.
- Jaboyedoff, M., Michoud, C., Derron, M.-H., Voumard, J., Leibundgut, G., Sudmeier-Rieux, K., Nadim, F., and Leroi, E.: Human-Induced Landslides: Toward the analysis of anthropogenic changes of the slope environment, in: *Landslides and Engineered Slopes – Experience, Theory and Practice*, edited by Aversa, S., Cascini, L., Picarelli, L., and Scavia, C., vol. 1, pp. 217–232, Associazione Geotecnica Italiana, Rome, Italy, CRC Press/Balkema, 2016.
- Jaboyedoff, M., Abellán, A., Carrea, D., Derron, M.-H., Matasci, B., and Michoud, C.: LiDAR use for Map-

- ping and Monitoring of Landslides, in: *Encyclopedia of Natural Hazards: Prediction, Assessment, and Mitigation*, edited by Singh, R. P., Taylor and Francis, in press.
- Jaiswal, P., van Westen, C. J., and Jetten, V.: Quantitative estimation of landslide risk from rapid debris slides on natural slopes in the Nilgiri hills, India, *Nat Hazard Earth Sys*, 11, 1723–1743, doi:[10.5194/nhess-11-1723-2011](https://doi.org/10.5194/nhess-11-1723-2011), 2011.
- Jakob, M., Stein, D., and Ulmi, M.: Vulnerability of buildings to debris flow impact, *Nat Hazards*, 60, 241–261, doi:[10.1007/s11069-011-0007-2](https://doi.org/10.1007/s11069-011-0007-2), 2012.
- James, M. R. and Robson, S.: Straightforward reconstruction of 3D surfaces and topography with a camera: Accuracy and geoscience application, *Journal of Geophysical Research: Earth Surface*, 117, F03 017, doi:[10.1029/2011JF002289](https://doi.org/10.1029/2011JF002289), 2012.
- James, M. R. and Robson, S.: Mitigating systematic error in topographic models derived from UAV and ground-based image networks, *Earth Surf Processes*, 39, 1413–1420, doi:[10.1002/esp.3609](https://doi.org/10.1002/esp.3609), 2014.
- Johnson, N. L. and Kotz, S.: *Continuous univariate distributions-1*, John Wiley & Sons, 1970.
- Joliquin, P., Schaeren, G., Perrin, R., and Balegno, P.: *Commune de Chardonne : Stabilisation de bancs rocheux : Secteurs « En Couralaz » et Hameau des Curnilles : Avant-projet*, Tech. rep., Norbert SA and Xylon SA and Cetrp SA, 2010.
- Jonkman, S., van Gelder, P., and Vrijling, J.: An overview of quantitative risk measures for loss of life and economic damage, *Journal of Hazardous Materials*, 99, 1–30, doi:[10.1016/S0304-3894\(02\)00283-2](https://doi.org/10.1016/S0304-3894(02)00283-2), 2003.
- Kahneman, D. and Tversky, A.: Intuitive prediction: Biases and corrective procedures, in: *Judgment under uncertainty: Heuristics and biases*, edited by Kahneman, D., Slovic, P., and Tversky, A., pp. 414–421, Cambridge University Press, 1982.
- Kanevski, M., Pozdnoukhov, A., and Timonin, V.: *Machine Learning for Spatial Environmental Data: theory, applications and software*, EPFL Press, 2009.
- Kaplan, S.: The Words of Risk Analysis, *Risk Anal*, 17, 407–417, doi:[10.1111/j.1539-6924.1997.tb00881.x](https://doi.org/10.1111/j.1539-6924.1997.tb00881.x), 1997.
- Kaplan, S. and Garrick, B. J.: On The Quantitative Definition of Risk, *Risk Anal*, 1, 11–27, doi:[10.1111/j.1539-6924.1981.tb01350.x](https://doi.org/10.1111/j.1539-6924.1981.tb01350.x), 1981.
- Kaplan, S., Haimès, Y. Y., and Garrick, B. J.: Fitting Hierarchical Holographic Modeling into the Theory of Scenario Structuring and a Resulting Refinement to the Quantitative Definition of Risk, *Risk Anal*, 21, 807–807, doi:[10.1111/0272-4332.215153](https://doi.org/10.1111/0272-4332.215153), 2001.
- Katz, R. W. and Garcia, R. R.: Statistical relationships between hailfall and damage to wheat, *Agricultural Meteorology*, 24, 29–43, doi:[10.1016/0002-1571\(81\)90031-5](https://doi.org/10.1016/0002-1571(81)90031-5), 1981.
- Kazhdan, M., Bolitho, M., and Hoppe, H.: Poisson surface reconstruction, in: *Proceedings of the fourth Eurographics symposium on Geometry processing*, vol. 7, 2006.
- Klimchouk, A.: Subsidence hazards in different types of karst: evolutionary and speleogenetic approach, *Environ Geol*, 48, 287–295, doi:[10.1007/s00254-005-1275-5](https://doi.org/10.1007/s00254-005-1275-5), 2005.
- Kohli, R.: *Tables de mortalité pour la Suisse 1998/2003*, Statistique de la suisse, Office Fédéral de la Statistique, Neuchâtel, 2005.
- Komac, B. and Zorn, M.: Geohazards, in: *Encyclopedia of Natural Hazards*, edited by Bobrowsky, P. T., p. 387, Springer, doi:[978-90-481-8699-0](https://doi.org/10.1007/978-90-481-8699-0), 2013.
- Kotz, S. and Van Dorp, J. R.: *Beyond beta: Other continuous Families of Distributions with Bounded Support and Applications*, World Scientific Publishing, 2004.
- Kuczera, G., Renard, B., Thyer, M., and Kavetski, D.: There are no hydrological monsters, just models and observations with large uncertainties!, *Hydrological Sciences Journal*, 55, 980–991, doi:[10.1080/02626667.2010.504677](https://doi.org/10.1080/02626667.2010.504677), 2010.
- Lacasse, S. and Nadim, F.: Landslide Risk Assessment and Mitigation Strategy, in: *Landslides – Disaster Risk Reduction*, edited by Sassa, K. and Canuti, P., chap. 3, pp. 31–61, Springer Berlin Heidelberg, Berlin, Heidelberg, doi:[10.1007/978-3-540-69970-5_3](https://doi.org/10.1007/978-3-540-69970-5_3), 2009.
- Lacasse, S., Eidsvik, U., Nadim, F., Hoeg, K., and Blikra, L. H.: Event tree analysis of Åknes rock slide hazard, in: *Proceedings of the 4th Canadian Conference on Geohazards: From Causes to Management*, edited by

- Locat, J., Perret, D., Turmel, D., Demers, D., and Leroueil, S., pp. 20–24, Presse de l'Université Laval, Québec, 2008.
- Lari, S., Frattini, P., and Crosta, G. B.: Integration of natural and technological risks in Lombardy, Italy, *Nat Hazard Earth Sys*, 9, 2085–2106, doi:10.5194/nhess-9-2085-2009, 2009.
- Lari, S., Frattini, P., and Crosta, G. B.: Local scale multiple quantitative risk assessment and uncertainty evaluation in a densely urbanised area (Brescia, Italy), *Nat Hazard Earth Sys*, 12, 3387–3406, doi:10.5194/nhess-12-3387-2012, 2012.
- Lateltin, O.: Prise en compte des dangers dus aux mouvements de terrain dans le cadre des activités de l'aménagement du territoire, Tech. rep., Office fédéral de l'aménagement du territoire (OFAT), Office fédéral de l'économie des eaux (OFEE), Office fédéral de l'environnement, des forêts et du paysage (OFEFP), Bern, Switzerland, 1997.
- Lateltin, O., Haemmig, C., Raetzo, H., and Bonnard, C.: Landslide risk management in Switzerland, *Landslides*, 2, 313–320, doi:10.1007/s10346-005-0018-8, 2005.
- Lato, M., Hutchinson, J., Diederichs, M., Ball, D., and Harrap, R.: Engineering monitoring of rockfall hazards along transportation corridors: using mobile terrestrial LiDAR, *Natural Hazards and Earth System Science*, 9, 935–946, doi:10.5194/nhess-9-935-2009, 2009.
- Liener, S., Kienholz, H., Liniger, M., and Krummenacher, B.: SLIDISP - A procedure to locate landslide prone areas, in: *Landslides — Glissements de terrain, Proceedings of the seventh international symposium on landslides, 17–21 June 1996, Trondheim, Norway*, edited by Senneset, K., Balkema, Rotterdam, 1996.
- Litai, D., Lanning, D. D., and Rasmussen, N. C.: The public perception of Risk, in: *The Analysis of Actual Versus Perceived Risks*, edited by Covelto, V. T., Gary, F. W., Rodricks, J. V., and Tardiff, R. G., *Advances in Risk Analysis*, pp. 213–224, Society for Risk Analysis, Plenum Press, 1983.
- Loat, R. and Petrascheck, A.: Consideration of Flood Hazards for Activities with Spatial Impact, Recommendations, Federal Office for Water Management, Federal Office for Spatial Planning, Federal Office for the Environment, Forests and Landscape, Biel/Bienne, Switzerland, 1997.
- Losey, S. and Wehrli, A.: Forêt protectrice en Suisse: Du projet SilvaProtect-CH à la forêt protectrice harmonisée, Tech. rep., Confédération Suisse, Office fédéral de l'environnement, Division Prévention des dangers, 2013.
- Lowe, D. G.: Distinctive Image Features from Scale-Invariant Keypoints, *Int J Comput Vision*, 60, 91–110, doi:10.1023/B:VISI.0000029664.99615.94, 2004.
- Ludy, J. and Kondolf, G. M.: Flood risk perception in lands "protected" by 100-year levees, *Nat Hazards*, 61, 829–842, doi:10.1007/s11069-011-0072-6, 2012.
- Lundgren, J.: Alpha shapes, Matlab File Exchange, <http://www.mathworks.com/matlabcentral/fileexchange/28851-alpha-shapes/content/alphavol.m>, 2012.
- Macciotta, R., Martin, C. D., Morgenstern, N. R., and Cruden, D. M.: Quantitative risk assessment of slope hazards along a section of railway in the Canadian Cordillera—a methodology considering the uncertainty in the results, *Landslides*, pp. 1–13, doi:10.1007/s10346-014-0551-4, 2015.
- Mainsant, G., Larose, E., Brönnimann, C., Jongmans, D., Michoud, C., and Jaboyedoff, M.: Ambient seismic noise monitoring of a clay landslide: Toward failure prediction, *J Geophys Res*, 117, doi:10.1029/2011JF002159, f01030, 2012.
- Malamud, B. D., Turcotte, D. L., Guzzetti, F., and Reichenbach, P.: Landslide inventories and their statistical properties, *Earth Surf Processes*, 29, 687–711, doi:10.1002/esp.1064, 2004.
- Marker, B. R.: Land subsidence, in: *Encyclopedia of Natural Hazards*, edited by Bobrowsky, P. T., pp. 583–590, Springer, doi:978-90-481-8699-0, 2013.
- Martius, O., Kunz, M., Nisi, L., and Hering, A.: Conference Report 1st European Hail Workshop, *Meteorol Z*, 24, 441–442, doi:10.1127/metz/2015/0667, 2015.
- Marzocchi, W. and Woo, G.: Principles of volcanic risk metrics: Theory and the case study of Mount Vesuvius and Campi Flegrei, Italy, *Journal of Geophysical Research: Solid Earth*, 114, B03213, doi:10.1029/2008JB005908, 2009.

- Matasci, B., Carrea, D., Abellan, A., Derron, M.-H., Humair, F., Jaboyedoff, M., and Metzger, R.: Geological mapping and fold modeling using Terrestrial Laser Scanning point clouds: application to the Dents-du-Midi limestone massif (Switzerland), *Eur. J. Remote Sens.*, 48, 569–591, doi:10.5721/EuJRS20154832, 2015.
- Mathai, A. M.: *An Introduction to Geometrical Probability: Distributional Aspects with Applications*, Gordon and Breach, Newark, 1999.
- Matsushi, Y. and Matsukura, Y.: Rainfall thresholds for shallow landsliding derived from pressure-head monitoring: cases with permeable and impermeable bedrocks in Boso Peninsula, Japan, *Earth Surf Processes*, 32, 1308–1322, doi:10.1002/esp.1491, 2007.
- Merriam-Webster: Scenario, <http://www.merriam-webster.com/dictionary/scenario>, last access: 22.07.2016.
- Merz, B., Kreibich, H., Thielen, A., and Schmidtke, R.: Estimation uncertainty of direct monetary flood damage to buildings, *Nat Hazard Earth Sys*, 4, 153–163, doi:10.5194/nhess-4-153-2004, 2004.
- meteoradar gmbh: meteoradar.ch, <http://www.meteoradar.ch/de/index.php>, last access: 14.08.2016.
- Meyer, V., Haase, D., and Scheuer, S.: Flood risk assessment in european river basins—concept, methods, and challenges exemplified at the mulde river, *Integr. Environ. Assess. Manag.*, 5, 17–26, doi:10.1897/IEAM_2008-031.1, 2009.
- Michel-Kerjan, E., Hochrainer-Stigler, S., Kunreuther, H., Linnerooth-Bayer, J., Mechler, R., Muir-Wood, R., Ranger, N., Vaziri, P., and Young, M.: Catastrophe Risk Models for Evaluating Disaster Risk Reduction Investments in Developing Countries, *Risk Anal*, pp. no–no, doi:10.1111/j.1539-6924.2012.01928.x, 2012.
- Micheletti, N., Chandler, J. H., and Lane, S. N.: Investigating the geomorphological potential of freely available and accessible structure-from-motion photogrammetry using a smartphone, *Earth Surf Processes*, 40, 473–486, doi:10.1002/esp.3648, 2015.
- Michoud, C., Derron, M.-H., Jaboyedoff, M., Nadim, F., and Leroi, E.: Classification of landslide-inducing anthropogenic activities, in: 5th Canadian Conference on Geotechnique and Natural Hazards, May 15–17, 2011, Kelowna, BC, Canada, 2011.
- Michoud, C., Derron, M.-H., Horton, P., Jaboyedoff, M., Baillifard, F.-J., Loye, A., Nicolet, P., Pedrazzini, A., and Queyrel, A.: Rockfall hazard and risk assessments along roads at a regional scale: example in Swiss Alps, *Nat Hazard Earth Sys*, 12, 615–629, doi:10.5194/nhess-12-615-2012, 2012a.
- Michoud, C., Nicolet, P., Jaboyedoff, M., Larose, E., Mainsant, G., Jongmans, D., and Brönnimann, C.: Glissement de Pont Bourquin: Rapport de synthèse des travaux menés par l'IGAR et ses partenaires de 2006 à 2012, Tech. rep., Universités de Lausanne et Grenoble, Ecole Polytechnique de Lausanne, (In French), 2012b.
- Michoud, C., Carrea, D., Costa, S., Derron, M.-H., Jaboyedoff, M., Delacourt, C., Maquaire, O., Letortu, P., and Davidson, R.: Landslide detection and monitoring capability of boat-based mobile laser scanning along Dieppe coastal cliffs, Normandy, *Landslides*, 12, 403–418, doi:10.1007/s10346-014-0542-5, 2015.
- Microsoft: PMT function, <https://support.office.com/en-us/article/PMT-function-0214DA64-9A63-4996-BC20-214433FA6441>, last access: 4.7.2016, 2016.
- Mignelli, C., Lo Russo, S., and Peila, D.: ROckfall risk MAnagement assessment: the RO.MA. approach, *Nat Hazards*, 62, 1109–1123, doi:10.1007/s11069-012-0137-1, 2012.
- Mikhail, E. M., Bethel, J. M., and McGlone, J. C.: *Introduction to Modern Photogrammetry*, chap. Mathematical concepts in photogrammetry, pp. 80–106, John Wiley & Sons, 2001.
- Monnet, J. M., Clouet, N., Bourrier, F., and Berger, F.: Using geomatics and airborne laser scanning for rockfall risk zoning: a case study in the French Alps, *The 2010 Canadian Geomatics Conference and Symposium of Commission I (ISPRS)*, Calgary Alberta : Canada (2010), 2010.
- Montgomery, D. and Dietrich, W.: A physically based model for the topographic control on shallow landsliding, *Water Resour Res*, 30, 1153–1171, 1994.
- Mooley, D. A.: Applicability of the Poisson Probability Model to the Severe Cyclonic Storms Striking the Coast around the Bay of Bengal, *Sankhyā: The Indian*

- Journal of Statistics, Series B (1960-2002), 43, 187–197, <http://www.jstor.org/stable/25052214>, 1981.
- Morgenroth, J. and Gomez, C.: Assessment of tree structure using a 3D image analysis technique—A proof of concept, *Urban Forestry & Urban Greening*, 13, 198–203, doi:10.1016/j.ufug.2013.10.005, 2014.
- Mueller, R. and Loew, S.: Predisposition and cause of the catastrophic landslides of August 2005 in Brienz (Switzerland), *Swiss J Geosci*, 102, 331–344, doi:10.1007/s00015-009-1315-3, 2009.
- Munich RE: Natural catastrophes 2013: Analyses, assessments, positions, Topics geo 302-08121, Münchener Rückversicherungs-Gesellschaft, <https://www.munichre.com/touch/publications/en/list/catalogue/706265/publication.html>, 2014.
- Nguyen, H., Wiatr, T., Fernández-Steeger, T., Reicherter, K., Rodrigues, D., and Azzam, R.: Landslide hazard and cascading effects following the extreme rainfall event on Madeira Island (February 2010), *Nat Hazards*, 65, 635–652, 2013.
- Niethammer, U., James, M., Rothmund, S., Travalletti, J., and Joswig, M.: UAV-based remote sensing of the Super-Sauze landslide: Evaluation and results, *Engineering Geology*, 128, 2 – 11, doi:10.1016/j.enggeo.2011.03.012, integration of Technologies for Landslide Monitoring and Quantitative Hazard Assessment, 2012.
- OFEV: EconoMe-Light 1.0: Programme d'évaluation en ligne du caractère économique des mesures de protection contre les dangers naturels, User manual, Office fédéral de l'environnement, <http://www.econome.admin.ch/>, last access: 17.09.2016, 2015.
- Oppikofer, T., Jaboyedoff, M., Blikra, L., Derron, M.-H., and Metzger, R.: Characterization and monitoring of the Åknes rockslide using terrestrial laser scanning, *Nat Hazard Earth Sys*, 9, 1003–1019, doi:10.5194/nhess-9-1003-2009, 2009.
- Pack, R., Tarboton, D. G., and Goodwin, C. N.: The SINMAP Approach to Terrain Stability Mapping, in: 8th Congress of the International Association of Engineering Geology, p. 8, Vancouver, British Columbia, Canada, 1998.
- Pantelidis, L.: A critical review of highway slope instability risk assessment systems, *B Eng Geol Environ*, 70, 395–400, doi:10.1007/s10064-010-0328-5, 2011.
- Papathoma-Köhle, M., Kappes, M., Keiler, M., and Glade, T.: Physical vulnerability assessment for alpine hazards: state of the art and future needs, *Nat Hazards*, 58, 645–680, doi:10.1007/s11069-010-9632-4, 2011.
- Parise, M.: A procedure for evaluating the susceptibility to natural and anthropogenic sinkholes, *Georisk: Assessment and Management of Risk for Engineered Systems and Geohazards*, 0, 1–14, doi:10.1080/17499518.2015.1045002, 2015.
- Paté-Cornell, E.: On "Black Swans" and "Perfect Storms": Risk Analysis and Management When Statistics Are Not Enough, *Risk Anal*, 32, 1823–1833, doi:10.1111/j.1539-6924.2011.01787.x, 2012.
- Paukštys, B., Cooper, A. H., and Arustiene, J.: Planning for gypsum geohazards in Lithuania and England, *Eng Geol*, 52, 93 – 103, doi:10.1016/S0013-7952(98)00061-1, 1999.
- Pei, S. and van de Lindt, J.: Methodology for earthquake-induced loss estimation: An application to woodframe buildings, *Structural Safety*, 31, 31–42, doi:<http://dx.doi.org/10.1016/j.strusafe.2007.12.002>, 2009.
- Peila, D. and Guardini, C.: Use of the event tree to assess the risk reduction obtained from rockfall protection devices, *Nat Hazard Earth Sys*, 8, 1441–1450, doi:10.5194/nhess-8-1441-2008, 2008.
- Pfiffner, A. O.: *Geology of the Alps*, Wiley-Blackwell, 2014.
- Pierrot-Deseilligny, M.: Modélisation automatique à partir de photos, in: *Atelier/séminaire Photogrammétrie terrestre*, EDYTEM, <http://edytem.univ-savoie.fr/actualites/atelier-seminaire-photogrammetrie>, 2013.
- Pierrot-Deseilligny, M. and Clery, I.: Apero, an open source bundle adjustment software for automatic calibration and orientation of set of images, in: 4th ISPRS International Workshop 3D-ARCH 2011: "3D Virtual Reconstruction and Visualization of Complex Architectures", Trento, Italy, edited by Remondino, F. and El-Hakim, S., pp. 269–276, 2011.

- Pierson, L. A.: Rockfall Hazard Rating System, Tech. Rep. FHWA-OR-GT-92-05, Oregon Department of Transportation, Salem, 1991.
- Pierson, L. A.: Rockfall Hazard Rating System, in: Rockfall: Characterization and Control, edited by Turner, A. K. and Schuster, R. L., Trans Res Board, Washington, D.C., 2012.
- Pierson, L. A. and Van Vickle, R.: Rockfall Hazard Rating System – Participant’s Manual, Final Report FHWA-SA-93-057, Federal Highway Administration, 1993.
- Pinter, N.: One Step Forward, Two Steps Back on U.S. Floodplains, *Int S Techn Pol Inn*, 308, 207–208, doi:10.1126/science.1108411, 2005.
- Pollefeys, M., Van Gool, L., Vergauwen, M., Verbiest, F., Cornelis, K., Tops, J., and Koch, R.: Visual Modeling with a Hand-Held Camera, *Int J Comput Vision*, 59, 207–232, doi:10.1023/B:VISI.0000025798.50602.3a, 2004.
- Preuth, T., Glade, T., and Demoulin, A.: Stability analysis of a human-influenced landslide in eastern Belgium, *Geomorphology*, 120, 38–47, doi:10.1016/j.geomorph.2009.09.013, landslide geomorphology in a changing environment, 2010.
- Pruppacher, H. R. and Klett, J.: *Microphysics of Clouds and Precipitation*, Springer, 2 edn., 2010.
- Pueyo Anchuela, O., Casas Sainz, A. M., Pocoví Juan, A., and Gil Garbí, H.: Assessing karst hazards in urbanized areas. Case study and methodological considerations in the mantle karst from Zaragoza city (NE Spain), *Eng Geol*, 184, 29 – 42, doi:10.1016/j.enggeo.2014.10.025, 2015.
- Purdy, G.: ISO 31000:2009—Setting a New Standard for Risk Management, *Risk Anal*, 30, 881–886, doi:10.1111/j.1539-6924.2010.01442.x, 2010.
- Raetzo, H. and Rickli, C.: Ereignisanalyse Hochwasser 2005 : Teil 1 – Prozesse, Schäden und erste Einordnung, chap. Rutschungen, pp. 195–210, Bundesamt für Umwelt BAFU, Eidg. Forschungsanstalt WSL, (in German), 2007.
- Raetzo, H., Lateltin, O., Bollinger, D., and Tripet, J. P.: Hazard assessment in Switzerland—Codes of Practice for mass movements, *B Eng Geol Environ*, 61, 263–268, 2002.
- Ragozin, A. and Yolkin, V.: Technique of Quantitative Assessment of Karst Risk on the Local and Regional Levels, in: *Engineering Geology for Infrastructure Planning in Europe: A European Perspective*, edited by Hack, R., Azzam, R., and Charlier, R., no. 104 in *Lecture Notes in Earth Sciences*, Springer, 2004.
- Remondino, F., Spera, M. G., Nocerino, E., Menna, F., and Nex, F.: State of the art in high density image matching, *The Photogrammetric Record*, 29, 144–166, doi:10.1111/phor.12063, 2014.
- Remondo, J., Bonachea, J., and Cendrero, A.: A statistical approach to landslide risk modelling at basin scale: from landslide susceptibility to quantitative risk assessment, *Landslides*, 2, 321–328, doi:10.1007/s10346-005-0016-x, 2005.
- Reynolds, D. W.: Observations of Damaging Hailstorms from Geosynchronous Satellite Digital Data, *Mon Weather Rev*, 108, 337–348, doi:10.1175/1520-0493(1980)108<0337:OODHFG>2.0.CO;2, 1980.
- Rickenmann, D. and Zimmermann, M.: The 1987 debris flows in Switzerland: documentation and analysis, *Geomorphology*, 8, 175–189, doi:10.1016/0169-555X(93)90036-2, 1993.
- Rickli, C., Raetzo, H., McArdell, B., and Presler, J.: Ereignisanalyse Hochwasser 2005 : Teil 2 – Analyse von Prozessen, Massnahmen und Gefahrengrundlagen, chap. Hanginstabilitäten, pp. 97–116, Bundesamt für Umwelt BAFU, Eidg. Forschungsanstalt WSL, 2008.
- Roberds, W.: Estimating temporal and spatial variability and vulnerability, in: *Landslide risk management*, edited by Hungr, O., Fell, R., Couture, R., and Eberhardt, E., pp. 129–157, Taylor and Francis, London, 2005.
- Robert-Diard, P.: Xynthia : l’ancien maire de La Faute-sur-Mer condamné à quatre ans de prison ferme, *Le Monde*, http://www.lemonde.fr/planete/article/2014/12/12/xynthia-l-ancien-maire-de-la-faute-sur-mer-condamne-a-quatre-ans-de-prison-ferme_4539436_3244.html, 2015.
- Robert-Diard, P.: Procès Xynthia : la peine de l’ancien maire allégée en appel, *Le Monde*, http://www.lemonde.fr/police-justice/article/2016/04/05/proces-xynthia-la-peine-de-l-ancien-maire-allegee-en-appel_4895907_1653578.html, 2016.

- Robertson, D. and Cipolla, R.: Structure from motion, in: Practical image processing and computer vision, edited by Varga, M., chap. 13, John Wiley & Sons, 2009.
- Rosa, E. A.: Metatheoretical foundations for post-normal risk, *J Risk Res*, 1, 15–44, doi:[10.1080/136698798377303](https://doi.org/10.1080/136698798377303), 1998.
- Ross, S. M.: A first course in probability, Pearson Education, Inc., 8 edn., 2010.
- Rotach, M., Appenzeller, C., and Albisser, P. E.: Starkniederschlagsereignis August 2005, *Arbeitsberichte 211*, MeteoSchweiz, Zürich, Switzerland, 2006.
- Rouiller, J. D., Jaboyedoff, M., Marro, C., Phlipposian, F., and Mamin, M.: Pentes instables dans le Pennique valaisan. Matterock: une méthodologie d'auscultation des falaises et de détection des éboulements majeurs potentiels, Rapport final du PNR31, VDF Hochschulverlag AG an der ETH Zürich, Zürich, Switzerland, in french, 1998.
- Sampson, C. C., Fewtrell, T. J., Duncan, A., Shaad, K., Horritt, M. S., and Bates, P. D.: Use of terrestrial laser scanning data to drive decimetric resolution urban inundation models, *Advances in Water Resources*, 41, 1 – 17, doi:[10.1016/j.advwatres.2012.02.010](https://doi.org/10.1016/j.advwatres.2012.02.010), 2012.
- Scaioni, M., Feng, T., Lu, P., Qiao, G., Tong, X., Li, R., Barazzetti, L., Previtali, M., and Roncella, R.: Close-Range Photogrammetric Techniques for Deformation Measurement: Applications to Landslides, in: *Modern Technologies for Landslide Monitoring and Prediction*, edited by Scaioni, M., Springer Natural Hazards, pp. 13–41, Springer Berlin Heidelberg, doi:[10.1007/978-3-662-45931-7_2](https://doi.org/10.1007/978-3-662-45931-7_2), 2015.
- Schiesser, H. H.: Hailfall: the relationship between radar measurements and crop damage, *Atmos Res*, 25, 559 – 582, doi:[10.1016/0169-8095\(90\)90038-E](https://doi.org/10.1016/0169-8095(90)90038-E), 1990.
- Schiesser, H. H.: Hagelstürme in der Schweiz: Wiederkehrperioden von schadenbringenden Hagelkorngrößen – eine Abschätzung, Teilprojekt, Zurich, (In German), 2006.
- Schmid, W. and Schiesser, H. H.: Assessment of hail size with radar and lightning data in an operational setting, in: 1st European Hail Workshop, 25–27 June 2014, University of Bern, Switzerland, edited by Romppainen-Martius, O., Kunz, M., Hering, A., Nisi, L., and Germann, U., http://www.oeschger.unibe.ch/events/conferences/hail/presentations/36_Schmid.pdf, 2014.
- Schmid, W., Schiesser, H. H., and Waldvogel, A.: The Kinetic Energy of Hailfalls. Part IV: Patterns of Hailpad and Radar Data, *J Appl Meteorol*, 31, 1165–1178, doi:[10.1175/1520-0450\(1992\)031<1165:TKEOHP>2.0.CO;2](https://doi.org/10.1175/1520-0450(1992)031<1165:TKEOHP>2.0.CO;2), 1992.
- Schmidberger, M., Daniell, J., and Kunz, M.: Hail hazard and hail risk modelling for Germany based on a combination of radar and insurance data, in: 1st European Hail Workshop, 25–27 June 2014, University of Bern, Switzerland, edited by Romppainen-Martius, O., Kunz, M., Hering, A., Nisi, L., and Germann, U., http://www.oeschger.unibe.ch/events/conferences/hail/presentations/14_Schmidberger.pdf, 2014.
- Schuster, S. S., Blong, R. J., and McAneney, K. J.: Relationship between radar-derived hail kinetic energy and damage to insured buildings for severe hailstorms in Eastern Australia, *Atmospheric Research*, 81, 215–235, doi:[10.1016/j.atmosres.2005.12.003](https://doi.org/10.1016/j.atmosres.2005.12.003), 2006.
- Seed, A. W., Srikanthan, R., and Menabde, M.: A space and time model for design storm rainfall, *J Geophys Res-atmos*, 104, 31 623–31 630, doi:[10.1029/1999JD900767](https://doi.org/10.1029/1999JD900767), 1999.
- Seitz, S., Curless, B., Diebel, J., Scharstein, D., and Szeliski, R.: A Comparison and Evaluation of Multi-View Stereo Reconstruction Algorithms, in: 2006 IEEE Computer Society Conference on Computer Vision and Pattern Recognition, vol. 1, pp. 519–528, doi:[10.1109/CVPR.2006.19](https://doi.org/10.1109/CVPR.2006.19), 2006.
- Seitz, S., Curless, B., Diebel, J., Scharstein, D., and Szeliski, R.: Multi-View Stereo Evaluation, <http://vision.middlebury.edu/mview/>, last access: 28.10.2015, 2015.
- Sensefly: <https://www.sensefly.com/about/company-profile.html>, last access: 02.11.2015, 2015.
- SGTK: Datenbeschreibung der geotechnischen, lithologisch-petrographischen Polygone, Tech. rep., Schweizerische Geotechnische Kommission, Zürich, Switzerland, 2012.
- Shi, Y., Jin, S., and Seeland, K.: Modeling business interruption impacts due to disrupted highway network of

- Shifang by the Wenchuan earthquake, *Nat Hazards*, 75, 1731–1745, doi:[10.1007/s11069-014-1391-1](https://doi.org/10.1007/s11069-014-1391-1), 2015.
- Sideris, I., Gabella, M., Erdin, R., and Germann, U.: Real-time radar-raingauge merging using spatiotemporal co-kriging with external drift in the alpine terrain of Switzerland, *Q J Roy Meteor Soc*, In Review, 2013.
- Silva, V., Crowley, H., Pagani, M., Monelli, D., and Pinho, R.: Development of the OpenQuake engine, the Global Earthquake Model's open-source software for seismic risk assessment, *Nat Hazards*, 72, 1409–1427, doi:[10.1007/s11069-013-0618-x](https://doi.org/10.1007/s11069-013-0618-x), 2014.
- Smith, K. and Petley, D. N.: *Environmental hazards: assessing risk and reducing disaster*, Routledge, 2009.
- Snaveley, N., Seitz, S., and Szeliski, R.: Photo tourism: exploring photo collections in 3D, in: *ACM Transactions on Graphics (TOG)*, vol. 25, pp. 835–846, ACM, proceedings of SIGGRAPH 2006, 2006.
- Snaveley, N., Seitz, S., and Szeliski, R.: Modeling the World from Internet Photo Collections, *Int J Comput Vision*, 80, 189–210, doi:[10.1007/s11263-007-0107-3](https://doi.org/10.1007/s11263-007-0107-3), 2008.
- Sornette, D. and Ouillon, G.: Dragon-kings: Mechanisms, statistical methods and empirical evidence, *The European Physical Journal Special Topics*, 205, 1–26, doi:[10.1140/epjst/e2012-01559-5](https://doi.org/10.1140/epjst/e2012-01559-5), 2012.
- Sowers, G. F.: *Building on sinkholes: design and construction of foundations in karst terrain*, ASCE Press, 1996.
- Steck, A., Jean-Luc, E., Escher, A., Gouffon, Y., and Masson, H.: Carte tectonique des Alpes de Suisse occidentale 1:100 000: Notice explicative, no. 123 in *Carte géologique spéciale*, Office Fédéral des Eaux et de la Géologie, (In French), 2001.
- Stein, J. and Stein, S.: Gray swans: comparison of natural and financial hazard assessment and mitigation, *Nat Hazards*, 72, 1279–1297, doi:[10.1007/s11069-012-0388-x](https://doi.org/10.1007/s11069-012-0388-x), 2014.
- Stein, S. and Wysession, M.: *An introduction to seismology, earthquakes and earth structure*, Blackwell Publishing Ltd, 2003.
- Strasser, M., Bonassi, A., Oramas-Dorta, D., De Aguinaga, J., Cheetham, R., Moehrlin, M., Riso, S., and Betz, H.-D.: Hail hazard derived from historic hail footprints; a probabilistic hail storm catalogue for central Europe, in: *EGU General Assembly 2015*, 2015.
- Stucki, M. and Egli, T.: Répertoire de la protection contre la grêle: Recherches sur le danger de grêle et la résistance de l'enveloppe des bâtiments, Rapport de synthèse, Fondation de prévention des Etablissements cantonaux d'assurance, http://praeventionsstiftung.ch/getmedia/0b633c62-cae7-43da-a727-76a284aeeef09/Hagel_f.pdf.aspx, (In French and German), 2007.
- Stumpf, A., Malet, J.-P., Allemand, P., Pierrot-Deseilligny, M., and Skupinski, G.: Ground-based multi-view photogrammetry for the monitoring of landslide deformation and erosion, *Geomorphology*, 231, 130 – 145, doi:[10.1016/j.geomorph.2014.10.039](https://doi.org/10.1016/j.geomorph.2014.10.039), 2015.
- Sturzenegger, M. and Stead, D.: Close-range terrestrial digital photogrammetry and terrestrial laser scanning for discontinuity characterization on rock cuts, *Eng Geol*, 106, 163–182, doi:[10.1016/j.enggeo.2009.03.004](https://doi.org/10.1016/j.enggeo.2009.03.004), 2009.
- Suresh, K.: Volume of a surface triangulation, *Matlab File Exchange*, <http://www.mathworks.com/matlabcentral/fileexchange/26982-volume-of-a-surface-triangulation/content/stlVolume.m>, 2010.
- Swiss Post: Address and geodata: Up-to-date reference data for correcting your addresses, <https://www.post.ch/en/business/a-z-of-subjects/maintaining-addresses-and-using-geodata/address-and-geodata>, 2016.
- Swiss Re: Natural catastrophes and man-made disasters in 2014: convective and winter storms generate most losses, sigma 2/2015, Swiss Re, http://media.swissre.com/documents/sigma2_2015_en_final.pdf, 2015.
- swisstopo: swissTLM3D 1.4, http://www.toposhop.admin.ch/en/shop/products/landscape/tlm3d_1, last access: 14.08.2016, 2015.
- Taleb, N. N.: *The Black Swan: The Impact of the Highly Improbable*, Random House and Penguin, 2007.
- Tarolli, P., Borga, M., Chang, K.-T., and Chiang, S.-H.: Modeling shallow landsliding susceptibility by incorporating heavy rainfall statistical properties, *Geomorphology*, 133, 199–211,

- doi:[10.1016/j.geomorph.2011.02.033](https://doi.org/10.1016/j.geomorph.2011.02.033), special issue: Modelling land dynamics in mountainous watersheds, 2011.
- Taylor, F. E., Santangelo, M., Marchesini, I., and Malamud, B. D.: A GRASS GIS Semi-Stochastic Model for Evaluating the Probability of Landslides Impacting Road Networks in Collazzone, Central Italy, in: EGU General Assembly 2013, Vienna, Austria, EGU2013-7624, 2013.
- Telesca, L., Cuomo, V., Lapenna, V., and Macchiato, M.: Identifying space–time clustering properties of the 1983–1997 Irpinia–Basilicata (Southern Italy) seismicity, *Tectonophysics*, 330, 93–102, doi:[10.1016/S0040-1951\(00\)00221-3](https://doi.org/10.1016/S0040-1951(00)00221-3), 2001.
- Terpstra, T. and Gutteling, J. M.: Households' Perceived Responsibilities in Flood Risk Management in The Netherlands, *Int J Water Resour D*, 24, 555–565, doi:[10.1080/07900620801923385](https://doi.org/10.1080/07900620801923385), 2008.
- Tihansky, A. B.: Sinkholes, west-central Florida, in: Land subsidence in the United States, edited by Galloway, D., Jones, D. R., and Ingebritsen, S., vol. 1182, pp. 121–140, U.S. Geological Survey, 1999.
- Tolmachev, V. and Leonenko, M.: Experience in Collapse Risk Assessment of Building on Covered Karst Landscapes in Russia, in: *Karst Management*, edited by Beynen, P. E., pp. 75–102, Springer Netherlands, doi:[10.1007/978-94-007-1207-2_4](https://doi.org/10.1007/978-94-007-1207-2_4), 2011.
- Triggs, B., McLauchlan, P., Hartley, R., and Fitzgibbon, A.: Bundle Adjustment—A Modern Synthesis, in: *Vision Algorithms: Theory and Practice*, edited by Triggs, B., Zisserman, A., and Szeliski, R., vol. 1883 of *Lecture Notes in Computer Science*, pp. 298–372, Springer Berlin Heidelberg, doi:[10.1007/3-540-44480-7_21](https://doi.org/10.1007/3-540-44480-7_21), 2000.
- Trümpy, R.: *Geology of Switzerland, Part A: An outline of the geology of Switzerland*, Wepf & Co. Verlag, 1980.
- Turcotte, D. L.: Self-organized criticality, *Rep Prog Phys*, 62, 1377, <http://stacks.iop.org/0034-4885/62/i=10/a=201>, 1999.
- UDN: *Cartographie des dangers naturels*, Vademecum, Canton de Vaud, Direction générale de l'environnement, Unité des dangers naturels, 2014.
- UNISDR: 2009 UNISDR Terminology on Disaster Risk Reduction, Geneva, <https://www.unisdr.org/we/inform/terminology>, 2009.
- University of Bern, G. and FOWG, F.: *Geological Map of Switzerland 1:500 000*, ISBN 3-906723-39-9, 2005a.
- University of Bern, G. and FOWG, F.: *Tectonic Map of Switzerland 1:500 000*, ISBN 3-906723-56-9, 2005b.
- Uzielli, M., Lacasse, S., and Nadim, F.: Probabilistic risk estimation for geohazards: a simulation approach, in: *Geotechnical Risk and Safety: Proceedings of the 2nd International Symposium on Geotechnical Safety and Risk*, Gifu, Japan, 11–12 June 2009, edited by Honjo, Y., Suzuki, M., Hara, T., and Zhang, F., pp. 355–362, CRC Press/Balkema, 2009.
- Valley, B., Thuro, K., Eberhardt, E., and Raetz, H.: Geological and geotechnical investigation of a shallow translational slide along a weathered rock/soil contact for the purpose of model development and hazard assessment, in: *Proceedings of the 9th International Symposium on Landslides, Rio de Janeiro*, edited by Lacerda, W. A., Ehrlich, M., Fontoura, S. A. B., and Sayão, A. S. F., pp. 385–391, A. A. Balkema, 2004.
- van Westen, C., van Asch, T., and Soeters, R.: Landslide hazard and risk zonation—why is it still so difficult?, *B Eng Geol Environ*, 65, 167–184, doi:[10.1007/s10064-005-0023-0](https://doi.org/10.1007/s10064-005-0023-0), 2006.
- Van Westen, C. J., Castellanos, E., and Kuriakose, S. L.: Spatial data for landslide susceptibility, hazard, and vulnerability assessment: An overview, *Eng Geol*, 102, 112–131, doi:[10.1016/j.enggeo.2008.03.010](https://doi.org/10.1016/j.enggeo.2008.03.010), special issue: "Landslide Susceptibility, Hazard and Risk Zoning for Land Use Planning", 2008.
- Ventsel, H.: *Théorie des probabilités*, Editions MIR, Moscou, 1973.
- von Ruette, J., Papritz, A., Lehmann, P., Rickli, C., and Or, D.: Spatial statistical modeling of shallow landslides—Validating predictions for different landslide inventories and rainfall events, *Geomorphology*, 133, 11–22, doi:[10.1016/j.geomorph.2011.06.010](https://doi.org/10.1016/j.geomorph.2011.06.010), 2011.
- Voumard, J., Caspar, O., Derron, M.-H., and Jaboyedoff, M.: Dynamic risk simulation to assess natural hazards risk along roads, *Nat Hazard Earth Sys*, 13, 2763–2777, doi:[10.5194/nhess-13-2763-2013](https://doi.org/10.5194/nhess-13-2763-2013), 2013.

- Voumard, J., Derron, M.-H., Jaboyedoff, M., and Andres, N.: Minor landslides and floods events affecting transportation network in Switzerland, preliminary results, in: *Landslides and Engineered Slopes – Experience, Theory and Practice*, edited by Aversa, S., Cascini, L., Picarelli, L., and Scavia, C., vol. 3, pp. 217–232, Associazione Geotecnica Italiana, Rome, Italy, CRC Press/Balkema, 2016.
- Waldvogel, A., Federer, B., and Grimm, P.: Criteria for the Detection of Hail Cells, *J Appl Meteorol*, 18, 1521–1525, doi:10.1175/1520-0450(1979)018<1521:CFTDOH>2.0.CO;2, 1979.
- Wallace, L., Lucieer, A., Watson, C., and Turner, D.: Development of a UAV-LiDAR System with Application to Forest Inventory, *Remote Sensing*, 4, 1519–1543, doi:10.3390/rs4061519, 2012.
- Wang, X., Frattini, P., Crosta, G., Zhang, L., Agliardi, F., Lari, S., and Yang, Z.: Uncertainty assessment in quantitative rockfall risk assessment, *Landslides*, 11, 711–722, doi:10.1007/s10346-013-0447-8, 2014.
- Ward, P. J., de Moel, H., and Aerts, J. C. J. H.: How are flood risk estimates affected by the choice of return-periods?, *Nat Hazard Earth Sys*, 11, 3181–3195, doi:10.5194/nhess-11-3181-2011, 2011.
- Weisstein, E. W.: Clean Tile Problem, <http://mathworld.wolfram.com/CleanTileProblem.html>, 2013.
- Werther, G. F. A.: When Black Swans Aren't: On Better Recognition, Assessment, and Forecasting of Large Scale, Large Impact, and Rare Event Change, *Risk Management and Insurance Review*, 16, 1–23, doi:10.1111/rmir.12000, 2013.
- Whittaker, K. A. and McShane, D.: Comparison of slope instability screening tools following a large storm event and application to forest management and policy, *Geomorphology*, 145–146, 115–122, doi:10.1016/j.geomorph.2012.01.001, 2012.
- Wieczorek: Landslide Triggering Mechanisms, in: *Landslides Investigation and Mitigation*, edited by Turner, A. K. and Schuster, R. L., Special Report 247, pp. 76–90, Transportation Research Board, National Research Council, National Academy Press, Washington, DC, 1996.
- Winkler, C.: 'En Courlaz', Commune de Chardonne, Risikobeurteilung, Beratung Kanton Waadt, Tech. rep., Natur.Ing, Brig-Glis, 2010.
- Wong, H. N., Ho, K., and Chan, Y. C.: Assessment of consequences of landslides, in: *Landslide risk assessment : proceedings of the International Workshop on Landslide Risk Assessment*, Honolulu, Hawaii, USA, 19–21 February 1997, edited by Cruden, D. M. and Fell, R., pp. 111–149, Balkema, 1997.
- WSL: Swiss flood and landslide damage database, http://www.wsl.ch/fe/gebirgshydrologie/HEX/projekte/schadendatenbank/index_EN, last access: 26.02.2013, 2012.
- WSL, Egli Engineering AG, GEOTEST SA, and B,S,S. Volkswirtschaftliche Beratung: Prevent-Building, une méthode et un outil d'évaluation de l'efficacité, de la rentabilité et de l'acceptabilité des mesures de protection des bâtiments, destinés à parer aux risques naturels gravitationnels et météorologiques, Tech. rep., Fondation de prévention des établissements cantonaux d'assurance, 2014.
- Wu, C.: SiftGPU: A GPU implementation of Scale Invariant Feature Transform (SIFT), <http://cs.unc.edu/~ccwu/siftgpu>, last access: 28.10.2015, 2007.
- Wu, C.: Critical Configurations For Radial Distortion Self-Calibration, in: *IEEE Conference on Computer Vision and Pattern Recognition 2014*, 2014.
- Wu, C.: VisualSFM : A Visual Structure from Motion System, <http://ccwu.me/vsfm/index.html>, (last access: 14.11.2015), 2015.
- Wüest, M., Frei, C., Altenhoff, A., Hagen, M., Litschi, M., and Schär, C.: A gridded hourly precipitation dataset for Switzerland using rain-gauge analysis and radar-based disaggregation, *Int J Climatol*, 30, 1764–1775, 2010.
- Yilmaz, I., Marschalko, M., and Bednarik, M.: Gypsum collapse hazards and importance of hazard mapping, *Carbonate Evaporite*, 26, 193–209, doi:10.1007/s13146-011-0055-4, 2011.
- Yu, F.-C., Chen, T.-C., Lin, M.-L., Chen, C.-Y., and Yu, W.-H.: Landslides and Rainfall Characteristics Analysis in Taipei City during the Typhoon Nari Event, *Nat*

Hazards, 37, 153–167, doi:[10.1007/s11069-005-4661-0](https://doi.org/10.1007/s11069-005-4661-0), 2006.

Zischg, A., Fuchs, S., Keiler, M., and Stötter, J.: Temporal variability of damage potential on roads as a conceptual contribution towards a short-term avalanche risk simulation, *Nat Hazard Earth Sys*, 5, 235–242, doi:[10.5194/nhess-5-235-2005](https://doi.org/10.5194/nhess-5-235-2005), 2005.

Appendices

Appendix A

Rockfall hazard and risk assessments along roads at a regional scale: example in Swiss Alps

Michoud, C., Derron, M.-H., Horton, P., Jaboyedoff, M., Baillifard, F.-J., Loye, A., Nicolet, P., Pedrazzini, A., and Queyrel, A.: Rockfall hazard and risk assessments along roads at a regional scale: example in Swiss Alps, *Nat Hazard Earth Sys*, 12, 615–629, doi:[10.5194/nhess-12-615-2012](https://doi.org/10.5194/nhess-12-615-2012), 2012.



Rockfall hazard and risk assessments along roads at a regional scale: example in Swiss Alps

C. Michoud¹, M.-H. Derron¹, P. Horton¹, M. Jaboyedoff¹, F.-J. Baillifard², A. Loye¹, P. Nicolet¹, A. Pedrazzini¹, and A. Queyrel³

¹Institute of Geomatics and Risk Analysis, University of Lausanne, Lausanne, Switzerland

²Security service, Bagnes municipality, Switzerland

³Ecole des Mines d'Alès, Alès, France

Correspondence to: C. Michoud (clement.michoud@unil.ch)

Received: 17 February 2011 – Revised: 27 January 2012 – Accepted: 2 February 2012 – Published: 14 March 2012

Abstract. Unlike fragmental rockfall runout assessments, there are only few robust methods to quantify rock-mass-failure susceptibilities at regional scale. A detailed slope angle analysis of recent Digital Elevation Models (DEM) can be used to detect potential rockfall source areas, thanks to the Slope Angle Distribution procedure. However, this method does not provide any information on block-release frequencies inside identified areas. The present paper adds to the Slope Angle Distribution of cliffs unit its normalized cumulative distribution function. This improvement is assimilated to a quantitative weighting of slope angles, introducing rock-mass-failure susceptibilities inside rockfall source areas previously detected. Then rockfall runout assessment is performed using the GIS- and process-based software Flow-R, providing relative frequencies for runout. Thus, taking into consideration both susceptibility results, this approach can be used to establish, after calibration, hazard and risk maps at regional scale. As an example, a risk analysis of vehicle traffic exposed to rockfalls is performed along the main roads of the Swiss alpine valley of Bagnes.

Cascini, 2008; Jaboyedoff et al., 2012). The field of propagation modeling is under fast development, aiming to compute runout probabilities with empirical, process-based and GIS-based models (Dorren, 2003; Volkwein et al., 2011), such as CONEFALL (Jaboyedoff and Labiouse, 2011), Rockyfor3D (Dorren, 2011), HY-STONE (Crosta et al., 2004) or ILWIS (van Dijke and van Westen, 1990). However, there are not yet robust and objective methods to detect source areas at a regional scale and quantify rock-mass-failure mean susceptibilities. In the present work, the authors intend to provide information about susceptibility indicators on potential rockfall source areas.

Rockfall is very likely to be found in steep slopes (Heim, 1932; Hoek and Bray, 1981; Crosta and Agliardi, 2003; Dorren, 2003). From a basic approach, unstable rock slopes can be delimited through the steepness of the topography. It can be done with a simple method of slope angle threshold, which can be defined from distinctive evidence (i.e. cliffs lying above scree deposits, fieldworks or historical events) when it is not arbitrary defined (Toppe, 1987; Dorren and Seijmonsbergen, 2003; Guzzetti et al., 2003; Jaboyedoff and Labiouse, 2003; Frattini et al., 2008).

Furthermore, several authors showed supplementary conditions influencing rock slope stability (Terzaghi, 1950, 1962; Bieniawski, 1976; Selby, 1982; Willie and Mah, 2004; Jaboyedoff and Derron, 2005), classified in internal parameters (IP, i.e. lithological, geo-mechanical and structural settings) and external factors (EF, e.g. active tectonic, water infiltration, weathering, etc.). Therefore, more complex models have been developed integrating these conditions to enhance the source detection at regional scale. They introduced rating systems following empirical multi-criteria

1 Introduction

Mountain roads are frequently exposed to fragmental rockfalls (Piteau and Peckover, 1978; Budetta, 2004), involving independent blocks of relatively small sizes characterized by high energy and mobility (Whalley, 1984; Willie and Mah, 2004). Recent advances of high resolution Digital Elevation Models (HRDEM) combined with Geographical Information System (GIS) technologies have made rockfall susceptibility mapping possible (Willie and Mah, 2004; Derron et al., 2005;

observations (Pierson et al., 1990; Baillifard et al., 2003), structural settings and kinematics analysis (Wagner et al., 1988; Jaboyedoff et al., 1999; Gokceoglu et al., 2000; Günther, 2003), safety factor computations (Hoek and Bray, 1981), or joining IP and EF conditions (Günther et al., 2004; Oppikofer et al., 2007).

But, all these methods obviously depend on the possibility of collecting a lot of complex and reliable information on the area of interest. For example, the simplified Rockfall Hazard Rating System method (Pierson et al., 1990; Budetta, 2004) requires eleven parameters per outcrop as an input to estimate the rockfall susceptibility along a road. Moreover, these methods usually use very high resolution datasets that are not often available at regional scale. For instance, Günther (2003) applied his model SLOPEMAP to extract structural features of the hard rock terrain using a 5×5 m DEM pixel size for a study area of 2.5 km^2 , which is inappropriate when only 10×10 up to 30×30 m DEM pixel sizes are available at regional scale. These methods require too high resolution information and too many parameters to be practically and rapidly applied on fairly large areas.

However, strong correlations between topography and earth surface processes have been suggested for many years (Powel, 1876 and Gilbert, 1877, cited in Montgomery and Brandon, 2002; Strahler, 1954). The terrain morphology reflects the compounded influence of these internal settings (Locat et al., 2000). Hence, Rouiller et al. (1998) and then Loye et al. (2009) proposed the Slope Angle Distribution (SAD) procedure to use the topography as a proxy to detect potential source locations. The next step is to assess the susceptibility level of rockfall release of the potential source locations previously detected. Therefore, this paper proposes to improve the SAD procedure by linking the cumulative distribution function of the slope angle to quantitative block release susceptibility.

The Flow-R software (Horton et al., 2008; Blahut et al., 2010; Kappes et al., 2011) is used to compute rockfall runout areas. It assesses propagations thanks to an open choice of algorithms and parameters of probabilistic spreading and basic energy balance, such as a multiple flow direction model (Holmgren, 1994) coupled with an inertial factor (Gamma, 2000) and a maximum runout distance based on a Coulomb friction model. Moreover, since Horton et al. (2008), the model has been modified to take into account the susceptibilities of block releases in the resulting spreading.

Finally, this improved methodology allows us to draw rockfall susceptibility maps. Then, after a calibration based on available rockfall inventories, hazard maps can be obtained, taking into consideration both relative frequencies of block release and propagation (Jaboyedoff et al., 2005; Corominas and Moya, 2008). Indeed, the hazard is always a challenging parameter to estimate in a Quantitative Risk Assessment (QRA) (Corominas et al., 2005).

As an example of the applicability of this procedure, the risk of fragmental rockfalls to vehicle traffic along the main



Fig. 1. Photography of a rockfalls event in 2006 that reached twice the road section near Le Plamproz, in the Bagnes Valley.

roads of the Swiss Alpine valley of Bagnes (Fig. 1) is assessed and expressed in terms of number of direct impacts per year of blocks on vehicles.

2 Methodology

2.1 Detection of sources areas

2.1.1 Slope Angle Distribution procedure

Strahler's law of constancy of slopes (Strahler, 1950) tells that the morphology of a slope topography tends to group predominantly around several mean slope angle values that are normally distributed with low dispersion. These particular slope angles of convergence can be often related to the most frequently encountered four major morphological units (Oppikofer et al., 2007; Loye et al., 2009):

- Plains formed by fluvio-glacial deposit; these correspond to the set of low slope angles;
- Bottom parts of the valley flanks comprising alluvial fans related to debris flow deposits and landslides mass. These correspond to the set of foot slopes angles;
- Talus slopes and valley sides (flank) covered by till, screes and debris mantles as well as rocky outcrops lightly covered with soil. These correspond to the set of steep slopes angles;
- Cliffs and rock faces corresponding to the very steep sets of slope angles.

Hence, the morphology of a terrain displays characteristic slope angles that can be directly related to the geomorphic

processes involved in slope stability. Rockfall source areas are commonly found in the steepest morphological units.

Based on these statements, Rouiller et al. (1998) and then Loye et al. (2009) have established a DEM-based geomorphometric approach to detect these morphological units and therefore rockfall source areas, named the Slope Angle Distribution (SAD) procedure. The classification is done by computing the Slope Angle Frequency Distribution (SAFD) of the study area, the frequency being normalized considering their real surface of occurrence. The SAFD is then decomposed into several Normal distributions f :

$$f(s) = w \cdot \frac{1}{\sigma\sqrt{2\pi}} \cdot \exp\left[-\frac{1}{2} \cdot \left(\frac{s - m_c}{\sigma}\right)^2\right] \quad (1)$$

where f is the normal probability distribution function (PDF) of the slope angle value s included within the interval $[0;90]$, σ its standard deviation, m_c its mean value (Kreyzig, 2006) and w a weighting factor which is linked to the proportions between unit surfaces inside study areas. The sum of these theoretical normal curves has to rebuild the real SAFD (Fig. 2a).

The above-mentioned sets of morphological units do not always exist in the study area; the number of normal curves is therefore given according to the number of morphological units present in the area of interest (as detailed in Loye et al., 2009). Moreover, in some cases (Fig. 3a), the distribution of the slope angles of cliffs units has to be decomposed into two normal functions f_1 and f_2 . This can be caused by the topography itself (potential high dispersion of this unit that possibly exists from 45° to 90°) or by the extent of the support (limits of the study domain). In theory, it could be divided into more than two distributions; but in our experience, two distributions are sufficient. Then, the total distribution f_i of cliffs units is simply defined as the sum of f_1 and f_2 :

$$f_i(s) = f_1(s) + f_2(s) \quad (2)$$

Technically, the input values for the initial normal distributions are defined according to the local maximum and minimum that can be visually identified along the SAFD. The fitting process is performed by minimizing the error between the most-likely sets of normal curves and the target function (namely the SAFD) using a simplex optimization solver. The morphological units are then delimited finally according to the sets of normal Slope Angle Distribution, where a normal curve becomes dominant over the others. An example of classified slope steepness map is shown in Fig. 4. The cliffs morphological unit f_i is then considered as the potential rockfall sources areas.

Finally, considering that the local morphology of an Alpine valley is partly controlled by structural settings and rock-mass properties (Terzaghi, 1962; Selby, 1982; Willie and Mah, 2004), different lithological and tectonic units have to be considered in order to refine the morphological analysis. Therefore, the study area is classified in homogeneous

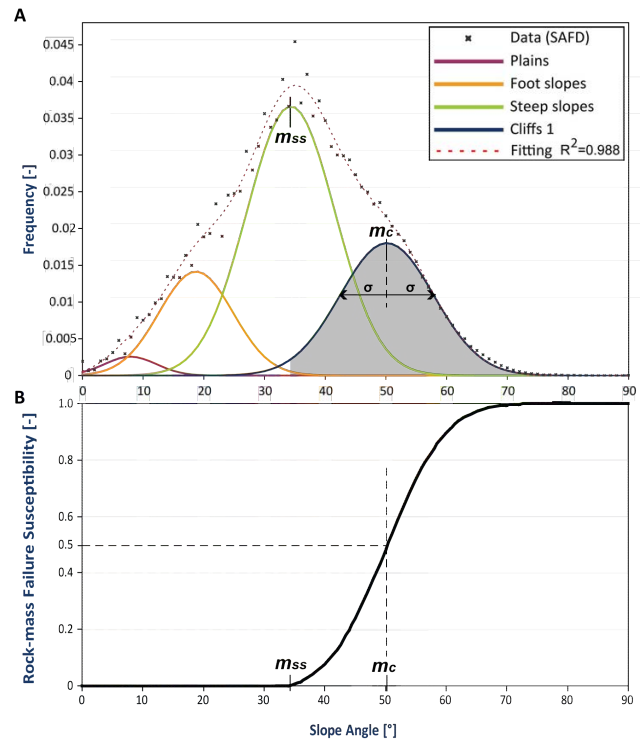


Fig. 2. (A) Normal distributions of the slope angles of the granitoids HMA in the Bagnes Valley, extracted from a 10 m-DEM. Three parameters are used to detect potential rockfall source areas: m_c which is the mean angle of the cliffs distribution and σ its standard deviation; m_{ss} which is the mean angle of the steep slopes distribution. In this case, cliffs units are decomposed in only one normal distribution. (B) Normalized cumulative distribution function (F_n) for the cliffs units, assimilated to a quantitative weighting of potential rockfall source areas, i.e. to a rock-mass-failure susceptibility. The mean angle of the steep slopes distribution m_{ss} is used as a first threshold to exclude lower values as potential rockfall source areas.

morphotectonic areas (HMA), following similar lithological characteristic rock mass structure and geomorphic activity, and one SAD procedure has to be done for each HMA.

To sum up, the SAD is a systematic approach to extract a slope angle lower threshold for each HMA, corresponding to the limit between the steep slopes and cliffs normal distributions. This procedure leads to Boolean results (i.e. in/out cliffs units) and cells included inside these cliffs areas are considered as potential sources of fragmental rockfalls.

2.1.2 Refinement of the Slope Angle Distribution

As stated in the introduction, taking into account all internal parameters and external factors can require too high resolution dataset and too many parameters to be applied on a fairly regional scale in order to precisely detect and rate potential rockfall source areas. But as topographies are strongly correlated with internal rock settings (Locat et al., 2000) and

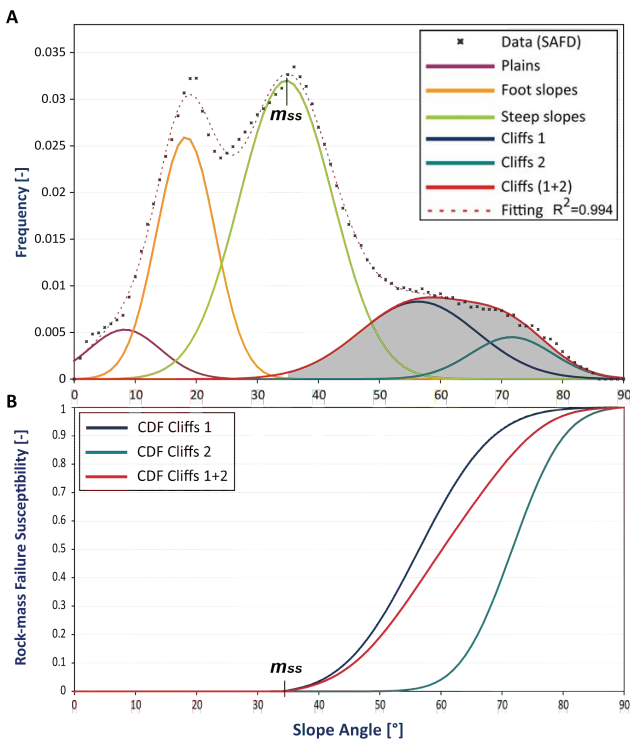


Fig. 3. (A) Normal distributions of the slope angles of the marbles HMA in the Bagnes Valley. Here, cliffs are decomposed in two normal distributions. (B) The normalized cumulative distribution function (F_n) of the sum of the two cliffs distributions (f_i) is shown by the red line. In comparison, the normalized cumulative distribution functions for the two cliffs distributions are shown in blue (f_1) and cyan (f_2).

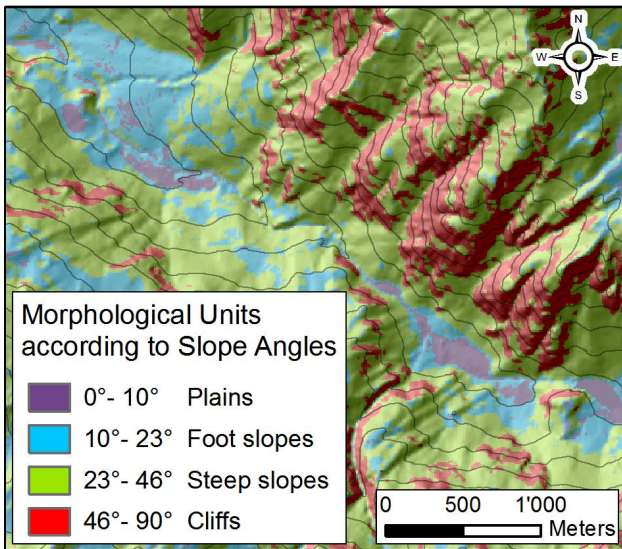


Fig. 4. Example of main morphological units in a region of the Bagnes valley according to slope angle thresholds got thanks to the SAD procedure. (Hillshade and 10 m isohypses: ©2008 swisstopo).



Fig. 5. Theoretical computation of rockfall runouts from two source areas on a DEM grid. These relative frequencies (numbers in the green and blue cells) of rockfall propagations take into account (1) the initial rock-mass-failure susceptibilities (numbers in the orange cells) and (2) the integration of all computed propagations with probabilistic spreading algorithms. The maximum runout distance is reached when the simple Coulomb friction model becomes zero.

Earth surface processes (Montgomery and Brandon, 2002), we assume that for large areas, the block release susceptibility is a function of slope angles. Thus, improving the SAD approach, this paper aims to link the cumulative distribution functions of slope angles of cliffs units to rock-mass-failure susceptibility inside rockfall source areas previously identified.

The explanations below will illustrate only the situation where cliffs units are decomposed in two distributions (Eq. 2). When it is not the case, f_i is equal to f_1 . The associated cumulative distribution function F of cliffs distribution is defined by:

$$F(\beta) = \int_0^\beta f_i(s) \cdot ds \quad (3)$$

where s and β are two slope angle values included within the interval $[0;90]$. By definition, Eq. (3) gives the probability that a slope angle s is lower than β (Kreyzig, 2006). Therefore, it is by extension assimilated to a quantitative block release susceptibility. Moreover, the mean value of the steep slopes distribution m_{ss} , extracted from the SAD procedure (Figs. 2a and 3a), relates to an apparent equilibrium slope angle of scree deposits (usually around 35°, that mainly compose steep slopes units). Thus, for higher slope angle values than m_{ss} , blocks can be mobilized; on the contrary, for lower slope angle values, blocks are not considered. As a consequence, m_{ss} is used as a lower threshold to exclude areas

not steep enough to be potential source of rockfalls. Thus, Eq. (3) has to be cutoff by m_{ss} and then normalized for slope angle values higher than m_{ss} ; the final cumulative function F_n is shown in Figs. 2b and 3b and defined by:

$$\begin{cases} \forall \beta \in [0 ; m_{ss}[\Rightarrow F_n(\beta) = 0 \\ \forall \beta \in [m_{ss} ; 90[\Rightarrow F_n(\beta) = \frac{F(\beta) - F(m_{ss})}{F(90) - F(m_{ss})} \end{cases} \quad (4)$$

The normalized cumulative distribution function F_n can be assimilated to a quantitative weighting of potential rockfall source areas, i.e. a rock-mass-failure susceptibility indicator (Fig. 7), identified according to the slope angles and the SAD procedures.

2.2 Runout assessment

Many tools have been developed to calculate runout areas of rolling, bouncing or falling blocks (Ritchie, 1963) and have been reviewed by Dorren (2003). In this study, the runout simulation is computed by the Flow-R software (Horton et al., 2008). The propagation is assessed by means of a probabilistic spreading and a basic energy balance, controlling respectively the lateral extent and the runout distance, merging several models and approaches. Everything is processed at the cell level and iterated on the DEM grid according to the propagation direction. This study is the first to use the Flow-R software for rockfall runout assessment. Thanks to the open choice of algorithms and parameters, it has been possible to parameterize the model according to our needs at regional scale. The model has also been modified to take into account the susceptibilities of the sources (calibrated on the base of F_n) in the resulting spreading, which is a step further in the frequency analysis. It allows us to approach the hazard frequency of a location more consistently than before by relating it to the source susceptibilities.

2.2.1 Probabilistic spreading

Probabilistic spreading is based on flow direction algorithms that process the probability of a cell to flow to its neighbors (Horton et al., 2008). The probability is integrated in a continuous way, meaning every neighboring cell having a non-null probability will be propagated further. Flow direction algorithms, that are the basis of the spreading, portion the probabilities according to the slope of the surrounding cells.

Fairfield and Leymarie (1991) have introduced the multiple flow direction algorithm as a stochastic method which gives a probability to every cell with a descending slope. Then Holmgren (1994) has suggested a variation of this method by introducing the exponent α on the slope gradient:

$$\forall \begin{cases} \tan \beta_i > 0 \\ \alpha \in [1; +\infty[\end{cases} \Rightarrow P_f(x) = \frac{(\tan \beta_i)^\alpha}{\sum_{j=1}^8 (\tan \beta_j)^\alpha} \quad (5)$$

where i, j are the flow directions, P_f is the probability proportion in direction i , $\tan \beta_i$ is the slope gradient between the

central cell and cell in direction i , and α is the exponent to calibrate.

The exponent α allows us to better control the spreading extent from the multiple flow direction algorithm. When $\alpha = 1$, Eq. (5) is equivalent to the multiple flow direction algorithm (Fairfield and Leymarie, 1991), and when $\alpha \rightarrow \infty$ to the D8 algorithm (propagation following only the steepest slope: O'Callaghan and Mark, 1984; Jensen and Domingue, 1988).

In addition to the flow direction algorithm, a persistence factor was introduced as in Gamma (2000), which is a weighting of the probability according to a direction change. The chosen values are the same as Gamma (2000), i.e. 1 when there is no change in direction and 2/3 in any other case. The role of this persistence factor is to take into consideration the inertia according to the previous directions of the moving blocks which can therefore deviate from the steepest paths.

2.2.2 Runout distance

The runout distance is assessed thanks to a basic energy balance including the potential and kinetic energy components and an energy loss function. As the source mass is unknown, the energy balance is processed on a unit mass. For the energy loss function, a simple Coulomb friction model (with a single friction coefficient) was used:

$$\Delta E_{\text{loss}} = g \times \Delta x \times \mu \quad (6)$$

where Δx is the increment of horizontal displacement, g the gravity acceleration and μ is the tangent of the friction angle. To this algorithm, we can add an upper threshold to limit the velocity of blocks or an equivalent kinetic energy (Horton et al., 2008). Then, the maximum runout distance is reached when the energy becomes zero, i.e. when the initial potential energy has been completely lost by friction.

2.2.3 Results in Flow-R

Flow-R can be used now to draw maps of relative frequencies of rockfall using: (1) the spreading probability based on a multiple flow algorithm including an inertial factor, and (2) the maximum runout distance based on a Coulomb friction model. Finally, Flow-R provides for each cell of the DEM the integration of relative frequencies, function of (1) the initial rock-mass-failure susceptibilities F_n of onset cells and (2) of all computed rockfall propagations P_f which can be superimposed (Fig. 5).

2.3 Rockfall quantitative hazard mapping along roads

The hazard H is the mean frequency of occurrence at a punctual location x of a defined phenomenon of magnitude equal or greater than E per year, i.e. the multiplication of a rock-mass-failure mean frequency and a probability (P_f) of

Table 1. Parameters used to assess rockfall hazard and risks along roads. Bold typo: input parameters needed to solve equations; normal typo: intermediary or final results solved during the assessment; italic typo: useless parameters because deleted during the equations' simplifications.

Acronym	Complete appellation
α	Exponent in the Holmgren's (1994) expression
d	Diameter of blocks considered
l	Mean length of the car
m_c	Mean values of cliffs distributions
m_{ss}	Mean values of steep slopes distributions
μ	Friction angle of the runout energy calculation
N_b	Number of rockfall events inventoried along road section
s and β	Slope angle values
σ	Standard deviations of cliffs distributions
T	Traffic per time period t_c
t_i	Time period of the inventory
v	Mean velocity
w	Weighting factor of normal distribution function
x_{rs}	Road section's cells locations
f, f_1, f_2 and f_t	Normal distribution function
F	Cumulative distribution function
F_n	Normalized F: rock-mass-failure susceptibility
H	Hazard
k	Calibration factor of hazard
R	Risk
E	<i>Magnitude of the rockfall event (function of d)</i>
Exp	<i>Exposure</i>
g	<i>Terrestrial acceleration</i>
i and j	<i>Flow directions in the Holmgren's (1994) expression</i>
L	<i>Mean length of the road within a pixel</i>
N_c	<i>Total number of vehicles during t_c</i>
P_{cell}	<i>Probability of a car to be hit inside a pixel</i>
P_f	<i>Relative frequency of propagation (in the Flow-R's results)</i>
t_c	<i>Considered period of time in the Risk equation</i>
x	<i>Punctual location</i>
x_p	<i>Pixel location</i>
Δx	<i>Increment of horizontal displacements in the friction model</i>

propagation (Leroi, 1996; Fell et al., 2005, 2008; Jaboyedoff et al., 2005; Volkwein et al., 2011).

However, the rock-mass-release susceptibilities F_n extracted from the improved SAD approach are relative to the slope angles and are not absolute numbers. Moreover, the frequencies of propagations P_f are assessed by Flow-R based on a unit mass and no different magnitudes of events (i.e. blocks volumes) can be considered. As a consequence, Flow-R results (namely F_n multiplied by P_f) have to be calibrated to adjust the hazard by a factor k which is a calibration term that links these results with observed events per year for a given magnitude:

$$H(E, x_p) = k(E) \times F_n \times P_f(x_p) \quad (7)$$

In Eq. (7), the rockfall hazard H (number of event per year) for a magnitude E is defined for a period of reference t_i at

a cell x_p and is equal to the product of rock-mass failure susceptibilities F_n times frequencies of propagation P_f up to a cell x_p and times a calibrating factor k , that depends on E .

This coefficient k depends on a known number of rockfall events with a given magnitude E in a cell x_p . However, in a context of rockfall studies along corridors, exact positions of impacts are unknown. For practical issues, inventories are frequently made along road sections. On a DEM, a road section is composed of a group of cells x_{rs} . So the inventoried number of events N_b along the section is the sum of all the rockfalls that occurred within the cells of this section during the time period t_i of the inventory. Thus, N_b has to be distributed in all the cells assessed following:

$$k(E) = N_b(E, t_r, x_{rs}) \times \frac{1}{\sum [F_n \times P_f(x_{rs})]} \times \frac{1}{t_i} \quad (8)$$

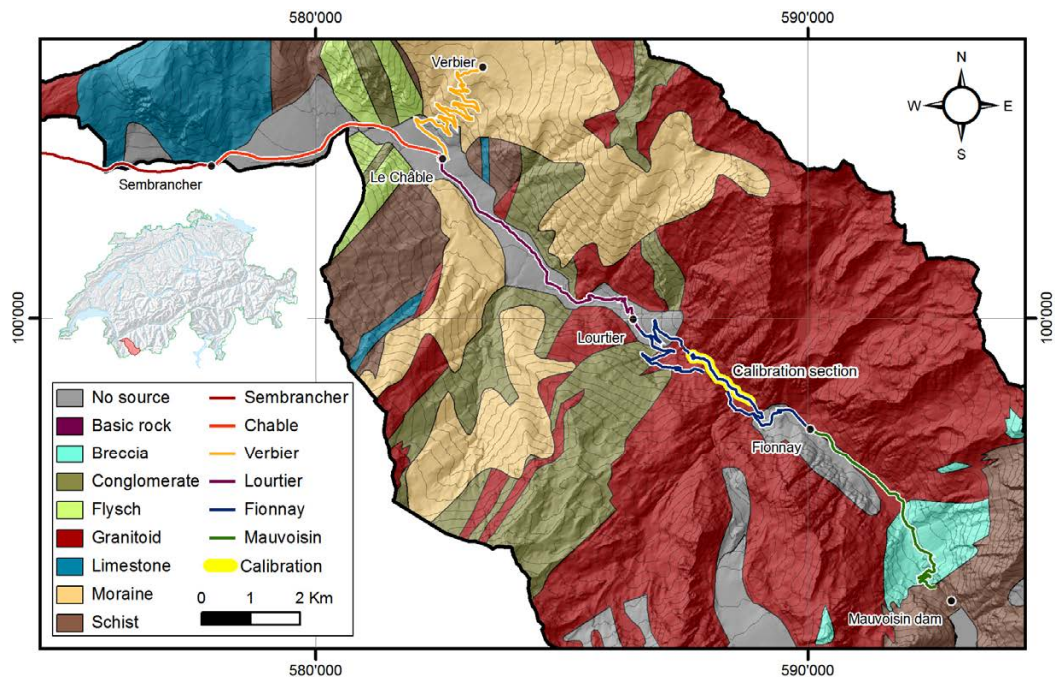


Fig. 6. Studied road sections and homogenous morphometric areas of the Bagnes Valley, located in the Swiss Alps, classified according to the swiss national geological atlas and the Vector25 (©swisstopo). They were identified differentiating daily traffic and mean velocities along the roads. The road section used to calibrate the rockfall hazard assessment is located between the second gallery after Lourtier and Le Plamproz (section underlined in yellow), where the rockfall activity is high, as shown in Fig. 1. (Hillshade and 10 m isohypses: ©2008 swisstopo).

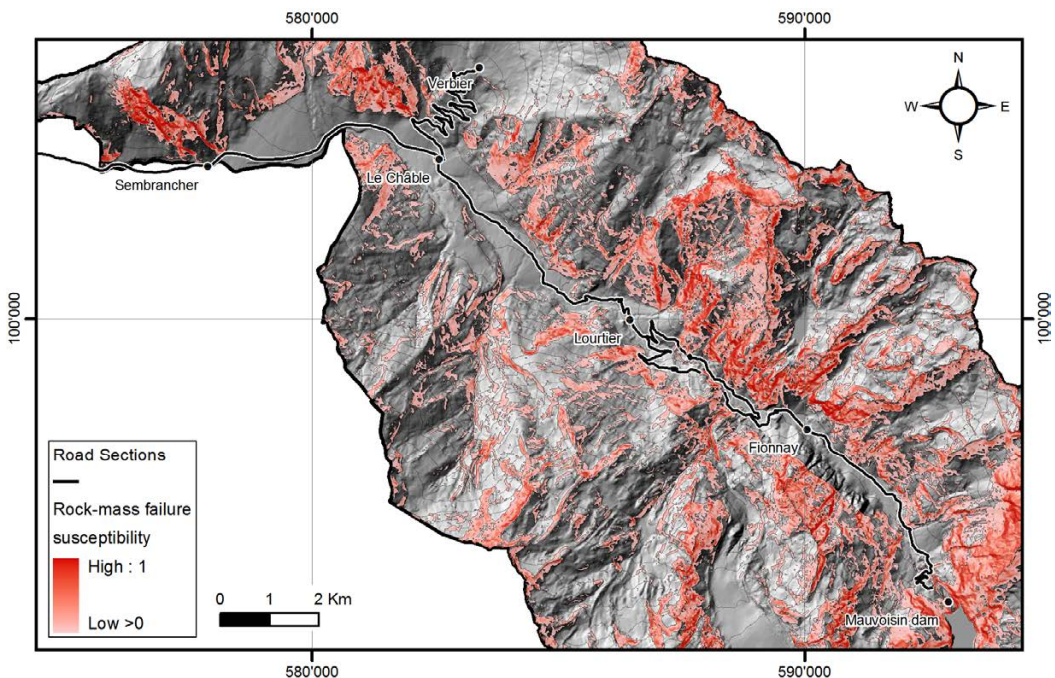


Fig. 7. Rock-mass failure susceptibility in the Bagnes Valley, identified thanks to the improved Slope Angle Distribution approach. (Hillshade and 10 m isohypses: © 2008 swisstopo).

where k is calibration factor with a frequency unit, function of a number of rockfall events N_b of magnitude E during a period of time t_i inventoried along a road section of cell x_{rs} divided by the sum of the Flow-R results within the whole road section.

2.4 Rockfall quantitative risk assessment along roads

Blocks frequently hit cars along Swiss mountain roads and occupants of vehicles are not necessarily killed or injured. Therefore, this paper is focused on the risk R of rockfalls to vehicle traffic; no considerations about vulnerabilities and elements at risk are provided, even if it would give proportional results. Adapting the risk equation of Fell et al. (2005) to this specific case, the annual risk can be defined by:

$$R(E, x_p) = H(E, x_p) \times \text{Exp}(x_p) \times N_c(x_p) \quad (9)$$

where R is the risk expressed in terms of number of direct impacts of blocks on cars per year, according to the hazard H and the exposure Exp , i.e. the probability that cars is hit in the hazardous area, and N_c the number of threatened vehicles. Modified after Fell et al. (2005), the exposure is presented as:

$$\text{Exp}(x_p) = \frac{L}{v(x_p)} \times \frac{1}{t_c} \times P_{\text{cell}}(x_p) \quad (10)$$

Exp depending on the mean length of the road inside cells L and the mean velocity v for a considered time period t_c (one year in this case) and the conditional probability P_{cell} :

$$P_{\text{cell}}(x_p) = \frac{d+l}{L} \quad (11)$$

where P_{cell} is the probability that a car of length l is hit by a block of diameter d on average inside a cell of length L , knowing that a block falls into a cell where a car is present. Indeed, in this study hazard and exposure are defined on a cell's scale x_p , not on a punctual location x . It is assumed that d is the minimum size block that will significantly affect the car and the magnitude E is equivalent to the block size. The diameter of blocks d has to tally with the inventoried events N_b considered to calibrate the hazard in Eq. (8). Then, the total number of vehicles attended on a road section is equal to Eq. (12):

$$N_c(x_p) = T(x_p) \times t_c \quad (12)$$

where T correspond to the daily traffic. Finally, the annual risk induced by rockfalls to vehicle traffic for an event with defined magnitude at a pixel x_p can be rewritten as follows:

$$R(E, x_p) = H(E, x_p) \times \frac{d+l}{v(x_p)} \times T(x_p) \quad (13)$$

R being a number of direct impacts of blocks of diameter d on cars of length l per year for a defined magnitude E at a cell x_p , function of the hazard H , the daily road traffic T ,

the mean velocity v , the mean car length l and the minimum block diameter d . Finally, the total risk along corridors is defined as the integration of all calculated $R(E, x_p)$ within the considered road sections.

3 Case study: the Val de Bagnes

3.1 Settings

The Val de Bagnes is located in the Canton of Valais in Switzerland. With a surface area of 300 km² and an elevation ranging from 677 m to 4313 m a.s.l., this municipality is under rapid development, in particular because of the fast growth of the Verbier ski resort. Moreover, an important power dam is located in the upper part of the valley. It means that the daily traffic is rather heavy, up to 5800 cars and 32 buses per day according to open-access databases (SRCE, 2009; CarPostal, 2010). Rockfall susceptibility maps at 1:25 000 were already performed (Michoud et al., 2010; Jaboyedoff et al., 2012). In this paper, a QRA of rockfalls to vehicle traffic is performed along the main roads (40 km) of the valley.

To achieve this goal, the authors used a 10 m cell size DEM derived from national maps at 1:25 000 (CN25, © swisstopo) to extract slope angles, the geological and tectonic vector atlas at 1:500 000 (© swisstopo) to classify the valley by HMA and the vectorized landscape model of Switzerland (Vector25, © swisstopo) to extract the location of the 40 km of roads.

3.2 Rockfall hazard assessments

3.2.1 Detection of block release areas

The rock type present is very large, from Cambrian polycyclic basements to Mesozoic and Cenozoic sedimentary covers (Sartori et al., 2006) of the Helvetic, Penninic and Austro-Alpine domains (Trümpy, 1980). Furthermore, large areas are covered by quaternary deposits that are fluvio-glacial deposits, colluvial fans or moraines. As the material diversity is wide, it justifies the importance of the HMA separation before further steps. Thus, each HMA was determined according to similar lithologies extracted from the 1:500 000 vectorised geological Atlas of Switzerland. Height classes were identified (Fig. 6): basic rocks, conglomerates, flyschs, granitoids, limestones, moraines, marble plus breccias and schists. In addition, some areas, such as lakes or alluvial deposits, were directly mapped as areas without any rockfall sources, due to absence of relief and/or material.

Then SAD analysis was performed from the 10 m DEM (©2008 swisstopo) and the useful slope angles (m_{ss} , m_c and σ for each HMA) were extracted to identify and weight potential rockfall source areas within the height HMAs. Results are presented in Table 2. This procedure was done thanks to the freeware Histofit (Loye et al., 2009) which decomposes

Table 2. Slope angles extracted from SAD analysis of each HMA. According to Fig. 2a and 3a, mean values and standard deviations of cliffs distributions correspond respectively to letters m_c and σ , and mean values of the steep slopes to letters m_{ss} .

Homogenous Morphometrical Areas	m_{ss}	1st normal distribution		2nd normal distribution (when necessary)	
		m_c	σ	m_c	σ
Basic rocks	33°	53°	8.3°	–	–
Conglomerates	31°	46°	8.7°	–	–
Flyschs	35°	48°	7.5°	60°	7.7°
Granitoids	34°	51°	7.7°	–	–
Limestones	35°	45°	8°	60°	8.0°
Marble and Breccias	33°	50°	6.4°	62°	7.4°
Moraines	33°	44°	6.1°	–	–
Schists	30°	47°	8.3°	61°	8.9°

the SAFD extracted from the software ArcGIS of Esri[®] and fits it with a predefined number of normal distributions. With the normal curves defined in Histofit and a slope angles map of the region, a MATLAB script allows to calculate directly rock-mass-failure susceptibilities F_n (Eq. 4) in each potential rockfall source cell of the map. Finally, the potential onset areas within each HMA were merged in one map (Fig. 7) before computing one propagation assessment.

3.2.2 Runout assessment

Taking into account local observations (Jaboyedoff et al., 2012) and detailed studies including computations of 2-D and 3-D rockfall modeling made for specific local cliffs into the valley, parameters of the runout assessment by Flow-R were calibrated as following: $\alpha = 1$ (Eq. 5) and $\mu = \tan 33^\circ$ (Eq. 6). Then, only one computation was done for the whole valley using the 10 m DEM (Fig. 8) to ensure continuous and homogenous results. Finally, these results were compared with a test simulation performed by the freeware CONEFALL (Jaboyedoff and Labiouse, 2011) based on an energy line angle equal to $\tan 33^\circ$ too. Both lateral and longitudinal extensions of computed runout areas are quite similar inside the Bagnes valley, which guarantee the coherence of the Flow-R runout assessment.

3.2.3 Rockfall hazard assessments

In order to achieve the normalized quantitative hazard assessment along the road sections, it is necessary to calibrate the Flow-R results with the factor k (Eq. 8 in Sect. 2.3). The road section used to calibrate the model is located on the NW side of the Dranse river, between the second gallery after Lourtier and Le Plamproz (Fig. 6), where the strong activity of cliffs has been well known for many years (Fig. 1). Along this section, covered by 237 cells with a sum of Flow-R results equal to 9453, it was assumed that 3 blocks with diameters d equal or greater than 25 cm reach the road every year ($t_i = 1$)

Table 3. Parameters for risk calculation along the different studied road sections (according to CarPostal, 2010, SRCE, 2009 and local road regulations). These road sections are mapped in Fig. 6.

Road Sections	T [daily traffic]	v [km h ⁻¹]	d [m]	l [m]
Sembrancher	10 600 cars	80	0.25	4
Chable	5800 cars	80	0.25	4
Verbier	5000 cars – 32 bus	60	0.25	4
Lourtier	2200 cars – 22 bus	70	0.25	4
Fionnay	800 cars – 8 bus	50	0.25	4
Mauvoisin	600 cars – 6 bus	40	0.25	4

according to our knowledge of past events. Then according to Eq. (8):

$$k(d \geq 25 \text{ cm}) = 3 \times \frac{1}{9453} [\text{events per year}] \quad (14)$$

An extract of the hazard map is presented in Fig. 9.

3.3 Rockfall risk assessment along the main roads of the valley

3.3.1 Inputs

The main important roads of the Val de Bagnes were extracted from the Vector25 (© swisstopo). The daily traffic along the valley roads considered T were obtained from open-access databases (SRCE, 2010 and CarPostal, 2010). Mean vehicles velocities v were estimated according to the local regulation and the state of the roads (roadwidth and ageing). Thus, six distinct road sections were distinguished and presented in Fig. 6 and Table 3, differentiating daily traffic and velocities along them. Moreover, the mean car length was set at 4 m, which corresponds to normal European compact car length. All parameters used in Eq. (13) are summarized in Table 3.

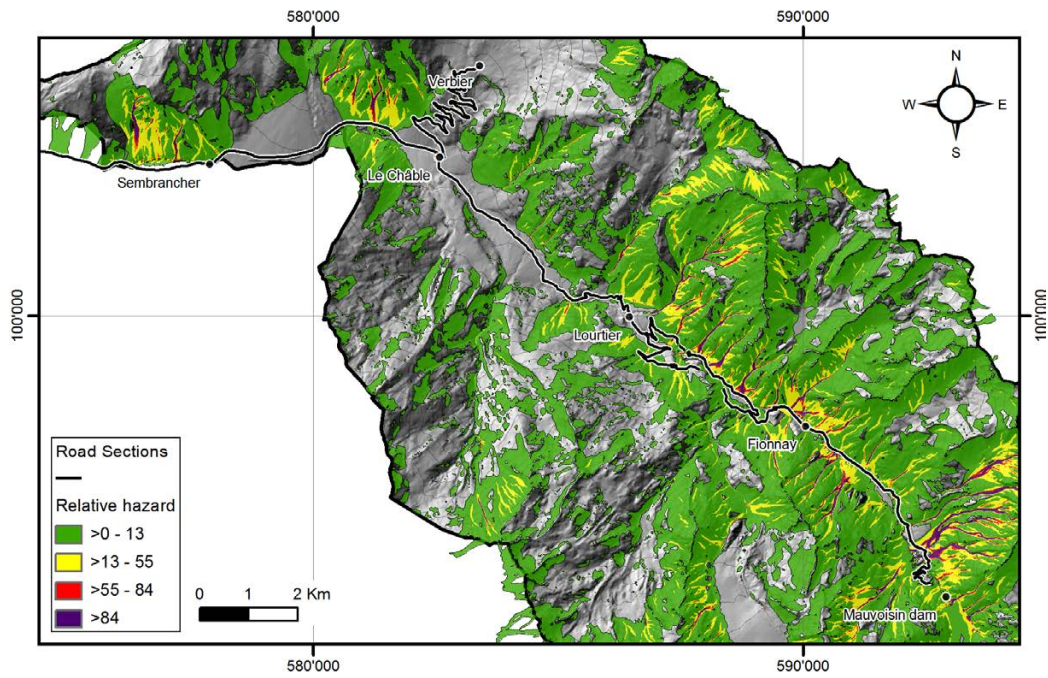


Fig. 8. Rockfalls relative hazard assessment in a part of the Bagnes Valley, performed by the software Flow-R. In the lower part of the valley (Sembrancher, Chable, Verbier), the daily traffic is rather heavy but the exposition is low. On the contrary, in the upper part of the valley (Fionnay and Mauvoisin), the daily traffic is lower but the hazard is pretty much higher. (Hillshade and 10 m isohypsés: ©2008 swisstopo).

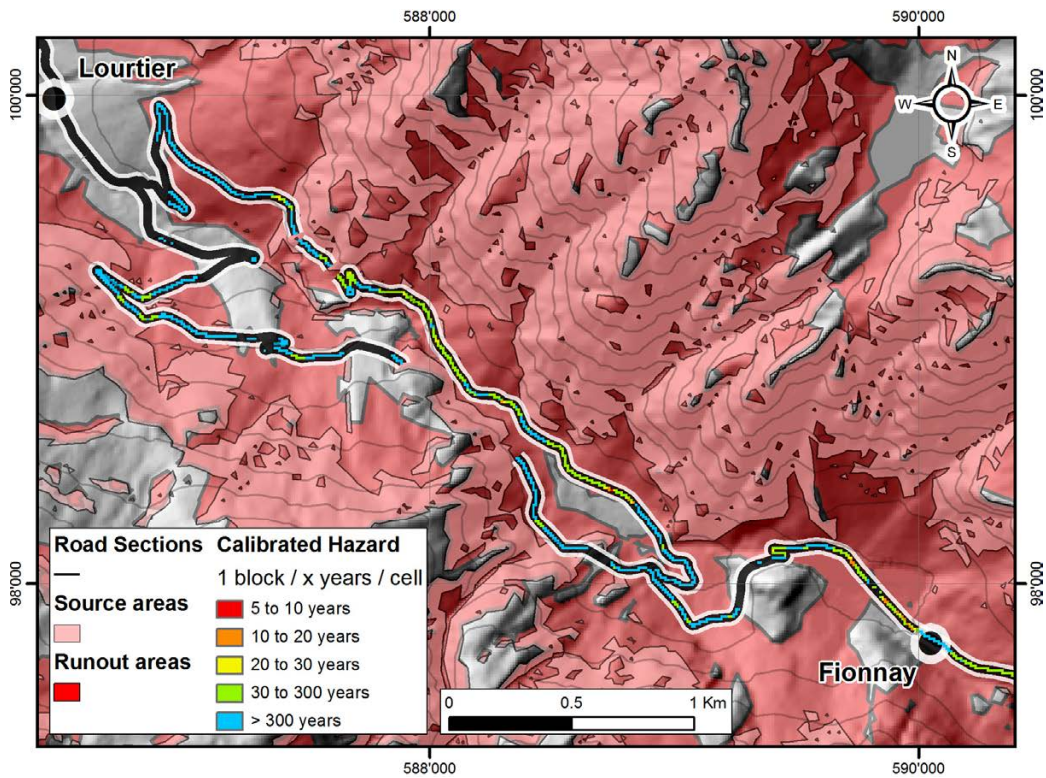


Fig. 9. Inverse hazard once the calibration has been performed, focused along the road section of Fionnay. Gaps along the section correspond to tunnels. (Hillshade and 10 m isohypsés: ©2008 swisstopo).

Table 4. Results of the quantitative risk assessment induced by rockfalls (mean diameter: 25 cm) to vehicle traffic along road sections of the Val de Bagnes. Finally, the whole risk is defined as the sum of all calculated pixel.

Road Sections	Total number of cells	Number of reached cells	Risk [x cars every year]	Inverse risk [1 car every x years]
Sembrancher	559	197(35%)	2.955×10^{-3}	~ 340
Chable	664	178 (27%)	4.626×10^{-3}	~ 220
Verbier	1031	98 (10%)	1.668×10^{-4}	~ 6000
Lourtier	851	63 (7%)	8.369×10^{-4}	~ 1200
Fionnay	1288	976 (76%)	1.676×10^{-2}	~ 60
Mauvoisin	742	591 (80%)	8.787×10^{-3}	~ 110
All roads	5135	2103 (41%)	3.414×10^{-2}	~ 30

3.3.2 Results

Finally, the annual risk induced by fragmental rockfalls greater or equal to a diameter of 25 cm to vehicle traffic was assessed along each road section of the Val de Bagnes. Results are summarized in Table 4. Along these sections, they vary a lot. In the lower part of the valley (Sembrancher, Chable and Verbier sections), where the daily traffic is important, there are only a few rockfall propagations that reach the road. This is why the risk is evaluated at one hit car every two hundreds to six thousands years. On the opposite, in the upper part of the valley (Lourtier, Fionnay and Barrage sections), the daily traffic is lower but there are a lot of blocks that reach the road; the risk is significantly higher, namely to one hit car every sixty years (Table 4). The integrated risk along all the road sections of the Val de Bagnes is evaluated to 0.03414 hit cars per year, i.e. approximately one incident every thirty years.

4 Discussions

4.1 Results within the study area

According to the authors' experience and testimonies from local security services and geologists, the results (i.e. the localization of potential rockfall onset areas, the runout computation and the risk assessment) are in agreement with observations. Nevertheless, the hazard calibration (Eq. 14) could be significantly improved with more complete inventories along these roads (detailed discussion in Sect. 4.5). In addition, the calculated risk is approximated and simplified, because it does not take into account some factors. First, the time lapse for the driver to react and the braking distance in front of blocks already on the road are ignored, considering that the velocity is low enough to avoid a collision along the most exposed sections. Moreover, all surveys and remediation measures already done (such as anchors, nets, removal of unstable blocks, monitoring systems, etc.) are ignored, except for tunnels and galleries which are mapped from orthophotos. Finally, the potential inhomogeneous repartitions of rockfall events and traffic during the day are ignored; for

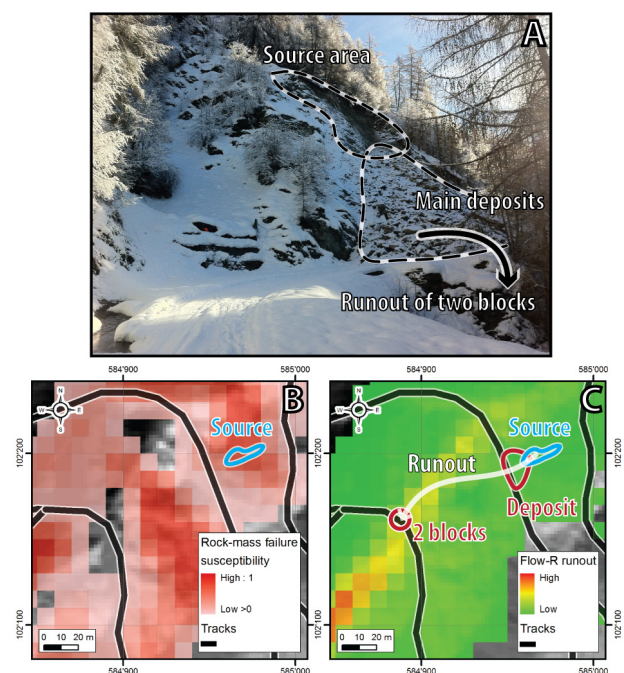


Fig. 10. (A) A recent rockfall event (2 January 2012) cut a mountain road with a deposit of approx. 1000 m^3 . The height difference between the fresh scarp and the road is about 30 m. (B) The rock-mass failure susceptibility map indicates that the onset is clearly defined as a potential rockfall source area with a high rock-mass failure susceptibility of about 0.8. (C) The trajectory of two blocks that reached a second road 80 m lower fit well with the predicted runout and confirms Flow-R results. (Hillshade: ©2008 swisstopo).

example, during winter periods, workers drive early in the morning and late in the afternoon, when the cliffs are frozen.

4.2 Recent rockfall event

A recent rockfall occurred on 2 January 2012, during the review process of this paper. The deposit of approx. 1000 m^3

cut a small road (Fig. 10a) and mostly stopped on it. The source area was localized in a zone clearly defined as a potential rockfall source area with a high rock-mass failure susceptibility of about 0.8 (scale: no susceptibility = 0 – highest susceptibility = 1; see Fig. 10b). The trajectories of two blocks that reached a second road 80 m lower fit well with the predicted runout using Flow-R (Fig. 10c). Thus, this event is in agreement with the improved SAD approach and the Flow-R results, showing its potential ability to predict hazard and risk zones.

4.3 Advantages and limitations of the presented approach

The combination of the improved SAD approach and the Flow-R software allows us to establish rockfall susceptibility, and when inventories are available, to obtain scaled hazard to assess risk along roads. This methodology has been optimized for studies at regional scale with only a little information available. Indeed, this procedure requires at least topography DEM and, if possible, a geological map in order to improve the rock-mass failures susceptibilities and spreading probabilities.

The refinement of the SAD approach is based on the assumption that the release susceptibility is related to the geomorphology, i.e. steepness of the topography, even if it is a simple rockfall activity factor. But, using geological information aims to indirectly take into account rock mass quality that influences the stability conditions, too. Nevertheless, it is also true that other very important local factors (such as weathering and/or deburstressing) cannot be taken into consideration for large areas, using documents available at regional scale. Then, regarding propagations, Flow-R assesses runout areas using only a DEM, since the parameters of the Holmgren's and the Coulomb's expressions (Eqs. 5 and 6) can be based on literature and/or past event records. This software is particularly optimized for regional studies and computation times are still acceptable with a normal workstation (five days for the study in Bagnes). Moreover, the approach can be even better calibrated according to other potential documents available for the study area (such as landuse maps, aerial images or information about mechanical rock parameters) in order to improve detection and runout settings. However, this procedure oversimplifies the laws governing rock-mass failures and block propagations, which are suitable at regional scale but become hazy for small studies' areas. Finally, this approach should be used as a preliminary quantitative assessment for large regions, highlighting hotspots requiring more detailed studies.

At local scales, robust empirical and physically-based methods have been developed for many years, allowing fine and realistic rock-mass failure detections & block propagations. For instance, the RSS-GIS method (Günther et al., 2004) allows us to deal with internal parameters and external factors of rockfalls. But, it requires a lot of data on topog-

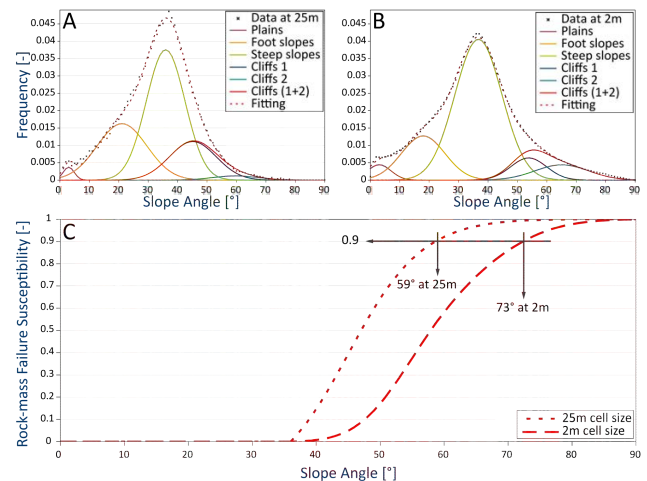


Fig. 11. (A) Normal distributions of the slope angles of the limestones HMA in the Bagnes Valley extracted from a 25 m resolution DEM. (B) Normal distributions of the slope angles of the same limestones HMA in the Bagnes Valley extracted now from a 2 m resolution DEM. (C) Cumulative distribution functions are shown for the same limestone HMA, once with a 25 m resolution DEM and once with a 2 m resolution.

raphy, structural geology, geotechnical settings and climatic conditions. The RHRS method (Pierson et al., 1990) is based on eleven parameters that have to be checked on the field. These two approaches are therefore indicated for studies at local scales to reliably and accurately detect and rate potential rockfall source areas; however, they would be too time-consuming for regional works if prioritized locations have not been defined before in-situ investigations. Then, regarding rockfall propagations, software like HY-STONE (Crosta et al., 2004; Frattini et al., 2008; Agliardi et al., 2009) is able to deal with both local and regional scales; moreover, it assesses probabilistic runout areas based on physical processes and computations of trajectographies. Furthermore, such software is able to consider countermeasures; fence design and location efficiencies can be estimated before their setup (Agliardi et al., 2009) to optimize them. However, it requires many inputs (such as rolling frictional angles, normal and tangential restitution coefficients) that have to be estimated and spatially distributed for all surface types of the study area, depending on landuses as well as superficial and bedrock geologies. Therefore, for studies at regional scale, it involves more time to acquire differentiated input parameters and compute runout than the Flow-R model.

4.4 Influences of the cell size DEM

The DEM resolution influences rockfall source detections: a coarse DEM tends to smooth high slope angle values. As stated in Loye et al. (2009), it implies that the higher resolution of the DEM, the smaller the potential source areas detected are. Furthermore, the coarser the DEM, the lower

the apparent slope angle of a vertical cliff is. For example, a 10 m vertical cliff has an apparent slope angle of 83° on a 2 m DEM instead of 55° on a 10 m DEM (Loye et al., 2009). As threshold angles which are used to identify block release susceptibilities (namely m_{ss} , m_c and σ) are extracted from slope maps, their values directly depend on the DEM cell size. Thus, for the same detected cliff, the coarser the DEM, the lower these threshold angles of cliff detection are (Fig. 11a, b). It means that the influence of the DEM cell size is implicitly taken into account during the SAD approach and no corrections have to be added. Fig. 11c illustrates a limestone cliff with an apparent slope angle of 59° on a 25 m DEM and 73° on a 2 m DEM having the same susceptibility of 0.9, regardless of the DEM cell size used during the SAD approach.

4.5 Hazard calibration

When it comes to converting rockfall susceptibilities into hazard (i.e. number of blocks per year per cell), the location of the calibration section associated to an inventory has a strong importance. Ideally, the section should be located along a non-forested slope without remediation systems. Therefore, if the calibration section is located along forested slopes, the final hazard would be underestimated along a non-forested adjacent slope because of a biased number of events due to blocks deviated or stopped by trees or anthropogenic countermeasures.

However, due to practical issues, the calibration step has to be achieved with inventories that are available (when they are), even if they are not always performed along optimum road sections. Nevertheless, a preliminary method to calibrate hazard is proposed and is still in progress; enhanced approaches will have to be developed in future work. Up to now, at least one section is needed to perform this calibration, but multiple road sections could also be used. Moreover, introducing two adjustment factors to take into account during the calibration step (i.e. Eq. 8) – (1) classical censoring effects inside inventories (Hungre et al., 1999) and (2) rockfall-forest interactions along forested slopes based on statistical studies (Dorren et al., 2005) – would be the first example of future evolution that could improve the reliability of the hazard calibration.

5 Conclusions

The improved approach of the Slope Angle Distribution and the Flow-R software were introduced and carried out along roads of the Val de Bagnes to assess the risk induced by fragmental rockfall to vehicle traffic. Linking the normal distributions of cliffs units with normalized cumulative functions, rockfall onset areas can be identified with rock-mass-failure susceptibility. Indeed, these indexes can be achieved at regional scale according to slope angle values inside homo-

geneous morphometric areas thanks to the enhanced SAD procedure. Then Flow-R software provides the relative frequencies of block propagations, using several approaches and susceptibilities of source areas. Thanks to these results, i.e. rock-mass-failure susceptibilities and relative frequencies of propagations, hazard maps can be achieved and calibrated with an inventoried number of events along a road section.

Even if the obtained quantitative risk assessment is an approximation, this improved approach allows us to deal at low cost with real hazard maps at a regional scale, requiring only few documents, namely a DEM and a geological map (if available). So this approach is indicated for regions which cannot afford systematic detailed assessments of the risk due to rockfalls; thus hotspots can be identified in order to prioritize sections on which detailed investigation and mitigation measures will be the most efficient.

Histofit and Flow-R software packages are available on request at www.flow-r.org.

Acknowledgements. The present work has been partially supported by the project SafeLand “Living with landslide risk in Europe: Assessment, effects of global change, and risk management strategies” (7th Framework Programme of the European Commission, Grant Agreement No. 226479). This support is gratefully acknowledged. The authors would like to thank the Bagnes municipality and its security service for allowing us to publish maps and results and for the useful discussions that allowed us to validate the models. Moreover, three reviewers helped us to significantly improve the present document thanks to pertinent remarks and suggestions. Finally, the authors appreciated the continuing questioning of Lucie Fournier and the support of Marc Choffet around chocolate breaks.

Edited by: P. Reichenbach

Reviewed by: A. Preh and two other anonymous referees

References

- Agliardi, F., Crosta, G. B., and Frattini, P.: Integrating rockfall risk assessment and countermeasure design by 3D modelling techniques, *Nat. Hazards Earth Syst. Sci.*, 9, 1059–1073, doi:10.5194/nhess-9-1059-2009, 2009.
- Baillifard, F., Jaboyedoff, M., and Sartori, M.: Rockfall hazard mapping along a mountainous road in Switzerland using a GIS-based parameter rating approach, *Nat. Hazards Earth Syst. Sci.*, 3, 435–442, doi:10.5194/nhess-3-435-2003, 2003.
- Bieniawski, Z. T.: Rock mass classification in rock engineering, in: *Proceeding of the Symposium on Exploration for Rock Engineering*, 1, edited by: Bieniawski, Z. T., Johannesburg, South Africa, 1–5 November 1976, 97–106, 1976.
- Blahut, J., Horton, P., Sterlacchini, S., and Jaboyedoff, M.: Debris flow hazard modelling on medium scale: Valtellina di Tirano, Italy, *Nat. Hazards Earth Syst. Sci.*, 10, 2379–2390, doi:10.5194/nhess-10-2379-2010, 2010.
- Budetta, P.: Assessment of rockfall risk along roads, *Nat. Hazards Earth Syst. Sci.*, 4, 71–81, doi:10.5194/nhess-4-71-2004, 2004.
- Cajos, J., Trocmé-Maillard, M., Huber, M., Arnold, P., Vollmer, U., Sandri, A., Raetzo, H., Dorren, L., Egli, T., Eberli, J., Knuchel,

- R., Kienholz, H., Donzel, M., Utelli, H. H., and Perren, B.: Risk concept for natural hazards on national roads, Federal Roads Office, 108 pp., available at <http://www.astra.admin.ch/>, 2009.
- CarPostal: <http://www.carpostal.ch/>, last access: 3 December 2010, 2010.
- Cascini, L.: Applicability of landslide susceptibility and hazard zoning at different scales, *Eng. Geol.*, 102, 164–177, 2008.
- Corominas, J. and Moya, J.: A review of assessing landslide frequency for hazard zoning purposes, *Eng. Geol.*, 102, 193–213, 2008.
- Corominas, J., Copons, R., Moya, J., Vilaplana, J., Altimir, J., and Amigó, J.: Quantitative assessment of the residual risk in a rockfall protected area, *Landslides*, 2, 343–357, 2005.
- Crosta, G. B. and Agliardi, F.: A methodology for physically based rockfall hazard assessment, *Nat. Hazards Earth Syst. Sci.*, 3, 407–422, doi:10.5194/nhess-3-407-2003, 2003.
- Crosta, G. B., Agliardi, F., Frattini, P., and Imposimato, S.: A three-dimensional hybrid numerical model for rockfall simulation, *Geophys. Res. Abstr.*, 6, 04502, 2004.
- Derron, M.-H., Jaboyedoff, M., and Blikra, L. H.: Preliminary assessment of rockslide and rockfall hazards using a DEM (Oppstadhornet, Norway), *Nat. Hazards Earth Syst. Sci.*, 5, 285–292, doi:10.5194/nhess-5-285-2005, 2005.
- Dorren, L. K. A.: A review of rockfall mechanics and modelling approaches, *Prog. Phys. Geogr.*, 27, 69–87, 2003.
- Dorren, L. K. A.: Rockyfor3D (v4.0) revealed – Transparent description of the complete 3D rockfall model, ecorisQ paper, 28 pp., 2011.
- Dorren, L. K. A. and Seijmonsbergen, A. C.: Comparison of the three GIS-based models for predicting rockfall runout zones at a regional scale, *Geomorphology*, 56, 49–64, 2003.
- Dorren, L. K. A., Berger, F., le Hir, C., Mermin, E., and Tardif, P.: Mechanisms, effects and management implications of rockfall in forests, *Forest Ecol. Manag.*, 215, 183–195, 2005.
- Fairfield, J. and Leymarie, P.: Drainage Networks from Grid Digital Elevation Models, *Water Resour. Res.*, 27, 709–717, 1991.
- Fell, R., Ho, K. K. S., Lacasse, S., and Leroi, E.: A framework for landslide risk assessment and management, in: *Landslide Risk Management*, edited by: Hungr, O., Fell, R., Couture, R., and Eberhardt, E., Proceedings of the International Conference on Landslide Risk Management in Vancouver, Canada, 31 May – 3 June 2005, 3–25, 2005.
- Fell, R., Corominas, J., Bonnard, C., Cascini, L., Leroi, E., and Savage, W. Z.: On behalf of the JTC-1 Joint Technical Committee on Landslides and Engineered Slopes: Guidelines for Landslide Susceptibility, Hazard and Risk Zoning for Land Use Planning, *Eng. Geol.*, 102, 85–98, 2008.
- Frattini, P., Crosta, G., Carrara, A., and Agliardi, F.: Assessment of rockfall susceptibility by integrating statistical and physically-based approaches, *Geomorphology*, 94, 419–437, 2008.
- Gamma, P.: Dfwalk - Ein Murgang-Simulationsprogramm zur Gefahrenzonierung, Geographisches Institut der Universität Bern, Switzerland, 158 pp., 2000.
- Gilbert, G. K.: *Geology of the Henry Mountains*, US Geological and Geographical Survey of the Rocky Mountain Region, Government Printing Office, Washington, DC, 1877.
- Gokceoglu, C., Sonmez, H., and Ercanoglu, M.: Discontinuity controlled probabilistic slope failure risk maps of the Altindag (settlement) region in Turkey, *Eng. Geol.*, 55, 277–296, 2000.
- Günther, A.: SLOPEMAP: programs for automated mapping of geometrical and kinematical properties of hard rock hill slopes, *Comput. Geosci.*, 29, 865–875, 2003.
- Günther, A., Carstensen, A., and Pohl, W.: Automated sliding susceptibility mapping of rock slopes, *Nat. Hazards Earth Syst. Sci.*, 4, 95–102, doi:10.5194/nhess-4-95-2004, 2004.
- Guzzetti, F., Reichenbach, P., and Wieczorek, G. F.: Rockfall hazard and risk assessment in the Yosemite Valley, California, USA, *Nat. Hazards Earth Syst. Sci.*, 3, 491–503, doi:10.5194/nhess-3-491-2003, 2003.
- Heim, A.: *Bergsturz und Menschenleben*, Fretz and Wasmuth Verlag, Zurich, 218 pp., 1932.
- Hoek, E. and Bray, J. W.: *Rock Slope Engineering*, 3rd edition, Institution of Mining and Metallurgy, London, 1981.
- Hoek, E., Marinis, P., and Benissi, M.: Applicability of the Geological Strength Index (GSI) classification for very weak and sheared rock masses. The case of the Athens Schist Formation, *Bull. Eng. Geol. Environ.*, 57, 151–160, 1998.
- Holmgren, P.: Multiple flow direction algorithms for runoff modeling in grid based elevation models: an empirical evaluation, *Hydrol. Process.*, 8, 327–334, 1994.
- Horton, P., Jaboyedoff, M., and Bardou, E.: Debris flow susceptibility at a regional scale, 4th Canadian Conference on Geohazards, Université Laval, Quebec, Canada, 20–24 May 2008, 8 pp., 2008.
- Hungr, O., Evans, S. G., and Hazzard, J.: Magnitude and frequency of rock falls and rock slides along the main transportation corridors of southwestern British Columbia, *Can. Geotech. J.*, 36, 227–238, 1999.
- Jaboyedoff, M. and Derron, M.-H.: Integrated risk assessment process for landslides, in: *Landslide risk management*, edited by Hungr, O., Fell, R., Couture, R. and Eberhardt, E., 776, Taylor and Francis, 2005.
- Jaboyedoff, M. and Labiouse, V.: Preliminary assessment of rockfall hazard based on GIS data, in: *Proceedings of the 10th International Congress on Rock Mechanics ISRM 2003 – Technology roadmap for rock mechanics*, South African Institute of Mining and Metallurgy, Johannesburg, South Africa, 8–12 September 2003, 575–778, 2003.
- Jaboyedoff, M. and Labiouse, V.: Technical Note: Preliminary estimation of rockfall runout zones, *Nat. Hazards Earth Syst. Sci.*, 11, 819–828, doi:10.5194/nhess-11-819-2011, 2011.
- Jaboyedoff, M., Baillifard, F. J., Marro, C., Philipposian, F., and Rouiller, J. D.: Detection of rock instabilities: Matterock Methodology, Joint Japan-Swiss Scientific on Impact Load by Rock Falls and Design of Protection Structures, Kanazawa, Japan, 4–7 October 1999, 37–43, 1999.
- Jaboyedoff, M., Dudd, J. P., and Labiouse, V.: An attempt to refine rockfall hazard zoning based on the kinetic energy, frequency and fragmentation degree, *Nat. Hazards Earth Syst. Sci.*, 5, 621–632, doi:10.5194/nhess-5-621-2005, 2005.
- Jaboyedoff, M., Oppikofer, T., Abellán, A., Derron, M.-H., Loye, A., Metzger, R. and Pedrazzini, A.: Use of LIDAR in landslide investigations: a review, *Nat. Hazards*, Springer Netherland, 61, 5–28, doi:10.1007/s11069-010-9634-22012a.
- Jaboyedoff, M., Choffet, M., Derron, M.-H., Horton, P., Loye, A., Longchamp, C., Mazotti, B., Michoud, C., and Pedrazzini, A.: Preliminary slope mass movements susceptibility mapping using DEM and LiDAR DEM, in: *Terrigenous Mass Movements*, edited by: Pradhan, B., and Buchroithner, Springer-Verlag Berlin

- Heidelberg, 64 pp., in press, 2012b.
- Jenson, S. K. and Domingue, J. O.: Extracting topographic structure from digital elevation data for geographic information system analysis, *Photogramm. Eng. Remote Sens.*, 54, 1593–1600, 1988.
- Kappes, M. S., Malet, J.-P., Rematre, A., Horton, P., Jaboyedoff, M., and Bell, R.: Assessment of debris-flow susceptibility at medium-scale in the Barcelonnette Basin, France, *Nat. Hazards Earth Syst. Sci.*, 11, 627–641, doi:10.5194/nhess-11-627-2011, 2011.
- Kreyszig, E.: *Advanced Engineering Mathematics*, 9th edition, John Wiley and Sons, 1248 pp., 2006.
- Leroi, E.: Landslides hazard – risk maps at different scales: objectives, tools and developments, in: *Proceedings of the 7th Int. Symp. on Landslides*, Trondheim, Norway, 1, 35–51, 1996.
- Locat, J., Leroueil, S., and Picarelli, L.: Some considerations on the role of geological history on slope stability and estimation of minimum apparent cohesion of a rock mass, in: *Landslides in research, theory and practice*, edited by: Bromhead, E., Dixon, N., and Ibsen, M. L., The 8th International Symposium on Landslides in Cardiff, Wales, 26–30 June 2000, 935–942, 2000.
- Loye, A., Jaboyedoff, M., and Pedrazzini, A.: Identification of potential rockfall source areas at a regional scale using a DEM-based geomorphometric analysis, *Nat. Hazards Earth Syst. Sci.*, 9, 1643–1653, doi:10.5194/nhess-9-1643-2009, 2009.
- Michoud, C., Mazotti, B., Choffet, M., Dubois, J., Breguet, A., Métraux, V., and Jaboyedoff, M.: *Advanced Susceptibility Mapping for Natural Hazards at a Local Scale – The Case of the Swiss Alpine Valley of Bagnes*, EGU General Assembly, Vienna, Austria, 3–7 May 2010, EGU2010-4606, 2010.
- Montgomery, D. R. and Brandon, M. T.: Topographic controls on erosion rates in tectonically active mountain ranges, *Earth Planet. Sci. Lett.*, 201, 481–489, 2002.
- O’Callaghan, J. F. and Mark, D. M.: The extraction of drainage networks from digital elevation data, *Comput. Vision Graphics Image Process.*, 28, 328–344, 1984.
- Oppikofer, T., Jaboyedoff, M., and Coe, J. A.: Rockfall hazard at Little Mill Campground, Uinta National Forest: Part 2. DEM analysis, in: *First North American Landslide Conference – Landslides and Society: Integrated Science, Engineering, Management, and Mitigation*, Vail, USA, 3–8 June 2007, 1351–1361, 2007.
- Pierson, L. A., David, S. A., and Van Vickle, R.: *Rockfall Hazard Rating System Implementation Manual*, Oregon, 1990.
- Piteau, D. R. and Peckover, F. L.: *Engineering of Rock Slope*, in: *Landslides, Analysis and Control*, Transportation Research Board, in: *Special Report 176*, edited by: Schuster, R. L. and Krizek, R. J., Washington, DC, 192–228, 1978.
- Powell, J. W.: *Report on the Geology of the Eastern Portion of the Uinta Mountains and a Region of Country Adjacent Thereto*, US Geological and Geographical Survey of the Territories, Government Printing Office, Washington, DC, 1876.
- Ritchie, A. M.: Evaluation of rockfall and its control, in: *Highway Research Record*, 17, Highway Research Board, National Research Council, Washington, DC, 13–28, 1963.
- Rouillier, J.-D., Jaboyedoff, M., Marro, C., Philipposian, F., and Mamin, M.: *Pentes instables dans le Pennique Valaisan. MATTEROCK: une méthodologie d’auscultation des falaises et de detection des éboulements majeurs potentiels*, Rapport final du PNR31, VDF Hochschulverlag AG, ETH Zürich, Switzerland, 1998.
- Sartori, M., Gouffon, Y., and Marthaler, M.: Harmonisation et définition des unités lithostratigraphiques briançonnaises dans les nappes penniques du Valais, *Ecolgae Geol. Helv.*, 99, 363–407, 2006.
- Selby, M. J.: Controls on the stability and inclinations of hillslopes formed on hard rock, *Earth Surf. Proc. Land.*, 7, 449–467, 1982.
- SRCE (Daily Traffic during 2007, by the Roads and Rivers Office of the Canton of Valais): <http://mapserver-srce.kiperti.com/srce/carte.html>, last access: 3 December 2010, 2009.
- Strahler, A. N.: Equilibrium theory of erosional slopes approached by frequency distribution analysis, *Am. J. Sci.*, 248, 673–696, 800–814, 1950.
- Strahler, A. N.: Quantitative geomorphology of erosional landscapes, *Compt. Rend.*, 19th Intern. Geol. Cong., Sec. 13, 341–354, 1954.
- Terzaghi, K.: *Mechanism of Landslides*, The Geological Society of America, Eng. Geol. (Berkeley), 83–123, 1950.
- Terzaghi, K.: Stability of Steep Slopes on Hard Unweathered Rock, *Géotechnique*, 12, 251–270, 1962.
- Toppe, R.: Terrain models – a tool for natural hazard mapping, *IAHS*, 162, 629–638, 1987.
- Trümpy, R.: *Geology of Switzerland – A Guide Book, Part A: An Outline of the Geology of Switzerland*, Wepf & Co, Basel, 104 pp., 1980.
- Van Dijke, J. J. and Van Westen, C. J.: Rockfall hazard: a geomorphological application of neighbourhood analysis with ILWIS, *ITC Journal*, 1, 40–44, 1990.
- Volkwein, A., Schellenberg, K., Labiouse, V., Agliardi, F., Berger, F., Bourrier, F., Dorren, L. K. A., Gerber, W., and Jaboyedoff, M.: Rockfall characterisation and structural protection – a review, *Nat. Hazards Earth Syst. Sci.*, 11, 2617–2651, doi:10.5194/nhess-11-2617-2011, 2011.
- Wagner, A., Leite, E., and Olivier, R.: Rock and debris-slides risk mapping in Nepal – A user-friendly PC system for risk mapping, in: *Proceedings of the fifth international symposium on landslides*, Lausanne, Switzerland, 10–15 July 1988, 1251–1258, 1988.
- Whalley, W. B.: Rockfalls, in: *Slope Instability*, edited by: Brunsden, D. and Prior, D. B., Wiley, Chichester, 217–256, 1984.
- Wyllie, D. C. and Mah, C. W.: *Rock Slope Engineering, Civil and Mining*, 4th Edition, Taylor & Francis, London and New-York, 2004.

Appendix B

Multi-scale debris flow vulnerability assessment and direct loss estimation of buildings in the Eastern Italian Alps

Ciurean, R. L., Hussin, H., van Westen, C. J., Jaboyedoff, M., Nicolet, P., Chen, L., Frigerio, S., and Glade, T.: Multi-scale debris flow vulnerability assessment and direct loss estimation of buildings in the Eastern Italian Alps, *Nat Hazards*, 85, 929–957, doi:[10.1007/s11069-016-2612-6](https://doi.org/10.1007/s11069-016-2612-6), 2017.



Multi-scale debris flow vulnerability assessment and direct loss estimation of buildings in the Eastern Italian Alps

R. L. Ciurean¹ · H. Hussin² · C. J. van Westen² ·
M. Jaboyedoff³ · P. Nicolet³ · L. Chen^{2,4} · S. Frigerio⁵ ·
T. Glade¹

Received: 15 February 2016 / Accepted: 27 September 2016 / Published online: 25 October 2016
© The Author(s) 2016. This article is published with open access at Springerlink.com

Abstract Vulnerability assessment, as a component of the consequence analysis, represents a fundamental stage in the risk assessment process because it relates the hazard intensity to the characteristics of the built environment that make it susceptible to damage and loss. The objective of this work is to develop a quantitative methodology for vulnerability and loss assessment of buildings exposed to debris flows and apply it to a study area in NE Italy at local and regional scale. Using existing conceptual models of vulnerability and loss, this paper seeks to identify solutions for maximizing the information gained from limited observational damage data and a heterogeneous building data set. Two vulnerability models are proposed: Model 1 is based on the generation of empirical vulnerability curves using observed intensities; Model 2 takes into account multiple resistance characteristics of buildings and uses modeled debris flow intensities. The process intensity descriptor in both cases is debris flow height. The vulnerability values obtained with the local (Model 1) and regional (Model 2) models are further multiplied with the building value to calculate the minimum and maximum loss for each building in the study area. Loss is also expressed as cumulative probability calculated with Model 1 using a Monte Carlo sampling technique. The methodology is applied in the Fella River valley (north-eastern Italian Alps), a region prone to multiple mountain hazards. Uncertainties are expressed as minimum and maximum values of vulnerability, market values and loss. The

✉ R. L. Ciurean
roxana.liliana.ciurean@univie.ac.at

¹ Department of Geography and Regional Research, University of Vienna, Vienna, Austria

² Faculty of Geo-Information Science and Earth Observation (ITC), University of Twente, Enschede, The Netherlands

³ Institute of Earth Sciences, Faculty of Geosciences and Environment, University of Lausanne, Lausanne, Switzerland

⁴ Institute of Geophysics and Geomatics, China University of Geosciences, Wuhan, China

⁵ Research Institute for Geo-Hydrological Protection, CNR-IRPI, National Research Council of Italy, Padua, Italy

results are compared with relevant published vulnerability curves and historical damage reports.

Keywords Building vulnerability · Loss · Uncertainty · Debris flow · Italy

1 Introduction

Extreme rainfall events frequently trigger slope instability phenomena of various types, as well as floods and flash floods in mountain regions worldwide. The reduction in possible future human and material losses is dependent on the design and implementation of effective mitigation strategies which require the assessment of risks before and after construction. These in turn rely not only on the analysis of the magnitude, frequency and intensity of the harmful events, but also on the comprehensive evaluation of exposed elements and their vulnerability (Hufschmidt et al. 2010; Mazzorana et al. 2012; Papathoma-Köhle et al. 2015). Risk in the context of disaster management is defined as “a combination of the consequences of an event and the associated likelihood/probability of its occurrence” (EC, p. 10, ISO 31010). For property, annual risk can be calculated as the product of the annual probability of the hazardous event, the probability of spatial impact by the hazard, the temporal spatial probability of the property, its vulnerability and value (AGS 2007; Fell et al. 2005).

Vulnerability is a key component in the quantitative risk assessment of natural hazards. Due to its complex nature and multitude of perspectives, many different concepts and methods to systematize vulnerability exist in the literature (Birkmann 2006; Cutter et al. 2003; Fuchs 2009). In general, the definitions within engineering or natural sciences describe physical vulnerability as the predisposition or inherent characteristics of an element at risk to be affected or susceptible to damage as a result of an impacting hazard with a given intensity (Glade 2003). In this work, vulnerability is defined as “the degree of loss to a given element, or set of elements, within the area affected by a hazard, expressed on a scale of 0 (no loss) to 1 (total loss)” (UNDRO 1984).

Landslide vulnerability assessment can be difficult due to the inherent complexity of the hazardous processes (Cardinali et al. 2002), as well as the spatial and temporal characteristics of the elements exposed (Glade and Crozier 2005b; van Westen et al. 2006). Some of the factors responsible for this are: complex characteristics of different landslide types and processes; limited information on preparatory, triggering and controlling conditions (Glade and Crozier 2005a); the lack of accurate or limited observational data for process intensity estimation (Papathoma-Köhle et al. 2011); absence or incomplete damage information, especially in terms of building damage data or lives lost related to the failure mechanism as a result of specific process impact (Fuchs et al. 2007); spatial and temporal variability of the exposed elements at risk. Due (but not limited) to these factors, uncertainty associated with the input data, models and output results is difficult to evaluate and was thus rarely considered in vulnerability assessments.

Within disaster risk modeling, different methodological approaches for landslide vulnerability assessment have been proposed, and these can be classified as qualitative, semiquantitative and quantitative (Fuchs et al. 2011). Uncertainty analysis is associated predominantly with the last category. Uncertainty can be defined as “any deviation from the unachievable ideal of completely deterministic knowledge of a relevant system”

(Walker et al. 2003). Uncertainty in probabilistic risk assessments is generally classified based on three factors (Walker et al. 2003): (1) the location of uncertainty within the modeled system (e.g., inputs, parameters, outputs); (2) the level of uncertainty, which can vary between total ignorance and deterministic knowledge; and (3) the nature of uncertainty, due to the natural variability of the phenomena being described—(aleatory uncertainty) or due to imperfection of our knowledge (epistemic uncertainty) (Fell et al. 2005; Pate-Cornell 1996; Rougier and Beven 2013).

A standardized method to quantify physical vulnerability is the use of a vulnerability curve, also referred to as a vulnerability function, which mathematically expresses the relationship between the hazard intensity and the expected degree of loss (Papathoma-Köhle et al. 2012). Also used are the fragility curves, which provide the conditional probability for a given element to be in or exceed a certain damage state for a given hazard intensity. Both vulnerability and fragility curves are derived from statistical analysis of loss/damage values which can be collected, modeled or assumed over a range of hazard intensities.

Physical vulnerability and associated uncertainty can be modeled empirically, using damage observations at building level as the main source of information. Although modeling based on observations is the most realistic, generation of vulnerability curves is often challenging because of data scarcity, inaccuracies, subjectivity and generalizations associated with building classification, damage state levels and intensity descriptors (Sterlacchini et al. 2014). Further advantages and limitations of this modeling approach are discussed in Papathoma-Köhle et al. (2015). Despite difficulties in collection and reliability of post-disaster information, as well as the uncertainty in selection of the approximation functions, they are most frequently used. Fuchs et al. (2007), Fuchs (2008), Akbas et al. (2009) and Papathoma-Köhle et al. (2012) developed vulnerability curves for torrent processes and debris flows based on real event damage information from the Austrian and Italian Alps. These studies used historical information as input data for both damage degree and process intensity. This is in contrast to Quan Luna et al. (2011), who combined numerically modeled debris flow intensities with building damage to calculate three empirical curves as a function of debris flow depth, impact pressure and kinematic viscosity. These outputs were applied in a quantitative debris flow risk assessment that expressed uncertainty using minimum, maximum and average values of direct economic losses to buildings (Quan Luna et al. 2014). Eidsvig et al. (2014) used confidence intervals and damage distribution probabilities for different intensity levels to indicate the uncertainty in the obtained empirical and fragility curves. The uncertainty in the hazard intensity was not taken into account. Similarly, Totschnig et al. (2011) and Totschnig and Fuchs (2013) investigated the uncertainties associated with the selection of a best-fit linear regression function and expressed it using uncertainty bands.

Analytical methods are less frequently used to model physical vulnerability than empirical ones because of their complexity and detailed input data requirements (Corominas et al. 2014). Nonetheless, the results take directly into account the uncertainty in parameters and models, providing an in-depth characterization of the structural behavior of buildings under different loads. Mavrouli and Corominas (2010) and Mavrouli et al. (2014) assessed vulnerability of reinforced concrete (RC) frame structures to rockfall impact, slow-moving landslides and rapid flow-type slides using finite element models and incorporating the uncertainty of the impact location and frame properties in the model. Negulescu and Foerster (2010) also proposed a methodology for deriving analytical fragility curves for RC frame structures subjected to differential settlements using a nonlinear static time-history analyses.

Finally, physical vulnerability can be estimated based on engineering judgment, where the relationship between the degree of loss and intensity resorts on expert opinion. Although this approach is subjected to high uncertainties due to its dependence on individual experience, different studies have demonstrated their usefulness in areas where information is sparse and the respondents are qualified in the investigated problem. Winter et al. (2014) used such a method to derive fragility functions that provide the conditional probability for a road to be in or exceed a certain damage state for a given debris flow volume. Godfrey et al. (2015) developed an expert-based vulnerability index for buildings impacted by hydro-meteorological hazards; this was used together with transferred vulnerability curves to generate a specific curve for the investigated area. The level of consistency in subjective judgments was quantified using an inconsistency ratio (IR). Similarly, Guillard-Gonçalves et al. (2015) measured the variability around an expert-based mean vulnerability value using standard deviation in a local-scale landslide risk study.

Other important examples of uncertainty analysis models used in landslide vulnerability analysis are given by Uzielli et al. (2008) and Kaynia et al. (2008), who applied a first-order second-moment (FOSM) approach to provide estimates of uncertainty in vulnerability by defining a central value (e.g., mean) and a measure of dispersion (e.g., variance) of the model input variables (i.e., susceptibility of structures and intensity).

Consequences are the effects resulting from the occurrence of a hazard, such as economic loss, disadvantage or gain, damage, injury or loss of life (Crozier and Glade 2005). In the case of buildings, the direct monetary loss associated with landslide activity is obtained by multiplying the vulnerability and monetary value of each building. There are two main approaches for the calculation of economic loss: using (1) building market value (Blahut et al. 2014; Remondo et al. 2008; Silva and Pereira 2014) or (2) based on building reconstruction costs (Fuchs et al. 2007; Papathoma-Kohle et al. 2012; Quan Luna et al. 2014).

The common approach for obtaining a vulnerability curve is the application of linear regression analysis (Totschnig and Fuchs 2013). A distribution function (e.g., Weibull, exponential, Gamma) is proposed, and best-fit parameters of an average function are calculated using different statistical tests, such as coefficient of determination. However, this approach can be misleading due to overfitting issues, especially when the number of observations is reduced, and it is difficult to apply when the amount of scatter in the data set is high (Harrell 2001). We propose to adapt this methodology so that a distribution function zone is calculated, which is bounded by a minimum and a maximum vulnerability curve. If the degree of scatter is high, a second distribution function can be used to describe the data set within the minimum and maximum vulnerability curves previously defined. This approach is applied at local scale in the study area in order to maximize the information gain from limited historical damage observations.

Similarly to the challenge of defining landslide hazard based on a single intensity descriptor (Keiler 2011), assessing the vulnerability of structures to landslide impact using one physical characteristic may contribute to increased levels of uncertainty in the vulnerability estimates. For example, it is expected that buildings pertaining to the same occupancy and structural type, such as residential brick–masonry buildings, are different in terms of height, geometry or age; this may result in different responses to debris flow impact. To better characterize the vulnerability of various building types in the study area, a parametric (resistance) model is applied at regional scale. Such a model takes into account different physical characteristics of the building to define quantitatively a relationship between its resistance and the debris flow intensity (Du et al. 2014; Li et al. 2010).

To our knowledge, the conceptual model applied herein has not been tested in a real case study. The two vulnerability models (empirical—Model 1, parametric—Model 2) are subsequently compared and used in direct loss estimation of the August 2003 extreme event in the Fella River valley, located in the northeastern Italian Alps.

The process of data collection regarding the value and structural characteristics of individual buildings at regional scale is very time-consuming and leads to difficulties in achieving accurate loss estimates, not only due to uncertainty in the physical effect of debris flow impact, but also due to disparities between areas with different land-use pattern (Blahut et al. 2014; Fuchs et al. 2012). To account for such differences, and due to the lack of information on reconstruction costs, a minimum and a maximum market value is used to assess direct economic loss. The obtained loss estimates are then compared with reported damages and results in other studies.

There are few regional vulnerability and loss studies that represent their pattern spatially, and most of them use discrete values (Silva and Pereira 2014). In this paper, discrete values of vulnerability and loss are represented spatially at individual building level, while continuous values are used to illustrate graphically the loss for a set of buildings, at local and regional scale. Maps representing the vulnerability and loss of exposed buildings can be useful in emergency planning, whereas vulnerability curves and probability loss distributions may help decision makers formulate strategies for rehabilitation/reconstruction investments in a given municipality or region.

The objective of this work is to develop a quantitative methodology for vulnerability and loss assessment of buildings exposed to debris flows and apply it to a study area in NE Italy at local and regional scale. The specific contribution of this work is the adaptation of existing vulnerability models to site-specific data sets and their application at various spatial scales. Moreover, the proposed methodology analyzes and partially quantifies uncertainties associated with vulnerability and loss assessment.

2 Study area

The Fella River valley is part of the upper section of the Tagliamento River Basin, which drains the Friuli-Venezia Giulia Region (FVG, northeastern Italian Alps). The area is characterized by rugged topography due to the faulted and densely fractured Permian and Triassic bedrock (mainly dolomite, limestone and calcareous marls), as well as high seismic activity. The landscape is predominantly mountainous, with high relief amplitude (between approximately 420–2750 m a.s.l) and slopes covered with deciduous or coniferous forests. Debris accumulation fans and alluvial deposits dominate the lower part of the slopes and river channels, respectively. The region is characterized by frequent heavy precipitation. Due to the lithological, structural and morphologic predisposition of the terrain, heavy convective precipitations result often in flash floods, floods, debris flows as well as shallow and deep-seated slides (Borga et al. 2007).

The administrative units overlapping the study area are Malborghetto-Valbruna, Pontebba, Tarvisio and Dogna municipalities. This territory presents high national interest due to its strategic position, at the border with Slovenia and Austria, which resulted in years of urbanization and development of a dense infrastructure network (Malek et al. 2014). Nevertheless, it has a low population density, ranging between 2.26 inhabitants/km² in Dogna and 22 inhabitants/km² in Tarvisio (ISTAT, 2014). Seasonal tourism, which is the main source of income in the area, accounts for a high variation in population density

throughout the year. Considering the available damage information and the objective of this paper, two scales of analysis are used: (1) regional, in which residential structures within the entire study area are considered, and (2) local, encompassing residential buildings within the Malborghetto-Valbruna commune (Fig. 1).

An intense rainfall in the afternoon of August 29, 2003, affected the easternmost sector of the Italian Alps over an area of approximately 200 km², overlapping mainly the Tarvisio, Malborghetto-Valbruna, Pontebba and Dogna communes. The convective system resulted as a combination of two extreme events, since very large accumulations of rainfall over 3–6 h occurred at the end of a climatic anomaly of prolonged drought and warm conditions in Europe and over the Mediterranean (Borga et al. 2007). The rainfall, lasting about 12 h in total, with a maximum intensity of 101.3 mm/h and a cumulative precipitation of 389 mm, resulted in debris flow processes with volumes ranging between few hundreds to ten thousand cubic meters and extreme values roughly attaining 100,000 m³ (Friuli-Venezia Giulia Civil Protection, 2012). The Fella River and its tributaries experienced floods and flash floods, respectively, with channel sections resulting in temporary sediment overload leading to destruction or burial of bridges, hundreds of meters of road

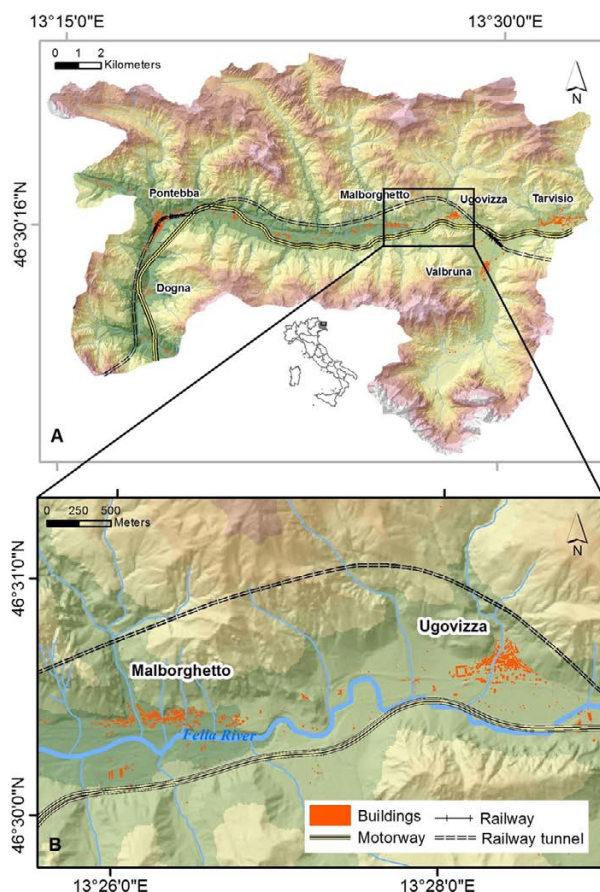


Fig. 1 Location of the study areas: **A** regional scale (Fella River valley); **B** local scale (Malborghetto and Ugovizza settlements, Malborghetto-Valbruna commune)

segments and narrow valley floors. Debris flow material, often 2 m thick, and muddy water flash-flood deposits affected settled areas or scattered houses along the lower part of the slopes, causing the loss of two lives and at least 1 billion Euros of damage costs (Fig. 2). Reports of the Civil Protection state that direct losses to companies and private buildings (excluding infrastructure and mitigation works) caused by floods and debris flows in Malborghetto-Valbruna, Pontebba, Tarvisio and Dogna communes reached a total of 59.5 million Euros, out of which 61 % were registered in Malborghetto-Valbruna alone.

3 Data and methodological framework

The methodological framework proposed in this study can be divided in two parts, each accounting for a conceptual model and scale of analysis. Each part consists of two methodological steps: (1) vulnerability assessment and (2) loss estimation. Figures 3 and 4 describe graphically the two methodological workflows. At local scale (Fig. 3), vulnerability is calculated empirically as the ratio between the damage costs and building monetary value (Model 1). Debris flow intensity described using debris height (measured in centimeters) is estimated at each impacted building from photo-documentation (Papa-thoma-Köhle et al. 2012). To generate minimum and maximum vulnerability curves, distribution functions are selected and their parameters calculated through regression analysis. In a second step, building market value is used together with the vulnerability value and its associated intensity to calculate the cumulative probability of loss using Monte Carlo sampling.

At regional scale (Fig. 4), vulnerability is calculated on the basis of a conceptual model proposed by Li et al. (2010), which takes into account multiple physical resistance characteristics of buildings (Model 2). The process intensity is estimated as a function of



Fig. 2 Damage produced by debris flows and flash floods to infrastructure and buildings in the aftermath of the August 2003 event (*source*: Civil Protection, FVG Region, 2012)

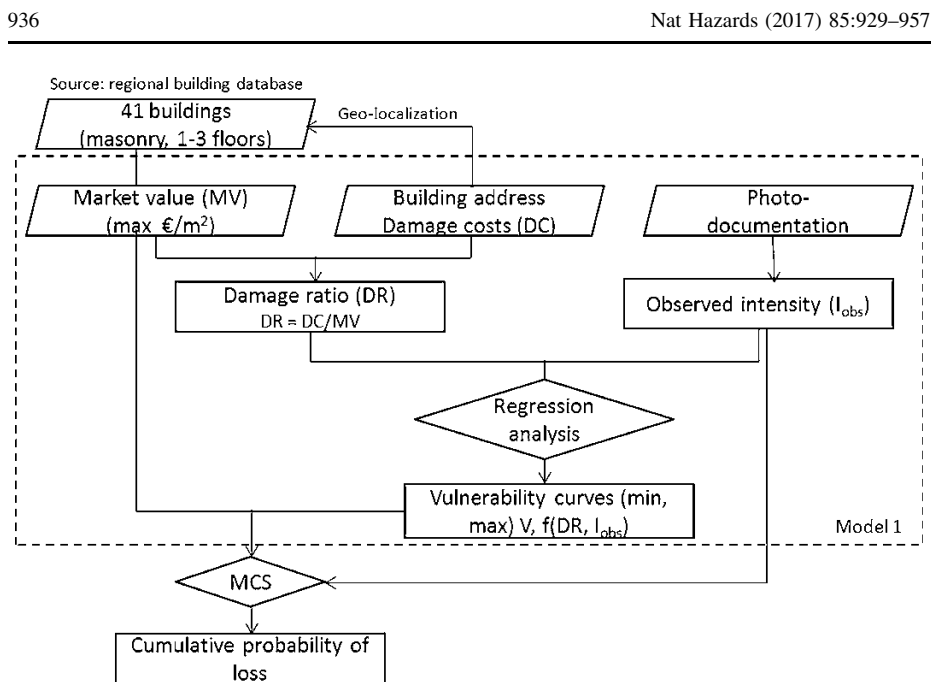


Fig. 3 Flow diagram showing the methodology used to obtain vulnerability curves and cumulative probability of loss at local scale. *MCS* Monte Carlo sampling

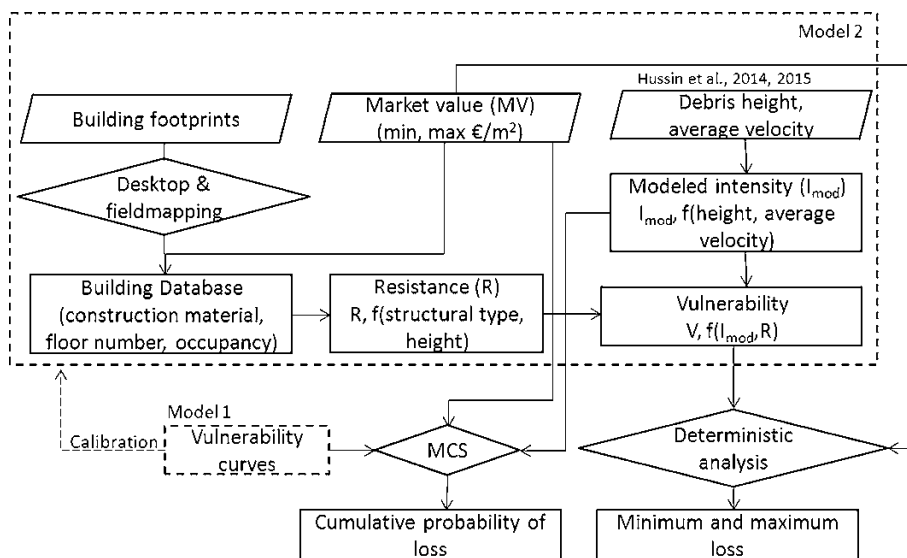


Fig. 4 Flow diagram showing the methodology used to obtain vulnerability values, minimum and maximum loss and cumulative probability of loss at regional scale. *MCS* Monte Carlo sampling

numerically modeled debris height (Chen et al. 2016; Hussin et al. 2014a, 2015); structural type and building height are used for the estimation of building resistance. Both resistance and intensity are expressed in non-dimensional terms and used to compute an

average vulnerability per building. In a second step, the obtained vulnerability values are used together with the market value to calculate the minimum and maximum loss for each building in the study area, from which a total (minimum and maximum) loss per commune is determined.

Finally, the vulnerability curves developed in Model 1 are applied at regional scale, and loss simulation results are compared with those obtained using vulnerability Model 2. In addition, a subset of the building stock is used to investigate differences in input data and vulnerability models. This work contributes to the risk assessment of debris flow hazard in Fella River valley together with other studies performed within the CHANGES FP7 Project.¹

3.1 Building database

Physical vulnerability assessment requires detailed and up-to-date, geo-localized information about the exposed elements at risk (Schwendtner et al. 2013; van Westen et al. 2006). Thus, the data that were needed to evaluate the resistance and value of buildings in the Fella River valley were inventoried through desktop mapping and field work. A building footprint map with basic attribute information was initially provided by the Civil Protection of the FVG Region. Later, Google Earth and Google Street View image interpretation, as well as field work, was used to acquire detailed information about building characteristics such as occupancy type, material of construction and number of floors.

The monetary value of buildings was obtained as standard minimum and maximum market price (Euros/m²) corresponding to each building type and cadastral zone from the Real Estate Observatory of the Italian Revenue Agency (Osservatorio del Mercato Immobiliare, Agenzia delle Entrate, 2013). The prices were obtained for the second semester of 2013 and adjusted for the effect of inflation using the Italian Consumer Price Index (ITCPI 2005). In this study, the reconstruction/rehabilitation cost was not available; therefore, we decided to use official market values which are easily accessible even for large areas (regional scale) and updatable in further studies. A similar approach was used by Blahut et al. (2014) to estimate the direct loss to debris flows of private properties in Valtellina di Tirano, Italy. The drawback of using these values is the fact that they reflect not only the value of the building, but also the price of the lot, and therefore, they are more sensitive to market fluctuations. Thus, the calculated loss estimations should be considered relevant only for the time of the analysis. To approximate the difference between the market value of a building and its reconstruction/rehabilitation cost, we compared the unit value of single residential houses with similar buildings in analogous socioeconomic contexts.

Finally, the database containing 4778 buildings was stored and processed in a GIS vector data model. In this study, only residential buildings of various occupancy types (apartment building, holiday apartment, house, etc.) are used for the assessment of vulnerability and direct economic loss. More information about the general characteristics of the regional building stock is presented in Chen et al. (2016).

Detailed damage information in the aftermath of the 2003 disaster event was available only for a limited number of buildings. This was collected as photo-documentation, damage cost reports and testimonies from local authorities, Geological Service and Civil

¹ CHANGES Project (Changing Hydro-meteorological Risks as Analyzed by a New Generation of European Scientists), Marie Curie Initial Training Network, FP7/2011–2014.

Protection of the FVG Region. Given the scarcity of damage documentation, empirical evidence was used to assess vulnerability of residential buildings only in Malborghetto-Valbruna commune, as described below.

3.2 Empirical vulnerability assessment (Model 1)

Vulnerability curves represent quantitative expressions of the relationship between hazard intensity and the expected damage degree of an element at risk. Intensity is usually estimated using one (rarely two or more) spatially distributed parameter(s) describing the destructive capacity of the process (Hungr, 1997) (e.g., for debris flows: average velocity, impact pressure, accumulation height). In this study, height of accumulated material is used as intensity proxy. Although it may not be the most relevant debris flow intensity descriptor, it is regularly used in empirical studies, since it is directly visible in the field and easy to interpret by decision makers (Quan Luna et al. 2011).

3.2.1 Process intensity estimation using damage photo-documentation

In a first step, photo-documentation of damaged structures and high-resolution aerial images were used to estimate the debris flow height. This method was developed and applied for similar processes by Papatoma-Köhle et al. (2012) in a well-documented case study in South Tyrol, Austrian Alps. The debris flow intensity was estimated by visually measuring the maximum deposit height against the upstream building wall (Fig. 3). Photo-documentation was acquired 1–3 days after the event (August 30–September 1, 2003) by the Civil Protection of FVG Region. Although a few photographs were difficult to assess, it was generally possible to estimate the height of the material and make observations about its nature (e.g., debris type and size, matrix granulometry). Figure 5 illustrates the differences in debris height between the upslope and the downslope part relative to a building, as well as the size and nature of the accumulated material. Depending on the position of the camera and the number of photographs per building, this situation may represent a source of error in measurement. It should also be noted that the observed debris height may not entirely correspond to the surge that caused the building damage, due to, for example, subsequent erosion.



Fig. 5 Building impacted by debris flow (A) 1 day after the August 2003 event and (B) during the field work campaign in 2013

3.2.2 Calculation of damage ratio

Studies on vulnerability of buildings to debris flows vary not only in terms of the use of various intensity proxies, but also due to different expressions of damage degree. Papathoma-Köhle et al. (2011) presented a list of vulnerability expressions, such as monetary loss, damage states or a combination of resistance (susceptibility) factors, which vary greatly as a consequence of data availability and scope of analysis. In this study, vulnerability is calculated as the ratio between the reported damage costs of a given building and its monetary value. The building monetary value was obtained by multiplying the maximum market value (Euros/m²), provided by the Real Estate Observatory of the Italian Revenue Agency, with the floor space (equal to the area multiplied by the number of floors). The maximum market value of single-house residential buildings in Malborghetto-Valbruna is equal to 1000 €/m². This value is comparable with the reconstruction/rehabilitation value (i.e., 1153 €/m²) of similar buildings in analogous socioeconomic regions, as for example in the Autonomous Province of Bolzano/Bozen, South Tyrol (Papathoma-Köhle et al. 2012).

Damage cost data were obtained from the Malborghetto-Valbruna municipality. These represent paid-out monetary compensation ranging from 75 to 90 % of the total loss, for damaged and destroyed buildings, as stated by the Decree No. 107/CD/2004, from May, 6 2004; from these values, a total damage cost was calculated. The reported losses were assessed separately for the building structure, technical costs (e.g., expenses related to cleaning debris material, sludge) and interior assets. In this study, we consider only the vulnerability and losses associated with the building envelope (structural damage).

The quality of the collected information and assumptions made to calculate the damage ratio resulted in a number of inaccuracies. The main errors might stem from the use of building market value as proxy for the reconstruction/rehabilitation value and the geolocalization of buildings based on the address. We also identified one mismatch between the reported costs and the building's damage state.

3.2.3 Quantification of vulnerability

To generate vulnerability curves, all buildings were represented as points in a two-dimensional space with intensity values on the x -axis and damage ratio on the y -axis. During the regression analysis, a high scatter in the data set was observed. One way to overcome this issue was to characterize the entire data set by using a type of distribution concordant with the level of knowledge, and for which the parameters are easiest to determine. In this study, a triangular cumulative function was used to represent the range of plausible vulnerability values. The advantage of this function is that it performs well even if little is known about the parameters outside the approximate estimate of its three known values (Haines 2009). Moreover, it fulfills the mathematical requirements of a vulnerability function, i.e., degree of loss between 0 and 1, and is monotonic increasing with the interval of the explaining variable (Papathoma-Köhle et al. 2012). The triangular cumulative function (CF) is defined mathematically as shown in Eq. 1:

$$V(I) = \begin{cases} 0, & I < a \\ \frac{(I-a)^2}{(b-a)(c-a)}, & a \leq I \leq c \\ 1 - \frac{(b-I)^2}{(b-a)(b-c)}, & c < I \leq b \\ 1, & I > b \end{cases} \quad (1)$$

where V is the vulnerability, I the intensity, a is the lowest intensity value (under which no damage is expected), b is the highest intensity value, and c is an intensity value varying between a and b and controlling the location of the inflection point. These values are obtained through curve fitting at the upper- and lowermost boundaries of the scattered data set. Equation 1 is used as input in regression analysis to generate minimum and a maximum vulnerability curves which envelop the data set. To simulate the scatter of the data set between the two vulnerability limits, a uniform distribution can be selected to characterize the space between them. The uniform cumulative distribution function (CDF) is defined mathematically as shown in Eq. 2:

$$V(X) = \begin{cases} 0, & X < a \\ \frac{X - a}{b - a}, & a \leq X < b \\ 1, & X \geq b \end{cases} \quad (2)$$

where a and b represent the minimum and the maximum vulnerability values (limits) calculated using Eq. 1, and X is a random variable uniformly distributed between them. Finally, the minimum and maximum vulnerability curves defined by the probability distributions and their parameters are used as input in the next phase of direct loss calculation (Sect. 4.4).

3.3 Parametric vulnerability assessment (Model 2)

Physical vulnerability of a building can also be calculated based on a set of factors (indicators) that reflect its capacity to withstand the impact of a hazard with a given intensity. For example, Du et al. (2014) used the structural type, ratio of service years to design service life and the difference between the flow direction and the longitudinal direction of the structure to calculate its vulnerability to debris flows. Such a model (called in this study parametric) is useful in areas where vulnerability curves are missing or for regional-scale assessments where the heterogeneity of buildings with the same occupancy and structural type is high.

In this paper, a conceptual vulnerability model was adapted from Li et al. (2010). The authors calculated the average vulnerability as a function of intensity-to-resistance ratio:

$$V = \begin{cases} 2 \frac{I^2}{R^2} & \frac{I}{R} \leq 0.5 \\ 1.0 - \frac{2(R - I)^2}{R^2} & 0.5 < \frac{I}{R} \leq 1.0 \\ 1.0 & \frac{I}{R} > 1.0 \end{cases} \quad (3)$$

where I is the hazard intensity associated with the exposed element at risk, and R is the resistance ability of the element to withstand the landslide. Both intensity and resistance are expressed in non-dimensional terms. Building resistance (R) to landslide hazard is defined in this paper using the function indicated by Li et al. (2010):

$$R = (\zeta_{\text{STR}} \times \zeta_{\text{SHT}})^{\frac{1}{2}} \quad (4)$$

where ζ_{STR} is the structural typology factor (represented by the material of construction), and ζ_{SHT} is the building height factor (represented by the number of floors). These two factors were selected because it was possible to collect information related to them over the

entire area, and they have been identified among the most relevant in previous studies (Silva and Pereira 2014; Uzielli et al. 2015). Through field work and desktop mapping, the following building categories were defined: wood single-story and low-rise (WO1, WO2); masonry single-story, low-rise and medium-rise (MA1, MA2, MA3); and reinforced concrete single-story, low-rise and medium-rise (RC1, RC2, RC3, RC4). A weight was assigned to each resistance factor based on literature survey and critical analysis of the values adopted by Li et al. (2010). Finally, resistance was computed for each building as shown in Eq. 4.

3.3.1 Process intensity estimation using dynamic runout modeling

The hazard intensity (I) is calculated by:

$$I = 0.1 \cdot D_{\text{dpt}} \quad (5)$$

where I is debris flow intensity and D_{dpt} is the debris height (measured in cm) obtained by Hussin et al. (2014b) using dynamic runout modeling. The model outputs were minimum, average and maximum runout maps with debris heights for four a priori defined hazard event scenarios. According to Chen et al. (2016), the August 2003 event corresponds to a major hazard event scenario, with a return period (RP) of around 133 years and within the 100–500 RP range. Thus, the maximum debris flow runout map was selected to perform the vulnerability assessment at regional scale. A detailed description of model parameterization and spatial probability calculation is provided in Hussin et al. (2015).

Li et al. (2010) proposed that in addition to debris flow height, average velocity can be used to estimate debris flow intensity. Hussin et al. (2014a) simulated landslide average velocities (and debris heights) for a post-August 2003 scenario in a representative sub-catchment in the Fella River valley. The authors found that the maximum velocity near houses was varying between 1.8 and 3.9 m/s. To improve the regional analysis with the addition of this parameter, flow velocity needs to be assessed at landslide or sub-catchment level over the entire study area. However, such an endeavor requires significant time, data and computational resources, which are rarely available even for smaller study areas. For this reason, and also to enhance the comparison of modeling results with those obtained in empirical approaches, we decided to use only accumulation height as intensity proxy for debris flows (Eq. 5). In order to reduce the uncertainty in vulnerability estimates, future studies should incorporate additional parameters such as impact pressure or average velocity in the analysis.

3.4 Loss estimation

In this study, we assess the direct economic loss to residential buildings affected by the August 2003 debris flow event with a return period of 100–500 years (Chen et al. 2016). Loss is calculated for each exposed building (polygon features in the GIS) as the product between its physical vulnerability and market value (Silva and Pereira 2014):

$$\text{Loss} = \text{PV} \cdot \text{MV} \quad (6)$$

where PV represents physical vulnerability (non-dimensional term), and MV is the market value (measured in Euro). Two different approaches are used to express economic loss starting from this mathematical relation: (1) using continuous values illustrated as cumulative probability of loss, and (2) discrete (minimum and maximum) values of loss.

The former approach is applied initially at local scale using the maximum market value, the observed debris flow height and the associated minimum and maximum vulnerability value (see Fig. 3). For example, the vulnerability of a given masonry building impacted by a debris flow front with a height of 2.8 m may vary between 0.27 and 0.89, according to the empirical analysis results (Model 1). A value between these minimum and maximum limits is then randomly selected and multiplied with the maximum market value to obtain a direct loss value. This process is iteratively performed in MATLAB[®] in 3000 iterations, and a cumulative probability curve of loss is plotted for the entire building stock. The result illustrates graphically the probability of being above or below a particular loss value, or of being within, or outside, a particular loss range. It should be noted that the probability in this context does not refer to the temporal probability of the debris flow event. To calculate the loss at regional scale using the same approach, we assumed that the vulnerability curves generated at local scale are representative for the residential building stock in Fella River valley. Therefore, the same methodological steps as described above were employed for the 721 buildings (see Fig. 4), with the difference that modeled intensities were used (Hussin et al. 2014b) instead of observed ones.

Finally, to express direct losses in discrete values, we took into account the vulnerability values obtained at regional scale (using Model 2), and the minimum and maximum market values. The loss was calculated according to Eq. 6 and expressed quantitatively as minimum and maximum loss for each building in the study area.

4 Results

4.1 Building characteristics

The application of the methodological framework is tested in Fella River valley, in the northeastern Italian Alps. In this study area, the majority of the 4778 buildings (81.3 %) are residential, out of which 721 were exposed to maximum modeled debris flow heights associated with the August 2003 event. The latter were obtained by intersecting the debris flow intensity map with the elements at risk map. From these, at least 26 % are seasonal (if we consider that holiday apartments and cabins are not occupied throughout the year), and 33 % are residential storage structures (garages and sheds). Buildings with mixed land use like commercial–residential buildings represent 0.6 % of the total building stock, out of which none were exposed to modeled debris flows. Figure 6 summarizes the main characteristics of the exposed structures.

Generally, the affected buildings were located at the contact between the slope and alluvial plain, below or in the immediate vicinity of debris flow channels. Two-thirds of the 721 impacted buildings were 2–3-story masonry houses (41 %) and one-story wooden cabins (34 %). Buildings constructed with mixed materials represented 17 % from the total, most of which (16 %) were 2–3-story masonry–wood houses. The least impacted were one-story brick sheds (4 %) and concrete apartment buildings of more than 3 stories height (3 %).

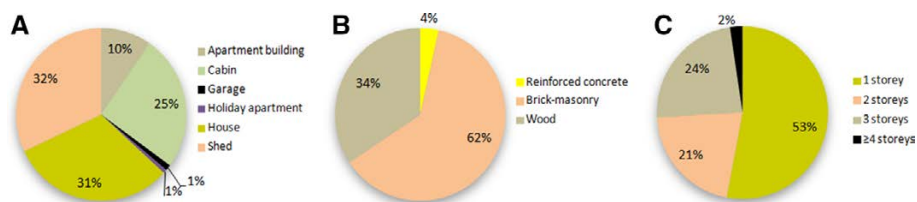


Fig. 6 Main characteristics of the exposed buildings to modeled debris flows representing the August 2003 event. The following attributes are shown: (A) use, (B) material of construction, and (C) number of storeys (data set: 721 buildings)

With regard to the data set of 41 buildings used for empirical vulnerability modeling at local scale, it is comprised out of structures of 1–3 storeys height, 13 of which are mixed masonry–wood, and 28 are masonry buildings. Figure 7 describes the variability within the data set in terms of material of construction and number of floors against the registered damage costs.

The data show that generally the damage distributions of multi-storey and masonry–wood buildings are positively skewed, with higher relative frequency of buildings in low damage classes (up to 50,000 €). The damage distribution of masonry buildings on the other hand seems to follow a bimodal uniform pattern. The median damage cost for 2- and 3-story buildings is 67,494 and 40,227 €, respectively. There are two buildings of 1 story height in the sample data set; the difference in registered damage costs might be explained (if no other variable is considered) by variations in hazard intensity (see Fig. 8), as both are masonry buildings. In terms of construction material, median damage value for masonry and masonry wood buildings is 64,268 and 24,801 €, respectively.

Damage to the 41 buildings was caused by different types of impact, depending on the location of buildings and the characteristics of the process. Since debris depth was measured from photographs at building level, Fig. 8 illustrates the spatial pattern of damage costs relative to debris flow intensity only for those buildings for which this information was available. In Malborghetto (Fig. 8A), buildings that were orthogonally facing the main flow direction were (partially) buried by depositional debris of 120–280 cm (for example, in Fig. 5). No buildings in this area collapsed due to dynamic impact pressure. As expected, the further away the building and the larger the angle between the structure and the main flow direction, the lower the damage costs for buildings with similar features. This pattern is more evident in Ugovizza, where buildings located closest to the flow

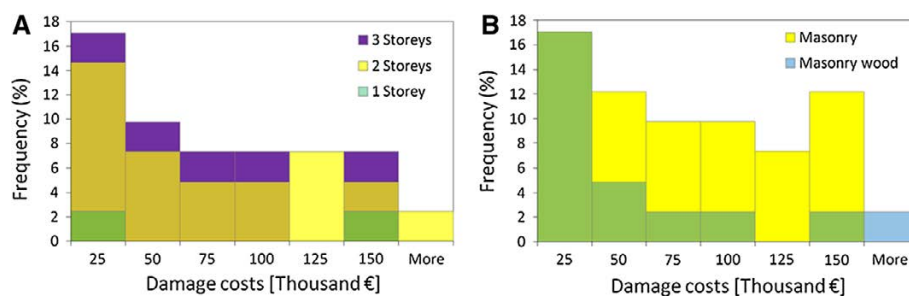


Fig. 7 Frequency plot of (A) material of construction and (B) number of storeys of buildings exposed to observed debris flow height in the August 2003 event (data set: 41 buildings). Overlapping bins are green and dark yellow

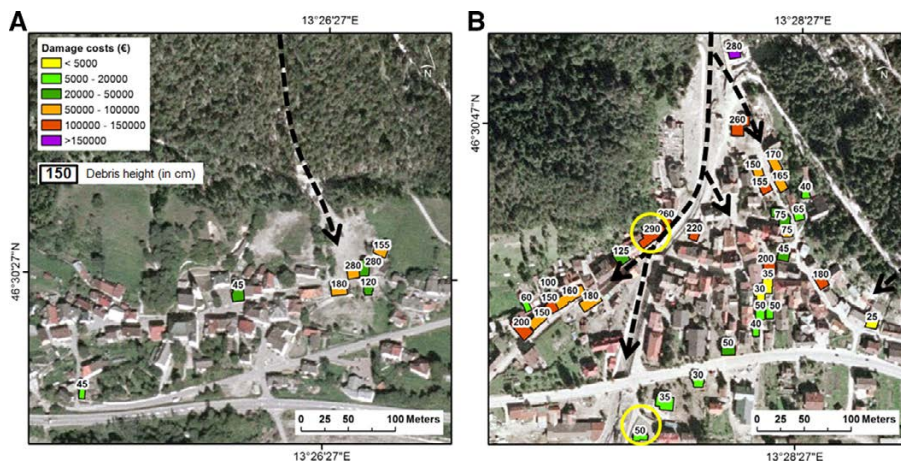


Fig. 8 Spatial pattern of damage costs and debris flow intensity in (A) Malborghetto and (B) Ugovizza. Black arrows indicate flow direction; yellow circles emphasize differences in damage costs/debris height for 1-story masonry buildings

channel are associated with the highest damage costs and vice versa (Fig. 8B). In this catchment, buildings were affected by direct flow impact, accumulation and abrasion. Moreover, the main flow had a strong flood character (debris flood) with high sediment concentration and secondary debris flows coming from lateral slopes carrying material with lower water content. It should be noted that due to the lack of damage information, not all affected buildings in the two impacted areas were mapped.

4.2 Building vulnerability assessment using Model 1

The methodology for vulnerability assessment at local scale is based on the generation of minimum and a maximum vulnerability curves from the empirical data set described above. Based on evidence presented in photo-documentation and damage reports, two empirical points were rejected from the analysis (red points in black circle in Fig. 9) due to mismatches between reported damage costs and observed impact effects. The parameter values used to calculate the vulnerability curves based on Eq. 1 are presented in Table 1.

Fig. 9 Minimum, average and maximum vulnerability as a function of debris height (data set: 39 buildings; see “Appendix”). Empirical points are classified according to building value (green $\lt; 200$ k Euros; orange 200–500 k Euros; red >500 k Euros). Data artefacts in black circle

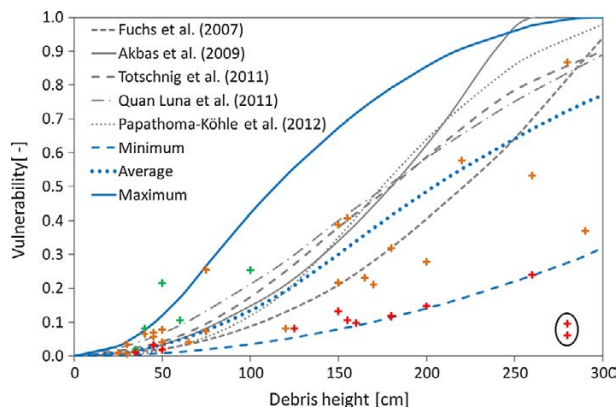


Table 1 Parameter values for Eq. 1 (*a*—lowest, *b*—highest and *c*—value varying between *a* and *b*) for minimum (min), average (average) and maximum (max) vulnerability curves

Intensity parameter (cm)	Min	Average	Max
<i>a</i>	0	0	0
<i>b</i>	300	650	1000
<i>c</i>	70	185	300

Initially, Eq. 2 was tested to simulate the scatter of the data set between the minimum and maximum vulnerability curves. However, relatively better results were obtained using only Eq. 1; therefore, we decided not to use Eq. 2 in the final analysis.

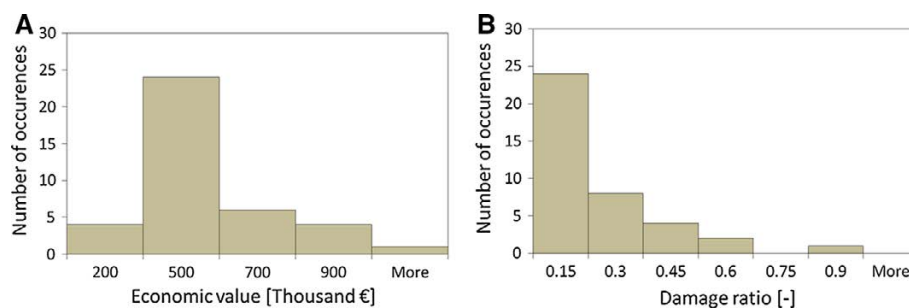
Figure 9 shows that the observations associated with debris heights of 25–100 cm and ≤ 0.25 degree of loss are well differentiated. However, for medium (100–200 cm) and high (>200 cm) process intensities, the spread is considerable, although for the latter fewer data points were available. For illustration purposes, an average vulnerability curve was also calculated. This falls within the range of variability of currently existent vulnerability functions, as the ones proposed by Akbas et al. (2009), Fuchs et al. (2007), Quan Luna et al. (2011), Totschnig et al. (2011) and Papathoma-Köhle et al. (2012) for similar buildings in north Italy and south Tyrol (Austria). For intensities up to 135 cm, the average curve coincides relatively well with that of Akbas et al. (2009) and Papathoma-Köhle et al. (2012). For intensities between 135 and 240 cm, it underestimates the values calculated by all authors with the exception of Fuchs et al. (2007). This might be explained by differences in process characteristics such as water-to-solid ratio, type of debris transported (e.g., wooden debris) or flow velocity in different study areas, but it is also related to the incomplete documentation of buildings that were impacted by high-intensity processes in Fella River valley. Other general differences between the six average vulnerability curves are attributed to the number of observation points used to generate them, the intensity assessment method, as well as possible discrepancies in building design and construction techniques.

In economic vulnerability approaches, the size of the building plays an important role as the damage ratio is lower for larger (more valuable) than for smaller (less valuable) buildings exposed to equal intensity levels. To account for this bias in the model, we normalized the intensity against the height of the building; however, the scatter showed no significant change. As the statistical spread of vulnerability values is expected to have an effect on the computation of loss using Monte Carlo sampling, we decided to split the local and regional data sets in three classes depending on the economic value of the building (Table 2; Fig. 10). Minimum and maximum vulnerability curves were then calculated for each class using the parameter values for Eq. 1 presented in Table 2.

The distribution of the damage ratio for the 39 buildings is positively skewed, with mean and median values of 0.17 and 0.1, respectively. From the total data set, 62 % of the buildings registered a damage ratio below 0.15 (24 buildings) and 8 % (3 buildings) above 0.5. The latter are related to debris heights of more than 220 cm. Note the absence of buildings within the 0.6–0.75 and >0.9 damage ratio intervals. The latter might be explained by the fact that damage was induced only by infill of debris and subsequent (partial) wall collapse or burial and not complete destruction.

Table 2 Parameter value for Eq. 1 (*a*—lowest, *b*—highest and *c*—value varying between *a* and *b*) for minimum (min) and maximum (max) vulnerability curves of each building class

Intensity parameter	<200 k Euro		200–500 k Euro		>500 k Euro	
	Min	Max	Min	Max	Min	Max
<i>a</i>	0	0	0	0	0	0
<i>b</i>	550	300	800	550	1000	800
<i>c</i>	80	70	150	80	300	150

**Fig. 10** Histograms of (A) economic value and (B) damage ratio of buildings exposed to observed debris flow height in the August 2003 event (data set: 39 buildings; see “Appendix”)

4.3 Building vulnerability assessment using Model 2

The methodology for vulnerability assessment at regional scale is based on the application of a conceptual model that takes into account the structural typology (represented by the material of construction) and height (represented by the number of floors) to determine a building’s resistance to a given hazard intensity level. Li et al. (2010) proposed a set of theoretical (non-dimensional) values of resistance for structural typology and height based on engineering judgment (Tables 3, 4).

Initially, these theoretical values were used as input to the model, and the resulting vulnerability estimates were compared with those obtained in other empirical studies. In a second step, the theoretical values of resistance were calibrated against the results obtained

Table 3 Values for structural typology resistance factor (ξ_{STR})

Structural typology ^a		This study	Li et al. (2010)
WO	Wood	0.25	0.2
MA	Masonry	0.90	0.8
RC	Reinforced concrete	1.95	1.3

^a Mixed structural types (e.g., masonry–wood) are counted in the category of the main material of construction (e.g., masonry)

Table 4 Values for building height resistance factor (ξ_{SHT})

Height	Number of floors	This study	Li et al. (2010)
Single-story	1	0.4	0.1
Low-rise	2	0.85	0.4
Medium-rise	3	1	0.9
Medium-rise	4	1.2	0.9

with empirical Model 1. Figure 11 indicates the change in coefficient of determination from $R^2 = 0.39$ to 0.52 for a sample data set of 20 buildings, as a result of modifying the values of resistance in Model 2.

As expected, the difference between the vulnerability estimates obtained with Model 2 and those obtained in other empirical studies reduced after the calibration. For the ease of comparison, the average curve developed with Model 1 and other curves existing in the literature are plotted together with the results of Model 2, in Fig. 12. This illustrates the range of vulnerability values for wooden (WO), masonry (MA) and reinforced concrete (RC) buildings of 1–4 storys height associated with debris flow intensities of maximum 300 cm. The results generally suggest that the higher the wall resistance, the lower the expected damage degree. Single-story buildings are significantly more vulnerable than multi-story buildings of the same structural type, possibly due to the different distribution of openings (doors and windows) that allow the material to enter the building. This, however, is highly dependent on the flow dynamic pressure, as the opening may actually decrease the probability of wall failure by reducing the applied pressure (Mavrouli et al. 2014).

The empirical curve developed with Model 1 coincides up to a debris height of 130 cm with the vulnerability values of medium-rise masonry buildings obtained in Model 2. This seems to suggest that the latter overestimates the degree of loss for higher process intensities. However, the dissimilarity is due to the different methods of intensity assessment and scales of analysis (i.e., Model 1, based on debris height observations; Model 2, using regional runout modeling).

4.4 Direct loss estimation using vulnerability Model 1

Vulnerability values estimated with Model 1 are further used together with building market values to calculate the direct economic loss at local and regional scale. The total reported

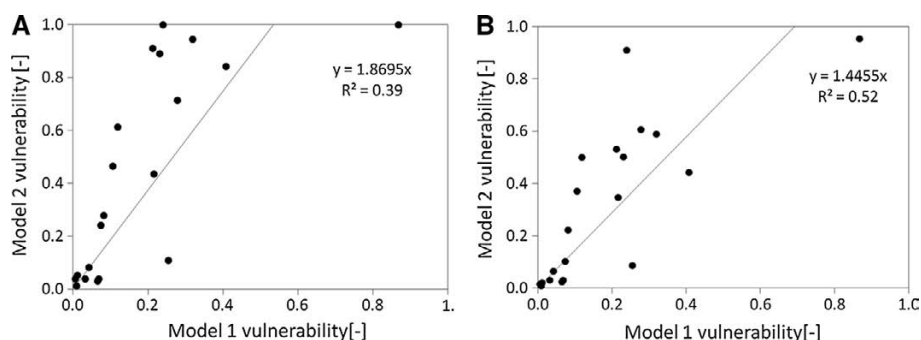


Fig. 11 Model 1 versus Model 2 vulnerability using (A) theoretical and (B) modified values of resistance for Model 2 (data set: 20 buildings). Observed debris heights were used in both models

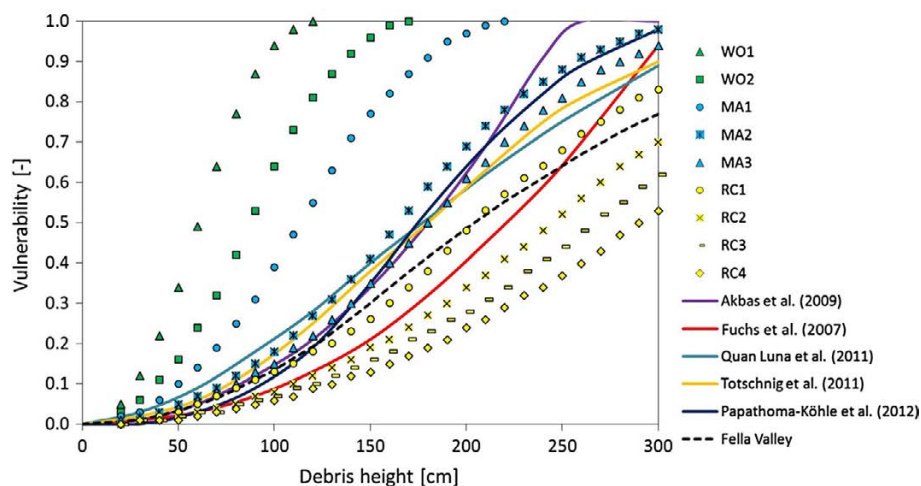


Fig. 12 Vulnerability values of wooden (WO), masonry (MA) and reinforced concrete (RC) buildings of 1–4 storeys as a function of debris height. Average vulnerability curve obtained with Model 1 and from the literature is indicated

damage costs for the 39 buildings in Malborghetto-Valbruna were equal to 2.42 million Euros. It should be noted that this amount does not reflect the technical costs or losses induced to interior assets, such as furniture and electronic equipment. The maximum value at risk for the same exposed buildings was 16 million Euros resulting in a direct economic loss of 14.2 % (Fig. 13). According to the simulations, there is a 10 % probability of having a direct economic loss below 2.37 million Euros and a 90 % probability that the loss is below 2.6 million Euros.

To compute the cumulative probability of loss for the regional building stock, we used the intensity parameter values presented in Table 2 and the maximum market value of the buildings exposed to modeled debris flows representing the August 2003 event. The results of the simulation show that there is an 80 % probability that the loss is between 44.3 million Euros and 45.4 million Euros for the exposed regional building stock.

4.5 Direct loss estimation using vulnerability Model 2

Direct loss was also calculated using vulnerability Model 2 for the entire study area. Figure 14 illustrates the maximum loss for buildings in Malborghetto and Ugovizza exposed to modeled debris heights. The maximum losses in both areas vary between less than 45 k Euros and over 500 k Euros, with higher values associated with debris height over 200 cm. A comparison of reported damage costs and estimated maximum losses for buildings exposed in both sub-catchments generally indicates an overestimation of losses at building level (between 13 and 178 %) for 14 out of 20 buildings. The reason for this might be that in Ugovizza the small debris flows coming from the side slopes interacted with the main flow which had a flash-flood character. This might have resulted in lower debris material accumulation than those estimated by the runoff model.

Figure 15 indicates the range of total loss values (minimum and maximum) per building type. Given the high proportion of multi-story masonry buildings in the study area, they registered an estimated loss between and 7.7 and 10.9 million Euros for MA2, and 19.1 and

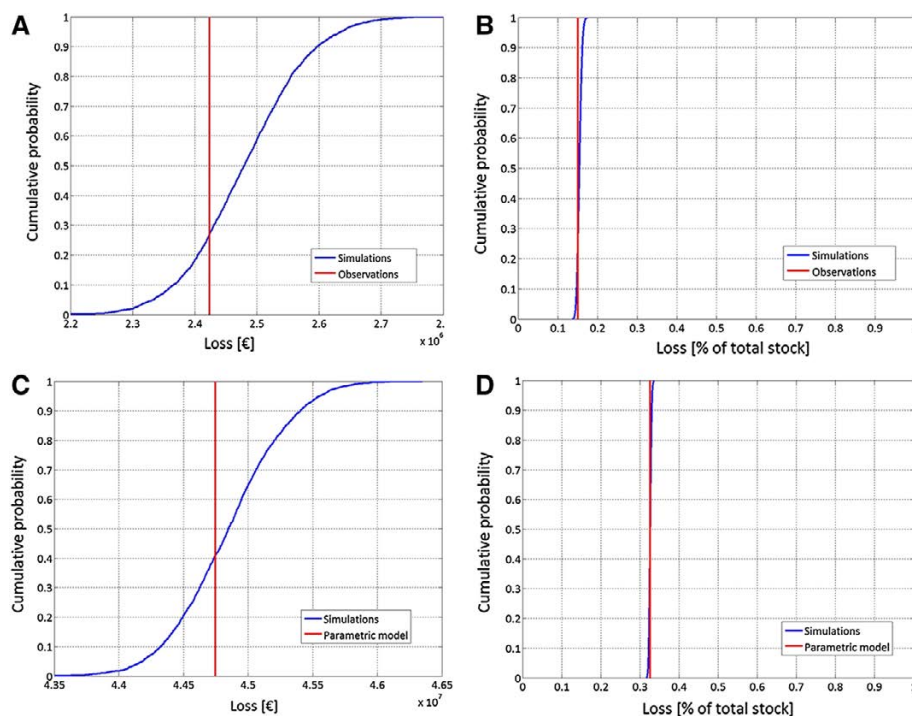


Fig. 13 Cumulative probability of loss for buildings affected by debris flows in the aftermath of the August 2003 event. Absolute and relative values of loss at (A, B) local and (C, D) regional scale. 3000 iterations have been computed

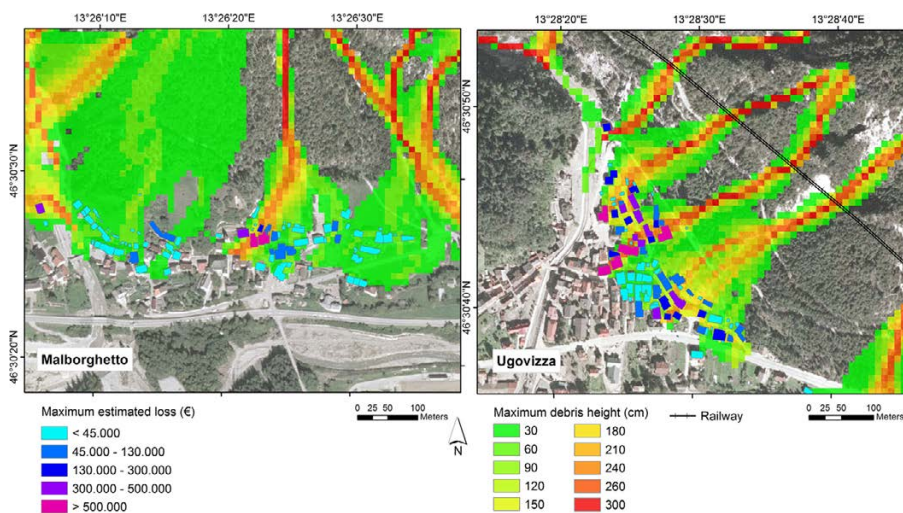


Fig. 14 Maximum direct loss estimated based on modeled debris heights and vulnerability Model 2

26.9 million Euros for MA3. A relatively significant loss value (between 1.8 and 2.6 million Euros) for a reduced number of buildings is associated with 4-story high RC buildings; these are apartment buildings located in Pontebba and Malborghetto-Valbruna.

Due to the limited damage information, a validation of the results at building level for the entire study area was not possible. However, zone-specific sums of damage costs were available from the Civil Protection of FVG Region. Table 5 presents a comparison between (maximum) modeled and documented monetary losses at commune level. The data show a relatively good estimation of damage costs for Pontebba and Malborghetto-Valbruna, the municipalities that suffered most of the losses in the study area.

A different situation is registered for Dogna and Tarvisio, where the modeled losses are underestimating or overestimating, respectively, the observed damage costs. Two explanations can be given for this: (1) The study site does not encompass the entire administrative area of the two communes (as opposed to the former ones); therefore, the building sample size is underestimated; (2) errors due to model transformations and simplifications. Table 5 also shows that the highest relative uncertainty (computed as the ratio between the maximum modeled loss and the documented loss) is associated with Dogna and Tarvisio communes.

5 Discussion and conclusions

Two vulnerability models were used in this study, each having limitations and introducing a number of uncertainties. The first vulnerability model was based on developing vulnerability curves from empirical data. The main drawback of this approach is that it is based on scarce process intensity data. Another important issue here is the definition of the damage ratio on the basis of the building value. One of the advantages of this approach is that it enhances the comparison of vulnerability curves developed in different economic regions. The limitation is that due to the heterogeneity of buildings and scale of analysis, rehabilitation/reconstruction values were not available; therefore, an approximation was used (i.e., market value).

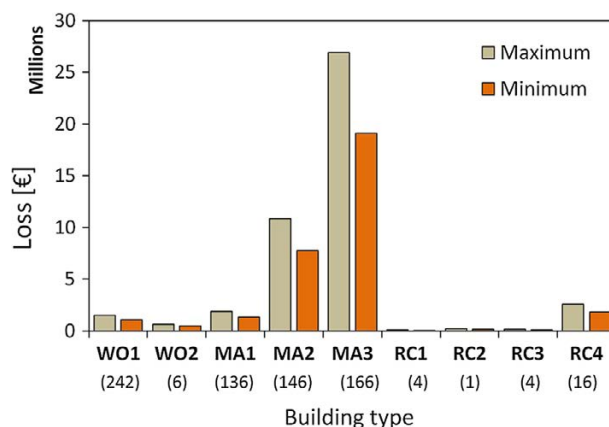


Fig. 15 Direct maximum and minimum loss values per building type in Fella River valley. The number in brackets represents the building class size

Table 5 Modeled maximum economic loss per commune (absolute and relative values) versus documented damages by the Civil Protection of the FVG Region

Commune	Documented (million Euro)	%	Modeled (million Euro)	%	Relative uncertainty ^a
Malborghetto-Valbruna	36	61	25.3	57	0.7
Pontebba	18	30	17.3	39	1
Tarvisio	0.5	1	1.8	4	3.5
Dogna	5	8	0.4	1	0.1
Total	59.5	100	44.7	100	

^a Ratio between the maximum modeled loss and the documented loss

A basic comparison between the results of Model 1 and other empirical curves from the literature shows that the average vulnerability curve developed here falls within the range of variability of the existent ones. Despite this, the wide range of the minimum–maximum curves indicates the level of uncertainty in the input data set.

The large scatter of empirical data is attributed partially to the heterogeneity of process intensity at sub-catchment level. The comparison between observed intensities and resulting damages gave an indication of the complexity and variability of process characteristics in two adjacent sub-catchment areas (e.g., from debris flows with low velocity, small debris clasts, which build up slowly a high wavefront, to high-energy velocity flows and even flash floods). Totschnig and Fuchs (2013) concluded that there is no need to distinguish between different sediment-laden torrent processes when assessing physical vulnerability of residential buildings toward torrent processes (e.g., debris flows, fluvial sediment transport). This study suggests that because of the differences in process characteristics, the use of accumulation height as intensity proxy should be replaced in the future with more relevant parameters like impact pressure or combined with flow velocity. This applies for the regional vulnerability assessment as well, although the spatial scale involves certain modeling challenges.

As demonstrated in previous studies (Alexander 2005; Fuchs 2008; Mavrouli et al. 2014), susceptibility of structures to damage induced by landslides is influenced by a number of technological and physical characteristics, among which structural typology, foundation depth and type, height and age are considered important. The second vulnerability model used in this study is based on a mathematical model that gives the opportunity to incorporate a number of resistance factors in the calculation of vulnerability. However, the values of these factors must be calibrated against empirical data or numerical (physical) modeling results to convey realistic values.

Regarding the regional loss analysis, the underestimation of total economic damages is related to the fact that reported values included losses to commercial and industrial facilities which are not considered in this study; neither are technical costs or damage to interior assets of buildings. Moreover, the analysis was performed using the present building stock and not taking into account the buildings destroyed in the August 2003 event. An integrated risk analysis to multi-hazards in Fella River valley was performed by Chen et al. (2016). The authors estimated that the economic loss associated with the August 2003 event to buildings impacted by debris flows and flash floods was 22.2 million Euros.

The interpretation of vulnerability and loss modeling results requires utmost care and should be done only considering the underlying assumptions and indicated uncertainties.

One assumption is related to use of building market values as proxy for building reconstruction/rehabilitation costs; another one allowed us to apply the empirical curves developed at local scale in the generation of the cumulative probability of loss at regional scale. Both assumptions increased the level of uncertainty in the results. Other important sources of uncertainty are presented in Table 6. From those partially treated, some are implicitly or explicitly included in the analysis. For example, the cumulative probability of loss (Fig. 13) takes into account explicitly the uncertainty in the vulnerability curves; however, the uncertainty in the process intensity estimates is only implicitly addressed (since no separate probability distribution was used to characterize it).

In order to improve the results obtained with Model 2, future applications can be amended with the use of additional resistance parameters like direction of building with respect to the direction of flow, depth of foundation or type/size building openings. However, one must decide to use only parameters whose variation has the greatest outcome in changing building resistance. This will avoid excessive computation and redundant information. Vulnerability results obtained with Model 1 can be improved by updating the damage database as soon as new information is available, as well as acquiring data about construction costs of different types of buildings. Finally, in order to fully quantify the propagation of errors between the different stages of consequence analysis, a fully probabilistic Monte Carlo simulation can be performed by substituting the range of minimum–maximum values with a probability distribution for each variable in the model.

Table 6 Sources of uncertainty in the two-phase methodologies at local and regional scale applied in this study

Source	Type	Cause	Treatment	Solution
<i>Vulnerability assessment</i>				
Selection of distribution function	E	Data set scatter	Partial	Triangular/uniform distributions
Intensity assessment	E/A	Measurement errors/natural variability	Partial	Parametrization of triangular CF
Market value	E/A	Proxy variable for building reconstruction cost	Partial	Calibration against reconstruction costs in other areas
Sampling error	E	Data set availability	No	Collection of additional data; use of confidence intervals
<i>Loss analysis</i>				
Application of Model 2	E	Testing of theoretical model	No	Validation in another study area
Resistance factors values	E/A	Heterogeneity of building stock; subjective judgment	Partial	Empirical calibration; modifying data sampling technique
Application of Model 1	E	Generalization/simplification	No	Transfer of vulnerability curves for other building types
Object value	E/A	Variability due to heterogeneity of building stock	Partial	Value ranges
Vulnerability results	E	Propagated errors	No	Monte Carlo simulation

Type: E—epistemic; A—aleatory

In this study, a multi-scale building vulnerability and loss assessment framework was developed and applied in a study area in the northeastern Italian Alps. In this work, former conceptual models were used in order to identify challenges and possible solutions in their application. The methodological framework is based on the generation of empirical vulnerability curves and vulnerability values for multiple types of buildings, which are then used to calculate the direct economic loss of individual buildings or for a set of building in a given area.

The results in this study indicate that vulnerability Model 1 simulates better the damages observed at local scale than vulnerability Model 2, due to the use of empirical data; however, the application of Model 2 at regional scale seems to be appropriate because of the heterogeneity of the building stock characteristics, which are not considered in Model 1.

The findings of this research support the idea that in order to obtain realistic vulnerability (and loss) estimates building vulnerability assessment to debris flows must take into account other intensity proxies than depth of accumulation. The variability of building responses to stresses induced by different flow-type processes cannot be explained solely by (post-event) assessment of accumulated material. This also implies that a better investigation of process characteristics is needed.

Although uncertainty was not fully accounted for/quantified in the Monte Carlo simulation, this approach enhanced the understanding of vulnerability model limitations and underlying data errors. Moreover, the expression of uncertainty as value ranges and cumulative probability plots has the advantage of being easy to convey to stakeholders and sufficiently informative to support the formulation of decision criteria, such as maximizing the minimum loss or minimizing the maximum loss (Haimes 2009).

Finally, the results obtained in this study may be used by stakeholder to identify hot spots for future mitigation planning which might lead to a reduction in future economic losses.

Acknowledgments Open access funding provided by the University of Vienna. This work is a part of the CHANGES Project (Changing Hydro-meteorological Risks as Analyzed by a New Generation of European Scientists), a Marie Curie Initial Training Network funded by the European Community, under Grant Agreement No. 263953. The research was partially supported through the Marietta Blau Grant, provided by the Austrian Federal Ministry of Science, Research and Economy (BMWFW). The authors would like to thank the stakeholders in Friuli-Venezia Giulia Region (especially the Civil Protection, Municipality of Malborghetto-Valbruna and Geological Survey) for data sharing and cooperation in the study area. We also like to thank Alessandro Pasuto (CNR-IRPI, Padua) for support in data collection and Simone Sterlacchini (CNR-IDPA, Milano, Italy) for constructive discussions. Finally, we are grateful to the anonymous reviewers for their valuable comments and suggestions on an earlier draft of this paper.

Open Access This article is distributed under the terms of the Creative Commons Attribution 4.0 International License (<http://creativecommons.org/licenses/by/4.0/>), which permits unrestricted use, distribution, and reproduction in any medium, provided you give appropriate credit to the original author(s) and the source, provide a link to the Creative Commons license, and indicate if changes were made.

Appendix

See Table 7.

Table 7 The data set used for the development of the vulnerability curves in Malborghetto-Valbruna, Eastern Italian Alps

No.	Observed intensity (cm)	Damage costs (€)	Max market value (€)	Damage ratio
1	30	2282.96	383,005.59	0.00
2	25	3476.92	393,584.87	0.00
3	35	3175.80	290,340.74	0.01
4	50	9725.99	500,793.00	0.01
5	35	14,800.81	758,351.44	0.01
6	45	24,801.87	768,554.12	0.03
7	30	9578.43	272,759.54	0.03
8	50	13,699.39	337,650.66	0.04
9	65	13,304.97	316,869.10	0.04
10	45	12,539.12	220,694.56	0.05
11	40	19,606.13	302,624.68	0.06
12	45	30,291.35	445,518.52	0.06
13	75	32,154.71	435,839.54	0.07
14	50	27,733.81	357,966.19	0.07
15	120	33,541.75	411,919.73	0.08
16	125	46,914.05	575,967.67	0.08
17	40	14,750.95	180,556.70	0.08
18	160	71,543.32	731,386.97	0.09
19	60	17,826.88	169,869.07	0.10
20	155	61,042.29	576,755.61	0.10
21	180	90,900.40	776,542.30	0.11
22	180	61,377.33	517,487.19	0.11
23	150	67,493.97	515,927.80	0.13
24	200	133,333.33	910,863.24	0.14
25	170	97,828.85	461,865.80	0.21
26	50	21,974.40	102,704.41	0.21
27	150	85,217.64	394,590.60	0.21
28	165	94,185.63	407,992.99	0.23
29	260	130,000.00	543,134.94	0.23
30	100	46,334.31	183,493.03	0.25
31	75	86,155.88	338,833.75	0.25
32	200	133,333.33	479,617.97	0.27
33	180	115,202.85	361,191.75	0.31
34	290	133,333.33	360,307.23	0.37
35	150	111,559.44	287,945.90	0.38
36	155	102,058.39	250,412.90	0.40
37	260	133,333.33	250,595.10	0.53
38	220	139,648.32	242,335.83	0.57
39	280	177,969.65	205,180.77	0.86

References

- AGS (2007) Practice note guidelines for landslide risk management. Australian Geomechanics Society Landslide Taskforce, Landslide Practice Note Working Group Australian Geomechanics, vol 42, pp 63–114
- Akbas SO, Blahut J, Sterlacchini S (2009) Critical assessment of existing physical vulnerability approaches for debris flows. In: Malet JP, Remaitre A, Bogaard T (eds) International conference—landslide processes: from geomorphologic mapping to landslide modelling, 6–7 February 2009, Strasbourg, France, 2009. pp 229–233
- Alexander D (2005) Vulnerability to landslides. In: Glade T, Anderson MG, Crozier M (eds) Landslide hazard and risk. Wiley, Chichester, pp 175–198
- Birkmann J (2006) Measuring vulnerability to promote disaster-resilient societies: conceptual frameworks and definitions. In: Birkmann J (ed) Measuring vulnerability to natural hazards: towards disaster resilient societies. United Nations University Press, Tokyo, pp 9–54
- Blahut J, Glade T, Sterlacchini S (2014) Debris flows risk analysis and direct loss estimation: the case study of Valtellina di Tirano, Italy. *J Mt Sci* 11:288–307. doi:[10.1007/s11629-013-2806-2](https://doi.org/10.1007/s11629-013-2806-2)
- Borga M, Boscolo P, Zanon F, Sangati M (2007) Hydrometeorological analysis of the 29 August 2003 flash flood in the eastern Italian Alps. *J Hydrometeorol* 8:1049–1067. doi:[10.1175/jhm593.1](https://doi.org/10.1175/jhm593.1)
- Cardinali M et al (2002) A geomorphological approach to the estimation of landslide hazards and risks in Umbria, Central Italy. *Nat Hazards Earth Syst Sci* 2:57–72. doi:[10.5194/nhess-2-57-2002](https://doi.org/10.5194/nhess-2-57-2002)
- Chen L, van Westen CJ, Hussin HY, Ciurean RL, Turkington T, Chavarro D, Shrestha DP (2016) Integrating expert opinion with modelling for quantitative multi-hazard risk assessment in the Eastern Italian Alps. *Geomorphology* 273:150–167
- Corominas J et al (2014) Recommendations for the quantitative analysis of landslide risk. *Bull Eng Geol Environ* 73:209–263. doi:[10.1007/s10064-013-0538-8](https://doi.org/10.1007/s10064-013-0538-8)
- Crozier MJ, Glade T (2005) Landslide hazard and risk: issues, concepts and approach. *Landslide hazard and risk*. Wiley, Chichester, pp 1–40. doi:[10.1002/9780470012659.ch1](https://doi.org/10.1002/9780470012659.ch1)
- Cutter SL, Boruff BJ, Shirley WL (2003) Social vulnerability to environmental hazards. *Soc Sci Q* 84:242–261. doi:[10.1111/1540-6237.8402002](https://doi.org/10.1111/1540-6237.8402002)
- Du J, Yin K, Lacasse S, Nadim F (2014) Quantitative vulnerability estimation of structures for individual landslide: application to the Metropolitan Area of San Salvador, El Salvador. *Electron J Geotech Eng* 19:1251–1264
- Eidsvig UMK, Papathoma-Köhle M, Du J, Glade T, Vangelsten BV (2014) Quantification of model uncertainty in debris flow vulnerability assessment. *Eng Geol* 181:15–26. doi:[10.1016/j.enggeo.2014.08.006](https://doi.org/10.1016/j.enggeo.2014.08.006)
- Fell R, Ho KKS, Lacasse S, Leroi E (2005) A framework for landslide risk assessment and management. In: Hungr O, Fell R, Couture R, Eberhardt E (eds) *Landslide risk management*. Taylor and Francis, London, pp 3–26
- Fuchs S (2008) Vulnerability to torrent processes. *Risk Anal* 6:289–298. doi:[10.2495/risk080291](https://doi.org/10.2495/risk080291)
- Fuchs S (2009) Susceptibility versus resilience to mountain hazards in Austria—paradigms of vulnerability revisited. *Nat Hazards Earth Syst Sci* 9:337–352. doi:[10.5194/nhess-9-337-2009](https://doi.org/10.5194/nhess-9-337-2009)
- Fuchs S, Heiss K, Hübl J (2007) Towards an empirical vulnerability function for use in debris flow risk assessment. *Nat Hazards Earth Syst Sci* 7:495–506
- Fuchs S, Kuhlicke C, Meyer V (2011) Editorial for the special issue: vulnerability to natural hazards—the challenge of integration. *Nat Hazards* 58:609–619. doi:[10.1007/s11069-011-9825-5](https://doi.org/10.1007/s11069-011-9825-5)
- Fuchs S, Ornetsmüller C, Totschnig R (2012) Spatial scan statistics in vulnerability assessment: an application to mountain hazards. *Nat Hazards* 64:2129–2151
- Glade T (2003) Vulnerability assessment in landslide risk analysis. *Erde* 134:123–146
- Glade T, Crozier MJ (2005a) The nature of landslide hazard impact. In: *Landslide hazard and risk*. Wiley, Chichester, pp 41–74. doi:[10.1002/9780470012659.ch2](https://doi.org/10.1002/9780470012659.ch2)
- Glade T, Crozier MJ (2005b) A review of scale dependency in landslide hazard and risk analysis. In: *Landslide hazard and risk*. Wiley, Chichester, pp 75–138. doi:[10.1002/9780470012659.ch3](https://doi.org/10.1002/9780470012659.ch3)
- Godfrey A, Ciurean RL, van Westen CJ, Kingma NC, Glade T (2015) Assessing vulnerability of buildings to hydro-meteorological hazards using an expert based approach—an application in Nehoiu Valley, Romania *Int J Disaster Risk Reduct* 13:229–241. doi:[10.1016/j.ijdr.2015.06.001](https://doi.org/10.1016/j.ijdr.2015.06.001)
- Guillard-Gonçalves C, Zêzere JL, Pereira S, Garcia RAC (2015) Assessment of physical vulnerability of buildings and analysis of landslide risk at the municipal scale—application to the Loures municipality, Portugal *Nat Hazards Earth Syst Sci Discuss* 3:5547–5597. doi:[10.5194/nhessd-3-5547-2015](https://doi.org/10.5194/nhessd-3-5547-2015)
- Haines YY (2009) Risk modeling, assessment, and management, 3rd edn. Wiley, London

- Harrell F, Jr (2001) General aspects of fitting regression models. In: Regression modeling strategies. Springer Series in Statistics. Springer, New York, pp 11–40. doi:[10.1007/978-1-4757-3462-1_2](https://doi.org/10.1007/978-1-4757-3462-1_2)
- Hufschmidt G, Glade T, Hufschmidt G, Glade T (2010) Vulnerability analysis in geomorphic risk assessment Geomorphological Hazards and Disaster Prevention. Cambridge University Press, Cambridge
- Hussin H et al (2014a) Assessing the effect of mitigation measures on landslide hazard using 2D numerical runout modelling. In: Sassa K, Canuti P, Yin Y (eds) Landslide science for a safer geoenvironment. Springer, Berlin, pp 679–684. doi:[10.1007/978-3-319-05050-8_105](https://doi.org/10.1007/978-3-319-05050-8_105)
- Hussin HY, Chen L, Ciurean RL, van Westen CJ, Reichenbach P (2014b) Analysing changes in landslide risk using multi temporal landslide susceptibility and run-out modeling on a regional scale. Paper presented at the International Conference on Analysis and Management of Changing Risks for Natural Hazards, Padova, Italy, 18–19 November 2014
- Hussin HY, van Westen CJ, Reichenbach P, Sterlacchini S, Frigerio S, Marcato G, Calligaris C (2015) Quantifying landslide intensity for hazard assessment on a regional scale in the Eastern Italian Alps (manuscript in preparation)
- Kaynia AM, Papathoma-Köhle M, Neuhäuser B, Ratzinger K, Wenzel H, Medina-Cetina Z (2008) Probabilistic assessment of vulnerability to landslide: application to the village of Lichtenstein, Baden-Württemberg, Germany. Eng Geol 101:33–48. doi:[10.1016/j.enggeo.2008.03.008](https://doi.org/10.1016/j.enggeo.2008.03.008)
- Keiler M (2011) Geomorphology and Complexity—inseparably connected? Zeitschrift für Geomorphologie 55:233–257
- Li Z, Nadim F, Huang H, Uzielli M, Lacasse S (2010) Quantitative vulnerability estimation for scenario-based landslide hazards. Landslides 7:125–134. doi:[10.1007/s10346-009-0190-3](https://doi.org/10.1007/s10346-009-0190-3)
- Malek Ž, Scolobig A, Schröter D (2014) Understanding land cover changes in the Italian Alps and Romanian Carpathians: combining remote sensing and stakeholder interviews. Land 3:52–73
- Mavrouli O, Corominas J (2010) Vulnerability of simple reinforced concrete buildings to damage by rockfalls. Landslides 7:169–180. doi:[10.1007/s10346-010-0200-5](https://doi.org/10.1007/s10346-010-0200-5)
- Mavrouli O et al (2014) Vulnerability assessment for reinforced concrete buildings exposed to landslides. Bull Eng Geol Environ 73:265–289. doi:[10.1007/s10064-014-0573-0](https://doi.org/10.1007/s10064-014-0573-0)
- Mazzorana B, Levaggi L, Formaggioni O, Volcan C (2012) Physical vulnerability assessment based on fluid and classical mechanics to support cost–benefit analysis of flood risk mitigation strategies. Water 4:196–218
- Negulescu C, Foerster E (2010) Parametric studies and quantitative assessment of the vulnerability of a RC frame building exposed to differential settlements. Nat Hazards Earth Syst Sci 10:1781–1792. doi:[10.5194/nhess-10-1781-2010](https://doi.org/10.5194/nhess-10-1781-2010)
- Papathoma-Köhle M, Totschnig R, Keiler M, Glade T (2012) A new vulnerability function for debris flow. The importance of physical vulnerability assessment in alpine areas. In: 12th Congress Interpraevent, April 23–26 2012, Grenoble, France
- Papathoma-Köhle M, Kappes M, Keiler M, Glade T (2011) Physical vulnerability assessment for alpine hazards: state of the art and future needs. Nat Hazards 58:645–680. doi:[10.1007/s11069-010-9632-4](https://doi.org/10.1007/s11069-010-9632-4)
- Papathoma-Köhle M, Keiler M, Totschnig R, Glade T (2012) Improvement of vulnerability curves using data from extreme events: debris flow event in South Tyrol. Nat Hazards 64:2083–2105. doi:[10.1007/s11069-012-0105-9](https://doi.org/10.1007/s11069-012-0105-9)
- Papathoma-Köhle M, Zischg A, Fuchs S, Glade T, Keiler M (2015) Loss estimation for landslides in mountain areas—an integrated toolbox for vulnerability assessment and damage documentation. Environ Model Softw 63:156–169. doi:[10.1016/j.envsoft.2014.10.003](https://doi.org/10.1016/j.envsoft.2014.10.003)
- Pate-Cornell ME (1996) Uncertainties in risk analysis: six levels of treatment. Reliab Eng Syst Saf 54:95–111
- Quan Luna B, Blahut J, van Westen CJ, Sterlacchini S, van Asch TWJ, Akbas SO (2011) The application of numerical debris flow modelling for the generation of physical vulnerability curves. Nat Hazards Earth Syst Sci 11:2047–2060. doi:[10.5194/nhess-11-2047-2011](https://doi.org/10.5194/nhess-11-2047-2011)
- Quan Luna B, Blahut J, Camera C, van Westen C, Apuani T, Jetten V, Sterlacchini S (2014) Physically based dynamic run-out modelling for quantitative debris flow risk assessment: a case study in Trensenda, northern Italy. Environ Earth Sci 72:645–661. doi:[10.1007/s12665-013-2986-7](https://doi.org/10.1007/s12665-013-2986-7)
- Remondo J, Bonachea J, Cendrero A (2008) Quantitative landslide risk assessment and mapping on the basis of recent occurrences. Geomorphology 94:496–507. doi:[10.1016/j.geomorph.2006.10.041](https://doi.org/10.1016/j.geomorph.2006.10.041)
- Rougier JC, Beven KJ (2013) Model and data limitations: the sources and implications of epistemic uncertainty. In: Rougier JC, Sparks S, Hill L (eds) Risk and uncertainty assessment for natural hazards. Cambridge University Press, Cambridge, pp 19–40
- Schwendtner B, Papathoma-Köhle M, Glade T (2013) Risk evolution: how can changes in the built environment influence the potential loss of natural hazards? Nat Hazards Earth Syst Sci 13:2195–2207. doi:[10.5194/nhess-13-2195-2013](https://doi.org/10.5194/nhess-13-2195-2013)

- Silva M, Pereira S (2014) Assessment of physical vulnerability and potential losses of buildings due to shallow slides. *Nat Hazards*. doi:[10.1007/s11069-014-1052-4](https://doi.org/10.1007/s11069-014-1052-4)
- Sterlacchini S, Akbas S, Blahut J, Mavrouli O-C, Garcia C, Luna B, Corominas J (2014) Methods for the characterization of the vulnerability of elements at risk. In: Van Asch T, Corominas J, Greiving S, Malet J-P, Sterlacchini S (eds) *Mountain risks: from prediction to management and governance*, vol 34: advances in natural and technological hazards research. Springer, Dordrecht, pp 233–273. doi:[10.1007/978-94-007-6769-0_8](https://doi.org/10.1007/978-94-007-6769-0_8)
- Totschnig R, Fuchs S (2013) Mountain torrents: quantifying vulnerability and assessing uncertainties. *Eng Geol* 155:31–44. doi:[10.1016/j.enggeo.2012.12.019](https://doi.org/10.1016/j.enggeo.2012.12.019)
- Totschnig R, Sedlacek W, Fuchs S (2011) A quantitative vulnerability function for fluvial sediment transport. *Nat Hazards* 58:681–703. doi:[10.1007/s11069-010-9623-5](https://doi.org/10.1007/s11069-010-9623-5)
- UNDRO (1984) *Disaster prevention and mitigation—a compendium of current knowledge Preparedness Aspects* 11
- Uzielli M, Catani F, Tofani V, Casagli N (2015) Risk analysis for the Ancona landslide—II: estimation of risk to buildings. *Landslides* 12(1):83–100. doi:[10.1007/s10346-014-0477-x](https://doi.org/10.1007/s10346-014-0477-x)
- Uzielli M, Nadim F, Lacasse S, Kaynia AM (2008) A conceptual framework for quantitative estimation of physical vulnerability to landslides. *Eng Geol* 102:251–256. doi:[10.1016/j.enggeo.2008.03.011](https://doi.org/10.1016/j.enggeo.2008.03.011)
- van Westen CJ, Asch TWJ, Soeters R (2006) Landslide hazard and risk zonation—why is it still so difficult? *Bull Eng Geol Environ* 65:167–184. doi:[10.1007/s10064-005-0023-0](https://doi.org/10.1007/s10064-005-0023-0)
- Walker WE, Harremoes P, Rotmans J, van der Sluijs JP, van Asselt MBA, Janssen P, van Krauss MPK (2003) Defining uncertainty: a conceptual basis for uncertainty management in model-based decision support. *Integr Assess* 4(1):5–17
- Winter MG, Smith JT, Fotopoulou S, Pitilakis K, Mavrouli O, Corominas J, Argyroudis S (2014) An expert judgement approach to determining the physical vulnerability of roads to debris flow. *Bull Eng Geol Environ*. doi:[10.1007/s10064-014-0570-3](https://doi.org/10.1007/s10064-014-0570-3)

Appendix C

La gestion des risques naturels est une dynamique

Jaboyedoff, M., Charriere, M. K. M., Derron, M.-H., Nicolet, P., and Sudmeier-Rieux, K.: Postface: La gestion des risques naturels est une dynamique, in: Les dangers naturels en Suisse: pratiques et développements: Comptes rendus de la deuxième Journée de Rencontre sur les Dangers Naturels (Université de Lausanne, 18 février 2011), edited by Nicolet, P., Jaboyedoff, M., and Derron, M.-H., no. 25 in *Memoires de la Societe Vaudoise des Sciences Naturelles*, pp. 393–428, http://wp.unil.ch/risk/files/2013/11/32_Postface_MemSVSN2013_C_Li.pdf, 2013.



32. Postface: La gestion des risques naturels est une dynamique

par

Michel JABOYEDOFF¹, Marie CHARRIÈRE², Marc-Henri DERRON¹,
Pierrick NICOLET¹ & Karen SUDMEIER-RIEUX^{1,3}

Résumé.—JABOYEDOFF M., CHARRIÈRE M., DERRON M.-H., NICOLET P. & SUDMEIER-RIEUX K., 2013. Postface: la gestion des risques naturels est une dynamique. *Mémoire de la Société vaudoise des Sciences naturelles* 25: 393-428.

Les risques sont contrôlés par de nombreux facteurs dont, en premier lieu, les dangers, exprimés par leur fréquence (aléa) à une intensité donnée, mais aussi relativement à un fonctionnement de la société. La gestion des risques, liés aux dangers naturels, implique de les évaluer, en premier lieu, en s'appuyant sur des estimations de fréquences d'événements dangereux; puis sur une quantification de la vulnérabilité ou des dommages potentiels aux objets en danger; mais aussi de tenir compte du système qui les génère. Lorsqu'on se préoccupe de l'impact total, il est nécessaire d'intégrer la capacité de retour à la normale de la société, soit la résilience, mais aussi de s'assurer de l'efficacité des stratégies de réduction des risques mises en place. Les problèmes que posent la mise en place d'une stratégie de gestion des risques ne sont, à ce jour, pas résolus. Cet article tente d'analyser les différents aspects de la gestion et de la quantification des risques dans le but de souligner les écueils et les problèmes à résoudre.

Il ressort de cette analyse qu'une lecture de l'équation du risque tant d'un point de vue quantitatif que d'un point de vue intuitif est possible, et permet de faire le lien entre les différents domaines qui touchent au risque. Cette approche permet d'identifier les problèmes qui sont communs à la quantification des risques et à leurs perceptions. Par exemple, la représentation des événements extrêmes pour l'ensemble des acteurs est peu précise, tant chez les experts que dans la population. Par ailleurs, il apparaît aussi que les experts, s'ils sont indispensables au processus d'évaluation des risques, sont malheureusement trop souvent soumis à des pressions externes qui biaisent leur propos. Plusieurs exemples sont invoqués pour illustrer ces situations. Une nouvelle définition de la résilience est proposée afin de quantifier les impacts post-catastrophe, de façon à séparer le risque des coûts indirects. L'analyse débouche sur une synthèse des défis futurs dans la gestion des risques, en particulier en Suisse.

Mots clés: dangers naturels, aléas, risque, résilience, société, fréquence.

¹Centre de Recherche en Environnement Terrestre (anciennement Institut de Géomatique et d'Analyse du Risque), Faculté des Géosciences et de l'Environnement, Université de Lausanne, CH-1015 Lausanne, Suisse.

²Water Resources (WR), Faculty of Civil Engineering and Geosciences, Delft University of Technology (TU Delft), 2600 GA Delft, Netherlands.

³IUCN Commission on Ecosystem Management - DRR thematic group, CH-1196 Gland.
E-mail: michel.jaboyedoff@unil.ch

INTRODUCTION

Dans sa préface, C. Bonnard nous incite à aller vers le risque. Les événements récents en Suisse et dans le monde (éboulements au Gurtellen, 2006 et 2012; tremblement de terre de l'Aquila, 2009; tsunami du Japon, 2012) nous ont montré à quel point il existe une nécessité d'anticiper les catastrophes afin de s'y préparer. L'évaluation des risques et leur gestion sont des outils parmi d'autres, mais ils ne sont pas les seuls. La gestion d'une société est plus complexe que celle des risques. C'est pourquoi la communication des risques ainsi que leur intégration dans la société elle-même, sont tout aussi importantes que leurs analyses. Pour mettre en perspective les risques naturels dans un contexte plus large, notons simplement que les coûts totaux qu'engendre la consommation d'alcool en Suisse, incluant les coûts indirects, ont été estimés à 6 milliards de francs par an (JEANRENAUD *et al.* 2003), alors que la catastrophe de 2005, la plus coûteuse pour la Suisse, n'a coûté «que» 3 milliards de francs suisses environ (HILKER *et al.* 2007). Ce type de comparaison permet de fournir aux décideurs des éléments afin de définir des priorités. Dès lors l'intégration des risques doit être réalisée avec rigueur, mais tout en sachant garder une certaine souplesse.

La société est en constant changement, avec le «progrès» qui fait disparaître certains risques alors que d'autres apparaissent (exemple: micropolluants tels que antibiotiques dans les eaux de surface; CHÈVRE *et al.* 2013); ou plus simplement en modifiant les facteurs qui influent sur le niveau du risque. L'apparition de nouveaux risques est parfois liée à une nouvelle perception du risque d'un groupe de personnes, la tolérance diminuant avec le temps. Par exemple les pollutions sont de moins en moins tolérées. Il est donc important de gérer les risques, c'est-à-dire d'avoir une stratégie qui va de l'identification des dangers à la communication à des publics variés et qui tient compte des contraintes et des implications pour la société. A la lumière de la condamnation à 6 ans de prison de 7 scientifiques et responsables italiens de la protection civile (RIDET 2012) suite au tremblement de terre de l'Aquila en 2009, les enjeux liés à la gestion des risques naturels prennent désormais une importance particulière.

Dans les lignes qui suivent, il s'agit tout d'abord de décrire ce qu'on entend par risque. Il faut s'interroger sur la façon dont on définit et quantifie le risque. Puis explorer les éléments qui nous permettent de «vivre avec», qui sont basés sur une réduction des risques adaptée aux situations particulières et à leur évolution dans le temps. La mise en équation des risques permet d'identifier les différents problèmes liés à leurs gestions. A noter que nous ne discutons pas ici des méthodes de quantification de l'aléa qui est un sujet en soit. Nous considérons donc que la qualification de l'aléa est réalisée d'une façon ou d'une autre, mais rappelons que la connaissance de l'aléa reste la base de la quantification et de la gestion des risques naturels.

Nous proposons également de faire un tour d'horizon des différents écueils qui jalonnent la gestion des risques, en les intégrant dans une perspective plus large.

LA QUANTIFICATION DU RISQUE

Une équation du risque parmi d'autres

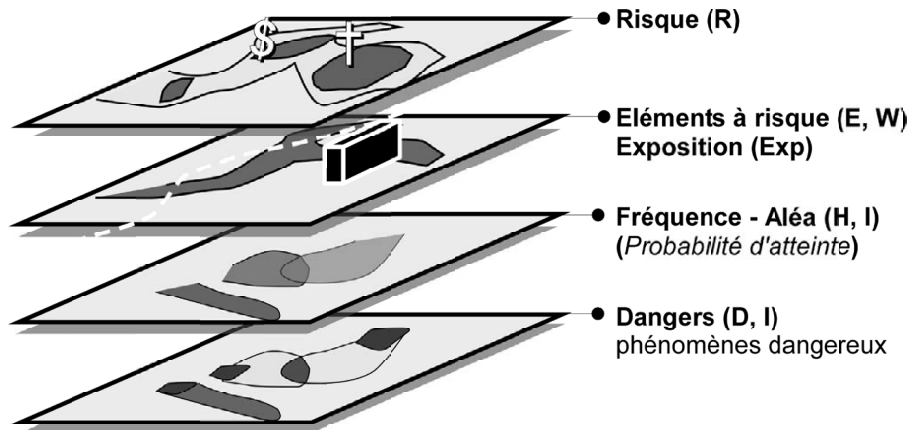


Figure 1.–les différentes couches nécessaires pour calculer un risque, selon l'équation 1 proposée.

Le risque est en principe une probabilité associée à un dommage potentiel causé par un phénomène dangereux qu'on appellera ici danger (D) (EINSTEIN 1988). Cependant, souvent on quantifie le risque par les coûts moyens annuels, ce qui revient à multiplier les dommages par leurs fréquences respectives. Le risque est la valeur attendue des dégâts directs (morts et objets), alors que la catastrophe est la réalisation d'un risque qui ne correspond pas forcément au calcul. Une des façons de calculer le risque est la suivante (FELL *et al.* 2005, JAKOB *et al.* 2012):

$$R(D, E, I, x, \Delta t) = H(D, I, x, \Delta t) \times \text{Exp}(E, \Delta t) \times V(D, I, E) \times W(D, E) \quad (\text{Equation 1})$$

Ou en d'autres termes:

Risque = aléa × exposition × vulnérabilité × dommage potentiel total

Les termes de cette formulation sont définis comme suit (figure 1):

- $H(D, I, x, \Delta t)$: aléa («hazard» en anglais) est équivalent à la fréquence d'un type de danger D pour des caractéristiques (p. ex. intensité I) données, en un lieu donné (x) et pour une période temps donnée (Δt). La période est importante puisque des phénomènes comme les cyclones, les avalanches de neiges, sont saisonniers.

- $\text{Exp}(E, \Delta t)$: l'exposition correspond au pourcentage de temps durant lequel un élément mobile (E) est soumis à un aléa durant une période donnée. Un élément immobile possède une exposition de 100%.

- $V(D, I, E)$: la vulnérabilité (degré de perte: 0-100%) est le taux de destruction d'un élément E atteint par un phénomène dangereux D d'intensité I. Elle s'exprime en termes de courbe de vulnérabilité (I-V) pour un type d'objet donné. D'une façon plus générale on peut l'assimiler au degré de disfonctionnement d'un système.

396 M. Jaboyedoff, M. Charrière, M.-H. Derron, P. Nicolet & K. Sudmeier-Rieux

- $W(D, E)$: dommage potentiel total en termes financiers ou en nombre d'unités d'objet ou personne, par exemple un nombre de victimes, pour un danger donné (D).

Cette formulation peut être simplifiée en estimant les conséquences globalement avec $C = \text{Exp} \times V \times W$, d'où (LEE & JONES 2004, VAN ALPHEN *et al.* 2009, ALE 2009, MARZOCCHI *et al.* 2012):

$$R = H \times C \quad (\text{Equation 2})$$

Souvent on remplace les courbes de vulnérabilité par des courbes de dommages, à savoir une courbe $I - V \times W$ (LEROI *et al.* 2013). Il est aussi possible de détailler la formulation [1], en y détaillant chaque terme. Par exemple, dans le cas des mouvements de versant, l'aléa peut s'écrire (JABOYEDOFF *et al.* 2005, HEINIMANN *et al.* 1999):

$$H_i(x) = \lambda_{ri} \times P_i(x) \quad (\text{Equation 3})$$

Ce qui signifie que l'aléa de l'instabilité «i» est le produit de la fréquence de rupture λ_{ri} de cette instabilité par la probabilité de sa propagation en un lieu x . Lorsqu'un lieu (x) est soumis à plusieurs types de danger et/ou d'aléas d'intensités différentes, on obtient:

$$R_{\text{total}}(x) = \sum_h \sum_j \sum_k \sum_l R(D_j(x), E_l(x), I_k(H_k, x), x, \Delta t_h) \quad (\text{Equation 4})$$

Les sommes sur les indices h, j, k et l se réfèrent respectivement aux périodes temps considérées, aux différents types de danger, à leurs intensités qui sont associées à un aléa H_k , et aux éléments à risque concernés. Cette formulation ne se réfère qu'aux coûts directs, et ne prend pas en compte les aspects indirects liés aux dysfonctionnements induits par un événement, comme par exemple la perte économique liée à une interruption du trafic suite à un éboulement sur une voie de communication.

Concernant le calcul du risque, rappelons qu'il ne faut pas confondre, les probabilités et les fréquences. Dans l'équation du risque présentée ici, les fréquences sont utilisées afin d'annualiser les coûts. Il existe cependant une relation entre fréquence et probabilité. Néanmoins, une probabilité varie de 0 à 1 alors que une fréquence peut excéder 1. On utilise plutôt les probabilités pour donner un poids à un scénario pour une période donnée, ce qui permet dès lors d'obtenir une fréquence pour chaque scénario. On peut aussi utiliser les probabilités pour indiquer la possibilité d'avoir 1, 2, 3 ou plus d'événements dans une période donnée, ce qui peut avoir un intérêt pour le calcul des risques.

Les termes du risque

L'avènement des systèmes d'information géographique (SIG) et la création de nombreuses bases de données spatiales, ainsi que de documents géoréférencés (par les régions, cantons ou états), permettent de réaliser des calculs de risque simples (MERZ *et al.* 2007).

Suivant les types de danger, l'aléa (H) reste encore le terme de l'équation du risque le plus difficile à évaluer. Les aléas sont souvent simplement qualifiés par des termes tels que: *insignifiant, faible, modéré, élevé, très élevé*, car ils sont souvent déduits de cartes

de susceptibilité qui ne renseignent pas explicitement sur les fréquences (VAN WESTEN *et al.* 2006). Pour décrire les intensités (I) on peut aussi associer une échelle: *insignifiante, faible, modérée, élevée, très élevée*. La quantification de l'aléa par son intensité et sa fréquence reste la base de toute analyse du risque, car si l'aléa n'existe pas, il n'y pas de risque. De nombreuses méthodes ont été et sont encore en développement pour résoudre cet important aspect de l'analyse du risque; mais les décrire en détail nécessiterait de longs développements qui dépassent le cadre de cet article.

Depuis quelques années, les publications sur la vulnérabilité ou/et les courbes de vulnérabilité des bâtiments se multiplient pour les inondations et le charriage (EGLI 2005, LEROI *et al.* 2013, FUCHS *et al.* 2012), pour les laves torrentielles (QUAN LUNA *et al.* 2011, JAKOB *et al.* 2012) ou encore pour les chutes de blocs (MAVROULI & COROMINAS 2010). Souvent le principe des courbes de vulnérabilité s'étend aux courbes de dommage qui mettent directement en relation les intensités avec les coûts (LEROI *et al.* 2013) ou encore au «damage ratio» qui est le ratio du coût du dommage rapporté au prix du bâtiment (FUCHS *et al.* 2012). Cette option est souvent plus judicieuse, notamment dans l'évaluation des coûts, car il est parfois difficile de calibrer la courbe intensité-vulnérabilité et parce que les frais engendrés par les catastrophes incluent aussi des aspects tels que le nettoyage après une inondation qui peuvent représenter une part importante des coûts. Ils peuvent se monter à 30% des couts totaux (CHOFFET in prep.).

Restent les dommages potentiels totaux (W) qui se réfèrent aux personnes, bâtiments ou infrastructures. Désormais, les SIG et les bases de données nous permettent, en principe, d'obtenir de bonnes estimations pour W. Il est évident que certaines données relatives à la propriété peuvent rester confidentielles et ne pas être accessibles simplement. Néanmoins, la valeur (W) des éléments à risque (E) est de mieux en mieux connue, et les statistiques de mobilité des personnes le sont aussi.

Lorsque les termes de l'équation du risque sont mal connus ou mal localisés, on peut, comme le font les assurances, réaliser des simulations de catastrophe afin d'obtenir des courbes d'excédence (KHATER & KUZAK 2002). Chaque terme peut être remplacé par une variable aléatoire de distribution connue afin de réaliser une simulation de Monte Carlo (MICHEL-KERJAN *et al.* 2012). Cette approche est surtout utilisée à l'échelle d'une région ou d'un pays tout entier, en particulier dans le secteur des assurances.

Le risque et son cadre

Si la quantification des risques est un outil d'aide à la décision en soit, elle n'est en aucun cas l'unique outil de décision quant à la gestion des risques, car de nombreux autres facteurs entrent en ligne de compte dans la gestion d'une société. La représentation des risques joue également un rôle important. La tolérance aux risques industriels peut être plus élevée dans un groupe d'habitants s'il bénéficie d'emplois au sein de l'entreprise dangereuse, par exemple dans le cas des centrales nucléaires (BERTRAND & MULLET 2006). Mais cela ne répond pas à la question de savoir lequel des groupes d'habitants possède une représentation plus objective de la réalité. De plus, la représentation des risques dépend aussi de la culture du groupe concerné (XIE *et al.* 2003, ALEXOPOULOS *et al.* 2009). Il faut donc tenir compte de l'acceptabilité et de la représentation des risques (PERRETI-WATEL 2000).

La quantification des risques est toutefois un outil puissant, notamment pour l'aide à la décision. L'analyse coûts-bénéfice (BRÜNDL 2009, FELL *et al.* 2005) permet de systématiser une approche afin de hiérarchiser les actions, c'est-à-dire de fournir des éléments pour les prioriser. Cette approche consiste à quantifier les risques avec différentes solutions de réduction des risques et de les comparer à l'état préexistant, de sorte qu'on puisse choisir la solution qui a un meilleur rapport coûts-bénéfices, c'est-à-dire celle qui réduit le risque (coût), et non l'impact, au maximum. Même si souvent les résultats sont relativement loin de la réalité, cette approche, appliquée avec rigueur, permet la comparaison de situations différentes.

Les mesures qui tendent à réduire le risque, si elles ne sont pas contextualisées, sont inutiles. Il ne sert à rien de mettre en place un système de surveillance sophistiqué si la maintenance et l'utilisation n'est pas garantie par des acteurs locaux responsables (en partie en tous les cas). De plus si une population est consciente des risques, elle peut non seulement potentiellement gérer des outils de surveillance mais aussi être apte à supporter les sollicitations d'un aléa plus important, car elle est mieux préparée.

L'équation du risque n'est donc pas tout, mais elle fournit un cadre conceptuel indispensable pour la gestion de l'impact des aléas sur la société. Nous partons du principe dans cette article que l'aléa est la base, nous ne discutons pas de la façon de le qualifier, mais plutôt de ses implications dans la gestion des risques.

LA LECTURE DU RISQUE

La formulation du risque n'est pas unique, elle dépend du degré de connaissance du contexte et du phénomène dangereux lui-même. Cependant les éléments essentiels à son appréhension se trouvent dans l'équation ci-dessus, à l'exception des coûts indirects du retour à la normale après une catastrophe, dont il est question plus loin.

Il est possible d'avoir une lecture de l'équation [1] en termes de représentation. Comment se comporte-t-on vis-à-vis du danger et de ses conséquences? Cela dépend de l'expérience, de la perception des risques (SLOVIC 1987) et de l'image que l'on s'en fait (PERETTI-WATEL 2000).

Cette lecture est fortement dépendante de la responsabilité des acteurs et de leurs états psychiques; une personne en bonne disposition est, a priori, plus encline à prendre des risques si cela lui bénéficie et inversement (SLOVIC & PETERS 2006, FINUCANE *et al.* 2000). En plus, la posture dans laquelle se trouvent les personnes impliquées est importante: si une situation à risque entraîne certains coûts, ou si quelqu'un doit prendre une responsabilité (doit signer) pour une communauté ou un groupe de personnes. La situation est différente pour une personne qui de sa propre décision s'expose volontairement aux risques. Il s'agit alors de prise de risque individuelle dont les potentielles conséquences affectent uniquement ou principalement la personne concernée ou un petit groupe.

Si l'on se livre à une lecture des termes de l'équation du risque, alors les constatations faites ci-dessus deviennent naturelles. Comment se représente-t-on H?, V, E et W? Quelles termes évalue-t-on lors de la pondération des risques? Premièrement, ces termes nous concernent-ils directement ou représentent-ils quelque chose de lointain dans le temps, dans

l'espace ou d'un point de vue du fonctionnement cognitif? Rappelons que les journalistes considèrent souvent pour communiquer que les personnes sont concernées au premier chef par le «moi», avec une décroissance en fonction de la proximité spatiale, affective, temporelle et du contexte social proche jusqu'au contexte culturel (AGNÈS 2002) (figure 2). Un bon exemple du «moi» est celui d'un enfant qui ne sait pas qu'il est vulnérable ($V = 0$). Le risque n'existe donc pas pour lui, même s'il en a une représentation. Le skieur hors-piste peut sous-estimer H ou V. Un propriétaire surestime très certainement W et V, mais sous-estime probablement H; bien que cela dépende aussi de l'assistance offerte par la communauté. Une autre interrogation à propos de la représentation de W est la façon dont elle est liée à la culture. W peut être un type d'environnement, des habitudes, des connaissances pratiques, des traditions, des structures sociales, qui tous sont vulnérables aux risques sociaux et naturels.

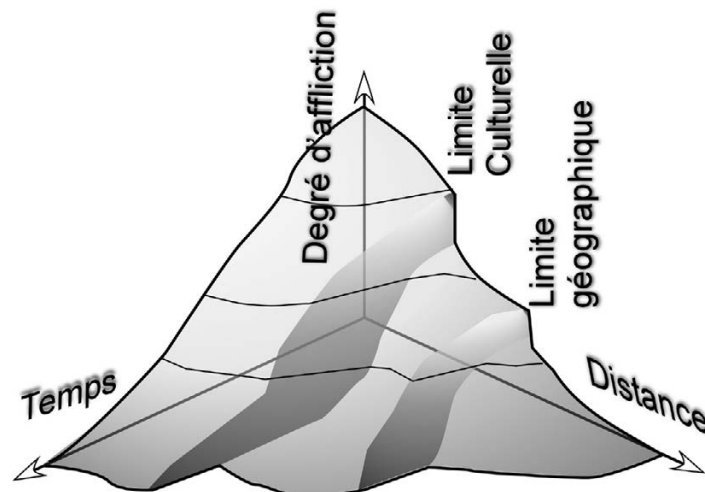


Figure 2.—Illustration du concept d'affliction qui signifie que plus le temps et l'espace qui sépare d'un événement catastrophique est grande, moins les personnes se sentent concernées.

L'état affectif d'une personne confrontée à l'évaluation de l'équation [1], pour quelque raison que soit, consciemment ou inconsciemment, va influencer son évaluation (KOUABENAN 2006). Prenons un exemple trivial: une personne qui veut en séduire une autre en pratiquant une activité dangereuse (saut en ski, vitesse en voiture ou moto, etc.), peut être entraînée à prendre des risques inconsidérés pour impressionner l'autre. L'équation [1] est une simplification du monde risqué, mais il peut être représenté de différentes manières, et elle fournit un cadre nécessaire à la réflexion. Ensuite, l'étude de l'ensemble de cette représentation est un support pour communiquer entre chaque acteur ou groupe concerné dans la gestion des risques. Tous les termes de [1] sont évalués par chaque acteurs ou groupes concernés par des risques. Ceux-ci sont inspectés sous l'angle de:

1. La responsabilité
2. La propriété
3. Les structures de la société

400 M. Jaboyedoff, M. Charrière, M.-H. Derron, P. Nicolet & K. Sudmeier-Rieux

4. Les contraintes administratives et politiques

5. Etc.

A la fin, tous ces points sont fonction de la spatialité et de la temporalité de tous les termes de l'équation du risque et tous les aspects ci-dessus doivent aussi être situés dans un contexte géographique au sens large ainsi qu'être liés au temps. Des modèles économiques récents, tenant compte des comportements, montrent que suivant les comportements adoptés par de nouveaux habitants dans des zones à risques côtiers, le niveau de risque augmente en raison de l'attrait pour certaines zones plus susceptibles d'être affectées et de l'absence de prise en compte du risque par les nouveaux habitants sans expérience (FILATOVA *et al.* 2011).

EXEMPLES DE SITUATIONS QUE DOIT RÉSOUDRE L'ANALYSE DE RISQUE

L'analyse de risque quelle qu'elle soit ne fournit qu'un des outils pour leur gestion. Néanmoins, il est primordial de comprendre les processus qui génèrent les risques ou/et qui s'y opposent. Plusieurs aspects sont encore mal maîtrisés, notamment en ce qui concerne les événements extrêmes dont on connaît assez mal les étendues, fréquences (aléas) et les intensités associées. Il en va souvent de même pour ce qui concerne les vulnérabilités. De plus, on sait désormais que dans le monde les grands moteurs de l'augmentation des risques naturels sont l'anthropisation, le manque de préparation et de moyens, mais aussi la pauvreté (UNISDR 2011, IPCC 2012). Où que l'on se trouve, les processus qui mènent à une situation à risque sont souvent issus des mêmes types de situations. En effet, les habitants d'un territoire sont souvent peu enclins à admettre les risques qui les touchent directement si aucun événement ne les a encore affectés, et cela est vrai autant en Europe qu'en Asie par exemple. De plus, si une mauvaise évaluation mène le plus souvent à une mauvaise gestion, une bonne évaluation ne mène pas forcément à une bonne gestion.

Les exemples de problèmes

Plusieurs événements récents ont montré les écueils de l'analyse des risques et de leur gestion. Ces événements ont souvent soulevé des problèmes connus et aussi parfois nouveaux. Les quelques cas qui suivent illustrent brièvement un certain nombre de ces problèmes.

Gurtellen (UR) et la fin des cartes de dangers

Le 31 mai 2006, un éboulement de 5000 m³ s'est produit au-dessus de l'autoroute du Saint-Gothard près de Gurtellen. 11 blocs d'environ 10 m³ chacun ont atteint la route, tuant deux touristes allemands dans leur voiture et touchant plusieurs véhicules (LINIGER & BIERI 2006). La route a été rouverte le 2 juin pour environ une heure, avant que de nouvelles chutes de blocs se produisent, sans toutefois atteindre l'autoroute. Puis, cet axe principal qui traverse les Alpes a été de nouveau fermé pour un mois. Avec six millions de véhicules en 2005, dont 1 million de camions, la fermeture de l'axe routier du Gothard en juin 2006 a notamment provoqué un excès de 260'000 véhicules sur l'itinéraire du San Bernardino (SWISSINFO 2006). Durant le mois de juin, la falaise, où restait 5000 m³ de matériel instable, a été purgée (LINIGER & BIERI 2006). Les blocs produits par le dynamitage se sont arrêtés au-dessus de l'autoroute. Notons qu'en mars 2004, trois blocs s'étaient arrêtés sur la place

de parking et un peu plus haut, indiquant que l'instabilité avait déjà été activée ou réactivée à ce moment-là.

Cet évènement a fait apparaître plusieurs lacunes: (1) La première réouverture de façon trop hâtive de l'autoroute; (2) La deuxième fermeture trop longue pour un axe de cette importance; (3) La démonstration que le concept de carte de danger (LATELTIN *et al.* 1997) n'était pas adéquat dans un tel cas et ceci pour plusieurs raisons: d'une part parce qu'il n'intègre pas le risque et d'autre part à cause de la mise en œuvre par un petit canton, qui possède des administrations trop restreintes pour gérer de façon adéquate des situations à risque particulières.

L'examen de l'instabilité a probablement été réalisé de façon trop rapide, et les pressions pour la réouverture ont dû être importantes. Malgré un impact économique important en termes de transport à travers les Alpes, il a ensuite été décidé de fermer l'axe du Gothard, pour éviter des problèmes, car la pression médiatique devenait élevée, notamment d'Allemagne. Pourtant, la création d'une digue sur la voie amont et une circulation alternée sur la voie aval, moyennant une inspection visuelle et instrumentée permanente, auraient permis de maintenir une partie du trafic, comme l'a fait remarquer Jean-Daniel Rouiller (ATS 2006). Ceci avec en plus une fermeture nocturne. L'aspect positif de cette expérience est que les lacunes de gestion ont été révélées et ont permis de mettre en place une nouvelle stratégie d'évaluation des risques le long des routes nationales en Suisse (DORREN *et al.* 2009, CAJOS *et al.* 2009). La plupart des outils avaient pourtant déjà été envisagés par la confédération (HEINIMANN *et al.* 1999, HEINIMANN & BORTER 1999). Il était en effet illusoire d'utiliser le concept de carte de danger pour la gestion d'axes de transport, et surtout de compter sur un canton d'un peu plus de 30'000 habitants pour gérer ce genre de situation. Le système a montré ses limites dans ce cas-là, ce qui a finalement été bénéfique.

Gurtellen II: la mauvaise évaluation des risques

Sur l'autre versant de la vallée, proche de Gurtellen, deux éboulements se sont produits au-dessus de la voie de chemin de fer. Le premier d'environ 400 m³, dont 5 m³ ont atteint les voies le 7 mars 2012, a provoqué la fermeture de la ligne pour 5 jours (20 MINUTES 2012, VOUMARD 2012). Cette falaise était l'objet de travaux d'assainissement le 5 juin 2012 lorsque 2'000 à 3'000 m³ se sont détachés et ont blessés deux ouvriers et tuant un troisième en l'ensevelissant. La ligne est restée fermée pendant un mois. Les causes sont attribuées à de fortes précipitations au début du mois de juin et au fait qu'une des structures géologiques ayant mené à la rupture n'avait pas été identifiée (Police cantonale uranaise citée par VOUMARD 2012).

Ce cas montre les difficultés de prévoir un éboulement (le premier), mais également qu'en général les mesures d'assainissement suivent. Néanmoins, les investigations et la surveillance avant et pendant le chantier ont visiblement été déficientes. Il reste à comprendre pourquoi, malgré une surveillance et des mesures a priori adéquates, celles-ci n'ont pas suffi.

Xynthia (Vendée, France) la gestion du territoire et la vulnérabilité

Le 28 février 2010, la tempête Xynthia a fait 47 morts dont 41 dus à des inondations par submersion. En particulier le village de la Faute-sur-Mer a compté 29 victimes, dont la plupart étaient des personnes de plus de 60 ans mortes dans leur sommeil (VINET *et al.* 2011).

Cette région de polders n'a pourtant pas été épargnée dans un passé récent avec plus de 6 événements de submersion depuis 1877 et jusque dans les années soixante (SAZEAU 2011). En 2010, le niveau de l'océan était de 4.7 m supérieur à la normale à cause des vents et de la forte marée (VINET *et al.* 2011). Plusieurs causes sont à l'origine de cette catastrophes (VINET *et al.* 2011): (1) le mauvais entretien des digues entraînant parfois leur destruction partielle; (2) une urbanisation déraisonnable dans des zones à risque. On constate que les bâtiments qui ont compté des décès ont été construits depuis 1980, alors qu'aucune victime n'a été déplorée dans les constructions antérieures à cette date; et (3) l'inadaptation des bâtiments, en majorité constitués d'un seul niveau et le plus souvent sans possibilité d'échappatoire sur le toit.

Rappelons aussi que le maire de la Faute-sur-Mer a été mis en examen le 14 avril 2011 (AFP 2011a), mais qu'ensuite, chose étrange, des graffitis d'insultes, en faveur du maire, ont été réalisés sur des tombes des victimes et sur la maison d'un défenseur des victimes (AFP 2011b).

L'Aquila (Italie)

Le 22 octobre 2012, un juge italien condamne 7 experts italiens (6 scientifiques et un haut fonctionnaire) à 6 ans de prison et à verser près de 8 millions d'Euros pour avoir incité des habitants à modifier leurs comportements face à une activité sismique accrue dans la région de L'Aquila (NOSENGO 2012, RIDET 2012, HALL 2011). Le tremblement de terre du 6 avril 2009 à L'Aquila a fait 1500 blessés, 20'000 bâtiments endommagés, 60'000 personnes déplacées et 309 victimes dont 29 personnes qui avaient pour habitude de quitter leurs maisons lorsqu'une activité sismique inhabituelle était ressentie. Mais cette fois-ci, ils ne le firent pas car les experts d'une commission des risques italiens s'étaient montrés rassurants lors d'une réunion à L'Aquila une semaine avant l'évènement.

Selon HALL (2011), ces experts ont constaté l'activité, mais ont conclu qu'il n'y avait pas plus de risque que le niveau habituel qui est de toute façon élevée dans cette zone. A la sortie d'une réunion d'information, ils ont rassuré la population en leur disant qu'ils pouvaient rentrer chez eux et qu'ils pouvaient boire un verre de vin tranquillement, sous prétexte qu'une activité sismique n'est pas un signe précurseur reconnu d'un séisme plus grand. D'autre part, un ancien technicien avait affolé une partie de la population en faisant des prévisions de séisme sur la base d'émission du gaz radon dont on sait qu'il peut augmenter, diminuer (IGARASHI *et al.* 1995, KUO *et al.* 2006), ou ne pas varier avant un tremblement de terre. A l'occasion du procès, plus de 5'000 scientifiques ont souligné que la prévision des séismes n'est pas possible.

Ainsi l'action du groupe de la commission des risques a aussi été influencée par des facteurs externes. Voulant mettre fin à une situation tendue, les responsables ont été jusqu'à se montrer trop rassurants, comme s'ils prédisaient qu'il n'y aurait pas de séismes, au lieu d'indiquer que la situation était préoccupante, mais que la prédiction n'était pas possible. Ils auraient en effet mieux fait de dire «si vous souhaitez dormir dehors, faites-le» et de rappeler les comportements à adopter en cas de séisme. Le plus regrettable dans cette affaire est que les personnes condamnées sont des personnes qui ont œuvré plus que beaucoup d'autres pour la réduction des risques en Italie. Malheureusement, ils ont fait une faute de communication qu'ils payent beaucoup trop cher. Il n'est pas injuste qu'ils aient été condamnés, car ils n'auraient pas dû se montrer aussi rassurants. Mais une peine d'au plus

un an, avec sursis et sans implication financière, aurait suffi, car cet événement crée un précédent qui amène inévitablement à la question suivante: qui désormais prendra des responsabilités dans le domaine de la gestion des risques? Ceci renvoie donc aux cadres légaux, mais également moraux et éthiques, qui définissent la répartition des différentes tâches et responsabilités de la gestion des risques entre les multiples acteurs, experts et décideurs; de l'évaluation du risque jusqu'à la communication et sensibilisation de la population en passant par sa réduction.

L'éboulement de St. Nicolas (VS)

Le 21 novembre 2002 à 15h20, 120'000 m³ s'éboulent au-dessus du village de St. Nicolas, alors qu'une partie du village a été évacuée depuis 6 jours et que l'évacuation complète a été faite depuis 20h (POINTER 2006). Cet éboulement n'atteint heureusement pas les bâtiments et aucune vie humaine n'a été mise en danger. L'activité de l'instabilité rocheuse commence en juillet 2002, une cellule de crise est formée début septembre dont fait partie le géologue Rovina, natif de l'endroit. Fin septembre, une évacuation est réalisée au vu des mouvements observés. Elle est levée 2 jours plus tard. La surveillance permet de prévoir la chute et d'évacuer avant l'éboulement (LADNER *et al.* 2004). La cellule de crise met sur pied des plans d'évacuation avec l'aide de M. Rovina, ce dernier favorisant une bonne communication et une gestion de la crise exemplaire.

Le problème des événements extrêmes

Il existe de nombreuses lois statistiques, que l'on tente d'ajuster sur des distributions observées. Il est relativement rare que l'on s'attarde sur leur origine et leur genèse. On sait que la loi normale est issue du théorème centrale limite (VENTSEL 1987), qui stipule que la somme de processus aléatoires possédant chacun une distribution quelconque de variance et moyenne définies aboutit à une loi normale. Lorsque la statistique suit une loi normale pour les valeurs logarithmique, alors la distribution, log-normale, est le résultat d'un processus multiplicatif. Les lois de type puissance sont, elles, issues de processus self-similaires ou en cascade, comme les énergies des ruptures de tremblements de terre, les glissements de terrain ou la surface de feux de forêts (SORNETTE 2006, MALAMUD & TURCOTTE 1999). La distribution de Poisson est le résultat de processus purement aléatoires alors que les lois des événements extrêmes proviennent d'extraits de distributions aléatoires (SORNETTE 2006).

Par conséquent, dans la plus part des cas, les distributions sont ajustées sur des données sans réellement prendre garde à leur validité «physique». De plus, bien des distributions ne possèdent pas de genèse claire (JOHNSON *et al.* 1995).

Des études récentes (SORNETTE & OUILLON 2012, ANCEY 2012) tendent à prouver que certains événements catastrophiques ont des valeurs d'intensités qui ne font partie de la statistique. Ils les appellent «Dragon-King». Or ceci indique que, compte tenu de leur rareté, nous n'avons pas accès aux lois statistiques qui régissent ces phénomènes, de sorte que les ajustements de lois aux valeurs courantes ne permettent pas d'en évaluer la fréquence. ANCEY (2012) indique que les avalanches de neige extraordinaires sont issues de situations singulières. Ceci s'ajoute bien sûr aux problèmes de changements de conditions qui modifient les paramètres des lois de distributions. C'est le cas du climat (SCHAËR *et al.* 2004), avec des températures mensuelles qui ont augmenté en moyenne de 0.8°, si les statistiques sont réalisées sur les périodes 1864-1923 et 1941-2000 (figure 3).

Il s'agit donc désormais d'analyser les signes précurseurs, c'est-à-dire de comprendre la dynamique des systèmes, soit la série temporelle précédant ces événements extraordinaires (SORNETTE & OUILLOIN 2012). Et ceci s'applique donc tant aux phénomènes naturels qu'à l'occupation du territoire puisque nous sommes concernés par tous les risques.

Il existe aussi des cas où la distribution des valeurs d'intensités du phénomène n'est pas la même pour les valeurs élevées et les faibles valeurs. C'est le cas des grands volumes des laves torrentielles en Valais qui suivent des lois puissances différentes de celles des plus petits volumes (figure 3c) (BARDOU & JABOYEDOFF 2008).

Les événements extrêmes sont encore très mal maîtrisés par la société, tant par les scientifiques que par la population, car ce que nous n'avons pas vécu, nous ne pouvons que difficilement l'imaginer sans surestimer ou sous-estimer le risque. Les études sur la perception de l'aléa d'inondation montrent d'ailleurs que celle-ci varie en fonction de l'information dispensée (KELLER *et al.* 2006).

Le vieillissement des infrastructures

Un fait marquant est que bon nombre de dangers naturels sont d'une origine anthropique. C'est notamment le cas de nombreux glissements de terrain (MICHOUUD *et al.* 2011); souvent dus à la déféctuosité d'une infrastructure telle que les conduites d'eau. Par exemple le 1^{er} septembre 2002, le glissement superficiel de Lutzenberg (canton d'Appenzell), de 2'500 m³, a détruit trois maisons et tué trois personnes (VALLEY *et al.* 2004). Des précipitations exceptionnelles associées à une conduite d'eau qui fuyait, ont permis de mettre en mouvement les matériaux superficiels d'un pâturage dans une pente d'environ 19°; ceci ayant été confirmé par des simulations numériques et des observations (VALLEY *et al.* 2004). Un exemple similaire de conduite percée, menant à un chalet quasiment désaffecté, s'est produit au-dessus des Diablerets (VD) durant des précipitations intenses mais pas exceptionnelles (temps de retour d'environ 3 ans). L'entretien était donc quasi inexistant depuis de nombreuses années. Un glissement de 500 m³ a ainsi coupé une petite route mais n'a fait aucun dégât majeur (JABOYEDOFF & BONNARD, 2008).

Un autre exemple est celui de la rupture d'un mur de soutènement le long de la voie de chemin de fer de Palézieux à Payerne, le 2 février 2013. Les matériaux du mur ont envahi la voie accompagnés d'un glissement de terrain d'une centaine de m³ (figure 4). Les précipitations, pas exceptionnelles mais accompagnées de fonte de neige fraîche, ont produit de grandes quantités d'eau qui ont probablement fait augmenter les pressions derrière le mur. Le dépôt sur les voies a fait dérailler le train, sans blesser les passagers (24HEURES 2013). Quelques mois plus tôt cette ligne avait déjà été affectée par un glissement quelques kilomètres plus loin (LA LIBERTÉ 2012). Il semble que les ouvrages commencent à être âgés et à céder.

En Suisse on observe clairement une dégradation des infrastructures et ouvrages durant ces dernières années. Ceci est souligné par le fait que de nombreux ouvrages en bétons, par exemple, sont rénovés en Suisse à cause de ces vieillissements. Un tel programme a déjà été identifié au cours des années 70 et planifié depuis le milieu des années 90 (OFQC 1994). Au Québec, l'effondrement du viaduc de la Concorde, qui a fait 5 morts et 6 blessés illustre aussi ce problème. Il a été provoqué par des négligences, mais en particulier par une

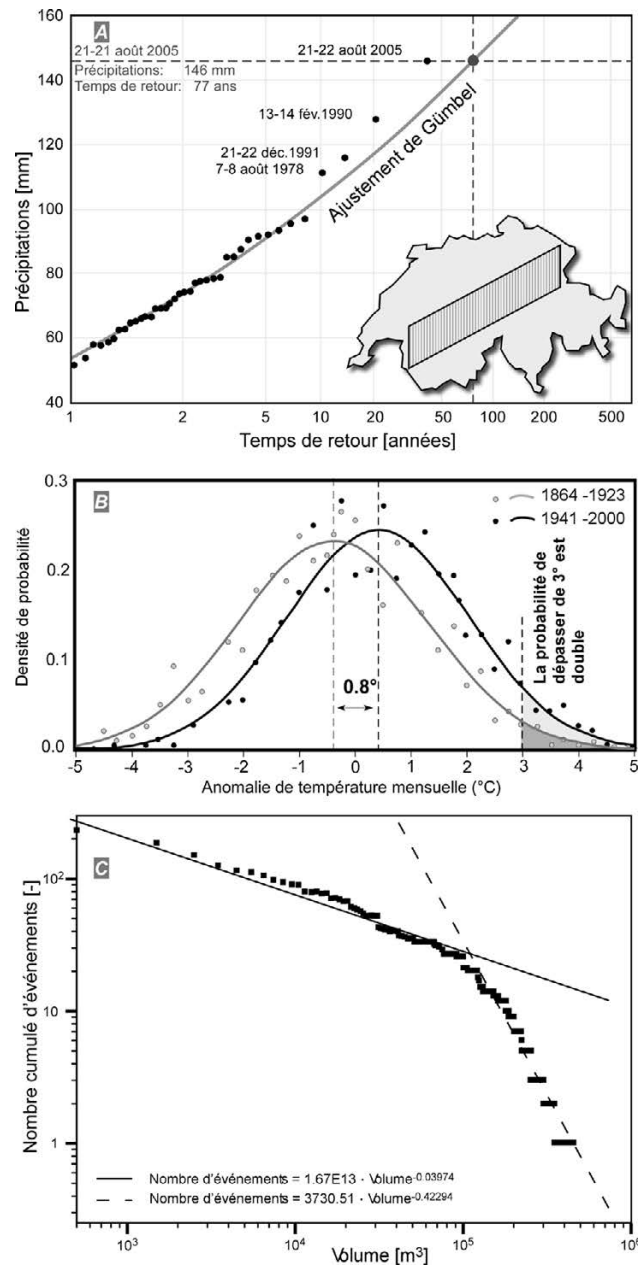


Figure 3.—(A) Précipitations en fonction du temps de retour. Les fortes précipitations récentes (y.c. neige) ne suivent pas l'ajustement de la loi de Gumbel (ligne du centre) des valeurs observées de précipitations pour 2 jours, 2005 en particulier (modifié d'après BEZZOLA & HEGG 2007). (B) Montée des températures moyennes en Suisse (Modifié d'après SCHÄER *et al.* 2004). (C) Les volumes de laves torrentielles en Valais sont distribués selon 2 lois de puissance (Modifié d'après BARDOU & JABOYEDOFF 2008).

406 M. Jaboyedoff, M. Charrière, M.-H. Derron, P. Nicolet & K. Sudmeier-Rieux

dégradation des matériaux (GOUVERNEMENTS DU QUÉBEC 2004). Les constatations ci-dessus s'appliquent bien entendu à d'autres ouvrages tels que les digues, les murs de protection, les filets de protection, les ancrages, etc. Ce problème n'est pas encore forcément bien documenté pour certaines de ces infrastructures, et il s'agit d'y prendre garde, notamment dans les zones où l'activité économique diminue et donc où beaucoup d'infrastructures ne sont plus entretenues.



Figure 4.–Train qui a déraillé en février 2013, avec le mur qui a cédé et le dépôt des matériaux.

INTÉGRATION DES RISQUES DANS UN CADRE PLUS LARGE: LEUR GESTION

Le contexte

Le but de l'analyse de risque et de leur gestion est de, in fine, réduire les risques et donc les impacts sur la société. Mais la poursuite de cet objectif doit tenir compte de la complexité des enjeux parmi lesquels les risques naturels ne constituent qu'une des composantes de la gestion du territoire (LEROI com. pers., LEROI *et al.* 2005) et de la société, qui notamment se préoccupe aussi des problèmes de santé publique. De plus, de nouvelles valeurs et enjeux environnementaux apparaissent tels que protection de la nature ou des eaux, gestion des forêts, etc., qui modifient le classement des valeurs affectées aux objets à risques. L'analyse coûts-bénéfices n'est désormais plus la méthode principale d'aide à la décision, cependant elle reste, comme il a déjà été indiqué, un outil très utile dans un processus décisionnel.

Les contraintes évoquées ci-dessus, qui sont de plus en plus nombreuses, impliquent inévitablement que la gestion du territoire ne peut se restreindre à des interdits ou à une classification rigide comme les cartes de danger suisses (les cartes de danger suisses sont en fait une évaluation des risques pour des bâtiments d'habitation). Au contraire, elle doit s'adapter aux contraintes, mais également mesurer et tolérer des prises de risques moyennant des mesures adéquates. Il est en effet préférable de vivre dans une zone rouge sachant qu'elle est rouge, que dans une zone de couleur inférieure dont l'affectation aurait été le fruit de décisions prises sous l'effet de pressions externes afin de minimiser le danger. Il existe plusieurs façons d'habiter des zones rouges, si les fréquences et les intensités restent raisonnables. On peut envisager des mesure d'évacuation grâce à un système d'alerte, comme cela a été fait temporairement à St-Nicolas, ou développer un habitat adapté comme cela aurait dû par exemple être le cas à la Faute-sur-Mer, des maisons à deux étages au moins avec échappatoire vers le toit ainsi que l'interdiction d'avoir des chambres à coucher au rez-de-chaussée. Lorsque des protections sont installées, la couleur du danger ne doit pas être supprimée, mais elle peut être assortie d'un figuré qui par sa couleur indique la réduction qui a été réalisée par la mesure prise et qui par son symbole indique le type de mesure (NICOLET *et al.* 2011) (figure 5).

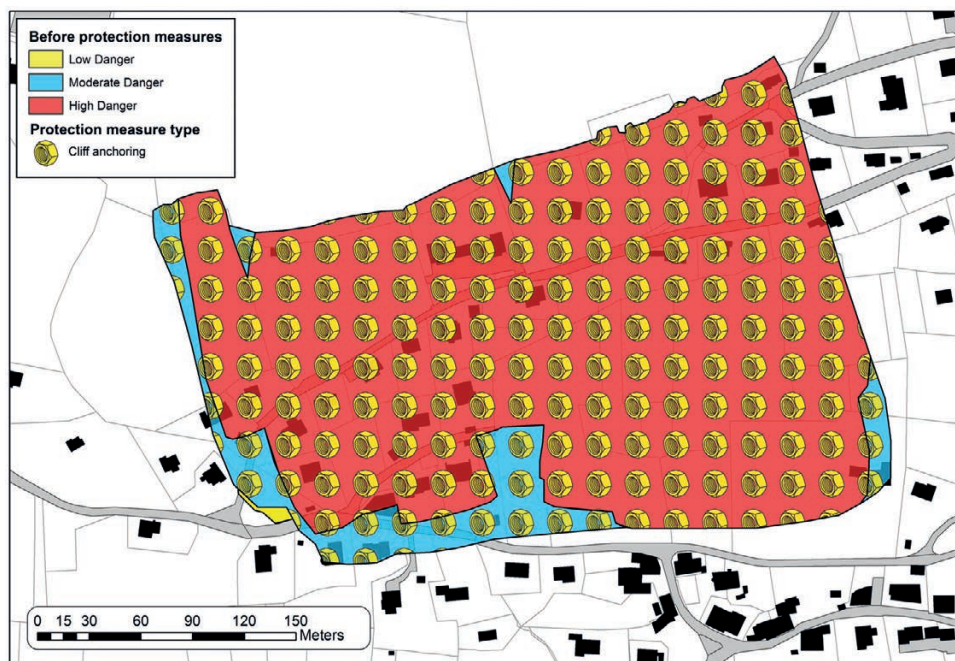


Figure 5.–Exemple de carte de danger chute de blocs pour la commune de Chardonne. Sans mesure de protection, le niveau de danger est élevé dans la majeure partie de la zone, tandis que les auteurs de l'étude estiment qu'il serait faible après les mesures de protection proposées (Géodonnées ©Etat de Vaud pour le fond cadastral / Norbert SA, Xylon SA et Cstp SA pour les cartes de dangers) (Tiré de NICOLET *et al.* 2011). (figure 32.5 en couleur en annexe)

Dans les cas de Gurntellen, on voit que d'une part la gestion des risques doit être indépendante des pressions, mais d'autre part des solutions doivent être trouvées. Ceci implique que la description du système à risque soit la plus complète possible. Nous y reviendrons plus loin. Mais surtout cela soulève la question de savoir quels sont les meilleurs outils pour gérer les risques?

Réduire le risque

Réduire le risque est important, mais de quelle manière? Il existe une panoplie de mesures structurelles, décisionnelles et organisationnelles, qui peuvent mener à cet objectif. Parmi celles-ci les systèmes de surveillances et d'alertes, la communication des risques ainsi que la prise de conscience des incertitudes dans l'appréhension des risques.

Les systèmes d'alertes

Les alertes qui concernent les événements météorologiques sont bien connues du public, mais ne sont pas toujours suivies par les populations. On peut s'en convaincre par le grand nombre de morts par imprudence lors des événements avalancheux de l'hiver 1999 dans les Alpes et lors de la tempête Lothar, et visiblement aussi de la part des autorités dans le cas de Xynthia.

Dans le cas des glissements de terrain, il existe plusieurs approches pour les «Early warning system» (EWS) ou systèmes d'alerte, suivant qu'il s'agisse de grands glissements ou de mouvements superficiels. Les glissements superficiels sont ce qu'on peut appeler «les glissements tueurs» comme celui de Lutzenberg, car bien que de petite taille, leur intensité est suffisante pour détruire des bâtiments en raison de vitesses relativement élevées, et il est difficile de prévoir leur localisation. C'est la raison pour laquelle plusieurs tentatives sont en cours dans le monde pour développer des systèmes d'alertes basés sur l'intensité des précipitations, la saturation des sols, les précipitations antécédentes, etc., afin d'être capable d'établir une alerte et d'éventuellement évacuer les zones les plus sensibles (BAUM *et al.* 2010). La même approche est en train d'être appliquée dans des zones urbanisées telles que Vancouver pour les laves torrentielles (JAKOB *et al.* 2011). La difficulté scientifique et technique de ce genre de systèmes est l'identification des seuils qui définissent les différents niveaux de l'alerte.

Les grands glissements peuvent présenter une rupture brutale, comme à Åknes (Norvège; BLIKRA 2008) ou à Turtle Mountain (Alberta, Canada; FROESE & MORENO 2011). Ces sites sont équipés de systèmes d'alerte complets, avec une chaîne de décision prédéfinie et de nombreux instruments sur site, avec de la redondance dans la transmission et dans les instruments eux-mêmes (figure 6). Dans le cas d'Åknes, le problème est compliqué puisqu'un tsunami peut être induit dans les fjords parmi les plus touristiques de Norvège. Ainsi, une infrastructure de chemins de fuite vers des points hauts a été créée. Ils sont signalés par des panneaux et un système de haut-parleur a été mis en place pour donner l'alerte, le tout en plusieurs langues. La population a aussi été impliquée dans des exercices et de nombreuses séances d'information ont été réalisées dans les villages.

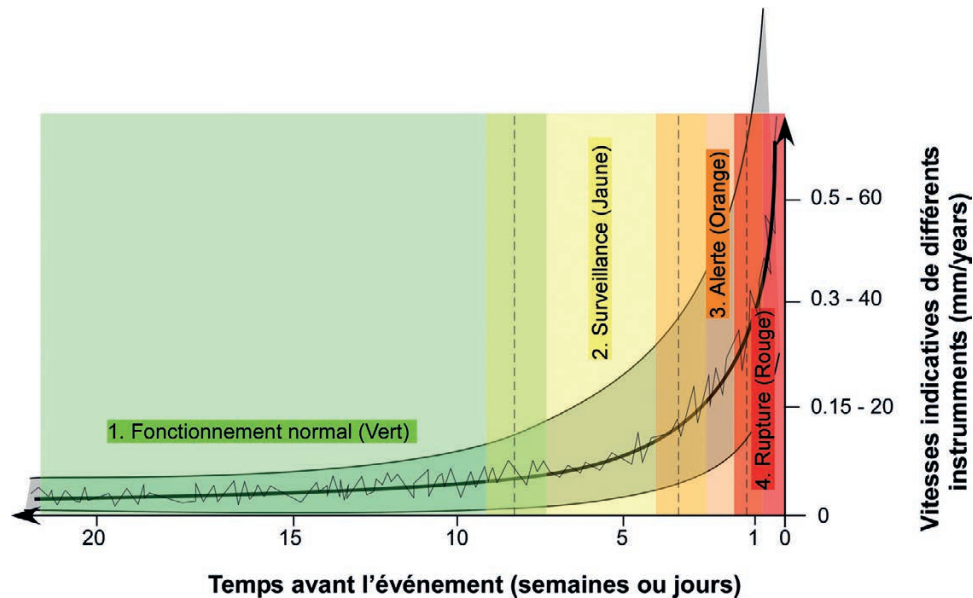


Figure 6.—Représentation schématique des niveaux d'alerte relatifs aux vitesses de capteurs de mouvement sur des glissements rocheux de plusieurs millions de m³. Notez que les périodes de décision sont floues en fonction des connaissances d'expert et que les valeurs seuils sont définies en fonction du capteur et de sa position (Modifié d'après FROESE *et al.* 2012; d'après BLIKRA 2008 et FROESE & MORENO 2011). (figure 32.6 en couleur en annexe)

Communiquer le risque

Comme l'exemple de L'Aquila le montre, la communication des risques est, et devient, primordiale dans la gestion des risques. Une des conditions pour que la communication du risque soit efficace est qu'elle soit développée considérant les caractéristiques de l'audience qu'elle vise (LUNDGREN & MCMAKIN 2009). Elle doit donc notamment tenir compte de la représentation des risques des personnes concernées et en particulier de leur perception (PERETTI-WATEL 2000). En effet, la perception que les gens se font du risque est le moteur de leur comportements face aux risques (ESPINER 1999, ENDERS 2001). La perception d'un risque dépend, en principe, de l'état affectif de l'individu concerné (FINUCANE *et al.* 2000) mais aussi de ses connaissances, de son vécu dans le contexte à risque, de son attitude face aux risques, de son exposition aux mesures de sensibilisation, de ses capacités de mitigation, de préparation et de réponse, ainsi que de ses caractéristiques personnelles (âge, genre, éducation, etc...) (ENDERS 2001). Dans le modèle de l'affect, selon SLOVIC & PETERS (2006), si l'individu se trouve dans de bonnes dispositions, il serait apte à prendre des risques si le bénéfice est important; ce qui démontre la difficulté d'appréhender la perception.

La perception est un processus complexe. KELLER *et al.* (2006) ont pu noter, par exemple, qu'un groupe de personnes informées des risques d'inondation dont les temps de retour sont plus longs est plus sensible aux risques, qu'un autre groupe informé d'événements à temps de retour plus faibles donc d'intensités plus faibles. Mais cela dépend aussi de l'expérience personnelle des individus ainsi que des autres facteurs cités ci-dessus. D'autre part, la

manière de présenter l'information peut avoir un impact sur la perception des risques. Par exemple, la présentation des photos d'inondation rend les personnes plus sensibles aux risques (KELLER *et al.* 2006). Il apparaît aussi que les médias semblent avoir une influence sur la perception des risques en général mais pas sur la perception personnelle du risque (WÄHLBERG & SJÖBERG 2000).

Il existe une tendance à considérer que les experts sont plus à même d'évaluer les risques et qu'ils seraient capables d'être objectifs (SLOVIC 1987). Ce modèle de perception des risques est contesté (JASANOFF 1997). Le problème des experts est qu'ils sont souvent proches de personnes impliquées de par leur statut d'expert et qu'ils entrent dans un jeu de pouvoir. Les experts indépendants, même qualifiés, sont souvent discrédités. Pourtant, les personnes les plus adéquates pour parler des dangers naturels sont celles qui les étudient, à savoir les techniciens, ingénieurs, scientifiques, géologues, etc., car ils connaissent les processus et prennent pour certains des responsabilités dans la gestion des risques. Il semble clair qu'une certaine proximité entre les personnes concernées par la réduction des risques et la population est nécessaire, comme le montre l'exemple de St-Nicolas. Il ne suffit pas de communiquer pour obtenir un résultat, il faut s'assurer de la confiance, montrer qu'on prend des responsabilités. Il faut absolument éviter les scénarios de médiatisation excessive décrit par DAUPHINÉ (2001):

1. Phase 1: La surmédiatisation induit:
 - Sensationnalisme
 - Voyeurisme
 - «Télé-réalité»
2. Phase 2: Souvent dans un deuxième temps les médias cherchent qui sont les coupables?
 - La recherche des causes, mais de façon à identifier des erreurs humaines ou des responsabilités individuelles
 - L'idée du complot s'insère: les choses arrivent, mais cela a été caché, et certaines personnes connaissaient le risque
 - ...

Bien sûr cela ne veut pas dire que la phase 2 ne soit pas légitime pour la société, car il existe souvent des responsables, que par exemple le journalisme d'investigation sérieux tente d'identifier. Mais lorsque que la catastrophe n'est pas imputable à des erreurs, il faut absolument éviter une surmédiatisation. Il existe notamment deux stratégies opposées pour tenter d'éviter «la médiatisation déviante»: la plus courante, c'est le secret, qui est souvent la source des deux phases décrites plus haut. La seconde consiste à être transparent, même si elle n'évite pas forcément les écueils de la communication.

Une communication efficace doit impérativement impliquer une connaissance de l'aléa par les communicants, qui doivent être les scientifiques, les techniciens, les politiques ou/ et des personnes des services de l'état concernés ou des spécialistes de communication ayant intégré la problématique de l'aléa dans leur discours. Mais la communication doit aussi s'appuyer sur une connaissance des populations ou intégrer un volet qui permette d'interagir avec la population et les groupes d'influences, afin de mieux comprendre le fonctionnement de la communauté concernée.

La société doit s'adapter aux incertitudes

Dans le processus de communication, il s'agit aussi de transmettre une partie de la connaissance tout en y incluant de l'incertitude. En effet, lors de la catastrophe de L'Aquila, c'est justement d'avoir voulu rassurer en induisant implicitement une prévision indirecte (en indiquant que les gens pouvaient rentrer chez eux) dans une situation plus incertaine qu'à l'accoutumée qui a mené aux condamnations. Il est donc important que cette incertitude soit transmise d'une façon ou d'une autre. Selon IBREKK & MORGAN (1987) l'incertitude peut être mieux transmise si les courbes d'excédence sont fournies en regard de la densité de probabilité; les personnes peuvent ainsi se figurer les probabilités (figure 7).

Mais l'incertitude doit aussi faire partie de tous le processus d'évaluation et de gestion des risques; les problèmes de Gurtneellen, de l'Aquila sont là pour nous le rappeler et l'exemple de St-Nicolas montre qu'une population peut l'accepter, si elle y est préparée.

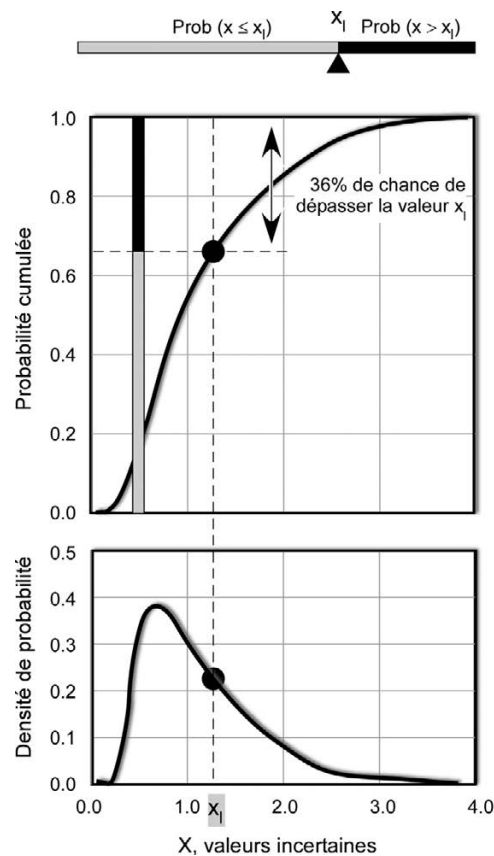


Figure 7.—Illustration de la façon de transmettre l'incertitude et les notions de probabilité au public (modifié d'après IBREKK & MORGAN 1987).

Structurer l'analyse des risques

Bien souvent les données nécessaires à la quantification des risques ne sont pas disponibles ou n'existent simplement pas. Il existe une série de méthodes qui tentent de pallier à ce manque. L'une d'elle consiste à réunir une équipe de personnes concernées par les risques et d'en tirer un tableau des aléas (fréquence ou probabilité) et des impacts potentiels (GILLET 1985, ALE 2009). Cette méthode a été systématisée par la Zürich assurance (méthode ZHA), qui a réalisé un outil (ZHA 2013) dont une version Excel est en libre accès. Sur cette base les tâches sont:

1. Réunir un groupe de personnes concernées
2. Choisir un leader
3. Définir les aléas
4. Définir les conséquences
5. Choisir des limites d'acceptabilité ou/et de tolérance
6. Proposer des scénarios de réduction du risque
7. Réalisation
8. Actualisation au cours du temps

Notons que cette méthode est, depuis quelques années, appliquée par la confédération pour la gestion des risques de projet (feuille Excel Risk-Cockpit) dans le cadre plus large de la gestion électronique des affaires (GEVER 2009). Cette approche a récemment été étendue à «l'élaboration d'une analyse des dangers à l'échelon cantonal - KATAPLAN» (OFPP 2013), qui a pour but de préparer et protéger une population en cas de catastrophe ou d'autres situations d'urgence. A cette procédure on peut ajouter les impacts en chaînes qui peuvent être induits par des mesures. Ceci peut aussi être abordé avec des arbres de décision, basé sur l'opinion d'un groupe d'experts pour affecter des probabilités à tous les scénarios en arborescence (EINSTEIN 1988, LACASSE *et al.* 2008, ALE 2009).

Prenons un exemple fictif pour illustrer la méthode ZHA, en la modifiant légèrement. Nous sauterons les deux premiers points, car ils sont difficiles à décrire de manière concise. Le cas suivant est posé: une zone constructible est proposée dans une zone de laves torrentielles, où l'aléa est élevé (figure 8). Cette zone étant la seule zone acceptable compte tenu de l'ensemble des contraintes auxquels les aménagistes font face. Le groupe envisage alors de mettre les bâtiments les uns derrière les autres dans la direction du flux afin de limiter l'impact éventuel. Compte tenu de l'aléa, on décide de placer les limites des zones de risque tolérable et inacceptable le long des couples impact-fréquence tel que sur la figure 8. Ensuite, une digue de protection est proposée en amont pour laquelle deux solutions sont envisagées. Dans les deux cas, la digue est oblique afin de dévier les matériaux. De plus, des monticules végétalisés de 2 m de haut sont proposés de part et d'autre des bâtiments. D'une part, on réduit le risque pour la zone construite, mais d'autre part, on prêterite des zones où l'aléa était faible ou inexistant avant les mesures de protection.

Dans la matrice impact-fréquence, les problèmes ainsi que l'effet de la réduction des risques se visualisent. L'aléa de la zone des bâtiments se réduit en termes de fréquences mais les conséquences augmentent, car au cas où la digue serait inefficace, alors l'aléa serait d'intensité plus forte. La déviation des laves torrentielles induit dans les deux cas de nouvelles zones à risque si celles-ci venaient à être habitées. Leurs fréquences augmentent,

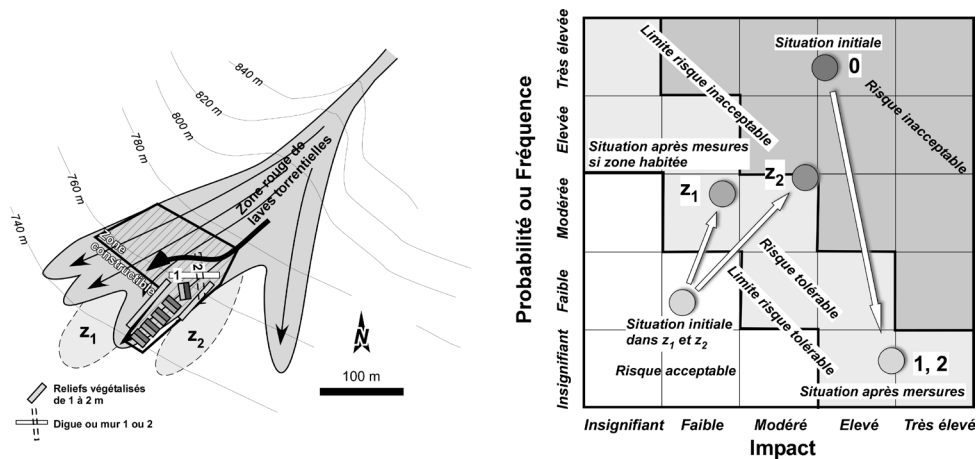


Figure 8.—Exemple de zone à bâtir potentielle dans une zone d'aléa élevé et illustration des solutions proposées. A droite représentation des degrés de risques à l'aide de la matrice impact-fréquence. Le champ du risque tolérable (gris clair) est compris entre la limite du risque tolérable et celle du risque inacceptable.

de même que leurs impacts, par rapport à la situation préexistante. La solution 1 est donc préférable car elle n'étend pas la zone de danger latéralement et l'intensité y est considérée comme plus faible que celle de la zone 2 qui indubitablement possédera une intensité élevée. La solution 2 induit donc un risque potentiel plus fort dans la zone de déviation que la solution 1, pour des zones affectées sensiblement identiques en superficie. Il est entendu que d'habiter une telle zone implique aussi un plan d'évacuation en cas de situation extrême.

Cette méthode autorise donc une approche multi-scénarios, mais elle peut aussi permettre d'insérer une approche multirisque. On voit par cet exemple qu'on peut représenter des chaînes d'évènements et leurs conséquences.

Le problème de la résilience

En général les risques sont évalués par les dommages, soit les coûts de remplacements sur la base d'un modèle économique, ou le nombre de morts attendus. Si les victimes n'ont aucune possibilité d'être ressuscitées, la réparation des dommages, a elle, en principe, un coût relativement bien connu (nous ne considérons pas ici les problèmes de couverture d'assurance et la volatilité du marché de l'immobilier). On considère alors le concept de résilience qui se définit comme la capacité à résister à un évènement catastrophique et à rétablir une situation normale dans un temps raisonnable (NISDR 2009). Ainsi, partant de ce qui précède, la résilience apparaît naturellement comme une quantification de l'inverse des degrés de «dommages» indirects induits par une catastrophe, mais dont l'impact varie en fonction du temps (figure 9), mais aussi des capacités sociétales de revenir à l'état pré-catastrophe, «normal», même si la définition de la normalité peut-être problématique en soi.

On peut donc définir le coût indirect induit par une catastrophe (C_{RE}) comme un «coût» financier ou social qui représente l'intégrale au cours du temps du degré de dysfonctionnement par unité de temps rapporté à la normale (BRUNEAU *et al.* 2003, ROSE 2007, SUDMEIER-RIEUX 2011, KRÖGER 2013):

$$C_{RE} = \int_{t_0}^{t_0+\Delta t} (1-r(t))M_n(t)dt \quad (\text{Equation 5})$$

Où $r(t)$ peut être défini comme la résilience instantanée dans la période post-catastrophe (une année par exemple), soit le rapport de la valeur post-catastrophe $M_c(t)$ à la valeur normale attendue $M_n(t)$ (échange, activité,...) à un temps t , l'évènement se produisant à t_0 , considérant une période de retour à la normale de durée Δt c'est à dire lorsque $r(t) = 1$ ou durablement proche de 1. On a alors:

$$r(t) = \frac{M_c(t)}{M_n(t)} \quad (\text{Equation 6})$$

Ainsi on peut proposer que la résilience soit définie comme:

$$Re = \int_{t_0}^{t_r} r(t)dt \quad (\text{Equation 7})$$

Où t_r est soit égal à $t_0+\Delta t$, soit à une valeur prédéfinie $t_r = t_0 + t_{ref}$ où t_{ref} est une durée prédéfinie qui permet de comparer différents cas. Re vaut au maximum Δt si $t_r = t_0+\Delta t$, c'est-à-dire une situation où il n'y a pas d'impact post-catastrophe. Re peut aussi être normée par rapport au temps afin d'obtenir un pourcentage. On voit bien que toutes ces équations sont difficiles à quantifier. Bien sûr, ($M_n(t)$) peut être un PIB, une quantité qui décrit la société, les transports, etc. Notons que $(1-r(t))$ représente l'écart à une situation normale. Lorsque que $r(t)$ est supérieur à 1 cela signifie que le système s'est amélioré, les coûts se sont réduits puisqu'il y a gain. Ainsi, pour joindre le risque habituel à la résilience et aux coûts indirects, on peut écrire que l'impact total vaut (I_t):

$$I_t = R + C_{RE} \quad (\text{Equation 8})$$

Selon certaines définitions I_t est équivalent au risque lorsque l'on considère le risque comme un calcul qui prend en compte l'ensemble des conséquences (HAIMES 2009). De la même manière que pour le risque, C_{RE} peut se lire de façon qualitative, c'est dire que $r(t)$ est l'écart à la situation normale, et cela peut être économique (ROSE 2007) ou relatif au fonctionnement de la société ou plus généralement d'un système (ALLENBY & FINK 2005, HAIMES 2009, SUDMEIER-RIEUX 2011).

Ce concept est important et il faut en tenir compte dans les calculs de risque ou plutôt dans le calcul de l'impact potentiel total d'une catastrophe. Le risque lui-même n'étant pas directement affecté par la résilience selon l'équation 8. Les premiers modèles appliqués en Suisse relatifs à la fermeture des autoroutes ne tiennent pas compte de la résilience (BRÜNDL 2009, ERATH *et al.* 2009). On suppose que la fermeture d'une autoroute a le même impact par jour sur toute la durée considérée. En fait, si l'autoroute du Gothard est fermée, de nos jours, les résidents tessinois qui doivent aller à Zürich peuvent communiquer par visio-conférence, ou si des fournitures ne sont plus accessibles, on peut se tourner vers l'Italie. Très vite la société sera résiliente, d'autant plus si l'état aménage des facilités. La mise en

réseau de beaucoup d'aspects de notre société la rend moins vulnérable et plus résiliente (ALLENBY & FINK 2005). Néanmoins cette assertion dépend de l'intensité des catastrophes qui affectent le système, car une atteinte au réseau tel un évènement comme Lothar ou d'une intensité supérieure pourrait avoir des conséquences plus grandes encore.

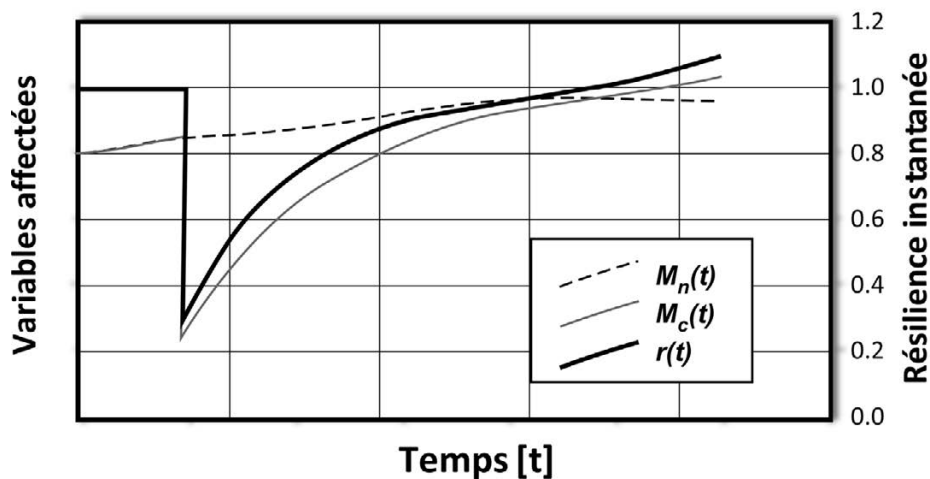


Figure 9.– Illustration de la notion de résilience instantanée ($r(t)$). $M_c(t)$ est une variable financière ou non qui a été affectée par un évènement catastrophique et dont la valeur normale attendue vaut hors catastrophe $M_n(t)$. Les M sont des «coûts» par unité de temps (modifié d'après BRUNEAU *et al.* 2003).

Un exemple: inondations en Thaïlande et disques durs

En automne 2011, la Thaïlande a été inondée en raison de précipitations exceptionnelles durant les mois de mai à octobre. En octobre, des zones industrielles de Bangkok ont été touchées par les inondations (KOMORI *et al.* 2012). Cet évènement a eu un impact mondial puisque plusieurs des principaux fabricants de disques durs possédaient des usines dans les régions affectées. Par conséquent, la production de disques durs a chuté au niveau mondial au lieu de d'augmenter, 30% de la production mondiale étant localisée à ce moment en Thaïlande (INFOWORLD 2011). Pour un chiffre d'affaire de 32\$ milliards en 2011 et 38\$ milliards en 2012 et une production en unités estimée en 2010 à 654 millions, en 2011 à 624 millions et en 2012 à 673 millions (WIKIPEDIA 2013, COUGHLIN & GROCHOWSKI 2012). Dès lors, on peut se poser la question des coûts globaux et du retour à la situation normale et calculer à postériori la résilience.

Partant de la courbe des prix d'un disque dur standard, nous pouvons définir la résilience instantanée par (figure 10a):

$$r(t) = \frac{M_c(t)}{M_n(t)} = 1 - \frac{\Delta C(t)}{C(t)} \quad (\text{Equation 9})$$

où $C(t)$ est le prix normal attendu à un temps donné et $\Delta C(t)$ l'écart à ce prix attendu. Partant du principe que le prix de ce disque dur standard est représentatif, on peut estimer

la résilience. Ne connaissant pas exactement la valeur de $C(t)$, mais en supposant que les périodes avant et après la crise sont indicatives, il est possible de tracer une droite qui joint ces périodes par la méthode des moindres carrés (figure 10A), et ainsi on obtient le prix normal attendu. Ensuite, on peut évaluer la résilience normée (Re_n) sur une période donnée, ici une année puisque cette durée a permis de revenir à la situation «normale» (figure 10B):

$$Re_n = \frac{1}{365} \int_{t_0=17.10.2011}^{t_0+365} r(t)dt = \frac{1}{365} \int_{t_0=17.10.2011}^{t_0+365} 1 - \frac{\Delta C(t)}{C(t)} dt = 69\% \quad (\text{Equation 10})$$

Il s'en suit que l'impact négatif est de 31% sur une année. En faisant la simplification que $C(t)$ est constant durant l'année considérée, il est possible d'estimer grossièrement à 10\$ milliards l'impact additionnel pour l'ensemble des utilisateurs finaux. Notons tout de même que les chiffres de production à disposition sont un peu contradictoires. Cependant ce résultat est proche de ce que prévoient COUGHLIN & GROCHOWSKI (2012) pour une bonne partie de 2012. Il est aussi probable que les compagnies productrices n'y aient pas trop perdu compte tenu de la hausse des prix, et qu'elles peuvent aussi avoir spéculé.

Cet exemple tente de quantifier l'impact d'une catastrophe naturelle sur l'économie mondiale. Dans ce cas l'impact est diffus, mais il est intéressant de voir le retour à la normale. On aurait pu aussi utiliser la production pour ce calcul, ce qui serait intéressant à analyser en regard des investissements et des prix du marché, mais il est à craindre que ces données ne soient pas disponibles.

On observe là que de concentrer la production des disques durs dans un site diminue la résilience du système, une localisation plus dispersée dans le monde aurait certainement diminué l'impact. Des effets similaires avaient été observés pour les mémoires d'ordinateur produites dans la région de Kobe après le tremblement de terre de 1995.

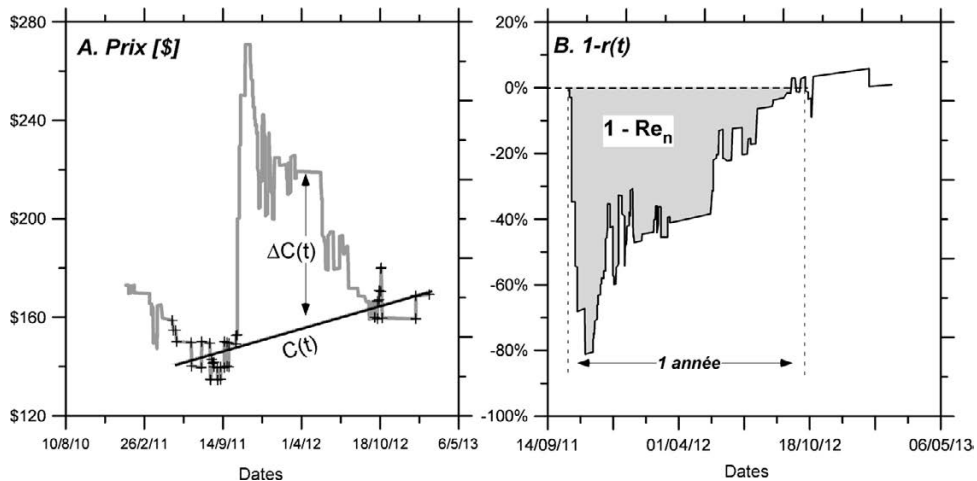


Figure 10.–(A) prix du disque dur Western Digital WD1002FAEX Caviar Black 1T SATA III 7200 RPM 64MB cache 3.5'' (tiré de HOMELAND SECURE IT 2013). (B) Graphique de $1 - Re_n(t)$ pour laquelle la zone grisée représente les pertes normée à 100% sur une année, les données sont extraites de (A).

LE RISQUE EST UNE DYNAMIQUE

Les exemples ci-dessus illustrent à quel point la gestion des risques nécessite une permanente remise en question, par exemple le simple fait que certains risques soient saisonniers, implique qu'il faut tenir compte de la période que l'on considère. Par conséquent, il est nécessaire de réaliser une analyse dynamique dans un monde qui change constamment. On ne peut plus se contenter d'attendre que des événements se produisent pour réagir, il faut anticiper.

Anticiper, c'est aussi tenir compte des incertitudes. C'est la raison pour laquelle plusieurs approches doivent être imaginées pour une prise en compte de futurs risques. Lorsqu'un système est modifié, il s'agit d'évaluer les impacts potentiels. Par exemple, dans le cas de Xynthia, l'urbanisation des polders a complètement changé les éléments à risque et des mesures de construction auraient dû être prises. Des changements dans les règles régissant des métiers à risque ou à responsabilité peuvent également produire de nouveaux risques, comme on peut le soupçonner dans les cas des accidents de trains début 2013 qui ont vraisemblablement été causés par l'ouverture du marché qui autorise des machinistes peu qualifiés à conduire des trains de marchandises (LE MATIN DIMANCHE 2013).

En matière de risques liés aux dangers naturels, il s'agit de s'interroger sur les implications de changement d'usage ou de fréquentation du territoire et des voies de communication. L'élaboration de scénarios est fondamentale, mais il s'agit surtout de tenter d'en explorer le plus possible. L'évaluation du risque de chacun d'entre eux doit être réalisée, si possible sans biais. C'est la raison pour laquelle l'ensemble des informations doivent être traitées, qu'elles soient historiques ou qu'elles puissent paraître a priori irrationnelles. La méthode des matrices impact-probabilité est un bon cadre pour l'évaluation des scénarios. Il faut aussi tenter d'y ajouter les incertitudes. Lorsque qu'un faisceau d'argument mène à une situation incertaine potentiellement risquée, le principe de précaution peut être appliqué. Néanmoins, un usage abusif de ce principe est néfaste dans la gestion des risques. Car c'est un moyen de ne pas prendre de responsabilités, alors que la gestion des risques nécessite une prise de responsabilité à un moment donné, lors d'une prise de décision.

Reste que les gestions des risques impliquent aussi de la transparence afin que les acteurs ne se sentent pas écartés. Ainsi la communication des risques, aussi difficile qu'elle soit à mettre en œuvre, doit être appropriée. Il est relativement évident que le contact direct avec les personnes en charge de la réalisation des évaluations des risques, et en particulier de l'aléa et des mesures à prendre dans les zones à risques, est la meilleure solution. Limiter les intermédiaires dans la chaîne de transmission de l'information est important pour éviter les malentendus. De plus, il ne faut pas utiliser de langages inappropriés. En effet, il y a une souvent une nécessité de traduire l'information technique vers un langage plus adaptée à l'audience qui est visée. En outre, en plus d'une transmission unidirectionnelle de l'information, il est évident qu'il doit y avoir un échange bi(multi)directionnelle, qui doit tendre à une confiance entre les personnes impliquées. Cela est nécessaire car il est important que les acteurs en charge des décisions, qui sont les responsables, soient bien perçus par le public.

Ce qui précède n'est pas facile à mettre en œuvre, car les contextes sont très variables (HÖPPNER *et al.* 2010, VAUGHAN 1995). Tout ceci n'est pas nouveau, mais il faut insister sur

le fait que ce sont les personnes qui possèdent les connaissances du système à risques qui doivent, dans la mesure du possible, en parler. Mais cela peut aussi impliquer des habitants qui connaissent leur territoire sans être scientifique ou technicien.

Le problème des experts

Un expert possède un agenda. Or, l'évaluation des risques doit justement s'absoudre de tout agenda, comme le montre le cas de L'Aquila. Il est évident que tous les acteurs sont importants. L'idée qu'une vision d'expert est plus importante que celles des non-experts ou de la population est juste et fautive à la fois. Il est vrai qu'évaluer certains phénomènes dangereux ne peut se faire que si on sait de quoi il en retourne, en particulier du point de vue de l'aléa (intensité fréquence ou probabilité-scénario). Par conséquent, ce sont les personnes qui savent qui peuvent donner leur avis, mais cela peut impliquer des anciens dans un village par exemple. Pour mieux illustrer le propos, nous allons prendre l'exemple de l'énergie nucléaire.

Comme cela a déjà été dit les experts possèdent souvent des intérêts contraires, ou ont une vision biaisée, en particulier en matière de nucléaire. Si cette énergie est fascinante, elle a montré sa capacité à polluer. C'est là où les experts ne s'en sortent plus: dans le cas de Fukushima, par exemple, on entend «... c'est une erreur qui nous amené à cette catastrophe...». Oui, cela est vrai, mais celles-ci doivent être intégrées dans l'appréciation des risques. C'est la raison pour laquelle les experts attestés (les opposants possédant de l'expertise ne sont souvent pas admis comme expert par les dirigeants) ne sont plus crédibles, car la confiance est rompue. Le nucléaire est le meilleur exemple, car justement, il a donné des arguments justifiés contre les sciences dures, ou plutôt les techniques, aux sociologues (SHORT 1984, PERETTI-WATEL 2000). Mais là encore, deux éléments brouillent les cartes. Les experts n'agissent trop souvent pas en tant que scientifiques (i.e. tenants de la méthode scientifique), mais en tant qu'acteurs soumis à un agenda qui biaise l'évaluation. Il ne s'agit donc pas de critiquer les scientifiques mais ceux qui font de la politique en se présentant sous leur étiquette de scientifique. Mais ce même biais apparaît en science humaine. Les travaux de SLOVIC (1987) sont parmi les plus biaisés quant à la prééminence des experts (JASANOFF 1997). Les écrits de SLOVIC (en particulier SLOVIC 1987) tentent de minimiser le risque nucléaire civil grâce à l'opinion des experts, sans prendre aucune distance par rapport à eux. Le risque nucléaire serait faible selon les «experts», mais au regard des récents événements, un petit calcul considérant les 450 réacteurs dans le monde montre que la fréquence résultante d'un accident pour un réacteur est de 2×10^{-4} . Ceci est le résultat du calcul du nombre de réacteurs \times an estimés à environ 11'250 depuis 1955 grâce aux données de WNISR (2009) et en comptant 3 événements ($3/11'250 \approx 2 \times 10^{-4}$). Ce résultat est à comparer aux limites proposées par la confédération, qui, pour 10 décès, la pollution de 1 km² d'eau ou 50 millions de francs de dégâts, se situent respectivement à 1×10^{-5} et à 1×10^{-7} pour le risque inacceptable et pour le risque tolérable (JORDI, 2006). Nous sommes donc, compte tenu de l'impact potentiel, au-delà des limites proposées.

Basé sur des domaines comme le nucléaire, la critique de la gestion des risques est pleinement justifiée, mais ce n'est pas si simple pour les risques liés aux dangers naturels. Les acteurs, dans ce dernier cas, sont plus nombreux et les enjeux plus variés et sont souvent le résultat qui permet d'identifier clairement les responsables potentiels. Le nucléaire vient

d'une décision unilatérale, qui n'autorise pas à désigner des responsables par la clause du besoin. Le manque de clarté des autorités fédérales en matière de fermetures de centrales sont instructifs à ce sujet (SWISSINFO 2011, 2013).

Dépendance du risque à la connaissance du système étudié et adaptation

L'équation du risque n'est pas tout, car elle n'est utile que si les paramètres choisis décrivent l'ensemble des situations à risque. Ainsi, poser une équation du risque ou gérer les risques dépendent de la connaissance du système étudié, tant du point de vue spatial que du point de vue temporel. L'anticipation d'un risque météorologique évolue au cours du temps qui précède une situation critique et permet de préciser l'intensité attendue, mais souvent cela ne suffit pas pour prévenir une catastrophe. Celle-ci est souvent non prévue car très fréquemment, c'est la conjonction de plusieurs phénomènes qui mène à la catastrophe, comme dans le cas de Xynthia. Pourtant, dans certains cas, des catastrophes auraient pu être anticipées. Par exemple, les effets d'un cyclone sur la ville de la Nouvelle-Orléans avaient été décrits assez précisément par LASKA (2004), mais on en n'a pas tenu compte avant le cyclone Katrina d'août 2005 (SWISSRE 2006). Cette capacité à prédire dépend du degré de connaissance préalable du système dangereux.

Le manque d'information à disposition peut être la cause d'une description lacunaire du système, ce qui est souvent le cas. Mais cela peut aussi provenir des acteurs en charge d'étudier, d'évaluer et/ou de gérer les risques. En effet «la lecture» d'un système dangereux dépend du bagage (formation et expérience) des personnes, mais aussi et surtout de l'agenda de ces dernières, comme c'est le cas des experts. On connaît par exemple les pressions que peuvent exercer une commune sur un bureau lors de la réalisation de cartes de danger. Le bureau pouvant avoir intérêt à satisfaire les autorités et services communaux afin de préserver des chances d'obtenir d'autres mandats. Le système va donc au-delà du système naturel, il est aussi tributaire du contexte social puisque les remarques faites au sujet des acteurs et des experts sont aussi valables pour les groupes sociaux. C'est une des raisons pour lesquelles une analyse coûts-bénéfices, si elle est utile à la décision, ne prend pas en compte le système dans son ensemble, et notamment l'aversion d'une population pour les risques (HALLEGATE & DUMAS 2012).

Trop souvent dans l'analyse de risque on entend: «... oui mais cette situation n'était pas prévue... on ne pensait pas que... et c'est une erreur». Justement l'analyse et la gestion des risque doit intégrer les situations imprévues autant que possible. En particulier dans le domaine nucléaire on parle «d'erreur humaine», de sous-estimation de l'impact de tsunami, même si les experts soulignent légitimement les manquements a posteriori (ACTON & HIBBS 2012). A l'inverse, la prise de conscience des changements climatiques essaie d'anticiper, mais on voit là toutes les difficultés d'une telle approche.

Notons aussi que les cultures de risques se perdent avec la mobilité des populations et l'attrait des beaux sites. L'exemple de Xynthia est là pour le souligner, puisque l'on a oublié que ces zones étaient assez fréquemment inondées (SAUZEAU 2011) et qu'on aurait pu s'adapter à la situation en construisant des maisons à deux étages. On peut toujours ajouter de nouveaux paramètres dans la description du système. Par exemple, FILATOVA *et al.* (2011) ont modélisé le comportement vis-à-vis du risque des habitants des côtes qui induit une

420 M. Jaboyedoff, M. Charrière, M.-H. Derron, P. Nicolet & K. Sudmeier-Rieux

augmentation des risques lorsque les membres d'une population présentent une perception des risques non uniforme.

Rappelons que les aspects techniques et l'histoire d'un site sont primordiaux dans la prise de responsabilités. Il s'agit de bien identifier les problèmes et ne pas hésiter à imaginer des événements extrêmes et d'en évaluer les conséquences potentielles, et de voir si des mesures simples peuvent permettre de limiter les risques. Dans la démarche de gestion des risques, on peut se tromper, mais si c'est le cas il faut immédiatement en tirer les conséquences. L'erreur, c'est de ne pas admettre ses erreurs. Dans un monde où nous communiquons beaucoup, cette nouvelle interaction par les nouvelles technologies ouvre des possibilités dans la gestion des risques, mais aussi dans la connaissance de ceux-ci. Il sera de plus en plus difficile de dire dans le futur qu'on n'était pas informé.

N'oublions pas que ce qui n'est pas envisagé dans la description d'un système à risque n'apparaît pas dans les résultats d'une étude de risque.

LES FUTURES DÉFIS

Conséquences pour la Suisse

Dans son ouvrage «Habiter la menace», LAMUNIÈRE (2006) se demande jusqu'où l'on peut aller. Même si des solutions peu réalistes sont proposées, le débat soulevé est le bon. La Suisse doit intégrer les risques dans sa gestion du territoire d'une façon dynamique. Il faut en effet habiter des zones à risque, là où les gens y trouvent un avantage (figure 11). Il s'agit d'anticiper les problèmes, puisque l'anthropisation du territoire suisse est rapide (OFS 2002). De plus, beaucoup d'infrastructures vieillissent, ce qui rend encore le territoire plus risqué.

La seule façon est de développer des zones où le risque serait supérieur au risque accepté, mais en le réduisant par la gestion pour retrouver un niveau de risque acceptable. Comme nous l'avons montré, de nombreuses pistes sont possibles: des bâtiments adéquats, une observation plus fine des phénomènes dangereux ou une prise de conscience de la population afin de vivre au quotidien avec les dangers naturels ou provoqués par l'homme.

Pour cela la philosophie de la gestion des risques et du territoire doit changer en Suisse, notamment la roue habituellement présentée (figure 12). Elle ne doit plus s'appuyer sur la réaction à une catastrophe, mais s'appuyer clairement sur la préparation à des événements qui ne se sont jamais produits. La gestion du territoire doit s'appuyer sur une gestion dynamique des risques, c'est-à-dire que la carte de danger n'est plus l'outil adéquat, comme le montre désormais la gestion des risques sur les routes nationales. Il faut également intégrer l'incertitude dans la transmission de l'information (LUNDGREN & McMAKIN 2009, FREWER 2004, LEISS 2004, OECD 2002). Du côté de la Confédération, on est d'ailleurs en train d'opérer ce virage vers le risque en matière de gestion du territoire mais aussi en matière de gestion du risque au niveau de tous les dangers en y intégrant les situations d'urgence (OFPP 2013).

Mais pour réussir tout cela, il faudra certainement édicter de nouvelles lois qui responsabilisent les habitants ainsi que les gestionnaire du territoire, tout en tenant compte

du fait que l'on peut se tromper, mais qu'on ne peut pas tromper les acteurs de la gestion des risques, à savoir la population concernée et les partenaires qui façonnent ce futur territoire.

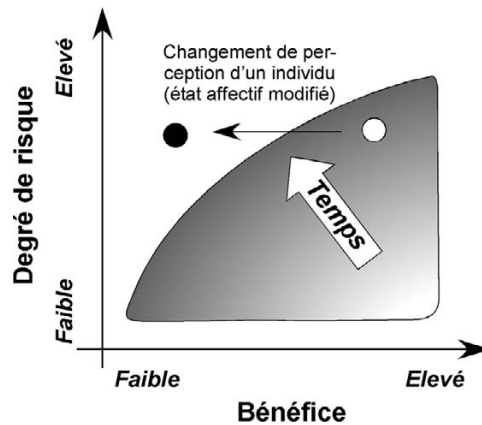


Figure 11.—Schéma illustrant les comportements à risque en fonction du bénéfice qu'on peut en tirer. La flèche temps et le dégradé indiquent dans quelle direction les populations devront accepter de vivre. Le problème étant essentiellement que les populations paniquent et ne voient pas le bénéfice d'une situation, comme l'illustre la flèche noire (modifié d'après FINUCANE *et al.* 2000).

Dans ce tournant, la Suisse est bien placée, sa population vit de longue date avec des risques (PFISTER 2002). Cependant, bien que la Suisse ait compté l'un des plus grands statisticiens, D. Bernoulli, la culture suisse n'a pas pour habitude d'intégrer les incertitudes et les probabilités. On aime bien le «propre en ordre», c'est-à-dire des choses figées, alors que le risque est dynamique. Les règles devront constamment être remises en question, mais il est certain que la Suisse possède le potentiel de vivre avec ses risques, la population par sa maturité pourra relever le défi.

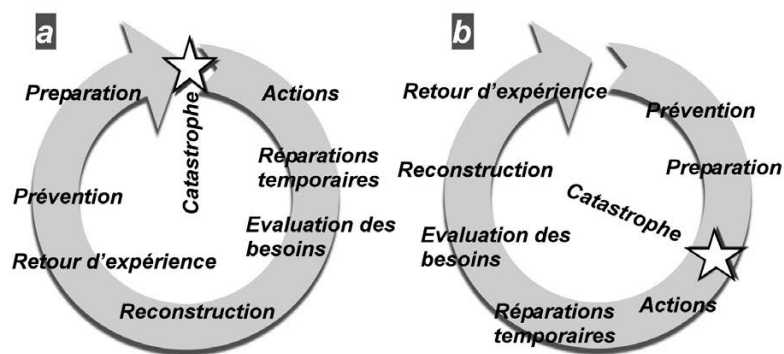


Figure 12.—(a) Roue de la gestion du risque de la PLANAT simplifiée (modifiée de www.planat.ch, OFPP 2010). Cette roue n'a pas réellement de point de départ, mais elle n'existe pas sans catastrophe et la catastrophe constitue donc implicitement le point de départ. (b) Roue tel qu'il faut qu'elle soit conçue en partant de la prévention, ceci a été récemment partiellement amélioré dans la dernière version (OFPP 2013).

422 M. Jaboyedoff, M. Charrière, M.-H. Derron, P. Nicolet & K. Sudmeier-Rieux

Le problème de la gestion des risques et de la responsabilité

Du côté des scientifiques en général, il existe un problème: la communauté scientifique ne peut pas clamer qu'elle a besoin de fonds pour la recherche sur les risques naturels et le jour où il faut se prononcer, que ses membres refusent de prendre des responsabilités. Car il est vraisemblable que dans un futur pas si lointain, la société n'accepte plus de financer des recherches sans résultat ou sans impact direct pour la société. D'un autre côté, la tendance des sciences sociales est à mélanger les concepts avec des définitions vagues ou multiples des termes qui décrivent les risques. Ce n'est pas une bonne chose, car cela apporte de la confusion. Il est nécessaire d'analyser de façon détaillée les impacts sur la gestion des risques par des études sociales, et il en existe de nombreuses qui éclairent la représentation des risques de façon utile. Néanmoins, contrairement aux techniciens et à certains scientifiques, les acteurs venant des sciences sociales ne prennent pas de responsabilité, au sens où les personnes qui sont censées connaître les risques naturels, et en particulier l'aléa, risquent la prison, comme c'est le cas en Italie.

Mais est-ce si difficile de prendre ses responsabilités? Les erreurs ne doivent pas être niées, mais au contraire enrichir la connaissance, afin de mieux se préparer aux prochains événements. Notons que tant les avalanches meurtrières d'Evolène de 1999, qui ont provoqué la condamnation d'un responsable guide de montagne et du président de la commune à la prison pour négligence (COMMUNIQUÉ DE PRESSE VS 2006), que l'éboulement de Gurtellen ont eu pour conséquence de modifier les approches et d'amener à une prise de conscience des manquements dans la gestion des risques. Il en ira de même pour la gestion des risques en Italie. La récente conférence de l'European Geosciences Union 2013 (session: Geoethics and natural hazards: the role and responsibility of the geoscientists; meetingorganizer. copernicus.org/EGU2013/orals/11853) a montré que le monde scientifique commence à s'en préoccuper.

Prendre ses responsabilités de façon transparente, c'est s'en dégager, car le fait de devoir prendre ses responsabilités, c'est se dégager des contingences et de s'en tenir à juger la situation à risque et non pas de tenir compte d'autres contingences de types politiciennes par exemple. Mais rappelons que la connaissance des systèmes est nécessaire à de bonnes décisions, mais celles-ci ne peuvent pas s'appliquer si la plupart des acteurs ne l'acceptent pas. En ce sens, la compréhension de la société et de ses acteurs est importante, le scientifique ou technicien non sociable ne peut pas gérer des risques. Souvent, les experts, pour se dégager des responsabilités, invoquent l'erreur humaine ou l'oubli, ce qui n'est pas sérieux dans le cadre d'une analyse de risque, où il est impératif d'essayer d'envisager toutes les possibilités. Dans le même ordre d'idées, la question de l'estimation des fréquences et périodes de retour des événements extrêmes reste ouverte, et il semble que nous sous-estimions souvent son impact. Il s'agit de toujours garder à l'esprit ce point.

Compte tenu des décisions à prendre, la gestion des risques est un problème qui dépend en grande partie du monde politique, l'aspect participatif pouvant en faire partie. Mais l'essentiel est que quelqu'un prenne des responsabilités, et ce ne peut être qu'en connaissance de cause. Mais le paradoxe et la difficulté sont que les décisions en matière de risque ne doivent pas être influencées par des attitudes politiciennes. Ainsi, tant les sciences naturelles qu'humaines doivent prendre leurs parts de responsabilités dans une société qui

se transforme rapidement et qui a besoin d'être étudiée. C'est là où les responsabilités sont les plus grandes qu'il faut essayer d'agir le plus rapidement.

Finalement, ce qui doit guider une bonne gestion signifie que les moins mauvaises solutions devraient être choisies, mais ceci ne peut pas se réaliser sans confiance entre les acteurs. D'un autre côté, si les connaissances ne sont pas suffisantes dans certains cas, il faut trouver des solutions pour palier à ces manques et ne pas hésiter à dire «non» si trop d'incertitudes subsistent.

REMERCIEMENTS

Cet article a été possible avec le support du projet européen Marie Curie CHANGES (FP7/2007-2013 under Grant Agreement No. 263953), qui finance les travaux de M. Charrière et de l'unité dangers naturels de l'état de Vaud, qui finance ceux de P. Nicolet.

REFERENCES

- 20 MINUTES, 2012. La voie du Gothard fermée jusqu'à lundi, <http://www.20min.ch/ro/lecteurreporter/story/25743642>. Consulté le 6.4.2013.
- 24HEURES, 2013. Un train voyageur déraile entre Palézieux et Payerne. <http://www.24heures.ch/vaud-regions/nord-vaudois-broye/Un-train-voyageur-deraille-entre-Palezieux-et-Payerne-/story/28880317>. Consulté le 6.4.2013.
- ACTON J.M. & HIBBS M., 2012. Why Fukushima was preventable. Carnegie Endowment for International Peace. 40 pp.
- AFP, 2011a. Xynthia: le maire de La Faut-Sur-Mer mis en examen. Paris, 15 avril 2011
- AFP, 2011b. Xynthia: graffitis et insultes contre les victimes à La Faut-Sur-Mer. Paris, 17 avril 2011
- AGNÈS Y., 2002. Manuel de journalisme. Paris: La découverte. 473 p.
- ALE, B. 2009. Risk: an introduction: the concepts of risk, danger and chance. Routledge, Taylor and Francis group, 134 p.
- ALEXOPOULOS E.C., KAVADI Z., BAKOYANNIS G. & PAPANTONOPOULOS S., 2009. Subjective Risk Assessment and Perception in the Greek and English Bakery Industries. *J. of Env. and Public Health*, Article ID 891754, 8 p. doi:10.1155/2009/891754
- ALLENBY B. & FINK J., 2005. Toward inherently secure and resilient societies. *Science* 309: 1034-1036.
- ANCEY C., 2012. Are there "dragon-king" events (i.e., genuine outliers) among extreme avalanches? *J. Phys Spec. Topics* 205: 117-129.
- ATS 2006. Fermeture du Gothard: le géologue cantonal valaisan s'étonne. Berne, 6 juin 2006
- BARDOU E. & JABOYEDOFF M., 2008. Debris Flows as a Factor of Hillslope Evolution controlled by a Continuous or a Pulse Process? In: GALLAGHER K., JONES S. J. & WAINWRIGHT J. (Eds.) Landscape Evolution: Denudation, Climate and Tectonics over Different Time and Space Scales. *Geol. Soc. London Spec. Publ.*: 63-78.
- BAUM R. L. & GODT J. W., 2010. Early warning of rainfall-induced shallow landslides and debris flows in the USA. *Landslides* 7: 259-272. DOI 10.1007/s10346.
- BERTRAND A. & MULLET E., 2006. La perception de la gravité des risques liés à la production et l'utilisation d'énergie. In: KOUABENAN D. R., CADET B., HERMAND D. & MUNOZ SASTRE M. T. (Eds.) Psychologie du risque. De Boeck. 167-184.
- BEZZOLA G.R. & HEGG C., 2007. Ereignisanalyse Hochwasser 2005: Teil1: Prozesse, Schädenunderste Einordnungen, Bern & Birmensdorf: Bundesamt für Umwelt & WSL. 252 p.
- BLIKRA L.H., 2008. The Åknes rockslide; monitoring, threshold values and early-warning. In: CHEN Z., ZHANG J, LI Z, WU F, HO K. (Eds.) Landslides and Engineered Slopes, From Past to Future. Proceedings of the 10th International Symposium on Landslides. Taylor and Francis Group. 1089-1094.

424 M. Jaboyedoff, M. Charrière, M.-H. Derron, P. Nicolet & K. Sudmeier-Rieux

- BRUNEAU M., CHANG S. E., EGUCHI R. T., LEE G. C., O'ROURKE T. D., REINHORN A. M., SHINOZUKA M., TIERNEY K., WALLACE W. A. & VON WINTERFELDT D., 2003. A framework to quantitatively assess and enhance the seismic resilience of communities. *Earthquake Spectra*, 19(4), 733-752.
- BRÜNDL M. (Ed.), 2009. Guide du concept de risque. Plate-forme nationale «Dangers naturels» PLANAT, Berne. 416 p.
- CAJOS J., TROCME MAILLARD M., HUBER M., ARNOLD P., VOLLMER U., SANDRI A., RAETZO H., DORREN L., EGLI T., EBERLI J., KNUCHEL R., KIENHOLZ H., DONZEL M., UTELLI H.-H. & PERREN B., 2009. Concept de risque pour les dangers naturels sur les routes nationales: Méthodologie basée sur les risques pour l'évaluation, la prévention et la maîtrise des dangers naturels gravitationnels sur les routes nationales. Confédération suisse, DETEC, OFROU, 89 001, édition V1.31.
- CHÈVRE N., COUTU S., MARGOT J., WYNN H. K., BADER H.-P., SCHEIDEGGER R. & ROSSI L., 2013. Substance flow analysis as a tool for mitigating the impact of pharmaceuticals on the aquatic system. *Water Research* 47: 2995-3005. 10.1016/j.watres.2013.03.004.
- CHOFFET M. In prep. Les coûts des dommages éléments naturels aux bâtiments et l'influence des facteurs du risque dans un contexte d'assurance immobilière. Thèse de l'Université de Lausanne, 213 p.
- COMMUNIQUÉ DE PRESSE VS, 2006. Avalanches d'Evolène: Le Tribunal cantonal confirme la condamnation d'André Georges et de Pierre-Henri Pralong. http://www.vs.ch/Press/DS_8/INFO-2006-01-17-16428/fr/Avalanches%20Evol%3%A8ne_F-D.pdf. Consulté le 18.04.2013.
- COUGHLIN T. & GROCHOWSKI E., 2012. Hard disk drive capital equipment market & technology report. Coughlin associates San Jose, California.
- DAUPHINÉ A., 2001. Risques et catastrophes. Armand Colin. 288 p.
- DORREN L.K.A., SANDRI A., RAETZO H. & ARNOLD P., 2009. Landslide risk mapping for the entire Swiss national road network. In: MALET J.-P., REMAÎTRE A., BOGAARD T. (Eds.) Landslide processes: from geomorphologic mapping to landslide modelling, Proceedings of the Conference, Strasbourg, 6-7 February 2009, CERG Editions: 277-281.
- EGLI T., 2005. Protection des objets contre les dangers naturels gravitationnels. Association des établissements cantonaux d'assurance incendie (AEIA). 109 p.
- EINSTEIN H. H., 1988. Special lecture: Landslide risk assessment procedure. In: BONNARD C. (Ed.) Proceedings of the 5th International Symposium on Landslides, Lausanne, Switzerland 2: 1075-1090
- ENDERS J., 2001. Measuring community awareness and preparedness for emergencies. *Australian Journal of Emergency Management* 16(3): 52-58.
- ERATH A., BIRDSALL J., AXHAUSEN K. & HAJDIN R. 2009. Vulnerability assessment methodology for Swiss road network. *Transportation Research Record: Journal of the Transportation Research Board* 2137: 118-126.
- ESPINER S. R., 1999. The use and effect of hazards warning signs – Managing visitor safety at Franz Josef and Fox Glaciers. *Science for Conservation*: 108.
- FELL R., HO K. K. S., LACASSE S. & LEROI E., 2005. A framework for landslide risk assessment and management. In: HUNGR O., FELL R., COUTURE R. & EBERHARDT E. (Eds.) Landslide Risk Management, Taylor & Francis Group, London. 3-26.
- FREWER L., 2004. The public and effective risk communication. *Toxicology letters* 149(1): 391-397.
- FILATOVA T., PARKER D.C., & VAN DER VEE A., 2011. The Implications of Skewed Risk Perception for a Dutch Coastal Land Market: Insights from an Agent-Based Computational Economics Model. *Agricultural and Resource Economics Review* 40: 405-423.
- FINUCANE M. L., ALHAKAMI A., SLOVIC P. & JOHNSON, S. M., 2000. The affect heuristic in judgments of risks and benefits. *Journal of Behavioral Decision Making* 13: 1-17.
- FROESE C., MORENO F., JABOYEDOFF M., HUMAIR F. & PEDRAZZINI A., 2012. Early-warning systems and instability modeling: the example of Turtle Mountain (Alberta, Canada). In: PICARELLI L., GRECO R. & URCIUOLI G. (Eds.) IWL 2011 Large slow active movements and risk management. 89-95.
- FROESE C.R. & MORENO F., 2011. Structure and components for the emergency response and warning system on Turtle Mountain. *Natural Hazards*, doi: 10.1007/s11069-011-9714-y.
- FUCHS S., ORNETSMULLER C. & TOTSCHNIGO R., 2012. Spatial scan statistics in vulnerability assessment: an application to mountain hazards. *Natural Hazards* 64: 2129-2151.
- GEVER, 2009. Guide GEVER à l'attention des dirigeants. Archives fédérales suisses – Département Fédéral de l'Intérieur, 18 p.

- GILLET J. E., 1985. Rapid ranking of hazards. *Process Engineering*, 19-22.
- GOVERNEMENTS DU QUÉBEC, 2004. Commission d'enquête sur l'effondrement d'une partie du viaduc de la Concorde. Rapport, 201 p.
- HALLEGATE S. & DUMAS P., 2012. Adaptation et risques: usages et limites de l'analyse coût-bénéfice. In: PRZYLUKSKI V. & HALLEGATE S. (Eds.) *Gestion des risques naturels*. Ed. Quae. 264 p.
- HAIMES Y. Y., 2009. On the complex definition of Risk: A system-based approach. *Risk Analysis* 29: 1647-1654.
- HALL S., 2011. Scientists on trial: At fault? *Nature* 477: 264-269.
- HEINIMANN H. R. & BORTER P., 1999. Risikoanalyse bei gravitativen Naturgefahren: Fallbeispiele und Daten. Bundesamt für Umwelt, Wald und Landschaft (BUWAL) 107/II
- HEINIMANN H. R., BORTER P., BART R., EGLI T. & GÄCHTER M., 1999. Risikoanalyse bei gravitativen Naturgefahren: Methode. Bundesamt für Umwelt, Wald und Landschaft (BUWAL) 107/I
- HILKER N., ALLER D. & HEGG C., 2007. Schäden. In: BEZZOLA G. R. & HEGG C. (Eds.) *Ereignisanalyse Hochwasser 2005 : Teil 1 -- Prozesse, Schäden und erste Einordnung*. Bundesamt für Umwelt BAFU, Eidg. Forschungsanstalt WSL. 127-148.
- HOMELAND SECURE IT, 2013. Visualization of Hard Drive Price Inflation Due to Thailand's Flood Induced Shortage. www.homelandsecureit.com/blog/2011/11/visualization-of-hard-drive-price-inflation-due-to-thailands-flood-induced-shortage. Visité le 15.04.2013.
- HÖPPNER C., BUCHECKER M. & BRÜNDL M., 2010. Risk communication and natural hazards. *CapHaz project*. Birmensdorf, Switzerland.
- IBREKK H. & MORGAN M.G., 1987. Graphical communication of uncertain quantities to nontechnical people. *Risk Analysis* 7: 519-529.
- IGARASHI G., SAEKI S., TAKAHATA N., SUMIKAWA K., TASAKA S., SASAKI Y., TAKAHASHI M., & SANO Y., 1995. Ground-water radon anomaly before the Kobe earthquake in Japan. *Science* 640: 60-61.
- INFOWORLD, 2011. The impending hard drive shortage - and possible price hikes. <http://www.infoworld.com/t/hard-drives/the-impending-hard-drive-shortage-and-possible-price-hikes-176453>. Consulté le 18.04.2013.
- IPCC. 2012. Managing the Risks of Extreme Events and Disasters to Advance Climate Change Adaptation. A Special Report of Working Groups I and II of the Intergovernmental Panel on Climate Change. FIELD C. B., BARROS V., STOCKER T. F., QIN D., DOKKEN D. J., EBI K. L., MASTRANDREA M. D., MACH K. J., PLATTNER G.-K., ALLEN S. K., TIGNOR M. & MIDGLEY P. M. (Eds.) , 582 p. Cambridge, UK, and New York, NY, USA.
- JABOYEDOFF M., DUDT J. P. & LABIOUSE V., 2005. An attempt to refine rockfall hazard zoning based on the kinetic energy, frequency and fragmentation degree. *Natural Hazards and Earth System Sciences* 5: 621-632.
- JABOYEDOFF M. & BONNARD CH., 2008. Report on landslide impacts and practices in Switzerland: need for new risk assessment strategies. In: Ho K. & Li V. (Eds.) *Proc. International Forum on Landslide Disaster Management*, 10 - 12 December 2007, Hong Kong, 79-97.
- JAKOB M., OWEN T. & SIMPSON T., 2011. A regional real-time debris-flow warning system for the District of North Vancouver, Canada. *Landslides*, doi:10.1007/s10346-011-0282-8.
- JAKOB M., STEIN D. & ULMI M., 2012. Vulnerability of buildings to debris flow impact. *Nat Hazards*, 60, 241-261. DOI 10.1007/s11069-011-0007-2
- JASANOFF S., 1997. The Political Science of Risk Perception. *Reliability Engineering and System Safety* 59: 91-99.
- JEANRENAUD C., PRIEZ F., PELLEGRINI S., CHEVROU-SÉVERAC H., VITALE S., MONNIN P., 2003. Le coût social de l'abus d'alcool en Suisse , IRER, Université de Neuchâtel, 266 p.
- JOHNSON N.L., KOTZ S. & BALAKRISHNAN N., 1995. Continuous univariate distributions Vol. 1 & 2, 2nd Ed. John Wiley, New York.
- JORDI B., 2006. Gestion des risques: Agir en connaissance de cause. *Environnement* 2/2006: 6-10.
- KOMORI D., NAKAMURA S., KIGUCHI M., NISHIJIMA A., YAMAZAKI D., SUZUKI S., KAWASAKI A., OKI K. & OKI T., 2012. Characteristics of the 2011 Chao Phraya River flood in Central Thailand. *Hydrological Research Letters* 6, 41-46.
- KELLER C., SIEGRIST M. & GUTSCHER H., 2006. The role of the affect and availability heuristics in risk communication. *Risk Analysis* 26: 631-639.
- KHATER M. & KUZAK D. E., 2002. Natural Catastrophe Loss Modelling. In: LANE M. (Ed.) *Alternative Risk Strategies*. RISK Books, London, 271 - 299.

- KOUABENAN D. R., 2006. Des facteurs structurants aux biais ou illusions dans la perception des risques. In: KOUABENAN D. R., CADET B., HERMAND D., MUNOZ SASTRE M. T.: *Psychologie du risque*. De Boeck. 125-145.
- KRÖGER W., 2013. Linked Activities Future Resilient Systems (FRS) - Evolving 2nd Program of the Singapore-ETH Center. 1st Dialogue Event, ETH Zurich, 18 January 2013.
- KUO T., FAN K., KUOCHEN H., HAN Y., CHU H., & LEE Y., 2006. 667 Anomalous decrease in groundwater radon before the Taiwan M6.8 Chengkung earthquake. *Journal of Environmental Radioactivity* 88: 101-106.
- LA LIBERTÉ, 2012. Trains remplacés par des bus entre Moudon et Ecublens-Rue, <http://www.laliberte.ch/node/383159>. Consulté le 18.04.2013.
- LACASSE S., EIDSVIK U., NADIM F., HØEG K. & BLIKRA L.H., 2008. Event Tree analysis of Åknes rock slide hazard. IV Geohazards Québec, 4th Canadian Conf. on Geohazards. 551-557.
- LADNER F., ROVINA H., POINTNER E., DRÄYER B., SAMBETH U., 2004. Ein angekündigter Felssturz. Geologische Überwachung und Instrumentierung des Felssturzes "Medji" bei St.Niklaus (Wallis). *Tec21* 130: 10-14.
- LAMUNIERE I., 2006. Habiter la menace. Presse polytechnique romande, 94 p.
- LATELTIN O., 1997. Prise en compte des dangers dus aux mouvements de terrain dans le cadre des activités de l'aménagement du territoire, Recommandations, OFEFP, 42 p.
- LASKA S., 2004. What if Hurricane Ivan Had Not Missed New Orleans? *Natural Hazards Observer*, November 2004, XXIX. <http://www.colorado.edu/hazards/o/archives/2004/nov04/nov04c.html>
- LE MATIN DIMANCHE, 2013. La sous-traitance menace la sécurité des trains. 24 mars 2013.
- LEE E. M. & JONES D. K. C., 2004. Landslide risk assessment. Thomas Telford, London. 454 p.
- LEISS W., 2004. Effective risk communication practice. *Toxicology Letters* 149(1): 399-404.
- LEROI E., CHOFFET M., MAYIS A., BIANCHI R., JABOYEDOFF M., KÖLZ E. & LATELTIN O., 2013. Outil d'analyse de la vulnérabilité du bâti aux inondations et de réduction du risque. In: NICOLET P., DERRON M.-H. & JABOYEDOFF M. (Eds.), 2013. Les dangers naturels en Suisse: pratiques et développements. Comptes rendus de la deuxième Journée de Rencontre sur les Dangers Naturels (Université de Lausanne, 18 février 2011). *Mémoire de la Société vaudoise de Sciences naturelles* 25: 127-135.
- LEROI E., BONNARD CH., FELL R., MCINNES R. 2005. Risk assessment and management. In: HUNGR O., FELL R., COUTURE R. & EBERHARDT E. (Eds.) *Landslide Risk Management*, Taylor & Francis Group, London. 159-198.
- LINIGER M. & BIERI D., 2006: A2, Goththardautobahn, Felssturz Gurtellen vom 31 mai 2006, Beurteilung und Massnahmen. *Pub. Soc. Suisse Mécanique Sols Roches* 153: 81-86.
- LUNDGREN R. E., & MCMAKIN A. H., 2009. Risk communication: A handbook for communicating environmental, safety, and health risks. Wiley-IEEE Press.
- MALAMUD B. D. & TURCOTTE D. L., 1999. Self-organized criticality applied to natural hazards. *Natural Hazards* 20: 93-116.
- MARZOCCHI W., GARCIA-ARISTIZABAL A., GASPARINI P., MASTELLONE M. & Di RUOCCO A. 2012. Basic principles of multi-risk assessment: a case study in Italy. *Natural Hazards* 62: 551-573.
- MAVROULI O. & COROMINAS J., 2010. Rockfall vulnerability assessment for reinforced concrete buildings. *Natural Hazards and Earth System Sciences* 10, 2055-2066.
- MERZ B., THIEKEN A. H. & GOCHT M., 2007. Flood risk mapping at the local scale: Concepts and challenges. In: BEGUIM S., STIVE M., HALL J. W. (Eds.) *Flood Risk Management in Europe: Innovation in Policy and Practice*, Springer, 231-251.
- MICHEL-KERJAN E., HOCHRAINER-STIGLER S., KUNREUTHER H., LINNEROTH-BAYER J., MECHLER R., MUIR-WOOD R., RANGER N., VAZIRI P. & YOUNG M., 2012. Catastrophe Risk Models for Evaluating Disaster Risk Reduction Investments in Developing Countries. *Risk Analysis*. DOI: 10.1111/j.1539-6924.2012.01928.x
- MICHOUD C., JABOYEDOFF M., DERRON M.-H., NADIM F. & LEROI E., 2011: Classification of landslide-inducing anthropogenic activities. 5th Canadian Conference on Geotechnique and Natural Hazards – GEOHAZARDS 2011, Kelowna, Canada, 10 p.
- NICOLET P., JABOYEDOFF M., GERBER C. & GIORGIS D., 2011. Des cartes de dangers plus informatives. *Geosciences ACTUEL* 2/2011: 21-24.
- NOSENGO N., 2012. Italian court finds seismologists guilty of manslaughter: Six scientists and one official face six years in prison over L'Aquila earthquake. *Nature News*. 23 October 2012. <http://www.nature.com/news/italian-court-finds-seismologists-guilty-of-manslaughter-1.11640>.

- OECD, 2002. OECD Guidance Document on Risk Communication for Chemicals Risk Management.
- OFPP, 2010. KATAPLAN.- Analyse et prévention des dangers à l'échelon cantonal. Factsheet, Office fédéral de la protection de la population, 4 p.
- OFPP, 2013. Aide-mémoire KATAPLAN.- Analyse et prévention des dangers et préparation aux situations d'urgence. Office fédéral de la protection de la population, 55p.
- OFQC, 1994. Réfection des ouvrages en béton. Office fédéral des questions conjoncturelles, Berne. 137 p.
- OFS, 2002. Environnement Suisse: statistique et analyse. Office fédérale de la statistique. 322p.
- PERETTI-WATEL P., 2000. Sociologie du risqué. Armand Colin. 286 p.
- PFISTER C., 2002. Le Jour d'après. Surmonter les catastrophes naturelles: le cas de la Suisse entre 1500 – 2000. Paul Haupt, Bern. 263 p.
- PLANT 2013. Le cycle de gestion intégrée des risques. www.planat.ch/fr/specialistes/gestion-des-risques, visité le 27.02.2013.
- POINTER E., 2006. Seuils d'alarme : Eboulement de Meidji (commune de Saint-Nicolas, Valais): surveillance géodésique et détermination des seuils d'alerte. In: INTERREG III A - Projet n°179 – RiskYdrogé; Actes de la Conférence finale – 24-26 oct. 2006. <http://www.risknat.org/projets/riskydrogeo/docs/conference/actes/a3.3.1-Pointer.pdf>
- QUAN LUNA B., BLAHUT J., VAN WESTEN C. J., STERLACCHINI S., VAN ASCH T. W. J., & AKBAS S. O., 2011. The application of numerical debris flow modeling for the generation of physical vulnerability curves. *Natural Hazards and Earth System Sciences* 11: 2047– 2060.
- RIDET P., 2012. Séisme de L'Aquila : prison ferme pour les experts. *Le Monde* 23.10.2012
- ROSE A., 2007. Economic resilience to natural and man-made disasters: multidisciplinary origins and contextual dimensions. *Environmental Hazards* 7: 383-398.
- SAZEAU T., 2011 Réinventer la culture du risque. In: MERCIER D. & ACERRA M. (Eds.) Xynthia: une tragédie prévisible. Place Publique. 45-50.
- SCHÄR C., VIDALE P. L., LÜTHI D., FREI C., HÄBERLI C., LINIGER M. A. & APPENZELLER C. 2004. The role of increasing temperature variability in European summer heatwaves. *Nature*, 427(6972): 332-336.
- SHORT J. F., 1984. The Social Fabric at Risk: Toward the Social Transformation of Risk Analysis. *American Sociological Review* 49/6: 711-725.
- SLOVIC P., 1987. Perception of Risk. *Science* 236(4799): 280-285
- SLOVIC P. & PETERS E., 2006. Risk Perception and Affect. *Current Directions in Psychological Science*: 322-325.
- SORNETTE D. & OUILLOIN G., 2012. Dragon-kings: mechanisms, statistical methods and empirical evidence. *The European Physical Journal Special Topics* 205: 1-26.
- SORNETTE D., 2006. Critical Phenomena in Natural Sciences, 2nd ed., Springer, 528 p.
- SUDMEIER-RIEUX K., 2011. On landslide risk, resilience and vulnerability of mountain communities in Central-Eastern Nepal., Thèse de l'Université de Lausanne, 312 p.
- SWISSINFO, 2006. Au Gothard, la route des vacances est rouverte. http://www.swissinfo.ch/fre/actualite/Au_Gothard_la_route_des_vacances_est_rouverte.html?cid=5293400. Consulté le 19.04.2013
- SWISSINFO, 2011. Swiss to phase out nuclear power by 2034. www.swissinfo.ch/eng/politics/internal_affairs/Swiss_to_phase_out_nuclear_power_by_2034.html?cid=30315730. Consulté le 18.04.2013.
- SWISSINFO, 2013. Feu vert au maintien de l'exploitation de la centrale de Mühleberg. www.swissinfo.ch/fre/nouvelles_agence/international/Feu_vert_au_maintien_de_l'exploitation_de_la_centrale_de_Muehleberg.html?cid=35345960, Consulté le 18.04.2013.
- SWISSRE, 2006. Natural catastrophes and man-made disasters 2005: high earthquake casualties, new dimension in windstorm losses. *SIGMA* 2/2006, 38 p.
- UNISDR, 2009. Terminology on Disaster Risk Reduction. Geneva: UNISDR. 30 p.
- UNISDR, 2011. Global Assessment Report. 178. Geneva: United Nations International Strategy for Disaster Reduction.
- VALLEY B., THURO K., EBERHARDT E. & RAETZO H., 2004. Geological and geotechnical investigation of a shallow translational slide along a weathered rock/soil contact for the purpose of model development and hazard assessment. In: LACERDA W. A., EHRLICH M., FONTOURA S. A. B. & SAYO A. S. F. (Eds.) IX International Symposium on Landslides. Vol. 1. A.A. Balkema, pp. 385-391.

428 M. Jaboyedoff, M. Charrière, M.-H. Derron, P. Nicolet & K. Sudmeier-Rieux

- VAN ALPHEN J., MARTINI F., LOAT R., SLOMP R. & PASSCHIER R., 2009. Flood risk mapping in Europe, experiences and best practices. *Journal of Flood Risk Management* 2: 285-292.
- VAN WESTEN C., VAN ASCH T. & SOETERS R., 2006. Landslide hazard and risk zonation—why is it still so difficult? *Bulletin of Engineering geology and the Environment* 65: 167-184, <http://dx.doi.org/10.1035/1007/s10064-005-0023-0>.
- VAUGHAN E., 1995. The significance of socioeconomic and ethnic diversity for the risk communication process. *Risk Analysis* 15(2): 169-180.
- VENTSEL H., 1987. Théorie des probabilités. MIR, Moscou. 584p.
- VINET F., DEFOSSÉZ S. & LECLERE J.-R., 2011. Comment se construit une catastrophe. In: MERCIER D. & ACERRA M. (Eds.) Xynthia: une tragédie prévisible. Place Publique. 45-50.
- VOUMARD J., 2012. Simulation dynamique du trafic routier pour l'estimation du risque sur les routes de montagne: Application à l'analyse du risque sur la route Aigle – Col du Pillon (VD). Mémoire de Master CRET-UNIL, 252 p.
- WÄHLBERG A. E. & SJÖBERG L., 2000. Risk perception and the media. *Journal of Risk Research* 3, 31-50.
- WIKIPEDIA, 2013. Hard disk drive. http://en.wikipedia.org/wiki/Hard_disk_drive#cite_note-AutoMK-101-109. Consulté le 18.4.2013.
- WNISR, 2009. The World Nuclear Industry Status Report 2009: With Particular Emphasis on Economic Issues. <http://www.worldnuclearreport.org/The-World-Nuclear-Industry-Status-52.html>, consulté le 18.04.2013.
- XIE X., WANG M. & XU L., 2003. What risks are Chinese People concerned about? *Risk Analysis* 23: 685-695.
- ZHA, 2013. Zurich Hazard Analysis: Methodology. www.zurich.com/riskengineering/global/services/strategic_risk_management/zha_services. Consulté le 18.4.2013.

Appendix D

Using the consequence - frequency matrix to reduce the risk: examples and teaching

Jaboyedoff, M., Derron, M.-H., Aye, Z. C., Nicolet, P., and Olyazadeh, R.: Using the consequence - frequency matrix to reduce the risk: examples and teaching, in: International Conference on the Analysis and Management of Changing Risk for Natural Hazards, 18–19 November 2014, Padua, Italy, CO1,http://www.changes-itn.eu/Portals/0/Content/2014/Final%20conference/abstracts/CO1_Abstract_Jaboyedoff_et_al.pdf, 2014.

Abstract code: CO1

Using the consequence - frequency matrix to reduce the risk: examples and teaching

M. Jaboyedoff¹, Z.C. Aye¹, M.-H. Derron¹, P. Nicolet¹ and R. Olyazadeh¹

¹Risk-group - ISTE - Institute of Earth Sciences - Faculté des géosciences et de l'environnement - University of Lausanne

Corresponding author details:

GEOPOLIS - 3793 - University of Lausanne - CH-1015 Lausanne – Switzerland; email: Michel.Jaboyedoff@unil.ch;

Keywords: Risk matrix, consequences, frequency.

Abstract:

Consequences-frequency matrices (CFM) are diagrams with consequence and frequency classes on the axes. They permit to classify risks based on expert knowledge with limited quantitative data. In this paper, we propose to introduce uncertainty using Bayesian approach, which allow obtaining exceedance curves for frequency, for consequences and for risk. An example of such an approach is given with the case of a landslide.

INTRODUCTION

Risk systems are often complex and do not allow to develop a full numerical approach, since many aspects are not fully quantifiable. “Risk filtering, ranking and management” methodologies have been developed since the nineties along with the NASA space shuttle program (Haimes, 2008). To rank the risky events and scenarios, these methods used the so called “risk matrix” displaying frequency (λ) or probability versus consequences (Co), divided in classes for each axis. This also permits to rank the risk ($R \propto \lambda \times Co$) in classes. Such approach had been developed earlier in industry production sector (Gillett, 1985). These Consequences-frequency matrices (CFM) are diagrams with consequence and frequency axes respectively, which are divided into classes. The CFM are often used and presented in text books (e.g. Ale, 2009) as a tool for assessing and comparing different situations for objects at risks. Nowadays, several approaches of decision making are inspired by these methods and are applied in many administrations including EU for health problem (ECDC, 2011). CFM is also used in evaluating risks related to corporate risk management (TBCS, 2011), commercial acquisitions (DOD, 2006), natural risks (OFPP, 2013) and in insurances (ZHA, 2013). This approach also permits to visualize the effects and consequences of risk reduction measures (Figure 1) and to give a framework to understand risk assessment, which is very useful for teaching.

These methods aim at providing solutions for encountered problems of a specific situation by answering to the questions (Haimes, 2008): *What can go wrong? What are their consequences and likelihood?* It follows several steps (Krause et al., 1995; Haimes, 2008):

1. Scope definitions: what are the problems?
2. Creation of a group of experts concerned by each level of the analysed risky system
3. Hazard identification, i.e. identification of potential events and their scenarios

4. Hazard filtering and ranking in several sub-stages which implies to establish frequency (probability) and impact classes and their corresponding limits (in loop with point 5)
5. Risk management, including the quantification of the potential risk reduction, which necessitate the understanding of causes and effects
6. Finalization of decision making process
7. Refinement of the process with the feedback

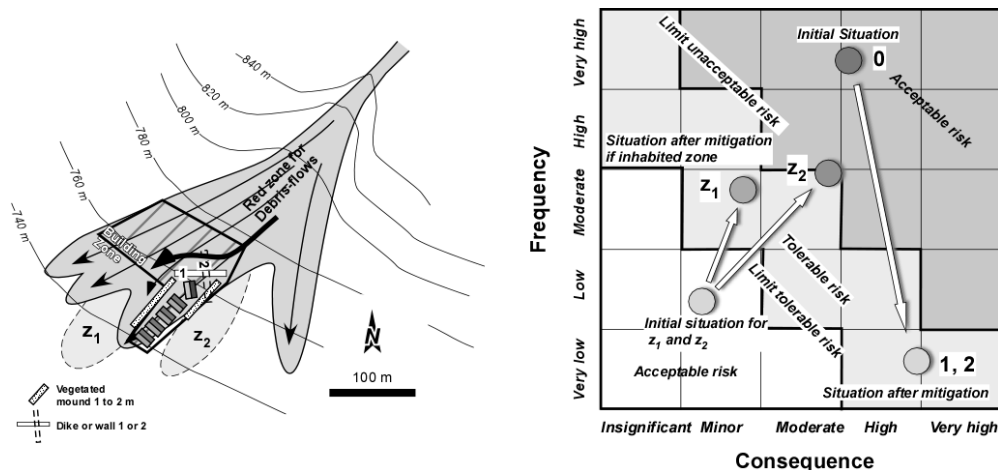


Figure 1: Example of potential building area in a high hazard area and illustration of the proposed solutions. CFM is used to represent the degree of risk. The scope of tolerable risk (light grey) is between the limits of tolerance and of acceptability (modified after Jaboyedoff et al., 2013).

However, these methods suffer from several weaknesses. First, the scales of risk level that are deduced from the CFM are often not consistent (Cox, 2008). For instance, if they are not well designed, a point at the corner of a class can belong to 3 different risk classes. Secondly, the uncertainties are often not assessed.

Some attempts have been performed to introduce uncertainty in the input data by using fuzzy logic for technical system (Krause et al., 1995): the classes are fuzzified by applying a membership function to the classes of frequencies and impacts.

In the present paper, we try to develop a method using CFM by developing the point 4 of the above mentioned list, with an example of landslide from the point 3 to 5. The basis of this method is to introduce Bayesian approach for the belonging classes, i.e. likelihood based on triangular distribution, using the prior probability given by experts. Then, the probabilities of an event to belong to a class of risk are calculated giving probability for each matrix element.

METHOD

The belonging to a class and its uncertainty

When experts give their opinions about the belonging to a class of events, which might for example be named “very low, low, medium, high, very high” and refers to the intensities, (or frequencies) and impacts (or consequences), uncertainties are involved. As it is proposed by the fuzzy logic framework (Zadeh, 1975), this is not unique and can also have a probability of belonging to other classes, which means that when an expert attributes an event to a class it implies also a “membership” to other neighbouring classes. Instead of using the fuzzy logic terminology as “membership”, it is preferred to use the likelihood $P(C_j|CE_i)$ of the attribution to a class CE_i by an expert to be distributed to neighbouring classes C_j .

The estimation of the uncertainty can be, for example, empirically decided by a group of experts, or an expert can give his definition of belonging to a class. This can be a way to introduce the uncertainty, but this not the one chosen here.

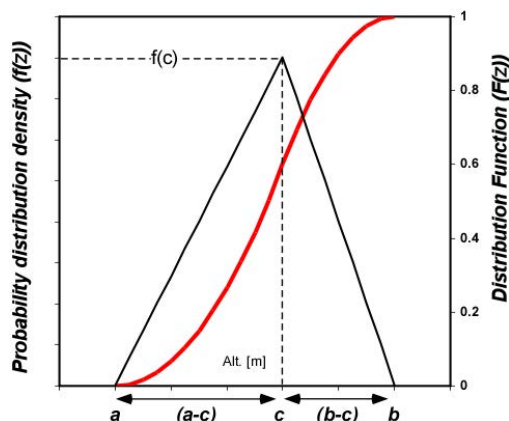


Figure 2: parameter defining triangular distributions.

Formally, if a class has a lower limit l_j and upper limit l_{j+1} and if the distribution of the weights from a class chosen by an expert CE_i to the others using a scale of value x is given by $f(x)dx$, then the likelihood or weight to belong effectively to the class C_j is given by:

$$P(C_j|CE_i) = \int_{l_j}^{l_{j+1}} f(x)dx \quad [1]$$

The function $f(x)$ can be of any type, and chosen in different ways by determining the variance, the mean, etc. Here, we will use the triangular distribution (Kotz and van Drop, 2004; Haimes, 2008) (Figure 2):

$$f(x) = \begin{cases} 0 & \text{for } x < a \\ \frac{2(x-a)}{(c-a)(b-a)} & \text{for } a \leq x \leq c \\ \frac{2(b-x)}{(b-c)(b-a)} & \text{for } c < x \leq b \\ 0 & \text{for } x > b \end{cases} \quad F(x) = \begin{cases} 0 & \text{for } x < a \\ \frac{(x-a)^2}{(c-a)(b-a)} & \text{for } a \leq x \leq c \\ 1 - \frac{(b-x)^2}{(b-c)(b-a)} & \text{for } c < x \leq b \\ 1 & \text{for } x > b \end{cases} \quad [2]$$

Where $F(x)$ is the repartition function of $f(x)$ ($F(x) = \int f(x)dx$), and the domain $[a, b]$ corresponds to non-zero $f(x)$ and c is the x value of the maximum of $f(x)$.

Classes definitions

The triangular density distribution is often used for expert knowledge (Vose, 2008). It presents the advantage to ask expert simple questions in order to define the distribution:

- What do you consider as the lower possible value (a) for an event (frequency, intensity, impacts, etc...), classified in the class C_j ?
- What do you consider as the upper possible value (b) for an event (frequency, intensity, damage, etc...), classified in the class C_j ?

Here, we will consider that the maximum of $f(x)$, i.e. $f(c)$ is located at the central value of the class considered by the expert as the most probable, but other choices can be used.

The expert assessment for a specific event

In the global procedure for all matrix approaches (Haimes, 2008), all the possible events (Ev) have to be listed. Each Ev corresponds to a process that can lead to different scenarios for consequence and frequency.

The class and their associated distribution definitions are independent of the events. An expert will have its own interpretation of a potential event Ev that leads to several scenarios

of impact and frequency independently. In that case, he must give, for each scenario, a weight to the corresponding class, i.e. for each class correspond a scenario (or more) for consequence corresponds, and this is also applicable for frequencies scenarios. Therefore, all couples of frequency or probability (p)/consequences (Co) related to an event Ev (p, Co) must be distributed following the potential scenarios. For instance, as proposed by Vengeon et al. (2001), the frequency can be set first by an array of probability – delay or more generally relative classes of probability. Then, the probability must be normalized to 1 and distributed among the respective belonging to the others classes, i.e. $P(CE_i)$ the expert weight distribution for one event (prior probability) (Figure 3a). This can be performed also for the impact. By following this logic, using the Bayesian theory, the probabilities $P(C_i)$ of a frequency or an impact in the class C_i are given by:

$$\begin{bmatrix} P(C_1|CE_1) & \dots & P(C_1|CE_n) \\ \vdots & \ddots & \vdots \\ P(C_n|CE_1) & \dots & P(C_n|CE_n) \end{bmatrix} \begin{bmatrix} P(CE_1) \\ \vdots \\ P(CE_n) \end{bmatrix} = \begin{bmatrix} P(C_1) \\ \vdots \\ P(C_n) \end{bmatrix} \quad [3]$$

By introducing values for the limits, it is then possible to provide exceedance curves for consequence or return period (Figure 3b).

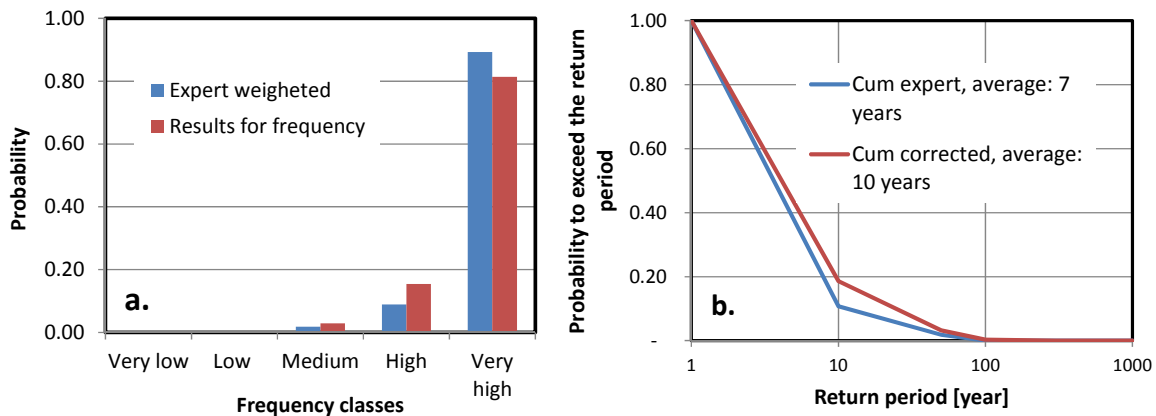


Figure 3: a. histogram of the probabilities $P(CE)$ (blue) and $P(E)$ (red). b. resulting curve of exceedance using the class limit (see in example for the limits).

The matrix

The different classes for probabilities and consequences can be multiplied to get a matrix of probability of each element (Figure 4), where each element of the risk matrix corresponds to a scenario of an event. This allows to obtain an exceedance curve of risk level that is attributed to each element. In the present case, we use the multiplication of the class value 1 to 5 with 5 being the highest.

As each element of the CFM possess a probability, using the scale of values for the class limits, the average risk can be calculated, as well as a curve of exceedance.

THE EXAMPLE OF A PARTICULAR UNSTABLE MASS OF PONT BOURQUIN LANDSLIDE

Landslide settings

Pont Bourquin Landslide (PBL) is located in the Swiss Prealps, close to Les Diablerets, Switzerland (Jaboyedoff et al., 2009). First evidences of recent gravitational deformation can be observed on aerial photos of the end of the Sixties. This activity gradually developed until 2004. The first large slope displacements happened in 2006, when movements up to 80 cm occurred on the head scarp. Subsequently, a mudflow reached the road just below the landslide on 5th of July 2007 and another flow destroyed the forest at the toe of the slide in

August 2010. For this second event, we were able to demonstrate the drop of surface shear wave seismic velocity at a depth of 9-11 m a few days before the collapse (Mainsant et al. 2012a). Afterwards, remedial works were carried out, including a trunk-framed box at the toe of the instability and gullies on the mass body to evacuate surface waters. However, the landslide body is still moving, with velocities similar to the former ones.

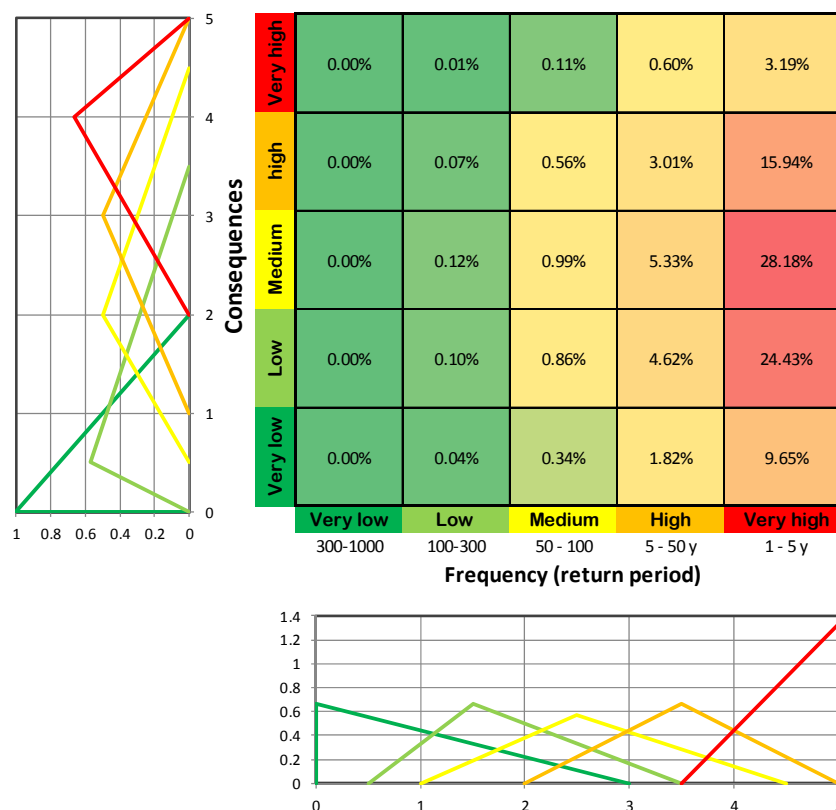


Figure 4: Example of matrix showing the proximity of each element of the matrix and the distribution function used to calculate the likelihood $P(C_j|CE_i)$ of both axes.

Nowadays, the landslide is still active and three zones are particularly threatening. In the present example, we will assess the risk for one of these potential source areas. It is an approximately 5000 m³ material that is detached on the north-eastern part of the landslide. The displacement is observable by visual inspection of the back scarp, sudden reactivation failure of this compartment and a fast propagation toward the road is expected. We will not mention a detailed description of the situation as it is not the goal of this paper. Therefore, we will simply present an example illustrating the general framework of the method.

The classes and scales

To create the limits of classes for the frequencies or return periods we use a modified version of the Swiss danger matrix (Lateltin, 1997): Very low (300-1000 years), Low (100-300 years), Medium (50-100 years), High (5-50 years) and Very high (1-5 years). A 1 year lower limit is used because a return period of zero would give an infinite frequency.

The classes of consequences have been designed depending on the considered scenario. We used 5 million CHF as the worst case scenario, which corresponds, according to the willingness-to-pay value generally used in Switzerland, to the death of one person (Figure 6). Each class is one order of magnitude different from its neighbours.

Setting the prior probabilities

Prior probabilities have been set using equation [1] and the triangular distributions shown in figure 4. For very low frequencies, looking at the likelihood function in figure 4 below the matrix, the error of attribution can be quite high towards the higher frequencies, while in a less extent, it is also the case for the very high frequencies towards the lower (Figure 4). For the intermediate classes, they are distributed nearly symmetrically over neighbouring classes.

The classes of consequences are defined by a decision tree as it is done in health disease prevention (ECDC, 2011). This starts by looking at if the landslide sudden reactivation failure will reach to the road or not, considering up to the possibility of killing one person in a vehicle. Please note that not all impacts have been taken into account here.



Figure 5: location of the unstable zone on the landslide and the national road that can be affected.

Results

First, we can see in figure 3 that the use of prior probability to correct expert assessment implies that the average return period changes from 7 to 10 years. The curve of exceedance shows that the corrected probability to exceed 10 years is around 20%, whereas it is 11% for the original value. Using the exceedance of the consequences, the values are more distributed for the corrected values than for the original one (Figure 7). This is clear from the average value of corrected costs (99'000.- CHF) which is double from the original one (41'000.- CHF). The probability to be above 500'000.- CHF for the corrected value is of 4% and zero for the non-corrected one.

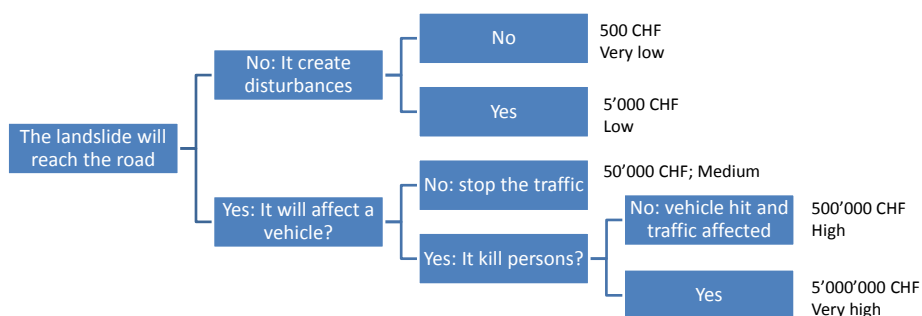


Figure 6: decision tree to deduce the consequences levels.

Now looking at the matrix results (Figure 4), we can extract the curve of exceedance for the risk level divided in five classes from 1 to 25 (5 × 5) in 5 equal classes (Figure 8). This clearly shows that there is 20% of chance to be in the very high risk class and less than 20% to be below medium risk. It is also possible to obtain the average risk, which is around 107'000 CHF/year.

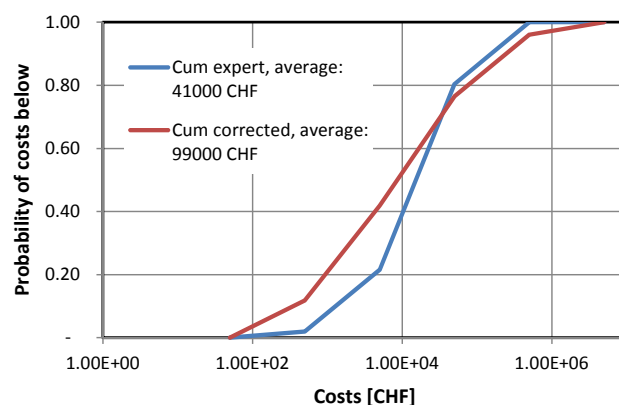


Figure 7: curve of exceedance using the limit of the classes for both corrected and uncorrected probabilities.

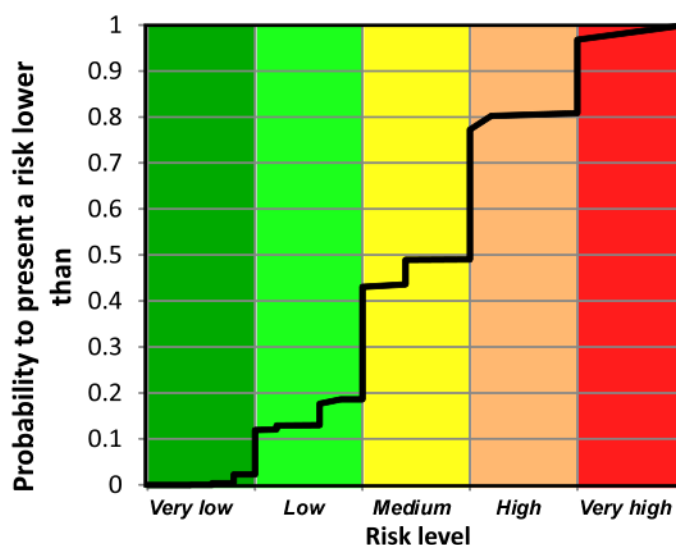


Figure 8: curve of exceedance for risk levels.

DISCUSSION AND CONCLUSION

The presented method is still in development; however, it already shows some interesting results. It allows to extend the domain of hazard and consequences that are often not considered by experts. In addition, it does not only give one result, but also gives exceedance curves. The fact that the experts must give two times their opinions, first for the likelihood, and second for the prior probability (weight for each class) is a way to introduce uncertainty, which is often lacking in the risk matrix approach. The use of Bayesian approach is also easier than fuzzy logic. Their results when compared to the results obtained from a more classical risk analysis have the same order of magnitude (Limousin, 2013), which give 278'000.- CHF / year for the 3 unstable masses. As a consequence, we think that this method must be tested on other sites. Nevertheless, there are several remaining problems:

- The discretization of the value by class which are not equal in width raises the problem of non-linearity and singular points at the limits. This has to be further explored, especially using function like power law or exponential.
- The way to calculate the risk and its distribution
- The extension of the classes to infinite and to zero is a problem. Until now, the sum of CFM probability matrix is equal to one, however, for instance, event with longer return period can be considered, but their weight has to be well assessed.

It is clear from the above results and figure 1 that this method provides also a good way to visualize the risk reduction, by changing the scenario and consequence weights, and it will keep the uncertainty which is not usually the case. In addition we experienced in courses that the use of risk matrix are a good way to promote collective work in a class and to address several different types of risks.

We think that the present method improves some of the weaknesses of the matrix approach, and which will give an excellent background for courses.

ACKNOWLEDGEMENT

The authors would like to thank all the members of risk team at ISTE, UNIL for their support and Prof. Kanevski who suggested us to use Bayesian approach. This research was funded by the European Commission within the Marie Curie Research and Training Network 'CHANGES: Changing Hydro-meteorological Risks as Analyzed by a New Generation of European Scientists' (2011-2014, Grant No. 263953) under 7th framework program.

REFERENCES

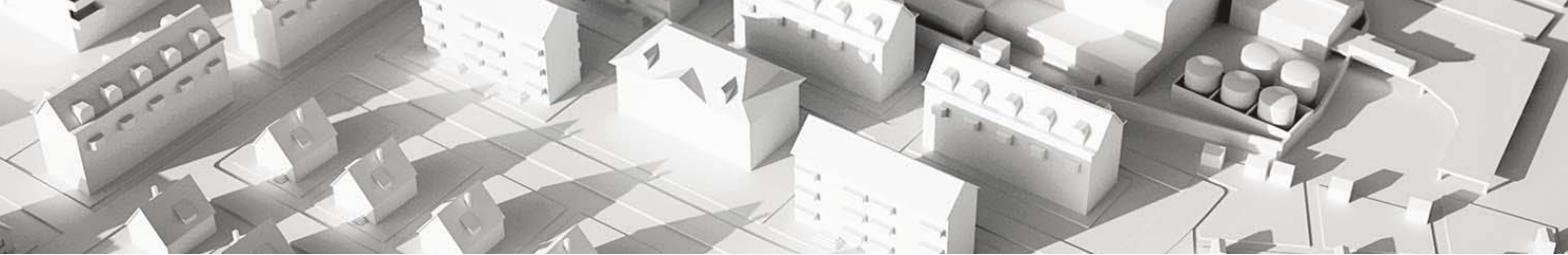
- Ale B. 2009, Risk: an introduction : the concepts of risk, danger and chance. Routledge, Taylor and Francis group, 134 p.
- Cox LA Jr. 2008, What's wrong with risk matrices? Risk Analysis, 28, 497–512.
- DOD, 2006, Risk management guide for DOD acquisition. Ed. 6th US Dept. of Defense. 34 p.
- ECDC, 2011, European centre for Disease Prevention and Control: Operational guidance on rapid risk assessment methodology. Stockholm, ECDC, 68p.
- Gillet J.E., 1985, 'Rapid Ranking of Process Hazard', *Process Engineering*, 66, 19-22.
- Haimes, Y.Y., 2009, 'Risk Modeling, Assessment, and Management'. 3rd Edition. John Wiley & Sons, 1009 p.
- Jaboyedoff M., Charrière M., Derron M.-H., Nicolet P. & Sudmeier-Rieux K. 2013, Postface: La gestion des risques naturels est une dynamique. Comptes rendus de la deuxième Journée de Rencontre sur les Dangers Naturels (Université de Lausanne, 18 février 2011). *Mém. Soc. vaud. Sc. nat.* 25, 393-428.
- Jaboyedoff M., Loye A., Oppikofer T., Pedrazzini A., Güell i Pons M. & Locat J. 2009, Earth-flow in a complex geological environment: the example of Pont Bourquin, Les

- Diablerets (Western Switzerland). In: Malet J.-P., Remaître A. and Bogaard T. (Eds): Landslide processes 131-137.
- Kotz S. & van Drop J.R. 2004, Beyond Beta: other continuous families of distributions with bounded support and applications. World Scientific, 289 p.
- Krause, J.-P. & R. Mock, Gheorghe A.D. 1995, Assessment of Risks from Technical Systems: Integrating Fuzzy Logic into the Zurich Hazard Analysis Method. in: *International Journal of Environment and Pollution* (IJEP) 5 (2-3), 278-296.
- Lateltin, O. 1997, Prise en compte des dangers dus aux mouvements de terrain dans le cadre des activités de l'aménagement du territoire. Recommandations, OFEFP, 42.
- Limousin P. 2013, De la caractérisation du sol, à l'étude de propagation et des risques induits : Les cas du glissement de Pont Bourquin. Univ. Lausanne Master Thesis, 100 p.
- Mainsant G., Larose E., Brönnimann C., Jongmans D., Michoud C. & Jaboyedoff M. 2012a, Ambient seismic noise monitoring of a clay landslide: toward failure prediction. *JGR-ES*, 117, F01030, 12 PP. doi:10.1029/2011JF002159
- OFPP, 2013, Aide-mémoire KATAPLAN.- Analyse et prévention des dangers et préparation aux situations d'urgence. Office fédéral de la protection de la population, 55p.
- Vengeon, J.M., Hantz, D., Dussauge, C. 2001, Prédicibilité des éboulements rocheux : approche probabiliste par combinaison d'études historiques et géomécaniques. *Revue Française de Géotechnique*, 95/96: 143-154.
- Vose, D. 2008. Risk Analysis: A Quantitative Guide, 3rd Edition. John Wiley & Sons, 752 p.
- Zadeh L.A. 1975, The Concept of a Linguistic Variable and Its Applications to approximate reasoning, Part I. *Information Sciences* 8: 199-249.
- ZHA 2013. Methodology Zurich Hazard Analysis. www.zurich.com/riskengineering/global/services/strategic_risk_management/zha_services, last access: 18.4.2013.

Appendix E

Hail 2011: Analysis of the 12–13 July 2011 hail event in the Canton of Aargau

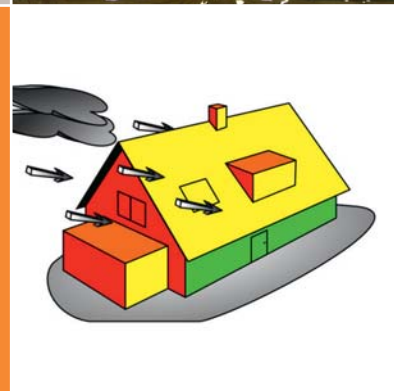
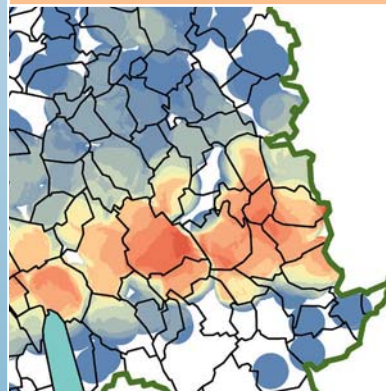
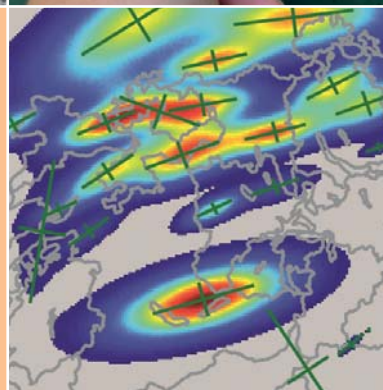
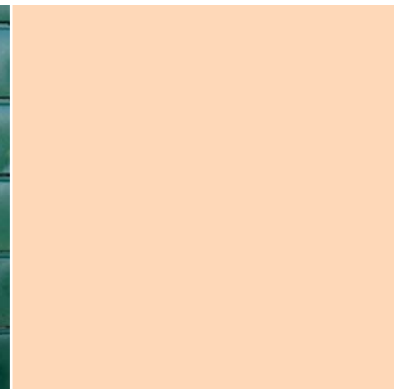
Imhof, M., Nicolet, P., Voumard, J., and Jaboyedoff, M.: Hail 2011: Analysis of the 12–13 July hail event in the Canton of Aargau, Event analysis, Intercantonal Reinsurance (IRV), http://irv.ch/getmedia/8007ce65-e40a-48d2-961f-0cd5c0d2f0c6/VKF_Brosch_Hagel_2011_DT_GzDb.pdf.aspx, (In German and French), 2015.



Analyse des événements

Grêle 2011

Étude de l'orage de grêle des 12 et 13 juillet 2011 dans le canton d'Argovie



Mentions légales

Éditeur

Tous droits réservés © 2015
Union intercantonale de réassurance UIR
Bundesgasse 20
CH-3001 Berne
www.uir.ch



Interkantonaler Rückversicherungsverband
Union intercantonale de réassurance

Auteurs

Markus Imhof, Union intercantonale de réassurance Berne (UIR)
Pierrick Nicolet, Institut des sciences de la Terre de l'université de Lausanne (ISTE)
Jérémy Voumard, Institut des sciences de la Terre de l'université de Lausanne (ISTE)
Michel Jaboyedoff, Institut des sciences de la Terre de l'université de Lausanne (ISTE)

Coordination

Markus Imhof, Union intercantonale de réassurance Berne (UIR)
Rolf Meier, Association des établissements cantonaux d'assurance incendie (AEAI)

Collaboration scientifique

Liliane Nguyen, Institut des sciences de la Terre de l'université de Lausanne (ISTE)
Martin Seiler, Union intercantonale de réassurance Berne (UIR)

Conseil technique

Martin Jordi, Association des établissements cantonaux d'assurance incendie (AEAI)
Armin Wittmer, Établissement cantonal d'assurance d'Argovie (AGV)

Traduction française

Carine Job, Union intercantonale de réassurance
Sarah Mettraux, Union intercantonale de réassurance

Réalisation et production

Rickli + Wyss, Berne

Tirage

500 exemplaires en allemand, 200 exemplaires en français

Sources de données ou d'informations

Établissement cantonal d'Argovie
Union intercantonale de réassurance
Office fédéral de topographie swisstopo
Office fédéral de météorologie et climatologie MétéoSuisse meteoradar GmbH: Willi Schmid
La Poste

Photos

Établissement cantonal d'assurance d'Argovie, Christine Oesch, Mühlethurnen BE

Illustrations de couverture

De gauche en haut à droite en bas :
Bâtiments ayant subi des dommages sur la toiture à Bremgarten AG
Bosses sur volet roulant
Modèle numérique grêle UNIL : cellules de grêle reproduites par des distributions gaussiennes
Toiture perforée en matière synthétique
Pourcentage des bâtiments endommagés par km² dans la partie orientale du canton d'Argovie
Éléments de l'enveloppe du bâtiment exposés aux impacts de grêle lorsque le vent souffle parallèlement au faîte du toit



Mentions légales	2
Table des matières	3
Résumé	4
1. Introduction	5
2. L'événement de grêle des 12 et 13 juillet 2011 dans le canton d'Argovie	5
2.1 Conditions météorologiques les 12 et 13 juillet 2011	5
2.2 Catégorisation statistique de l'événement	6
2.3 Distribution spatiale des dommages : analyse du parc immobilier touché	8
2.4 Observation des dommages suivant les communes	11
2.5 Coup d'œil sur les chiffres	14
3. Analyse des dommages par genre et fonction des éléments de construction	17
3.1 Catégories de dommages	17
3.2 Répartition des dommages par élément de construction touché	18
3.3 Analyse des dommages par matériau des éléments de construction	20
3.4 Coût moyen des dommages par élément de construction	20
3.5 Comparaison avec l'événement de mai 2009 dans le canton de Thurgovie	20
3.6 Les vingt bâtiments ayant les dommages les plus chers au m ²	23
3.7 Dommages en fonction de l'année de construction	25
4. Potentiel d'économie par l'utilisation d'éléments de construction avec un indice de résistance à la grêle RG 3	27
5. Analyse de la relation dommages – orientation du bâtiment	28
5.1 Introduction	28
5.2 Méthodologie	28
5.3 Résultats de l'analyse à l'échelle du canton	29
5.4 Résultats de l'analyse locale	33
5.5 Validation des orientations automatiques	39
5.6 Discussion des résultats	40
6. Estimation rapide des dommages après l'événement	42
6.1 Introduction	42
6.2 Dommages aux bâtiments suite aux deux importants événements de grêle de 2009	42
6.3 Dommages aux bâtiments suite à l'événement de grêle de 2011	44
6.4 Estimation rapide des dommages	46
7. Analyse du risque	49
7.1 Danger	49
7.2 Calcul du risque annuel moyen	51
7.3 Évolution ultérieure du risque	52
7.4 Simulation	52
8. Conclusions, résultats, perspectives	55
9. Remerciements	58
10. Bibliographie	59
Annexe A: Carte d'orientation indiquant l'emplacement des localités mentionnées dans le rapport	61
Annexe B: Code d'affectation AEAI	62



Résumé

Deux ans après les orages de grêle qui ont occasionné de graves dommages aux bâtiments de Suisse occidentale et dans le canton de Thurgovie (UIR, 2012 : voir Analyse des événements grêle 2009), un nouvel orage de grêle d'intensité semblable a traversé le Plateau suisse. L'événement a causé d'importants dommages en particulier dans les cantons d'Argovie et de Zurich. Les grêlons, dont le diamètre atteignait pour certains 6,5 cm (grosseur d'une balle de tennis), étaient accompagnés de rafales de vent et d'inondations localisées, en particulier à l'ouest du canton d'Argovie, près de Zofingue. En plus des dommages habituels dus à la grêle sur les toits, les façades, les stores et les fenêtres, des toits arrachés par la tempête et des caves inondées ont été signalés. Comme deux ans auparavant pour les établissements cantonaux d'assurance de Thurgovie et de Fribourg, cet événement s'est avéré être le sinistre éléments naturels le plus important jamais recensé pour l'établissement d'assurance d'Argovie. Contrairement à l'événement de 2009, la tempête de grêle ne s'est pas abattue l'après-midi mais dans les heures après minuit, ce qui s'est traduit par un constat des dommages quelque peu différent : le nombre de bâtiments dont des dommages aux stores ont été déclarés n'était certes pas plus élevé proportionnellement, mais le montant des dommages aux stores était sensiblement plus important.

Cette seconde analyse de l'événement par rapport au processus de grêle sur une période relativement courte fut l'occasion d'étudier et d'interpréter à nouveau les déclarations de sinistre reçues par un établissement cantonal d'assurance. Outre une comparaison avec les relevés de 2009, l'objectif était de vérifier les hypothèses établies dans la première étude. Contrairement à l'étude précédente, c'est l'ensemble des cas de sinistre qui a été examiné, et non pas un simple échantillon. Les résultats n'en sont donc que plus pertinents. Il a été ainsi confirmé une nouvelle fois que les stores, les toits et les façades représentent les principaux facteurs de coûts dans un événement de grêle, que les bâtiments d'habitation sont plus sensibles à la grêle que les bâtiments sans affectation d'habitation et que leur vulnérabilité a nettement augmenté, surtout depuis les années 90.

Comme dans l'étude réalisée à l'occasion de l'événement de 2009, les calculs effectués pour l'événement d'Argovie démontrent aussi le potentiel d'économie des éléments de construction avec un indice de résistance à la grêle $RG \geq 3$ (résistance jusqu'à un diamètre de grêlon de 3 cm) : concrètement, l'économie se serait située autour de CHF 25 millions pour cet événement.

Autre critère analysé : l'influence de l'orientation des bâtiments par rapport au nord et par rapport à la trajectoire de la cellule de grêle à l'origine des dommages. Une méthode d'analyse automatique a été développée en ce sens. Il en est ressorti que les bâtiments les plus endommagés sont ceux dont l'axe du faite du toit est orienté dans un angle de 40 à 70° par rapport à la trajectoire moyenne de la cellule de grêle, exposant ainsi la plus grande section de bâtiment aux grêlons.

Une nouvelle modélisation informatisée de l'université de Lausanne a servi à réaliser des essais de reproduction des dommages provoqués par des événements de grêle et d'évaluer sur cette base le risque grêle dans le canton. Le chapitre correspondant présente les courbes dommages / fréquence pour deux modèles de scénario. Grâce à la modélisation, il sera possible à l'avenir de fournir, peu de temps après l'événement de grêle, des indications utiles sur la répartition et la somme globale des dommages, au moyen de données radar.

La modélisation permet également d'évaluer le risque grêle actuel dans le canton d'Argovie ainsi que les périodes de récurrence correspondantes. En s'appuyant sur des scénarios de l'Office fédéral de la statistique concernant l'évolution de la population, il est même possible d'effectuer une évaluation de la progression du risque grêle dans vingt ans.

Les auteurs espèrent que cette deuxième étude grêle suscitera autant d'intérêt que celle sur les événements de 2009.

L'essentiel en bref

Date de l'événement :	12 et 13 juillet 2011
Principalement touchés :	Cantons AG et ZH
Diamètre maximal des grêlons constaté :	6.7 cm
Montant total des dommages AG (brut / net) :	CHF 151 / 145 millions
Nombre de sinistres reconnus AG :	20'600
Dommage moyen AG (brut / net) :	CHF 7'380 / 7'080
Dommage médian AG (brut / net) :	CHF 5'300 / 5'000
Plus gros dommage individuel grêle AG :	près de CHF 2 millions (jardinierie)
Classification :	Montant du dommage éléments naturels le plus important enregistré par l'ECA d'Argovie. Événement estimé comme survenant environ tous les 50 (à 100) ans.

1. Introduction

1. Introduction

La dernière phase des travaux sur le rapport « Analyse des événements de grêle 2009 » était encore en cours que déjà un nouvel orage de grêle d'une exceptionnelle intensité s'abattait sur le Plateau suisse, provoquant de graves dommages aux bâtiments dans le canton d'Argovie en particulier. C'est pourquoi cet événement a fait l'objet d'une attention toute particulière. L'analyse a également soulevé de nouvelles questions auxquelles les données de 2009 ne pouvaient apporter aucune réponse. L'Union intercantonale de réassurance a donc décidé de procéder également à une analyse des résultats pour l'événement de grêle des 12 et 13 juillet 2011.

Tout comme ses partenaires deux ans auparavant, l'établissement cantonal d'assurance d'Argovie a été mis à rude épreuve. Il a en effet dû apprendre ce que signifie avoir des milliers de clients qui veulent déclarer leur sinistre en l'espace de quelques jours. Littéralement d'un coup, la charge de travail a été multipliée par dix. D'une part, en raison du très grand nombre de dommages et, d'autre part, parce que l'examen des dommages grêle est nettement plus contraignant que pour les dommages dus à une tempête ou une inondation par exemple. 26 postes supplémentaires à temps plein ont même dû être créés spécifiquement pendant environ un an et demi (AZ 2012).

Cet événement a été pour l'AGV l'occasion d'améliorer son organisation administrative.

L'étude grêle a été confrontée cette fois aux questions suivantes :

- La méthodologie d'interprétation détaillée des données, développée à l'exemple de l'établissement cantonal d'assurance de Thurgovie, peut-elle être aussi appliquée auprès d'autres établissements d'assurance ?
- La tempête de grêle s'étant abattue cette fois en pleine nuit, dans quelle mesure la part des stores endommagés

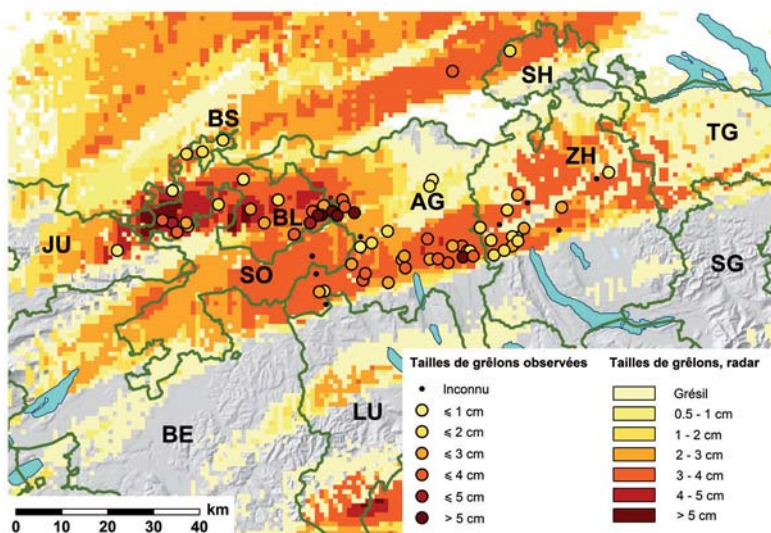
par rapport à l'ensemble des éléments de construction touchés diffère-t-elle de 2009 ?

- Le potentiel d'économie, grâce à une utilisation d'éléments de construction avec un indice de résistance à la grêle d'au moins RG3, s'avérerait-il aussi élevé que lors de l'événement de grêle de 2009 ?
- En ce qui concerne l'étendue des dommages, existe-t-il un lien entre l'orientation du bâtiment et la trajectoire suivie par les cellules de grêle ?
- Est-il possible de réaliser une estimation fiable peu après un événement, en se basant sur des données radar et sur une relation empirique intensité / dommages ?
- Le risque grêle actuel dans le canton d'Argovie est-il chiffrable ?
- À quel risque grêle doit-on s'attendre à l'avenir dans le canton d'Argovie ?

2. L'événement de grêle des 12 et 13 juillet 2011 dans le canton d'Argovie

2.1 Conditions météorologiques les 12 et 13 juillet 2011 (extrait d'après MétéoSuisse)

Le mardi 12 juillet 2011, une zone de basse pression s'est formée sur le centre de la France, alimentant des vents d'altitude de secteur sud-ouest sur l'arc alpin. La masse d'air entraînée depuis l'Espagne s'est révélée très chaude et orageuse. Par la suite, la température est passée en Suisse de 29 à 35°C. Les valeurs les plus élevées ont été relevées en Valais et dans la vallée du Rhin près de Coire. Dans la zone de convergence, en amont du front froid, les premières cellules orageuses se sont formées en soirée dans l'ouest du Jura. Ces cellules se sont ensuite déplacées en se renforçant le long du Jura, en direction de l'est. À ce moment-là, la grêle est tombée dans le « triangle » composé des cantons d'Argovie, de Bâle-Campagne et de Soleure. Le diamètre des grêlons dépassait nettement les 6 cm, ce qui correspond à peu près à la taille d'une balle de tennis (ill. 1).



Ill. 1: distribution des tailles de grêlons des 12 et 13 juillet 2011 sur les deux orages de grêle dans le nord de la Suisse; observées ou tirées de données radar (données radar: meteoradar; bases cartographiques: swisstopo).

2. L'événement de grêle des 12 et 13 juillet 2011 dans le canton d'Argovie

D'autres orages ont éclaté dans l'ouest des Préalpes d'où ils se sont déplacés en direction de l'est, jusque dans les Grisons.

Après une accalmie intervenue plus tard dans la soirée, une nouvelle cellule orageuse intense s'est formée vers minuit. Elle s'est déplacée du sud vers l'est au pied du Jura et elle a généré sur sa trajectoire de fortes averses de grêle avec des grêlons atteignant 6 cm, depuis Zofingue en passant par les cantons d'Argovie et de Zurich jusqu'après Winterthur.

C'est surtout dans les régions du nord du pays que des dommages dus à la grêle ont été répertoriés, principalement le long d'une bande légèrement courbée reliant le Jura bernois au lac de Constance. Fait marquant : la cellule orageuse la plus dévastatrice a déversé sa grêle au milieu de la nuit dans les cantons d'Argovie et de Zurich alors que la grêle tombe habituellement plutôt entre le début d'après-midi et la soirée. La fréquence élevée des éclairs était également étonnante : à Granges SO, 48 éclairs au total se sont produits à 3 km à la ronde. Il s'agit là d'une fréquence que l'on constate en général seulement dans les stations de montagne exposées.

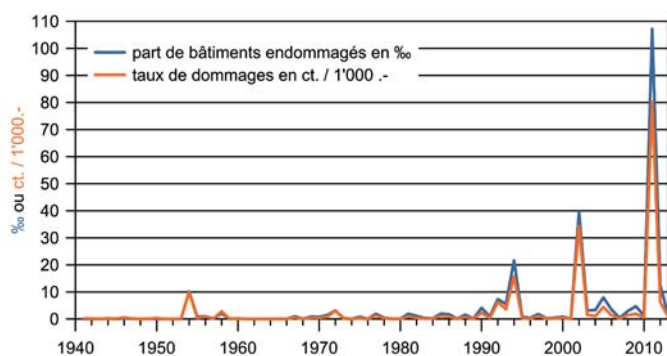
Après les orages préfrontaux, un front froid actif a envahi la Suisse le mercredi, causant un refroidissement et de fortes pluies, notamment sur le versant sud des Alpes.

L'établissement d'assurance du canton d'Argovie a recensé les 12 et 13 juillet 2011 des dommages dus à la grêle pour une valeur de 145 millions de francs (nets, c'est-à-dire après déduction des franchises). Il s'agit là du plus important événement dommageable de son histoire (rapport de gestion 2011). La tempête «Lothar» de décembre 2009 et l'averse de grêle du 24 juin 2002 étaient considérés tous deux comme les événements dommageables les plus importants

jusqu'à-là. Leur niveau de gravité n'est en fait pratiquement que de moitié moins élevé que ce qui s'est produit ces 12 et 13 juillet 2011. Les événements suivants en terme de dommages sont les inondations de mai 1999, de mai 1994 et d'août 2007 (UIR, 2005; statistique des dommages AEA).

2.2 Catégorisation statistique de l'événement

Il est difficile d'évaluer exactement la période de récurrence statistique des événements de grêle car peu de données de mesure sont disponibles, contrairement aux données sur le débit des crues ou sur la quantité des précipitations. Il existe toutefois des données sur les dommages causés aux bâtiments : depuis la première statistique des dommages éléments naturels établie pour l'année 1941, jamais un montant de dommages éléments naturels aussi élevé n'a été enregistré (voir ill. 2). Il serait toutefois dangereux d'en déduire directement la période de récurrence à partir des données de dommages disponibles auprès de l'établissement cantonal d'assurance d'Argovie et de définir l'averse de grêle des 12 et 13 juillet 2011 comme un événement survenant tous les 74 ans, soit une fois sur la période considérée. D'une part, parce qu'un événement (hypothétique) comparable survenu en 1940 et donc non inclus dans les données modifierait déjà fortement cette estimation. D'autre part, parce que l'averse de grêle n'était pas limitée uniquement au canton d'Argovie. En fonction de la situation et de l'étendue de sa zone d'impact, chaque orage de grêle est unique. C'est pourquoi, il convient de définir clairement la région pour laquelle une période de récurrence doit être déterminée. Est-il question de la période de récurrence sur tout le pays, pour le canton d'Argovie seulement ou du point de vue d'un seul bâtiment ? Le résultat ne sera pas le même suivant les cas. Dans le cadre de notre analyse de l'événement, il paraît approprié de se centrer sur le canton d'Argovie.



III. 2: évolution des dommages annuels aux bâtiments causés par la grêle (taux de sinistres) dans le canton d'Argovie depuis 1941, année de création de la couverture des risques naturels. L'événement de grêle des 12 et 13 juillet 2011 n'est pas seulement de loin le plus important de l'histoire de l'établissement d'assurance du canton d'Argovie en termes de dommages mais il s'agit de l'événement isolé le plus important dû aux éléments naturels (source : statistique des dommages AEA).

Une étude des sources permet en tout cas de catégoriser approximativement l'averse de grêle de juillet 2011 pour le canton d'Argovie. Les rapports historiques d'événements ont généralement été rédigés de manière non systématique. Ils sont par ailleurs emprunts de subjectivité et les observations que l'on peut y lire sont en général toutes impressionnantes. On y trouve en revanche peu d'indications quantitatives sur les surfaces touchées et sur le montant des dommages. Les quelques chiffres avancés sont de plus difficilement comparables avec ceux d'aujourd'hui. Par ailleurs, il n'est pas certain que la totalité des sources soient bien prises en compte dans ces rapports, ce qui pose un autre problème. Il est en effet difficile d'estimer combien d'événements significatifs n'ont pas été répertoriés par la grille de recherche.

Une recherche effectuée dans différentes sources (Riniker, 1881; Lanz-Stauffer / Rommel, 1936; Steigmeier, 2004; archives de journaux en ligne, recherche «Google») a permis d'aboutir à la conclusion suivante : les événements



Date	Région touchée dans le canton d'Argovie	Estimation à l'époque	Taille des grêlons	Domages
30 juillet 1824	Du Ruedertal et du Wynental à Schynznach et Bözberg; districts de Brugg, Lenzburg, Mellingen, Bremgarten, Baden	« destructeur » « cause de détérioration »	Près de Brugg, jusqu'à la taille d'un œuf de poule (env. 5 cm), sinon pour la plupart de la taille d'un œuf de pigeon (3,5 cm) et d'une noix (3 cm).	Toits en tuile et en chaume détruits, fenêtres brisées, oiseaux et lapins écrasés, nombreuses personnes blessées, feuilles des arbres et des vignes arrachées, cultures écrasées comme après le passage de chevaux (<i>Sauerländer, 1824; Riniker, 1881</i>)
31 mai 1838	Avant tout, les districts de Rheinfelden, Laufenburg et Zurzach ainsi que quelques communes isolées dans les districts de Brugg et de Zofingue	« meurtrier » « dévastateur »	Des grêlons d'env. 3,75 cm de diamètre ont été retrouvés le lendemain	Semences, arbres, vignes lourdement endommagés; presque toutes les vitres de l'église de Weiach ZH (à la limite du canton d'Argovie) ont été brisées (<i>Lanz-Stauffler / Rommel, 1936; Brandenberger, 2011</i>).
14 juillet 1873	Nord du Freiamt, en particulier la région autour de Büttikon, Waltenschwil et Boswil	« horreur indescriptible »	Jusqu'à la taille d'un œuf de poule (env. 5 cm) dans la vallée du Bünzthal; on aurait encore trouvé des grêlons près de Kallern 8 jours après	Toits en tuile et en chaume gravement endommagés, cheminées pulvérisées, fenêtres brisées et certains bâtiments « moitié démolis » Cultures et arbres fruitiers anéantis. (<i>Riniker, 1881</i>)

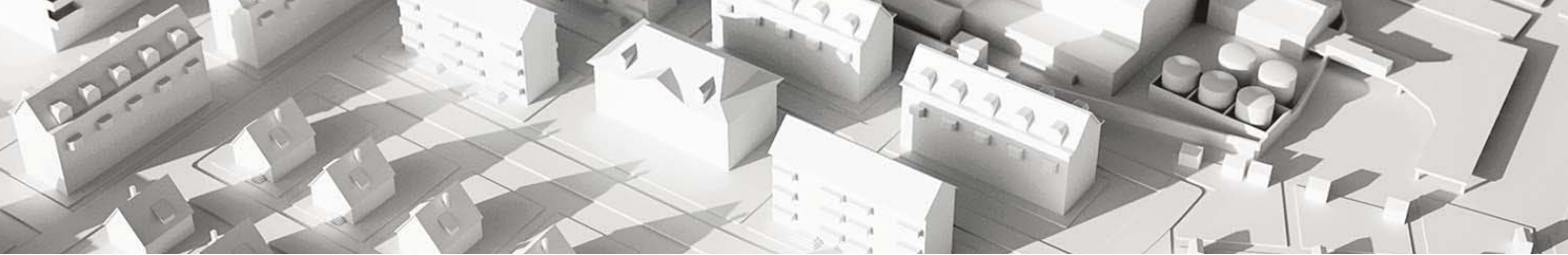
retrouvés entre 1800 et 1940 et perçus à l'époque comme significatifs ne donnent que trois renseignements sur des tailles de grêlons et sur les conséquences dommageables susceptibles de pouvoir être comparés avec juillet 2011.

Le deuxième plus important événement de grêle survenu dans le canton d'Argovie pendant la période documentée par les données sur les dommages aux bâtiments remonte au 24 juin 2002. Une cellule de grêle intense suivit une trajectoire très proche de celle des 12 et 13 juillet 2011, avec une trajectoire traversant le canton d'Argovie un peu plus au nord. Elle fut à l'origine de dommages aux bâtiments de l'ordre de 50 millions de francs (valeur nominale; rapport de gestion 2002 de l'AGV). Les plus gros grêlons retrouvés dans le canton atteignaient 4 cm de diamètre. Cet événement du canton d'Argovie n'égalait ainsi pas les événements cités précédemment, au moins en ce qui concerne la taille maximum des grêlons.

Avec l'averse de grêle des 12 et 13 juillet 2011, si l'on se base sur un ordre de grandeur comparable aux trois évé-

nements historiques, il apparaît donc que la période de récurrence pour ces quatre événements survenus en 214 ans depuis 1800 dans le canton d'Argovie correspond à une bonne cinquantaine d'années. Partant de l'hypothèse que la liste des événements répertoriés n'est pas complète, il apparaît probable qu'il se soit davantage agi en juillet 2011 d'un événement survenant tous les 50 ans et non tous les 100 ans.

Le rapport ci-après laisse supposer que d'autres événements encore plus dévastateurs ont été possibles en Argovie :



En 1591, un terrible nuage de grêle se forma le 5 juillet à 5 heures du soir, reliant l'Argovie au lac [de Zurich] en passant au-dessus de l'Albis jusqu'à la région du «Grüninger Amt» [≈ Oberland zurichois]. Toits, fontaines, vignes et champs de céréales ont subi de tels dommages qu'il ne restait encore qu'à peine les graines à de nombreux endroits. À Ottenbach [ZH, à la limite directe du canton de AG], des grêlons de deux livres et plus sont tombés. Dans certains endroits, les cochons ont été tués en plein champ, tout comme des bergers. «Après tant d'années de pénurie, la grêle a encore appauvri beaucoup de gens. Que Dieu ait pitié de nous, Amen».

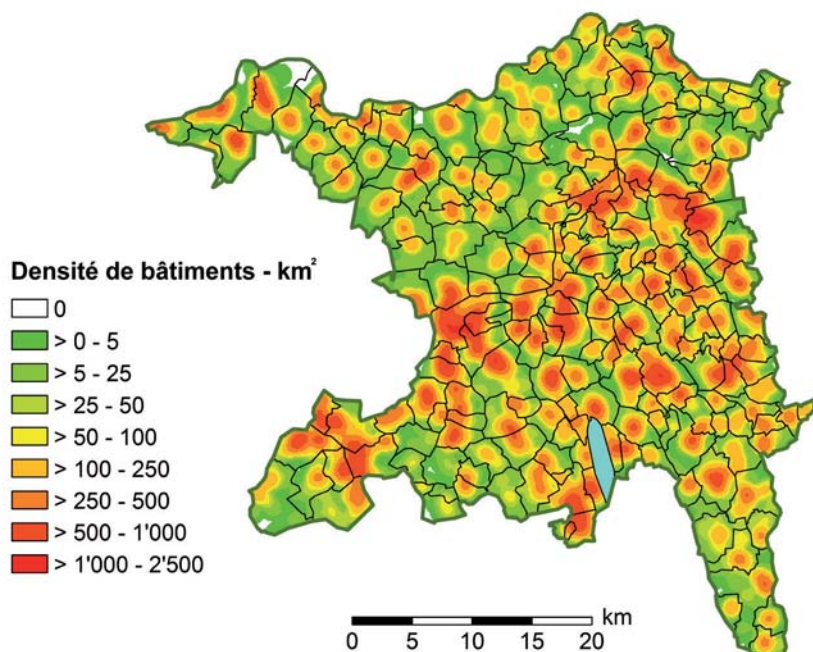
(Sigg, 1994)

2.3 Distribution spatiale des dommages: analyse du parc immobilier touché

Grâce à la banque de données d'adresses «GeoPost Coordinates» de la Poste Suisse (La Poste, 2013), les bâtiments dépendant de l'établissement cantonal d'assurance d'Argovie ont pu être géoréférencés¹ dans une proportion de 88,6%. Ainsi, des analyses pertinentes axées sur les bâtiments ont pu être réalisées dans le système d'information géographique (SIG) «ArcMap®». Il fut alors possible de procéder à des analyses au niveau communal d'une part, et de réunir dans le SIG d'autre part les emplacements individuels des bâtiments qui sont exploités pour des cartes de distribution de densité.

Des grêlons de plus de 2 livres (soit environ 1 kg) correspondaient à des boules de glace de 13 cm de diamètre. La fiabilité de cette information n'est toutefois pas garantie. Il a quand même été fait mention à Undingen (Baden-Württemberg, D), d'un grêlon de forme ovoïde tombé le 6 août 2013 et mesurant 14 cm dans son axe longitudinal (GEA, 2013). Il ne pesait toutefois «que» 360 g. Mais le fait que des bergers et des cochons aient été tués en 1591, cela veut tout dire.

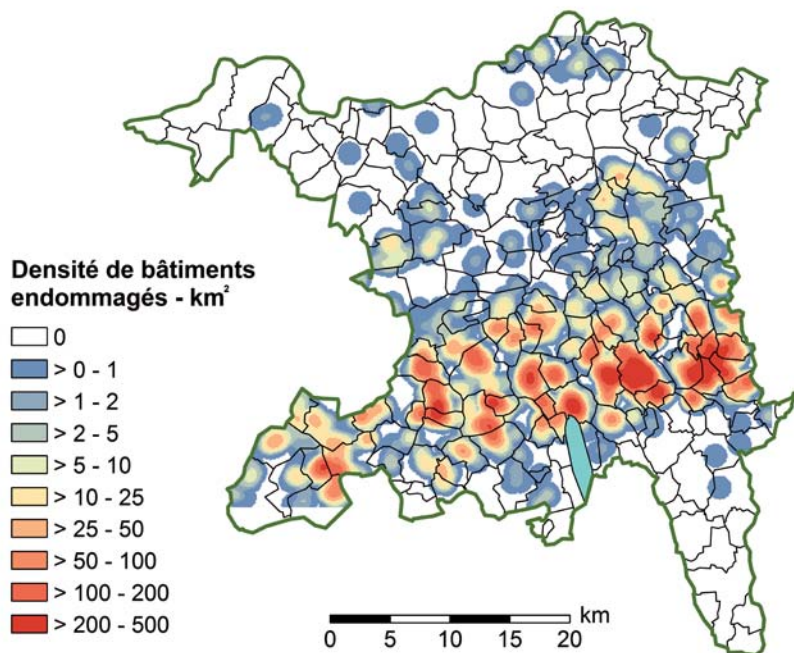
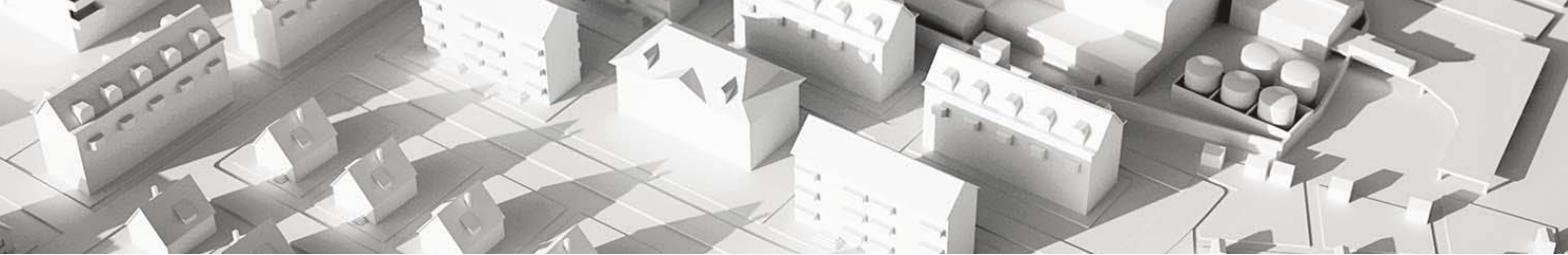
L'ill. 3 présente la distribution spatiale des bâtiments existants dans le canton d'Argovie en termes de densité (nombre de bâtiments au km²). Les plus grandes agglomérations se situent d'après cette carte dans les zones les plus basses, notamment dans les vallées le long de l'Aar², de la Limmat et de la Reuss ainsi que sur les rives du Rhin près de Möhlin. D'autres noyaux plus petits se trouvent également dans les vallées de la Wigger, de la Suhre, de la Bünz et de la Sissle. Les hauteurs souvent boisées du Jura au nord (p. ex. Böz-



III. 3: densité de bâtiments au km² dans le canton d'Argovie (recherche sur un rayon de 1 km pour le calcul; base cartographique: swisstopo).

¹ Le géoréférencement spécifie l'emplacement de localités par l'attribution de coordonnées; dans le cas présent, une paire de coordonnées a été attribuée aux adresses de bâtiments se trouvant dans le portefeuille de l'établissement cantonal d'assurance d'Argovie, selon le système de coordonnées nationales suisse.

² Une carte du canton d'Argovie en annexe A présente la situation des localités mentionnées dans le rapport.

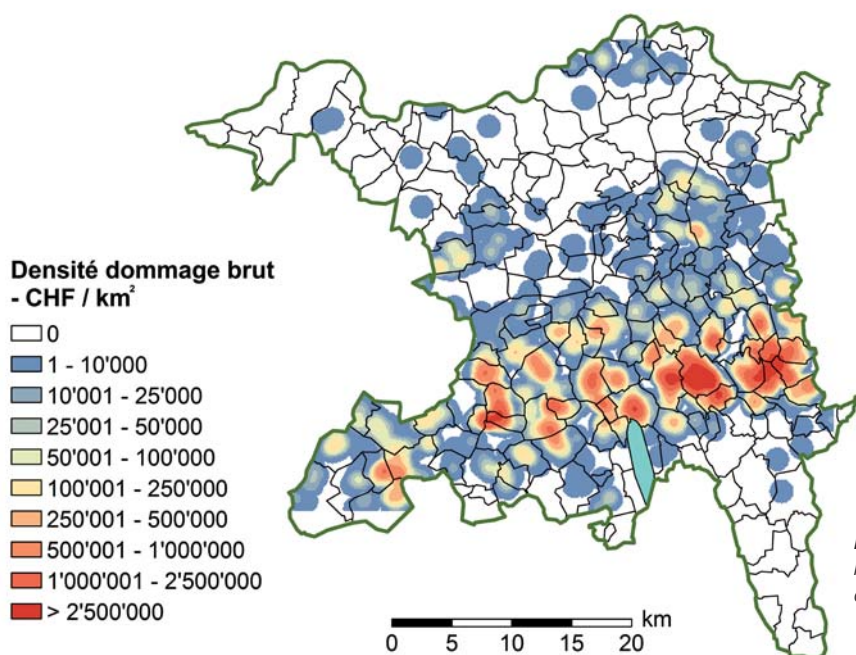


III. 4: densité de bâtiments endommagés au km² (recherche sur un rayon de 1 km pour le calcul ; base cartographique: swisstopo).

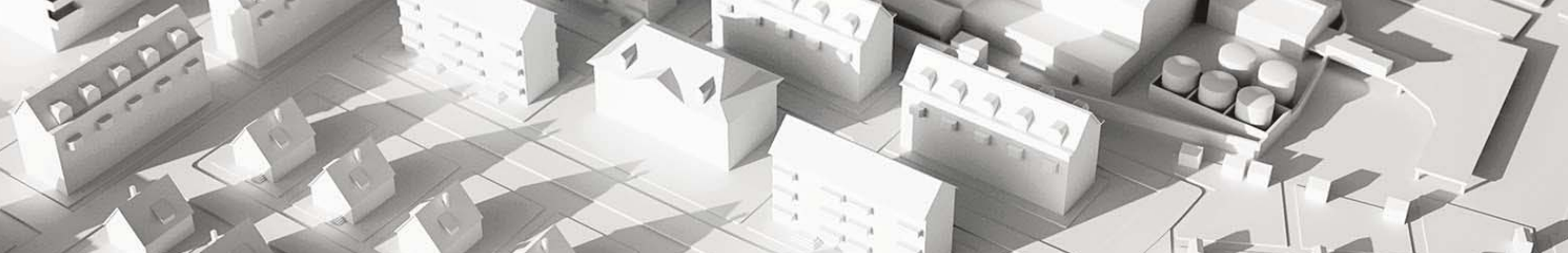
berg) et les chaînes entre les vallées fluviales du Plateau au sud du canton (p. ex. Lindenberg) sont nettement moins habitées. La carte sert de base de comparaison pour les cartes de dommages dus à la grêle, présentées ci-après.

L'ill. 4 indique la concentration des 20'600 bâtiments environ qui ont été endommagés par la grêle les 12 et 13 juillet 2011 (nombre de bâtiments par km²). Les zones de dommages se détachent nettement, par exemple près de

Wohlen et de Bremgarten où la densité de bâtiments endommagés atteignait des valeurs correspondant à plusieurs centaines de bâtiments au km². Des valeurs semblables ont été relevées en 2009 dans le canton de Thurgovie. La large bande rouge transversale dans la partie sud du canton reflète explicitement la trajectoire suivie par la grêle. Les tâches rouges ne doivent toutefois pas être directement perçues comme une représentation de l'intensité de la grêle car elles sont en fait étroitement liées à la densité des bâtiments existants.



III. 5: densité des dommages bruts en francs / km² (recherche sur un rayon de 1 km pour le calcul ; base cartographique: swisstopo).



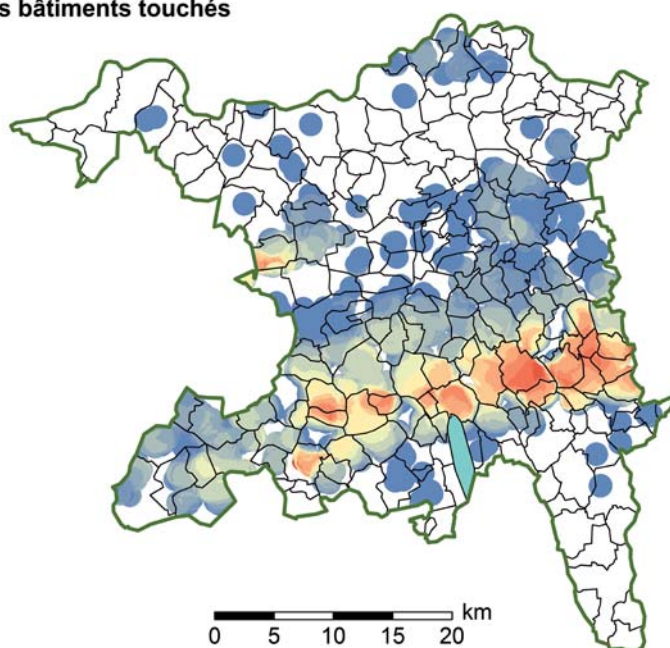
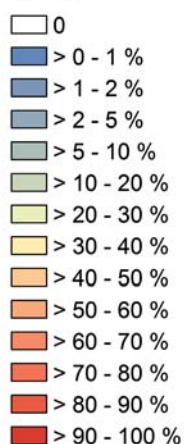
Une image très proche fournit une analyse selon la densité des dommages (somme brute des dommages aux bâtiments au km²; ill. 5). Des densités de dommages de plusieurs millions de francs / km² ont été atteints dans les noyaux de dommages précédemment cités: des valeurs identiques à celles recensées en Thurgovie en mai 2009. Les valeurs maximales se limitent obligatoirement aux zones présentant la plus forte densité de constructions de telle sorte que cette représentation ne permet pas d'en déduire directement l'intensité de la grêle. Pour estimer l'intensité de la grêle, il faut compenser l'influence de la densité très variable des constructions dans l'espace en divisant les données de la carte de l'ill. 4 par celles de l'ill. 3.

Le résultat est présenté dans l'ill. 6 avec le pourcentage de bâtiments touchés au km². Cette formule aboutit à un lissage de la structure dominée par des noyaux. Le modèle devient plus uniforme en comparaison avec les images présentées antérieurement. Ressortent en outre désormais des structures que l'on distinguait à peine sur les cartes précédentes. Par exemple, le noyau d'intensité d'un autre nuage de grêle qui a traversé le canton de Bâle-Campagne tôt dans la soirée et qui s'est délité peu de temps après son avancée dans le canton d'Argovie au Bözberg, tel que le montre distinctement l'image radar (ill. 1). C'est d'ailleurs dans cette région du col de la Salhöhe que les plus gros grêlons ont été rapportés, avec un diamètre atteignant bien 6,5 cm. Leurs conséquences dommageables ont toutefois à peine été prises en considération dans la somme finale en raison de la faible densité de bâtiments dans cette zone.

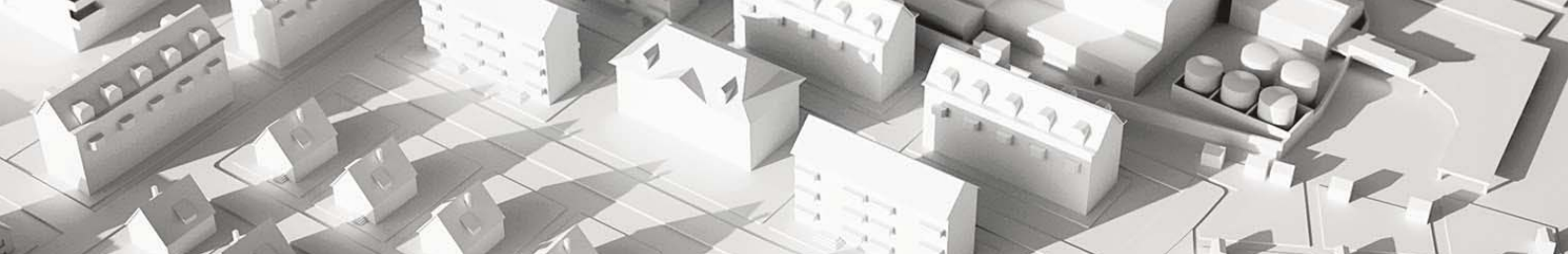
Par contre, la concentration des dommages reconnaissables localement sur l'ill. 5 disparaît presque complètement à Baden, loin de l'axe principal de l'orage de grêle. La part des bâtiments touchés tournait autour de 5% mais la forte concentration de valeurs a suffi à faire augmenter de manière significative la densité des dommages et à la faire ressortir dans l'ill. 5 comme une zone isolée ayant subi un maximum de dommages.

L'ill. 6 offre un bon rendu de l'intensité réelle de l'averse de grêle. La carte reproduit par exemple également les forts gradients d'intensité reconnaissables sur l'image radar dans le Freiamt: tandis que des grêlons de 6 cm de diamètre étaient signalés à Bremgarten, la grêle n'est absolument pas tombée à Besenbüren, située à seulement 3,5 km au sud. De telles variations entre des localités rapprochées avaient déjà été constatées en mai 2009 dans le canton de Thurgovie (UIR, 2012). L'ill. 6 ne montre toutefois bien sûr que les effets de la grêle et non pas sa véritable intensité (énergie cinétique): dans les zones non construites, la carte reste vide malgré une intensité vraisemblablement élevée. C'est le cas par exemple à Wegenstetten dont la densité de population est proportionnellement faible. Le radar indique la présence de grêlons de 4 à 5 cm mais aucun dommage n'a été pour autant signalé. Il n'existe malheureusement aucune indication sur la taille des grêlons effectivement tombés à Wegenstetten afin de confirmer les données radar.

Pourcentage des bâtiments touchés par km²



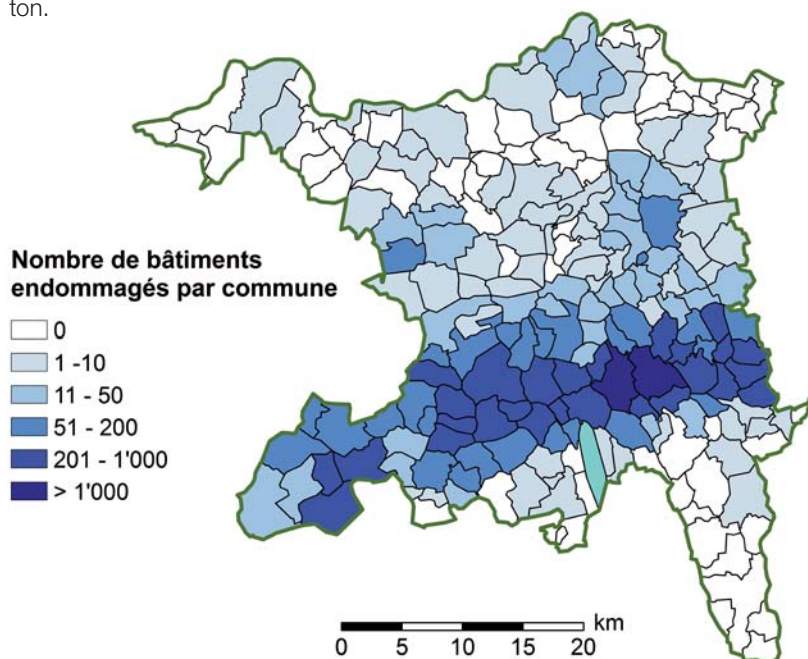
III. 6: pourcentage de bâtiments endommagés au km² (recherche sur un rayon de 1 km pour le calcul ; base cartographique: swisstopo).



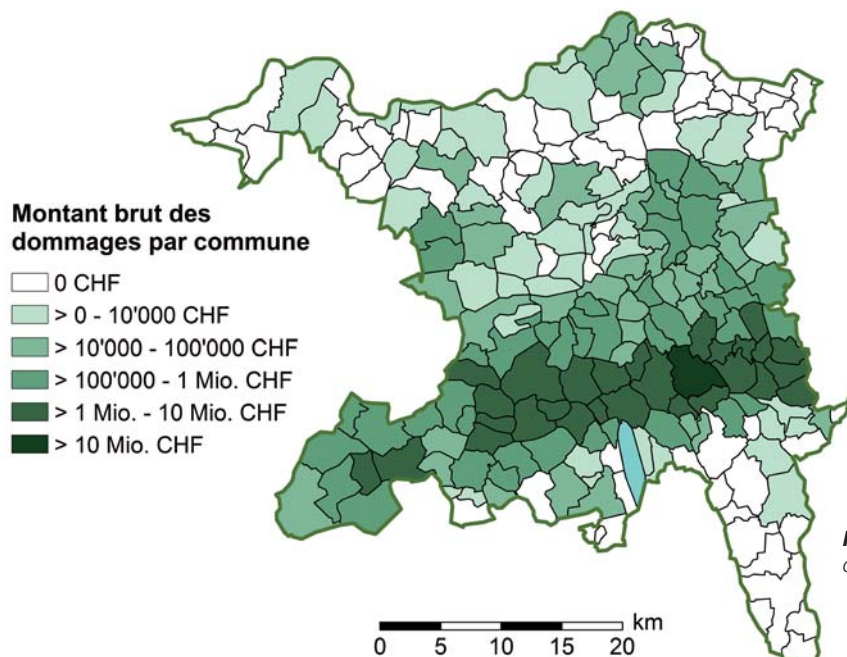
2.4 Observation des dommages suivant les communes

L'observation par commune fournit d'autres explications. La plupart des bâtiments endommagés (soit environ 2'900) ont été enregistrés dans la commune de Wohlen. Bien plus de 1'000 bâtiments touchés ont également été signalés à Villmergen. Une bande constituée de communes ayant subi chacune plus de 200 dommages aux bâtiments s'étend sur pratiquement toute la partie sud du canton, ce qui souligne les effets destructeurs de l'orage de grêle (ill. 7). Le nombre de dommages est nettement inférieur dans le reste du canton.

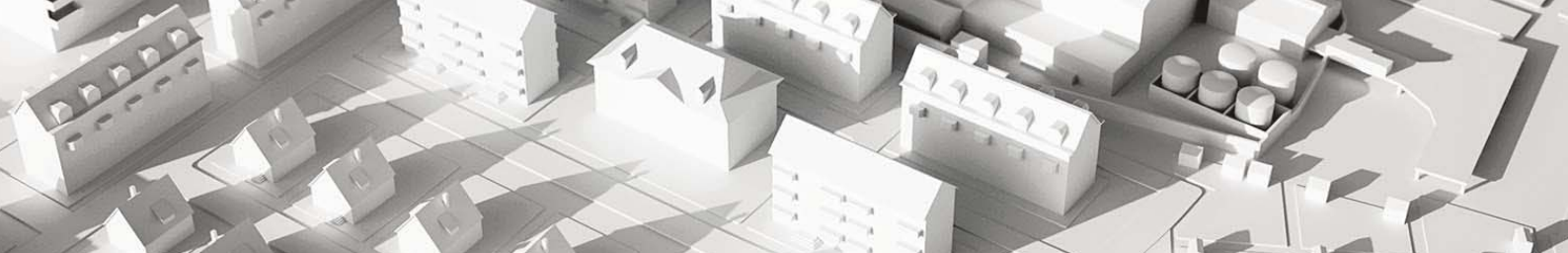
La carte représentant le montant des dommages par commune (ill. 8) ne se distingue visuellement que légèrement de la précédente. Avec 35 millions de francs au moins, Wohlen est en tête. Les communes voisines de Villmergen avec à peine 10 millions de francs et Bremgarten avec à peine 8 millions de francs sont déjà loin derrière. L'orage de grêle a atteint son intensité maximum ici, dans le nord du Freiamt, sur l'une des plus importantes concentrations de valeurs du canton d'Argovie.



III. 7: nombre de bâtiments endommagés par commune (base cartographique: swisstopo).



III. 8: somme des dommages aux bâtiments par commune (base cartographique: swisstopo).



L'ill. 9 est le résultat de la division des données représentées sur la carte de l'ill. 8 par les données de l'ill. 7. Elle indique le dommage moyen aux bâtiments dans les différentes communes. L'influence des agglomérations dans ce calcul a été compensée afin de faire ressortir également les plus petites communes sévèrement touchées. Comme un faible nombre de dommages importants peut quand même aboutir à une valeur moyenne élevée, une fausse impression serait rendue dans certains cas si l'on ne procédait pas à une compensation. Ainsi, à Freienwil, le dommage moyen très élevé de 24'400 francs était à imputer à un seul bâtiment essentiellement. À Neuhof, Gipf-Oberfrick et Ehrendingen, c'est même un seul et unique bâtiment qui est à l'origine de dommages moyens estimés respectivement dans ces communes à presque 22'000 francs, environ 12'000 francs et bien 10'000 francs.

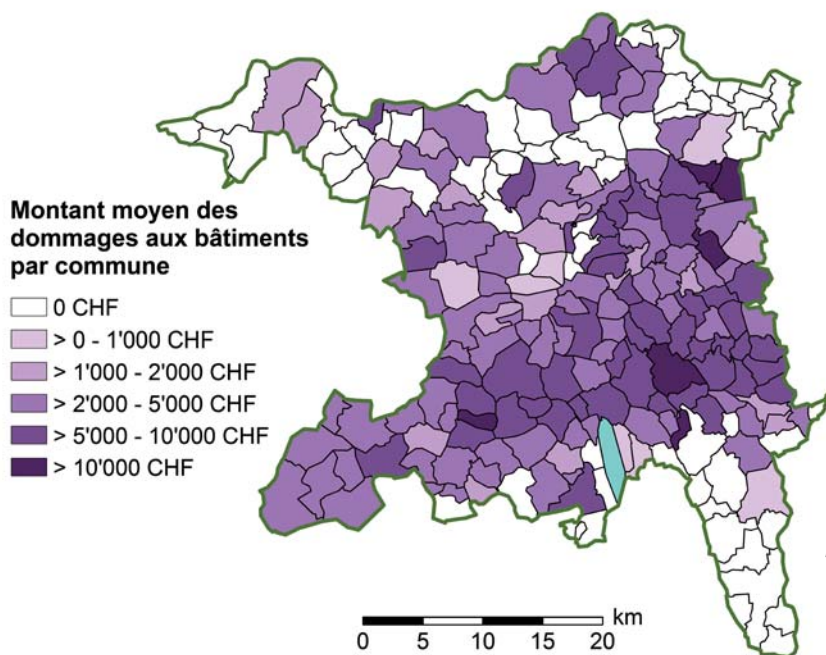
À l'inverse, les communes de Hirschthal et de Wohlen ont été fortement touchées. On a pu y observer des grêlons mesurant jusqu'à 4 cm de diamètre, ce qui est aussi établi par les données radar. C'est pourquoi, les moyennes élevées de dommages s'élevant à 14'700 francs (Hirschthal) et à 12'200 francs (Wohlen) sont pertinentes.

À première vue, il est surprenant de constater un dommage moyen relativement élevé de 6'800 francs à Leibstadt, correspondant à 12 dommages aux bâtiments. En effet, au-

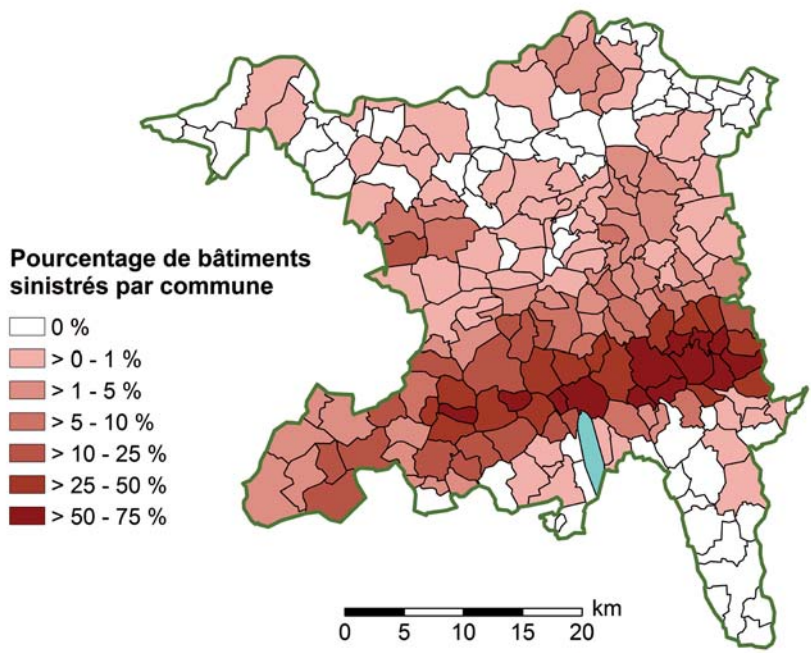
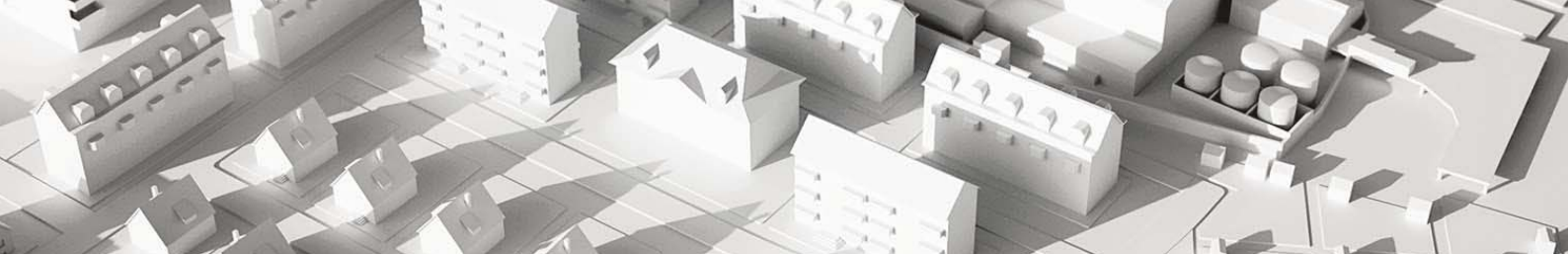
cune grêle n'a été signalée dans cette zone et le radar n'a rien enregistré, si ce n'est du grésil.

Il est vrai que la région autour de Leibstadt a été touchée le 22 juin 2011 par une forte averse de grêle. Il est donc probable que la plupart des dommages signalés dans la région provenait de cet événement. Toutefois, ce tableau ne reflète pas le cas de la ville de Koblenz située non loin de là et qui avait été également touchée le 22 juin. Les données concernant les dommages pour cette ville ne contiennent en effet aucun dommage aux bâtiments.

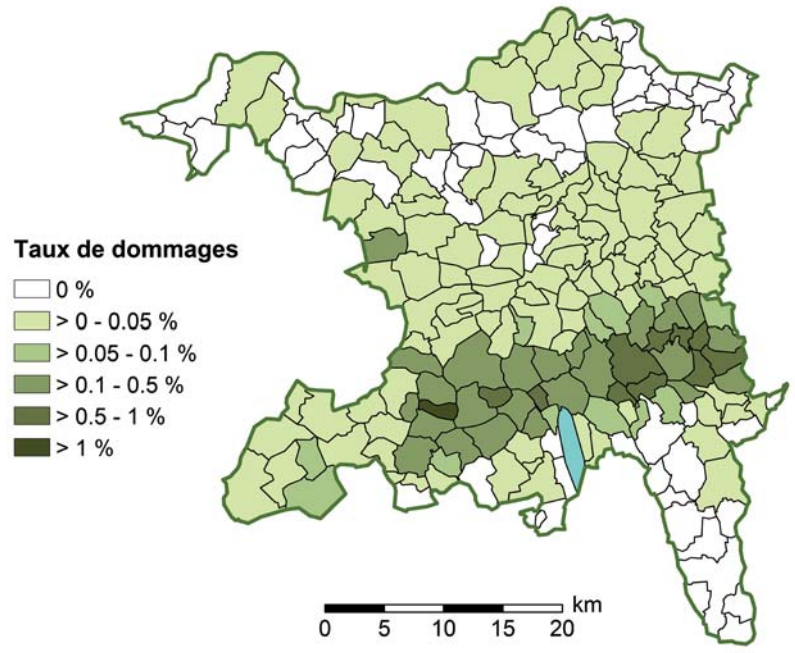
L'ill. 10 donne une bonne représentation de la gravité de l'événement de grêle en reprenant le pourcentage de bâtiments endommagés par rapport à la totalité des bâtiments existants dans chaque commune (voir également l'ill. 6) L'orage de grêle au sud en particulier apparaît à nouveau nettement. La carte donne une vue réaliste des rapports d'intensité car les répercussions de la densité de population sont estompées par le caractère relatif des chiffres. La région autour de Wohlen et Bremgarten ressort une fois encore de façon marquée, car plus de la moitié des bâtiments d'un bon nombre de communes a subi des dommages. Par ailleurs, d'autres zones situées plus à l'ouest ont aussi relevé de forts pourcentages de dommages. Avec 70 %, Hirschthal enregistre par exemple la part la plus élevée.



III. 9: niveau du dommage moyen aux bâtiments par commune (base cartographique: swisstopo).



III. 10: proportion relative des bâtiments endommagés par commune (base cartographique: swisstopo).



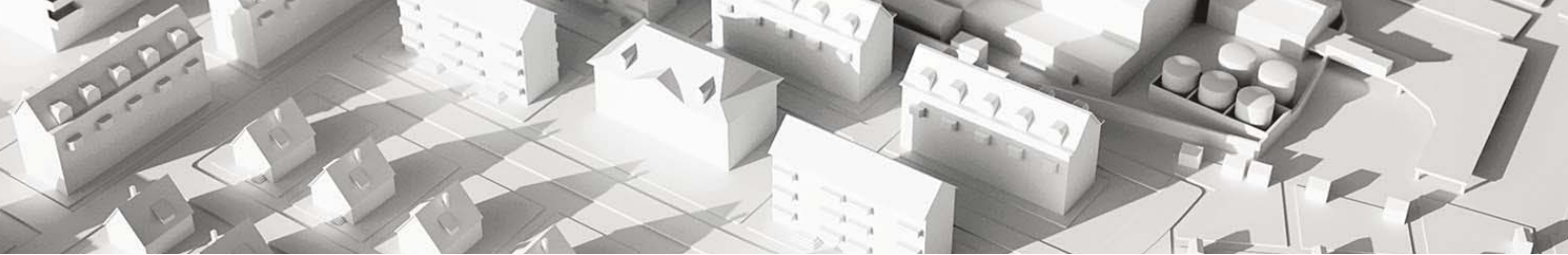
III. 11: taux de dommage, soit le rapport entre le montant du dommage et la valeur d'assurance par commune (base cartographique: swisstopo).

Si l'on établit un rapport entre le montant des dommages par commune et la somme totale assurée, on obtient alors le taux de dommage, c'est-à-dire le pourcentage de la valeur d'assurance (ill. 11). Il s'agit donc d'une mesure des effets destructeurs de la grêle. Par conséquent, les taux de dommages les plus élevés ne coïncident pas avec les intensités de grêle les plus fortes. Il existe toutefois des exceptions, comme le montrent les exemples suivants :

- À Gansingen, seul un abri pour petits animaux a été endommagé. En raison de la valeur d'assurance insignifiante, ce dommage relativement faible a suffi à entraîner un haut taux de dommage. Ceci est caractéristique des petits bâtiments et des dépendances (ill. 16). La taille maximum des grêlons était d'env. 3 cm d'après le radar.

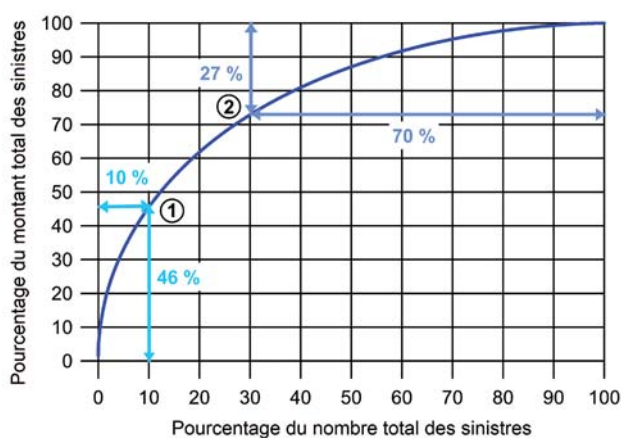
- Effingen se distingue également pour la même raison en principe: une seule maison d'habitation a subi un dommage de gravité moyenne mais non défini précisément, causant ainsi un taux de dommage élevé. D'après le radar, la taille des grêlons atteignait 3 cm ici aussi.
- À Freienwil, les dommages causés sur le revêtement d'étanchéité d'un seul bâtiment ont donné un taux de dommage élevé malgré une intensité de grêle relativement faible (jusqu'à 2 cm de diamètre).

En résumé, il faut convenir que le canton d'Argovie a eu de la chance dans son malheur les 12 et 13 juillet 2011, dans la mesure où seuls les bords du nuage de grêle ont touché les régions présentant les concentrations de valeurs les plus élevées (voir ill. 3).



2.5 Coup d'œil sur les chiffres

Si l'on compare le nombre de déclarations de sinistre aux montants des dommages isolés triés par ordre décroissant, on obtient la courbe de l'ill. 12. Si tous les dommages étaient d'un montant parfaitement égal, la « courbe » se présenterait sous forme de bissectrice, tirée de l'angle inférieur gauche à l'angle supérieur droit. Mais puisque les montants de dommages sont différents, la courbe des dommages totaux s'approche davantage d'une branche de parabole, l'importance de la courbure étant déterminée par la divergence entre les dommages les plus gros et les plus petits.



III. 12: proportion relative des dommages triés par ordre décroissant dans la somme totale des dommages.

Outre la courbure, les deux extrémités de la courbe présentent un intérêt particulier :

Les 10 % de sinistres individuels les plus importants (2'066 sur 20'656 sinistres) sont responsables à eux seuls de 46 % de la somme totale (brute) des dommages de près de 150 millions de francs : (1). Un faible nombre d'importants sinistres définit donc dans une large mesure la somme totale des dommages. Ainsi, seuls 15 sinistres individuels (dont neuf à Wohlen) dépassent un montant (brut) de dommages de 200'000 francs chacun et s'élèvent au total à 7,9 millions de francs, ce qui correspond à presque 20 % de la somme totale des dommages.

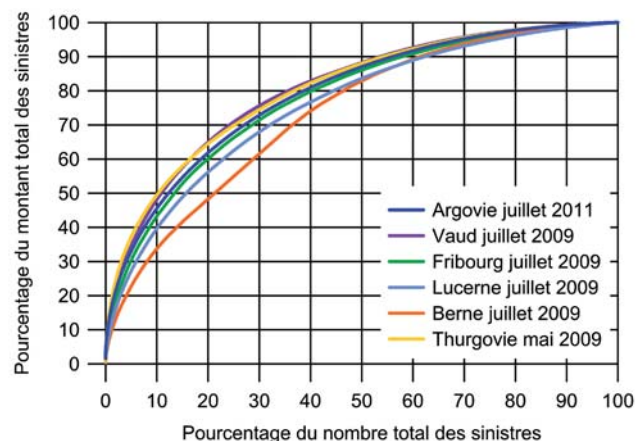
Les trois sinistres les plus importants sont cités ci-après :

- Le sinistre le plus important avec presque 2 millions de francs est survenu dans une entreprise artisanale constituée de plusieurs bâtiments. Les dommages étaient si considérables surtout sur la toiture que le bâtiment principal a dû être reconstruit.
- Le deuxième dommage le plus important avec presque 1,2 millions de francs concernait la toiture métallique d'un bâtiment industriel. La vaste surface et le matériau sensible à la grêle ont contribué au montant élevé des dommages.

- Des dommages pour un montant de presque 1 million de francs sont survenus sur le toit, les fenêtres de toit et les stores d'un autre bâtiment industriel. Les pompiers ont dû par ailleurs pomper l'eau qui avait pénétré dans la cave.

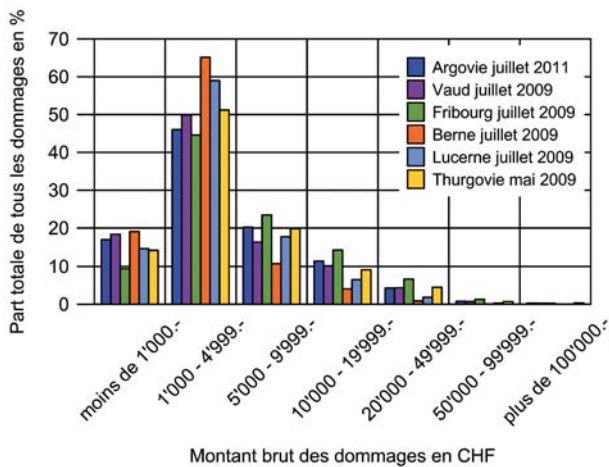
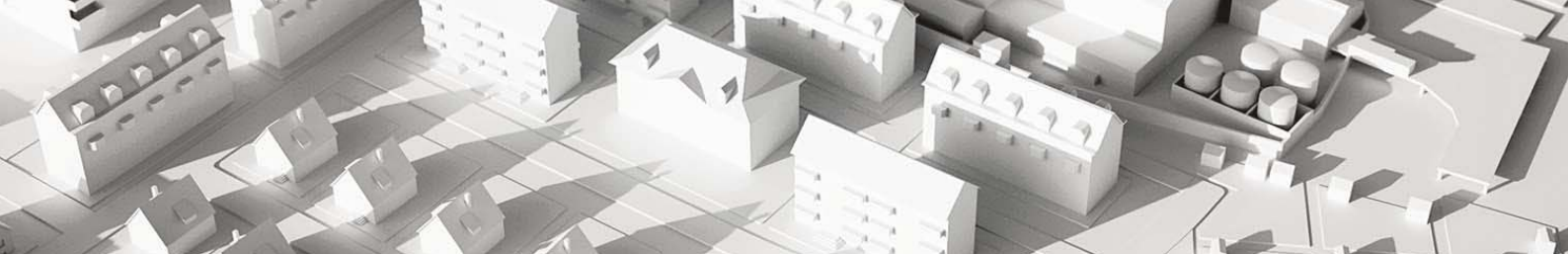
En revanche, les 70 % de petits sinistres ne correspondent qu'à 27 % de la somme totale des dommages : (2). 4'381 cas se situent ainsi au-dessous d'un montant (brut) de dommages de 1'500 francs. En raison de leur nombre, ces dommages relativement faibles entraînent toutefois d'importants frais administratifs et logistiques.

La courbe des dommages totaux d'Argovie présentée sous l'ill. 12 coïncide bien avec les événements de grêle comparables dans d'autres cantons (ill. 13). Sa pente se situe entre les courbes des cantons de Vaud / Thurgovie et celle du canton de Fribourg. Il s'agit là des cantons qui furent les plus touchés par les averses de grêle de 2009. Une forte courbure dénote manifestement une certaine virulence, la divergence entre les grands et les petits dommages étant plus importante.

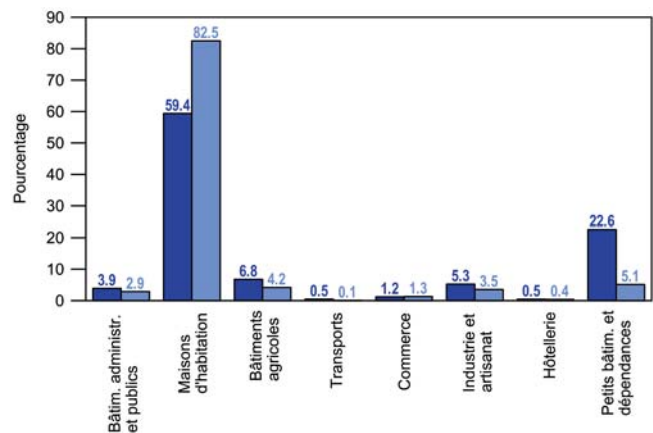


III. 13: comparaison de la courbe de l'ill. 12 avec les courbes des deux grands événements de grêle de 2009 (complété selon UIR, 2012).

L'ill. 14 subdivise la structure des coûts des dommages en différentes catégories. Elle montre que presque la moitié des dommages isolés dans le canton d'Argovie correspondait à des montants compris entre 1'000 et 5'000 francs. Des montants de dommages supérieurs à 20'000 francs n'ont été atteints que dans bien 5 % des cas. Les montants dépassant 100'000 francs étaient de 0,3 % et constituaient ainsi une infime minorité. La répartition est caractéristique et s'inscrit bien dans celle des cantons analysés dans le cadre de l'étude de 2009 (UIR, 2012). Comme présenté dans l'ill. 13, c'est surtout le canton de Berne qui se distingue par une plus large part de catégories inférieures ou une plus petite part de catégories correspondant à des montants élevés de dommages. Cela indique que la conséquence dommageable est moindre en moyenne.



III. 14 : structure des coûts des dommages bruts aux bâtiments dus à la grêle pour les événements de 2009 et 2011 : proportion relative des différentes classes de coûts dans le nombre total des dommages.



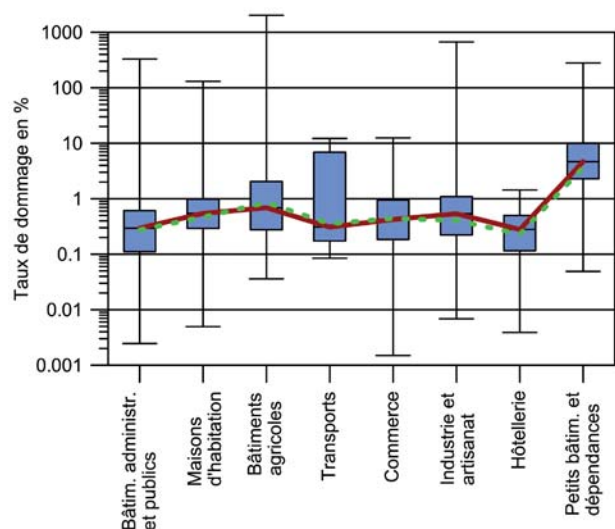
III. 15 : proportion relative des catégories de bâtiments (affectation) dans le nombre total de bâtiments du canton d'Argovie (colonnes sombres), ou dans le nombre de bâtiments endommagés (colonnes claires).

Si l'on compare le pourcentage des catégories de bâtiments touchées avec la part que ces catégories représentent sur l'ensemble des bâtiments existants dans le canton d'Argovie (ill. 15), les mêmes observations peuvent être faites que pour l'étude de 2009. Les bâtiments d'habitation sont nettement sur-représentés en termes de part du portefeuille de bâtiments. Par contre, les petits bâtiments et les dépendances sont massivement sous-représentés ainsi que, dans une moindre mesure, les bâtiments agricoles et les bâtiments industriels et artisanaux. Tous les autres bâtiments apparaissent dans les données sur les dommages à peu près dans la même proportion que dans l'ensemble des bâtiments existants. Les chiffres d'Argovie se placent donc immédiatement entre ceux des cantons de Thurgovie, de Vaud, de Fribourg, de Berne et de Lucerne (UIR, 2012). Les conclusions de l'étude de 2009 ne sont pas remises en question par les données 2011 :

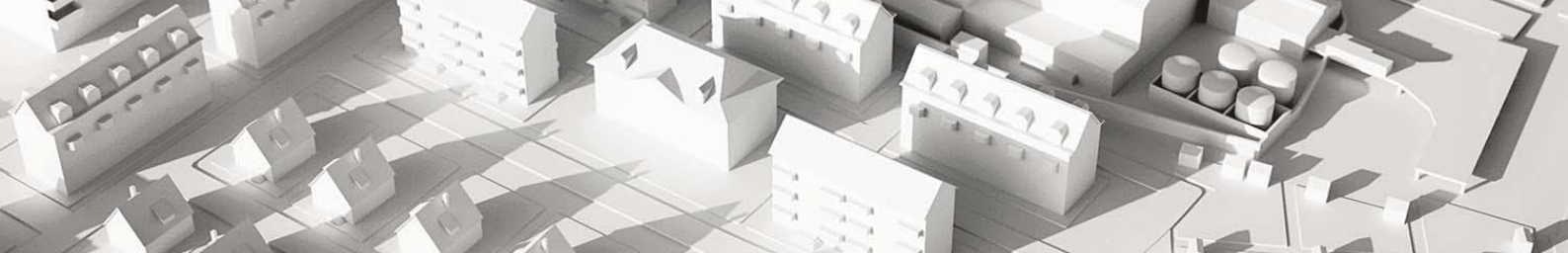
- Les bâtiments d'habitation présentent en moyenne une plus forte sensibilité à la grêle que les autres catégories de bâtiments.
- Les propriétaires de bâtiments d'habitation se montrent plus exigeants envers leur établissement cantonal d'assurance : ils ont tendance à déclarer à l'ECA même les petits dommages sur leur objet, tandis que c'est vraisemblablement moins souvent le cas chez les propriétaires de toutes les autres catégories de bâtiments.

Le premier constat ressort plus ou moins de l'analyse de la part des éléments de construction touchés (voir chapitres suivants), tandis que les attentes des clients ne sont que difficilement perceptibles dans les seules données de dommages.

Une comparaison du taux de dommage dans les différentes catégories de bâtiments permet d'examiner la vulnérabilité des bâtiments à la grêle. Il faut comprendre par taux de dommage d'un bâtiment le quotient du montant (brut) des dommages et de sa valeur d'assurance. L'ill. 16 représente l'analyse correspondante pour le canton d'Argovie.



III. 16 : box plots des taux de dommages (quotient montant brut des dommages / somme d'assurance) par catégorie de bâtiment (affectation) dans le canton d'Argovie. La courbe rouge relie la médiane (50% quantile). En vert, pour comparaison : la courbe correspondante du canton de Thurgovie.



Les taux de dommages calculés varient essentiellement entre 0,1 et 10 % mais des tendances caractéristiques demeurent :

Les taux de dommages des **petits bâtiments et des dépendances** sont clairement les plus élevés : la médiane des taux de dommages de cette catégorie se situe presque à 5 %. Plusieurs raisons pourraient être à l'origine de ces valeurs élevées : la valeur d'assurance moyenne des petits bâtiments et des dépendances se situe en moyenne considérablement en dessous de celle des autres catégories de bâtiments ; elle s'élève par exemple à seulement environ 1/9 de celle des bâtiments d'habitation. En cas de dommage comparable sur une construction de ce type, le quotient montant des dommages / valeur d'assurance s'avère inévitablement plus élevé que pour les autres classes de bâtiments. Même lorsque les dommages sont au total plus limités en raison des dimensions inférieures et, par conséquent, de la surface réduite des petits bâtiments et des dépendances, les proportions entre surface et volume (et aussi par rapport à la valeur d'assurance) sont malgré tout moins favorables. Si le montant des dommages par unité de surface de l'enveloppe du bâtiment se situe dans un même ordre de grandeur, le dommage sur les petits bâtiments et les dépendances en relation avec la valeur d'assurance est alors plus élevé par rapport aux autres classes. À cela s'ajoute que le couvreur, le ferblantier ou le plâtrier calcule évidemment ses tarifs de travaux de réparation sans tenir compte du type de bâtiment, ce qui aboutit à un taux de dommage plus élevé pour une valeur d'assurance plus faible.

Avec une médiane de 0,7 %, les **bâtiments agricoles** sont en deuxième position en ce qui concerne le taux de dommage. 56 % des bâtiments touchés ne sont pas des bâtiments d'habitation agricoles mais sont l'équivalent agricole des petits bâtiments et dépendances, soit des granges, des abris pour machines, des étables, des serres, etc. C'est pourquoi, les mêmes constatations que précédemment peuvent être faites sous une forme atténuée.

Le lien mentionné précédemment du taux de dommages correspondant à la relation surfaces/volumes est confirmé par le fait que **les bâtiments administratifs et les bâtiments publics** présentent des taux de dommages moins élevés (médiane 0,3 %). Ce genre de bâtiment est en général assez grand, entraînant ainsi un rapport plus favorable entre la surface de l'enveloppe du bâtiment et le volume (et la valeur d'assurance). Toute autre interprétation est difficile au vu des modes de construction très variables dans cette catégorie.

Avec une médiane de degré de dommage de bien 0,5 %, les **bâtiments d'habitation** occupent la troisième position. Ces bâtiments sont modernisés à intervalles relativement

rapprochés et des nouvelles. La part de constructions modernes est par conséquent relativement importante dans cette catégorie. On peut supposer que le taux élevé de dommages s'explique au moins en partie justement en raison de cette part élevée d'éléments de construction modernes : Ces derniers se dégradent en effet souvent rapidement et sont de ce fait plus vulnérables (stores, toits en fibres-ciment, revêtements en tôle, crépi sur isolation extérieure, avant-toits et coupoles en plastique). On ne peut que spéculer sur le rapport de cause à effet entre les attentes présumées plus élevées de la part des propriétaires de bâtiments d'habitation et le taux élevé de dommage.

Les taux de dommages les plus faibles concernent les **bâtiments de l'hôtellerie** (médiane 0,3 %). Cela peut paraître surprenant au premier abord car ces bâtiments ressemblent fortement aux bâtiments d'habitation en règle générale. Il existe toutefois une différence essentielle : ces bâtiments ont tendance à être bien plus résistants dans leur configuration. Malgré des changements de propriétaire relativement plus fréquents, l'affectation et l'aspect extérieur ne changent généralement pas pendant des décennies. Il est rare qu'un hôtel issu d'une longue tradition soit transformé du tout au tout. Quant aux nouvelles constructions, leur pourcentage est faible. Dans cette catégorie, les bâtiments répondant à des modes de construction plus anciens prédominent en moyenne. Avec leurs larges toits en tuile, leur



III. 17 : auberge de village typique, de construction « traditionnelle » : colombages crépis sous un large toit de tuiles et volets en bois. Ce genre de construction est comparativement plus résistant à la grêle (photo : C. Oesch).

maçonnerie crépie et leurs volets en bois, ils témoignent un certain attachement à la tradition et au confort chaleureux d'une maison tout en étant apparemment très résistants à la grêle (III. 17). Cette constatation devrait peut-être trouver plus d'écho dans les futurs projets de bâtiments d'habitation.

La même analyse a été faite à partir des données sur les dommages de mai 2009 dans le canton de Thurgovie. Afin

3. Analyse des dommages par genre et fonction des éléments de construction

de ne pas surcharger le graphique, seule la ligne de liaison entre les valeurs médianes de Thurgovie est visible sur l'ill. 16. Le tracé peu divergent de la ligne correspondante pour le canton d'Argovie révèle que les résultats ne sont pas dus au hasard mais qu'ils sont bien caractéristiques de ce type d'événement même pour d'autres cantons.

Il découle également de ce qui précède que le taux de dommage ne peut être assimilé à la vulnérabilité des matériaux constituant l'enveloppe d'un bâtiment. Un grand bâtiment de bureaux doté d'éléments de construction sensibles à la grêle n'enregistre qu'un faible taux de dommage en raison de l'importance de sa valeur même s'il est fortement endommagé. En revanche, même de petits dommages dans un abri de jardin de construction solide peuvent engendrer un taux de dommage élevé.

3. Analyse des dommages par genre et fonction des éléments de construction

3.1 Catégories de dommages

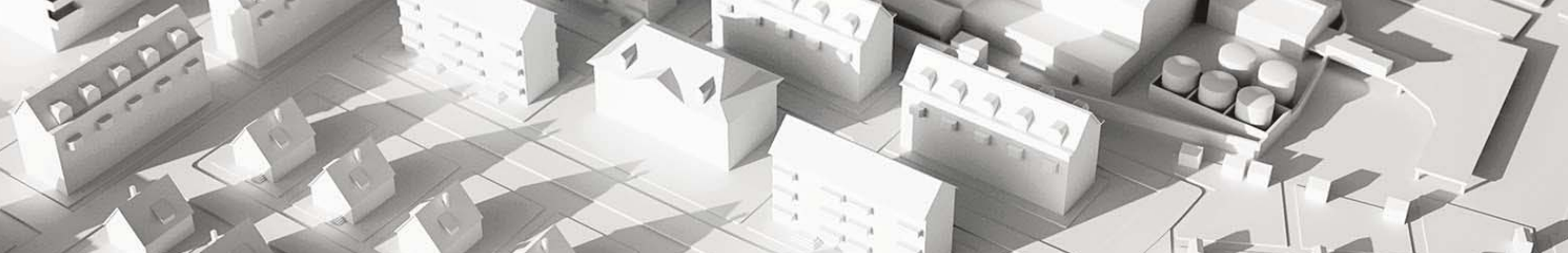
Afin d'étudier le profil des dommages survenus sur les bâtiments, les données concernant les dommages isolés fournies par l'établissement cantonal d'assurance d'Argovie ont été catégorisées selon les éléments de construction touchés. Ces données n'étant pas triées de manière détaillée dans le fichier de données sur les montants de dommages versés, on a eu recours à la place au fichier de données sur les montants de dommages budgétisés, qui est conçu avec plus de précision. Les 40 catégories d'éléments de construction suivants ont été déterminées sur cette base :

Toit
Avant-toits
Parois, façades
Fenêtres, vitrage
Volets
Stores
Stores de fenêtres de toit
Voile pare-soleil
Paravents
Portes, portails
Impostes, coupoles d'éclairage
Fenêtres de toit, lucarnes
Cheminées
Vérandas
Installations d'énergie solaire
Balcons
Garde-corps, balustrades
Boîtes aux lettres
Éclairage extérieur
Anémomètres et sondes solaires

Installations de chauffage
Installations de climatisation
Systèmes de ventilation
Installations sanitaires
Piscine (et couverture de piscine)
Revêtements de sol
Carreaux (faïence, carrelage)
Aménagements de cuisine
Éléments en tôle / en métal, travaux de ferblanterie
Travaux de menuiserie
Installations électriques, travaux d'électricité
Aménagements extérieurs
Travaux de nettoyage
Travaux d'assèchement
Direction des travaux
Échafaudages (provisoires)
Démontage, élimination
Autres (connus)
Inconnus
Adaptations du budget (non spécifié)

Si la désignation de la plupart des catégories parle quasiment d'elle-même, certaines méritent d'être précisées :

- La catégorie *Toit* prend en considération les dommages et les travaux de réparation sur la couverture (tuiles, fibres-ciment, lés d'étanchéité) ainsi que sur la toiture. Les panneaux en fibres-ciment translucides qui constituent des surfaces de toit sont également inclus dans cette catégorie. Les fenêtres de toit proprement dites ainsi que les éléments en tôle et en métal constituent en revanche leur propre catégorie.
- La catégorie *Parois*, façades englobe tous les dommages et travaux de réparation liés aux façades et aux parois extérieures, comme les travaux de peinture et de plâtrerie (réparations sur le crépi, sur l'isolation extérieure, sur les façades, sur les revêtements et nettoyage de façades).
- La catégorie *Stores* comprend les stores à lamelles (stores d'obscurcissement orientables), les volets roulants (stores à enroulement) et les stores en toile. Les voiles pare-soleil (éléments verticaux pouvant être installés par exemples sur les terrasses) et les stores sur les fenêtres de toit constituent par contre des catégories séparées.
- *Autres* englobe tous les éléments de construction qui sont certes mentionnés mais qui n'entrent dans aucune des catégories restantes ou pour lesquels aucune catégorie propre n'a été créée.
- *Inconnus* désigne des éléments de construction dont le bordereau ne permet pas de définir la nature; p. ex. si le fichier de données sur les dommages mentionne seulement «Travaux de peinture», il n'est pas clair si cela concerne des façades ou des (cadres de) fenêtres.
- Sous *Adaptations du budget* figurent les montants dont l'utilisation finale prévue n'est pas mentionnée dans le fichier de données sur les dommages.



Dans la suite de ce document, le terme « dommages » se rapporte aux sinistres déclarés à l'assurance. Ceux-ci sont décrits dans les données de l'établissement d'assurance et sont caractérisés par un montant (en francs suisses) et par un type de dommage (catégorie). Comme la distinction est établie par type de dommage, plusieurs dommages peuvent être consignés dans les données concernant un même bâtiment (par ex. dommages aux stores, à la toiture, à la façade et à la couverture de piscine). Un bâtiment est considéré comme « bâtiment endommagé » si un ou plusieurs sinistres ont été déclarés pour celui-ci.

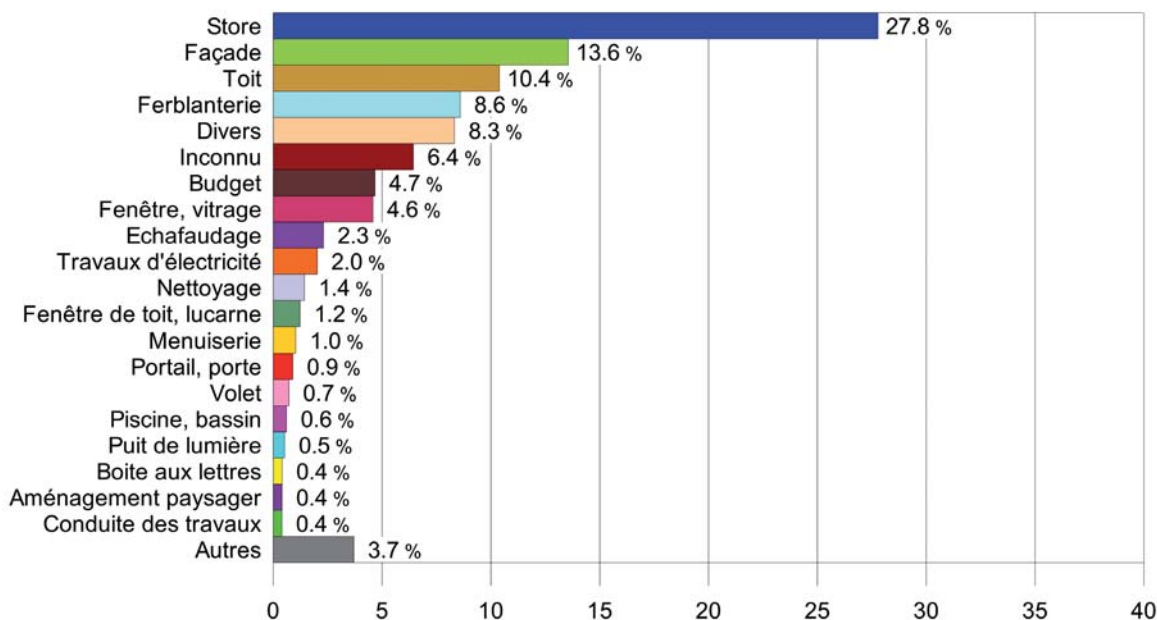
Il était prévu de comparer les chiffres de l'établissement cantonal d'assurance d'Argovie avec les chiffres de mai 2009 de l'établissement cantonal d'assurance de Thurgovie. Toutefois, les conditions d'assurance des deux ECA sont en partie divergentes. Par exemple, contrairement à l'ECA de Thurgovie, l'ECA d'Argovie assure les dispositifs textiles de protection solaire (stores extérieurs, voiles pare-soleil). Par ailleurs, les données sur les dommages des deux ECA étaient présentées sous des formes différentes pour l'analyse: les données analysées de l'ECA d'Argovie décrivent les dommages de manière relativement succincte, tandis que les décisions analysées de l'ECA de Thurgovie à l'attention de ses clients sont formulées de manière plus approfondie. C'est pourquoi, il n'était pas possible d'appliquer

la méthode d'analyse semi-automatique développée dans le cadre de l'étude de la grêle de 2009 (VBA-Script of Choffet et al., 2011 et IRV, 2012). L'analyse des données d'Argovie a donc été réalisée au moyen de critères de sélection ciblés directement dans les rapports de sinistres.

Pour les raisons invoquées, les catégories d'éléments de construction touchés analysées dans la présente étude divergent en partie par rapport à l'étude « Grêle 2009 » (UIR, 2012) et ne sont par conséquent comparables avec cette étude que de manière limitée. Des comparaisons avec l'événement 2009 ne seront donc effectuées qu'au cas par cas.

3.2 Répartition des dommages selon les éléments de construction touchés

Les 43'618 dommages³ dont la somme totale budgétisée s'élève à 155 millions de francs ont été analysés selon la part que représentent les différents éléments de construction touchés dans le nombre total de dommages (ill. 18) ainsi que selon la part du montant des dommages par rapport à la somme totale des dommages (ill. 22). En termes de nombre de dommages, c'est la catégorie « Stores » avec 12'119 cas, soit 27,8 % du nombre total de dommages, qui est seule en tête.



III. 18: pourcentage du nombre de dommages par éléments de construction. Exemple: les dommages de la catégorie stores représentent 27,8 % du nombre total de dommages (43'618 dommages au total).

³ 43'618 dommages partiels sont survenus sur 20'656 bâtiments. De nombreux bâtiments ont donc subi des dommages multiples (c'est-à-dire sur différents éléments de construction).



III. 19: *Dompage grêle typique sur un volet roulant : les grêlons ont provoqué des bosses bien marquées (photo : ECA d'Argovie).*



III. 21: *Dompage grêle typique sur un toit en eternit ondulé : les grêlons ont provoqué des éclatements et des fissures (non visibles sur la photo) (photo : ECA d'Argovie).*

Avec une part presque égale à la moitié de cette catégorie (13,6% ou 5'911 sinistres), la catégorie «Parois, façades» occupe la deuxième place. 4'530 cas, soit un pourcentage de 10,4%, sont à attribuer à la catégorie «Toits». Viennent ensuite les éléments en tôle et en métal avec 8,6% de sinistres qui nécessitaient des travaux de ferblanterie. Les trois catégories suivantes sont plus difficiles à cerner: il s'agit de sinistres sur des éléments de construction mentionnés certes dans les données de dommages mais pour lesquels aucune catégorie n'a été créée (réunis sous «Autres»). Ce sont aussi des sinistres et des adaptations de budget en rapport avec les éléments de construction non identifiables dans le fichier de sinistres. Viennent ensuite à nouveau des catégories concrètes telles que Fenêtres / vitrages, Coûts des échafaudages, Travaux d'électricité et de nettoyage, Fenêtres de toit / lucarnes ainsi que Travaux de menuiserie. Toutes les autres catégories se situent en dessous de 1% en ce qui concerne le nombre de sinistres. À elles seules, les trois plus grandes catégories (stores, façades et toits) représentent la majorité de tous les cas de sinistre avec 51,7%.

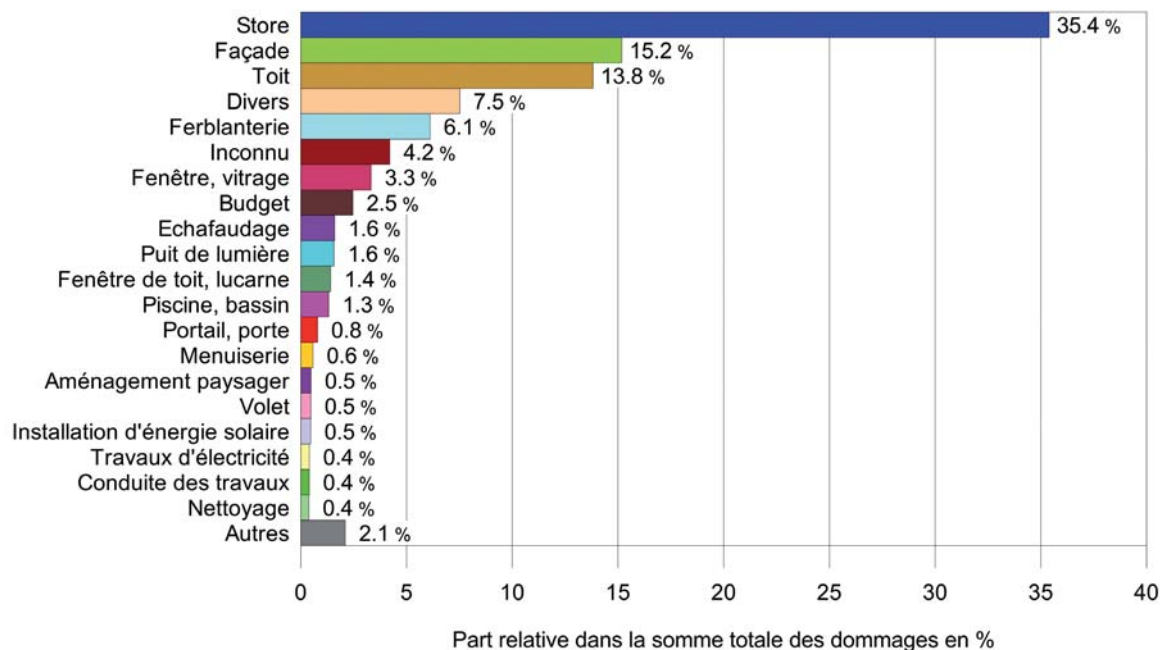
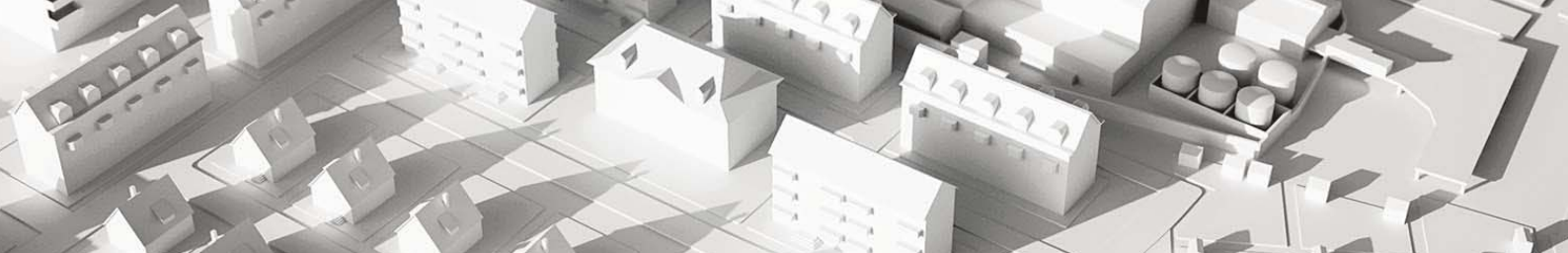


III. 20: *dompage grêle typique sur une façade : fissures et éclatements dans le crépi (photo : ECA d'Argovie)*

Les stores sont aussi très nettement en tête en ce qui concerne la somme totale des dommages (155 millions de francs). Ils en représentent 35,4% (54,8 millions de francs) (ill. 22). Une fois encore, les stores sont suivis des parois et façades dont la part de 15,2% (23,5 millions de francs) n'atteint même pas la moitié de celle des stores. Tout comme pour le nombre des cas de dommages, la catégorie «Toits» se trouve en troisième position avec 13,8% (21,4 millions de francs). Elle est rejointe derrière par les éléments en tôle et en métal, la catégorie «Inconnus», les fenêtres / vitrages, les adaptations de budget et les échafaudages.

Avec 1,6%, la catégorie «Impostes, coupoles d'éclairage» arrive ensuite. En ce qui concerne le nombre de dommages, elle ne représente que 0,5%. Il s'agit donc ici apparemment de montants de dommages élevés au-dessus de la moyenne (vraisemblablement en raison de dommages subséquents dus aux infiltrations d'eau de pluie). Il en est de même pour les piscines qui représentent 1,3% du montant des dommages, derrière les Fenêtres de toit et les lucarnes, ce qui correspond en nombre à 0,6% seulement. Toutes les catégories restantes se situent en dessous de 1% en ce qui concerne le montant des dommages.

Les trois catégories Stores, Parois et Façades ainsi que les Toits sont responsables à elles seules de presque les deux tiers (64,4%) du montant total des dommages. Elles s'avèrent être ainsi de loin les principaux facteurs de coûts dans les dommages grêle du canton d'Argovie. Il est vrai que ceci n'est pas étonnant si l'on considère la large proportion, en termes de surface, de ces trois types éléments de construction sur les bâtiments.



III. 22: pourcentage du montant de dommages par élément de construction. Exemple: les dommages de la catégorie stores représentent 35,4 % du montant total des dommages qui s'élève à 155 millions de francs.

3.3 Analyse des dommages suivant le matériau des éléments de construction

Les bordereaux de sinistre de l'ECA de Thurgovie analysés dans le cadre de l'étude 2009 (UIR, 2012) faisaient souvent également mention du matériau des éléments de construction endommagés. Les possibilités d'analyse des données sur les dommages fournies par l'établissement cantonal d'assurance d'Argovie sont très limitées en raison des formulations plus succinctes. Environ 2/3 des sinistres ont dû être attribués à la catégorie « Inconnus » pour manque d'informations sur le matériau.

S'il est possible de déduire assez clairement le type de matériau à partir de certains éléments de construction et travaux de réparation (p. ex. « revêtement en eternit », « stores en toile », « toiture en tôle »), ce n'est pas le cas pour d'autres (« volets », « stores », « couverture de toit »). L'analyse a donc été systématiquement faussée. C'est pour cette raison que les résultats de l'analyse des matériaux ne sont pas repris ici.

3.4 Coût moyen des dommages par élément de construction

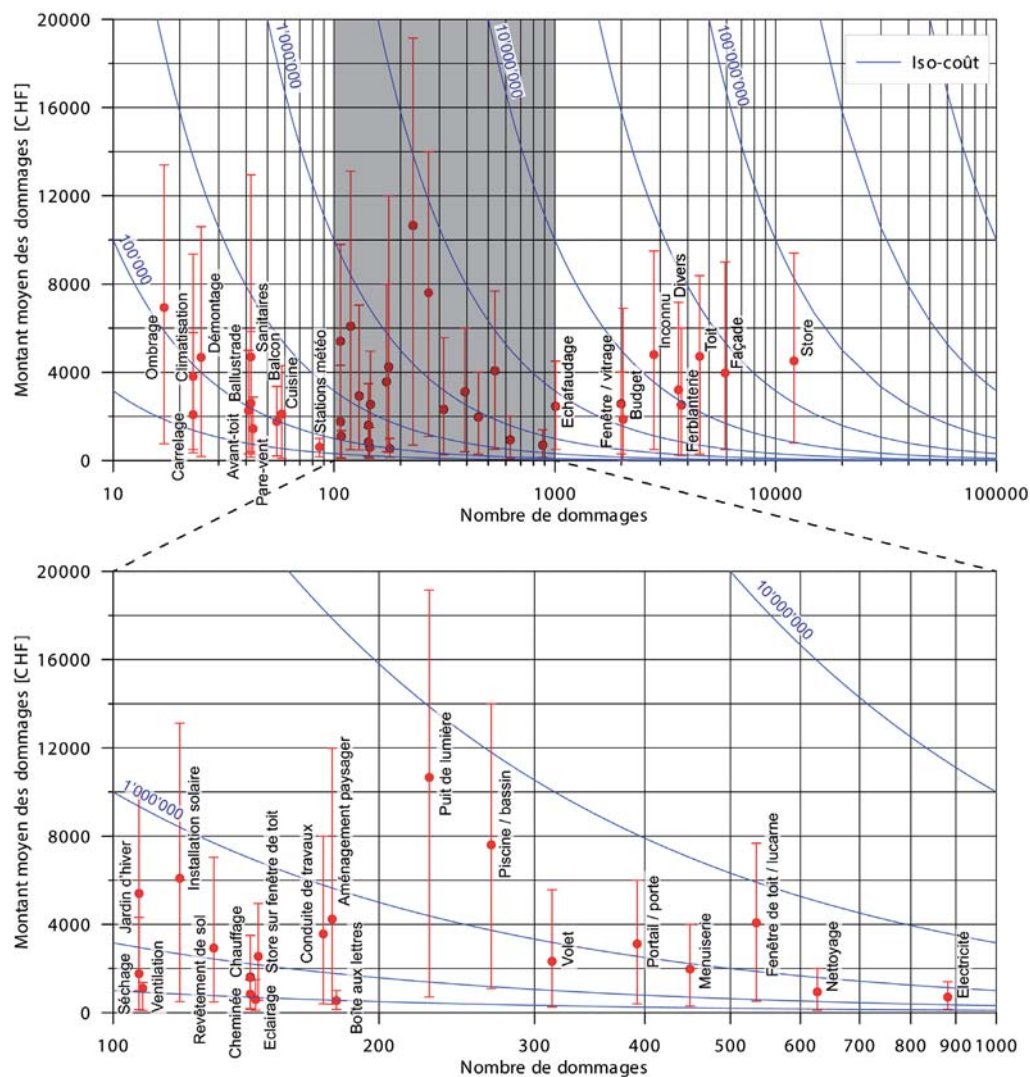
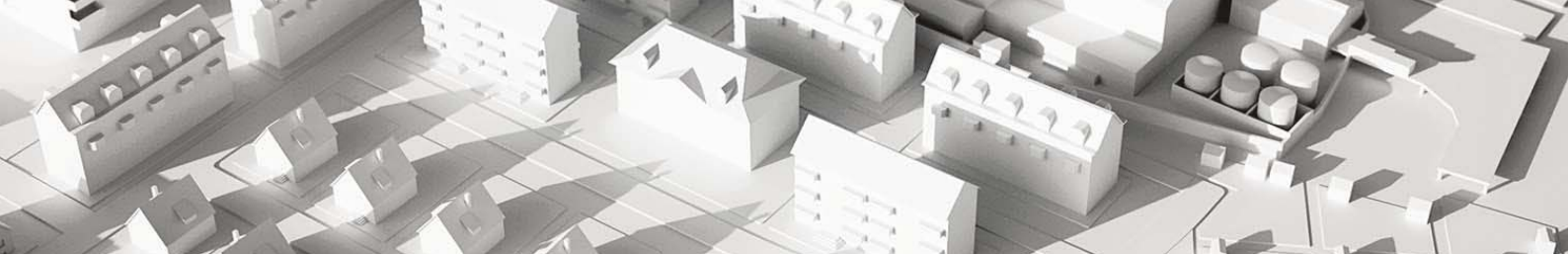
Il est possible de calculer le coût moyen des dommages par catégorie à partir de la somme et du nombre de dommages. Avec un montant moyen de 10'667 francs par cas, les dommages sur les impostes / coupoles d'éclairage sont en tête (voir ci dessus). Ils sont loin devant la deuxième catégorie, les piscines (et leur couverture), qui représente 6'944 francs.

Viennent ensuite les voiles pare-soleil avec 6'609 francs et les installations d'énergie solaire avec 6'095 francs.

Avec 4'727 francs, les toits se trouvent à la septième position sur les 40 catégories. Les stores (la catégorie la plus importante en termes de nombre et de montant des dommages) occupent la dixième place avec 4'526 francs. Ainsi, les catégories d'éléments de construction qui contribuent le plus aux dommages totaux (stores, façades, toits) ne sont pas en tête en ce qui concerne la moyenne du montant des dommages par élément de construction. Il convient toutefois de préciser que la représentativité du coût moyen des dommages dépend du nombre de dommages dans chaque catégorie. En effet, dans une catégorie contenant un nombre de 10 dommages, un dommage deux fois supérieur au montant moyen va augmenter le montant moyen de 10 %, alors que pour une catégorie de 100 dommages, cette augmentation sera de 1 %, et elle ne sera plus que de 0,1 % pour une catégorie comprenant 1000 dommages. Afin de mieux se rendre compte de l'importance de chaque catégorie, l'ill. 23 met en relation le nombre de cas par catégorie d'élément de construction avec le coût moyen de ces dommages. Les « antennes » sur le graphique illustrent la dispersion partiellement vaste des montants des dommages isolés pour les différentes catégories.

3.5 Comparaison avec l'événement de mai 2009 dans le canton de Thurgovie

La comparaison des parts en pourcentage des différentes catégories d'éléments de construction dans le canton



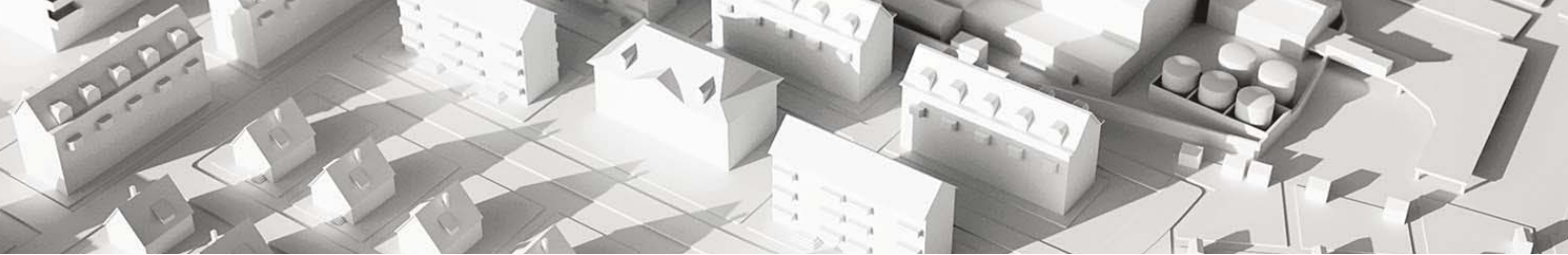
III. 23: nombre de dommages par catégorie d'éléments de construction et montant moyen des dommages de ces catégories. Les lignes d'iso-coût représentent des lignes pour lesquelles le montant total des dommages (nombre de dommages multipliés par le coût moyen) est identique. Les catégories importantes pour le montant total des dommages ont ainsi tendance à se situer en haut à droite et les moins significatives sont en bas à gauche. Le bas et le haut des barres d'erreur, les «antennes», marquent les quantiles de 10% et 90%.

d'Argovie avec les chiffres correspondants de l'événement de grêle du 26 mai 2009 dans le canton de Thurgovie révèle quelques divergences intéressantes en dépit des réserves déjà émises sur la comparabilité.

La part en pourcentage des cas de sinistres dans la catégorie «Stores» est identique dans les deux cantons avec presque 30% du nombre total de dommages (ill. 25). Ce qui est surprenant au premier abord car l'averse de grêle a eu lieu en pleine nuit en Argovie et dès la fin de l'après-midi en Thurgovie. Mais si l'on compare la proportion des stores par rapport au montant des dommages pour les deux cantons, les chiffres sont remarquablement plus élevés dans le canton d'Argovie. Il n'y a pas eu plus proportionnellement de

stores endommagés en Thurgovie mais les stores ont subi des dommages nettement plus coûteux. L'explication la plus plausible est que dans les deux cantons au moment de l'averse de grêle, au moins un store était descendu sur la plupart des bâtiments touchés. Un sinistre de grêle sur des stores a été recensé pour ces bâtiments et la proportion par rapport au nombre de dommages était identique dans les deux cantons.

Toutefois, comme l'averse de grêle en Argovie est survenue pendant la nuit, les stores descendus sur chaque bâtiment étaient proportionnellement nettement plus nombreux, si bien qu'une plus grande surface de stores était exposée à la grêle. Par conséquent, les montants des dommages pour



les stores sur les bâtiments qui en étaient pourvus étaient en moyenne plus élevés. L'heure à laquelle s'est produit l'événement a donc eu une influence décisive sur les sinistres : non pas en ce qui concerne le nombre de bâtiments présentant des stores endommagés mais en ce qui concerne le montant des dommages.

Cette constatation confirme l'utilité des systèmes de commande qui déclenchent l'enroulement automatique des stores en cas de menace de grêle. Un système de ce type se trouve actuellement en phase de test (cf encadré).

Projet «Alerte grêle pour relever à temps les équipements de protection solaire» de la fondation de prévention des Établissements cantonaux d'assurance.

En collaboration avec SRF Meteo et d'autres partenaires, l'AEAI a développé un système moderne d'alerte grêle pour protéger les stores et d'autres équipements de protection solaire. Dès qu'un bâtiment est menacé par un danger de grêle accru, SRF Meteo envoie un signal à un système électronique de gestion du bâtiment. Ensuite, les stores remontent automatiquement et sont épargnés par la grêle. Quand l'averse de grêle est terminée, un deuxième signal fait en sorte que les stores reviennent dans leur position antérieure.

Pour que le dispositif d'alerte soit en mesure de prévenir efficacement les dommages, une fiabilité maximale est requise. Les prévisions correspondantes nécessitent des calculs complexes et coûteux, eux-mêmes basés sur des modèles météorologiques dont les données proviennent des radars, des éclairs et des stations météorologiques. Le système a également recours à des analyses statistiques. Il calcule en tout plus de 714 millions de valeurs par jour, ce qui permet d'établir une prévision grêle fiable toutes les 5 minutes. Si un événement a lieu, le signal est transmis aussi bien par Internet que par SMS à l'appareil de commande.

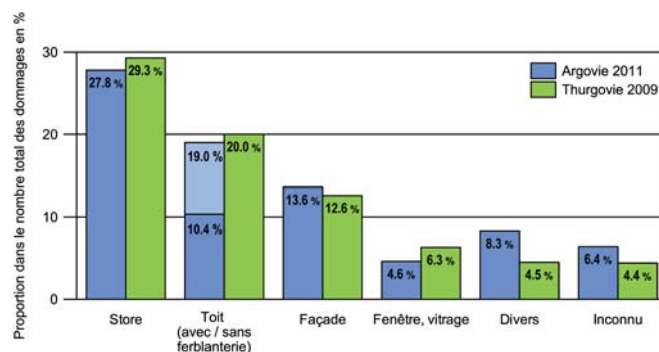
Le système d'alerte est encore actuellement en phase de test. Cette phase dure au total trois ans et se terminera à la fin de l'année 2015.

Dans la catégorie «Toit», avec 10,4%, la proportion de dommages aux toits correspond à seulement la moitié du nombre relevé dans le canton de Thurgovie pour lequel l'étude grêle de 2009 (UIR, 2012) indiquait 20%: À ce sujet, il faut toutefois noter que le contenu de la catégorie «Toit» n'est pas le même dans les deux études.

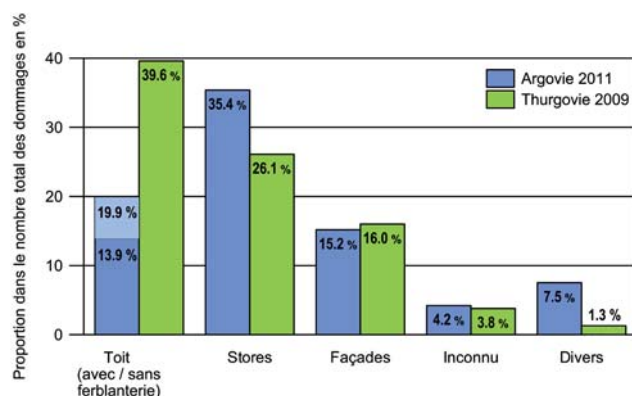
Les chiffres sur les sinistres aux parois et aux façades suivent un modèle semblable : par rapport à l'événement de Thurgovie, si la part quantitative des façades endomma-

gées est légèrement plus élevée, elle est toutefois plus faible si l'on regarde le montant des dommages. Notons à cet égard que la part élevée des stores en termes de montant des dommages dans le canton d'Argovie diminue celle des autres catégories. La catégorie «Autres» a aussi le même effet. Elle est beaucoup plus forte dans le canton d'Argovie que dans le canton de Thurgovie. C'est pour cette raison que la comparaison des chiffres entre les deux cantons n'est possible qu'avec certaines réserves.

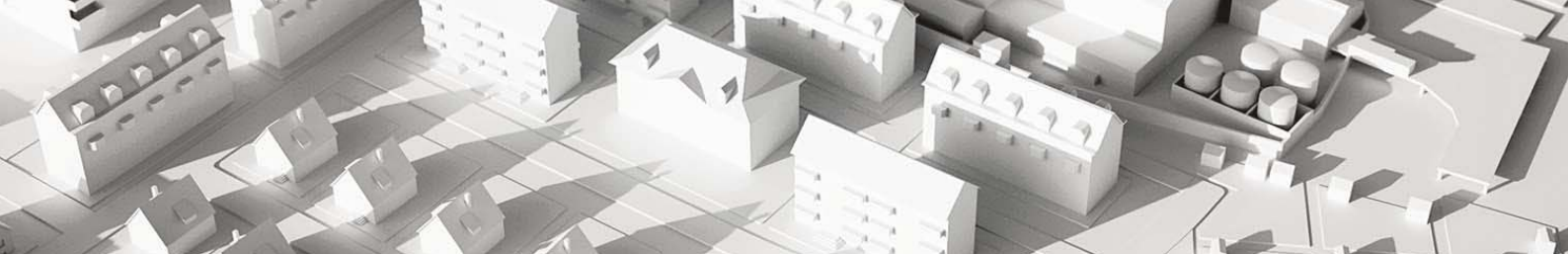
En un mot, tant en Thurgovie qu'en Argovie, les stores, les toits et les parois / façades représentent les plus importants facteurs de coûts. Une situation qu'il convient de prendre en considération pour les mesures de prévention (p. ex. Répertoire suisse de la protection contre la grêle).



III. 24: comparaison de la proportion du nombre de dommages par éléments de construction par rapport au nombre total des dommages entre l'événement du canton d'Argovie en 2011 et celui de Thurgovie en 2009.

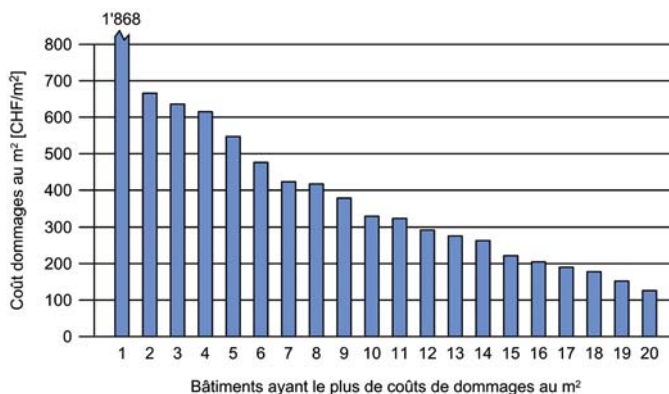


III. 25: comparaison de la proportion du montant de dommages par éléments de construction par rapport au montant total des dommages entre l'événement du canton d'Argovie en 2011 et celui de Thurgovie en 2009.



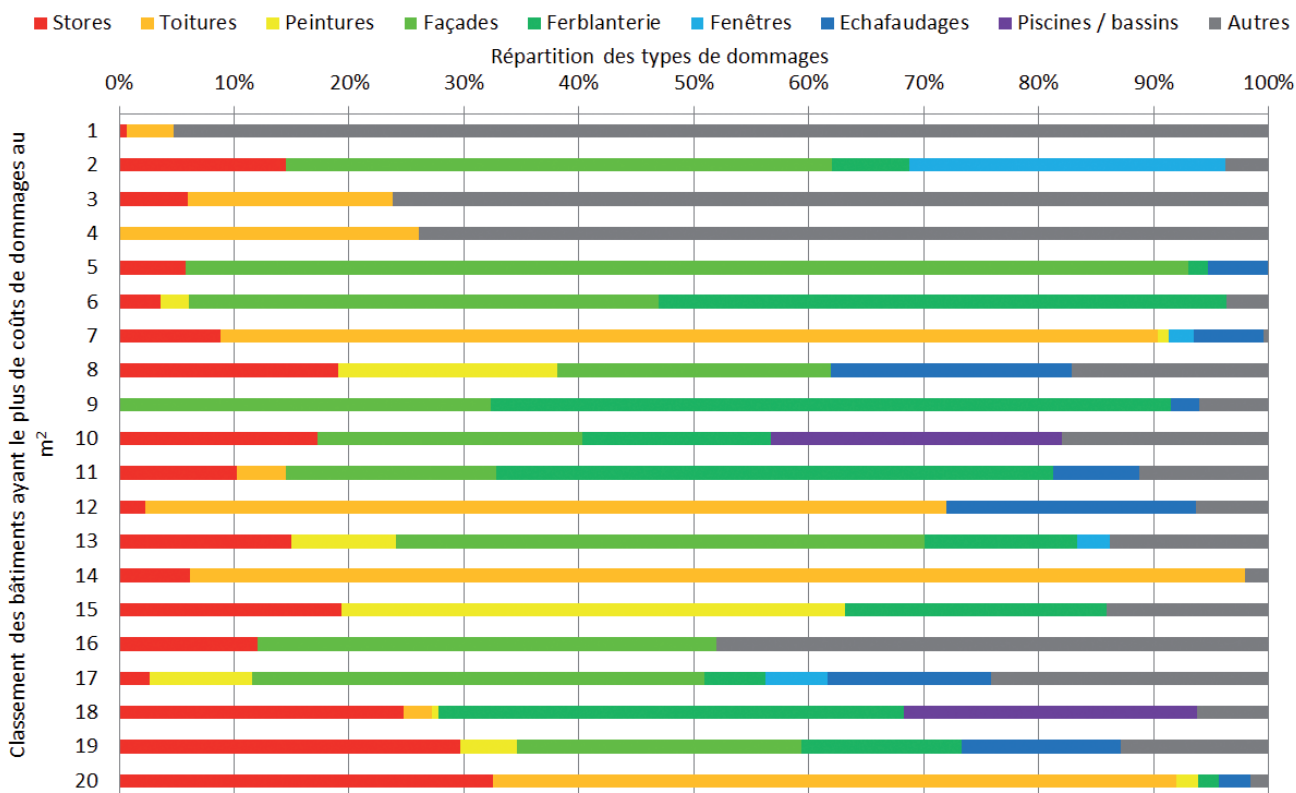
3.6 Les vingt bâtiments ayant les dommages les plus chers au m²

Les dommages d'un montant particulièrement élevé présentent un certain intérêt. Les vingt bâtiments avec les montants de dommages les plus élevés par surface au sol ont donc fait l'objet d'une analyse plus approfondie (ill. 26). C'est surtout le bâtiment atteignant une valeur maximum extraordinaire de 1'868 francs/m², soit un montant total des dommages de près de 375'000 francs, qui ressort de l'analyse. Les données ne permettent malheureusement pas d'attribuer précisément la majeure partie de ce montant élevé pour ce bâtiment à une catégorie d'élément de construction concrète (ill. 27). Avec un montant de dommages de 660 francs / m² de surface, le bâtiment occupant la deuxième place se trouve nettement en retrait. Dans ce bâtiment, c'est la façade qui est responsable de la plus grande partie du montant. À la vingtième position, ce montant atteint finalement 126 francs/m².

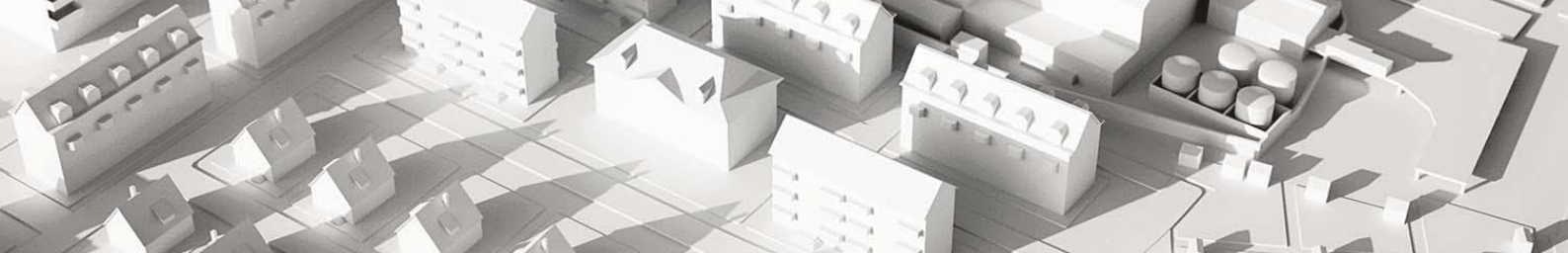


III. 26: les vingt bâtiments ayant les dommages les plus chers au m². La colonne avec la valeur maximale de 1'868 francs / m² a été coupée pour permettre une meilleure lisibilité du graphique.

Selon la description contenue dans le fichier de dommages, les stores, les toits, les façades et les éléments en tôle et en métal constituent également la majeure partie du montant des dommages pour ces vingt bâtiments.



III. 27: répartition des dommages par catégorie d'élément de construction pour les vingt bâtiments présentant le montant de dommages le plus élevé par surface au sol



Installations d'énergie solaire: une épée de Damoclès pour les établissements cantonaux d'assurance?

Dès l'événement de grêle de 2009 dans le canton de Thurgovie (Choffet et al., 2011; UIR, 2012), la question s'est posée: les installations d'énergie solaire pourraient-elles finir par poser problème aux ECA? Toujours est-il que l'on peut s'attendre à ce que le «virage énergétique» recherché, en vue de s'éloigner du fossile et de se rapprocher du renouvelable, continue de faire augmenter le nombre d'installations d'énergie solaire sur les toits. Les chiffres des ventes d'éléments photovoltaïques montrent que c'est bien le cas (Swissolar, 2012): entre 2007 et 2012, la puissance photovoltaïque vendue chaque année en Suisse a fait un bond de presque 10'000 kW à pratiquement 160'000 kW. La «rétribution à prix coûtant du courant injecté (RPC)» allouée depuis le 1er janvier 2009 a sûrement sa part de responsabilité dans le «boom photovoltaïque».

L'avancée des collecteurs thermiques est un peu moins forte mais quand même évidente: la surface des collecteurs thermiques vendue par année a presque doublé entre 2007 et 2012.

Certaines inquiétudes découlent du fait que le montant moyen des dommages sur les installations d'énergie solaire était relativement élevé par rapport à d'autres éléments de construction, tant en mai 2009 qu'en juillet 2011. Comme le montrent les chiffres de l'analyse de l'événement de grêle de juillet 2011, le dommage moyen des installations d'énergie solaire touchées correspond à:

- environ 1,3 fois celui des toits ou des stores
- bien 1,5 fois celui des parois et façades,
- environ 2,4 fois celui des éléments en tôle et en métal.

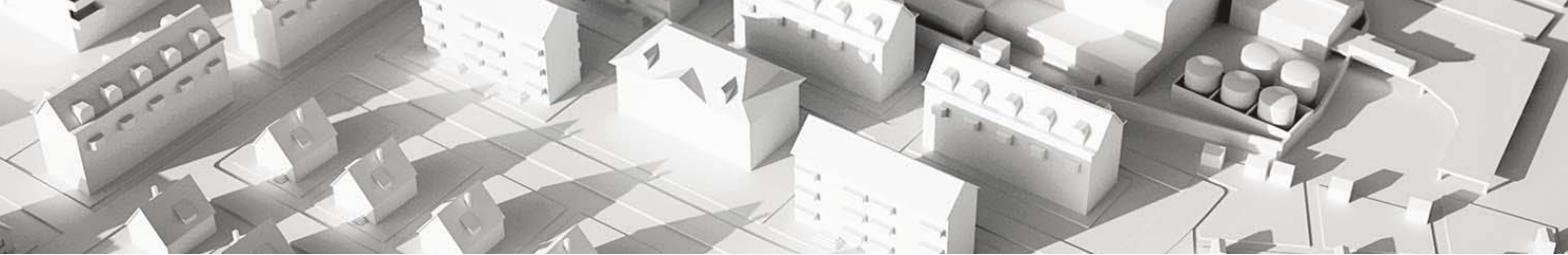
Faut-il donc s'attendre à l'avenir à une forte augmentation des coûts des dommages dus à la grêle à cause de l'utilisation croissante d'installations d'énergie solaire?

La réponse n'est pas si simple. La part des dommages sur les installations d'énergie solaire est actuellement assez insignifiante dans les chiffres absolus et en comparaison avec d'autres éléments de construction. Son importance à l'avenir ne peut être évaluée qu'à condition de savoir ce que représente la part des installations d'énergie solaire endommagées par rapport à leur nombre total. C'est là le seul moyen d'en déterminer la vulnérabilité et l'évolution future. D'importants moyens sont toutefois nécessaires pour connaître le nombre des installations d'énergie solaire en place. Le fait est que le problème a aussi été reconnu par les fabricants.



III. 28: en haut, élément photovoltaïque défectueux. En bas, capteur à tubes endommagé (photos: ECA d'Argovie).

Par le passé, les capteurs à tubes se sont révélés particulièrement sensibles aux averses de grêle. Ils ne représentent cependant que 10% environ des surfaces de capteurs installées en Suisse. Pour ce type de construction, il est par ailleurs possible de remplacer des tubes individuellement afin de limiter éventuellement le sinistre. Un coup d'œil au Répertoire suisse de la protection contre la grêle (www.rpgonline.ch) montre toutefois qu'aujourd'hui les collecteurs à tubes et les collecteurs plats sur le marché présentent des degrés de résistance à la grêle de 3 et 4. Des éléments photovoltaïques atteignent même des degrés de résistance à la grêle de 5. Ce n'est donc pas l'existence ou non de produits résistants à la grêle qui pose problème, mais le fait que ces produits soient installés ou non. Et comme pour tout, ici aussi: la qualité a un prix. Les établissements cantonaux d'assurance doivent donc réussir à rendre les architectes et les maîtres d'ouvrage attentifs aux différences de qualité. Ils doivent leur démontrer qu'une variante moins chère au départ peut s'avérer être une fausse solution. Il convient d'évoquer au moins l'éventualité d'exclure les installations qui ne résistent pas suffisamment à la grêle.



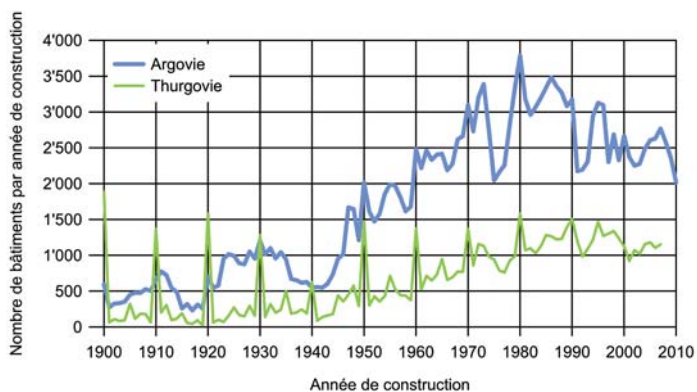
3.7 Dommages en fonction de l'année de construction

Dans l'étude 2009, l'analyse des sinistres en fonction de l'année de construction des bâtiments touchés a abouti à des résultats dont on pouvait tirer des conclusions intéressantes sur la sensibilité à la grêle ainsi que sur les attentes de la clientèle. Un point restait toutefois incertain: s'agissait-il de résultats spécifiques aux cas en question ou bien les résultats pouvaient-ils être transposés à d'autres événements de grêle et d'autres cantons? On a ainsi pu constater une nette augmentation de la vulnérabilité entre les bâtiments d'habitation anciens et récents. De plus, les données étayaient la thèse selon laquelle des propriétaires d'habitations neuves déclarent leurs sinistres de manière particulièrement pointilleuse.

Comme pour la publication UIR (2012), le nombre de bâtiments touchés selon leur année de construction a aussi fait l'objet d'une analyse dans le canton d'Argovie.

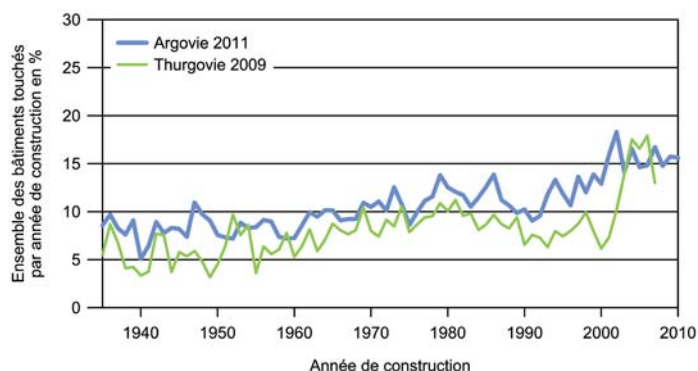
Afin de pouvoir procéder à une comparaison avec l'événement du 26 mai 2009, les bâtiments construits à partir de 1935 ont été analysés (18'972 bâtiments endommagés). Comme dans le canton de Thurgovie, la part des bâtiments datant d'avant 1945 est faible: l'essor économique d'après-guerre se reflète nettement dans l'augmentation marquée du nombre de bâtiments (ill. 29). Sans oublier bien sûr que bon nombre de bâtiments anciens ont été démolis entre temps et ont été remplacés par des neufs. Mis à part les pics tous les dix ans (1900, 1910, 1920...) qui sont sensiblement moins marqués sur la courbe d'Argovie, les deux courbes suivent la même évolution si l'on considère que la population du canton d'Argovie équivaut à plus du double de celle du canton de Thurgovie. On reconnaît nettement sur les deux courbes par exemple les baisses au milieu des années 1970 et au début des années 1990 (périodes de récession économique).

Ill. 30 présente le pourcentage de bâtiments endommagés par les événements de grêle de mai 2009 ou juillet 2011 par rapport à l'ensemble des bâtiments existants pour chaque année de construction à partir de 1935.



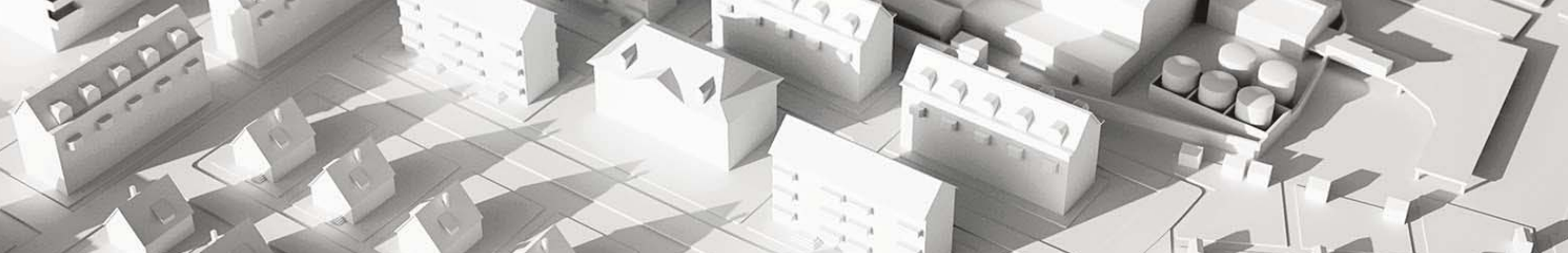
Ill. 29: nombre de bâtiments par année de construction dans les cantons d'Argovie et de Thurgovie.

Cela compense ainsi le fait que, comme indiqué sur l'ill. 29, le nombre de bâtiments existants par année de construction est très différemment élevé. Les courbes permettent ainsi de mettre en évidence une sensibilité moyenne à la grêle des bâtiments existants pour chaque année de construction. Lors de la comparaison directe des deux courbes, il ne faut pas oublier que le pourcentage ne dépend pas seulement de la sensibilité à la grêle mais aussi de l'intensité de l'événement. Il apparaît donc plus probable que l'averse de grêle dans le canton d'Argovie ait été en fait plus intense et/ou plus étendue et non pas que les bâtiments de ce canton soient plus sensibles à la grêle. Les deux courbes ont en commun une augmentation de la proportion de bâtiments endommagés au fur et à mesure que l'on avance dans les années de construction. Dans le canton de Thurgovie, les valeurs sont multipliées par trois par rapport aux valeurs de départ. Elles sont presque doublées dans le canton d'Argovie. En raison du plus grand nombre de bâtiments, la courbe d'Argovie évolue de manière plus régulière. Une nette augmentation apparaît toutefois ici aussi entre les années 1990 et 2000. Tandis que 8% environ des bâtiments des années 1940 ont subi des dommages, ce fut le cas pour près de 15% des bâtiments construits après l'an 2000.

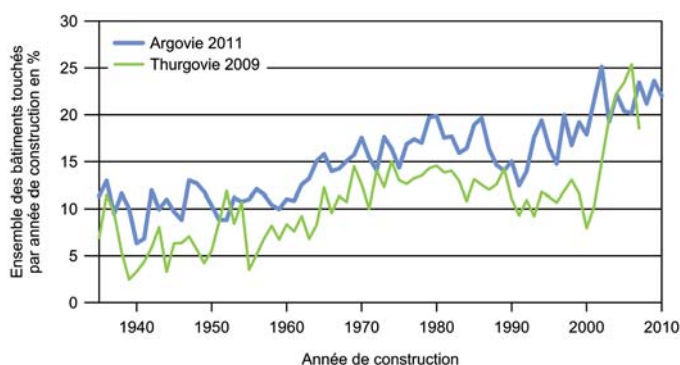


Ill. 30: pourcentage de bâtiments endommagés sur l'ensemble des bâtiments existants dans les communes concernées en Argovie et Thurgovie en fonction de leur année de construction.

Comme pour le canton de Thurgovie dans l'étude «Grêle 2009» (UIR, 2012), les bâtiments d'habitation d'Argovie (code d'affectation 20 - 29) ont été traités séparément (ill. 31). La courbe correspondante révèle une augmentation marquée et relativement régulière à partir des années de construction autour de 1990. La courbe d'Argovie ne présente pas de pic abrupt comme celui de la courbe de Thurgovie à partir de l'an 2000. Le bond de Thurgovie a été interprété dans l'étude précédente par le fait que les propriétaires avaient déclaré particulièrement consciencieusement leurs sinistres sur leurs bâtiments quasi neufs car, habituellement, le premier dommage survenu sur un objet neuf affecte particulièrement le propriétaire.

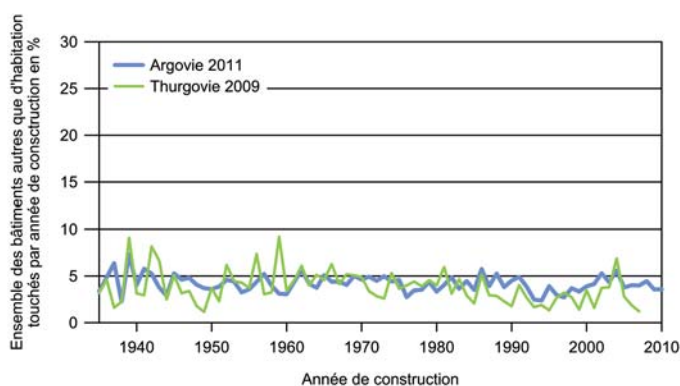


Les données d'Argovie ne contredisent au moins pas cette interprétation car le même niveau y est atteint. Les valeurs tournent en effet entre 20 et 25 %. Il est intéressant de constater que la courbe d'Argovie révèle une légère tendance à la baisse entre les années de construction de 1980 à 1990, tout comme la courbe de Thurgovie. Une analyse du mode de construction des habitations pendant les périodes en question ainsi qu'au cours des années antérieures et ultérieures serait à cet égard intéressante, quoique difficile.



III. 31 : pourcentage d'habitations endommagées (affectation 20–29 du code AEA) sur l'ensemble des habitations existantes dans les communes concernées en **Argovie** et **Thurgovie** en fonction de leur année de construction

L'ill. 32 présente les courbes correspondantes pour les bâtiments autres que des habitations (codes d'affectation 10–19 ou 30–90). Les deux courbes évoluent de manière très rapprochée dans les niveaux inférieurs et ne montrent pas de tendance claire. Dans le canton d'Argovie, les pourcentages varient entre 4 et 7 % et sont donc ainsi bien en dessous de ceux des habitations. Le problème d'une augmentation de la vulnérabilité à la grêle ou en tout cas de la plus forte sensibilité des propriétaires de bâtiments récents n'est

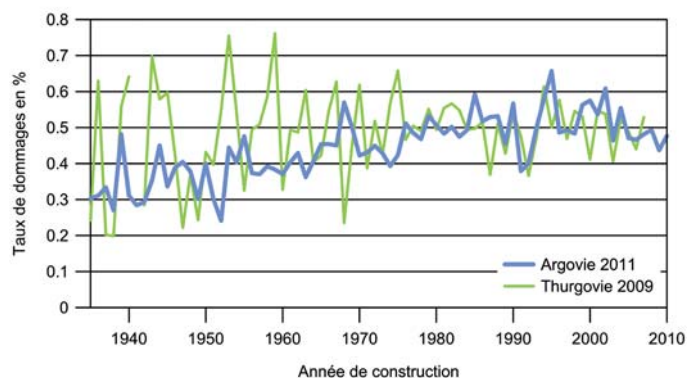


III. 32 : pourcentage de bâtiments autres qu'habitations (affectation 10–19 ou 30–90 du code AEA) sur l'ensemble des bâtiments existants autres qu'habitations dans les communes concernées en **Argovie** et **Thurgovie** en fonction de leur année de construction.

pas manifeste ici. Cela est quelque peu surprenant quand on pense que les bâtiments industriels modernes sont recouverts de tôle et de lés d'étanchéité.

Il est possible d'expliquer en partie les valeurs plus faibles des bâtiments sans affectation d'habitation par le fait que les ECA et les clients s'entendent plus fréquemment que dans le cas d'une habitation sur une indemnité partielle pour des dommages esthétiques et non fonctionnels (p. ex. bosses sur les revêtements en tôle), en particulier si les parties touchées ne sont que peu visibles.

Les courbes présentées précédemment se réfèrent uniquement au pourcentage de bâtiments touchés par année de construction, l'étendue des sinistres n'étant pas prise en considération. Mais la thèse d'une augmentation de la vulnérabilité est-elle aussi étayée par le taux de dommage, c'est-à-dire le rapport entre le montant des dommages et la valeur d'assurance (en d'autres termes : la part des valeurs détruites) ? L'analyse correspondante pour les cantons d'Argovie et de Thurgovie (ill. 33) montre en effet pour les deux courbes une légère augmentation partant d'environ 0,4 % pour atteindre près de 0,5 % entre les bâtiments anciens et les bâtiments récents. La modification est mineure mais elle peut aboutir à des montants non négligeables pour un gros événement : pour un bâtiment d'habitation moyen d'Argovie (code d'affectation AEA 20) avec une valeur d'assurance de 900'000 francs, l'augmentation du taux de dommage de 0,1 pour cent signifie tout de même un montant de dommage plus élevé de 900 francs. Au vu des 120'000 bâtiments d'habitation environ, dont près de 14 % ont été touchés en 2011, l'économie réalisable lors d'un événement de grêle comparable pourrait être de l'ordre de 10 millions de francs si l'on parvenait à rendre les bâtiments modernes aussi résistants à la grêle que ceux des années 40 !



III. 33 : valeurs médianes des taux de dommages des bâtiments d'habitation endommagés (affectation 20–29) dans les cantons d'Argovie et Thurgovie en fonction de l'année de construction.

4. Potentiel d'économie par l'utilisation d'éléments de construction avec un indice de résistance à la grêle $RG \geq 3$

4. Potentiel d'économie par l'utilisation d'éléments de construction avec un indice de résistance à la grêle $RG \geq 3$

D'après la carte des dangers de grêle de l'Association des établissements cantonaux d'assurance incendie (ECA, 2007), un bâtiment dans le canton d'Argovie se retrouve environ une fois tous les 50 ans exposé à une averse de grêle avec des grêlons de ≥ 3 cm. L'AEAI recommande donc pour le canton l'utilisation d'éléments de construction présentant un indice de résistance à la grêle de 3 et plus, afin de leur permettre de résister au moins à des grêlons d'un diamètre pouvant atteindre 3 cm. Les répercussions sur le montant des dommages d'une utilisation notable de ce type d'éléments de construction sont évaluées grâce à une analyse correspondante de l'événement de juillet 2011.

Dans un souci de simplification, on a admis que les bâtiments n'avaient subi aucun dommage en dehors des zones où la carte radar avait enregistré les grêlons de plus de 3 cm le jour de l'événement. Ces bâtiments ont été exclus au moyen d'une analyse SIG, leur contribution au montant total des dommages a été déterminée et cette part a été déduite (ill. 34). L'analyse a abouti aux résultats suivants :

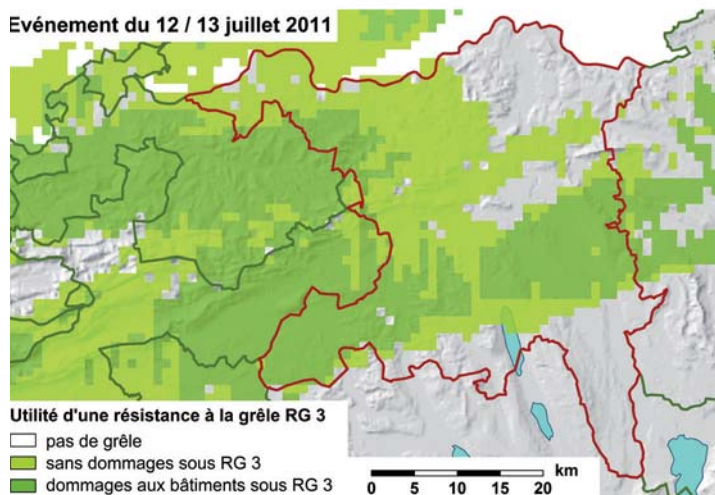
sur les 18'000 bâtiments environ endommagés et géoréférencés, environ 4'100 se situent en dehors de la zone d'intensité où sont tombés des grêlons de plus de 3 cm. Ils ont participé à hauteur de 17 % environ au montant total des dommages de 151 millions de francs (bruts) ou 145 millions de francs (nets). En d'autres termes : l'utilisation importante d'éléments de construction aurait permis d'empêcher environ 25 millions de francs de dommages. L'établissement cantonal d'assurance d'Argovie aurait économisé près de 24 millions de francs en indemnités (la différence correspond à la franchise des propriétaires).

Après l'événement du 23 juillet 2009, le potentiel d'économie pour les cantons de Vaud, Fribourg, Berne et Lucerne a été évalué dans l'étude portant sur ce sujet entre 5 et 15 %, ce qui correspond à la somme de 15 à 40 millions de francs (UIR, 2012).

Il s'agit bien sûr d'une simplification sommaire puisque l'on a supposé qu'absolument aucun sinistre n'était survenu dans les régions où les grêlons présentaient un diamètre ≤ 3 cm. On peut considérer en outre qu'une application conséquente de la consigne $RG \geq 3$ aurait contribué à réduire les dommages également dans les régions touchées par des grêlons plus gros. Par ex. les coupoles d'éclairage à double vitrage ou les toits en fibres-ciment auraient été certes endommagés mais sans être complètement brisés, ce qui aurait permis d'éviter des dommages supplémentaires dus à l'infiltration des eaux de pluie. Par ailleurs, les tailles de grêlons déterminées à partir des données radar ne sont pas des valeurs exactes et on ne connaît pas non plus la part des éléments de construction déjà installés à ce jour présentant un indice $RG \geq 3$ sur l'ensemble des bâtiments assurés par l'ECA d'Argovie. La valeur de 17 % pour le potentiel d'économie ne doit donc pas être considérée comme un chiffre exact. Ce chiffre est toutefois tout à fait plausible et il justifie de façon saisissante le potentiel de cette mesure de prévention.

Remonter les stores pendant une averse de grêle constitue une mesure encore plus efficace pour faire diminuer les sinistres : comme le montre l'ill. 22, le potentiel d'économie correspondant pour juillet 2011 aurait atteint 35,4 % de la somme totale des dommages, ce qui équivaut à environ 50 millions de francs en chiffres absolus. Peu importe que les stores soient remontés à la main ou automatiquement. En cas d'intervention manuelle, il est toutefois difficile, pour des raisons évidentes, de garantir la fiabilité requise.

Le projet AEA « Alerte grêle », décrit à l'alinéa 3.5, pour que se déclenche automatiquement la remontée des stores, vise justement à combler cette lacune



Ill. 34 : étendue des régions touchées par des grêlons > 3 cm (vert foncé) et ≤ 3 cm (vert clair) dans le canton d'Argovie selon les données radar de meteoradar (cf ill. 1). Zones non colorées : soit elles n'ont pas été touchées par l'averse, soit c'est du grésil et/ou de la pluie qui est tombé (bases cartographiques : swisstopo).

5. Analyse de la relation dommages – orientation des bâtiments

5. Analyse de la relation dommages – orientation des bâtiments

5.1 Introduction

S'il est connu que l'altération des matériaux les rend plus vulnérables à la grêle (e.g. Cullen, 1992; Crenshaw & Koontz, 2001; Hohl et al., 2002), l'influence de l'orientation des bâtiments sur leur vulnérabilité n'a à ce jour pas été étudiée. L'altération est notamment déterminée par l'orientation du bâtiment, surtout en ce qui concerne la couverture des toits en pente. De plus, l'orientation d'un bâtiment peut aussi être déterminante si l'orage de grêle est accompagné de vent. Afin d'étudier la relation entre les dommages et l'orientation des bâtiments par rapport au nord, respectivement par rapport à la trajectoire suivie par la cellule de grêle, deux analyses ont été réalisées. Pour ces analyses, il a été estimé, à partir des données radar disponibles, que la trajectoire moyenne suivie par la cellule de grêle des 12 et 13 juillet 2011 était de 73°, c'est-à-dire que l'orage se déplaçait de OSO vers ENE. La première analyse concerne la totalité des bâtiments du canton d'Argovie. La deuxième étude, plus précise dans la manière de calculer les orientations des bâtiments, porte sur les bâtiments de deux communes du canton fortement touchées.

Lors de la comparaison avec la trajectoire suivie par l'orage de grêle, la totalité des dommages par bâtiment a été prise en compte, ainsi que les dommages seulement aux toits et les dommages seulement aux stores. Pour ce qui est des dommages comparés à l'orientation par rapport au nord, les mêmes catégories ont été étudiées, mais seuls les dommages aux toits sont présentés, puisque l'effet supposé du vieillissement en fonction de l'orientation affecte surtout les tuiles.

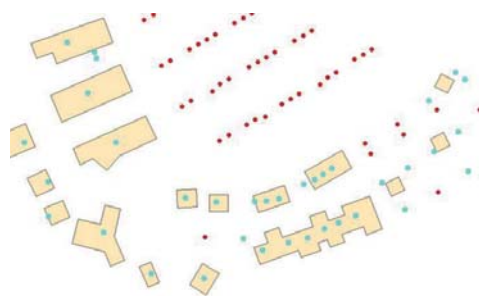
5.2 Méthodologie

Analyse à l'échelle du canton d'Argovie

Première étape dans l'analyse cantonale: le calcul des orientations de l'ensemble des bâtiments argoviens.

Ce calcul a pu être effectué grâce à une fonction du système d'information géographique «ArcMap 10®» nommée «Calculate Polygon Main Angle» sur la base des données «VECTOR25»⁴ de l'Office fédéral de topographie (swisstopo). L'hypothèse de travail est que le faîte du toit d'un bâtiment est orienté dans le sens du plus long côté du bâtiment. Si cette hypothèse est particulièrement vraie pour la majorité des immeubles d'habitation avec toiture en deux pans, elle ne l'est pas toujours pour des bâtiments au périmètre presque carré (le faîte du toit pouvant se trouver aussi bien dans un sens que dans l'autre) ou pour les bâtiments à géométrie autre que rectangulaire (ill. 35).

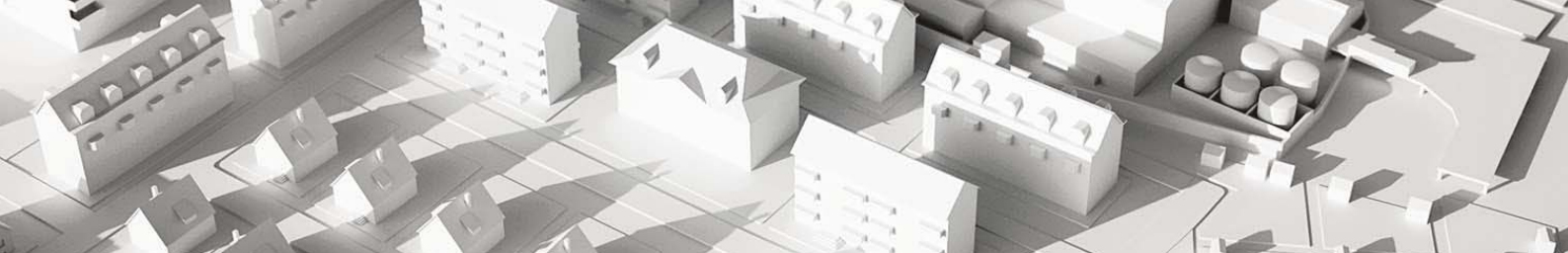
Autre problématique de cette méthode: le polygone de la carte VECTOR25 ne correspond pas toujours à l'apparence dans la vue aérienne rectifiée (orthophoto). Les emplacements des bâtiments ont été géolocalisés à l'aide des données GéoPost⁵, puis liés spatialement avec les polygones des bâtiments de la carte VECTOR25. Les coordonnées de position de chaque bâtiment endommagé ont été reliées au polygone le plus proche, à condition que celui-ci se trouve à moins de 10 m. Sinon, aucune liaison n'a lieu. Le but de cette condition est d'éviter de lier des dommages à des bâtiments auxquels ils n'appartiennent pas



II. 35: image illustrant les liens entre les bâtiments de la carte VECTOR25 et les coordonnées de bâtiments selon la base de données d'adresses GeoPost. Un point de coordonnées et un polygone de bâtiment sont ensuite reliés si le premier se situe à l'intérieur du polygone ou s'il se trouve dans une zone autour de celui-ci sans dépasser une distance de 10 m. Les points bleus correspondent à une attribution réussie, les rouges représentent une attribution qui a échoué (distance par rapport au bâtiment suivant > 10 m ou bâtiment pas encore contenu dans la carte VECTOR25). L'orientation des bâtiments n'a été calculée que pour les points bleus.

⁴ Modèle numérique de paysage de la Suisse dont le contenu et la géométrie sont basés sur la carte nationale au 1:25'000. Les objets naturels et artificiels du paysage sont représentés sous forme de vecteurs.

⁵ Base de données d'adresses de la Poste, comprenant entre autres les coordonnées de position des entrées de bâtiments.



En conséquence, cette manière de calculer l'orientation d'un bâtiment est correcte à trois conditions :

1. le faîte du toit du bâtiment est orienté du même côté que le plus long côté dudit bâtiment,
2. le polygone du cadastre suisse illustrant l'empreinte au sol réelle du bâtiment correspond à la réalité,
3. les coordonnées des bâtiments endommagés tirées de GeoPost se situent à moins de 10 m du polygone ou sont à l'intérieur de celui-ci sur la carte VECTOR25.

Si les orientations de bâtiments obtenues par cette méthodologie sont parfois approximatives, cette hypothèse de travail a comme avantage l'obtention en peu de temps et de façon standardisée des orientations d'un grand nombre de bâtiments. L'orientation calculée des bâtiments a été observée par rapport au sens de déplacement de la cellule de grêle et par rapport au nord. Le taux de dommage a été calculé, c'est-à-dire le ratio entre le montant des dommages (total / stores / toiture) et la valeur d'assurance.

Analyse locale à Bremgarten et à Widen

L'analyse locale a été réalisée sur les deux communes voisines Bremgarten et Widen, dans l'est argovien. Bremgarten, bourgade de 6'423 habitants fin 2011, est située à 390 m d'altitude et est traversée par la Reuss. La commune comprenait 3'702 logements et 12 exploitations agricoles au moment de l'événement. Widen, qui comptait 3'536 habitants et 7 exploitations agricoles en 2011, est une commune orientée sud-ouest située sur un flanc de colline à une altitude variant de 470 m à 700 m. Bremgarten est située au pied de cette colline.

Ces deux localités comprennent un large spectre de bâtiments tels que des villas individuelles ou des immeubles locatifs en passant par des bâtiments historiques au centre-ville. Pour effectuer l'analyse, il importait tout d'abord de déterminer l'orientation des bâtiments. Les bâtiments spéciaux tels que les bâtiments industriels ont été écartés de l'analyse.

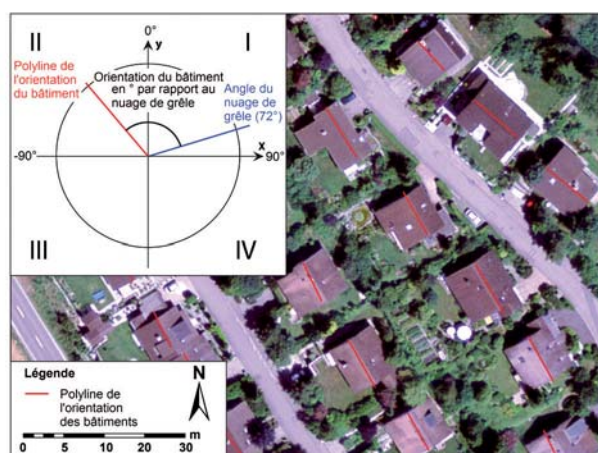
L'orientation du faîte du toit a été déterminée sur la base d'orthophotos de swisstopo datant de 2006, soit 5 ans avant l'événement. La résolution des orthophotos est de 25 cm.

Pour chaque faîte de toit compris dans le périmètre de l'analyse, une ligne a été tracée manuellement dans le SIG (polyligne). Les coordonnées X et Y des points de départ et de fin de chaque ligne ont été sauvegardés.

Les orientations des faîtes ont ensuite été calculées à partir de ces coordonnées par trigonométrie dans le logiciel Matlab® 2013. Les orientations en degrés de chaque polyligne par rapport à la trajectoire suivie par la cellule de grêle et par rapport au nord ont été calculées dans un premier

temps sur les quatre quadrants, (-180° à 180°), puis rapportées sur les deux quadrants puisque les orientations des faîtes avec un angle α par rapport au nord (azimut) sont équivalentes aux orientations des faîtes de $\alpha + 180^\circ$. Les orientations ont ensuite été reliées aux coordonnées des bâtiments ainsi qu'aux données de dommages par les numéros de contrats d'assurance des bâtiments.

Les bâtiments construits ou transformés structurellement de manière significative entre 2006 et 2011 n'apparaissant pas sur les orthophotos, leur orientation n'a donc pas pu être déterminée.



III. 36: caractérisation de l'orientation des faîtes par le SIG ArcMap 10[®] grâce à une orthophoto (prise de vue: swisstopo).

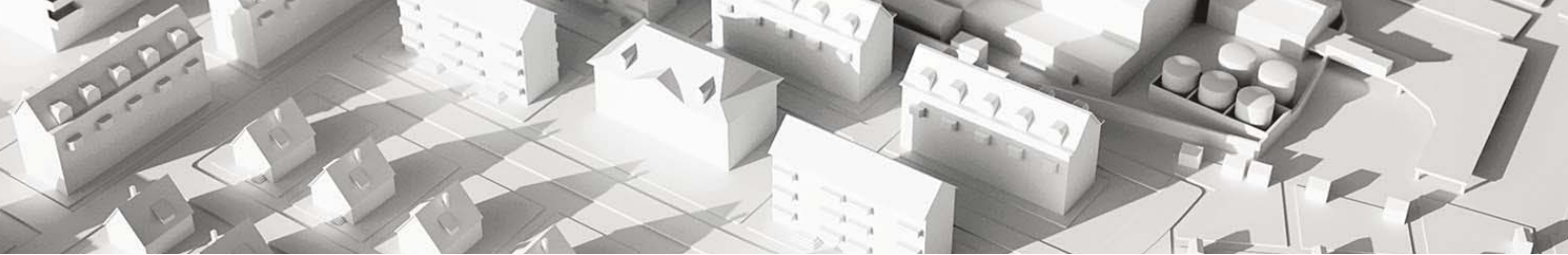
5.3 Résultats de l'analyse à l'échelle du canton

Les analyses ont porté sur les dommages dans leur ensemble (désignés par « dommage totaux » ci-après). Elles ont été menées d'autre part pour les dommages aux stores ainsi qu'aux toits. En ce qui concerne l'analyse par rapport au nord, seuls les résultats pour les dommages aux toits sont présentés. Chaque résultat d'analyse est illustré par deux graphiques :

- Un histogramme présentant la proportion de bâtiments endommagés en fonction de leur orientation.
- Un box plot représentant le rapport entre taux de dommage et orientation du bâtiment.

Données

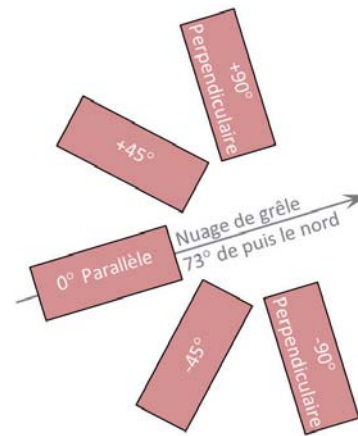
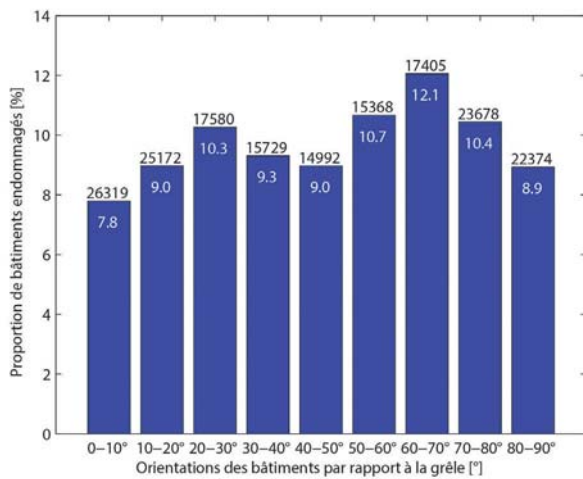
Pour le calcul de l'orientation des bâtiments, 139'076 orientations de polygones de bâtiments ont été définies dans la base de données de VECTOR25. Les 219'042 bâtiments assurés par l'ECA d'Argovie ont pu être géoréférencés avec la base de données GeoPost et reliés avec la base de données VECTOR25 et les orientations calculées.



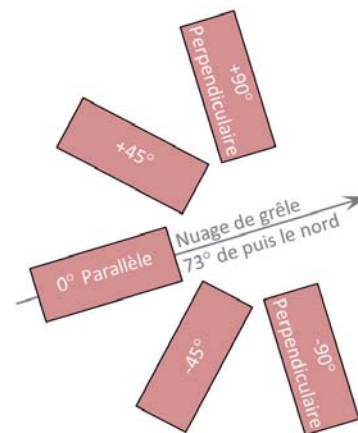
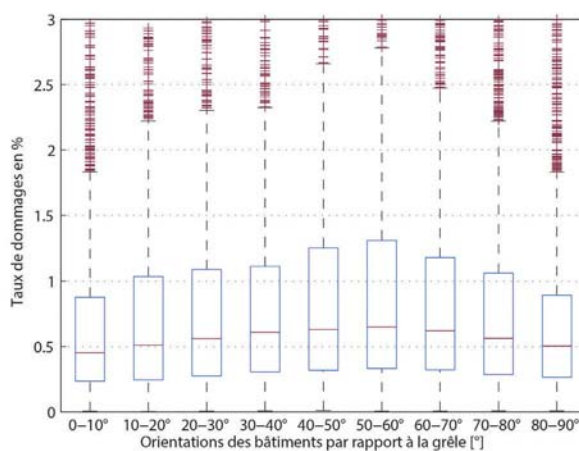
L'orientation de 179'923 bâtiments assurés a ainsi pu être déterminée. Parmi ces bâtiments, il y a beaucoup de maisons mitoyennes pour lesquelles plusieurs coordonnées se retrouvent dans un même polygone de la carte VECTOR25. Ces 179'923 bâtiments sont liés aux 53'495 dommages individuels (plusieurs dommages possibles par bâtiments) dont 13'443 dommages aux stores et 5'068 dommages aux toits. Il faut comprendre par taux de dommage d'un bâtiment le quotient « montant des dommages divisé par valeur d'assurance ».

Dommmages totaux

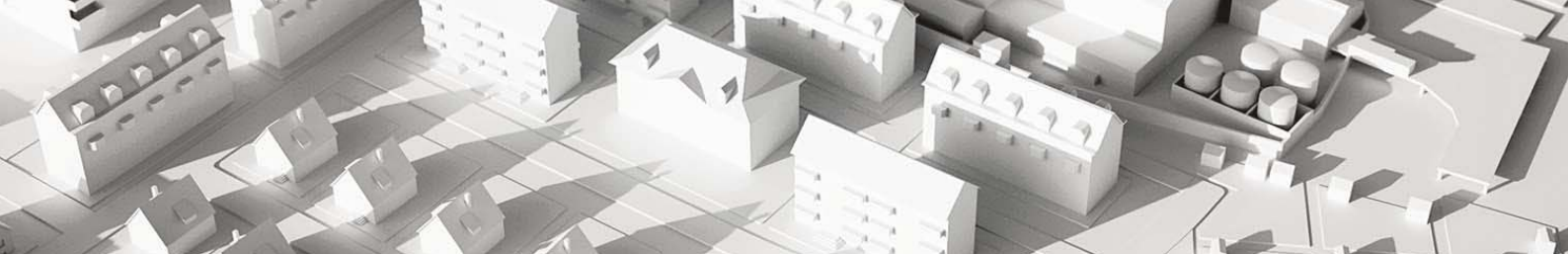
Les proportions de bâtiments endommagés selon leur orientation varient entre 7,8% (pour des orientations comprises entre 0° et 10°, c'est-à-dire pour les bâtiments les plus parallèles à la trajectoire de la cellule de grêle) et 12,1% (orientation entre 60° et 70°). Les bâtiments dont l'axe du faîte diverge fortement de la trajectoire suivie par l'orage (entre 50° et 80°) sont dans l'ensemble beaucoup plus fréquemment endommagés (taux de bâtiments endommagés entre 10,4% et 12,1%) que les bâtiments dont la longueur diverge moins, entre 0 et 50% (taux de bâtiments endommagés entre 7,8% et 10,3%, voir ill. 37).



III. 37: proportion de bâtiments endommagés, l'orientation des bâtiments étant classée par rapport à la trajectoire de la cellule de grêle de 0 à 90°. Les pourcentages sont indiqués en blanc. Les valeurs inscrites au-dessus des barres indiquent le nombre de bâtiments appartenant à la classe d'orientation.



III. 38: taux de dommages des bâtiments endommagés, l'orientation des bâtiments étant classée par rapport à la trajectoire de la cellule de grêle de 0 à 90°.



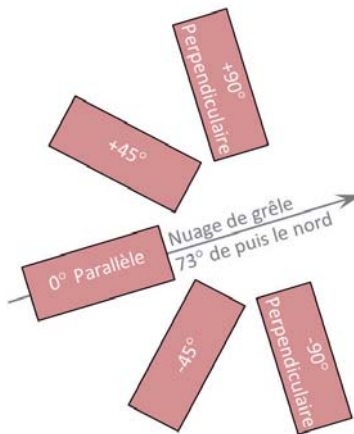
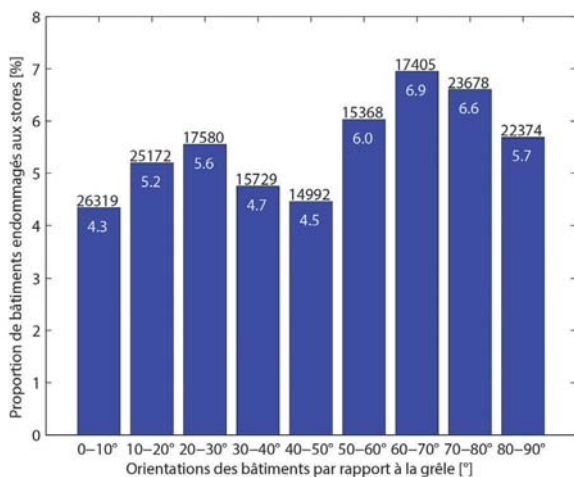
Les taux de dommages médians varient entre 0,45 % (orientation de 0 à 20° par rapport à la trajectoire de la cellule) et presque 0,65 % (orientation de 40 à 60°) ; voir ill. 38.

Dommages aux stores

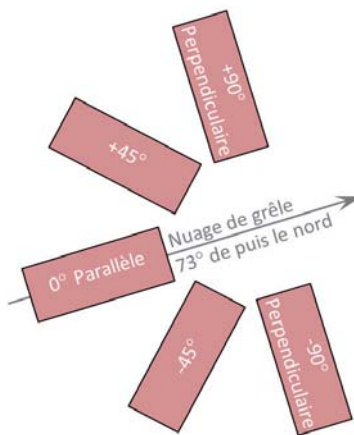
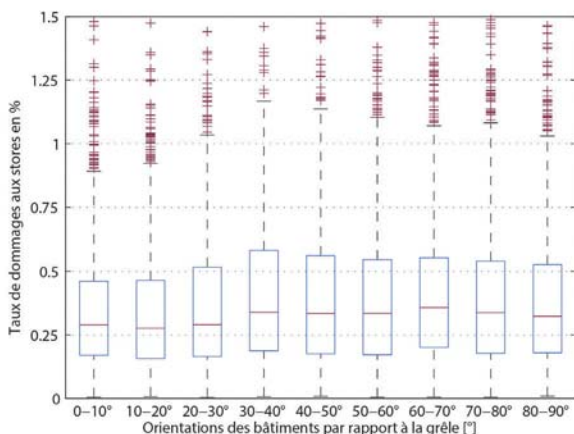
La proportion des bâtiments dont les stores sont endommagés varie entre 4,3 % pour les classes présentant les degrés de divergence les plus faibles par rapport à la trajectoire de la cellule et 6,9 % pour les classes dont la divergence est située entre 60° et 70°. Ces valeurs sont ainsi comparables à celles des dommages totaux.

Les stores des bâtiments orientés entre 50° et 90° par rapport à la trajectoire de la cellule sont endommagés dans 5,7 à 6,9 % des cas contre 4,3 % à 5,6 % pour les bâtiments dont l'orientation est située entre 0° et 50° (ill. 39).

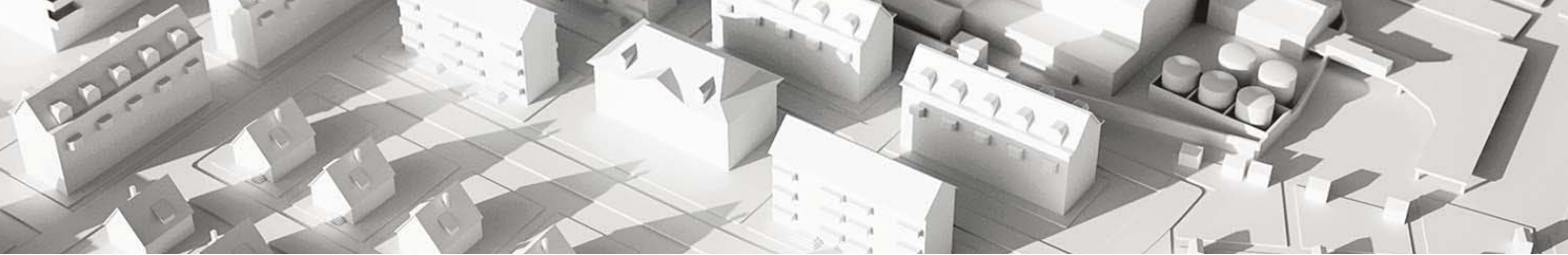
Les taux de dommages médians varient entre 0,28 % (orientation de 0 à 20° par rapport à la trajectoire de la cellule) et 0,36 % (orientation de 60 à 70°) ; voir ill. 40. Le taux des dommages aux stores dépend ainsi très faiblement de l'orientation des bâtiments



III. 39: proportion de bâtiments endommagés, l'orientation des bâtiments étant classée par rapport à la trajectoire suivie par la cellule de grêle de 0 à 90°. Les pourcentages sont indiqués en blanc. Les valeurs inscrites au-dessus des barres indiquent le nombre de bâtiments appartenant à la classe d'orientation.



III. 40: taux de dommages des stores de bâtiments endommagés, l'orientation des bâtiments étant classée par rapport à la trajectoire suivie par la cellule de grêle de 0 à 90°.



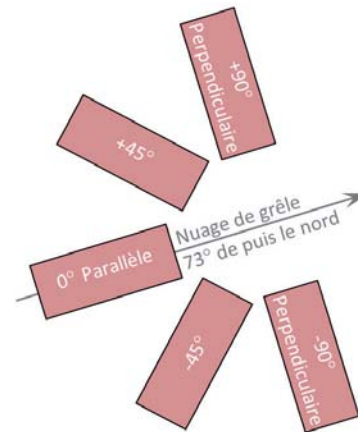
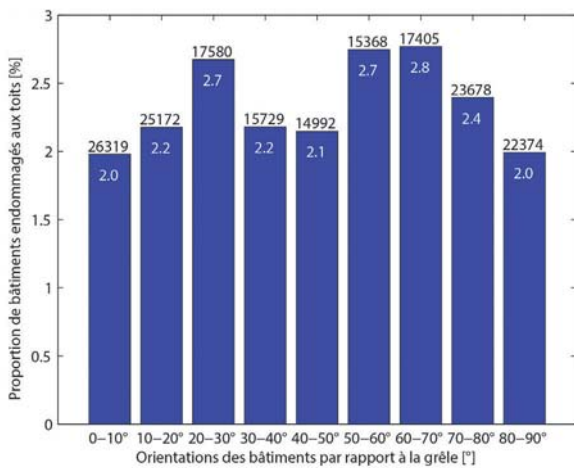
Dommmages aux toits

Les proportions de bâtiments dont le toit a été endommagé selon leur orientation par rapport à la trajectoire de la grêle varient entre 2 % (orientation entre 0 et 10° et entre 80 et 90°) et 2,8 % (orientation entre 50 et 70°). Ces chiffres sont comparables aux valeurs des bâtiments dont les stores ont été touchés. La répartition présente un maximum de 2,7 % pour une orientation entre 20 et 30 ° (ill. 41).

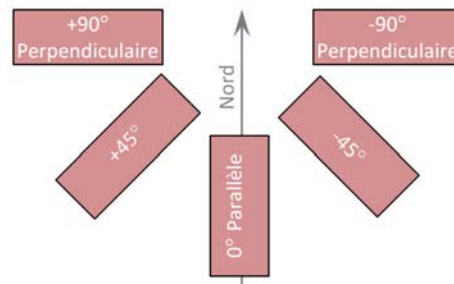
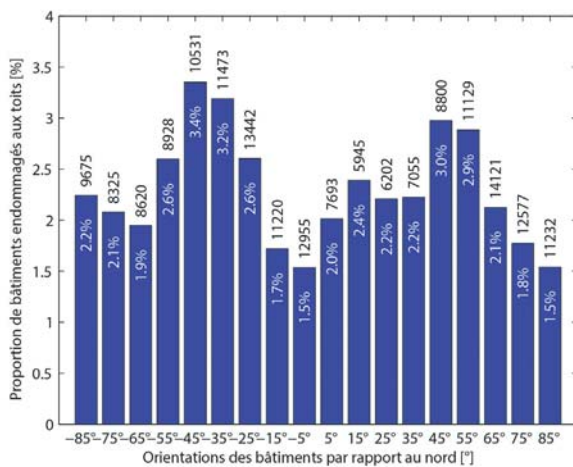
au nord-est et au nord-ouest. Le taux de dommage varie entre 1,5 et 3,4 % (ill. 42).

Le taux de dommage des bâtiments dont la toiture a été endommagée ne varie que faiblement selon leur orientation par rapport à la trajectoire suivie par la grêle. Il se situe entre 0,18 et 0,28 % (ill. 43). Logiquement, il en est de même pour le taux de dommage selon l'orientation par rapport au nord (ill. 44).

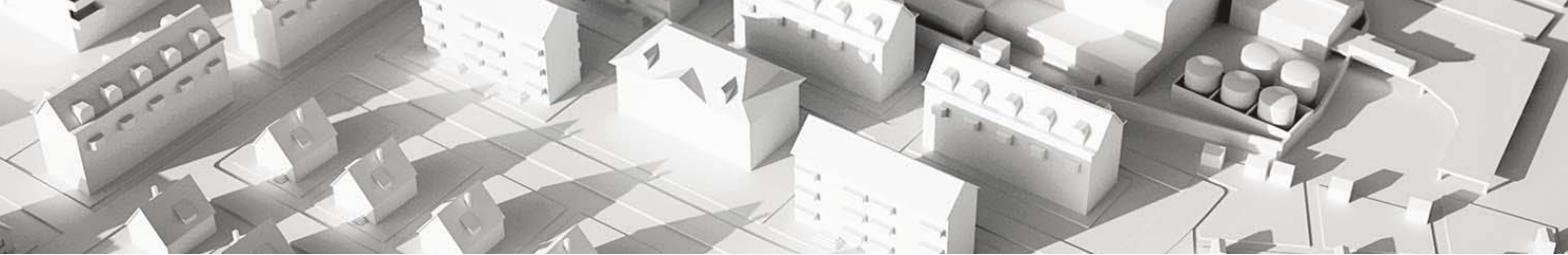
Le diagramme en barres des proportions de bâtiments endommagés des bâtiments dont la toiture a été endommagée selon leur orientation par rapport au nord présente deux pics :



III. 41: Proportion de bâtiments dont la toiture est endommagée selon leur orientation par rapport à la trajectoire suivie par la cellule de grêle de 0 à 90°. Les pourcentages sont indiqués en blanc. Les valeurs inscrites au-dessus des barres indiquent le nombre de bâtiments appartenant à la classe d'orientation.



III. 42: proportion de bâtiments dont la toiture a été endommagée selon leur orientation par rapport au nord (0°), classés de -90° (est) à +90° (ouest). Les pourcentages sont indiqués en blanc. Les valeurs inscrites au-dessus des barres indiquent le nombre de bâtiments appartenant à la classe d'orientation.

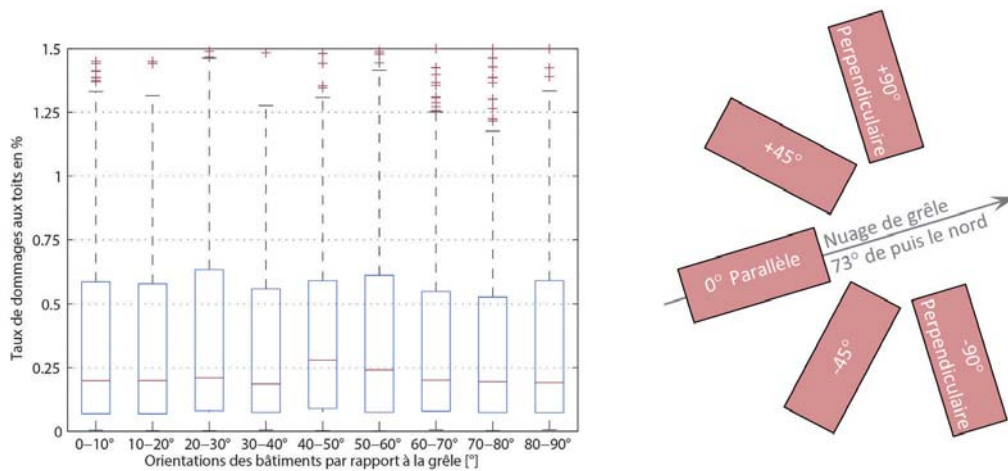


5.4 Résultats de l'analyse locale

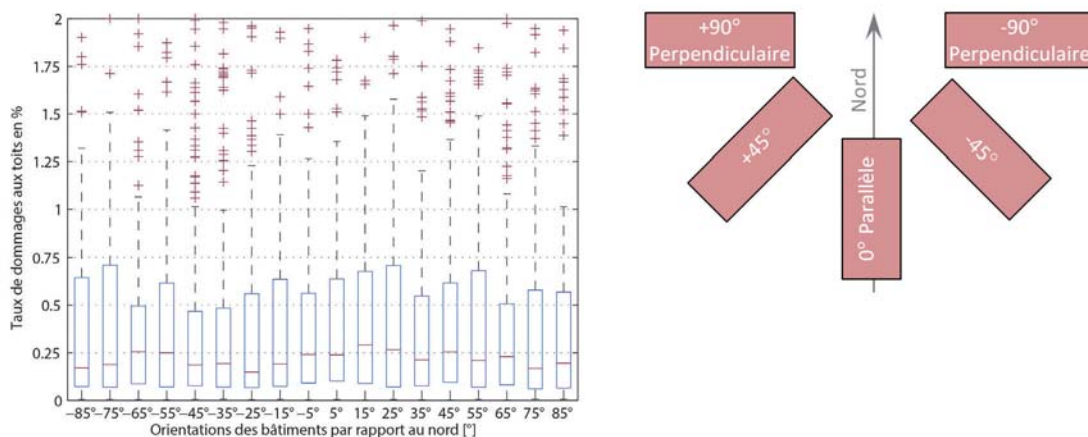
Avant d'examiner de plus près les résultats de l'analyse locale, il convient de rappeler que le faible nombre de bâtiments pris en compte dans cette analyse ne permet pas d'obtenir des valeurs absolument fiables mais délivre seulement certaines tendances. C'est pour cette raison que les graphiques présentent seulement 9 classes d'orientation par rapport au nord au lieu de 18, le faible nombre dans chaque classe ne permettant pas de tirer des conclusions fiables pour un si grand nombre de classes.

Données

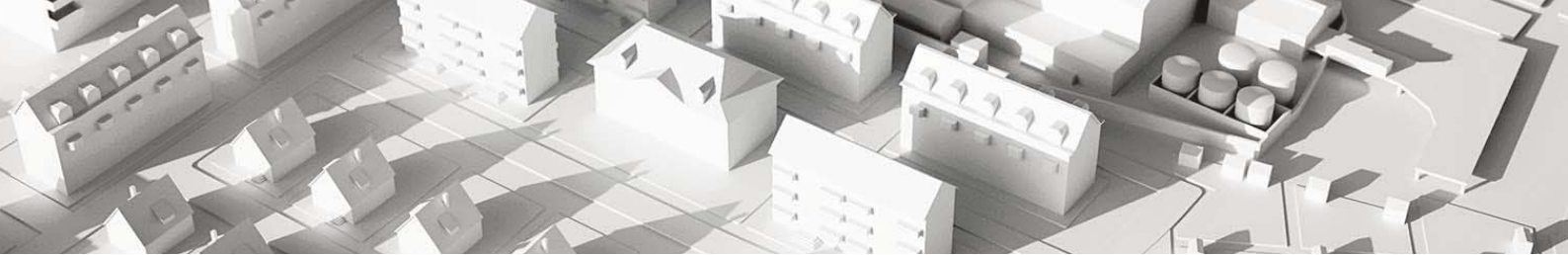
1'931 orientations de toits au total ont été définies manuellement et calculées au moyen de la vue aérienne (orthophoto) dans le logiciel SIG ArcMap®. Le nombre de dommages individuels dans ces deux communes est de 3'725 cas (plusieurs dommages possibles par bâtiment), dont 906 dommages aux stores et 418 dommages aux toits. Tous ces dommages sont pris en compte dans l'analyse locale. Le taux de dommage d'un bâtiment correspond au quotient du montant des dommages (dommages totaux ou dommages aux stores ainsi qu'aux toits) et de la valeur d'assurance.



III. 43: taux de dommages de la toiture des bâtiments endommagés en fonction de leur orientation classée par rapport à la trajectoire de la cellule de grêle de 0 à 90°.



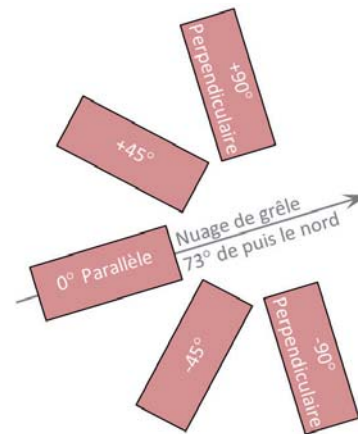
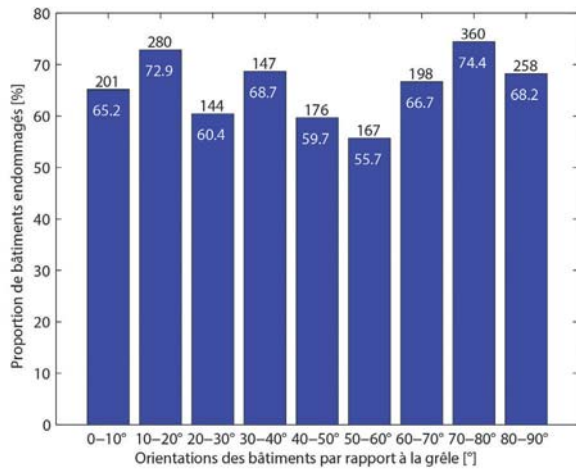
III. 44: taux de dommages de la toiture des bâtiments endommagés en fonction de leur orientation, classée par rapport au nord de -90 à +90°.



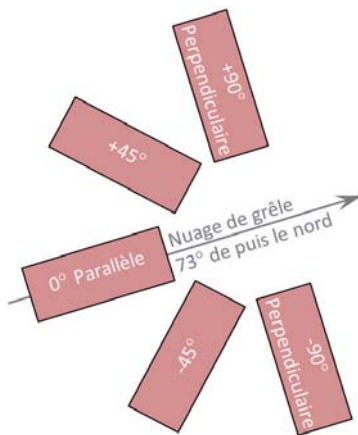
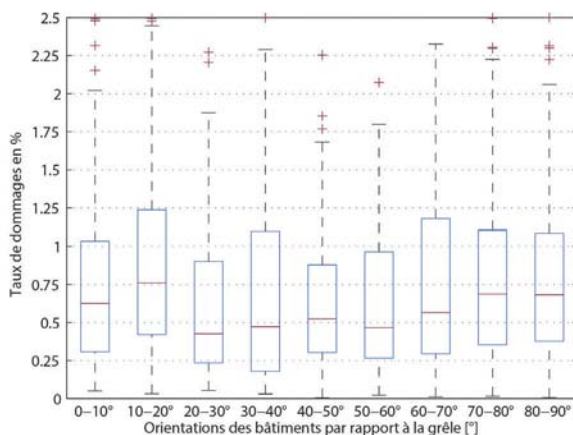
Dommmages totaux

Il apparaît que la proportion de bâtiments endommagés selon leur orientation par rapport à la trajectoire de la grêle dans les communes de Bremgarten et Widen est la plus faible dans la classe d'orientation entre 50 et 60° avec 55,7% (ill. 45). Pour les bâtiments orientés à peu près transversalement (catégorie 70 - 80°), la proportion s'élève à 74,4%. Elle est de 65% pour les bâtiments parallèles ou presque à l'orage. Il n'en ressort toutefois aucune tendance nette.

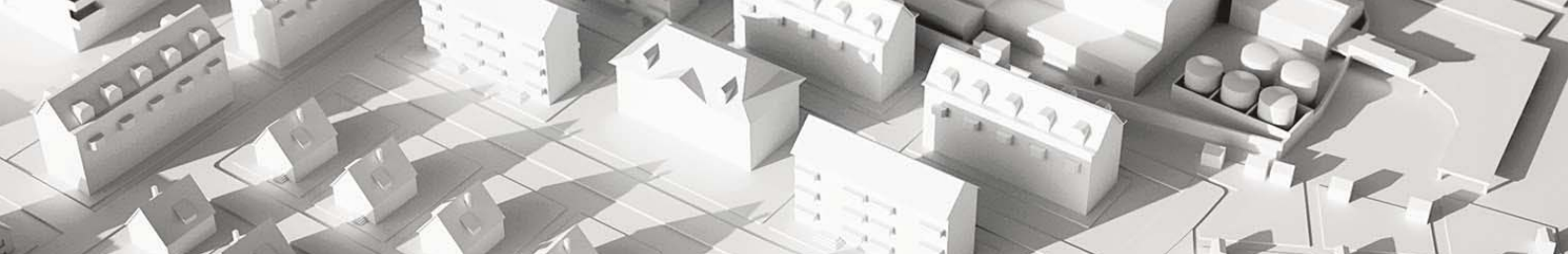
Le taux de dommage des bâtiments endommagés révèle en grande partie des valeurs similaires, quelle que soit l'orientation du bâtiment par rapport à la trajectoire de la grêle



III. 45: proportion de bâtiments endommagés à Bremgarten et Widen selon l'orientation du faite par rapport à la trajectoire de la cellule de grêle de 0 à 90°. Les pourcentages sont indiqués en blanc. Les valeurs inscrites au-dessus des barres indiquent le nombre de bâtiments appartenant à la classe d'orientation.



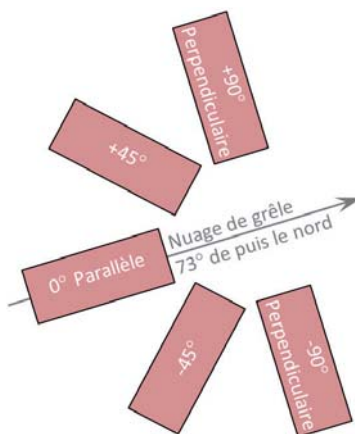
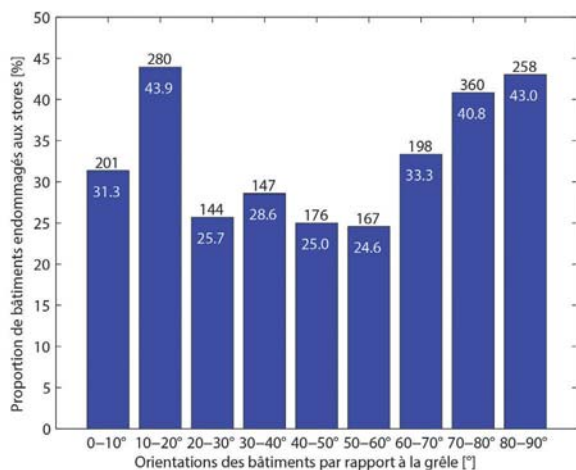
III. 46: taux de dommages des bâtiments touchés à Bremgarten et Widen selon leur orientation par rapport à la trajectoire de la cellule de grêle de 0 à 90°.



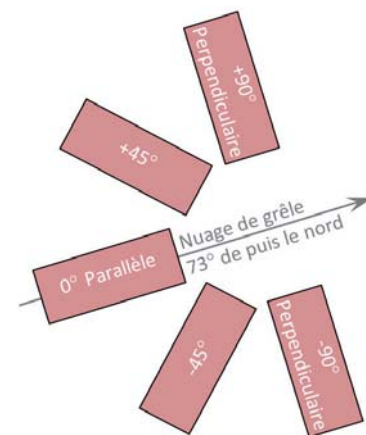
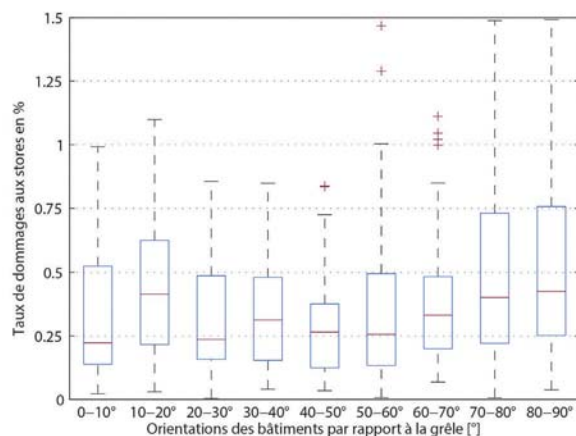
Domages aux stores

Selon l'ill. 47, la proportion des bâtiments dont les stores ont été endommagés est la plus faible pour les deux communes avec 24,6 % lorsque l'orientation par rapport à la trajectoire de la grêle se situe dans la classe 50–60°. Elle est la plus élevée dans la classe 10–20° avec 43,9 % ainsi que dans la classe transversale à l'orage (80–90°) avec 43,0 %. Il semble que les proportions ont légèrement tendance à être plus élevées pour les bâtiments dont l'orientation est supérieure à 60° par rapport à la trajectoire suivie par la grêle. Mais le pic entre 10–20° semble plutôt indiquer que cette constatation n'est pas significative.

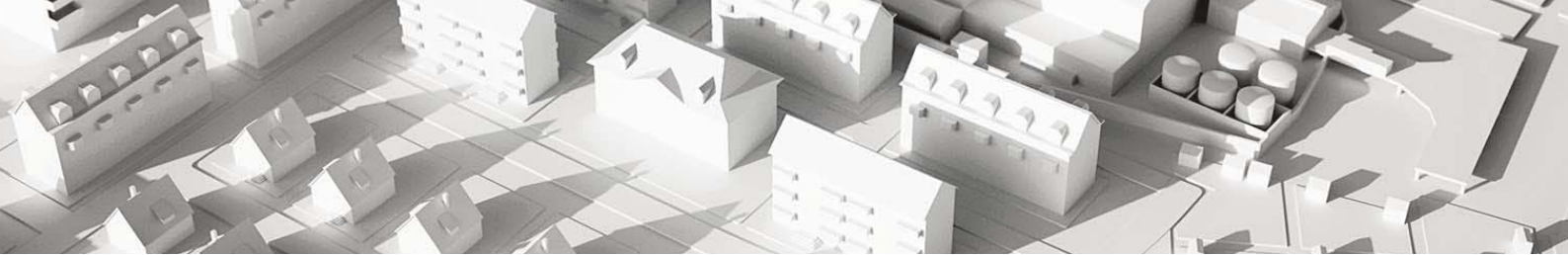
Les valeurs médianes des taux de dommages aux bâtiments dont les stores ont été endommagés dans les communes de Bremgarten et Widen selon leur orientation par rapport à la trajectoire de la grêle sont comprises entre 0,23 % et 0,44 % (ill. 48). Elles reflètent largement les relations de l'ill. 47. Elles montrent ainsi les valeurs les plus élevées en cas d'orientation transversale par rapport à la trajectoire de la grêle ainsi que dans la classe 1–20°.



III. 47: proportion de stores endommagés dans les communes de Bremgarten et Widen selon leur orientation par rapport à la trajectoire de la cellule de grêle de 0 à 90°. Les pourcentages sont indiqués en blanc. Les valeurs inscrites au-dessus des barres indiquent le nombre de bâtiments appartenant à la classe d'orientation.



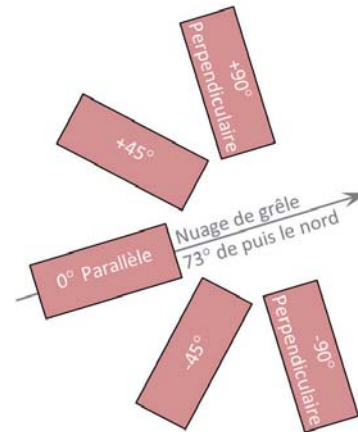
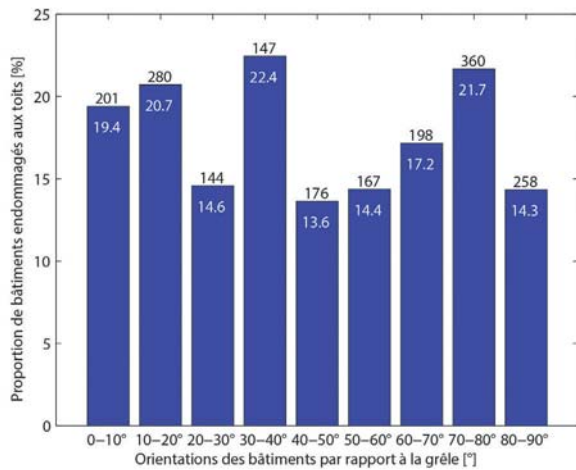
III. 48: taux de dommages sur les stores endommagés dans les communes de Bremgarten et Widen selon leur orientation par rapport à la trajectoire de la cellule de grêle de 0 à 90°.



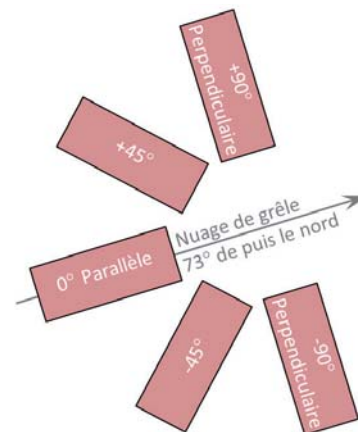
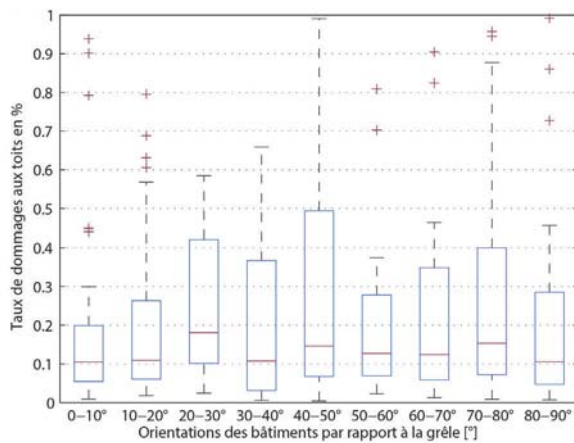
Dommmages aux toits

La proportion de bâtiments dont les toits ont été endommagés dans les communes de Bremgarten et de Widen selon leur orientation par rapport à la trajectoire de la grêle s'élève à 13,6% (bâtiments orientés entre 40 et 50°) et 22,4% (bâtiments orientés entre 30 et 40°) ; voir ill. 49. Il n'en ressort toutefois aucune tendance nette ici non plus.

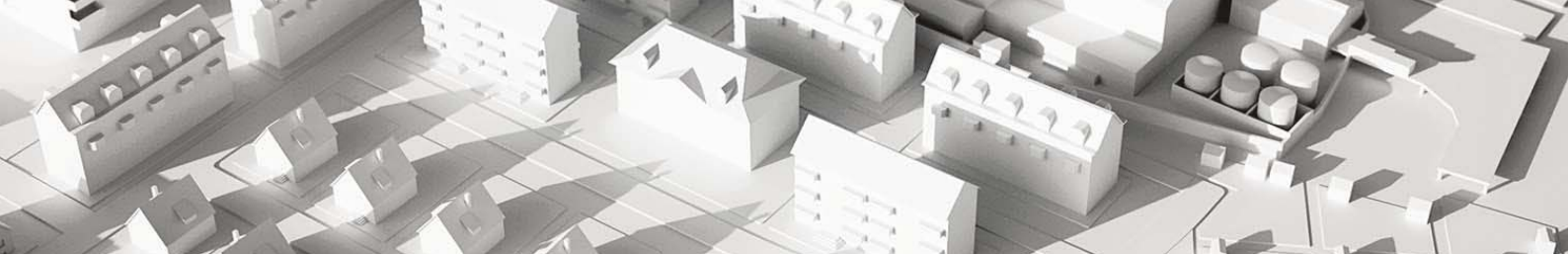
Les taux de dommages aux toits des bâtiments touchés dans les communes de Bremgarten et Widen selon leur orientation par rapport à la trajectoire de la grêle sont compris entre 0,10% et 0,18% (ill. 50). Là encore, aucune tendance ne se dégage.



III. 49: proportion de toits endommagés dans les communes de Bremgarten et Widen selon leur orientation par rapport à la trajectoire suivie par la cellule de grêle de 0 à 90°. Les pourcentages sont indiqués en blanc. Les valeurs inscrites au-dessus des barres indiquent le nombre de bâtiments appartenant à la classe d'orientation.



III. 50: taux de dommages sur les toits des bâtiments touchés dans les communes de Bremgarten et Widen selon leur orientation par rapport à la trajectoire de la cellule de grêle de 0 à 90°.

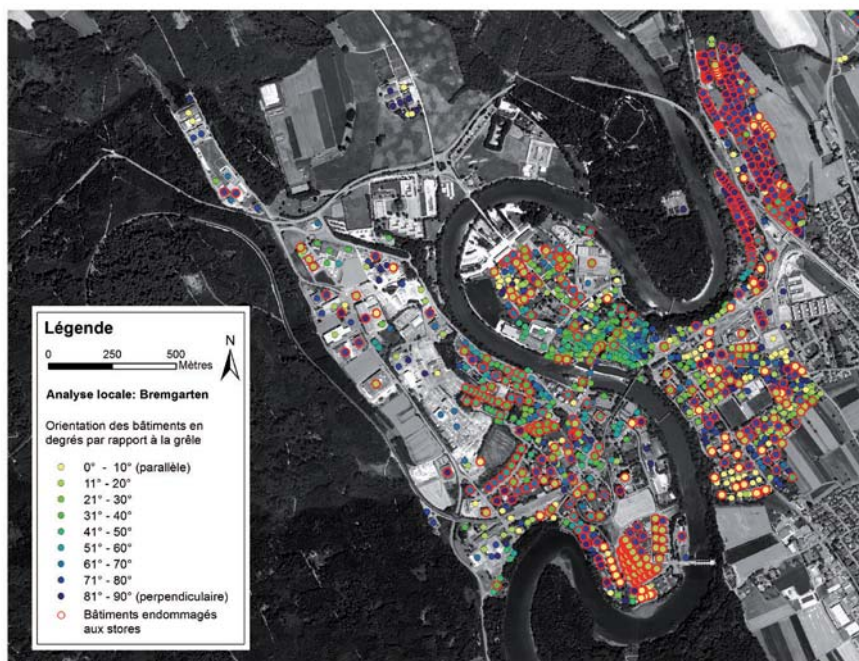


Analyse spatiale

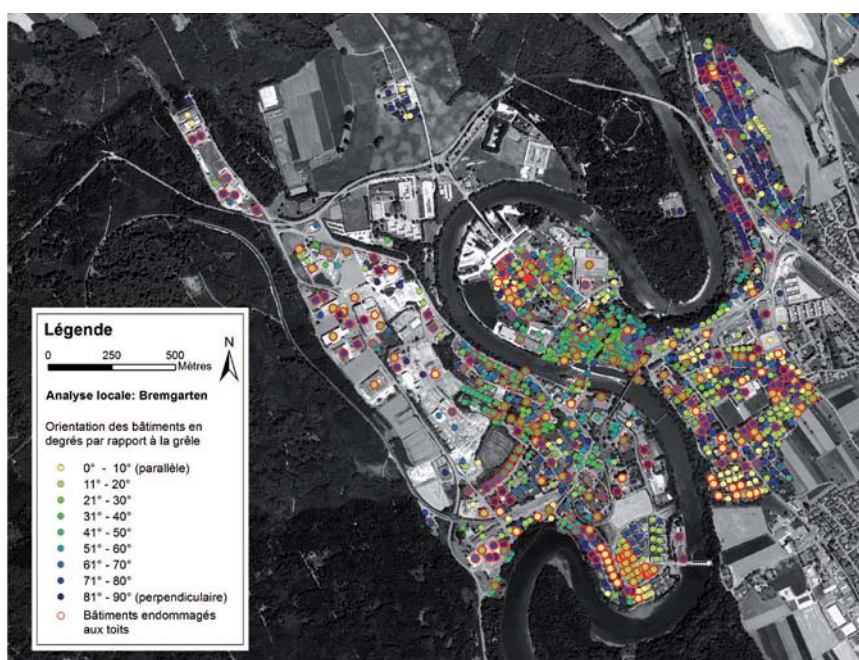
Les vues aériennes ci-après permettent d'observer les résultats de l'analyse selon l'orientation des bâtiments endommagés dans les communes de Bremgarten et Widen dans leur contexte spatial (ill. 51 à 54). Les bâtiments dont les stores ou la toiture ont subi des dommages sont mis en évidence par un cercle rouge tandis que les bâtiments dont l'orientation a été calculée sont représentés par des points de différentes couleurs en fonction de leur orientation par rapport au nuage de grêle.

Comme on peut s'y attendre, les bâtiments d'un même quartier ont généralement des orientations similaires, comme l'on peut le constater à Bremgarten et à Widen.

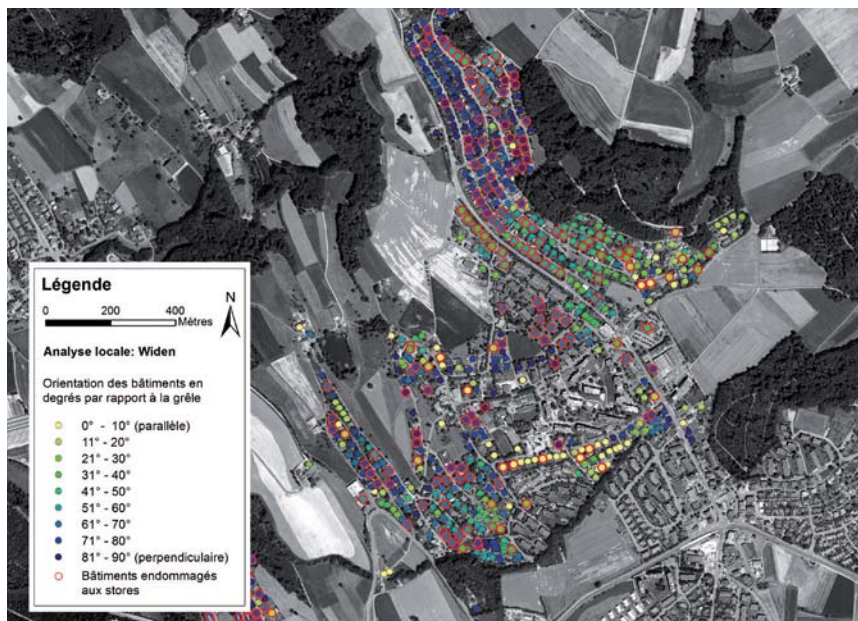
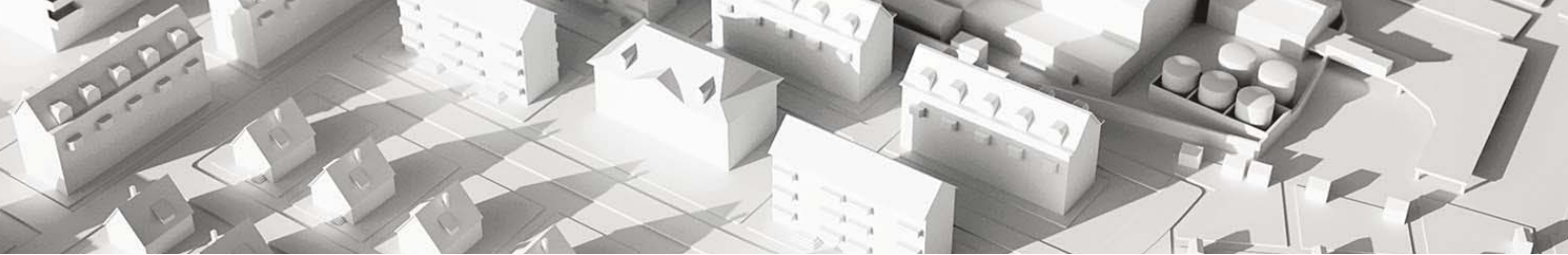
Les bâtiments dont la toiture a été endommagée ont, dans une grande majorité, également subi des dommages aux stores. Ceci n'est toutefois pas le cas dans le cœur historique de Bremgarten où il y a plus de toits endommagés que de stores. Cela est dû au fait que les toits des maisons souvent construites de manière très rapprochée protègent les façades (et aussi les stores) ; il y a peu de distance entre les bâtiments (effet écran) et surtout les stores sont très peu présents dans les centres historiques. Les stores sont également moins souvent concernés que les toits dans les secteurs industriels et agricoles où les types de bâtiments spécifiques sont rarement pourvus de stores.



III. 51: photo aérienne de Bremgarten ; les cercles rouges désignent les bâtiments dont les stores ont été endommagés, les points de couleur désignent l'orientation par rapport à la trajectoire suivie par la grêle (voir légende). (Prise de vue : swisstopo)



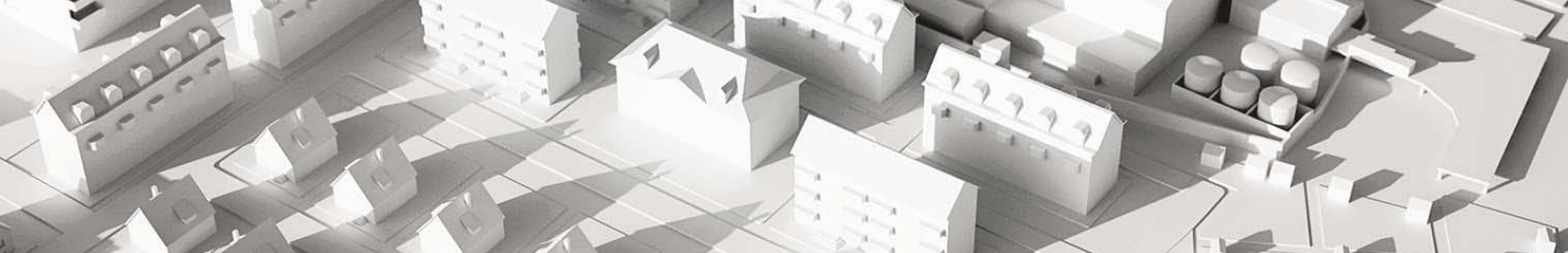
III. 52: photo aérienne de Bremgarten ; les cercles rouges désignent les bâtiments dont les toits ont été endommagés, les points de couleur désignent l'orientation par rapport à la trajectoire suivie par la grêle (voir légende). (Prise de vue : swisstopo)



III. 53: photo aérienne de Widen ; les cercles rouges désignent les bâtiments dont les stores ont été endommagés, les points de couleur désignent l'orientation par rapport à la trajectoire suivie par la grêle (voir légende). (Prise de vue: swisstopo)



III. 54: photo aérienne de Widen ; les cercles rouges désignent les bâtiments dont les toits ont été endommagés, les points de couleur désignent l'orientation par rapport à la trajectoire suivie par la grêle (voir légende). (Prise de vue: swisstopo)



5.5 Validation des orientations automatiques

L'analyse automatique des orientations de bâtiments effectuée à l'échelle cantonale sur le long côté des polygones offre l'avantage de traiter rapidement et de manière standardisée un grand nombre de bâtiments. Comme précisé précédemment, les résultats sont en revanche moins sûrs. Afin de vérifier la fiabilité de la méthode, les orientations de bâtiments définies automatiquement dans les communes de Widen et de Bremgarten ont été comparées avec les orientations définies manuellement (ill. 55 à gauche). Il en ressort que dans 68 % des cas, l'orientation obtenue automatiquement se situe dans une marge de tolérance de $\pm 20^\circ$ par rapport aux orientations obtenues manuellement. Pour 29 % des cas, l'axe longitudinal se situe en revanche dans une même plage de tolérance transversale par rapport à l'orientation définie manuellement, ce qui signifie que le faite de ces bâtiments correspond à l'axe du petit côté. Il est à noter que la différence d'angle entre l'orientation et l'axe longitudinal peut être de 90° au maximum, dans la mesure où les axes ne sont pas considérés comme des vecteurs d'orientation (c'est-à-dire qu'une ligne du nord au sud est équivalente à une ligne du sud au nord). Ce résultat mérite toutefois d'être relativisé, du fait que certains bâtiments complexes, dont l'orientation ne pouvait pas être définie manuellement, ont été ignorés, tandis que la méthode automatique leur a attribué une orientation malgré que celle-ci ne soit pas significative.

Une fois transformés en une valeur d'angle par rapport à la trajectoire suivie par la grêle, 73 % des axes déterminés automatiquement et manuellement se situent dans une plage de tolérance de $\pm 20^\circ$, le reste des différences étant réparti de manière relativement homogène entre 20 et 90° .

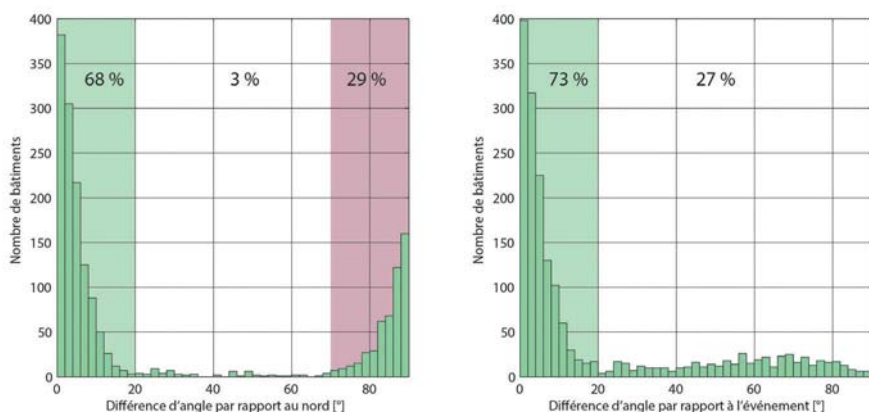
Aucun maximum n'est visible à 90° puisque, pour que la différence soit de 90° entre l'axe défini automatiquement et l'axe défini manuellement, un axe doit se situer sur un angle de 90° par rapport à la trajectoire de la grêle et l'autre axe doit obligatoirement correspondre à la direction de l'orage. En effet, si les deux axes sont perpendiculaires et que le premier forme un angle de 62° par exemple avec la trajec-

toire suivie par la grêle, alors le deuxième formera forcément un angle de 28° par rapport à la trajectoire de la grêle (ill. 56).

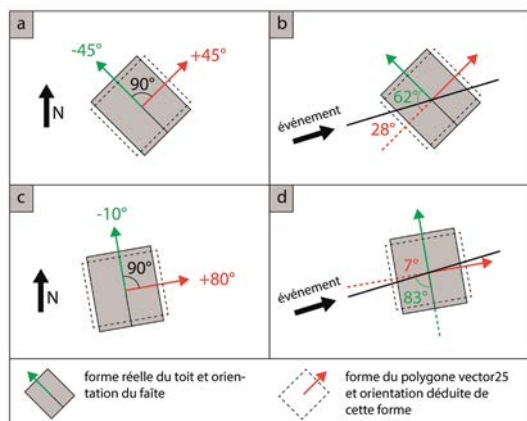
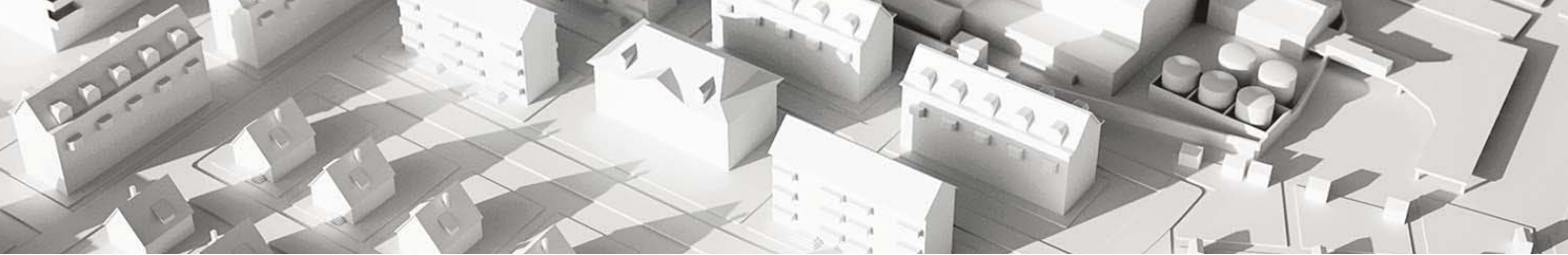
Pour un même angle de 90° entre l'orientation réelle et l'orientation déterminée à partir du polygone Vector25, l'angle par rapport à l'autre direction du bâtiment principal est obligatoirement de 83° si l'angle de l'un de deux axes du bâtiment est de 7° , ce qui implique que les orientations différentes de 90° sont réparties entre 0° et 90° par rapport à la trajectoire suivie par la grêle.

Il ressort de ces deux graphiques qu'environ 70 % des valeurs définies automatiquement sont acceptables. Tant qu'un lien de causalité demeure entre l'orientation et les dommages du bâtiment, il faut s'attendre à un deuxième maximum décalé de 90° par rapport au premier pour l'analyse de l'orientation du bâtiment par rapport au nord. Pour l'analyse en rapport avec la trajectoire de la grêle, il n'existe aucun second maximum car les axes non convergents sont répartis de manière homogène.

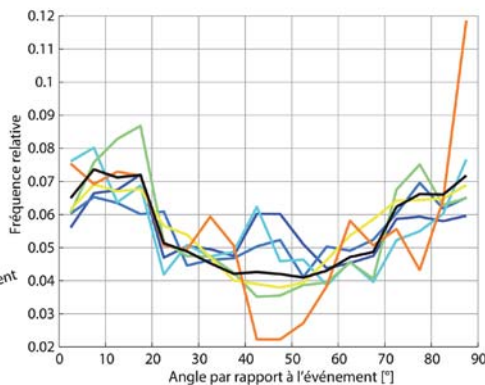
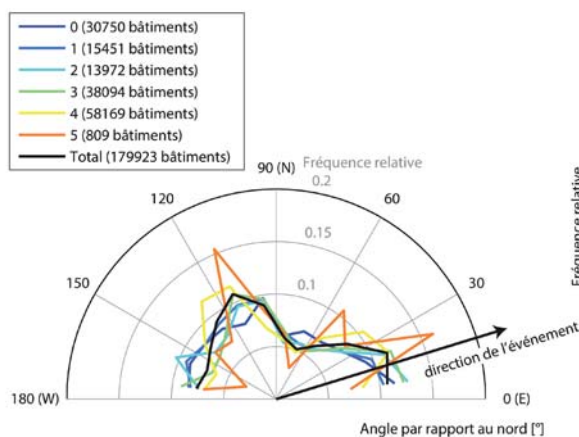
Outre les problèmes liés à la définition de l'orientation des bâtiments, l'analyse à l'échelle cantonale pourrait être faussée si la distribution des orientations des bâtiments n'était pas homogène spatialement et si elle était déterminée par la topographie, par exemple le cours de la vallée. Afin de déterminer si l'analyse est biaisée par un tel effet, la répartition de l'orientation des bâtiments a été analysée pour chaque catégorie de taille de grêlon déduite des données radar (ill. 57). Mise à part la catégorie 5 cm qui ne concerne que peu de bâtiments, les répartitions sont généralement similaires dans les différentes catégories. On observe néanmoins pour les intensités les plus faibles (catégories de taille de grêlon de 0 à 2 cm) que les orientations proches de 45° par rapport à la trajectoire de la cellule de grêle sont légèrement surreprésentées. Cela pourrait avoir pour effet une diminution de la proportion de bâtiments endommagés, ainsi que des taux de dommages, pour les bâtiments orientés avec un angle d'environ 45° par rapport à la trajectoire de la grêle.



III. 55: différence d'angle entre les orientations définies manuellement et celles définies automatiquement. À gauche par rapport à l'axe nord, à droite par rapport à la trajectoire suivie par la grêle.



III. 56: différence des axes de bâtiments par rapport au nord (a et c) entre les valeurs effectives (vert) et les valeurs déduites de VECTOR25 (rouge). Dans les 2 cas, on admet que les axes déduits du VECTOR25 divergent de 90° par rapport aux axes réels. Pour une même différence d'orientation de 90° par rapport à la trajectoire suivie par la grêle (b et d), les différences se situent entre 0 (si les deux axes forment un angle de 45° avec la direction de l'orage) et 90° (si l'un des deux axes se trouve exactement sur la direction suivie par l'orage) Dans les cas b et d, les différences d'angle par rapport à la trajectoire sont respectivement de 34° (62°-34°) et 76° (83°-7°).



III. 57: fréquence relative des orientations des bâtiments par rapport au nord (gauche) et par rapport à la trajectoire de la grêle (droite) dans chaque catégorie de taille de grêlon. Les valeurs pour chaque catégorie ont été normalisées de manière à ce que le total soit égal à 1. Le nombre de bâtiments dans chaque catégorie est indiqué dans la légende et donne une idée de la représentativité des courbes. Les points des courbes sont situés au milieu de chaque classe d'angle. La fourchette des différentes classes d'angle est de 10° pour le graphique de gauche et de 5° pour le graphique de droite.

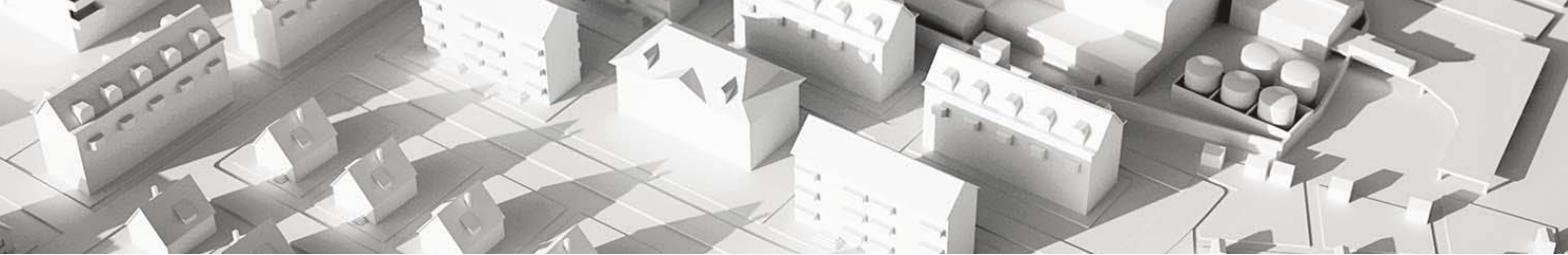
5.6 Discussion des résultats

Certains éléments de construction sont plus ou moins fortement exposés à la grêle en fonction de leur orientation. Cette affirmation s'appuie au moins en partie sur les résultats de l'analyse cantonale et locale et elle peut par exemple être prise en considération pour les mesures de prévention.

A l'échelle cantonale, il semble que les taux de dommages (des bâtiments touchés) soient les plus élevés pour les bâtiments dont l'angle avec l'orage de grêle est d'environ 50° (ill. 58) par rapport à la trajectoire suivie par la grêle. Ce constat est particulièrement vrai pour les dommages totaux, tandis que la tendance est moins claire pour les dommages aux stores. Un léger seuil est en effet visible pour ceux-ci, entre 0-30° (les moins endommagés) et entre 30-90° (les plus endommagés) (ill. 40). Les taux de dommages aux toits, quant à eux, sont relativement homogènes, sauf pour les classes de 40 à 60° où les dommages sont légèrement

plus élevés (ill. 43). Cause éventuelle: lorsque l'angle est de 45°, deux faces (ou deux pans de toit) du bâtiment sont exposées, tandis que quand le bâtiment est parallèle ou perpendiculaire à la direction de la grêle, seule une face peut être atteinte.

En ce qui concerne la proportion de bâtiments endommagés, deux pics sont visibles à environ 20-30° et 60-70° (ill. 37). Il est plus difficile d'en déterminer la cause. Il pourrait s'agir d'orientations défavorables pour lesquelles plusieurs faces seraient exposées, l'une d'entre elles étant soumise pratiquement de face aux impacts de la grêle, tandis que l'autre y serait relativement moins soumise, mais les objets les plus sensibles pourraient tout de même être abîmés. Les choses sont un peu moins évidentes pour les bâtiments dont la toiture a été endommagée. Ceci pourrait être dû au fait que les surfaces de toit sont en principe toujours exposées aux impacts de grêle. L'ill. 58 présente les orientations favorables et défavorables



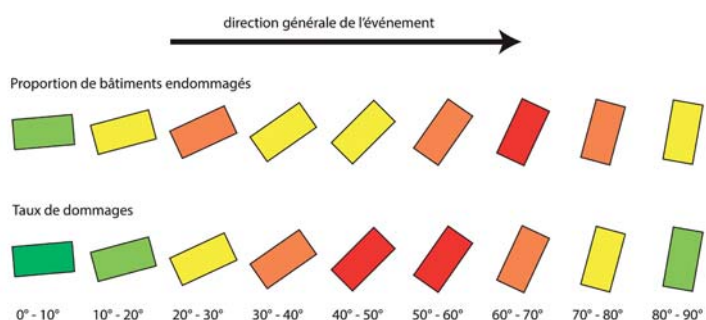
selon l'analyse par rapport à la trajectoire de la cellule de grêle. Elle repose essentiellement sur les évaluations des dommages totaux.

L'analyse à l'échelle locale de la proportion des bâtiments endommagés fait ressortir également deux pics (toutefois seulement faiblement prononcés). Ils apparaissent dans la zone des 25° ou 75° (ill. 45). L'explication doit être la même que pour l'analyse cantonale. Il est difficile en revanche de tirer des conclusions définitives à partir des taux de dommages sur les bâtiments touchés (ill. 46).

L'analyse des dommages par rapport au nord n'a été réalisée que pour les dommages sur la toiture, en supposant qu'il existe un lien de cause à effet entre les cycles de gel-dégel et la dégradation des tuiles. Pour ce qui est de la proportion de bâtiments touchés, deux pics se distinguent autour de -45° et de +45° (ill. 42). Ces deux pics étant situés à 90° d'intervalle, ils peuvent vraisemblablement s'expliquer par la méthode de calcul selon laquelle certains bâtiments presque carrés se voient attribuer à tort une orientation perpendiculaire à l'orientation réelle. Cela impliquerait qu'il ne s'agirait en réalité que d'un seul pic, probablement le plus prononcé aux environs de -45°. Ce pic correspond bien à l'orientation de 57° par rapport au nuage de grêle, orientation dans laquelle les bâtiments ont été le plus fortement touchés. Cet état de fait dépend davantage de la trajectoire suivie par la cellule de grêle que des cycles de gel-dégel, car les bâtiments dont l'orientation est de $\pm 90^\circ$ (orientation de l'un des pans de toit vers le sud) ne présentent pas de taux de dommages extraordinairement élevés.

Les tendances observées ne peuvent toutefois pas faire office de norme pour les dommages futurs et passés. Un facteur météorologique peut en effet influencer cette tendance, à savoir l'angle d'impact des grêlons sur les éléments de construction touchés (ill. 59). L'exemple extrême est un orage avec un vent très violent faisant tomber les grêlons selon une orientation proche de l'horizontale (B et C) : La surface d'un toit à deux pans pour un bâtiment parallèle au déplacement de la grêle ne devrait être que relativement peu endommagée, car les grêlons le percutent avec un angle proche de l'horizontale (B), tandis que le toit d'un bâtiment perpendiculaire à la grêle devrait être très endommagé, les grêlons arrivant tout droit sur la surface du toit (C).

A contrario, des grêlons tombant quasi verticalement par vent faible vont épargner les façades protégées par la toiture mais ils vont atteindre cette dernière indépendamment de l'orientation du toit (A).



III. 58: représentation schématique des orientations les plus favorables (en vert) et les plus défavorables (en rouge) par rapport à la trajectoire suivie par la cellule de grêle. En haut, selon la proportion de bâtiments touchés. En bas, selon le taux de dommage des bâtiments touchés.



III. 59: représentation schématique de l'influence de l'angle d'impact des grêlons sur les dommages. Cas A: sans vent, les grêlons tombent presque verticalement. Cas B: poussés par un vent fort, les grêlons tombent avec un angle d'incidence proche de l'horizontale sur le toit dont le faîte est parallèle au sens du vent. Cas C: poussés par un vent fort, les grêlons tombent à l'angle droit sur le toit dont le faîte est perpendiculaire au sens du vent. Les éléments de construction perpendiculaires au sens de l'impact sont exposés fortement, voire très fortement à la grêle. Les éléments de construction parallèles ne sont en revanche que moyennement à faiblement exposés, selon qu'ils soient protégés par un avant-toit ou non.

Cette partie de l'analyse doit servir à clarifier s'il existe un lien entre la trajectoire généralement suivie par la grêle et le taux de dommage, c'est-à-dire si l'on constate une différence entre les cas B et C. Les données permettent de mettre à jour des tendances. Toutefois, l'angle d'incidence est directement déterminé par la vitesse et le sens du vent près du sol. Il dépend aussi de différents facteurs tels que la topographie et le recouvrement du sol (bâtiments, forêt, haies) qui crée des tourbillons dont la trajectoire peut diverger fortement de celle suivie par la cellule de grêle. La relation entre sol et vent pendant l'événement de grêle de juillet 2011 n'étant pas connue, seule une trajectoire moyenne de 73° a pu être prise en compte pour la présente étude. Afin que les futures analyses de ce type puissent aboutir à des résultats plus fiables, il conviendra de viser une meilleure connaissance de la relation entre sol et vent.

6. Estimation rapide des dommages après l'événement

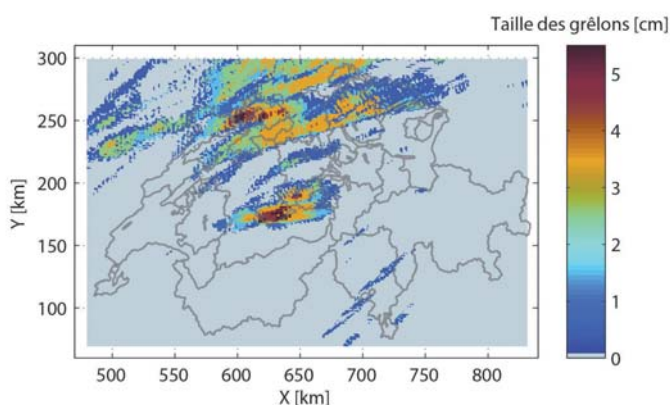
6. Estimation rapide des dommages après l'événement

6.1 Introduction

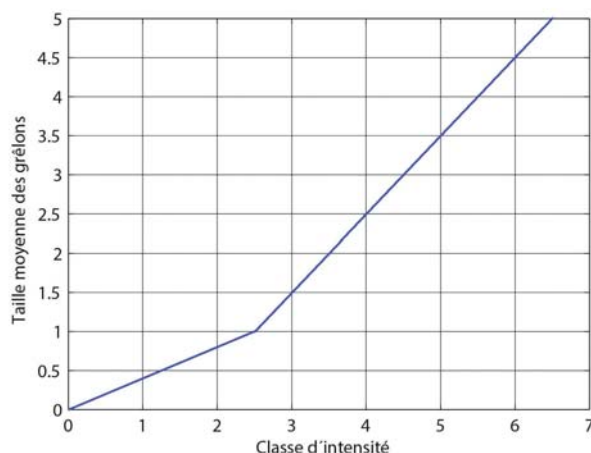
Lors d'un événement tel que celui des 12 et 13 juillet 2011, la charge de travail pour les établissements d'assurance devant traiter un nombre important de dossiers est considérable. L'ECA d'Argovie a ainsi été obligé de créer 26 nouveaux postes à plein temps à compter de l'événement jusqu'à fin 2012 afin de pouvoir faire face au volume de travail. Le délai de paiement moyen des indemnisations est malgré tout passé de six jours habituellement à 30 jours (AZ, 2012). De ce point de vue, il s'avère très important de pouvoir estimer rapidement la quantité de travail supplémentaire, ainsi que le montant escompté des dommages.

Parmi les données rapidement disponibles après un événement figurent les données radar. La société meteoradar gmbh fournit sur demande une carte des intensités maximales atteintes durant un événement en chaque endroit de la Suisse (ill. 60 et 61). Ces intensités correspondent à une estimation de la taille des grêlons au sol qui est ainsi directement liée à l'énergie cinétique.

Afin de tester dans quelle mesure les données radar peuvent être utilisées pour estimer les dommages rapidement après un événement, l'analyse décrite ci-après a été réalisée à partir des données de dommages aux bâtiments au cours des deux gros événements de grêle qui se sont produits en 2009.



III. 60: carte des grêlons de taille moyenne, tirée de l'intensité des précipitations selon l'ill. 61 (données : meteoradar).

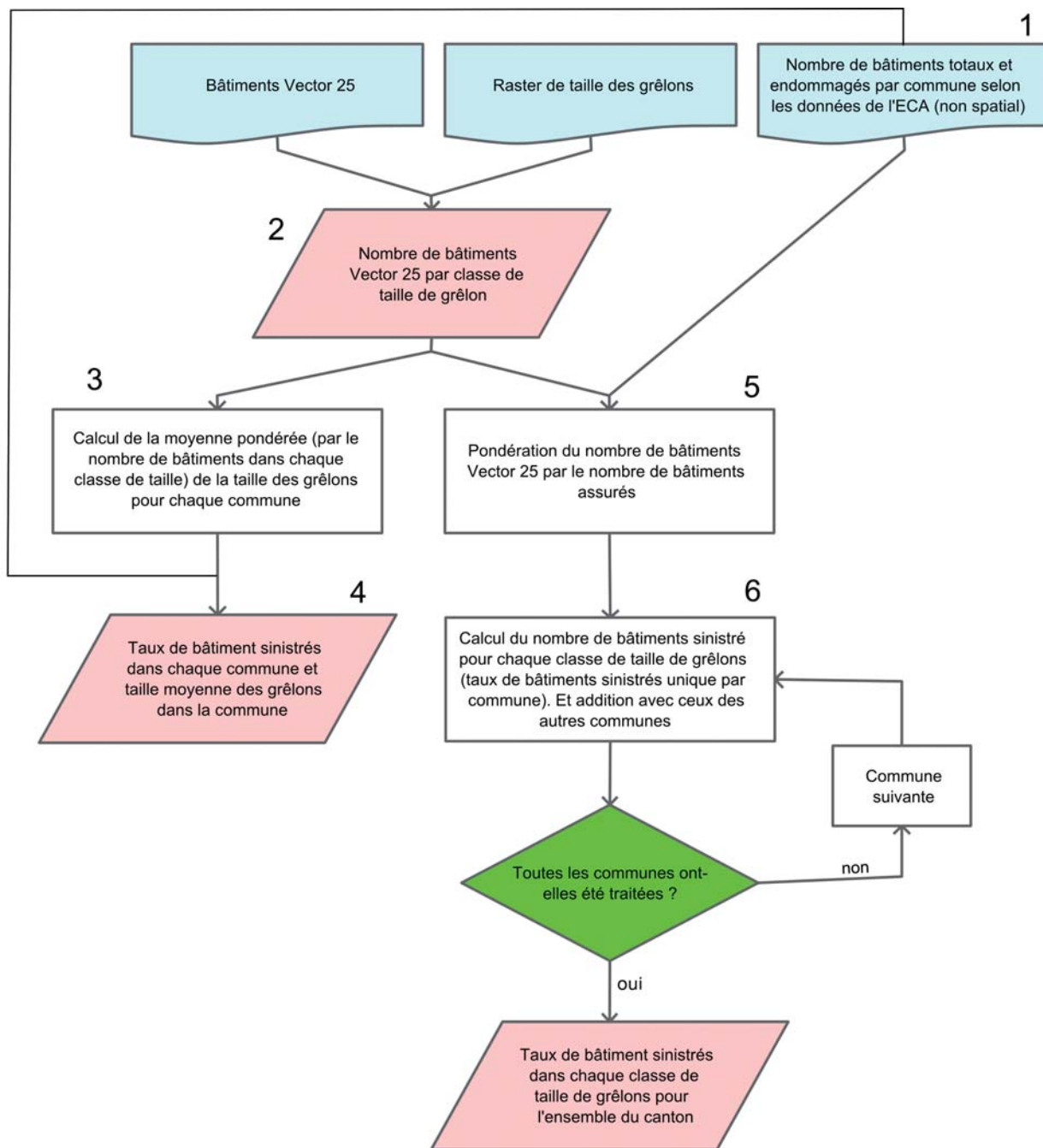
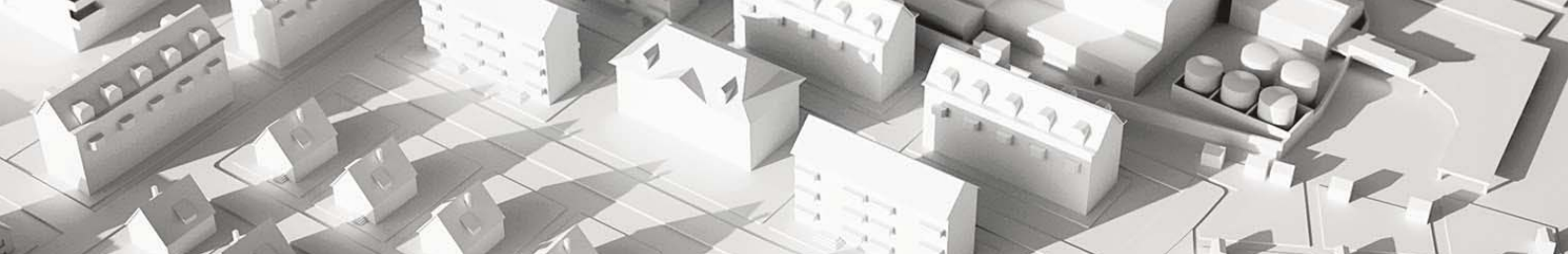


III. 61: relation entre les catégories d'intensité fournies par meteoradar gmbh et la taille approximative correspondante des grêlons.

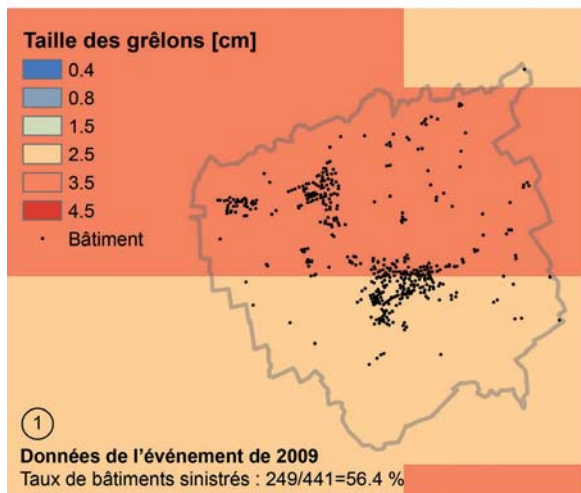
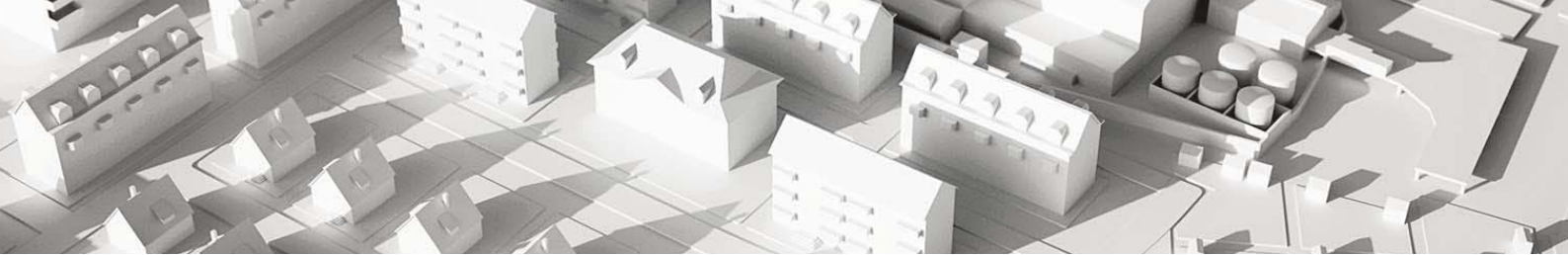
6.2 Dommages aux bâtiments suite aux deux importants événements de grêle de 2009

Une régression linéaire a été établie sur la base des données concernant les dommages de l'événement de grêle du 23 juillet 2009 dans les cantons de Vaud, de Fribourg, de Berne et de Lucerne ainsi que sur les tailles des grêlons issues des données radar (UIR 2012).

Ce calcul permet de déduire, en fonction de la taille des grêlons, l'ampleur escomptée des dommages aux bâtiments. Toutefois, cette relation ne permet pas de connaître la proportion des bâtiments touchés. Pour connaître cette proportion, un autre événement de 2009 a été utilisé, à savoir celui du 26 mai, qui a touché le canton de Thurgovie. L'information n'est pas disponible directement, mais le nombre de bâtiments sinistrés et le nombre total de bâtiments existants de chaque commune est connu.

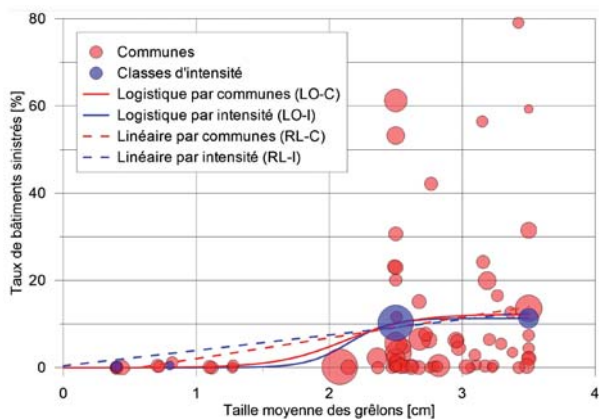


III. 62: schéma de la procédure utilisée pour calculer les proportions des bâtiments endommagés par classe d'intensité et par commune. Les chiffres correspondent aux étapes de l'exemple présenté dans l'ill. 63. Les deux types de résultats sont présentés dans l'ill. 64.



- 2 Bâtiments "Vector 25"
153 dans la classe 2.5 cm
284 dans la classe 3.5 cm
437 au total
- 3 Regroupement par communes
Taille moyenne des grêlons :
 $((153 \cdot 2.5) + (284 \cdot 3.5)) / (153 + 284) = 3.15 \text{ cm}$
Taux de sinistralité : 56.4%
- 4 Regroupement par intensité radar
Nombre de bâtiments ajoutés à la classe 2.5 cm :
5 $(153 - 441) / 437 = 154.4$
Dont sinistrés :
6 $154.4 \cdot 0.564 = 87$
- 5 Nombre de bâtiments ajoutés à la classe 3.5 cm :
5 $(284 - 441) / 437 = 286.6$
Dont sinistrés :
6 $286.6 \cdot 0.564 = 162.5$

III. 63: Exemple de calcul de taille des grêlons et de répartition des bâtiments par classe d'intensité pour une commune du canton de Thurgovie. Les points de situation des bâtiments proviennent de la carte «VECTOR25» (swisstopo). Les nombres correspondent aux étapes décrites dans le flow-chart (ill. 62).



III. 64: proportion de bâtiments sinistrés dans chaque classe d'intensité (en bleu) et dans chaque commune (en rouge), en fonction de la taille moyenne des grêlons dans la commune.

Dans les deux cas, les droites de régression et des fonctions logistiques ont été ajustées aux données, en pondérant par le nombre de bâtiments concernés pour chaque point (la taille de chaque point indique le nombre de bâtiments concernés ; les cercles rouges et les cercles bleus ont des échelles différentes). Les fonctions logistiques ont été contraintes de manière à ce que le paramètre k (valeur de l'asymptote supérieure) soit compris entre 0 et 1, que l'ordonnée à l'origine soit inférieure à 0,1 % et que le point d'inflexion soit situé entre 1 et 6 cm.

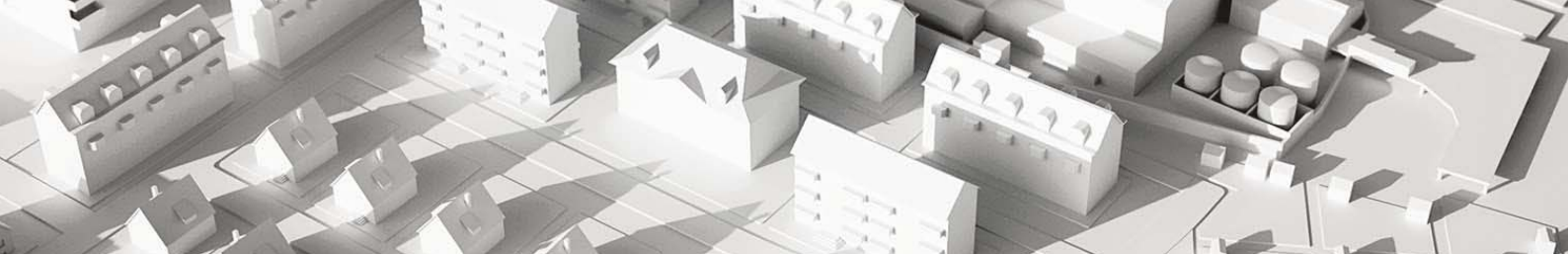
Afin de déterminer la proportion de bâtiments sinistrés dans chaque classe d'intensité, les données à disposition ont été traitées en 2 étapes: premièrement, l'empreinte des bâtiments de la carte vector25 (swisstopo) a été recoupée avec les données radar, ce qui permet d'estimer la proportion de bâtiments de chaque commune dans les différentes zones d'intensité définies par le radar. Dans un deuxième temps, le nombre de bâtiments sinistrés et le nombre de bâtiments au total dans chaque commune ont été attribués aux différentes classes d'intensité, proportionnellement à la répartition définie précédemment, en partant du principe que les bâtiments endommagés sont répartis équitablement sur toute la commune, c'est-à-dire que la proportion de bâtiments sinistrés est la même dans chaque classe d'intensité pour une commune donnée. Il est vrai que cette hypothèse est simpliste, mais il n'est pas possible de définir les proportions réelles à partir des données disponibles. Le nombre de bâtiments sinistrés et le nombre total de bâtiments existants par commune ont été finalement regroupés dans chacune des classes d'intensité pour établir une proportion à l'échelle du canton (ill. 61 et 62).

Une régression linéaire ainsi qu'une fonction logistique ont été adaptées à ces données (ill. 63).

6.3 Dommages aux bâtiments suite à l'événement de grêle de 2011

Pour cette partie de l'étude, 194'122 bâtiments géoréférencés à l'aide des données Geopost ont été utilisés, ce qui représente 88,6% du nombre total des bâtiments assurés par l'ECA, tandis que le montant des dommages liés à ces bâtiments représente 123 millions de CHF, soit 94 % de l'ensemble des dommages.

La proportion de bâtiments sinistrés dans chaque classe de taille de grêlons est présentée dans l'ill. 65. Une fonction logistique a été ajustée sur la base de ces données. Cette fonction a été choisie parce que sa pente augmente progressivement dans sa première partie, et parce qu'elle peut être limitée à une valeur maximale, ce qui est utile dans la mesure où la proportion de bâtiments endommagés ne



peut pas être plus élevée que 1 (ou 100%). Il n'est toutefois pas très facile d'ajuster cette courbe. Certaines conditions s'imposent.

Premièrement, l'ajustement a été effectué en tenant compte du nombre de bâtiments dans chaque classe, de manière à ce que le faible nombre de bâtiments touchés par des grêlons de taille 4,5 et 5,5 cm n'influence pas excessivement le résultat. En effet, une fonction gaussienne, par exemple, permettrait de reproduire plus précisément la diminution observée dans l'ill. 65 des bâtiments endommagés par des grêlons de plus de 4 cm, mais elle n'aurait pas de sens, puisque cette diminution provient manifestement du manque de représentativité des proportions observées dans ces catégories. Ensuite, l'ajustement de la courbe selon la méthode du plus petit écart quadratique forme une marche d'escaliers, ce qui signifierait que la proportion augmente brusquement lorsque la taille de grêlons dépasse 2,5 cm, alors qu'une progression plus douce semble plus réaliste. Deux courbes sont ainsi proposées en fixant les limites suivantes, pour la première courbe :

- Valeur maximale (k) comprise entre 0 et 1
- Pente maximale inférieure ou égale à la pente maximale observée (en l'occurrence entre les catégories 2,5 cm et 3,5 cm)
- Point d'inflexion situé entre 1 et 6 cm
- Ordonnée à l'origine inférieure ou égale à 0,1 %

Pour la seconde courbe :

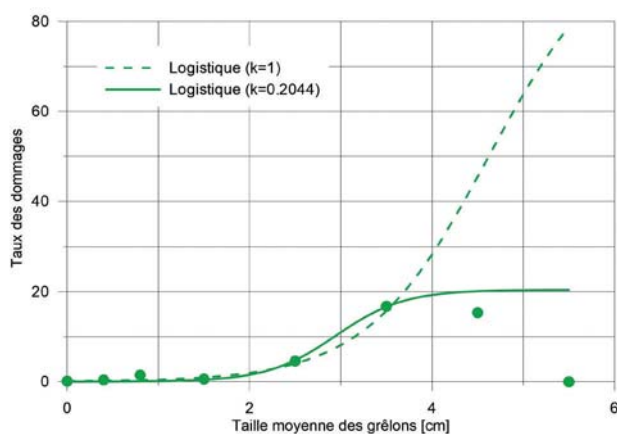
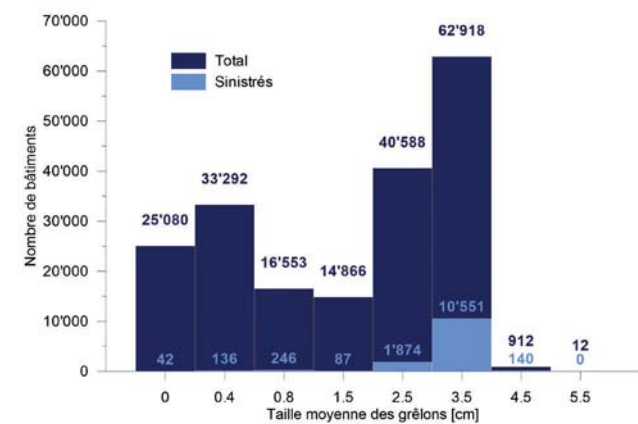
- Valeur maximale (k) égale à 1
- Point d'inflexion situé entre 1 et 10 cm
- Ordonnée à l'origine inférieure ou égale à 0,1 %

Les deux courbes ainsi que le nombre de bâtiments endommagés et le nombre total de bâtiments pour chaque catégorie sont présentés dans l'ill. 65. De par les contraintes imposées pour ajuster ces courbes et les différences entre les deux courbes, il est relativement évident que l'incertitude est grande en ce qui concerne les taux réels de dommages prévisibles. Toutefois, elles forment tout de même deux solutions plausibles qui seront comparées afin d'évaluer le niveau d'incertitude sur le nombre réel de bâtiments touchés.

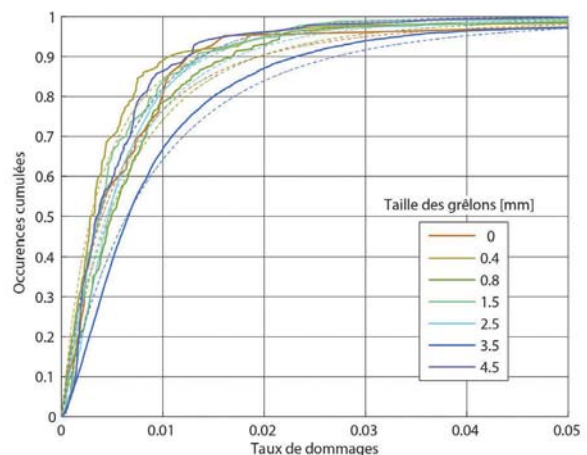
Le taux de dommages pour chaque bâtiment est calculé en divisant le montant des dommages par la valeur d'assurance. La distribution des taux de dommages de chaque catégorie est ensuite représentée à l'aide d'une distribution de Pareto généralisée, dont la fonction de distribution cumulée vaut

$$F(x) = 1 - \left(1 + \beta \frac{x}{\alpha}\right)^{-\frac{1}{\beta}}$$

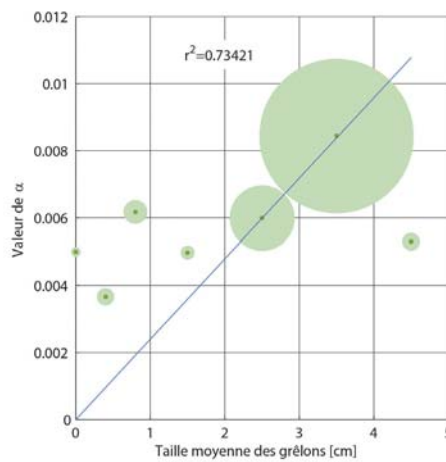
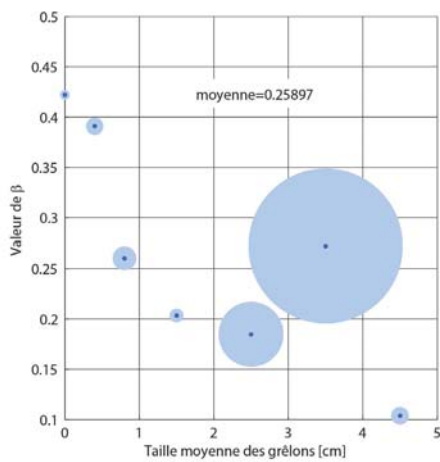
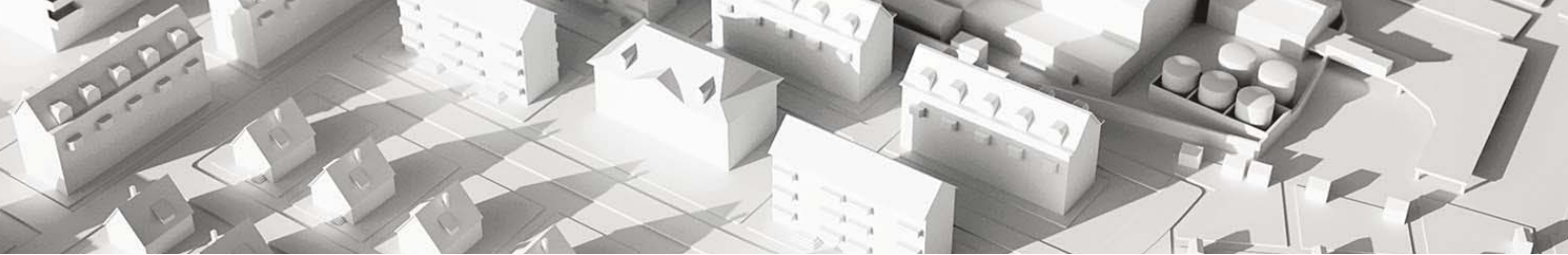
Où α détermine l'échelle et β la forme. Les fonctions d'évaluation ajustées sont présentées dans l'ill. 66 sous forme de courbes en traitillés. Pour apprécier la cohérence des résultats et donner ensuite une portée plus générale



III. 65 : nombre de bâtiments endommagés et nombre total de bâtiments dans chaque catégorie de taille de grêlons (en haut) et fonctions logistiques ajustées aux proportions de bâtiments endommagés (en bas).



III. 66 : occurrences cumulées de différents taux de dommages (traits pleins) pour chaque catégorie de grêlons. Les courbes en traitillés sont les distributions de Pareto tirées des données.



III. 67 : paramètres α et β des fonctions de Pareto tirées des données et régression linéaire utilisée pour généraliser le paramètre. Le paramètre β est généralisé à l'aide d'une moyenne, étant donné qu'aucune dépendance par rapport à la taille des grêlons ne ressort. La taille des cercles indique le nombre de données dans la catégorie qui a été utilisée pour pondérer les ajustements.

aux fonctions, les paramètres α et β sont placés dans des graphiques. La variable β ne révèle pas de tendance marquée, mais la variable α est plus ou moins proportionnelle aux catégories de tailles des grêlons. Cette dernière est donc ajustée à l'aide d'une fonction linéaire en pondérant l'ajustement par le nombre de bâtiments endommagés dans chaque catégorie (ill. 67).

La droite ajustée sur la variable α a été contrainte à passer par l'origine, de manière à ce qu'une intensité nulle ne produise pas de dommage. Cette contrainte est néanmoins discutable, dans la mesure où une autre fonction (fonction logistique « oui/non ») détermine si un bâtiment est endommagé ou non et dans la mesure où des travaux de réparation entraînent forcément un certain montant minimum (frais de base). Ces fonctions ajustées seront toutefois utilisées pour la suite des analyses et sont présentées dans l'ill. 68. Dans la suite de ce rapport, il est supposé que ces fonctions sont représentatives du bâti argovien.

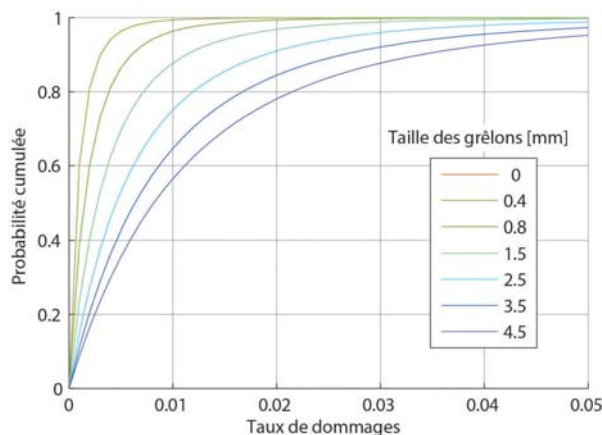
6.4 Estimation rapide des dommages

Les dommages sont évalués en estimant la proportion de bâtiments touchés ainsi que le montant des dommages à l'aide du tableau 2. Pour chaque bâtiment, le modèle détermine s'il a été touché ou non en générant une variable aléatoire « u » dont la valeur est comprise entre 0 et 1, avec une densité de probabilité uniforme entre ces deux bornes (voir ill. 69).

Si la variable aléatoire est inférieure à la valeur de la courbe à l'abscisse définie par la taille de grêlons (déduite à partir des données radar sur le lieu d'implantation du bâtiment), le bâtiment est considéré comme étant endommagé. Si tel est le cas, le montant des dommages est défini directement par la relation linéaire établie pour l'événement de juillet 2009 (UIR 2012), à savoir :

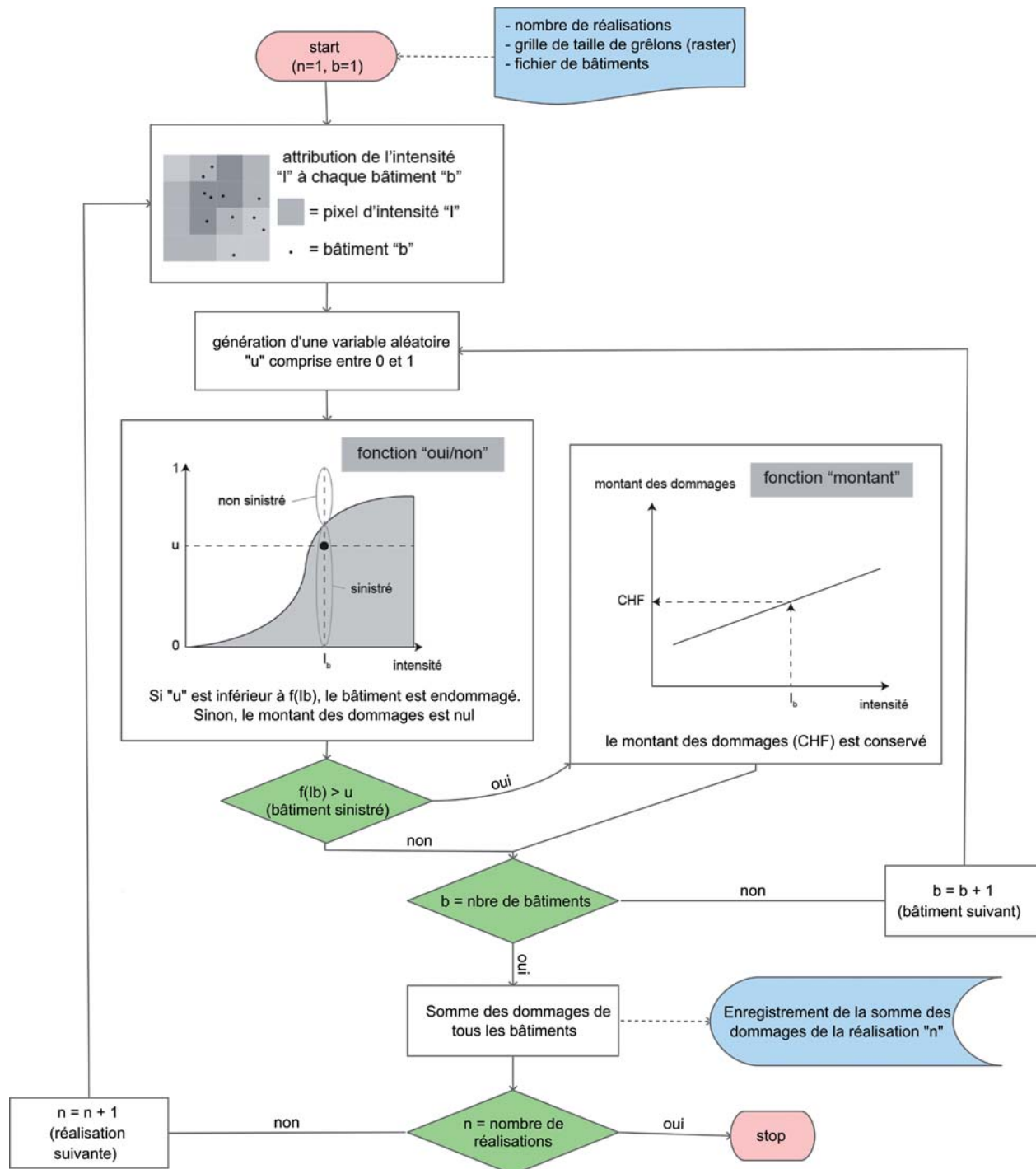
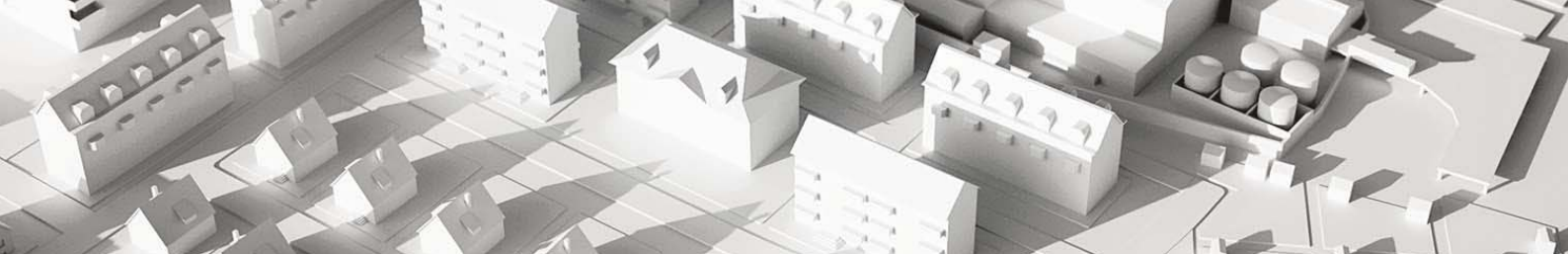
$$S = 695 \times d + 1'623$$

S correspondant au montant des dommages en CHF et d au diamètre des grêlons en cm.



La proportion de bâtiments touchés pour une intensité donnée semble similaire entre les deux événements puisque, à l'exception de la droite de régression ajustée sur les données de Thurgovie regroupées par catégorie d'intensité (RL-I), les droites de régression selon les communes et les fonctions logistiques reflètent relativement bien le nombre de bâtiments endommagés en 2011. En effet, même si les deux fonctions logistiques sont environ 10 % au-dessous de la valeur attendue, celles ajustées sur l'événement de 2011 ne reproduisent pas parfaitement le nombre de bâtiments touchés, mais toutes se situent dans une marge d'erreur acceptable.

III. 68 : fonctions de probabilité des taux de dommages pour différentes catégories de taille de grêlons. La courbe pour la catégorie 0 cm n'est pas visible, parce qu'on suppose qu'aucun dommage n'est possible dans cette classe.



III. 69: schéma expliquant la démarche utilisée pour l'attribution du montant des dommages. La fonction « oui/non » sert à définir si le bâtiment est endommagé ou non, tandis que la fonction « montant » permet, dans le cas où celui-ci est endommagé, de définir le montant des dommages. Pour établir une courbe moyenne des résultats, plusieurs réalisations du modèle peuvent être effectuées.



Fonction « oui / non »	Fonction «montant»	Montant du dommage (en millions de francs)	Taux	Nombre de bâtiments endommagés	Taux
RL-C	Relation linéaire (juillet 2009)	51.1	0.42	13'514	1.03
RL-I		75.8	0.61	22'500	1.72
LO-C		46	0.37	12'076	0.92
LO-I		43.4	0.35	11'400	0.87
LO-AG ($k = 0.2044$)		50.1	0.41	12'686	0.97
LO-AG ($k = 1$)		48.4	0.39	12'267	0.94
LO-AG ($k = 0.2044$)	Pareto AG	123	1	12'676	0.97
LO-AG ($k = 1$)		119	0.97	12'273	0.94
Valeur («réelle») attendue		123	1	13'076	1

Tab. 2: montants de dommages et nombre de bâtiments endommagés selon les différentes fonctions. Les colonnes «taux» indiquent le rapport entre le montant estimé de dommages ou proportion estimée de bâtiments endommagés et la valeur («réelle») correspondante escomptée. Les proportions de bâtiments touchés sont définies soit par une régression linéaire (RL), soit par une fonction logistique (LO), déduite soit de l'événement de 2009 en Thurgovie (C et I, voir ill. 64), soit de l'événement de 2011 en Argovie (AG, voir ill. 65). Les montants de dommages des bâtiments sinistrés sont estimés soit à l'aide de la relation linéaire présentée ci-dessus, soit à l'aide des fonctions de Pareto présentées dans l'ill. 68.

Pour ce qui est du montant des dommages estimé à l'aide de la relation linéaire définie pour les événements de 2009, celui-ci est systématiquement trop bas, même lorsque le nombre de bâtiments sinistrés est largement surévalué. Les données disponibles ne permettent pas d'en déterminer la cause, mais plusieurs hypothèses peuvent être émises pour tenter de l'expliquer :

- L'événement de 2011 s'est produit pendant la nuit, et donc à un moment où les stores sont généralement baissés. La part des stores sur le montant total des dommages était sensiblement plus élevée qu'en mai 2009, ce qui pourrait expliquer la différence.
- Autre explication possible : l'angle d'impact des grêlons en juillet 2011 pourrait avoir été plus horizontal en raison du vent, ce qui impliquerait que des éléments de construction différents (ou les mêmes éléments mais en proportions différentes) aient été touchés sur un bâtiment similaire. Il est à noter toutefois que les proportions des différents éléments touchés sont comparées avec les chiffres de l'événement de mai 2009 en Thurgovie, tandis que les montants de dommages totaux sont comparés avec l'événement de juillet 2009. L'absence de données pertinentes ne permet pas de tirer de conclusions plus approfondies.
- Outre la grêle, la tempête, l'infiltration des eaux de pluie et les inondations ont également causé des dommages aux bâtiments. Les établissements d'assurance classifiant⁶ la cause des dommages premièrement selon le principe du phénomène dominant (un seul phénomène par bâtiment) et deuxièmement selon la cause initiale, d'autres dommages sont également inclus en partie par ces processus secondaires dans les dommages dus à la grêle. De ce fait, la part des classes de dommages «toits» et «stores» pourrait être réduite au profit d'autres éléments de construction (principalement à l'intérieur des bâtiments). L'analyse des dommages isolés n'a cependant fait ressortir aucun transfert de ce genre.
- Explication probable : dans les villages particulièrement fortement touchés, les bâtiments endommagés sont essentiellement des villas construites de manière non traditionnelle, constituées de nombreux éléments potentiellement coûteux. Ceci pourrait expliquer que le montant des dommages survenus en 2011 est plus élevé que lors de l'événement de juillet 2009. De plus, la proportion de maisons individuelles est plus élevée en Argovie qu'en Thurgovie et que dans les quatre cantons touchés par l'événement de juillet 2009 (OFS 2014c).

⁶ Les dommages liés à l'eau qui s'infiltré par une fenêtre de toit brisée figurent également sous la cause «Grêle».

7. Analyse du risque

Une des grandes sources d'incertitude dans cette analyse est la taille réelle des grêlons. Même en supposant que les mesures radar soient parfaites, il est évident que la résolution ne permet pas d'affecter les tailles de grêlons aux bâtiments avec une exactitude absolue. Ainsi, l'ill. 63 montre une commune où la taille de grêlons est divisée en deux groupes séparés par une frontière nette, ce qui n'est évidemment pas réaliste. Lorsque la différence de taille entre 2 cellules adjacentes est faible (saut d'une catégorie seulement par exemple), l'erreur induite est relativement limitée. Si la différence est plus importante, l'incertitude sur la taille «réelle» des grêlons est plus grande en conséquence.

Le nombre de bâtiments constitue une autre source d'erreur possible : si l'étude repose sur les données géoréférencées de l'établissement d'assurance, le nombre de bâtiments sera plus élevé que si elle découle, par exemple, des contours des bâtiments dans VECTOR25. En effet, dans le second cas, des maisons mitoyennes ne seront représentées que sous forme d'un seul objet par le contour global, tandis que l'établissement d'assurance considère qu'il s'agit de plusieurs logements. Dans ce cas, il serait plus adapté de recourir à un taux de dommage plutôt qu'à un montant pour répartir la valeur d'assurance totale entre les différents bâtiments, afin d'obtenir des montants de dommages potentiellement plus proches de la réalité.

Cette approche ignore quelques paramètres importants pour calculer les taux de dommages, tels que le type de bâtiments, l'orientation du vent, le fait que les stores sont baissés ou non au moment de l'événement, et encore bien d'autres points. Ces facteurs pourraient relativement facilement être intégrés à l'estimation, pour autant que leur effet soit connu. Pour cela, comme pour réduire l'incertitude sur les fonctions de dommages dont la définition est encore très vague (ill. 64), il est important d'analyser d'autres événements.

7. Analyse du risque

7.1 Danger

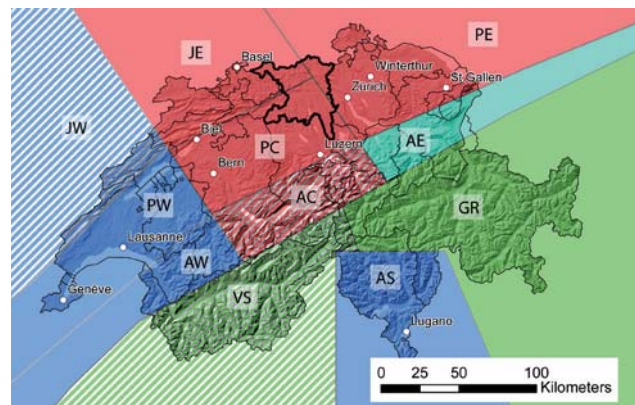
Une carte des différentes zones de danger pour l'ensemble de la Suisse a été établie dans le cadre du projet « Répertoire suisse de la protection contre la grêle » de la Fondation de prévention (ECA, 2007, voir ill. 70). Cette carte indique, pour différentes périodes de récurrence, la taille minimale des grêlons à attendre dans chacune de ces zones. Le canton d'Argovie se trouve dans la zone pour laquelle le danger est le plus élevé. Pour n'importe quel bâtiment implanté dans cette zone, il faut s'attendre en moyenne à des grêlons de 1 cm de diamètre une fois par an, de 2 cm une fois tous les 5 ans, de 3 cm une fois tous les 20 ans et de 4 cm une

fois tous les 100 ans. Cela n'exclut pas que plusieurs événements aient lieu au sein d'un même canton avec les tailles de grêlons mentionnées sur les différentes périodes, car les orages de grêle ne concernent la plupart du temps qu'une partie du canton.

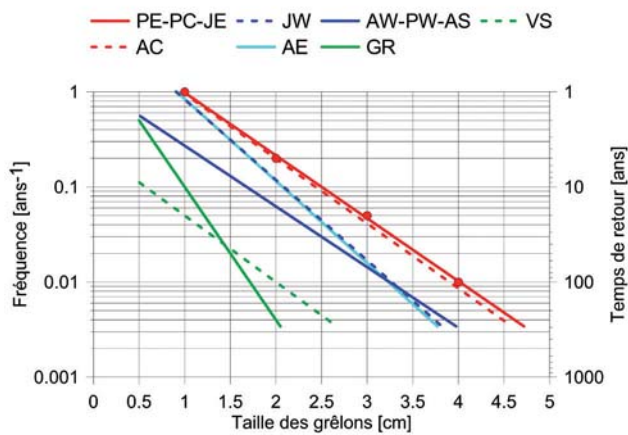
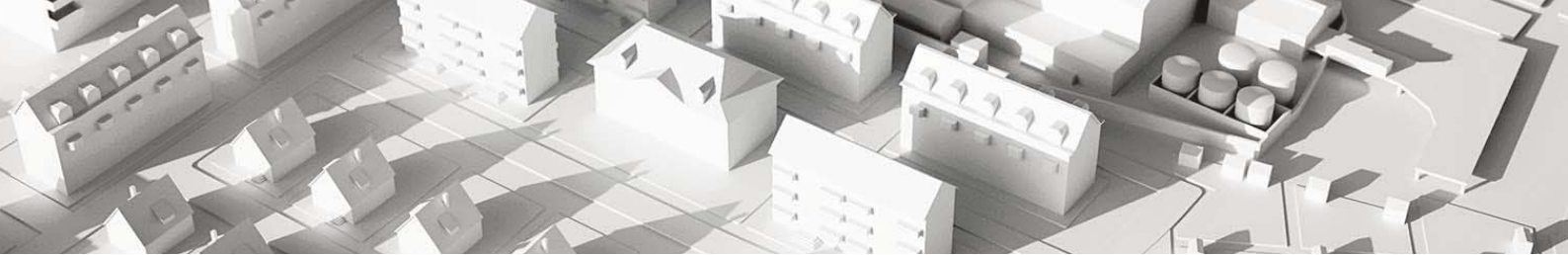
En ce qui concerne la distribution des tailles de grêlons au sein d'un événement, Pruppacher et Klett (2010) signalent que la plupart des auteurs utilisent, pour ajuster les données, une loi exponentielle de type « Marshall-Palmer » :

$$n(d) = n_0 e^{-\lambda d}$$

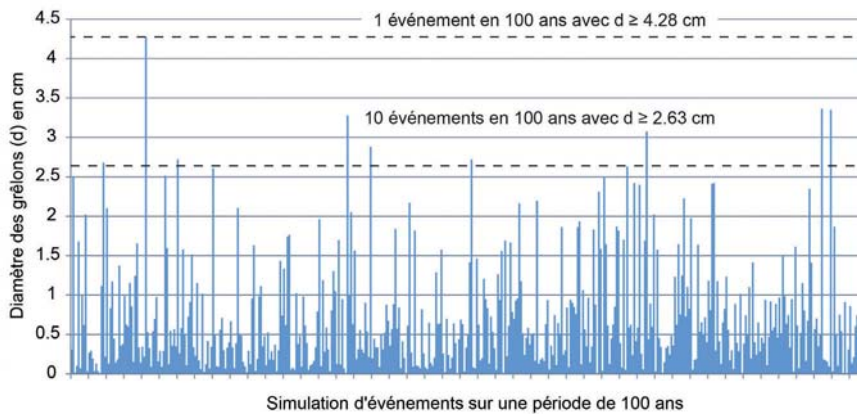
Où $n(d)$ correspond au nombre de grêlons de diamètre supérieur ou égal à d , tandis que d ; n_0 et λ sont des paramètres dépendants de l'événement ou de la région. Cette loi permet également de relativement bien décrire les premières apparitions des catégories de taille de la carte présentée dans ECA (2007). L'ill. 71 montre les différentes fonctions ajustées aux données, ainsi que les points des zones du plateau central (PC), du plateau est (PE) et du jura est (JE) dont Argovie fait partie. Punge et al. (2014) utilisent également une relation dérivée de la distribution exponentielle citée (avec $n_0 = \lambda$), pour ajuster la fréquence relative des tailles de grêlons entre différents événements.



III. 70 : zones de danger définies par l'étude de l'ECA (2007), pour lesquelles des relations fréquence-taille de grêlons ont été définies (ill. 71). Les couleurs de la carte correspondent aux couleurs des courbes de l'ill. 71. Les zones de danger ont été prolongées au-delà des frontières de la Suisse pour les besoins de la modélisation.



III. 71 : fonctions exponentielles ajustées sur les périodes de récurrence des tailles minimales de grêlons selon ECA (2007). Les points correspondent aux données brutes des zones du plateau est et du plateau central (PE et PC), ainsi que du Jura est (JE). L'ill. 70 montre la situation des zones correspondantes.



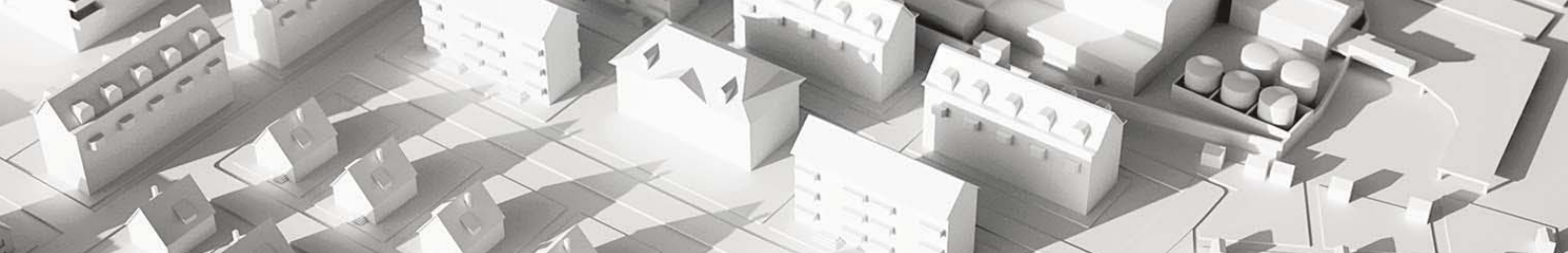
III. 72 : exemple de données générées aléatoirement à partir de la formule ajustée pour le canton d'Argovie et représentant 100 ans de données. À partir de ces données brutes, sans ajuster de loi de distribution, le scénario pris en compte pour la période de récurrence de 100 ans donnerait des grêlons de 4,28 cm, puisque cette taille est atteinte une fois. La taille de 2,63 cm serait atteinte ou dépassée dans un scénario de 10 ans. Si les scénarios 10 ans et 100 ans sont utilisés pour calculer le risque total, alors la fréquence $f'_{10} = 0.09$ (soit $0.1 - 0.01$) doit être utilisée pour le scénario de 10 ans. On évite ainsi que l'événement avec des grêlons de 4,28 cm soit pris en compte 2 fois. En effet, la fréquence à laquelle les grêlons ont une taille comprise entre 2,63 cm (inclus) et 4,28 cm (non inclus) vaut $9/100$, soit 0,09.

Si l'on considère la fréquence d'un événement i défini par une taille de grêlons minimum, la fréquence d'un événement plus rare « $i+1$ » est comprise dans le scénario « i ». En effet, si le scénario 30 ans est défini par la taille de grêlons atteinte ou dépassée en moyenne un fois tous les 30 ans, un événement dont la taille des grêlons est atteinte ou dépassée en moyenne une fois tous les 100 ans est déjà pris en compte pour le scénario 30 ans. Ainsi, la fréquence utilisée pour pouvoir additionner plusieurs scénarios est la suivante :

$$f'_i = f_i - f_{i+1}$$

f_i étant la fréquence du scénario i indépendamment des autres scénarios considérés et f_{i+1} étant la fréquence du scénario immédiatement supérieur. f'_i est ainsi la fréquence des grêlons compris entre les tailles définies pour les scénarios i et $i+1$.

C'est également sur cet ajustement que se base le fameux outil d'analyse «EconoMe» pour déterminer le risque lié aux dangers naturels (Bründl et al. 2011). L'ill 72 en offre une illustration à l'aide d'une série de données générées aléatoirement.

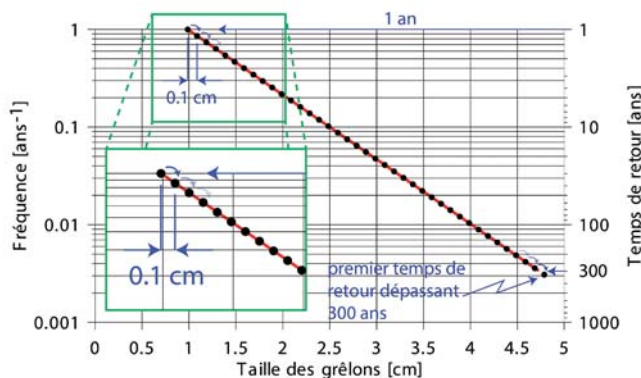


7.2 Calcul du risque annuel moyen

Afin d'estimer les risques pour les périodes de récurrence définies préalablement au moyen des données de dommages disponibles, un modèle simple a été développé dans le logiciel « Matlab® ». Pour chaque carte de taille de grêlons disponible, le dommage prévisible est calculé au moyen de la fonction logistique en générant, bâtiment par bâtiment, une variable aléatoire qui sert à définir si le bâtiment est sinistré ou non. Un taux de dommages est ensuite attribué à chaque bâtiment endommagé au moyen d'une autre variable aléatoire selon l'ill. 68: Ce taux de dommages est alors multiplié par la valeur d'assurance afin d'obtenir le montant des dommages en CHF. Les montants des dommages de tous les bâtiments sont ensuite additionnés. Le processus est répété une vingtaine de fois afin d'établir un montant total moyen des dommages. Cette moyenne est ensuite multipliée par la fréquence correspondante afin d'obtenir le risque en CHF/an.

Cette approche a été appliquée à l'aide des deux fonctions logistiques ajustées sur les données de l'événement de 2011 au moyen des cartes de danger de grêle (ECA 2007), puis avec des cartes de danger générées à partir de la fonction exponentielle. Ces dernières sont générées de la manière suivante (voir également l'ill. 73):

1. L'utilisateur indique les périodes de récurrence minimale et maximale, tout comme la « résolution » (ou pas d'augmentation), c'est-à-dire la différence de taille de grêlons entre 2 étapes de calcul.
2. La taille des grêlons est calculée pour la plus petite période de récurrence, puis cette taille est augmentée de la valeur correspondant au pas de résolution défini par l'utilisateur. La période de récurrence correspondant à la taille de grêlons est ensuite calculée. Si les bâtiments sont situés sur des zones avec différentes fonctions exponentielles, le modèle s'adapte de manière à ce que la différence moyenne de taille corresponde à la valeur définie par l'utilisateur. Le montant des dommages est cal-



Ill. 73: dans cet exemple de calcul de la période de récurrence, l'utilisateur a défini une période de récurrence minimale de 1 an, une période de récurrence maximale de 300 ans et un pas d'augmentation de 0,1 cm. La taille des grêlons correspondant à une période de récurrence de 1 an est tout d'abord calculée, puis, pour la deuxième étape de calcul, la taille est augmentée de 0,1 cm et la période de récurrence est déduite de la fonction exponentielle. Cette procédure est répétée jusqu'à ce qu'une période de récurrence atteigne ou dépasse la valeur maximale (300 ans). A chaque pas, le risque est calculé.

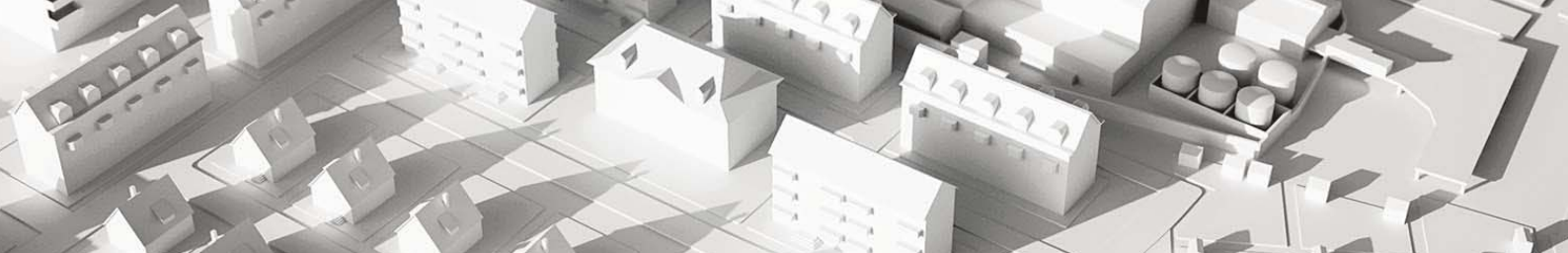
culé par chaque étape de calcul, en admettant que tout le canton est touché en même temps par la taille de grêlons définie.

3. Le calcul s'arrête lorsque la période de récurrence maximale définie est atteinte ou dépassée.

Le risque a été calculé au moyen des fonctions exponentielles pour 3 différents intervalles de périodes de récurrence, à savoir 1 à 300 ans, soit la plage couverte par les cartes de danger de grêle de l'ECA (2007), 0,1 à 300 ans et 1 à 1000 ans, cela dans le but d'analyser l'influence sur le calcul du risque des périodes de récurrence très petites et des périodes très longues. Les résultats sont présentés dans le tab. 3:

Danger	Modèle de dommages	Intervalles des périodes de récurrence		
		0.1–300 ans	1–300 ans	1–1000 ans
Cartes	AG (k = 0.2044)		15.2 mio CHF/an	
Cartes	AG (k = 1)		17.4 mio CHF/an	
Fonction exponentielle	AG (k = 0.2044)	27.3 mio CHF/an	27.1 mio CHF/an	27.2 mio CHF/an
Fonction exponentielle	AG (k = 1)	35.5 mio CHF/an	34.1 mio CHF/an	35.8 mio CHF/an

Tab. 3: Le pas de la taille de grêlons pour les analyses faites à partir des fonctions exponentielles est de 0,1 cm. Les risques calculés concernent exclusivement les bâtiments géoréférencés, qui représentent 88,6% du nombre total des bâtiments assurés par l'ECA (les autres bâtiments ne font pas partie des bases de calcul).



L'utilisation des fonctions exponentielles donne des résultats largement supérieurs à ceux issus du calcul reposant sur les cartes de danger de l'ECA (2007). Cela s'explique par le pas d'augmentation appliqué dans le calcul. En effet, si celui-ci est fixé à 1 cm en faisant l'analyse avec la fonction exponentielle, le risque est calculé pour des périodes de récurrence de 1, 5, 21 et 439 ans et le résultat obtenu pour le canton d'Argovie est également de 15,2 millions de CHF/an. À l'opposé, si le pas est fixé à 0,01 cm, le résultat sera plus élevé (28,8 millions CHF/an), mais la différence sera comparativement faible. Cela est dû au fait que la manière de calculer implique que la taille des grêlons (et ainsi le taux de dommages) reste la même jusqu'à la valeur immédiatement supérieure. Plus le pas de calcul est fin, plus les résultats seront mathématiquement corrects.

Lorsque la fonction logistique bornée à 1 est utilisée, les montants de dommages sont plus élevés pour une taille de grêlons supérieure à 3,5 cm environ (correspondant à une période de récurrence d'environ 90 ans), car le nombre de bâtiments sinistrés augmente fortement dans ce cas. L'augmentation relative du risque entre l'intervalle 1–300 et l'intervalle 0,1–300 ans est également plus élevée lorsque cette fonction est utilisée. Cela est dû à une ordonnée à l'origine légèrement supérieure pour cette courbe qui provoque des proportions de bâtiments sinistrés légèrement plus élevées dans les catégories inférieures de tailles de grêlons (la différence entre les deux fonctions logistiques pour les petites tailles de grêlons n'est toutefois pas visible sur le graphique). Même si cette différence est relativement peu significative, elle illustre l'importance de limiter les courbes d'ajustement pour que les courbes soient réalistes.

7.3 Évolution future du risque

La question de l'évolution future du risque lié à la grêle est certes délicate, mais des scénarios simples peuvent tout de même être établis. Si l'on considère que la fréquence des événements de grêle ne change pas dans le futur, toute évolution du risque grêle sera alors uniquement conditionnée par les modifications dans le bâti. Selon les projections de l'office fédéral de la statistique (OFS, 2014a), la population devrait augmenter entre 2010 et 2035 dans le canton d'Argovie, pour passer de 608'000 à 725'000 habitants. Plus ou moins sur la même période, le nombre de personnes par ménage devrait passer de 2,17 en 2010, à 2,02 en 2030 (OFS 2014b). En considérant que ce chiffre de 2,02 personnes par ménage est également valide pour 2035, le nombre de ménages passerait d'environ 280'000 à 360'000 environ.

Si l'on observe le nombre de bâtiments assurés (et géoréférencés) en 2011, il est possible de constater qu'il y a actuellement 3,13 personnes par bâtiment assuré.

Si l'on tient compte de l'augmentation de la population et de la diminution du nombre de personnes par ménage, le nombre de bâtiments augmenterait ainsi de 55'000 environ d'ici 2035.

La localisation des bâtiments au sein du canton n'est pas essentielle, dans la mesure où le danger est relativement semblable en tous points du territoire (voir ill. 70). Si nous envisageons que les bâtiments ont la même fonction de dommage que les bâtiments existants, le risque augmenterait de 7,7 millions de francs par an. Cette augmentation signifie, pour les habitants d'Argovie, que le risque par personne passerait de 45 CHF par an aujourd'hui à 48 CHF en 2035 (en francs actuels).

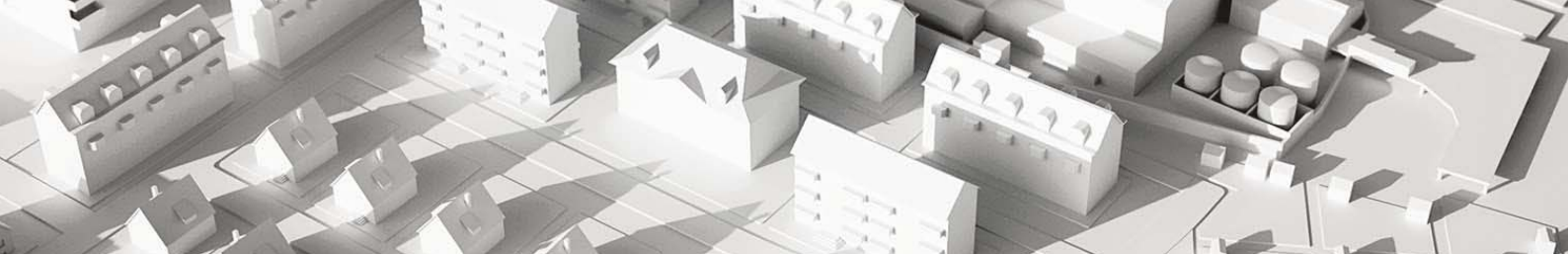
Si l'ECA d'Argovie parvenait par contre à imposer comme standard le degré de résistance RG3 recommandé par l'AEAI et si l'on pose l'hypothèse simpliste que les dommages sont inexistantes en dessous de 3 cm et identiques à maintenant au-dessus de 3 cm, le risque total augmenterait seulement de 4,1 millions de francs par an. Le risque par habitant et par an passerait ainsi de 45 à 43 francs.

7.4 Simulation

La démarche présentée ci-dessus permet de se faire une idée du risque moyen, mais ne permet pas de savoir quel montant de dommages attendre d'un événement de grêle, dans la mesure où il n'est pas probable qu'une taille donnée de grêlons tombe uniformément sur l'ensemble du canton lors du même événement. Afin d'avoir une idée de la distribution des dommages des événements de grêle, un simulateur est actuellement en cours de développement. Ce simulateur est constitué de deux modules. Dans le premier module, des fonctions gaussiennes en deux dimensions sont ajustées sur l'image radar fournie par meteoradar gmbh, tandis que de nouveaux événements (artificiels) sont créés dans le second module à partir des paramètres issus du premier module.

Ajustement des paramètres

Afin de pouvoir ajuster des fonctions gaussiennes sur l'image radar, leur contenu doit d'abord être converti dans les différentes catégories de tailles de grêlons. L'image est ensuite lissée. Les valeurs maximum locales servent à définir la position ainsi que le nombre de fonctions gaussiennes requises. Ainsi, plus l'image radar est lissée, plus le nombre de maximums locaux est faible et plus le nombre de fonctions gaussiennes nécessaires diminue. Les fonctions gaussiennes sont définies par 6 paramètres, à savoir les coordonnées X et Y de leur centre, l'orientation, l'écart-type de l'axe transversal, l'excentricité (rapport entre l'écart-type de l'axe transversal et de l'axe longitudinal), ainsi que l'intensité. Chacun de ces paramètres peut avoir n'importe quelle valeur entre des limites définies par l'utilisateur, de manière à



ce que l'erreur quadratique moyenne (RMSE) entre les pixels de l'image radar et les pixels de l'image produite par les gaussiennes soit la plus petite possible.

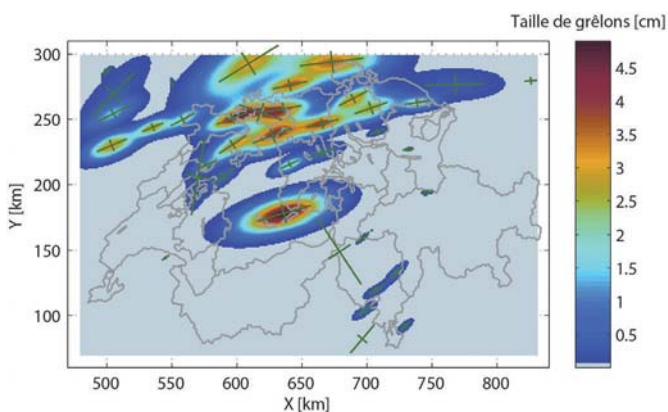
Il s'agit, en outre, de trouver un compromis idéal entre une possibilité d'erreur la plus faible possible et une solution simple à modéliser. En effet, utiliser un grand nombre de fonctions gaussiennes aboutira à une bonne solution, mais dont les paramètres seront compliqués à appliquer dans la phase de modélisation, puisque la carte finale sera le produit d'une superposition complexe entre les fonctions gau-

siennes. L'ill. 74 présente l'exemple d'un bon compromis. Un exemple de paramètres déduits des courbes d'ajustement, en l'occurrence la taille de grêlons, est présenté dans l'ill. 75.

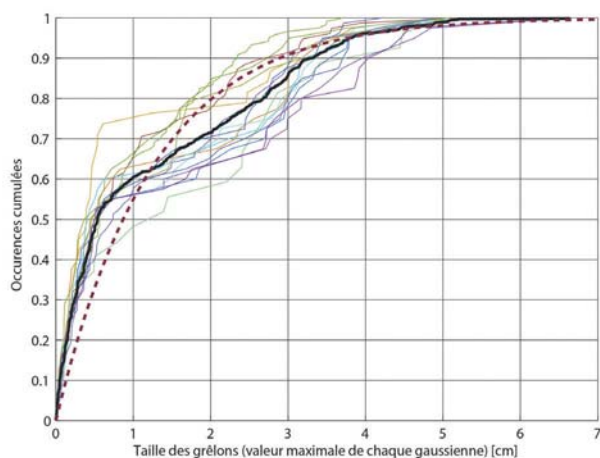
Simulation d'événements synthétiques

La simulation des événements synthétiques a lieu de la manière suivante (voir aussi ill. 76).

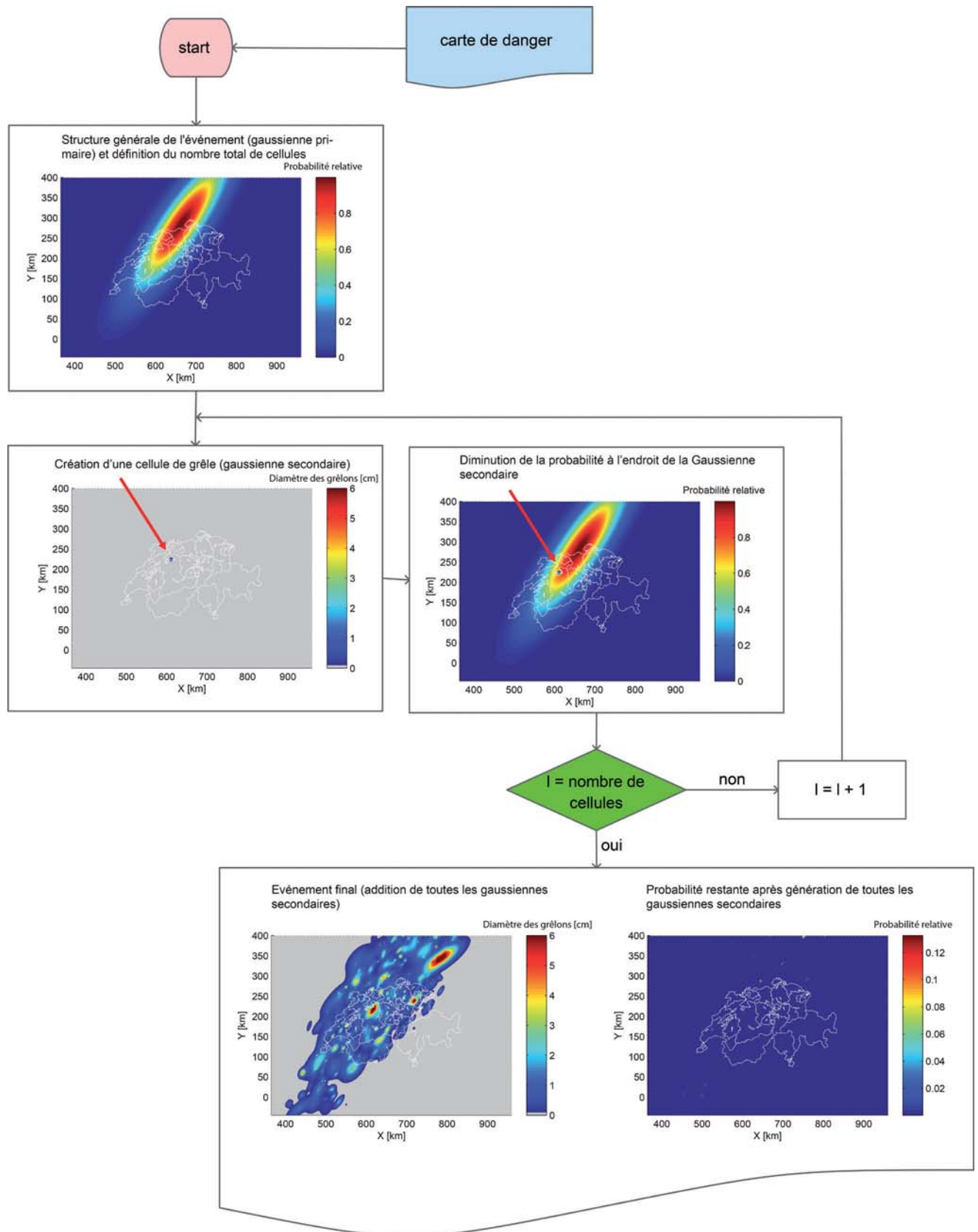
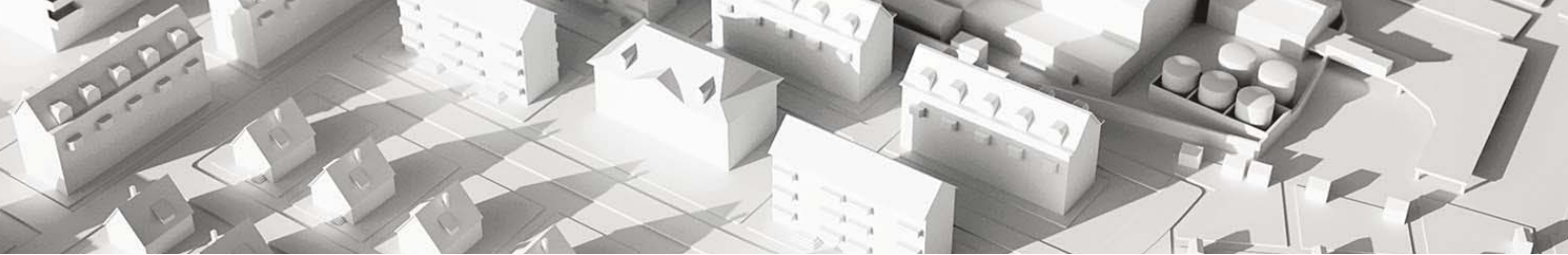
1. Une fonction gaussienne en 2 dimensions est définie et représente la structure générale de l'événement (ci-après «gaussienne de type primaire»). Ses différents paramètres sont définis au moyen des fréquences relatives de la carte de danger (position) et avec des distributions prédéfinies (orientation et excentricité). La valeur maximale est toujours de 1 (échelle relative) et le volume de la fonction gaussienne est utilisé pour définir le nombre d'orages de grêle.
2. Une première cellule de grêle est créée aussi à l'aide d'une fonction gaussienne (ci-après «gaussienne de type secondaire»). La fonction qui représente l'événement dans son ensemble (gaussienne de type primaire) sert de carte de probabilité pour la position de la cellule de grêle, tandis que l'orientation globale de l'événement sert de valeur escomptée pour la variable aléatoire «orientation de la cellule de grêle». L'excentricité de la cellule est définie avec une fonction aléatoire, à savoir l'écart-type de son axe transversal selon une fonction exponentielle dans les limites de 500 m et 10 km.
3. Une fois que la cellule de grêle est créée au moyen de la gaussienne de type secondaire, elle est soustraite à la gaussienne de type primaire qui forme l'événement dans son ensemble, de manière à ce que les cellules de grêle suivantes ne soit pas positionnées trop proches des cellules existantes.
4. Les étapes 2 et 3 sont répétées jusqu'à ce que le nombre de cellules de grêle défini au départ soit atteint, ou jusqu'à ce que ce qu'il ne reste plus assez d'espace pour créer de nouvelles cellules.
5. Une fois l'événement reproduit artificiellement, les éventuels dommages sont calculés et stockés afin d'être disponibles pour de futures analyses. Les catégories de tailles de grêlons calculées en différents endroits du territoire sont également conservées pour valider les résultats.



III. 74 : résultat de l'ajustement de 40 fonctions gaussiennes. Les axes principaux sont présentés à l'aide de traits verts. Ils s'étendent de moins un écart-type à plus un écart-type. Les limites fixées pour l'ajustement sont : déplacement en X et en Y de plus ou moins 10 km, par rapport à la solution initiale, une intensité comprise entre 1/10 et 2 fois la valeur initiale issue de l'image radar lissée, une orientation quelconque, un écart-type de l'axe transversal compris entre 500 m et 10 km ainsi qu'une excentricité comprise entre 1 et 3. Pour plus de clarté, la classe des plus petites intensités est présentée en gris.



III. 75 : occurrences cumulées des tailles de grêlons selon le procédé des fonctions gaussiennes issues de différents ajustements du même événement. La courbe noire correspond au total de différentes courbes, tandis que la courbe rouge en traitillés est une fonction exponentielle ajustée sur la courbe noire. Le paramètre μ de cette fonction (1,25) est utilisé pour les simulations.



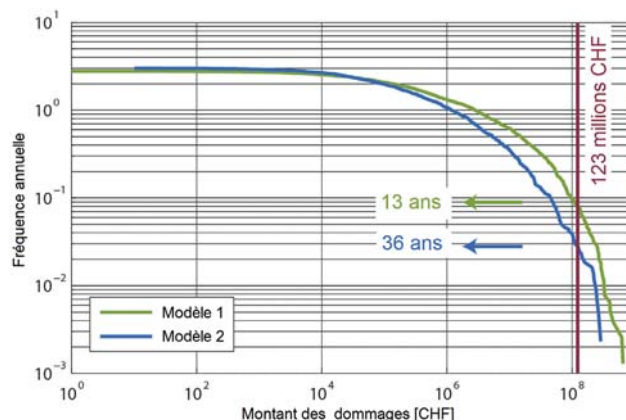
III. 76: flow-chart pour la création artificielle d'un événement de grêle.

8. Conclusions, résultats, perspectives

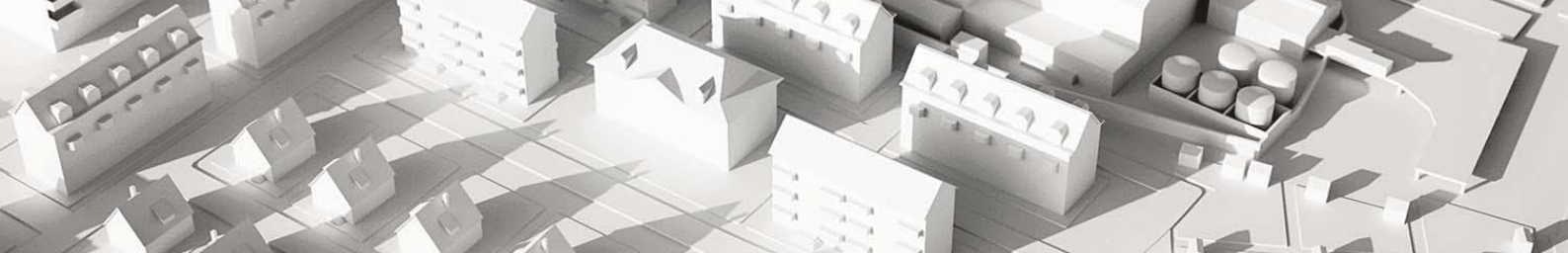
Lorsqu'un grand nombre d'événements artificiels a été créé, une fonction exponentielle est ajustée dans chaque cellule de la grille, de manière à contrôler si les événements générés suivent une courbe similaire à celle obtenue à partir des cartes de danger (ECA 2007), en particulier le paramètre α qui définit la pente de la fonction et indique ainsi si les proportions entre les différentes fréquences de tailles de grêlons sont cohérentes avec celles représentées sur les cartes de danger de grêle (ECA 2007). Le paramètre n_0 doit par contre être mis à l'échelle, de manière à définir quelle fréquence est décrite par les différentes modélisations, soit combien de ces simulations représentent une année dans la réalité. Une fois la mise à l'échelle réalisée, le risque peut être calculé.

Les résultats de deux modèles différents sont présentés ci-dessous. Dans le premier, l'intensité maximale de chaque cellule suit la distribution présentée dans l'ill. 77, tandis que dans le deuxième modèle, la moyenne de cette distribution est ajustée à chaque simulation de manière à ce que les intensités maximales d'un événement de petite ampleur soient en moyenne plus basses que celles d'un événement plus conséquent. Le premier modèle permet d'obtenir un risque moyen légèrement supérieur à celui calculé au point 7.2 (40,8 millions de CHF/an au lieu d'environ 30 millions de CHF/an), mais la pente des exponentielles est par contre trop faible. À l'inverse, le second modèle permet de mieux reproduire la pente des fonctions exponentielles, mais le risque est plus bas que celui attendu (18,1 millions de CHF/an au lieu d'environ 30 millions de CHF/an).

Ces deux modèles permettent de donner une idée de la période de récurrence d'événements d'ampleur semblable à celui de 2011 en termes de dommages. Dans le premier modèle, la période de récurrence serait d'environ 13 ans, ce qui est évidemment à considérer comme la limite inférieure pour un événement de ce type. Dans le deuxième modèle, la période de récurrence serait de 36 ans. Ces simulations sont très sensibles aux paramètres d'entrée. Par conséquent, d'autres tests sont encore nécessaires pour affiner les résultats et les faire correspondre le plus possible aux différents paramètres attendus, tels que le risque moyen ou la pente de la relation « Marshall-Palmer » ajustée sur les tailles de grêlons escomptées en chaque point du canton. Il est tout à fait possible que dans les deux cas, la répartition des coûts, et donc aussi la pente et la forme des courbes, soit fautive. L'incertitude porte en particulier sur les petits événements fréquents, puisqu'aucune image radar d'un événement de ce type n'est disponible.



III. 77 : dans le premier modèle (vert), le montant des dommages de l'événement de 2011 est atteint environ tous les 13 ans et des dommages de 2,8 millions ou plus sont à attendre en moyenne une fois par année. Dans le deuxième modèle (bleu), la période de récurrence de l'événement est d'environ 36 ans. 560'000 simulations ont été effectuées pour le modèle 1 (dont 2'153 provoquant des dommages dans le canton d'Argovie) et 360'000 pour le modèle 2 (dont 1'299 provoquant des dommages dans le canton d'Argovie).



8. Conclusions, résultats, perspectives

Outre des propositions d'amélioration pour des analyses futures, le prochain objectif à long terme a aussi été formulé dans les conclusions du rapport «Analyse des événements Grêle 2009»: «... une estimation aussi rapide et, même si elle repose sur des informations incomplètes, aussi fiable que possible des dommages causés par un futur événement de grêle». Avec le modèle de grêle présenté, nous nous sommes nettement rapprochés de cet objectif. Le nouveau modèle est fonctionnel. Il manque encore principalement une vaste base de données pouvant servir à la calibration afin d'affiner les paramètres. Le modèle réagit en effet à ces derniers de manière relativement sensible, tout comme les abondants essais sur des événements de différentes intensités.

La représentativité des échantillons analysés de données concernant les dommages a également été abordée dans l'étude précédente. Le fait que l'analyse dans la nouvelle étude porte directement sur l'ensemble des données au lieu d'un échantillon permet de résoudre le problème de la représentativité pour l'événement analysé. Cela ne vaut pas bien sûr pour la représentativité des connaissances acquises en ce qui concerne le transfert sur d'autres événements de grêle. La très bonne concordance partielle avec les données des averses de grêle de mai et juillet 2009 (en particulier la proportion des catégories de bâtiments touchés par rapport à l'ensemble des bâtiments existants, le taux de dommages par catégorie de bâtiment ainsi que l'interdépendance de la proportion des bâtiments touchés par année de construction) laisse toutefois supposer que de nombreux résultats peuvent également être transférés sur d'autres événements de grêle ou sur d'autres cantons.

L'étude «Grêle 2009» voit en particulier ses résultats suivants confirmés par la présente analyse :

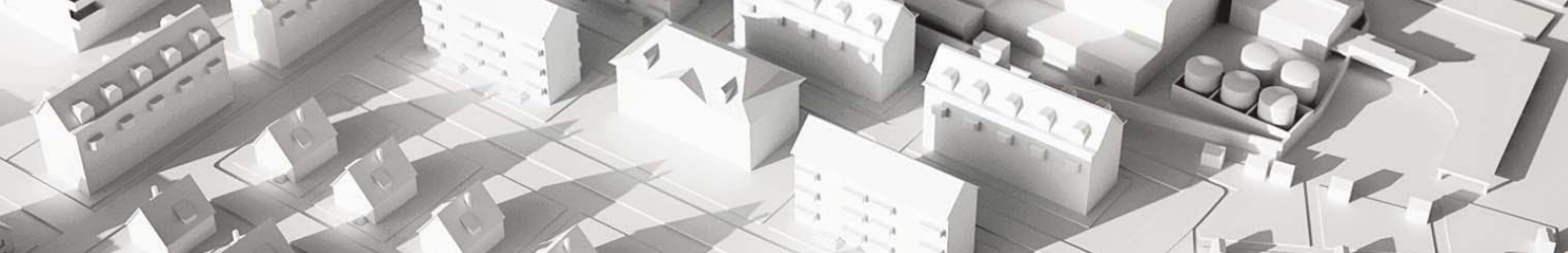
- Plus de la moitié du montant des dommages des événements de grêle résulte des dommages causés aux stores, au toit et aux parois / façades.
- Les maisons d'habitation sont en moyenne clairement plus sensibles à la grêle que les autres types de bâtiments.
- Les maisons d'habitation récentes sont en moyenne nettement plus sensibles à la grêle que les plus anciennes.
- Les maisons d'habitation récentes sont non seulement nettement plus souvent concernées par des dommages de grêle que les anciennes mais elles sont aussi plus fortement endommagées (taux de dommages plus élevé).
- L'utilisation d'éléments de construction avec une résistance à la grêle RG 3 au moins peuvent permettre de réduire efficacement les dommages dus à la grêle et de réaliser des économies substantielles. En raison des modes de construction non adaptés au danger de grêle,

la solidarité entre les personnes qui paient les primes s'épuise car les primes sont revues à la hausse pour tous les clients.

- Les efforts des ECA en termes de prévention devraient porter principalement sur les maisons d'habitation car celles-ci sont nombreuses et présentent une sensibilité marquée à la grêle.

Par rapport à l'étude sur l'orage de grêle de 2009, la nouvelle étude a toutefois aussi permis d'obtenir de nouvelles informations :

- L'événement de grêle des 12 et 13 juillet 2011 fut certes le plus important événement de dommages éléments naturels jamais répertorié pour l'établissement d'assurance d'Argovie (soit depuis 1941), mais la période de récurrence statistique d'un tel événement devrait plutôt être de 50 ans que de 100 ans. C'est ce qu'indiquent également les calculs modélisés de l'université de Lausanne.
- Si la cellule de grêle avait suivi une trajectoire légèrement plus au nord, les dommages auraient été encore plus élevés, mais les plus grandes agglomérations du canton n'ont été en réalité que «frôlées». Même sans l'augmentation de l'intensité de la grêle due au changement climatique, on peut s'attendre à constater des événements encore plus dommageables.
- Le fait que l'orage de grêle ait eu lieu la nuit n'a pas eu de répercussion sur le nombre de cas de sinistres, mais sur le montant des dommages des stores touchés. C'est la raison pour laquelle il s'avère judicieux, notamment pour les orages survenant la nuit, d'avoir recours à un système automatique reposant sur des prévisions à court terme pour faire remonter les stores pendant des événements de grêle. Ce genre de solution devrait également être avantageux d'un point de vue économique.
- Une utilisation systématique d'éléments de construction avec une résistance à la grêle RG 3 au moins permettrait de réduire encore davantage le risque grêle par rapport à aujourd'hui, même dans l'hypothèse où le taux de croissance actuel du bâti argovien se maintient d'ici à 2035.
- En ce qui concerne la fréquence ou le taux des dommages, il existe un lien statistique entre l'orientation des bâtiments d'habitation et la trajectoire des cellules de grêle.
- Les bâtiments les plus fréquemment et les plus gravement endommagés n'étaient pas les bâtiments (avec toit en pente) implantés à angle droit par rapport à la trajectoire de la cellule de grêle, mais bien plus ceux dont l'axe longitudinal était orienté de 40 à 70°, une plus vaste surface de bâtiment étant ainsi exposée aux impacts de grêle (entraînée par le vent).
- Selon l'orientation des bâtiments, les dommages peuvent donc être plus ou moins importants. C'est justement pour les orientations défavorables qu'il peut être payant d'utiliser des éléments de construction plus résistants à la grêle, surtout sur la face «exposée aux intempéries» du



bâtiment, car les cellules de grêle suivent souvent des « itinéraires fixes ».

- Grâce aux données radar, il est possible avec un modèle adapté, comme celui décrit dans le présent rapport, d'établir rapidement après un événement une estimation approximative de l'étendue et de l'ordre de grandeur des dommages survenus. Le choix judicieux des paramètres est ici déterminant.
- Contrairement aux attentes, la méthode d'analyse de l'événement 2009 n'a pas pu être reprise pour l'événement de juillet 2011. Il a fallu choisir un autre procédé.

Dans le premier cas, les décisions rendues par l'ECA de Thurgovie envers ses clients ont été analysées depuis des fichiers Excel séparés, ce qui a nécessité le développement d'un outil de sélection de données adapté. Dans le canton d'Argovie en revanche, les informations nécessaires se trouvaient dans une base de données, ce qui simplifiait l'analyse. Les entrées correspondantes étaient rédigées par contre de manière plus concise, de telle sorte que le matériau notamment des éléments de construction endommagés n'était pas souvent évident, ce qui empêchait de mener une analyse statistique pertinente.

Il reste toutefois des questions sans réponse. Comment établir une statistique sur la vulnérabilité des éléments de construction face à la grêle ? Il s'agit là d'un problème qui n'a toujours pas trouvé de solution. Pour cela, les chiffres des éléments de construction non endommagés seraient aussi nécessaires, en plus des chiffres des éléments de construction endommagés. Ces données ne sont malheureusement pas facilement accessibles car elles nécessiteraient des relevés coûteux.

Le manque d'informations rend également impossible l'analyse statistique de l'incidence de l'usure de certains éléments de construction sur leur degré de résistance à la grêle (en particulier des matières synthétiques). Des essais systématiques en laboratoire sont ici de toute façon plus appropriés pour obtenir des résultats pertinents.

La fiabilité des données radar pour estimer rapidement les dommages aux bâtiments dus à la grêle dépend en grande partie de l'exactitude du rapport établi entre la puissance de l'écho radar et l'intensité de la grêle qui en est déduite.

Il existe aujourd'hui des systèmes de mesure offrant une saisie permanente de l'intensité de la grêle mais la Suisse ne dispose toutefois actuellement d'aucun réseau de mesure pour une saisie globale en continu. C'est pourquoi le calibrage s'effectue le plus simplement possible, au moyen des grêlons retrouvés. La société meteoradar GmbH invite la population à indiquer sur son site Internet (www.meteoradar.ch) la taille des grêlons ainsi que le lieu et l'heure où ils ont été observés.

La pertinence du modèle de grêle présenté dans ce rapport est étroitement dépendante de la qualité des données issues de la carte des dangers et notamment par les fonctions exponentielles sous-jacentes à celle-ci. Cette pertinence du modèle repose ainsi sur des données radar de 1992 à 2004 ainsi que sur une série chronologique des situations météorologiques selon Hess / Brezowsky de 1881 à 2001 (Schiesser, 2006 ; ECA, 2007). Les grands événements de grêle des années passées (2005, 2009, 2011, 2013) ne sont ainsi pas pris en considération. En raison de la série chronologique relativement courte de données radar, la Suisse a été partagée en onze zones de danger, la résolution spatiale de la carte des dangers étant inévitablement limitée. C'est la raison pour laquelle, on prévoit de réimprimer prochainement la carte en tenant compte des données des dix dernières années. Cette nouvelle version doit reproduire plus en détail la situation actuelle des dangers et donner une nouvelle base à la prévention de mesures de prévention.



9. Remerciements

9. Remerciements

L'UIR et l'ISTE remercient sincèrement l'établissement d'assurance d'Argovie pour leur agréable collaboration et les nombreuses informations.

Nos remerciements s'adressent tout particulièrement à :

- Monsieur Armin Wittmer de l'établissement d'assurance d'Argovie pour les nombreux renseignements et conseils sur les données concernant les dommages de l'événement des 12 et 13 juillet 2011.
- Monsieur Matthieu Weber de l'établissement d'assurance d'Argovie pour la mise à disposition des nombreuses images et photos.

10. Bibliographie

10. Bibliographie

AZ (2012): Gebäudeversicherung zieht Lehren aus dem Hagel-GAU. Journal Aargauer Zeitung du 3 août 2012. (<http://www.aargauerzeitung.ch/aargau/kanton-aargau/gebaeudeversicherung-zieht-lehren-aus-dem-hagel-gau-124955840>; dernière consultation le 6 nov. 2014)

OFS (2014a): Évolution future de la population - Données, indicateurs - Scénarios cantonaux (http://www.bfs.admin.ch/bfs/portal/fr/index/themen/01/03/blank/key_kant/01.html; dernière consultation le 12 sept. 2014).

OFS (2014b): Évolution future de la population - Données, indicateurs - Scénarios des ménages (http://www.bfs.admin.ch/bfs/portal/fr/index/themen/01/03/blank/key_hhsz.html; dernière consultation le 12 sept. 2014).

OFS (2014c): Atlas statistique de la Suisse (http://www.atlas.bfs.admin.ch/maps/13/map/mapIdOnly/0_de.html; dernière consultation le 25 sept. 2014).

Brandenberger, U. (2011) Weiach – Aus der Geschichte eines Unterländer Dorfes. 4. Überarbeitete Auflage von Zollinger, W. (1972): «Weiach. 1271–1971. Aus der Vergangenheit des Dorfes Weiach». Édition en ligne (<http://weiachergeschichten.ch/wp-content/uploads/2011/06/GeschWeiach-Ausg2011-06.pdf>). 80 p. ; dernière consultation le 17 nov. 2014).

Bründl, M., Krummenacher, B., Rheinberger, C. & Winkler, C. (2011): Formeln zur Berechnung des Risikos bei Naturgefahren. (http://www.econome.admin.ch/doc/Formeln_Risiko_111221_D.pdf; dernière consultation le 17 nov. 2014).

Choffet, M., Imhof, M., Caspard, O. & Jaboyedoff, M. (2011): Analyse des événements de grêle de 2009 – Étude pilote dans le canton de Thurgovie. Institut de Géomatique et d'Analyse du Risque, Université de Lausanne, n° rapp IGAR-Grêle-R001. 47 p.

Crenshaw, V. & Koontz, J. D. (2001): Simulated hail damage and impact resistance test procedures for roofing coverings and membranes. Roofing Industry Committee on Weather Issues (RICOWI) meeting Oct. 27, 2000. Dallas, Texas. 10 p.

Cullen, W. C. (1992): Hail damage to roofing: assessment and classification. Proceedings of the 4th International Symposium on Roofing Technology, NRCA/NIST. p. 211–216.

La Poste (2013): GeoPost Coordinates – Haute précision dans les adresses de bâtiments. La Poste (<http://www.post.ch/post-startseite/post-adress-services-match/post-gis/post-gis-geopost-coordinates>; dernière consultation le 9 oct. 2014). 4 p.

GEA (2013): Dickstes Hagelkorn Deutschlands. Reutlinger Generalanzeiger du 27 août 2013. (https://www.facebook.com/gea.reutlingen/posts/641601495857987?stream_ref=5 ; dernière consultation le 9 oct. 2014).

Hohl, R., Schiesser, H.-H. & Aller, D. (2002): Hailfall: the relationship between radar-derived hail kinetic energy and hail damage to buildings. Atmospheric Research 63 (2002). p. 177–207.

UIR (Éd. ; 2008): Analyse des événements crues 8 / 9 août 2007. Étude de l'Union intercantonale de réassurance. Berne. 27 p.

UIR (Éd. ; 2012): Analyse des événements Grêle 2009. Étude de l'orage de grêle du 26 mai et du 23 juillet 2009. Étude de l'Union intercantonale de réassurance. Berne. 51 p.

ECA (Éd. ; 2007): Répertoire de la protection contre la grêle - Recherches sur le danger de grêle et la résistance de l'enveloppe des bâtiments. Rapport de synthèse Fondations de prévention des établissements cantonaux d'assurance. Berne. 34 p.

Lanz-Stauffer, H. & Rommel, C. (1936): Elementarschäden und Versicherung. Studie des Rückversicherungsverbandes kantonal-schweizerischer Feuerversicherungsanstalten zur Förderung der Elementarschadenversicherung. II. Tome Berne. 1154 p.

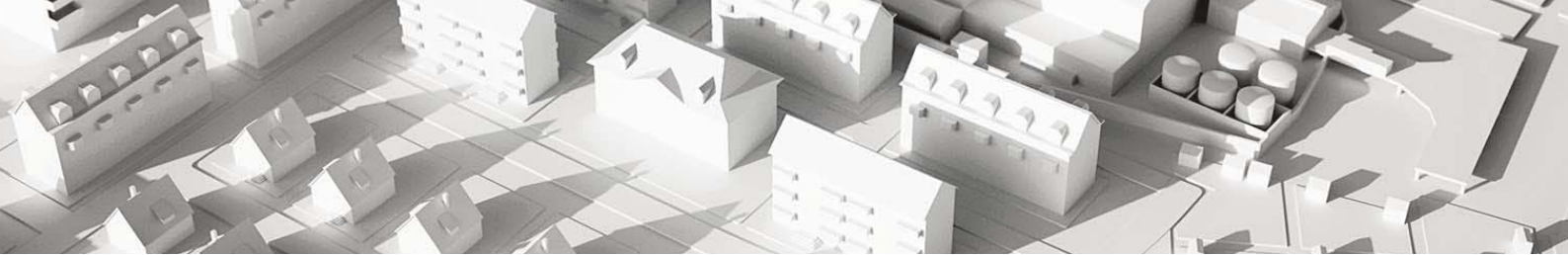
Pruppacher, H. R. & Klett, J. (2010): Microphysics of Clouds and Precipitation. Springer. 976 p.

Punge, H., Bedka, K., Kunz, M. & Werner, A. (2014): A new physically based stochastic event catalog for hail in Europe. Natural Hazards Vol. 73. Springer Dordrecht. p. 1625-1645.

Riniker, H. (1881): Die Hagelschläge und ihre Abhängigkeit von Oberfläche und Bewaldung des Bodens im Kanton Aarau nach Beobachtungen des Forstpersonals und amtlichen Quellen. Springer-Verlag Berlin Heidelberg GmbH. 152 p.

Sauerländer, H. R. (Hrsg.; 1824): Der aufrichtige und wohlverfahrene Schweizer-Bote. n° 32. Aarau. p. 250-251.

Schiesser H.-H. (2006): Hagelstürme in der Schweiz: Wiederkehrperioden von schadenbringenden Hagelkorngrößen – eine Abschätzung. Étude non publiée, élaborée pour la fondation de prévention des Établissements cantonaux d'assurance. Zurich. 23 p.



Sigg, O. (1994): «Inclementia aeris» – Wetter, Teuerung und Armut in den Jahrzehnten um 1600. Tirage spécial de: Vom Luxus des Geistes. Cadeau à l'occasion du 80e anniversaire de Bruno Schmid. Schulthess Polygraphischer Verlag, Zurich. 13 p.

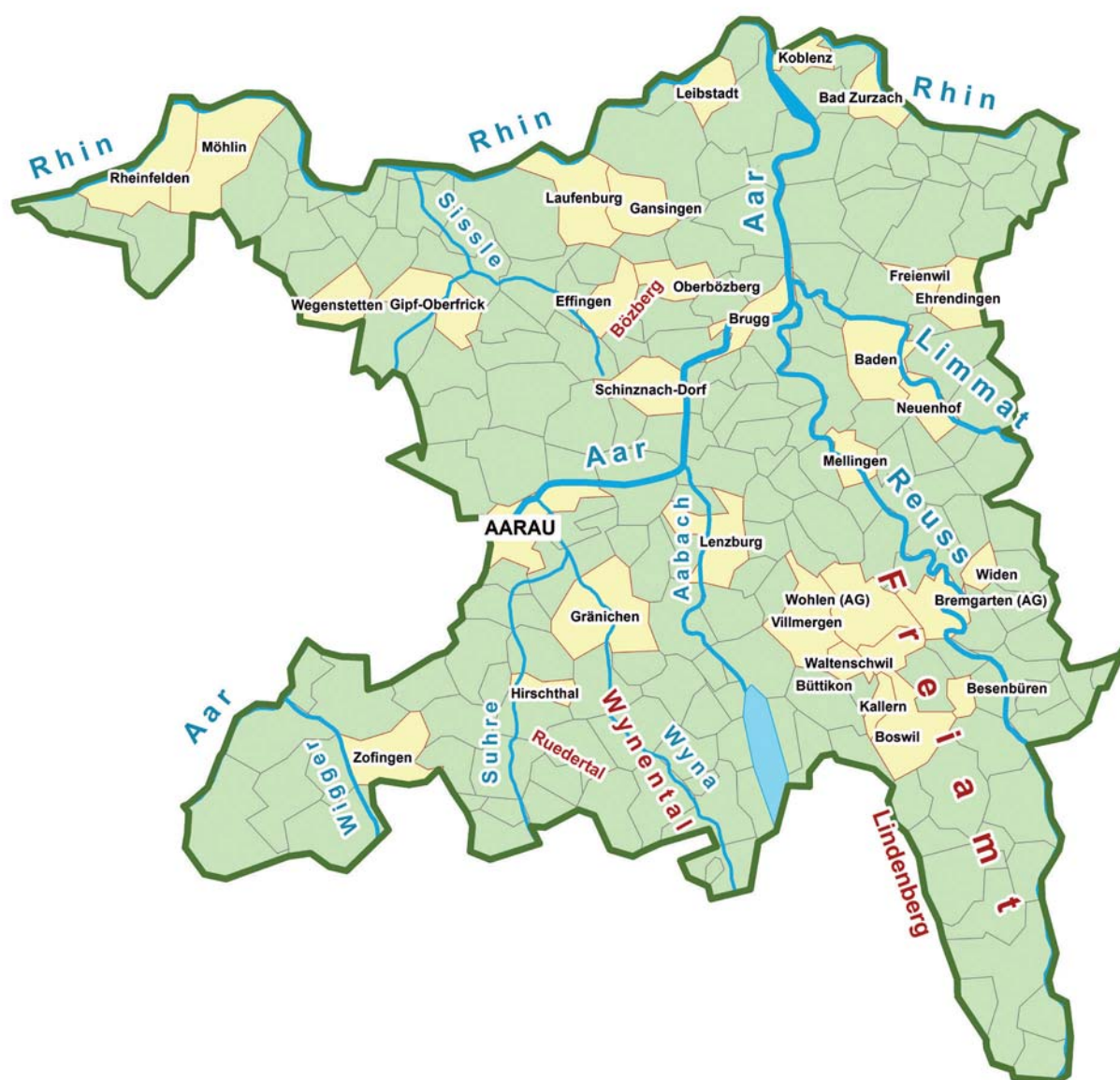
Steigmeier, A. (2004): Feuer, Wind und Wasser. 200 Jahre Gebäudeversicherung im Aargau. Kasimir Meyer AG, Wohlen. 119 p.

Swissolar (2012): L'industrie solaire suisse. Savoir-faire pour le tournant énergétique. Association suisse des professionnels de l'énergie solaire. Zurich: 18 p.

Annexe A: carte d'orientation indiquant l'emplacement des localités mentionnées

Annexe A: Carte d'orientation indiquant l'emplacement des localités mentionnées dans le rapport

Canton d'Argovie
(base cartographique swisstopo)





Annexe B: Code d'affectation AEAI

Annexe B: Code d'affectation AEAI

Bâtiments administratifs et bâtiments publics

10	Bâtiments de l'administration
11	Bâtiments scolaires
12	Bâtiments ecclésiastiques
13 (14)	Hôpitaux, maisons spécialisées dans les soins
16	Bâtiments consacrés à l'art, à la culture et au sport
19 (15)	Autres

Maisons d'habitation

20	Habitation uniquement
29 (21–29)	Affectation mixte

Bâtiments agricoles

30	Bâtiments agricoles habités
39 (31–39)	Autres bâtiments agricoles

Transports

40 (40–49)	
------------	--

Commerce

50 (55)	Magasins et immeubles commerciaux
51	Entrepôts

Industrie et artisanat

60 (61)	Travail de la pierre et de la terre
62	Industrie du bâtiment (sans le bois)
63	Produits alimentaires et de luxe
64 (65,69)	Industrie textile, vêtements, cuir
66	Travail du bois (y compris industrie du bâtiment)
67 (68)	Industrie du papier, arts graphiques
70	Industrie des matières synthétiques
71	Industrie chimique
72 (73)	Industrie métallurgique et mécanique

Hôtellerie

80	Approvisionnement et élimination des déchets
79 (75,77–79)	Autres

Petits bâtiments et dépendances

90	
----	--